Konya Mühendislik Bilimleri Dergisi
Konya Journal of Engineering Sciences

Editorial Board/Yayın Kurulu

İÇİNDEKİLER (CONTENTS)

Araştırma Makalesi (Research Article)

THE EFFECT OF WOOD VENEER TYPE ON THE REDUCTION OF SOUND TRANSMISSION BETWEEN NOISE-PRODUCING INTERIOR SPACES IN BUILDINGS

[1] **Eda Nur ERZURUM SONUÇ** , [2] **Mustafa DERELİ**

[1,2] *Necmettin Erbakan University, Fine Arts and Architecture Faculty, Architecture Department, Konya, TÜRKİYE*
[1] arceda.eda@gmail.com, [2] mustafa.dereli@erbakan.edu.tr

Highlights

- The effect of wood veneer materials on sound transmission between spaces was investigated.
- The sound transmission amounts of different wood species were measured with the help of a special device.
- An evaluation was made by comparing the sound transmission amounts of wood veneer types.

*Corresponding Author: Mustafa Dereli, mustafa.dereli@erbakan.edu.tr

THE EFFECT OF WOOD VENEER TYPE ON THE REDUCTION OF SOUND TRANSMISSION BETWEEN NOISE-PRODUCING INTERIOR SPACES IN BUILDINGS

[1] **Eda Nur ERZURUM SONUÇ** [iD], [2] **Mustafa DERELİ** [iD]

[1,2] *Necmettin Erbakan University, Fine Arts and Architecture Faculty, Architecture Department, Konya, TÜRKİYE*
[1] arceda.eda@gmail.com, [2] mustafa.dereli@erbakan.edu.tr

ABSTRACT: In order to provide auditory comfort indoors, it is necessary to prevent noise generation and transmission. In this respect, coating materials are essential in reducing sound transmission between interior spaces in noise-generating buildings. Wood is one of the most widely used materials for interior walls and floor coverings. Wood cladding materials can reduce noise transmission. However, the wide variety of types of wood cladding material will create differences in its contribution to noise insulation in this sense. In this direction, the study aimed to investigate the noise transmission properties of different types of wood veneer materials. This study measured the sound transmission amounts of different wood veneer materials with a particular device. This apparatus was used to determine the amount of sound transmitted from the inner face of the veneer material to the outer face of the veneer material of the noise source in an isolated environment with other surfaces touching only the inner face of the veneer material. The measurements were made with the help of this box so that the sound transmission data of different types of wood veneer materials with the same environment and noise source were evaluated using the comparative analysis method. For the study, 24 different wood veneer materials were tested. As a result of the research, it was concluded that the wood cladding material effectively reduces the amount of sound transmission and that there is variability in sound transmission performance depending on the wood species.

Keywords: Auditory Comfort, Decibel, Noise, Sound Transmission Measurement, Wood Veneer Material

1. INTRODUCTION

Spaces should provide comfort conditions while meeting the functional needs of the user. Auditory comfort, one of these features, is the condition that the acoustic environment characteristics of the spaces are suitable for the user [1];noise is defined as unwanted sounds that disturb the user [2]. In this respect, attention should be paid to preventing the formation and transmission of noise in space design. Noise can be prevented by measures taken at the source, receiver and environment [2]. The indoor environmental quality of spaces impacts on health, comfort, productivity, perception, mental and physical performances [3, 4]. Acoustic properties also have significant effects on indoor ambient comfort [3]. Acoustic, thermal and lighting conditions are the most influential factors on indoor comfort [5]. In addition, exposure to high noise levels negatively affects focus, productivity, communication and learning skills, psychological, health and general well-being [6-8].

Since covering materials are effective in sound transmission and noise transmission, the intended use of the space should be taken into considered when choosing materials [9]. The shape of the space, acoustic properties of the materials and objects in the space are practical on sound transmission. For example, porous materials such as carpets, drapery and upholstery absorb high frequencies well, while wood panels absorb low frequencies. In concert halls, the use of wood in combination with textiles for flooring, seating, reflective panels and wall coverings provides both aesthetics and optimization of the sound field, reverberation time and brightness [10].

*Corresponding Author: Mustafa DERELİ, mustafa.dereli@erbakan.edu.tr

1.1. Wood as a Cladding Material and Sound Transmission

Wood was one of the first building materials that people used to meet their shelter needs and is still used today. In this respect, with the development of wood, which has been used for a long time, its usage area has also diversified considerably. Wood was one of the first building materials that people used to meet their shelter needs and is still used today. In this respect, with the development of wood, which has been used for a long time, its usage area has also diversified considerably.

Due to the good sound absorbing properties of wood, it is preferred as a coating material. Its fibrous structure, dampens impact sounds and prevents sound transmission and echoing [11].

In wooden materials, sound can both spread and suffocate. In this respect, wood material shows a superior feature compared to other materials [12]. The speed of sound in a structural material varies according to flexibility and density. In wood, the speed of sound also varies according to the grain direction, as the transverse modulus of elasticity is much less than the longitudinal value. In wood, the speed of sound along the grain is about one-fifth to one-third of the longitudinal value [13].

Studies have shown that wood materials provide sound insulation thanks to their ability to absorb sound [14] and their sound absorption values depend on the type of wood used [15, 16] the inner layer structure of the wood material [12], the perforated structure [17], heat treatment [18], and the type of varnish used [19].

1.2. Industrial Wood Species That Can Be Used As Cladding Materials

Industrial wood is obtained by combining wood pieces, boards, timber, chips, and fibers with different techniques and binding agents to strengthen the properties of wood and add homogeneous properties [20]. Industrial wood materials provide various features that solid wood cannot provide and provide ease of use (Figure 1) [21].
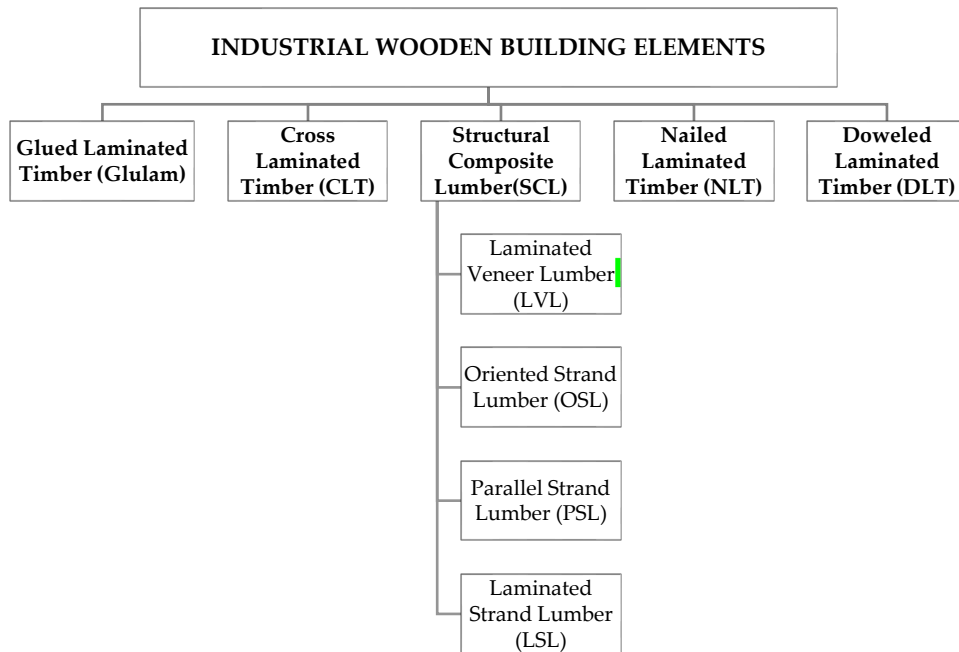
Figure 1. Classification of Industrial Wooden Building Elements [21]

Wood materials used in construction are generally divided into solid wood and composite wood. Solid wood is the state of the tree that has not undergone any treatment other than drying and shaping after cutting. Composites are materials formed by combining two or more materials. Various processes are carried out in these materials to increase the strength and functionality of wood according to environmental conditions. Wood composites are obtained by combining wood-wood or wood with other

materials. The classification of wood composites that differ in terms of their properties is given in Table 1 [22].

Table 1. Classes of wood composite materials

WOOD COMPOSITE CLASSES				
Board Products	**Structural Composites**	**Mechanically Laminated Components**	**Molded Products**	**Wood-Non-Wood Product Composites**
• Plywood • Contrablas • Particleboards [Particleboard, Waferboard, Flakeboard, OSB (Oriented Strand Board) • Fibreboards [MDF (Medium Density Fiber Board), HDF (High-Density Fibre Board), Insulation Board]	• Structural Composite Timbers [Parallel strand lumber (PSL), Laminated Strand Lumber (LSL), Oriented Strand Lumber (OSL), Laminated Veneer Lumber (LVL), Glued Laminated Timber (GLULAM)] • Structural Board Products [Structural Plywood, Structural Flakeboards (Waferboard, OSB)] • Wooden I beams • COM-PLY timbers*	• Elements obtained by joining timbers with nails, screws, etc.	• Products where fibre or particle boards are produced in a form suitable for the place of use	• Composites using in organic materials as binders (Plaster Boards, Magnesium Cement Boards, Portland Cement Boards)

A product obtained by compressing a center section of oriented or randomly positioned chips between at least two veneer boards. It was developed by the USDA Forest Service (Forestry Division of the United States Department of Agriculture) in the 1970s.

The properties of wood composites obtained with inorganic binders differ according to the binder used. Gypsum, magnesium cement and Portland cement are used as binders. The most preferred type is Portland cement composites, which also provide sound insulation. Since it is resistant to moisture, it is used indoors and outdoors. Gypsum binder wood composites, also called dry wall, are generally used in interior wall and ceiling construction and are not resistant to moisture [23].

The so-called thermoplastics are polypropylene, polystyrene, vinyl, low-high density polyethylene. Wood flour is used for filling in thermoplastic composites. Depending on the amount of thermoplastic, there are composites with high and low thermoplastic content. Thermoplastics are also used in nonwoven textile type composites. Long fibers obtained from jute, hemp or synthetic thermoplastics are used in their production [23].

1.3. Psychological Effect of Wood on the User

Wood materials have a different perceptual effect on people than other materials because they are natural materials consisting of living organisms. Studies on this subject have shown that wood is warm, friendly, pleasant and preferred in the environment compared to other materials[24-26] and the positive effects of the use of natural wood and its smell have been shown to reduce fatigue and depression [27, 28].

1.4. Wood Production and Recycling

Compression and densification processes are carried out in the wood production stages to improve the physical and mechanical properties of wood. This process increases its smoothness, moisture resistance and hardness. However, as a result of the heat treatment applied to prevent stretching, color change occurs and weight, mechanical, gloss and smoothness properties decrease [29].

Wood is a valuable material for being a recyclable and reusable material. In this respect, the wastes

generated while producing of wood materials are also utilized again in material production processes [30, 31]. In addition, wood is an ecological material that offers the opportunity to create different materials by combining with other waste materials [32].

Today, with the deterioration of the natural ecosystem and global warming, the tendency towards natural materials, ecological and sustainable design has increased. Accordingly, the use of wood, which is environmentally sensitive, renewable and has low embodied carbon energy [33], is increasing daily. In order to meet the increasing demand, industrial afforestation is carried out by growing needle and broad-leaved tree species, also called industrial plantations, which are generally fast-growing [34].

2.MATERIAL AND METHODS

The study used 24 wood and wood-containing building materials to evaluate the sound transmission amounts. Iroko, tar, sapelli (mahogany), red pine (heat treated), black pine, meranti, yellow pine, red pine as laminate parquet; red pine and fir as solid blocks; MDF separator, double-sided veneered MDF, double-sided veneered perforated MDF, MDF with out veneer, double-sided veneered chipboard, wood-like textured MDF veneer, plywood, laminate parquet with 2 different appearances, pool edge cladding with grooved bottom, MDF wall cladding, thin MDF without veneer, thin rose veneer and thin beech veneer were used as experimental materials in the research. In addition, the amount of sound passing through the combination of MDF with out veneer and MDF separator, thin rose and thin beech veneers were tested separately. The materials subjected to the research were tested with the thicknesses normally used in applications, while their widths and lengths were prepared to fit into the 20x20 cm chamber created for the material in the sound measurement box. The thicknesses of the building materials used were measured and recorded with an electronic caliper with a precision of 0.01 mm.

A specially prepared insulated noise measurement box, as shown in Figure 2, was used in the measurements and the sound permeability of the materials was evaluated by the comparison method. The measurements were made and recorded on the same day and time in the same environment.

Figure 2. Specially Prepared Insulated Sound Transmission Measurement Box

The test box used to measure the sound transmission of building materials consists of a 60x60x60 cm bottom part and a 15 cm high cover part. The outer part of the box is made of 8mm fiberboard, the inner part is insulated with rock wool and the lid is insulated with insulation foam. With the help of a noise generating sound device and sound measuring devices, the amount of sound passing through the materials was evaluated. Thanks to the glass section on the lid of the device, the values shown on the sound meter were recorded non-contact. A schematic representation of the noise measurement box is shown in Figure 3.
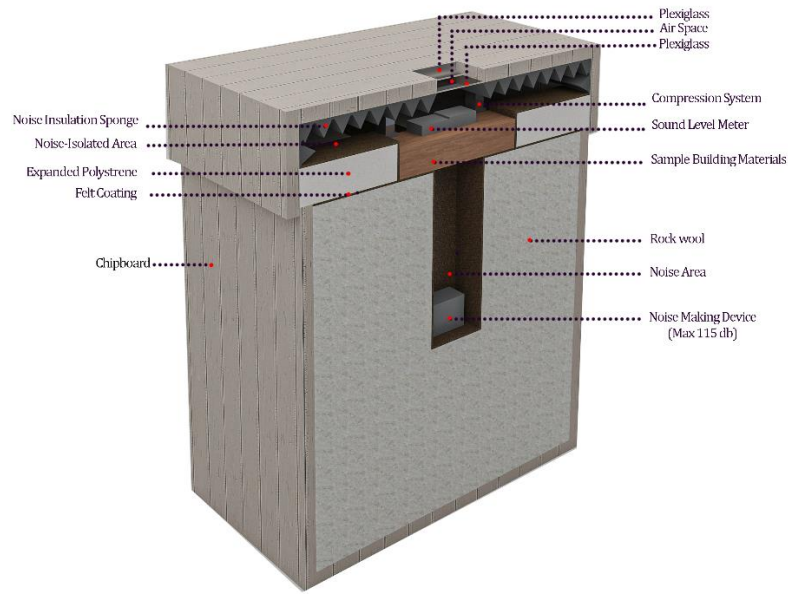
Figure 3. Schematic Material Display

3. RESULTS AND DISCUSSION

In the prepared sound measurement box, the amount of sound transmission was recorded as 103.00 dB in the empty state without any material. Then, readings were taken for each material and the amount of sound transmitted to the upper surface of the material was determined. According to this process, the thickness of the wood-based coating materials tested, and the sound transmission amounts obtained as a result of the experiment are shown in Table 2.

Table 2. Utilization Thicknesses and Sound Transmission Amounts of Building Materials

Building Material	Material Utilization Thickness (mm)	Sound Transmission Amount (dB)	Building Material	Material Utilization Thickness (mm)	Sound Transmission Amount (dB)
Iroko	17,85	61,80	Tar	17,90	62,70
Sapelli (Mahogany)	17,75	57,60	RedPine (heat treated)	17,50	59,90
Black Pine	16,90	61,80	Meranti	18,00	65,40

YellowPine	17,85	62,90	**RedPine**	16,93	61,50
Red Pine Solid Block	16,55	58,20	**Fir Solid Block**	16,50	61,80
MDF Separator	2,85	92,40	**Double-Sided Veneered MDF**	17,93	53,90
Double-Sided Veneered Perforated MDF	18,15	81,30	**Double-Sided Veneered Chipboard**	18,20	56,00
MDF Without Veneer	18,25	58,00	**Wood-Like Textured MDF Veneer**	3,50	65,00
LaminantParquet(A)	7,85	58,00	**Laminant Parquet (B)**	7,75	56,00
Pool Edge Cladding With Grooved Bottom	19,30 / 11,10	67,00	**MDF Wall Cladding**	13,80	73,00

Plywood	6,30	62,00	**Thin MDF Without Veneer**	5,95	59,00
Thin Rose Surface Veneer	0,60	73,90	**Thin Beech Surface Veneer**	0,65	70,80

As a result of the measurements obtained, the wood veneer material with the lowest sound transmission amount was MDF with double-sided veneer. In constrast the veneer material with the highest sound transmission amount was MDF separator. In addition, measurements were also made on uncoated MDF, thin rose and beech surface coatings and the use of MDF separators. As a result of the measurements;

- MDF with out veneer + Thin Beech Surface Veneer with a measurement of 51.30 dB,
- MDF with out veneer + Thin Rose Surface Veneer with 53,70 dB and,
- MDF with out veneer + MDF Separator with 51.40 dB recorded.

Thus, since the sound transmission amount measured from the thin beech surface coating with MDF with out veneer was 51.30 dB, it was the material that prevented the noise the most by producing better results than the double-sided veneered MDFbuilding material with the lowest sound transmission amount with 53.90 dB. In addition, in the sound measurements, the measurement made with MDF with out veneer and MDF separator placed on one side was lower than the measurement made with double-sided coated MDF.

As a result of the sound measurements made in the study, it was determined that alder has better sound retention properties compared to fir. In addition, it was observed that double-sided veneered MDF passes less sound compared to double-sided veneered chipboards.

In the sound measurements made with double-sided veneered MDFs, it was observed that the sound transmission amount of perforated MDF increased significantly.

Among the iroko, tar, sapelli (mahogany), heat-treated red pine, black pine, meranti, yellow pine, red pine materials used as laminate parquet, sapelli (mahogany) had the lowest sound transmission amount in the sound measurement made in the study.

In sound measurements with thin surface veneers, Beech showed less sound transmission compared to Rose material.

Although the wood-like textured MDF cladding material is a thin, in the sound measurements made, it transmitted a lower amount of sound than the thicker meranti, pool edge cladding with grooved bottom, MDF wall cladding and double-sided veneered perforated MDF materials.

Altunok, in their 2012 study, stated that yellow pine panels were less sound permeable than iroko in sound measurements, However in the comparison measurements made in this study, the amount of sound permeability of iroko was found to be less than that of yellow pine [15].

In Ayan's doctoral thesis study in 2012, it was stated that the sound absorption property of heat-treated wood increased in the sound measurements made, and in our study, the sound transmission amount of heat-treated red pine was lower compared to red pine, and similar results were obtained [18].

Çavuş stated that black pine has less sound transmission properties than yellow pine due to measurements within the scope of his study in 2020 [35]. It is seen that a similar result was reached with

this study.

4. CONCLUSIONS

In the study, sound transmission values of wood veneer materials were measured using the same environment and noise source, and the following results were obtained by comparative analysis in terms of sound transmission potentials. According to this:

- The contribution of wood materials in sound transmission in the interior varies depending on the type of wood,
- In the sound transmission measurements, sapelli (mahogany) was the slightest sound transmitting among the laminate parquets. According to this result, sapelli (mahogany) can be preferred as laminate parquet in interior spaces because it also contributes to noise control,
- The heat-treated material shows a better sound transmission performance compared to its normal state,
- Especially in noisy interiors, double-sided veneered MDF material can be preferred instead of double-sided veneered chipboard as it prevents sound transmission more,
- Separators, which are generally used to divide spaces into different areas, also have an effect on sound transmission, and in this respect, especially in multi-use areas such as open office areas, the use of separators will provide auditory comfort,
- Among all the measurements made, it was concluded that the least sound-permeable coating material was MDF with beech veneer, and that it may even be the best wood veneer material to be used to prevent sound transmission between interior spaces of noise-producing structures by absorbing almost half of the sound produced by the sound generating device.

The study showed that noise permeability can be reduced according to the type of wood coating materials.

The fact that similar findings were obtained in this study and other studies in the literature reveals that the study method is appropriate. In this direction, it is recommended that new studies be conducted with different coating materials. Reducing the noise with the studies to be carried out will ensure the protection of the auditory comfort environment in other spaces.

Declaration of Ethical Standards

The authors declare that they have carried out this completely original study by adhering to all ethical rules including authorship, citation and data reporting.

Credit Authorship Contribution Statement

E. N. ERZURUM SONUÇ: Methodology, Conceptualization, Resources, Investigation, Writing.
M. DERELİ: Methodology, Conceptualization, Resources, Investigation, Writing -review & editing, Supervision.

Declaration of Competing Interest

The authors declared that they have no conflict of interest.

Funding / Acknowledgements

Data Availability

Data supporting the findings of this study can be obtained from the corresponding author with reasonable requests to assist in scientific studies.

REFERENCES

[1]   R. Kutlu, "Çevresel Faktörlerin Mekan Kalitesi ve İnsan Sağlığına Etkileri," Turkish Online Journal of Design Art and Communication, vol. 8, no. 1, pp. 67-78, 2018.

[2]   Ç. Güler, "Ergonomiye giriş," Çevre Sağlığı Temel Kaynak Dizisi, vol. 45, no. 9-12, 1997.

[3]   Y. Al Horr, M. Arif, A. Kaushik, A. Mazroei, M. Katafygiotou, and E. Elsarrag, "Occupant productivity and office indoor environment quality: A review of the literature," Building and environment, vol. 105, pp. 369-389, 2016.

[4]   T. Alapieti, R. Mikkola, P. Pasanen, and H. Salonen, "The influence of wooden interior materials on indoor environment: a review," European Journal of Wood and Wood Products, vol. 78, pp. 617-634, 2020.

[5]   W. Yang and H. J. Moon, "Combined Effects of Acoustic, Thermal, and Illumination Conditions on the Comfort of Discrete Senses and Overall Indoor Environment," Building and Environment, vol. 148, pp. 623-633, 2019.

[6]   Z. Akan, A. Yilmaz, O. Özdemir, and M. A. Korpinar, "Noise pollution, psychiatric symptoms and quality of life: noise problem in the east region of Turkey," Journal of Inonu University Medical Faculty, vol. 19, no. 2, pp. 75-81, 2012.

[7]   M. Dovjak, N. Šubic, R. Kunič, A. Repše, and R. Prislan, "Holistic Solutions for Acoustic Comfort in Day-Care Facilities," 2018.

[8]   A. Şahmurova and P. Sezgin, "Gürültü kirliliğinin dikkat eksikliği ve hiperaktivite bozukluğu üzerindeki etkileri," Avrasya Sosyal ve Ekonomi Araştırmaları Dergisi, vol. 6, no. 3, pp. 566-579, 2019.

[9]   V. Bucur, "Wood and Wood-Based Materials in Architectural Acoustics," in Acoustics of wood 2006, pp. 21-36.

[10]   U. G. Wegst, "Wood for sound," American Journal of Botany, vol. 93, no. 10, pp. 1439-1448, 2006.

[11]   G. Özdöl, "Masif Ahşap Parklerin Boyutsal Kararlılığının Araştırılması," Doktora, İstanbul Teknik Üniversitesi,Fen Bilimleri Enstitüsü, İstanbul, 2010.

[12]   V. Öztürk, "Ahşap Esaslı Akustik Kompozit Panellerin Bazı Teknolojik Özellikleri," Yüksek Lisans Tezi, Gazi Üniversitesi, Fen Bilimleri Enstitüsü, Ankara, 2019.

[13]   D. Kretschmann, "Mechanical Properties of Wood," in Wood Handbook: Wood as an Engineering Material, vol. 190. USA,44: Madison, WI, 2010, ch. 5, pp. 5.1-5.46.

[14]   K. Işıktaş and A. Nurgül, "Ahşap Akustik Panellerin Sesi Absorbe Etme Yeteneği ile İç ve Dış Ortamlardaki Ses Yalıtımının İyileştirilmesi," Mesleki Bilimler Dergisi (MBD), vol. 5, no. 1, pp. 16-21, 2016.

[15]   M. Altunok and S. Ayan, "Lamine Panellerde Ses Yutma Katsayısı Değerlerinin Belirlenmesi," Politeknik Dergisi, vol. 15, no. 3, pp. 117-125, 2012.

[16]   J. Smardzewski et al., "Experimental study of wood acoustic absorption characteristics," Holzforschung, vol. 68, no. 4, pp. 467-476, 2014.

[17]   F. Negro, C. Cremonini, R. Zanuttini, and M. Fringuellino, "Development of framed poplar plywood for acoustic improvement," Wood Research, vol. 61, no. 1, pp. 121-128, 2016.

[18]   S. Ayan, "Isıl İşlemli Ahşap Lamine Panellerin Akustik Özelliklerinin Belirlenmesi," Doktora Tezi, Gazi Üniversitesi Fen Bilimleri Enstitüsü, Ankara, 2012.

[19]   M. S. Muslu, "İç Mekânda Kullanılan Bazı Ahşap Esaslı Kompozit Levha Türlerinde Ses Yutma Katsayısının Belirlenmesi," Politeknik Dergisi, pp. 1-1, 2022.

[20]   N. Öztank, "Orta Yükseklikteki (4-8 Kat) Konut Yapılarında Ahşap Teknolojisinin Uygulanabilirliği," Doktora, Dokuz Eylül Üniversitesi, Fen Bilimleri Enstitüsü, İzmir, 2004.

[21]   Ş. N. Caştur, "Günümüz Mimarisinde Kullanılan Endüstriyel Ahşap Yapı Elemanları ve Yapı Örneklerinin İncelenmesi," Yüksek Lisans Tezi, Fatih Sultan Mehmet Vakıf Üniversitesi, Lisansüstü Eğitim Enstitüsü, İstanbul, 2021.

[22]   M. Çolak and S. Değirmentepe, "İç ve Dış Mekanlarda Ahşap Malzemelerin Mobilya ve Yapı Malzemesi Olarak Kullanımı," Türk Doğa ve Fen Dergisi, vol. 9, no. Özel Sayı, pp. 190-199, 2020.

[23]   B. Güller, "Odun Kompozitleri," (in tr scheme="ISO639-1"), Orijinal Araştırma Makalesi vol. 2, no. 1, pp. 135-160, 2001, doi: https://dergipark.org.tr/tr/pub/tjf/issue/20877/224202. [Accessed May. 22, 2024].

[24]   N. Podrekar Loredan, D. Lipovac, S. Jordan, M. D. Burnard, and N. Šarabon, "Thermal effusivity of different tabletop materials in relation to users' perception," Applied Ergonomics, vol. 100, p. 103664, 2022.

[25]   M. Watchman, A. Potvin, and C. M. Demers, "A post-occupancy evaluation of the influence of wood on environmental comfort," BioResources, vol. 12, no. 4, pp. 8704-8724, 2017.

[26]   C. H. Wong and A. A. Aziz, "Perceptions of youngsters on interior space quality in relation to materiality and spatial design," International Journal of Built Environment and Sustainability, vol. 8, no. 1, pp. 103-119, 2021.

[27]   S. R. Bhatta, K. Tiippana, K. Vahtikari, M. Hughes, and M. Kyttä, "Sensory and emotional perception of wooden surfaces through fingertip touch," Frontiers in psychology, vol. 8, p. 367, 2017.

[28]   C.-P. Yu, W.-C. Weng, J. Ramanpong, C.-D. Wu, M.-J. Tsai, and J. D. Spengler, "Physiological and psychological responses to olfactory simulation by Taiwania (Taiwania cryptomerioides) essential oil and the influence of cognitive bias," Journal of Wood Science, vol. 68, no. 1, pp. 1-12, 2022.

[29]   M. Tosun and S. D. Sofuoğlu, "Ağaç Malzemenin Sıkıştırılarak Yoğunlaştırılması Konusunda Yapılan Çalışmalar," Mobilya ve Ahşap Malzeme Araştırmaları Dergisi, vol. 4, no. 1, pp. 91-102, 2021.

[30]   C. Demirkır and S. Çolak, "Odun kökenli atıkların levha endüstrisinde yeniden kullanım imkanları," Kafkas Üniversitesi, Artvin Orman Fakültesi Dergisi, vol. 7, no. 1, pp. 41-50, 2006.

[31]   N. Özmen, N. S. Çetin, N. Narlıoğlu, V. Çavuş, and E. Altuntaş, "MDF atıklarının odun plastik kompozitlerin üretiminde değerlendirilmesi," SDÜ Orman Fakültesi Dergisi, vol. 15, pp. 65-71, 2014.

[32]   F. Özdemir and D. Ramazanoğlu, "Atık muz kabuğu, biber sapı ve kızılçam odun unu kullanılarak biyoplastik kompozit üretimi," Turkish Journal of Forestry, vol. 20, no. 3, pp. 267-273, 2019.

[33]   H. S. Azkur and F. Canan, "Farklı Taşıyıcı Sistemlerin Gömülü Enerji ve Gömülü Karbon Değerlerinin Müstakil Konutlar Bağlamında Karşılaştırılması," (in tr scheme="ISO639-1"), 26, no. 1, pp. 35-46, 2022, doi: https://dergipark.org.tr/tr/pub/sdufenbed/issue/69379/860348. [Accessed May. 22, 2024].

[34]   Ö. Görücü, A. Tolunay, Y. Güneş, and P. Topçu, "Endüstriyel Plantasyonlar Ve Orman Ürünleri Endüstrisi," Bartın Orman Fakültesi Dergisi, vol. 22, no. 3, pp. 939-952, 2020.

[35]   V. Çavuş, "Kokulu ardıç odununun bazı fiziksel ve mekanik özellikleri üzerine bir araştırma," Mobilya ve Ahşap Malzeme Araştırmaları Dergisi, vol. 3, no. 1, pp. 1-9, 2020.

NEW HYBRID WINDOWS BASED ON COSH WINDOW AND THEIR PERFORMANCE ANALYSIS IN FIR DIGITAL FILTER DESIGN

[1] **Oğuzhan COŞKUN** [ID] **,** [2, *] **Kemal AVCI** [ID]

[1] *Emko Elektronik A.Ş., Bursa, TÜRKİYE*
[2] *Izmir Democracy University, Engineering Faculty, Electrical and Electronics Engineering Department, Izmir,*
TÜRKİYE
[1] oguzhan.coskun@emkoelektronik.com.tr, [2] kemal.avci@idu.edu.tr

Highlights

- Twenty hybrid window functions are proposed by hybridizing two-parameter Cosh window with various one-parameter windows in the existing literature

- Simulations in Matlab programming environment are performed to design FIR digital filter by using proposed window functions

- Comparative simulation results showed that nine proposed hybrid windows exhibit better filter characteristics compared to the Cosh window

- Among the proposed windows, Cosh-Hamming and Cosh-Von Hann hybrid windows outperformed other well-known two-parameter windows in the literature in designing FIR filters

*Corresponding Author: Kemal AVCI, kemal.avci@idu.edu.tr

NEW HYBRID WINDOWS BASED ON COSH WINDOW AND THEIR PERFORMANCE ANALYSIS IN FIR DIGITAL FILTER DESIGN

¹Oğuzhan COŞKUN [iD] , ², * Kemal AVCI [iD]

¹ Emko Elektronik A.Ş., Bursa, TÜRKİYE
² Izmir Democracy University, Engineering Faculty, Electrical and Electronics Engineering Department, Izmir, TÜRKİYE
¹ oguzhan.coskun@emkoelektronik.com.tr, ² kemal.avci@idu.edu.tr

ABSTRACT: FIR filters find extensive use in various applications such as audio processing, image processing, communications, and control systems. Improving the design methods for FIR filters can lead to better performance in these critical areas. This study introduces novel hybrid window functions, or abbreviated as "windows", to design FIR filters. These newly proposed windows are created by hybridizing two-parameter Cosh window with various one-parameter windows in the existing literature. The performance of these hybrid windows in designing filters is thoroughly examined. Simulation results, conducted in Matlab programming environment, demonstrate that nine proposed hybrid windows exhibit better filter characteristics compared to the Cosh window. Furthermore, for the filter lengths of N = 51 and 101, the filters designed using the proposed windows are compared with those designed using two-parameter windows from the literature, focusing on achieving minimum stopband attenuation for a fixed transition width. The findings reveal that the Cosh-Hamming and Cosh-Von Hann hybrid windows outperform other well-known windows in producing filtering.

Keywords: Cosh Window, Digital Filter Design, FIR Filters, Hybrid Windows, Window Functions

1. INTRODUCTION

A digital filter is used to perform filtering operation on digital signals, such as audio, images, or other time-dependent data, to achieve specific desired effects. Software and hardware realization, non-critical circuit element tolerance, high accuracy, small physical size, high reliability, insignificance of the effect of environmental electrical noises, more efficient cost and being the only option in non-real time systems can be listed as the advantages of digital filters compared to analog filters [1].

Digital filters can be categorized into finite impulse response (FIR) and infinite impulse response (IIR) based on the length of their impulse response. Both FIR and IIR filters come with their own advantages and disadvantages. For example, FIR filters are always stable. This means they won't exhibit unstable behavior, even for certain types of filter designs. IIR filters, on the other hand, can become unstable if not designed properly. FIR filters can achieve a linear phase response, meaning that the input signal experiences a uniform delay across all its frequency components. This is important in applications like audio processing where phase distortion can cause audible artifacts.

Among the FIR filter design techniques, the most superior designs are achieved through optimization methods, and ongoing research is dedicated to advancing this methodology [2-5]. Nonetheless, optimization-driven approaches demand substantial computational resources, rendering them impractical for real-time applications. Conversely, the windowing-based Fourier series method stands out as the most direct method for designing FIR filters, entailing considerably fewer computational requirements compared to alternative methods. The incorporation of a window function in Fourier series serves to truncate and smooth out the ideal filter [6].

A window is a discrete time-domain function that is non-zero only in a certain time interval as in Figure 1 [7]. Windows are classified as either fixed or adjustable. Windows that depend on a single parameter are called fixed, and those with two or more are called adjustable. Practical applications often

---

*Corresponding Author: Kemal AVCI, kemal.avci@idu.edu.tr

favor the use of adjustable windows because of their flexibility. Among the window functions, the rectangular window is the most simple one and it performs a straightforward cut without any smoothing effect. Other well-known fixed windows include Von Hann, Hamming, and Blackman [1].
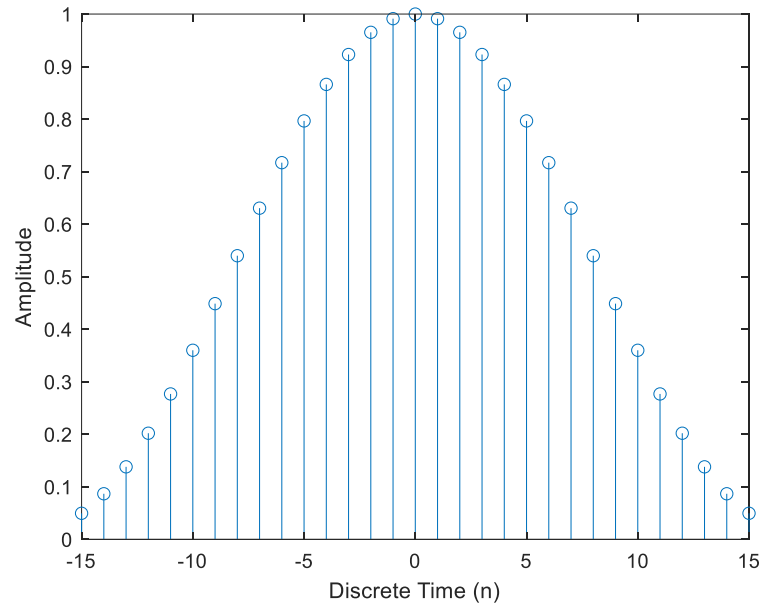
Figure 1. A discrete time domain window for N = 31

As for the adjustable windows, there are well known two [8-10] and three parameter [11-13] windows. The Dolph-Chebyshev window, introduced by Dolph in 1946, yields the narrowest main lobe width for a given maximum sidelobe level, outperforming all other windows in literature. Kaiser, in 1966, introduced the Kaiser window, which is among the most known adjustable windows in the field. Subsequently, Kaiser published the Kaiser window related filter design equations in 1974. This window exhibits superior performance in FIR filter design applications when compared to many two parameter windows in literature. In 1989, Saramaki proposed a two-parameter window, known as Saramaki window [9]. The findings of this study demonstrated that filters designed using the Saramaki window exhibited better stopband attenuation compared to those designed with the Kaiser window. However, it relies on iterative expressions as in the Dolph-Chebyshev window in the time domain, which could be considered a drawback. Various two-parameter adjustable windows were suggested in the literature, including the Poisson, Cauchy, Gaussian, and Parzen-Cos6 (πt) window families. However, these alternatives do not surpass the performance of the Kaiser window in filter design. Bergen and Antoniou [11] conducted an in-depth study on the use of three-parameter Ultraspherical windows in non-recursive digital filter design. Their research demonstrated that the Ultraspherical window family allows for the design of filters with lower degrees compared to those designed using the Saramaki, Kaiser, and Dolph-Chebyshev windows. The Ultraspherical family of windows has one important feature that is special cases of Saramaki and Dolph-Chebyshev windows. In recent years, studies have been continuing to increase the effectiveness of window functions in different application areas [14-23].

The motivation behind proposing new window functions for digital FIR filter design in literature lies in overcoming limitations associated with existing window functions to achieve improved filter characteristics, making them more suitable for diverse signal processing applications. In order to enhance filter design, it is essential for a window function to effectively minimize undesirable Gibbs oscillations and optimize filtering performance metrics, thereby improving the overall frequency response of the filter. By definition, Gibbs oscillations refer to the phenomenon where oscillations or ripples occur in the vicinity of a sharp transition in a function. Gibbs oscillations are inherent in Fourier Series based FIR filter design method due to the need to truncate the infinite ideal impulse response of

the filter derived from the desired frequency response which is identified by specifying passbands, stopbands, and transition bands, as well as any other relevant parameters based on the application requirements. In the frequency domain, truncating process corresponds to convolving with a sinc function, leading to overshoot and ringing (i.e., Gibbs oscillations) in the frequency response [1]. Minimizing these oscillations lead to an improvement in filter design. Various performance metrics such as minimum stopband attenuation, maximum passband attenuation, and transition width are used to evaluate and compare different filters. Stopband and passband attenuations are related with the ripples in stopband and passband, respectively. The transition width of a filter refers to the rate at which the filter response changes from the passband to the stopband. Proposing new window functions allows for the optimization of these performance metrics, tailoring the filter design to achieve the best compromise based on the specific application requirements. For example, different window functions can provide different transition width characteristics, therefore developing new window functions allows for the exploration of designs that provide sharper or smoother transitions.

Since undesired Gibbs oscillations inherently occur in the windowing-based filter design method, it is important to minimize them to obtain a better filter design by proposing new window functions. In this study, it is aimed to propose new adjustable hybrid windows based on Cosh window [10], which will allow to design better window method-based filters in terms of transition width and minimum stop band attenuation parameters.

The article is organized as follows: The second section provides an overview of fixed and adjustable windows used in this study and introduces the method for designing FIR filters using windows, along with the proposed window functions. In the third section, the performance of filters designed with the proposed windows is analyzed through a comparison with digital filters designed using adjustable windows in the literature. The last section summarizes the results obtained in this study.

2. MATERIAL AND METHODS

2.1. Fixed Windows in The Literature

Window functions that have only window length as their argument, that is, that depend on only one parameter, are called fixed window functions. Fixed window functions proposed in the literature are given below for the range $|n| \leq (N-1)/2$ in alphabetical order.

The Bartlett window is defined by Eq. (1) [24].

$$w(n) = \begin{cases} \dfrac{n + \dfrac{N-1}{2}}{\dfrac{N-1}{2}} & -\dfrac{N-1}{2} \leq n \leq 0 \\ 2 - \dfrac{n + \dfrac{N-1}{2}}{\dfrac{N-1}{2}} & 0 \leq n \leq \dfrac{N-1}{2} \end{cases} \tag{1}$$

The Bartlett-Hann window is a modified version of the Bartlett and Von Hann windows. It is defined by Eq.(2) [25].

$$w(n) = 0.62 - 0.48 \left| \dfrac{n + \dfrac{N-1}{2}}{N-1} - 0.5 \right| + 0.38 \cos\left(2\pi \left(\dfrac{n + \dfrac{N-1}{2}}{N-1} - 0.5 \right) \right) \tag{2}$$

Blackman window is defined as in Eq. (3) [26].

$$w(n) = 0.42 + 0.5cos\ 2\pi n/(N-1) + 0.08cos\ 4\pi n/(N-1)$$

(3)

Blackman-Harris Window is defined by Eq. (4) [26].

$$w(n) = 0.35875 - 0.48829\cos\left(\frac{2\pi\left(n+\frac{N-1}{2}\right)}{N-1}\right) + 0.14128cos\left(\frac{4\pi\left(n+\frac{N-1}{2}\right)}{N-1}\right)$$
$$- 0.01168cos\left(\frac{6\pi\left(n+\frac{N-1}{2}\right)}{N-1}\right)$$

(4)

Bohman window is defined as in Eq. (5) [26].

$$w(n) = \left(1 - \frac{|n|}{(N-1)/2}\right)cos\left(\frac{\pi n}{(N-1)/2}\right) + \frac{1}{\pi}\frac{sin(\pi|n|)}{(N-1)/2}$$

(5)

Cos(x) window is defined as in Eq. (6) [8].

$$w(n) = cos\left(\frac{\pi n}{N-1}\right)$$

(6)

Cos³(x) window is defined as in Eq. (7) [8].

$$w(n) = 0.75cos\left(\frac{\pi n}{N-1}\right) + 0.25cos\left(\frac{3\pi n}{N-1}\right)$$

(7)

Cos⁴(x) window is defined as in Eq. (8) [8].

$$w(n) = 0.375 + 0.5cos\left(\frac{2\pi n}{N-1}\right) + 0.125cos\left(\frac{4\pi n}{N-1}\right)$$

(8)

Flat-Top window is defined as in Eq. (9) [27].

$$w(n) = 0.21557895 - 0.41663158\cos\left(\frac{2\pi\left(n+\frac{N-1}{2}\right)}{N-1}\right) + 0.277263158cos\left(\frac{4\pi\left(n+\frac{N-1}{2}\right)}{N-1}\right) -$$
$$0.083578947cos\left(\frac{6\pi\left(n+\frac{N-1}{2}\right)}{N-1}\right) + 0.006947368cos\left(\frac{8\pi\left(n+\frac{N-1}{2}\right)}{N-1}\right)$$

(9)

Hamming window is defined as in Eq. (10) [25].

$$w(n) = 0.54 + 0.46cos\frac{2\pi n}{N-1}$$

(10)

Lanczos window is defined as in Eq. (11) [28].

$$w(n) = sinc\left(\frac{2n}{N-1}\right)$$

(11)

The Nuttal Window is formed by modifying the coefficients of the Blackman-Harris window equation. It is given in Eq. (12) [29].

$$w(n) = 0.3635819 - 0.4891775\cos\left(\frac{2\pi\left(n + \frac{N-1}{2}\right)}{N-1}\right) + 0.1365995\cos\left(\frac{4\pi\left(n + \frac{N-1}{2}\right)}{N-1}\right)$$
$$- 0.106411\cos\left(\frac{6\pi\left(n + \frac{N-1}{2}\right)}{N-1}\right) \tag{12}$$

The Optimized Blackman Window is created by changing the coefficients in the Blackman window equation. It is given in Eq. (13) [8].

$$w(n) = 0.412 + 0.5\cos\frac{2\pi n}{N-1} + 0.088\cos\frac{4\pi n}{N-1} \tag{13}$$

Parabolic window is defined as in Eq. (14) [8].

$$w(n) = 1 - \left(\frac{2n}{N-1}\right)^2 \tag{14}$$

The Parzen window is defined as in Eq. (15) [30].

$$w(n) = \begin{cases} 1 - 6\left[\frac{n}{(N)/2}\right]^2 + 6\left[\frac{n}{(N)/2}\right]^3 & 0 \leq |n| \leq \frac{N-1}{4} \\ 2\left[1 - \frac{|n|}{N/2}\right]^3 & \frac{N-1}{4} \leq |n| \leq \frac{N-1}{2} \end{cases} \tag{15}$$

Rectangular window is defined as in Eq. (16) [1].

$$w(n) = 1 \tag{16}$$

The Riemann window is defined as in Eq. (17) [8].

$$w(n) = \frac{\sin\left(\frac{2\pi n}{N-1}\right)}{\frac{2\pi n}{N-1}} \tag{17}$$

Triangular window is defined as in Eq. (18) [31].

$$w(n) = 1 - \frac{|2n|}{N} \tag{18}$$

Von-Hann window is defined as in Eq. (19) [21].

$$w(n) = 0.5 + 0.5\cos\frac{2\pi n}{N-1} \tag{19}$$

Welch window is defined as in Eq. (20) [32].

$$w(n) = 1 - \left(\frac{n - \frac{N-1}{2}}{\frac{N-1}{2}}\right)^2 \tag{20}$$

2.2. Adjustable Windows in The Literature

Window functions that depend on more than one parameter are called adjustable window functions. There are various adjustable window functions proposed in the literature. Some well-known adjustable windows used in this study are given below for the range $|n| \leq (N-1)/2$ in alphabetical order.

Cosh window is defined as in Eq. (21) [10].

$$w(n) = \frac{\cosh\left(\alpha\sqrt{1 - \left(\frac{2n}{N-1}\right)^2}\right)}{\cosh(\alpha)} \tag{21}$$

Cosh-Hamming window is defined as in Eq. (22) [33].

$$w(n) = \frac{\cosh\left(\alpha\sqrt{1 - \left(\frac{2n}{N-1}\right)^2}\right)}{2\cosh(\alpha)} + 0.27 - 0.23\cos2\pi\left(\frac{n}{N-1} + 0.5\right) \tag{22}$$

Dolph Chebyshev window is defined as in Eq. (23) [1].

$$w(n) = \frac{1}{N}\left[\frac{1}{r} + 2\sum_{i=1}^{\frac{N-1}{2}} T_{N-1}\left(x_0\cos\left(\frac{i\pi}{N}\right)\right)\cos\left(\frac{2ni\pi}{N}\right)\right] \tag{23}$$

where

$$r = 10^{-R/20}, \; x_0 = \cosh\left(\frac{1}{N-1}\cosh^{-1}\left(\frac{1}{r}\right)\right), \; T_k(x) = \begin{cases} \cos(k\cos^{-1}(x)) & |x| \leq 1 \\ \cosh(\cosh^{-1}(x)) & |x| \geq 1 \end{cases} \tag{24}$$

Exponential window is defined as in Eq. (25) [34].

$$w(n) = \frac{\exp\left(\alpha\sqrt{1 - \left(\frac{2n}{N-1}\right)^2}\right)}{\exp(\alpha)} \tag{25}$$

Exponential-Hamming window is defined as in Eq. (26) [35].

$$w(n) = \frac{\exp\left(\alpha\sqrt{1 - \left(\frac{2n}{N-1}\right)^2}\right)}{2\exp(\alpha)} + 0.27 - 0.23\cos2\pi\left(\frac{n}{N-1} + 0.5\right) \tag{26}$$

Gaussian window is defined as in Eq. (27) [8].

$$w(n) = e^{-\frac{1}{2}\left[\alpha\frac{2n}{N-1}\right]^2} \tag{27}$$

Hann-Poisson window is defined as in Eq. (28) [8].

$$w(n) = 0.5\left[1 + \cos\left(\frac{2\pi n}{N-1}\right)\right]e^{\alpha\frac{2|n|}{N-1}} \tag{28}$$

Kaiser window is defined as in Eq. (29) [1].

$$w(n) = \frac{I_0\left(\alpha\sqrt{1 - \left(\frac{2n}{N-1}\right)^2}\right)}{I_0(\alpha)} \tag{29}$$

where

$$I_0(x) = 1 + \sum_{k=1}^{\infty}\left[\frac{1}{k!}\left(\frac{x}{2}\right)^k\right]^2 \tag{30}$$

Kaiser-Hamming window is defined as in Eq. (31) [7].

$$w(n) = \frac{I_0\left(\alpha\sqrt{1 - \left(\frac{2n}{N-1}\right)^2}\right)}{2I_0(\alpha)} + 0.27 - 0.23cos2\pi\left(\frac{n}{N-1} + 0.5\right) \tag{31}$$

Poisson window is defined as in Eq. (32) [8].

$$w(n) = e^{\alpha\frac{2|n|}{N-1}} \tag{32}$$

Saramaki window is defined as in Eq. (33) [9].

$$w(n) = \hat{w}(n)/\hat{w}(0) \quad |n| \le \frac{N-1}{2} \tag{33}$$

where

$$\hat{w}(n) = v_0(n) + 2\sum_{k=1}^{(N-1)/2} v_k(n), \quad v_0(n) = \begin{cases} 1 & n=0 \\ 0 & \text{other} \end{cases}, \quad v_1(n) = \begin{cases} \gamma - 1 & n=0 \\ \gamma/2 & |n|=1 \\ 0 & \text{other} \end{cases} \tag{34}$$

$$v_k(n) = \begin{cases} 2(\gamma-1)v_{k-1}(n) - v_{k-2}(n) + \gamma[v_{k-1}(n-1) - v_{k-2}(n-1)] & |n| \le k \\ 0 & \text{other} \end{cases} \tag{35}$$

2.3. FIR Filter Design Using Window Functions

The Fourier series method is one of the FIR filter design methods. The purpose of using a window in this method is to cut and smooth the ideal filter having the infinite impulse response. The impulse response of the noncausal filter obtained using the window is found from Eq. (36) [1,7].

$$h_{nc}(n) = w(n)h_{id}(n) \tag{36}$$

where $h_{id}(nT)$ is the infinite time impulse response of the ideal filter that cannot be realized. For a low pass filter, this impulse response can be found from Eq. (37) [1,7].

$$h_{id}(n) = \begin{cases} \dfrac{w_{ct}}{\pi} & for\ n = 0 \\ \dfrac{sinw_{ct}n}{n\pi} & for\ n \ne 0 \end{cases} \tag{37}$$

The undesired oscillations in the passband and stopband regions of filters designed using windows are equal. Therefore, when finding the simulation results, it is sufficient to calculate the attenuation parameter (Generally As) in only one of the two regions.

The amplitude spectrum and spectral parameters of a low-pass filter are given in Figure 2.
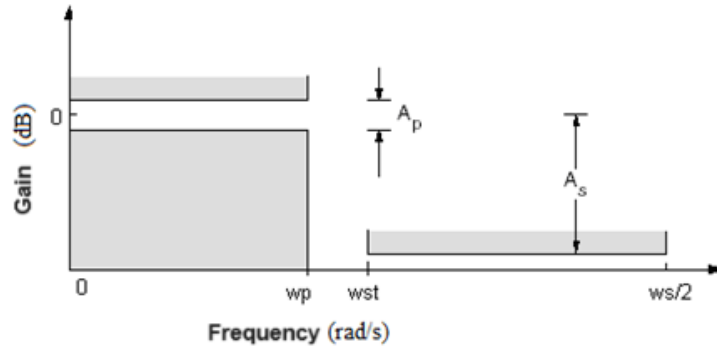
Figure 2. Amplitude spectrum and spectral parameters of a low-pass filter

The specified parameters in Figure 2 are: pass-band frequency (ω_P), stop-band frequency (ω_{st}), sampling frequency (ω_s), maximum pass-band attenuation (A_P), minimum stop-band attenuation (A_s).

Apart from these, there are also cut-off frequency (ω_c) and transition width ($\Delta\omega$) parameters defined by Eq. (38), respectively.

$$\omega_c = (\omega_{st} + \omega_p)/2 \text{ and } \Delta\omega = \omega_{st} - \omega_p \tag{38}$$

2.4. Proposed Hybrid Windows

When the fixed windows given in Section 2.1 are combined with the Cosh windows in equal weight, the hybrid windows given in Table 1 are obtained [36].

Table 1. Proposed hybrid windows.

Window	Equation	Window	Equation
w1	0.5(Cosh + Bartlett)	w11	0.5(Cosh + Lanczos)
w2	0.5(Cosh + Bartlett-Hann)	w12	0.5(Cosh + Nuttal)
w3	0.5(Cosh + Blackman)	w13	0.5(Cosh + Optimized
w4	0.5(Cosh + Blackman-Harris)	w14	0.5(Cosh + Parabolic)
w5	0.5(Cosh + Bohman)	w15	0.5(Cosh + Parzen)
w6	0.5(Cosh + Cos(x))	w16	0.5(Cosh + Rectangular)
w7	0.5(Cosh + Cos³(x))	w17	0.5(Cosh + Riemann)
w8	0.5(Cosh + Cos⁴(x))	w18	0.5(Cosh + Triangular)
w9	0.5(Cosh + Flat-Top)	w19	0.5(Cosh + Von-Hann)
w10	0.5(Cosh + Hamming)	w20	0.5(Cosh + Welch)

In Figure 3, time domain amplitude characteristics of 20 hybrid windows plotted for N = 51 and α = 3 are given**.**
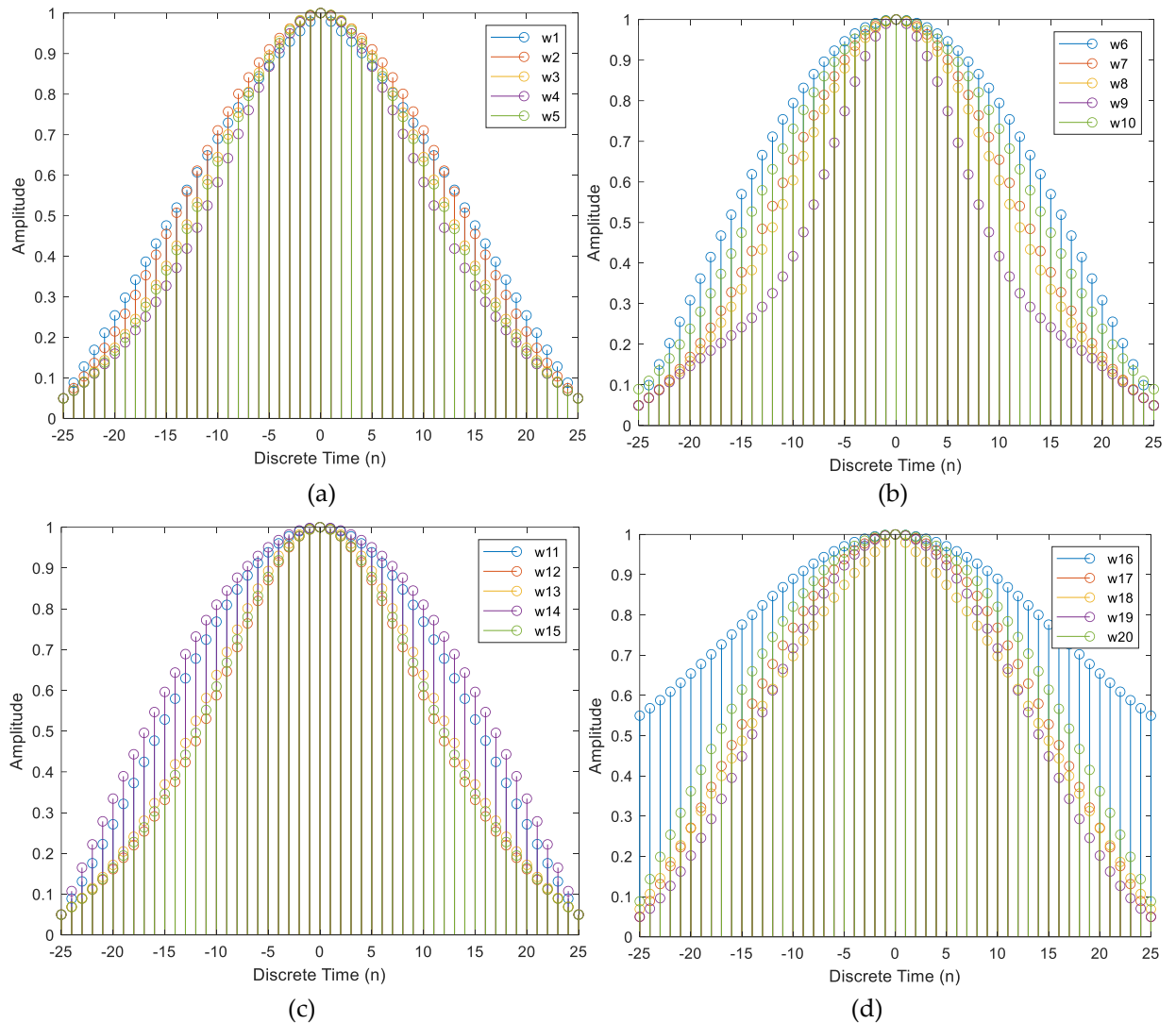
Figure 3. For N = 51 and α = 3, time domain plots of a) w1-w5 b) w6-w10 c) w11-w15 d) w16-w20

3. RESULTS AND DISCUSSION

In this section, first, the effect of window parameters α and N on the filter characteristics will be observed through the Cosh-Von Hann window, which is one of the hybrid windows. Then, the minimum stopband attenuation and transition width characteristics of 20 hybrid windows obtained by many filter design results will be achieved and the filter performances will be observed by comparing them with the filters designed with Cosh window. Then, the numerical filter design performances of the proposed hybrid windows and two parameter adjustable windows in the literature will be compared.

3.1. Effect of Proposed Hybrid Windows Parameters on Designed Filter Characteristics

In this section, performance analyzes in terms of minimum stop band attenuation and transition width parameters of digital filters designed with equal filter length - different alpha values and equal alpha value - different filter lengths for the new hybrid window obtained by hybridizing Cosh window and Von-Hann window are given. Figure 4a shows the effect of α on the filter characteristic at a fixed filter length. It is observed that when α value increases, $\Delta\omega$ increases (gets worse) and A_s increases (gets better). Figure 4b illustrates the impact of the filter length on the filter characteristic at a constant α

value. It is seen that as N increases, $\Delta\omega$ decreases (gets better) and A_s remains almost the same. The numerical data of the filters designed in Figure 4 are presented in Table 2. The effects of the window parameters on the filter spectral parameters are also seen in this table explicitly.
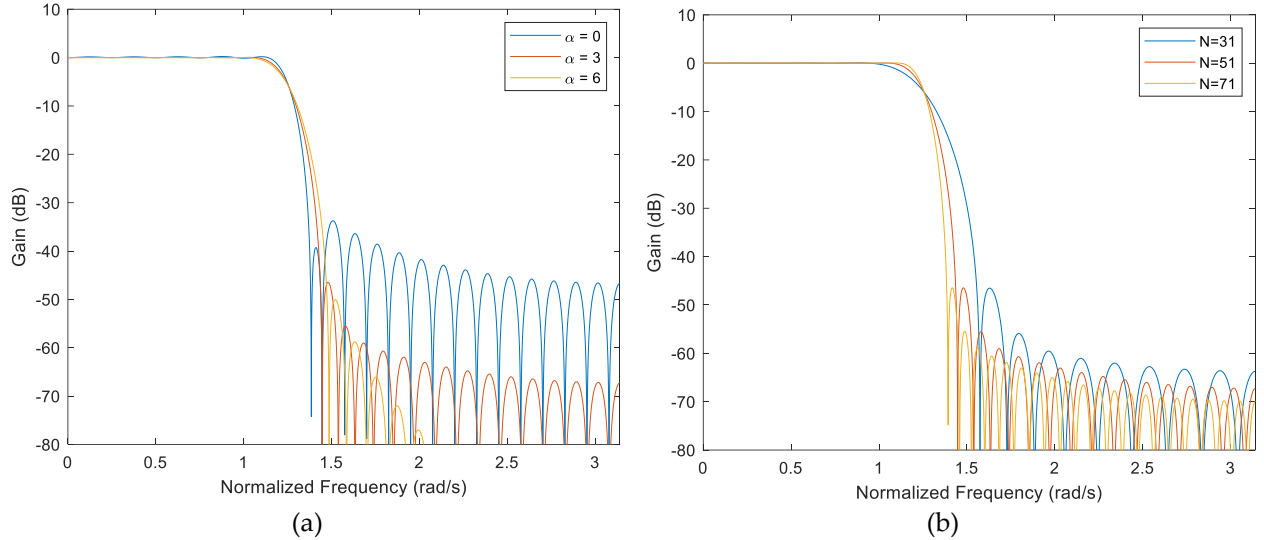
Figure 4. Amplitude spectra of filters designed with a Cosh-Von Hann hybrid window a) for different values of α at a fixed filter length and b) for different filter lengths at a fixed value of α

Table 2. Transition width and minimum stopband attenuation values for filters designed with Cosh-Von Hann window at different lengths and α values

	N = 31		N = 51		N = 71	
α	$\Delta\omega$ (rad/s)	A_s (dB)	$\Delta\omega$ (rad/s)	A_s (dB)	$\Delta\omega$ (rad/s)	A_s (dB)
0	0.368	33.77	0.221	33.74	0.158	33.70
3	0.610	46.52	0.365	46.22	0.261	46.46
6	0.737	50.06	0.443	50.06	0.316	50.06

3.2. Comparison of Filters Designed with Proposed Hybrid Windows and Cosh Window

In this section, the comparisons of filters designed for 20 hybrid windows obtained by hybridization of Cosh window and fixed windows with filters designed with Cosh window in terms of minimum stopband attenuation and transition width parameters for a filter length of N = 51 are presented.

In Figure 5a, it is seen that none of the filters designed with Cosh-based hybrid windows exhibited better filter spectral characteristics than Cosh-based filters. From Figure 5b, it is observed that the filters designed with hybrid windows based on w6 and w7 can exhibit better filter spectral characteristics than Cosh based filters at certain intervals. As for Figure 5c, it is seen that filters designed with hybrid windows based on w10 and w11 can exhibit better filter spectral characteristics than Cosh based filters at certain intervals. In Figure 5d, it is seen that filters designed with hybrid windows based on w14 and w16 can exhibit better filter spectral characteristics than Cosh based filters at certain intervals. And, from Figure 5e, it is observed that the filters designed with hybrid windows based on w17, w19 and w20 can exhibit better filter spectral characteristics than Cosh based filters at certain intervals. As a result, since the filter performance of w1, w2, w3, w4, w5, w8, w9, w12, w13, w15 and w18 hybrid windows is always worse than the Cosh window, the hybridization in these windows was not significant for filter design applications.

(a)

(b)

(c)

(d)

(e)
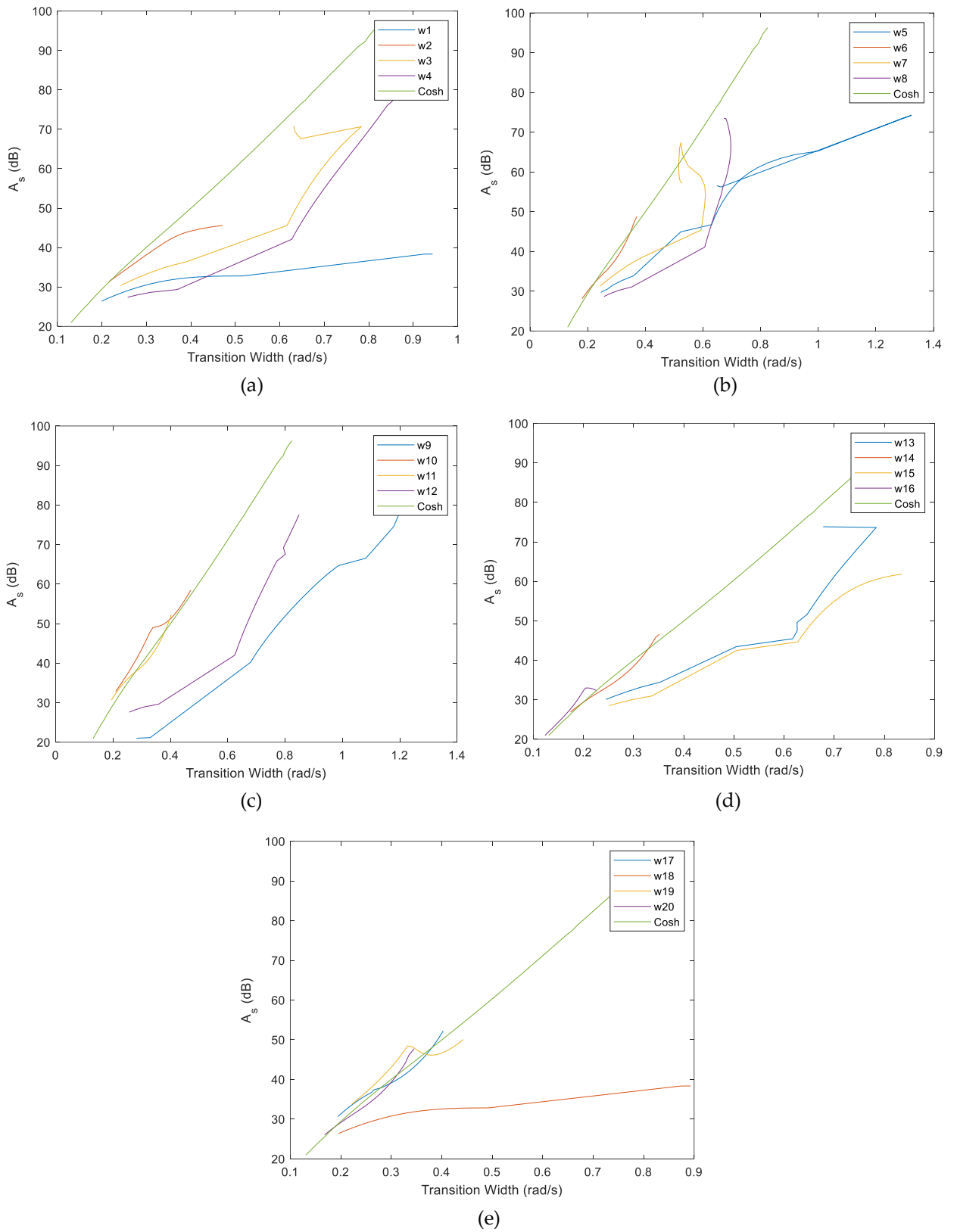
Figure 5. For window length N = 51 a) w1-w4, b) w5-w8, c) w9-w12, d) w13-w16 and e) w17-w20 hybrid windows with minimum stop band attenuation of filters designed with Cosh window-pass band width characteristics.

3.3. Comparison of Filters Designed Using Proposed Hybrid Windows with Filters Designed Using Other Two-Parameter Windows in The Literature

As a result of the filter spectral analysis performed in the previous section, it was seen that filters designed with hybrid windows based on w6, w7, w10, w11, w14, w16, w17, w19 and w20 can exhibit better filter spectral characteristics than Cosh based filters at certain intervals. Therefore, in this section, the performance of these 9 hybrid windows proposed in the filter design with other two-parameter windows proposed in the literature is examined. For a fair comparison, the minimum stopband attenuation values of the designed filters are compared while the filter lengths and transition widths are selected to be the same. Fixed window functions such as Hamming window are not included in the comparison, because they cannot provide the filter characteristics specified in the comparison, because they can perform only one filter characteristic for a fixed filter length.

Table 3 presents the filter spectral numerical values related to the digital filters designed by using nine mentioned proposed windows and well known two parameter adjustable windows (Kaiser-Hamming, Dolph-Chebyshev, Exponential-Hamming, Saramaki, Kaiser, Cosh, Exponential, Gaussian, Hann-Poisson and Poisson windows) in literature for the filter lengths N = 51 and 101. The amplitude spectrums of the designed filters for a filter length N = 51 are shown in Figure 6. The results show that the best filter design performance is exhibited by filters designed with Cosh-Hamming and Cosh-Von Hann windows, respectively, while the worst performance is exhibited by filters designed with Poisson and Cosh-Nuttal windows. In addition, from the values given in Table 3, it is seen that when the filter length is increased, the minimum stop band attenuation remains almost the same, while the transition bandwidth is reduced by half to a better value.

Table 3. Comparison of the digital filters designed with hybrid windows and other two-parameter windows in terms of minimum stop band attenuation at different filter length values

Window	N = 51		N = 101	
	$\Delta\omega$ (rad/s)	A_s (dB)	$\Delta\omega$ (rad/s)	A_s (dB)
Cosh-Hamming (w10)	0.1065π	48.92	0.0533π	48.75
Cosh-Von Hann (w19)	0.1065π	48.86	0.0533π	48.71
Kaiser-Hamming [7]	0.1065π	48.16	0.0533π	48.01
Dolp-Chebyshev [1]	0.1065π	48.10	0.0533π	47.99
Exponential-Hamming [35]	0.1065π	47.10	0.0533π	47.07
Saramaki [9]	0.1065π	46.23	0.0533π	46.07
Kaiser [1]	0.1065π	45.89	0.0533π	45.86
Cosh-Welch (w20)	0.1065π	45.68	0.0533π	44.84
Gaussian [8]	0.1065π	44.15	0.0533π	44.02
Cosh-Parabolic (w14)	0.1065π	43.91	0.0533π	44.01
Cosh [10]	0.1065π	43.91	0.0533π	43.88
Exponential [34]	0.1065π	43.47	0.0533π	43.51
Cosh-Cosx (w6)	0.1065π	42.68	0.0533π	42.71
Cosh-Lancsoz (w11)	0.1065π	42.02	0.0533π	42.04
Cosh-Riemann (w17)	0.1065π	42.02	0.0533π	42.04
Cosh-Bartlett Hann (w2)	0.1065π	40.78	0.0533π	40.74
Cosh-Cos³x (w7)	0.1065π	36.30	0.0533π	36.24
Cosh-Blackman (w3)	0.1065π	34.70	0.0533π	34.66
Cosh-Opt. Blackman (w13)	0.1065π	33.90	0.0533π	33.86
Hann-Poisson [8]	0.1065π	33.46	0.0533π	33.70
Cosh-Bohman (w5)	0.1065π	33.21	0.0533π	33.18
Cosh-Triangular (w18)	0.1065π	31.65	0.0533π	31.47
Cosh-Nuttal (w12)	0.1065π	29.36	0.0533π	29.36
Poisson [8]	0.1065π	22.11	0.0533π	22.15
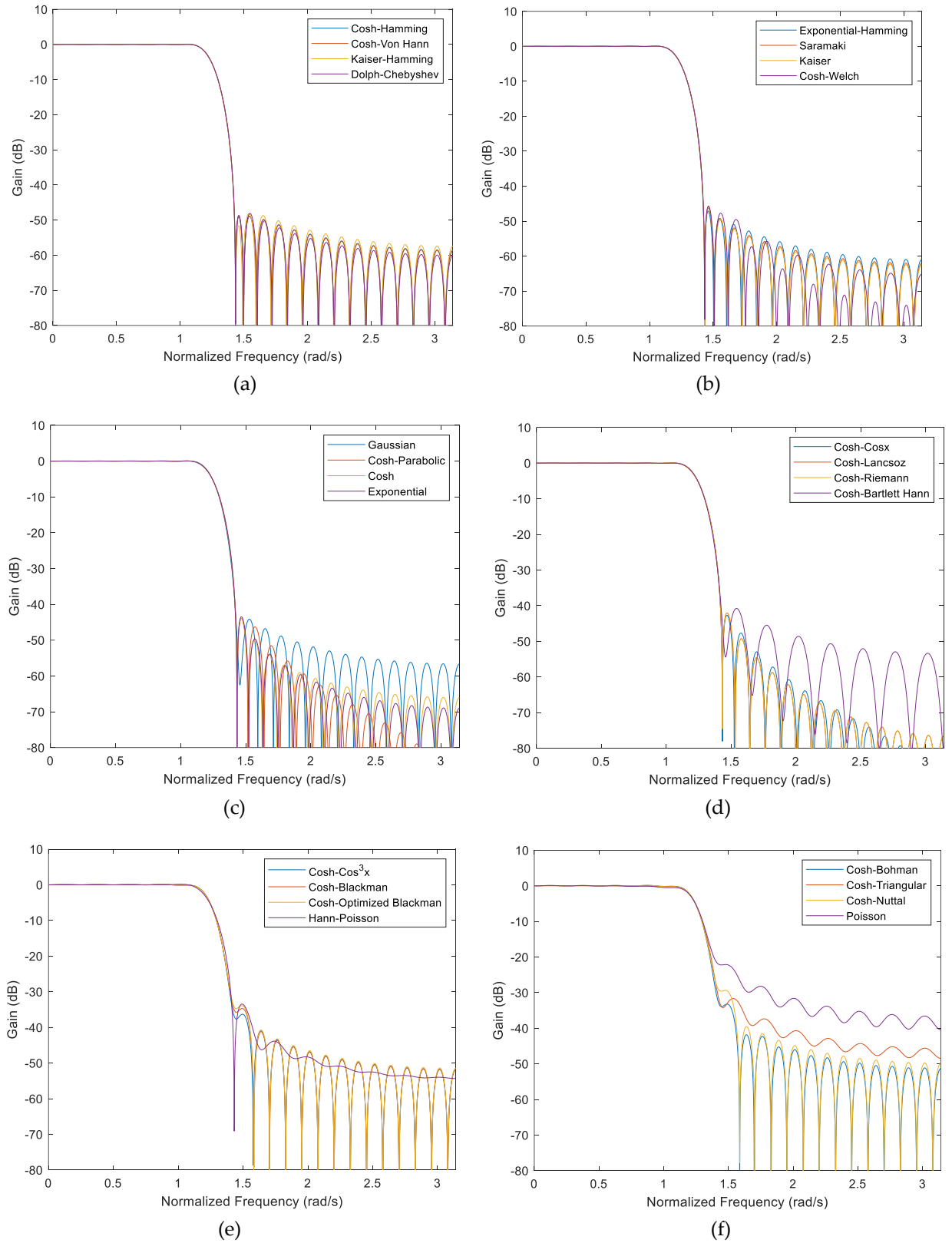
Figure 6. Amplitude spectrums of digital filters designed with the proposed windows and the adjustable windows in the literature for filter length of N = 51

4. CONCLUSIONS

In this study, new hybrid windows are proposed by weighting the fixed windows in the literature with equal coefficients with the two-parameter adjustable window, namely Cosh window, and their performances in filter design are examined, as extended version of our study [36]. First, the minimum stop band attenuation and transition width characteristics of 20 hybrid windows obtained by many filter design results are achieved. The filter performances are observed by comparing them with the filters designed with the Cosh window. The results show that filters designed with only nine hybrid windows (Cosh-Cosx, Cosh-Cos³x, Cosh-Hamming, Cosh-Lancsoz, Cosh-Parabolic, Cosh-Rectangular, Cosh-Riemann, Cosh-Von Hann, and Cosh-Welch) can exhibit better filter spectral characteristics than Cosh window-based filters at certain intervals. Meanwhile, among hybrid windows, the filtering performances of Cosh-Bartlett, Cosh-Bartlett Hann, Cosh-Blackman, Cosh-Blackman Harris, Cosh-Bohman, Cosh-Cos⁴(x), Cosh-Flat Top, Cosh-Nuttal, Cosh- Optimized Blackman, Cosh-Parzen, Cosh-Triangular are always worse than the Cosh window, therefore the hybridization in these windows is not significant for filter design applications. Finally, the performances of the nine hybrid windows in filter design are examined in comparison with other two-parameter windows in the literature. As a result of the filter spectral analysis for N = 51 and N = 101, it is observed that the filters designed based on Cosh-Hamming and Cosh-Von Hann windows can provide better results than filters designed with other windows. The proposed windows can also be used in applications such as communication [37-39], image processing [40, 41] and biomedical processing [42, 43] instead of the Kaiser window and other well-known windows.

Declaration of Ethical Standards

As the authors of this study, we declare that all ethical standards have been complied with.

Credit Authorship Contribution Statement

Author contribution rates are equal in this study.

Declaration of Competing Interest

The authors declare that there is no conflict of interest.

Funding / Acknowledgements

No funding is available for this research.

Data Availability

This study does not contain any dataset.

REFERENCES

[1]   A. Antoniou, *Digital Signal Processing: Signal, Systems and Filters*, NY, USA: McGraw-Hill, 2005.

[2]   A. Jiang, H. K. Kwan, Y. Tang, and Y. Zhu, "Sparse FIR filter design via partial 1-norm optimization," *IEEE Transactions on Circuits and Systems II: Express Briefs*, vol. 67, no. 8, pp. 1482-1486, Aug. 2020. [Online]. Available: https://doi.org/10.1109/TCSII.2019.2937343.

[3]   M. H. Nassralla, N. Akl, and Z. Dawy, "A clustering-based approach for designing low complexity FIR filters," *IEEE Signal Processing Letters*, vol. 28, pp. 299-303, 2021. [Online]. Available: https://doi.org/10.1109/LSP.2021.3050916.

[4]   A. L. Jayaweera, D. Pakiyarajah, and C. U. Edussooriya, "Minimax design of MD sparse FIR

filters with arbitrary frequency response using SOCP," *IEEE Transactions on Circuits and Systems II: Express Briefs*, vol. 69, no. 5, pp. 2403-2407, May 2022. [Online]. Available: https://doi.org/10.1109/TCSII.2022.3160400.

[5]   J. Yang, H. Yang, X. Yang, and J. Yang, "Optimal design of digital FIR filters based on back propagation neural network," *IEICE Electronics Express*, vol. 20, no. 1, pp. 1-6, 2023. [Online]. Available: https://doi.org/10.1587/elex.19.20220491.

[6]   P. Bloomfield, *Fourier Analysis of Time Series: An Introduction*, NY, USA: Wiley-Interscience, 2000.

[7]   K. Avci, "Kaiser-hamming window and its performance analysis for nonrecursive digital filter design," *Journal of the Faculty of Engineering and Architecture of Gazi University*, vol. 29, no.4, pp. 823-833, 2014. [Online]. Available: https://doi.org/10.29109/http-gujsc-gazi-edu-tr.335872.

[8]   K. M. M. Prabhu, *Window Functions and Their Applications in Signal Processing*, Taylor & Francis, 2014.

[9]   T. Saramaki, "Adjustable windows for the design of FIR filters-a tutorial," In Proc. 6th Mediterranean Electrotechnical Conference, Ljubljana, Slovenia, 1991, pp. 28–33.

[10]   K. Avci and A. Nacaroğlu, "Cosh window family and its application to FIR filter design", *Int. Journal of Electronics and Communications (AEÜ)*, vol. 63, no. 11, pp. 907-916, 2009. [Online]. Available: https://doi.org/10.1016/j.aeue.2008.07.013.

[11]   S. W. A. Bergen and A. Antoniou, "Design of nonrecursive digital filters using the ultraspherical window function," *EURASIP Journal on Appl. Signal Proc.*, vol. 12, pp.1910-1922, 2005. [Online]. Available: https://doi.org/10.1155/ASP.2005.1910.

[12]   K. Avci and A. Nacaroğlu, "Modification of cosh window family," In Proc. Third International Conference on Information and Communication Technologies (ICTTA'08), Damascus, Syria, 2008, pp. 291-292.

[13]   K. Avci and A. Nacaroğlu, "An efficient study on the modification of kaiser window", In Proc. 7th International Conference *COMMUNICATIONS*, Bucharest, Romania, 2008, pp. 63-66.

[14]   R. G. Kulkarni, "Synthesis of a new signal processing window," *Electronics Letters*, vol. 55, no. 20, pp. 1108-1110, 2019. [Online]. Available: https://doi.org/10.1049/el.2019.2116.

[15]   J. F. Justo and W. Beccaro, "Generalized adaptive polynomial window function," *IEEE Access*, vol. 8, Oct., pp. 187584-187589, 2020. [Online]. Available: https://doi.org/10.1109/ACCESS.2020.3030903.

[16]   Y. C. Lim, T. Saramaki, P. S. Diniz, and Q. Liu, "A method for scaling window sidelobe magnitude," *IEEE Signal Processing Letters*, vol. 28, pp. 1056-1059, 2021. [Online]. Available: https://doi.org/10.1109/LSP.2021.3079847.

[17]   Y. C. Lim, Q. Liu, P. S. Diniz, and T. Saramaki, "Efficient scaling of window function expressed as sum of exponentials," *IEEE Signal Processing Letters*, vol. 29, pp. 1814-1817, 2022. [Online]. Available: https://doi.org/10.1109/LSP.2021.3050916.

[18]   Y. C. Lim, Q. Liu, P. S. Diniz, and T. Saramaki, "Efficient design of scaled rectangular (Saramaki) window," *IEEE Signal Processing Letters*, vol. 29, pp. 489-492, 2022. [Online]. Available: https://doi.org/10.1109/LSP.2022.3141309.

[19]   A. Noureddine, M. Boussif, and C. Adnane, "A modified ultraspherical window and its application for speech enhancement," *Traitement du Signal*, vol. 39, no. 1, pp. 79-86, 2022. [Online]. Available: https://doi.org/10.18280/ts.390108.

[20]   R. Avanzato, F. Beritelli, G. Capizzi, and G. L. Sciuto, "A new design methodology for window-based FIR filters," *Electronics Letters*, vol. 59, no. 11, pp. 1-3, 2023. [Online]. Available: https://doi.org/10.1049/ell2.12815.

[21]   T. Yamaoka, and S. Kageme, "New class of cosine-sum windows," *IEEE Access*, vol. 11, pp. 5296-5305, 2023. [Online]. Available: https://doi.org/10.1109/ACCESS.2023.3236606.

[22]   V. Misra, N. Singh, and M. Shukla, "Performance analysis of cosine window function," *Applications and Applied Mathematics: An International Journal (AAM)*, vol. 17, no. 3, pp. 108-118, 2022. [Online]. Available: https://digitalcommons.pvamu.edu/aam/vol17/iss3/9.

[23] H. N. Uzo, H. U. Nonyelu, J. N. Eneh, T. I. Ozue, E. C. Anoliefo, V. C. Chijindu, and O. U. Oparaku, "FIR filter design using raised semi-ellipse window function," *Indonesian Journal of Electrical Engineering and Informatics (IJEEI)*, vol. 10, no. 3, pp. 592-603, 2022. [Online]. Available: http://dx.doi.org/10.52549/ijeei.v10i3.3799.

[24] J. K. Gautam, A. Kumar, and R. Saxena, "On the modified bartlett-hanning window (family)," *IEEE Transactions on Signal Processing*, vol. 44, no. 8, pp. 2098-2102, 1996. [Online]. Available: https://doi.org/10.1109/78.533733.

[25] A. V. Oppenheim, R. W. Schafer, and J. R. Buck, *Discrete-Time Signal Processing*, Upper Saddle River, NJ: Prentice Hall, 1999.

[26] F. J. Harris and J. Fredric, "On the use of windows for harmonic analysis with the discrete Fourier transform," *Proceedings of the IEEE*, vol. 66, no.1, pp. 51-83, 1978. [Online]. Available: https://doi.org/10.1109/PROC.1978.10837.

[27] G. D'Antona and A. Ferrero, *Digital Signal Processing for Measurement Systems*, NY, USA: Springer Media, 2006.

[28] C. Lanczos, *Applied Analysis*, Courier Corporation, 1988.

[29] A. H. Nuttall, "Some windows with very good sidelobe behavior," *IEEE Transactions on Acoustics, Speech, and Signal Processing*, vol. 29, no. 1, Feb., pp. 84-91, 1981. [Online]. Available: https://doi.org/10.1109/TASSP.1981.1163506.

[30] S. N. Sharma, R. Saxena and A. Jain, "FIR digital filter design with Parzen and Cos6(πt) combinational window family," In Proc. 6th International Conference on Signal Processing, Beijing, China, 2002, pp. 92-95.

[31] J. W. Adams, "A new optimal window", *IEEE Transactions on Signal Processing*, vol. 39, no. 8, pp. 1753-1769, Aug. 1991. [Online]. Available: https://doi.org/10.1109/78.91146.

[32] A.E. Abed and G. Cain, "The host windowing technique for FIR digital filter design," *IEEE Transactions on Acoustics, Speech and Signal Processing*, vol. 32, no. 4, pp. 683-694, Aug. 1984. [Online]. Available: https://doi.org/10.1109/TASSP.1984.1164414.

[33] B. Üstün and K. Avci, "A New hybrid window based on Cosh and Hamming windows for nonrecursive digital filter design," In Proc. 23rd Signal Processing and Communications Applications Conference (SIU), Malatya, Turkey, 2015, pp. 2282-2285.

[34] K. Avci and A. Nacaroğlu, "A New window based on exponential function", In Proc. IEEE Ph.D. Research in Microelectronics and Electronics (PRIME 2008), Istanbul, Turkey, 2008, pp. 69-72.

[35] K. Avci, "Design of FIR filters using exponential–hamming window family", *Turkish Journal of Electrical Engineeing & Computer Sciences*, vol. 24, no. 4, pp. 2513 – 2524, 2016. [Online]. Available: https://doi.org/10.3906/elk-1312-246.

[36] K. Avcı and O. Coşkun, "Spectral performance analysis of cosh window based new two parameter hybrid windows," In Proc. 26th Signal Processing and Communications Applications Conference (SIU), Izmir, Turkey, 2018, pp. 1-4.

[37] W. Wei, X. Yu, Q. Lu, X. Wang, and G. Cui, "Window function design for asymmetric beampattern synthesis and applications," *IEEE Signal Processing Letters*, vol. *30*, pp. 284-288, 2023. [Online]. Available: https://doi.org/10.1109/LSP.2023.3259163.

[38] E. Simsek *et al.*, "Fast evaluation of RF power spectrum of photodetectors with windowing functions," *IEEE Transactions on Electron Devices*, vol. 70, no. 7, pp. 3643-3648, July 2023. [Online]. Available: https://doi.org/10.1109/TED.2023.3275553.

[39] K. Karwowska and D. Wierzbicki, "Improving spatial resolution of satellite imagery using generative adversarial networks and window functions," *Remote Sensing*, vol. 14, no. 24, pp. 6285, 2022. [Online]. Available: https://doi.org/10.3390/rs14246285.

[40] G. P. K.R., A. K. Gande and G. Ram, "A novel very low power leakage factor window for image processing applications," *IEEE Geoscience and Remote Sensing Letters*, vol. 20, pp. 1-5, 2023. [Online]. Available: https://doi.org/10.1109/LGRS.2023.3234903.

[41] P. Walek and J. Jan, "Two-dimensional shape-adaptive windowing functions for image

analysis," *IET Image Processing*, vol. 13, no. 11, pp. 1853-1861, 2019. [Online]. Available: https://doi.org/10.1049/iet-ipr.2018.5697.

[42]   T. Karmaker, M. S. Anower, M. A. G. Khan and M. A. Habib, "A new adjustable window function to design FIR filter and its application in noise reduction from contaminated ECG signal," In Proc. IEEE Region 10 Humanitarian Technology Conference (R10-HTC), Dhaka, Bangladesh, 2017, pp. 51-54.

[43]   F. Serbet, and T. Kaya, "Statistical analysis and EEG signal filtering using design of window function based on optimization methods," *Journal of Circuits, Systems and Computers*, vol. 32, no. 8, 2023, [Online]. Available: https://doi.org/10.1142/S0218126623503061.

EFFECT OF PILE GEOMETRY AND SOIL SATURATION DEGREE ON POINT BEARING CAPACITY FOR BORED PILES IN SANDS

1,* Yavuz YENGİNAR [iD] **, ² Bekir FİDAN** [iD] **, ³ Murat OLGUN** [iD]

¹ *Necmettin Erbakan University, Engineering Faculty, Civil Engineering Department, Konya, TÜRKİYE*
² *Ministry of Interior Disaster and Emergency Management Presidency (AFAD) Konya Provincial Directorate of Disaster and Emergency, Konya, TÜRKİYE*
³ *Konya Technical University, Engineering and Natural Sciences Faculty, Civil Engineering Department, Konya, TÜRKİYE*

¹ yyenginar@erbakan.edu.tr, ² bekirfidann@gmail.com, ³ molgun@ktun.edu.tr

Highlights

- Loading speed does not affect the ultimate point and total bearing capacities of the pile significantly.
- The base, shaft, and total bearing capacities of piles mobilized at different settlement values.
- The base and total capacities of piles decrease 65 to 75% when the dry soil becomes saturated.
- Experimental N_q coefficients were smaller than coefficients of Vesic and Meyerhof but closer to Janbu's.
- N_q value depends on the internal friction angle of soil, effective stress, pile diameter, and saturation degree.
- In dry and saturated sands, N_q value decreases since the pile length/pile diameter ratio increases.

Graphical Abstract
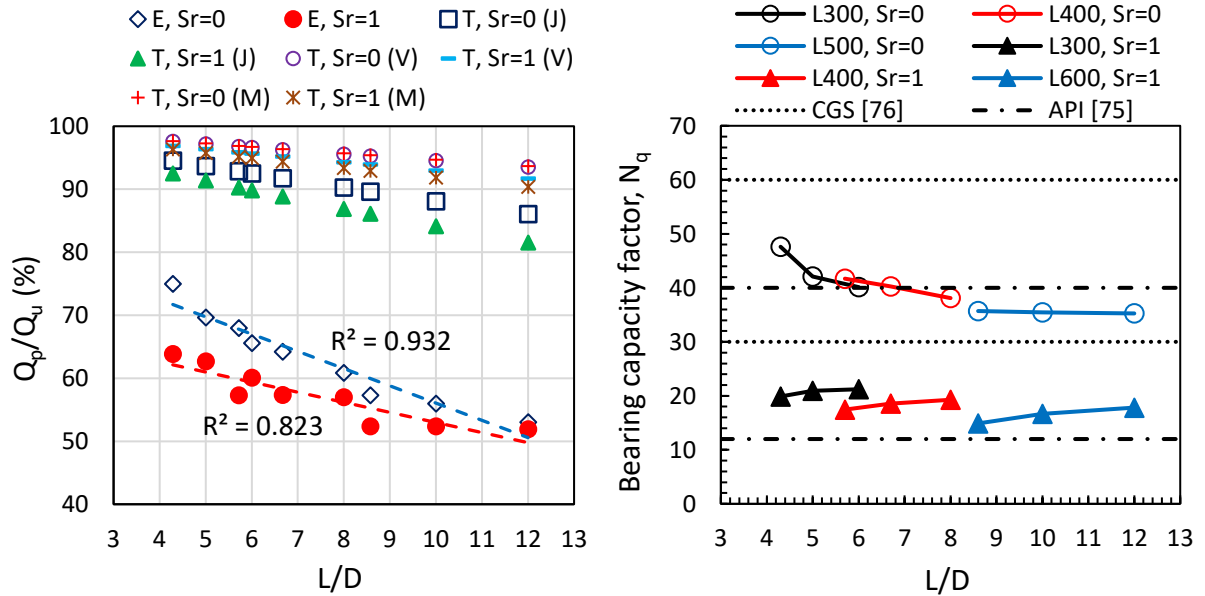
The percentage of point capacity in ultimate bearing capacity (left) and the variation of N_q values depending on L/D (right)
(Q_P: point capacity, Q_u: ultimate capacity, L: pile length, D: pile diameter, Sr: saturation degree of soil, E: experimental, T: theoretical, J: Janbu, V: Vesic, M: Meyerhof,)

*Corresponding Author: Yavuz YENGİNAR, yyenginar@erbakan.edu.tr

EFFECT OF PILE GEOMETRY AND SOIL SATURATION DEGREE ON POINT BEARING CAPACITY FOR BORED PILES IN SANDS

1,* Yavuz YENGİNAR , **2 Bekir FİDAN** , **3 Murat OLGUN**

1 Necmettin Erbakan University, Engineering Faculty, Civil Engineering Department, Konya, TÜRKİYE
2 Ministry of Interior Disaster and Emergency Management Presidency (AFAD) Konya Provincial Directorate of Disaster and Emergency, Konya, TÜRKİYE
3 Konya Technical University, Engineering and Natural Sciences Faculty, Civil Engineering Department, Konya, TÜRKİYE
1 yyenginar@erbakan.edu.tr, 2 bekirfidann@gmail.com, 3 molgun@ktun.edu.tr

ABSTRACT: In the present paper, an experimental study was conducted to determine the factors affecting the point bearing capacity of pile foundations constructed in dry and saturated sandy soils. Model piles were installed as reinforced concrete bored piles cast-in-situ. Model pile foundations of various geometries resting at different depths in homogeneous sand of different saturation degrees (%0-100) were loaded statically to failure. The test results showed that the bearing capacity of piles did not significantly affect by the loading rate. At most 10% difference was observed in pile bearing capacity when the loading rate was between 0.7 and 2.5 mm/min. Subsequently, the load bearing capacities of the piles were determined at a specified constant loading rate. The point and total capacities of the piles were measured separately in the experiments, then test results were compared with theoretical values. Pile point capacities provided from pile load tests are smaller than the theoretical values. The differences between experimental and theoretical results have been attributed to the N_q values. The N_q values not only dependent on the internal friction angle of the soil but also the saturation degree of the soil, the pile diameter, and the effective stress. N_q values decrease since the pile length/pile diameter ratio increases.

Keywords: *Bearing Capacity Factor, Pile Load Test, Point Resistance, Sand, Saturation Degree, Single Pile*

1. INTRODUCTION

Pile foundations are the most preferred practices in solving the foundation problems, such as bearing capacity, settlement, stability problems, liquefaction, and groundwater flow. In field applications, pile foundations are manufactured for soldier piles (lateral loaded piles) [1], [2] or soil reinforcement piles (vertical loaded piles) [3], [4], [5]. In soil reinforcement works, more than one pile is manufactured according to the project requirements, and the piles are ensured to carry the load as a group. If a raft plate is manufactured on the pile group, the system becomes a piled raft. In the pile foundation systems (single pile, pile group, and pile raft), the load-bearing capacity and load-settlement behavior of each pile are different [6]. The piled raft system is mostly used in soil reinforcement works and the load transfer mechanism between the pile-soil-raft is very complex [6], [7], [8]. If the load-settlement behavior of single piles can be determined accurately, it will enable more reliable designs of pile groups and piled rafts.

Pile foundations are classified as point bearing or friction piles according to the mechanisms of load transfer. The total bearing capacity of the pile is mostly met by the shaft capacity in friction piles and by the point capacity in the point bearing piles [9], [10]. However, the point capacity of piles installed in sandy soil constitutes a significant portion of the pile bearing capacity [11], [12], [13], [14]. Point and shaft capacities are not independent of one another because improving the load-bearing layer at the pile base is not only increases point capacity but at the same time improves the shaft capacity [15].

The soil properties (soil type, shear strength parameters), pile material type (steel, concrete, wood), the construction method (driven or bored piles), the loading direction (axial or lateral), and groundwater

---

*Corresponding Author: Yavuz YENGİNAR, yyenginar@erbakan.edu.tr

conditions (effective stress and pore water pressure) have decisive effects on the load-settlement characteristics of pile. There are still some uncertainties on the pile behavior since many factors affect the pile-soil interactions. In the last decade, empirical or semi-empirical methods enhanced to determine the load transfer mechanism of bored piles [16], [17], [18], [19], [20]. In addition, some analytical models have been developed to estimate pile capacity considering the pile diameter, soil properties, and stress in soil body [21], [22], [23], [24], [25], [26]. In non-displacement piles, Han et al. [27] reported that increments of relative density of sand and lateral stress at pile base increase the ultimate base resistance but pile diameter has no effect on base resistance.

The bearing capacity factor (N_q) is the most important parameter affecting the pile point resistance. N_q values usually get constant values according to the internal friction angle of the soil (ϕ). Many researchers have developed equations or graphs for the N_q coefficient depending on the ϕ [28], [29], [30], [31], [32], [33]. Cheng [34] proposed to increase the N_q values developed by Berezantzev [28] by 4 to 10%.

The pile point resistance also increases by the effective stress in soil body. However, pile load tests in the field cases indicate that a linear increase was not observed on point resistance, depending on the effective stress in soil. Consequently, the expression of "limit point pressure" to limit the point resistance has been developed [31], [35]. The limitation of the point resistance is caused by the arching and clamping effects occurring in the soil. The pile point resistance increases with depth at a gradually decreasing rate and it is stated that there is no limit value [28], [29], [36], [37]. Meyerhof [38] and Bolton [39] reported that the main reason for the decrease in "the amount of increase in the point resistance" is the reduction in the internal friction angle of the soil because of increasing confining pressure with depth.

The groundwater level may change depending on the seasonal conditions. This situation affects the bearing capacity of pile foundations and may lead to an increase in settlement. Studies, where groundwater level has been taken into account, are generally on structures manufactured on the seashore or offshore and are mostly performed on driven steel piles [40], [41], [42], [43], [44]. Very few studies investigated the load-settlement behavior of bored (nondisplacement) piles in saturated soils. Nguyen et al. [45] reported that as a result of the lowering of groundwater, the bending moments on piles and the amount of settlement are increasing and then structural damage occurs. Sheikhtaheri [46] stated that the point and shaft capacities of the piles in saturated sandy soil decrease by 2-2.5 and 5 times, respectively, as compared with the piles installed in non-saturated soil. Olgun et al. [47] reported that the pile shaft capacity decreases by 55.7% to 68.2% depending to pile length/diameter ratio when groundwater level rises. Mukhlisin *et al.* [48] stated that increasing soil moisture content cause a decrease in friction resistance. Pile shaft capacity decreases when groundwater level increases since effective stress in soil mass decreases [49], [50]. Chong and Ong [51] observed relatively large settlements in contiguous bored pile due to the sudden decrease of groundwater during tunnel construction. In addition, axial force on the pile increases due to the negative skin friction if settlement of soil is more than pile settlement during groundwater lowering [52]. This phenomenon decreases the pile bearing capacity [53].

In this study, model piles have diameters of 50-60-70 mm and lengths of 300-400-600 mm were installed in sandy soil. Thus, piles similar to one in the field are modeled in the laboratory. Firstly, a model pile loaded in nine different loading rates (between 0.7 and 2.5 mm/min) and the differences in bearing capacity were investigated. Subsequently, the load-settlement behaviors of the model piles constructed in dry and saturated sandy soils having the same void ratio were investigated with constant penetration load tests. In the tests, the point and total bearing capacities of the piles were measured separately. The effect of the soil saturation degree, pile length, and pile diameter on the point and total bearing capacities of piles were investigated. This study is an extended version of the previous study [54], in which only the load-bearing capacity of the pile base was investigated. The novel approaches of this study are model piles have more realistic surface roughness since they are manufactured as cast-in-place reinforced concrete, load-settlement values of the pile base are measured directly, pile loading tests carried out in a large-scale test setup, and groundwater effect is included.

2. PILE BEARING CAPACITY

The ultimate load capacity of the pile can be determined with the following equation:

$$Q_u = Q_f + Q_p \tag{1}$$

where; Q_u=ultimate pile capacity in compression, Q_f=ultimate load capacity of pile shaft, Q_p=ultimate load capacity of the pile point.

2.1 Point Capacity

Generally, the point capacity of piles installed in sandy soil could be found by the following relationship [31]:

$$Q_p = \sigma' N_q A_p \tag{2}$$

where; σ'=effective vertical stress at the level of pile end, N_q=bearing capacity factor, A_p=area of pile point.

The N_q value suggested by Vesic [33] and Janbu [30] is given in Eq. 3 and Eq. 4, respectively. Meyerhof [55] developed a graphical chart for N_q values depending on ϕ (Figure 13), but there is no analytical formula.

$$N_q = \frac{3}{3-sin\,\phi}\left\{exp\left[\left(\frac{\pi}{2} - \phi\right)tan\,\phi\right]tan^2\left(45^0 + \frac{\phi}{2}\right)Irr^{\frac{1.333\,sin\,\phi}{1+sin\,\phi}}\right\} \tag{3}$$

$$N_q = \left(tan\,\phi + \sqrt{1 + tan^2\,\phi}\right)^2 exp(2\psi\,tan\,\phi) \tag{4}$$

where; I_{rr}=reduced rigidity index ($I_{rr} = I_r/(1 + I_r \Delta)$), I_r=rigidity index (for sand 75-150), Δ=average volumetric strain in the plastic zone below the pile point, ψ angle is given in Figure 1 and changes between 60° (loose sand) and 105º (dense sand).
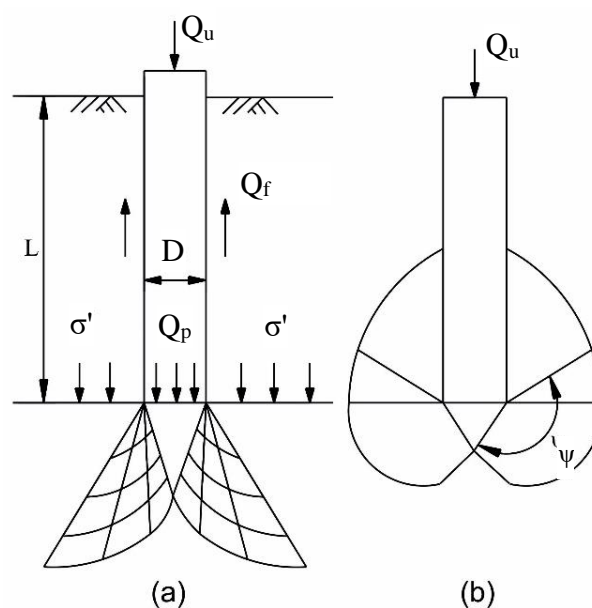
Figure 1. The shear surfaces at the pile point at failure a) Vesic, b) Janbu, and Meyerhof [56]

Equation (2) indicates that the pile point capacity increases linearly depending on the effective stress since N_q and A_P have constant values according to soil and pile properties, respectively. However, Vesic [33] stated that due to the coupling effect on the soil after a depth of 20D, the pile point capacity remains constant. In addition, critical pile depth (L_{cr}) is recommended as 10D, 15D, and 20D for loose, medium dense, and dense sands, respectively [57]. Poulos and Davis [35] defined the L_{cr} depending on the internal friction angle as follows:

$$L_{cr}/D = 5 + 0.24(\phi - 28) \qquad 28<\phi<36.5 \tag{5}$$
$$L_{cr}/D = 7 + 2.35(\phi - 36.5) \qquad 36.5<\phi<42 \tag{6}$$
$$\phi = \phi_1 - 3 \quad \text{for bored piles} \tag{7}$$

where; L_{cr}=critical depth, D=pile diameter, ϕ_1=angle of internal friction prior to the installation of the pile

2.2 Shaft Capacity

Burland [58] has proposed the following relationship for piles installed in sandy soil for shaft capacity:

$$Q_f = \beta \cdot \sigma_o' \cdot A_s \tag{8}$$
$$\beta = K \cdot \tan \delta \tag{9}$$

where; σ_o' =average effective vertical stress, K=the lateral earth pressure coefficient, δ=effective friction angle between soil and pile material, A_s=pile surface area

The shaft capacity increases linearly but the shaft capacity remains constant, as with the pile point capacity, after a critical depth (15D) [10].

3. EXPERIMENTAL SETUP

The experimental setup has a model tank box or container, a loading frame, a hydraulic piston, hydraulic control unit, and data acquisition unit, load cells, and dial gauges (Figure 2). Diameter and height of the model tank are 65 cm and 110 cm, respectively. The hydraulic loading unit, which has 100 kN-capacity, is fixed to the upper part of the loading frame. The loading speed of the piston can be adjusted from a hydraulic control unit. The load and settlement values measured during the test are recorded by a software with the help of a data collection unit.
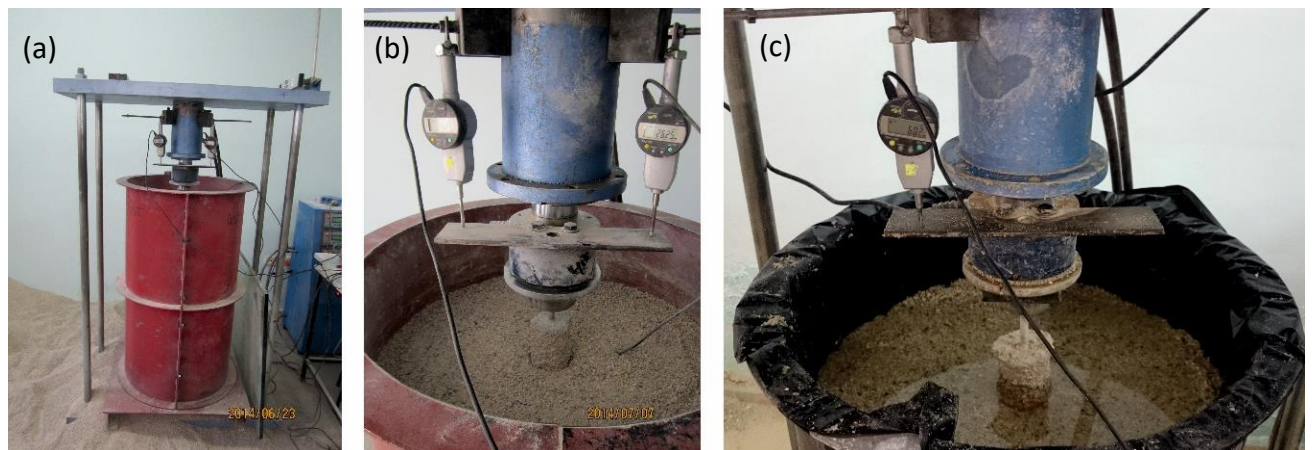
Figure 2. a) The general view of pile loading experimental setup on condition of b) S_r=0 and c) S_r=1

3.1 Geotechnical Properties of Soil

Sandy soil was used in the model pile loading tests. The sandy soil contains 44% coarse sand, 47% medium sand, and 9% fine sand (Figure 3). Sandy soil is classified as SP (poorly graded sand) according to USCS [59]. The geotechnical properties of the sand were given in Table 1. In the pile loading experiments, dry and saturated sandy soil masses having same void ratio were placed into the tank. The relative density of the soil was 39.4% by ASTM D4254-1 [60]. Internal friction angles of the soils were determined to be 37.2° and 34.5° in dry and saturated states, respectively, resulting from shear box tests [61].
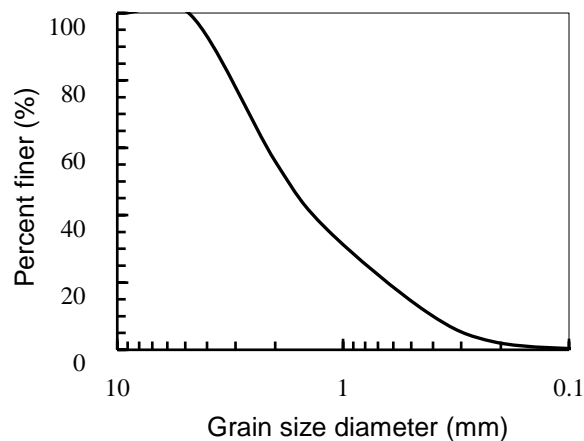
Figure 3. Grain size distribution of soil

Table 1. Geotechnical properties of sand

Coefficient of uniformity	C_u	4.87
Coefficient of curvature	C_c	1.09
Unit weight of soil particles	γ_s (kN/m³)	26.20
Dry unit weight	γ_d (kN/m³)	16.37
Saturated unit weight	γ_{sat} (kN/m³)	20.05
Maximum void ratio	e_{max}	0.730
Minimum void ratio	e_{min}	0.400

3.2 Construction of Model Piles

Model piles were manufactured as cast in-situ, reinforced concrete, and bored piles in the laboratory. During the pile installation process, casing pipes were used because the piles were manufactured in cohesionless soil. Firstly, the model container or box was filled with some amount of sand and then casing pipes were placed vertically on the sand surface. After that, the remaining part of the tank between the casing pipes was filled with sandy soil. Before the concreting process, a 12 mm diameter threaded rod was placed at the center of the casing pipe vertically. The threaded rod has been used for the reinforcement function and mounting the s-type load cell to the pile bottom. In the pile loading experiments, pile base capacity is measured directly by the virtue of load cell. During the concreting process, the piles were created by pulling up the casing pipe simultaneously (Figure 4a). Piles were being left two days in the soil to gain resistance against breakage (Figure 4b). After two days, the model piles were removed from the soil environment and they were cured in the curing pool for seven days to gain enough strength. The pile surface roughness and pile-soil interaction are provided to be similar to the field conditions by manufacturing model piles using this technique (Figure 4c). Constructed piles had diameters (D) of 50-60-

70 mm and lengths (L) of 300-400-600 mm and they were been named by diameter-length (D70L600, D50L300…).
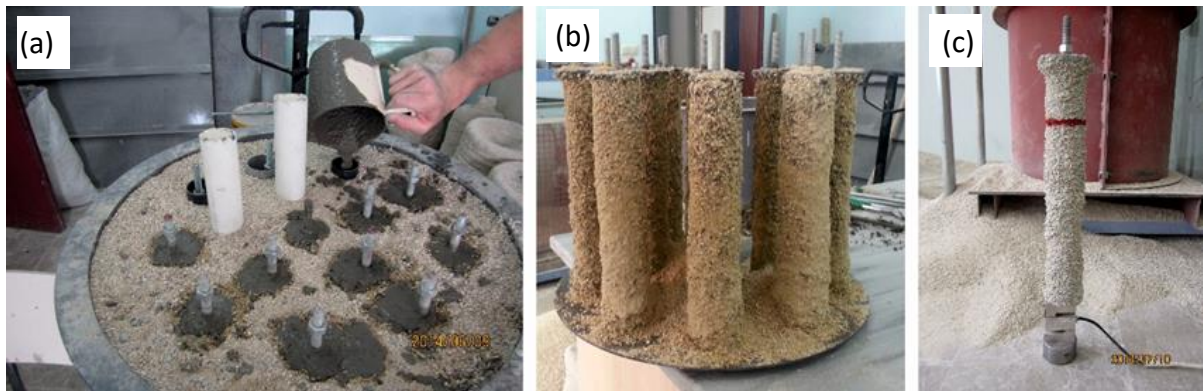
Figure 4. a, b) Construction of the piles in sandy soil, c) a model pile

3.3 Test Program and Methods

One of the aims of this study is to determine the changes in the pile bearing capacity due to changes in groundwater level. For this reason, in the model pile loading experiments, the soil condition must be in the same void ratio in dry and saturated conditions. The void ratio of dry and saturated soil mass is 0.6 (Dr=39.4%). In order to obtain same void ratio for both soil state, the mass of the soil at a certain height was determined using the grain density and dry/saturated unit weight properties of the soil. Then, the materials were weighed and placed in the tank. In the experiments performed in the dry state, the sand inside a funnel was always dropped from the same height (pluviation technique), flowing by its weight, into the test tank. In the experiments performed in saturated sand, the soil was placed into the test tank by tamping, laying, and compressing layer by layer. Compacting energy applied to soil (hammer weight, number of blows, and height of drop) was arranged to obtain the same void ratio with the sand of dry state. Before loading the model piles, static groundwater level raised up to soil surface and all voids between soil grains filled with water. To prevent water infiltration, a seamless plastic bag was used in experiments on saturated sandy soils (Figure 2c). In both soil conditions, the distance between pile end and bottom of the test tank is 40-70 cm (5.7D-10D) and 28-30 cm (3.8D-5.5D) from the tank surface to the pile surface (Figure 5a). Minimum distance between pile and container boundary is required 2.5D along the horizontal direction and 4D along the vertical direction for axial loading, where D is the pile diameter [62], [63]. In addition, D70L600 pile is modelled in Plaxis 3D software, and the stress at the container boundary is close to 0 kPa when the pile is loaded at ultimate capacity (2.36 kN or 653 kPa) (Figure 5b). The adequate distance between pile and tank surface exists in the model tests. Therefore, the stresses transferred from the pile to the soil do not reach the tank boundary.

The load-settlement behavior of the model piles was determined by loading the piles with a load larger than the failure load. That is, model piles were loaded until 40 mm settlement amount at which they were already reached to failure load. The ultimate pile capacity (Q_u) was measured with the total load applied from hydraulic piston. The load transferred to the pile end was measured by the load cell mounted to pile bottom, which gave the pile point capacity (Q_P). The pile shaft capacity (Q_f) was the difference between total and point capacities of the model pile. During the pile loading experiment, Q_P, Q_u and settlement (ΔH) values were recorded through the data acquisition system. After drawing the Q_P-ΔH and Q_u-ΔH curves, the limit values of Q_P and Q_u were determined by the tangent method [64]. In this method, the intersection points of the tangent lines drawn at the beginning and end parts of the load-settlement curve gives the limit load. The pile is mobilized at the settlement value corresponding to the limit load (Figure 6). In order to increase the reliability of the test results, each pile installed in identical soil conditions was subjected to the loading test at least twice. In case of a difference of less than 10% between repeated experiments, the average of them was taken; otherwise, an additional loading test were performed.
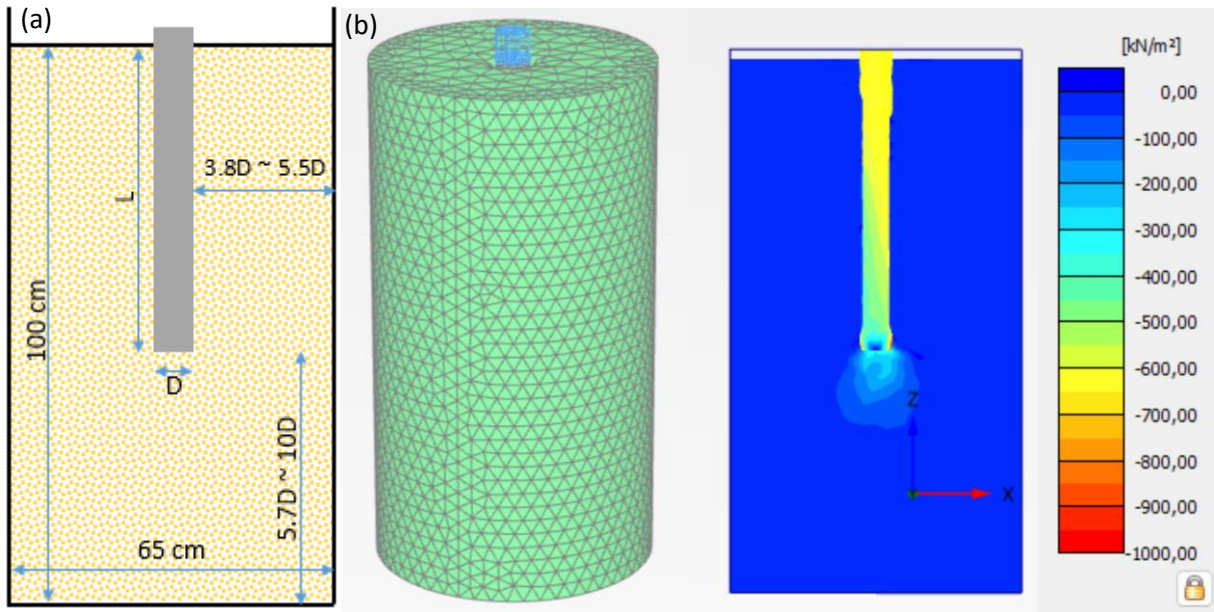
Figure 5. a) Experimental and b) numerical modelling of test pile in sand mass
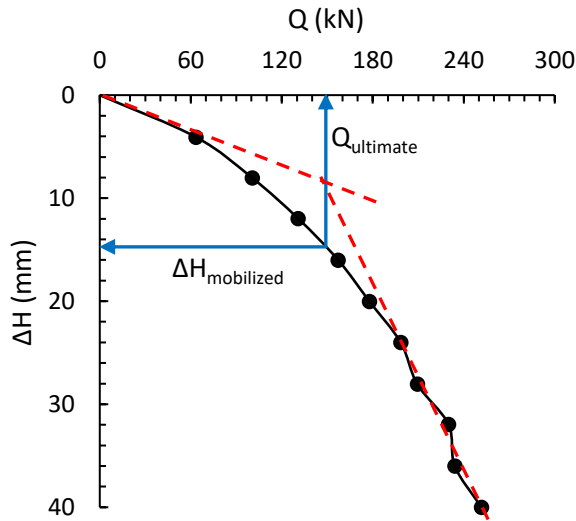
Figure 6. Application of tangent method

4. EXPERIMENTAL RESULTS

4.1 Effect of Loading Rate

Piles buried in dry and saturated soils were subjected to static loading. For this purpose, EN 1536:1999 [65] recommends the loading rate of piles as 1 mm/min, while ASTM D 1143-81 [66] suggests it as 1.25 mm/min. To examine the effect of loading rate on pile bearing capacity, the D70L600 pile was loaded at loading rates of 0.4-0.8-1.5-2.3-2.9-3.6-4.4-5.3-5.8 mm/min. According to the load-settlement curves (Q_P-ΔH, Q_u-ΔH), the rates of change in Q_P and Q_u values for different settlement amounts remained within the 6-10% level (Figure 7). This result shows that loading speed does not have a major effect on pile bearing capacity. Therefore, loading speed is 1.25 mm/min in pile loading tests.
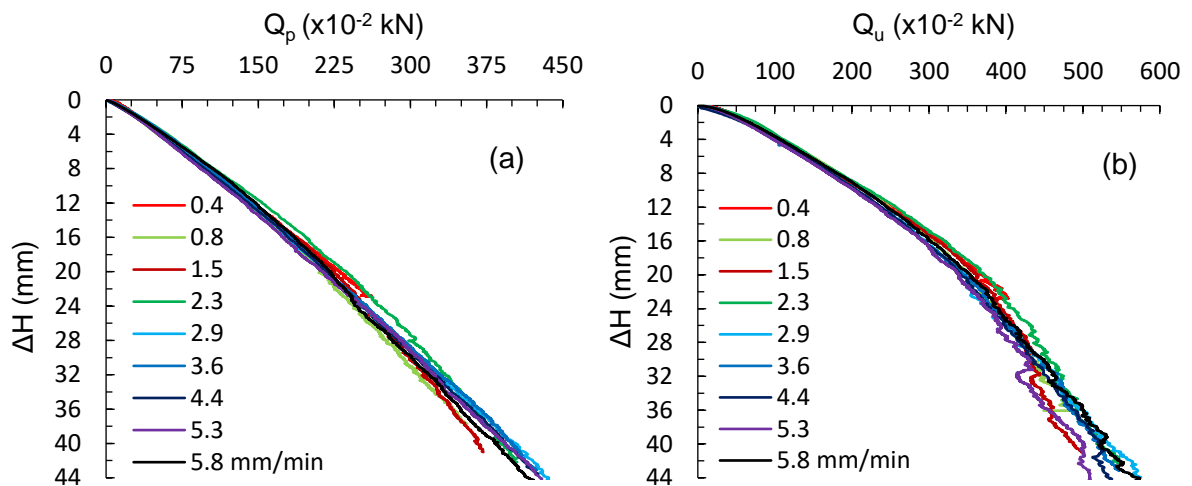
Figure 7. The load-settlement curves for D70L600 pile loaded in different loading speeds a) Q_P-ΔH curves, b) Q_u-ΔH curves

4.2 Pile Load Test Results

After the pile loading tests, the ultimate point and total bearing capacities of piles were determined by using the load-settlement curves given in Figure 8. The intersection points of tangent lines, which were drawn to the starting and ending portions of the load-settlement curves, was assumed to represent the ultimate bearing capacity of the pile [32] (Table 2). Ultimate bearing capacities of model piles were also calculated with analytical formulas (Equations 1-9). Theoretical ultimate base capacities of piles, using N_q coefficients developed by Janbu, Vesic, and Meyerhof, were calculated separately for each pile (Table 3 and Table 4).

In calculations made by existing theories, point capacities of piles are decreasing by 55.6%, 52.3%, and 60.8% according to methods of Janbu, Vesic, and Meyerhof, respectively, when soil changes from a dry state to a saturated state. The total bearing capacity reduce by 51.4 to 60.3% (Table 3 and Table 4). These reductions of the theoretical bearing capacities were not affected by the piles' geometry. K, tan δ, and N_q values used in formulas have fixed values depending on the internal friction angle of the soil (ϕ) having the same property. Therefore, pile point capacity increases linearly with depth depending on increment in effective stress. The internal friction angle of soil is modified by a few degrees since the saturation degree of the soil changes. However, change in ϕ does not affect the $K \cdot tan\,\delta$ value significantly. Due to the logarithmic increase in the value of N_q, changing a few degrees of ϕ affects the N_q value appreciably. However, the decrease in point capacity has been mostly caused by change in effective stress since the dry soil becomes saturated state. Pile loading test results show that the base capacities of piles decrease by 66.9 to 73.9% and 63.9 to 71.5% in total capacities when the dry soil becomes saturated (Table 2). In addition, decreasing amount of pile bearing capacity in the experiments is larger than the theory. Pile loading test results also reveal that variations on pile length and pile diameter affect reductions in pile bearing capacity proportionally.
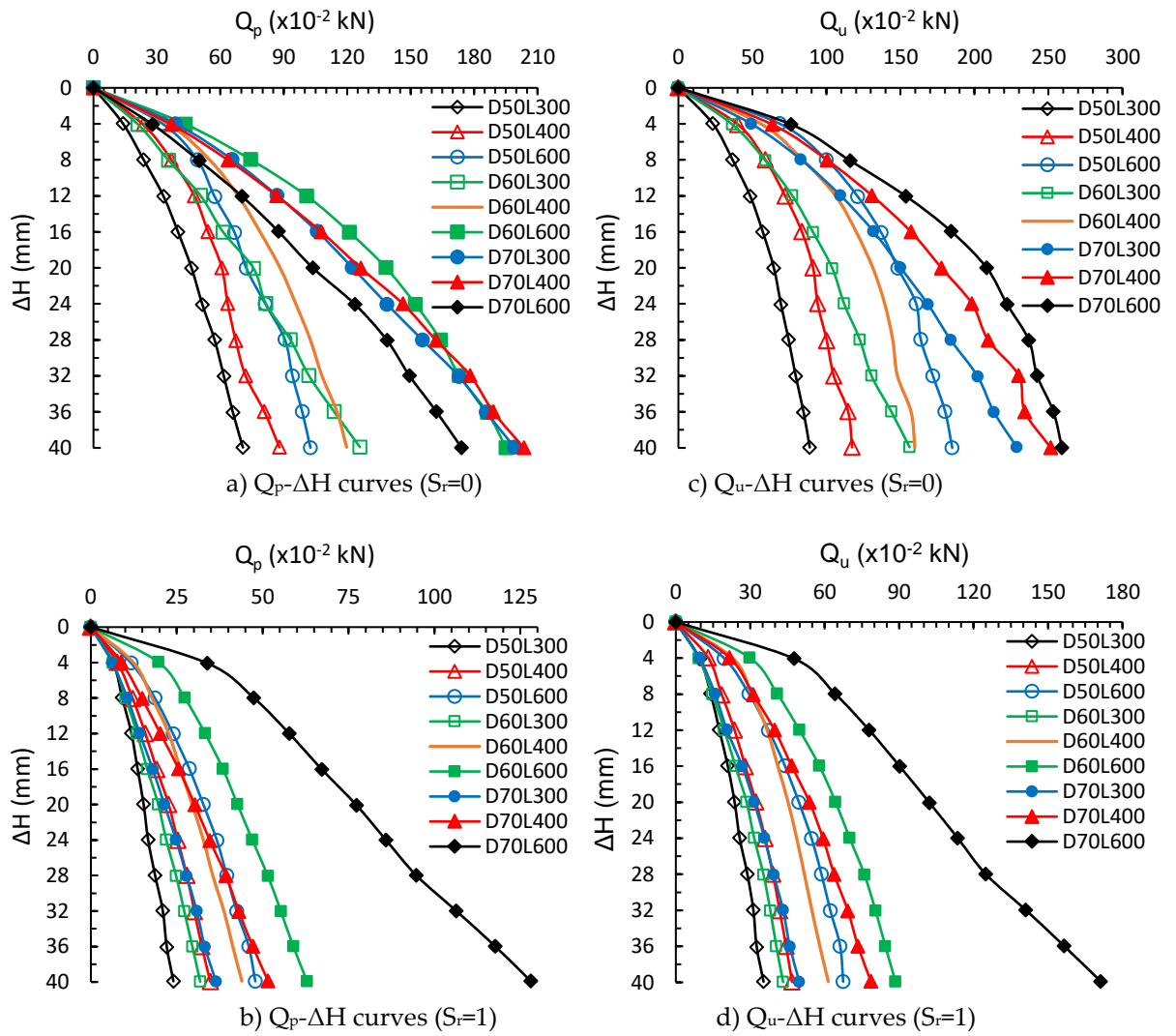
Figure 8. Load-settlement curves obtained from pile loading tests in dry (S_r=0) and saturated (S_r=1) sands

Table 2. Experimental results of ultimate bearing capacity values of the model piles in dry (S_r=0) and saturated (S_r=1) sandy soils

Piles	L/D	S_r=0				S_r=1			
		Q_p (kN)	ΔH (mm)	Q_u (kN)	ΔH (mm)	Q_p (kN)	ΔH (mm)	Q_u (kN)	ΔH (mm)
D70 L600	8.6	1.35	26.0	2.36	28.0	0.35	6.8	0.67	10.1
D70 L400	5.7	1.05	15.8	1.54	16.3	0.28	12.0	0.49	14.9
D70 L300	4.3	0.90	12.1	1.20	13.9	0.24	13.5	0.37	16.0
D60 L600	10.0	0.99	12.9	1.76	14.4	0.29	10.0	0.55	13.8
D60 L400	6.7	0.75	15.9	1.17	16.0	0.22	11.9	0.38	12.2
D60 L300	5.0	0.59	13.8	0.85	14.3	0.18	14.2	0.29	16.0
D50 L600	12.0	0.68	13.1	1.28	14.1	0.22	11.8	0.42	12.5
D50 L400	8.0	0.49	12.1	0.81	15.9	0.16	11.9	0.28	15.6
D50 L300	6.0	0.39	15.9	0.59	16.2	0.13	12.1	0.21	15.8

Table 3. Theoretical ultimate bearing capacity values of the model piles in dry soil (S_r=0)

Piles	Q_f (kN)	Q_p [a] (kN)			Q_u (kN)		
		Janbu	Vesic	Meyerhof	Janbu	Vesic	Meyerhof
D70 L600	0.20	1.68	3.92	4.05	1.88	4.12	4.25
D70 L400	0.09	1.12	2.61	2.70	1.21	2.70	2.79
D70 L300	0.05	0.84	1.96	2.02	0.89	2.01	2.07
D60 L600	0.17	1.24	2.88	2.97	1.41	3.05	3.14
D60 L400	0.07	0.82	1.92	1.98	0.89	1.99	2.05
D60 L300	0.04	0.62	1.44	1.49	0.66	1.48	1.53
D50 L600	0.14	0.86	2.00	2.06	1.00	2.14	2.20
D50 L400	0.06	0.57	1.33	1.38	0.63	1.39	1.44
D50 L300	0.04	0.43	1.00	1.03	0.47	1.04	1.07

[a] N_q values for ϕ=37.2° recommended by Janbu, Vesic, and Meyerhof are 44.5, 103.7, and 107, respectively. In the Janbu method, ψ is accepted as 90° at the pile base and in the Vesic method, I_{rr} is accepted as 100.

Table 4. Theoretical ultimate bearing capacity values of the model piles in saturated soil (S_r=1)

Piles	Q_f (kN)	Q_p [a] (kN)			Q_u (kN)		
		Janbu	Vesic	Meyerhof	Janbu	Vesic	Meyerhof
D70 L600	0.12	0.75	1.87	1.58	0.87	1.99	1.70
D70 L400	0.05	0.50	1.25	1.06	0.55	1.30	1.11
D70 L300	0.03	0.37	0.93	0.79	0.40	0.96	0.82
D60 L600	0.10	0.55	1.37	1.16	0.65	1.47	1.26
D60 L400	0.05	0.37	0.92	0.78	0.42	0.97	0.83
D60 L300	0.03	0.27	0.69	0.58	0.30	0.72	0.61
D50 L600	0.09	0.38	0.95	0.81	0.47	1.04	0.89
D50 L400	0.04	0.25	0.64	0.54	0.29	0.68	0.58
D50 L300	0.02	0.19	0.48	0.40	0.21	0.50	0.42

[a] N_q values for ϕ=34.5° recommended by Janbu, Vesic, and Meyerhof are 31.6, 79, and 67, respectively. In the Janbu method, ψ is accepted as 90° at the pile base and in the Vesic method, I_{rr} is accepted as 100.

Experimental results obtained in dry soil show that base capacity values of piles, according to the methods of Janbu, Vesic, and Meyerhof, were lower, by 0 to 20.8%, 54.1 to 66.0%, and 55.5 to 67.0%, respectively. The experimental ultimate load-bearing capacity of the piles was more than the method of Janbu at 25.4-34.9%, and less than the methods of Vesic and Meyerhof at 40-45% (Table 2 and Table 3). Experimental results obtained in saturated soil show that base capacity of piles was found lower by 32.8 to 52.9%, 73.1 to 81.2%, and 68.3 to 77.8% according to Janbu, Vesic, and Meyerhof, respectively. In terms of total capacity, according to Janbu, Vesic, and Meyerhof they were found lower, by 0.4 to 22.6%, 57.2 to 63.0%, and 50.0 to 60.6%, respectively (Table 3 and Table 4).

In general, base and total bearing capacity of piles installed in dry and saturated sands in the experiments were smaller than theoretical values. Dissimilarity in theoretical and experimental results discussed below.

4.2.1 Load-settlement behavior

The ultimate base and total capacities of single piles loaded in dry sands observed at the settlement levels of 12.1-26.0 mm and 13.9-28.0 mm, respectively. In saturated sand, the base and total capacities of piles mobilized at 6.8-14.2 mm and 10.1-16.0 mm settlement values (Table 2). The settlement values correspond to ultimate bearing capacity of pile, at the time of failure, are similar to Munaga et al. [67]. In the dry state, Q_p and Q_u were mobilized at normalized settlement values ($\Delta H/D$) of 17.3-31.8% (average of 25%). In the saturated state, Q_p and Q_u were mobilized at normalized settlement values of 9.7-23.8% (average of 20%) and 14.4-31.6% (average of 24%), respectively (Figure 9). Shakeel and Ng [68] observed 2% normalized pile settlement (45-50 mm) at the working load of 0.75Q_u for large scale field tests (D=0.6m,

L=20m). Wang et al. [69] observed that piles, whose diameters of 1.5-1.8m and lengths of 52-83m, were mobilized at settlement values of 55.5-87.4 mm corresponding to 2.5-6.0% of pile diameter. The normalized settlement values obtained in the laboratory were greater than the pile loading test results in the field. This difference may be due to the geometry of the piles (L/D ratio) at laboratory and field scales. The L/D ratio of piles in the laboratory is at most 12, but this ratio can be 30-55 in the field. Depending on the pile length, vertical and horizontal stresses in the ground affect the settlement of the pile. On the other hand, the results obtained from this study were similar to other laboratory-scale studies since the piles have a diameter of 2.84 cm and a length of 25.3 cm reached their ultimate bearing capacity at 20-25% normalized settlement value [70].

In general, piles in the saturated sand reached their limit base and total capacities at lower settlement levels than piles in the dry sand. Moreover, Q_u is mobilized at greater settlement value than Q_p in the dry and saturated state. That is, each of the base and total capacities of piles reached their ultimate capacities at different settlement levels in dry and saturated sandy soils (Figure 9). Consequently, the pile shaft capacity mobilized at smaller settlement values than the base and total capacities. The use of different safety factors for shaft and base capacities to calculate the allowable bearing capacity may provide the opportunity to make a more economical design [71], [72]. TBEC [73] recommends using safety factors of 1.5 and 2.0 for ultimate shaft and base capacities of piles, respectively.
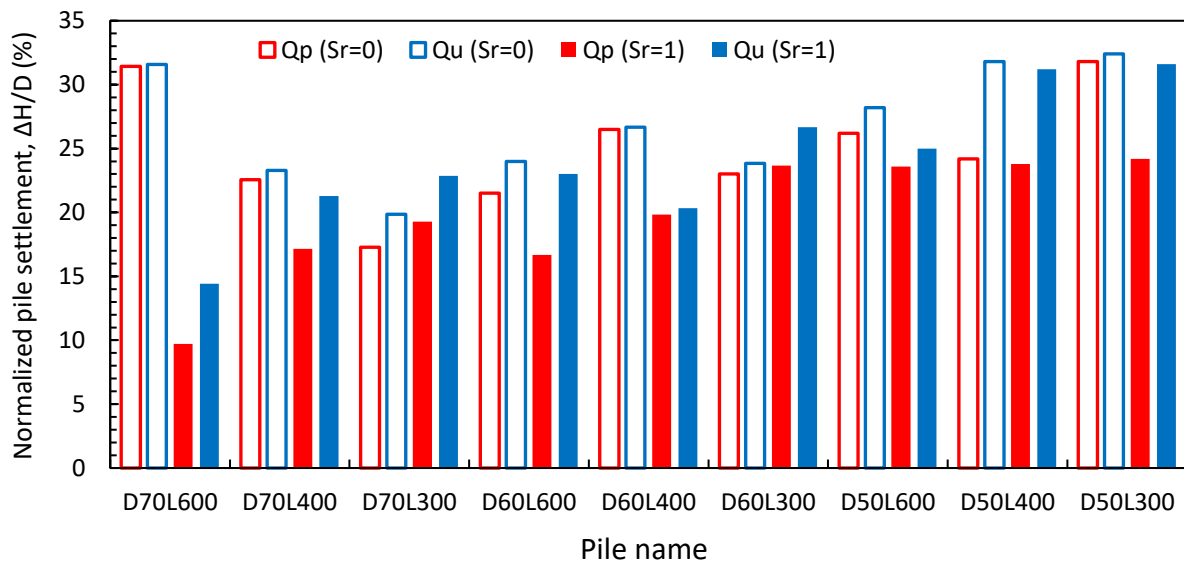
Figure 9. Normalized pile settlement values

A pile compresses the sandy soil under the pile bottom during the loading stage since settlement increases. Thus, the relative density and bearing capacity of soil under pile bottom increase. For this reason, point load-settlement curves of piles obtained from experiments exhibit quasi-linear behavior (Figure 8). Nevertheless, there is a point on the load-settlement curve at which the initial slope of the curve changes. In particular, piles installed in loose and medium dense sands exhibit similar behavior, and hence it is difficult to decide the ultimate base capacity of the pile in these soils [6], [54]. Compared with the piles in dry soils, the base capacities of piles in saturated sands reach their ultimate value at lower settlement values because the shear strength of saturated sand is less than dry sand having same relative density. In addition, the soil under the pile bottom moves more freely in vertical and lateral directions in saturated sands, when compared with dry sands.

4.2.2 Point resistance

There are differences between the experimental and theoretical results in pile base and total capacities. In the theoretical calculations, pile base capacities are 86 to 97.6% of the total bearing capacity in dry soil

and 81.5 to 97% in saturated soil. These results show that the pile point capacity constitutes a considerable part of the total load [9], [10], [32]. In the experimental results, the ratio of pile base capacity in the total bearing capacity represents 53 to 75% in dry soil, and 52 to 64% in saturated soil (Figure 10). Experimental results are closer to the load transfer mechanism of friction piles than theoretical results. The coefficients used to calculate the bearing capacity of the pile lead to the difference between experimental and theoretical results. Moreover, pile base capacity decreases if the L/D ratio increases (Figure 10). The same result was observed by Li et al. [74] in model pile loading experiments in sandy soils.
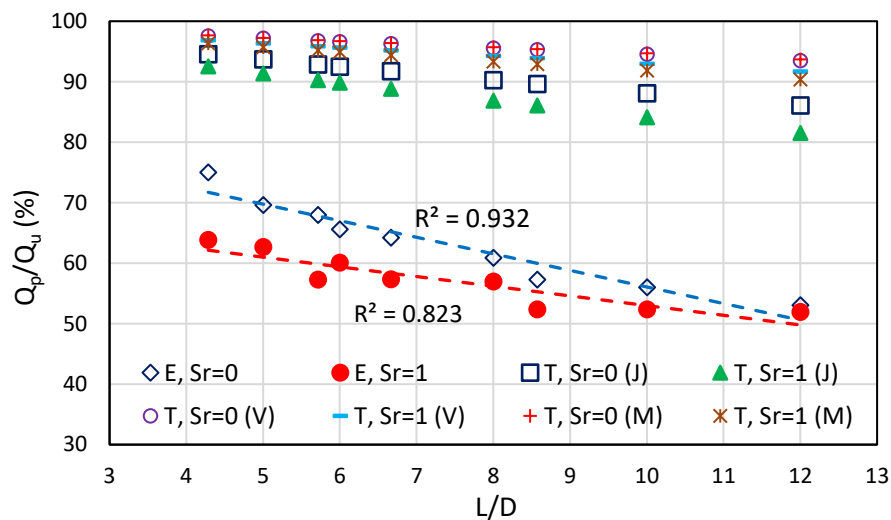
Figure 10. The percentage of point capacity in ultimate bearing capacity (E: experimental, T: theoretical, J: Janbu, V: Vesic, M: Meyerhof)

In theoretical methods, only the internal friction angle of the soil and the effective stress are considered while calculating the pile point resistance. However, the test results revealed that the diameter of the pile also affects the pile point resistance. In dry sands, the point resistance of same length piles decreases when L/D increases. That is, the point resistance increases when the pile diameter increases for piles having the same length (Figure 11). The contact area between soil particles and the pile bottom increases since the pile diameter increases. Therefore, point resistance increases. In saturated sands, for piles having the same length, the point resistance decreases as the pile diameter increases (when L/D decreases) (Figure 11). This is caused by the pore water pressure at the depth of pile base because a wider area is influenced by pore pressure.

The most important parameter affecting pile point resistance is the N_q value. In theory, N_q values vary depending on the ϕ of the soil. However, according to the test results, as the length of the same diameter piles in dry and saturated soil increases, the N_q values decrease (Figure 12). Since the L/D ratio increases, the shaft resistance of the pile increases and the load transferred to the pile end decreases (Figure 10). For the same length piles, increments of N_q values are the same with increments of point resistance if pile diameter increases. It is concluded that the N_q value is affected by pile geometry (L, D), saturation degree of soil (S_r), and effective stress (σ'). In addition, API [75] and CGS [76] recommend taking N_q values in the range of 12-40 and 30-60, respectively, for piles installed in medium dense sand. Experimental N_q values valid for dry sands are in good agreement with CGS [76]. N_q values recommended by API [75] are more representative of experimental N_q values obtained from the saturated state.
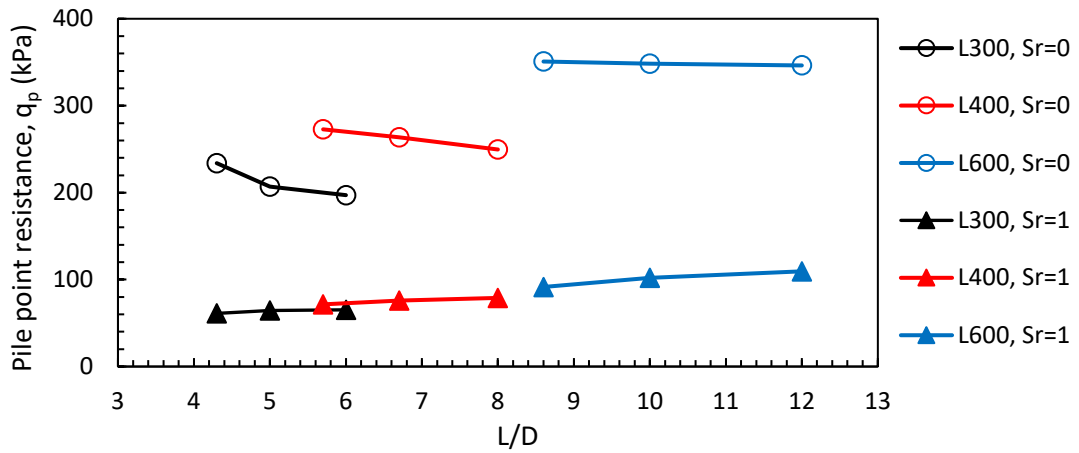
Figure 11. The variation of unit point resistance depending on L/D (modified from Yenginar et al. [54])
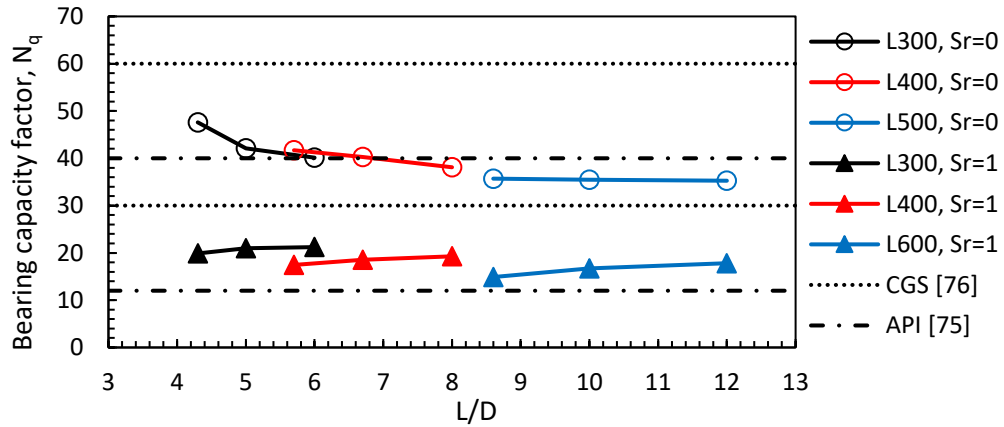
Figure 12. The variation of Nq values depending on L/D (modified from Yenginar et al. [54])
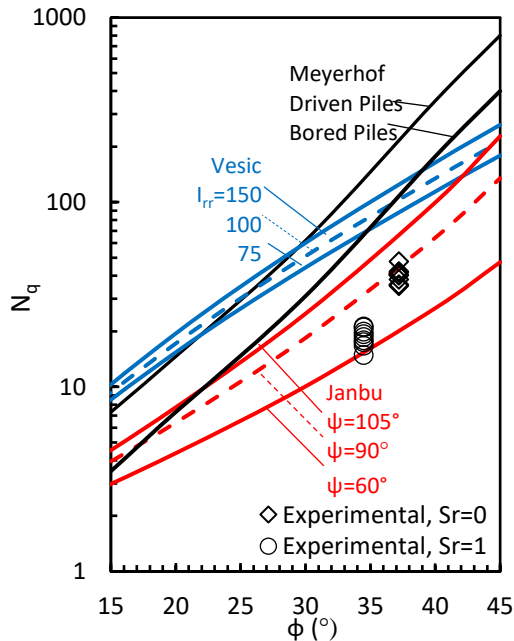
Figure 13. Theoretical and experimental N_q values depending on internal frictional angle (modified from Yenginar et al. [54])

Other than Janbu and Vesic, graphical charts presenting the variation in N_q values depending on ϕ have been developed by some researchers [28], [29], [31], [32]. In these curves, N_q values vary in a wide range even if the ϕ value is constant (Figure 13). For instance, the N_q values change between 10 and 60 for $\phi=30°$ while they vary between 30 and 180 for $\phi=40°$. Field loading test results of piles installed in sandy soils having ϕ of 32-40° reveal that N_q values changes between 30 and 150 [77]. In this study, experimental N_q values are smaller than the Meyerhof and Vesic coefficients, and they are within the boundaries of Janbu (Figure 13).

5. CONCLUSION

In the present study, the load-settlement behavior of model piles was investigated with laboratory pile loading tests performed in dry ($S_r=0$) and saturated ($S_r=1$) sandy soils. The main findings of the study are given below.

- Loading speed during pile load test does not affect the ultimate point and total bearing capacities of the pile installed in sandy soils significantly.
- In saturated and dry sandy soils, ultimate values of the base, shaft, and total bearing capacities mobilized at different settlement values. Therefore, using different safety factors for base and shaft capacities is recommended to determine the allowable bearing capacity of piles.
- Total and base bearing capacities approximately decrease by 50 to 60% in theory when dry soil becomes saturated. In the pile loading test results, however, it is concluded that the reduction in base and total capacities of piles was 65 to 75% when the dry soil becomes saturated. The bearing capacity of the piled foundations will decrease more than expected since the groundwater level increase. In theory, the reason of the decrease in the bearing capacity is only decreasing amount of effective stress, but experimental results indicate that diameter of pile has also an influence in this reduction.
- Experimental N_q values are smaller than the Meyerhof and Vesic coefficients, and they are within the boundaries of Janbu. Thus, the authors recommend using Janbu's bearing capacity coefficients for medium-dense sandy soils.
- N_q values change depending on the effective stress, pile diameter, and saturation degree of soil. Defining the N_q value depending only on the internal friction angle of soil (ϕ) could be misleading.
- In dry and saturated sands, N_q value decreases since the pile length/pile diameter ratio increases.

The authors made some criticisms about the N_q parameter in the light of the pile loading test results obtained in the laboratory. The fact that the N_q values vary over a wide range and this makes it difficult to know the actual value, especially in the calculation of the pile base capacity. If the actual value of N_q can be determined more precisely using the pile and soil properties, the pile bearing capacity can be determined more accurately in the preliminary design. The results obtained in the study are valid for nondisplacement piles (L/D≤12), which are installed in medium dense sand in dry and saturated conditions. For this reason, new relationships based on pile and soil parameters can be developed for the N_q parameter by continuing experimental studies on the piles with different geometries (for practical concern, L/D>20) constructed in soils having different grain distributions, relative density, and saturation degree.

Declaration of Ethical Standards

The authors declare that they comply with all ethical standards.

Credit Authorship Contribution Statement

Author 1: Resources, Investigation, Experimentation, Formal analysis, Validation, Methodology, Visualization, Writing – original draft **Author 2:** Resources, Investigation, Experimentation, Writing – original draft **Author 3:** Investigation, Validation, Methodology, Reviewing - original draft

Declaration of Competing Interest

The authors have no competing interests to declare that are relevant to the content of this article.

Funding / Acknowledgements

Data Avaibility

All data generated or analyzed during this study are included in this published article.

REFERENCES

[1]   C. Cakiroglu, K. Islam, G. Bekdaş, and M. L. Nehdi, "Data-driven ensemble learning approach for optimal design of cantilever soldier pile retaining walls," *Structures*, vol. 51, pp. 1268–1280, May 2023, doi: 10.1016/j.istruc.2023.03.109.

[2]   G. Bekdaş, Z. A. Arama, A. E. Kayabekir, and Z. W. Geem, "Optimal Design of Cantilever Soldier Pile Retaining Walls Embedded in Frictional Soils with Harmony Search Algorithm," *Applied Sciences*, vol. 10, no. 9, p. 3232, May 2020, doi: 10.3390/app10093232.

[3]   H. Bolouri Bazaz, A. Akhtarpour, and A. Karamodin, "A study on the effects of piled-raft foundations on the seismic response of a high rise building resting on clayey soil," *Soil Dynamics and Earthquake Engineering*, vol. 145, p. 106712, Jun. 2021, doi: 10.1016/j.soildyn.2021.106712.

[4]   I. Jamil *et al.*, "Analysis and Design of Piled Raft Foundation Taking into Account Interaction Factors," *Advances in Civil Engineering*, vol. 2022, pp. 1–11, Mar. 2022, doi: 10.1155/2022/1334136.

[5]   R. Zhu *et al.*, "Improving the Performance of Piled Raft Foundations Using Deformation Adjustors: A Case Study," *Buildings*, vol. 12, no. 11, p. 1903, Nov. 2022, doi: 10.3390/buildings12111903.

[6]   Y. Yenginar, "Investigation of group effect with model piled foundations [in Turkish]," Selcuk University, Institute of Science and Technology, Konya, Turkey, 2014.

[7]   H. Bolouri Bazaz, A. Akhtarpour, and A. Karamodin, "A study on the effects of piled-raft foundations on the seismic response of a high rise building resting on clayey soil," *Soil Dynamics and Earthquake Engineering*, vol. 145, p. 106712, Jun. 2021, doi: 10.1016/j.soildyn.2021.106712.

[8]   E. E. Başar, İ. D. Çelik, M. Fındık, and S. Uzundurukan, "Kohezyonsuz Zeminde Kazık Aralığının Belirlenmesi ve Temel Davranışının Deneysel İncelenmesi," *Turkish Journal of Civil Engineering*, vol. 34, no. 2, pp. 145–172, Mar. 2023, doi: 10.18400/tjce.1244594.

[9]   J. E. Bowles, *Foundation analysis and design*. McGraw-Hill Book Company, NY, 1997.

[10]   B. M. Das, *Principles of foundation engineering*. Thomson Canada Limited, Canada, 2007.

[11]   S. Manandhar and N. Yasufuku, "Analytical Model for the End-Bearing Capacity of Tapered Piles Using Cavity Expansion Theory," *Advances in Civil Engineering*, vol. 2012, pp. 1–9, 2012, doi: 10.1155/2012/749540.

[12]   N. Miura, "Point resistance of piles in sand," *Technology reports of the Yamaguchi University*, vol. 3, no. 2, pp. 129–139, 1983.

[13]   S. Ohno and S. Sawada, "Bearing capacity of piles in sands with different crushabilities under various stress conditions," in *Proceeding 11th Asian Regional Conf on Soil Mechanics and Geotech Eng,*

1999, pp. 249–252.

[14]   N. Yasufuku and A. F. L. Hyde, "Pile end-bearing capacity in crushable sands," *Géotechnique*, vol. 45, no. 4, pp. 663–676, Dec. 1995, doi: 10.1680/geot.1995.45.4.663.

[15]   Q. Zhang, Z. Zhang, and S. Li, "Investigation into Skin Friction of Bored Pile Including Influence of Soil Strength at Pile Base," *Marine Georesources & Geotechnology*, vol. 31, no. 1, pp. 1–16, Jan. 2013, doi: 10.1080/1064119X.2011.626506.

[16]   Z. Jia-Jin, G. Xiao-Nan, Z. Ri-Hong, W. Kui-Hua, and Y. Tian-Long, "Shaft capacity of pre-bored grouted planted nodular pile under various overburden pressures in dense sand," *Marine Georesources & Geotechnology*, vol. 38, no. 1, pp. 97–107, Jan. 2020, doi: 10.1080/1064119X.2018.1553214.

[17]   A. Mishra and V. A. Sawant, "Optimization of Empirical Methods in Determining the Load Capacity of Rock Socketed Piles," *Indian Geotechnical Journal*, vol. 52, no. 4, pp. 852–864, Aug. 2022, doi: 10.1007/s40098-022-00629-9.

[18]   E. C. Junior and A. S. Moura, "Evaluation of the Group Effect's Simulation on the Bearing Capacity of Bored Piles in Granular Soil, Using Load Transfer Functions," *Geotechnical and Geological Engineering*, vol. 40, no. 7, pp. 3393–3412, Jul. 2022, doi: 10.1007/s10706-022-02100-1.

[19]   R. Wang, D. E. L. Ong, J. Zhou, S. Liu, and E. Oh, "Validation of Analytical Solutions for Predicting Drilled Pile Behaviour under Bi-Directional Static Load Tests," *Geosciences (Basel)*, vol. 12, no. 8, p. 284, Jul. 2022, doi: 10.3390/geosciences12080284.

[20]   E. M. Comodromos and M. F. Randolph, "Improved Relationships for the Pile Base Response in Sandy Soils," *Journal of Geotechnical and Geoenvironmental Engineering*, vol. 149, no. 8, Aug. 2023, doi: 10.1061/JGGEFK.GTENG-11035.

[21]   G. Cao, X. Ding, Z. Yin, H. Zhou, and P. Zhou, "A new soil reaction model for large-diameter monopiles in clay," *Comput Geotech*, vol. 137, p. 104311, Sep. 2021, doi: 10.1016/j.compgeo.2021.104311.

[22]   Y. Zhang *et al.*, "A new approach for estimating the vertical elastic settlement of a single pile based on the fictitious soil pile model," *Comput Geotech*, vol. 134, p. 104100, Jun. 2021, doi: 10.1016/j.compgeo.2021.104100.

[23]   T. A. Pham and M. Sutman, "A Simplified Method for Bearing-Capacity Analysis of Energy Piles Integrating Temperature-Dependent Model of Soil–Water Characteristic Curve," *Journal of Geotechnical and Geoenvironmental Engineering*, vol. 149, no. 9, Sep. 2023, doi: 10.1061/JGGEFK.GTENG-11095.

[24]   X.-Y. Li, J.-H. Wan, H.-P. Zhao, and S.-W. Liu, "Three-Dimensional Analysis of Nonlinear Pile–Soil Interaction Responses Using 3D Pile Element Model," *International Journal of Geomechanics*, vol. 21, no. 8, Aug. 2021, doi: 10.1061/(ASCE)GM.1943-5622.0002076.

[25]   X. Zhang, B. Jiao, and B. Hou, "Reliability analysis of horizontally loaded pile considering spatial variability of soil parameters," *Soil Dynamics and Earthquake Engineering*, vol. 143, p. 106648, Apr. 2021, doi: 10.1016/j.soildyn.2021.106648.

[26]   A. Akbari Garakani, B. Heidari, S. Mokhtari Jozani, and O. Ghasemi-Fare, "Numerical and Analytical Study on Axial Ultimate Bearing Capacity of Fixed-Head Energy Piles in Different Soils," *International Journal of Geomechanics*, vol. 22, no. 1, Jan. 2022, doi: 10.1061/(ASCE)GM.1943-5622.0002223.

[27]   F. Han, R. odrigo Salgado, M. Prezzi, and J. Lim, "Shaft and base resistance of non-displacement piles in sand," *Comput Geotech*, vol. 83, pp. 184–197, Mar. 2017, doi: 10.1016/j.compgeo.2016.11.006.

[28]   V. G. Berezantzev, "Load bearing capacity and deformation of piled foundations," in *Proceeding 5th Int Conf ISSMFE*, Paris, FR: ISSMFE, 1961, pp. 11–12.

[29]   J. B. Hansen, "A general formula for bearing capacity. ," 1961.

[30]   N. Janbu, "Static bearing capacity of friction piles," *J of Soil Mec. and Found Eng Div ASCE*, vol. 95, 1976.

[31]   G. G. Meyerhof, " Bearing capacity and settlement of pile foundations," *J of Geotech Eng Div*, vol.

102, no. GT3, 1976.

[32] M. J. Tomlinson, *Foundation design and construction*. New York: John Willey and Sons, 1986.

[33] A. S. Vesic, *Design of pile foundations*. Washington, DC: Synthesis of Highway Practice 42 Res Bd, 1977.

[34] Y. M. Cheng, "Nq factor for pile foundations by Berezantzev," *Géotechnique*, vol. 54, no. 2, pp. 149–150, Mar. 2004, doi: 10.1680/geot.2004.54.2.149.

[35] H. G. Poulos and E. H. Davis, *Pile foundation analysis and design*. New York: John Willey and Sons, New York, 1980.

[36] F. H. Kulhawy, "Limiting tip and side resistance: fact or fallacy?," in *Proceeding Symp on Analysis and Design of Pile Foundations, ASCE*, 1984, pp. 80–98.

[37] W. J. Neely, "Bearing Capacity of Expanded-Base Piles in Sand," *Journal of Geotechnical Engineering*, vol. 116, no. 1, pp. 73–87, Jan. 1990, doi: 10.1061/(ASCE)0733-9410(1990)116:1(73).

[38] G. G. Meyerhof, "Scale Effects of Ultimate Pile Capacity," *Journal of Geotechnical Engineering*, vol. 109, no. 6, pp. 797–806, Jun. 1983, doi: 10.1061/(ASCE)0733-9410(1983)109:6(797).

[39] M. D. Bolton, "The strength and dilatancy of sands," *Géotechnique*, vol. 36, no. 1, pp. 65–78, Mar. 1986, doi: 10.1680/geot.1986.36.1.65.

[40] X. Jia, H. Zhang, C. Wang, F. Liang, and X. Chen, "Influence on the lateral response of offshore pile foundations of an asymmetric heart-shaped scour hole," *Applied Ocean Research*, vol. 133, p. 103485, Apr. 2023, doi: 10.1016/j.apor.2023.103485.

[41] K. Natarajan and G. S. P. Madabhushi, "Seismic response of an offshore wind turbine jacket structure with pile foundations," *Soil Dynamics and Earthquake Engineering*, vol. 162, p. 107427, Nov. 2022, doi: 10.1016/j.soildyn.2022.107427.

[42] Z. Xiao-ling, L. Cheng-rui, W. Pi-guang, and Z. Guo-liang, "Experimental simulation study on dynamic response of offshore wind power pile foundation under complex marine loadings," *Soil Dynamics and Earthquake Engineering*, vol. 156, p. 107232, May 2022, doi: 10.1016/j.soildyn.2022.107232.

[43] L. Wang and T. Ishihara, "A semi-analytical one-dimensional model for offshore pile foundations considering effects of pile diameter and aspect ratio," *Ocean Engineering*, vol. 250, p. 110874, Apr. 2022, doi: 10.1016/j.oceaneng.2022.110874.

[44] X. Wang, S. Li, and J. Li, "Effect of pile arrangement on lateral response of group-pile foundation for offshore wind turbines in sand," *Applied Ocean Research*, vol. 124, p. 103194, Jul. 2022, doi: 10.1016/j.apor.2022.103194.

[45] V. D. Nguyen, J. C. Small, and H. G. Poulos, "The Effects of Groundwater Pumping on Piled Foundations," in *Computational Mechanics–New Frontiers for the New Millennium*, Elsevier, 2001, pp. 433–438. doi: 10.1016/B978-0-08-043981-5.50067-5.

[46] M. Sheikhtaheri, " Experimental and numerical modeling studies for interpreting and estimating the p–δ behavior of single model piles in unsaturated sand ," University of Ottawa, Canada, 2014.

[47] M. Olgun, B. Fidan, and Y. Yenginar, "Model Studies of Lateral Soil Pressure on Drilling Piles in Dry and Saturated Sands," *Soil Mechanics and Foundation Engineering*, vol. 56, no. 4, pp. 280–286, Sep. 2019, doi: 10.1007/s11204-019-09603-9.

[48] M. Mukhlisin, B. Hamdani, E. Novita, S. Sukoyo, and A. H. Rabinah, "Behaviour of Friction Resistance of Pile Groups on Clay Soil During Loading Tests: Case Study in Semarang and Temanggung, Central Java, Indonesia," *Indonesian Journal on Geoscience*, vol. 9, no. 1, 2021, doi: 10.17014/ijog.9.1.61-69.

[49] H. Phoban, U. Seeboonruang, and P. Lueprasert, "Numerical Modeling of Single Pile Behaviors Due to Groundwater Level Rising," *Applied Sciences*, vol. 11, no. 13, p. 5782, Jun. 2021, doi: 10.3390/app11135782.

[50] Y. Roh, I. Kim, G. Kim, and J. Lee, "Comparative Analysis of Axial Load Capacity for Piled-Raft Foundation with Changes in Groundwater Level," *KSCE Journal of Civil Engineering*, vol. 23, no. 10, pp. 4250–4258, Oct. 2019, doi: 10.1007/s12205-019-0239-3.

[51]   E. E.-M. Chong and D. E.-L. Ong, "Data-Driven Field Observational Method of a Contiguous Bored Pile Wall System Affected by Accidental Groundwater Drawdown," *Geosciences (Basel)*, vol. 10, no. 7, p. 268, Jul. 2020, doi: 10.3390/geosciences10070268.

[52]   K. Amornfa, H. T. Quang, and T. V Tuan, "Effect of groundwater level change on piled raft foundation in Ho Chi Minh City, Viet Nam using 3D-FEM," *Geomech. Eng*, vol. 32, no. 4, pp. 387–396, 2023.

[53]   T. L. Gia, L. T. Duy, T. D. T. Kieu, and H. N. Thu, "The impact of groundwater lowering on pile bearing capacity in Hanoi – Vietnam," 2020, pp. 137–144. doi: 10.1007/978-981-15-2184-3_17.

[54]   Y. Yenginar, B. Fidan, and M. Olgun, "Experimental and theoretical Nq values for dry and saturated sands," in *4th International Conference on New Developments in Soil Mechanics and Geotechnical Engineering*, 2016, pp. 149–156.

[55]   Gg. Meyerhof, "The bearing capacity of foundations under eccentric and inclined loads," in *Proc. of the 3rd Int. Conf. on SMFE*, 1953, pp. 440–445.

[56]   B. M. Das and N. Sivakugan, *Principles of foundation engineering*. Cengage learning, 2018.

[57]   D. NAVFAC, "Foundation and Earth Structures," *US Department of the Navy*, 1984.

[58]   J. B. Burland, "Shaft friction piles in clay-a simple fundamental approach," *Ground Engineering*, vol. 3, pp. 30–42, 1973.

[59]   ASTM D2487-17e1, "Standard practice for classification of soils for engineering purposes (Unified Soil Classification System)," in *Book of Standards Volume: 04.08*, ASTM International, West Conshohocken, PA, USA., 2020, pp. 1–10.

[60]   ASTM D4254-16, "Standard test methods for minimum index density and unit weight of soils and calculation of relative density," in *Book of Standards Volume: 04.08*, 8th ed., vol. 4, West Conshohocken, PA: ASTM International, 2016, pp. 1–9.

[61]   C. Tang, R. H. Borden, and M. A. Gabr, "A Simplified Direct Shear Testing Procedure to Evaluate Unsaturated Shear Strength," *Geotechnical Testing Journal*, vol. 41, no. 2, p. 20150161, Mar. 2018, doi: 10.1520/GTJ20150161.

[62]   ASTM D1143, "Standard Test Methods for Deep Foundations Under Static Axial Compressive Load," in *Book of Standards*, West Conshohocken, PA, USA: ASTM International, 2013.

[63]   J. M. O. Hughes, N. J. Withers, and D. A. Greenwood, "A field trial of the reinforcing effect of a stone column in soil," *Géotechnique*, vol. 25, no. 1, pp. 31–44, Mar. 1975, doi: 10.1680/geot.1975.25.1.31.

[64]   US Army Corps of Engineers, "EL 02 CO97," US Army Publication, USA, 1997.

[65]   EN:1536, "Execution of special geotechnical work-bored piles," 1999.

[66]   ASTM D1143, "Standard Test Methods for Deep Foundations Under Static Axial Compressive Load," in *Book of Standards*, West Conshohocken, PA, USA: ASTM International, 2013.

[67]   T. Munaga, M. M. Khan, and K. K. Gonavaram, "Axial and Lateral Loading Behaviour of Pervious Concrete Pile," *Indian Geotechnical Journal*, vol. 50, no. 3, pp. 505–513, Jun. 2020, doi: 10.1007/s40098-019-00377-3.

[68]   M. Shakeel and C. W. W. Ng, "Settlement and load transfer mechanism of a pile group adjacent to a deep excavation in soft clay," *Comput Geotech*, vol. 96, pp. 55–72, Apr. 2018, doi: 10.1016/j.compgeo.2017.10.010.

[69]   P. Wang, H. Ding, J. Zhou, W. Hu, X. Gu, and E. Oh, "Field Tests of Super-Long and Large-Diameter Drilled Shaft Pile Foundations," *Advances in Civil Engineering*, vol. 2020, pp. 1–12, Jun. 2020, doi: 10.1155/2020/8814257.

[70]   M. Sharafkhah and I. Shooshpasha, "Physical modeling of behaviors of cast-in-place concrete piled raft compared to free-standing pile group in sand," *Journal of Rock Mechanics and Geotechnical Engineering*, vol. 10, no. 4, pp. 703–716, Aug. 2018, doi: 10.1016/j.jrmge.2017.12.007.

[71]   V. N. S. Murthy, *Advanced foundation engineering*. . New Delhi, India: CBS Publishers and Distributors, 2007.

[72]   Y. Yenginar and Ö. Tan, "Kumlu Zeminlerdeki Tekil Kazığın Eksenel Yük Altındaki Yük-Oturma

Davranışının Model Deneylerle Araştırılması," in *6. Geoteknik Sempozyumu*, 2015.

[73]   TBEC, "Turkish building earthquake code," Disaster and Emergency Management Authority (AFAD), Ankara, Turkey, 2019.

[74]   Y. Li, C. Liu, and J. Song, "The Pile End Mechanism of Jacked Pile in Layered Soils," *Indian Geotechnical Journal*, vol. 51, no. 5, pp. 1087–1098, Oct. 2021, doi: 10.1007/s40098-021-00510-1.

[75]   API (American Petroleum Institute), "Planning, designing and constructing fixed offshore platforms — Working stress design," API Recommended Practice 2A-WSD (RP 2A-WSD). Washington, DC:API, 2003.

[76]   CGS (Canadian Geotechnical Society), "Canadian foundation engineering manual," 4th ed. Alberta, Canada: CGS, 2006.

[77]   B. H. Fellenius, *Basics of foundation design*, Electronic Edition. Sidney, British Columbia, Canada: See www.Fellenius.net., 2015.

RANKING OF THE MEMBER COUNTRIES IN THE BLACK SEA ECONOMIC COOPERATION ORGANIZATION USING MULTI-CRITERIA DECISION-MAKING METHODS

1, *Ahmet SARUCAN [iD], **2 Mehmet Emin BAYSAL** [iD], **3 Orhan ENGİN** [iD]

1.2.3 Konya Technical University, Engineering and Natural Sciences Faculty, Industrial Engineering Department, Konya, TÜRKİYE

1 asarucan@ktun.edu.tr, 2 mebaysal@ktun.edu.tr, 3 oengin@ktun.edu.tr

Highlights

- A ranking of member countries in BSECO with MCDM in terms of basic energy indicator are made.
- The MCDM approach is used consist of CRITIC, COPRAS, and the Borda Count method.
- Two scenarios are created in the study.
- Seven different solutions are found.

*Corresponding Author: Ahmet SARUCAN, asarucan@ktun.edu.tr

RANKING OF THE MEMBER COUNTRIES IN THE BLACK SEA ECONOMIC COOPERATION ORGANIZATION USING MULTI-CRITERIA DECISION-MAKING METHODS

1, *Ahmet SARUCAN , **2 Mehmet Emin BAYSAL** , **3 Orhan ENGİN**

1,2,3 Konya Technical University, Engineering and Natural Sciences Faculty, Industrial Engineering Department, Konya, TÜRKİYE
1 asarucan@ktun.edu.tr, 2 mebaysal@ktun.edu.tr, 3 oengin@ktun.edu.tr

ABSTRACT: The objective of the study is to measure and rank the performance of the Black Sea Economic Cooperation Organization (BSECO) member countries for the different four years using Multi-Criteria Decision Making (MCDM) techniques widely used in performance measurement. This is the first study using CRITIC (Criteria Importance through Intercritera Correlation), COPRAS (Compress PRoportional ASsessment- Complex Relative Assessment) and Borda Count Methods to rank countries on basic energy indicators using MCDM. The CRITIC method was used to calculate the critical weights of the criteria established in the first stage of the three-stage work. It is an objective method of MCDM. The performance of BSECO member countries is ranked using the COPRAS method. The weights calculated in the second stage are used for the ranking. In the last stage, using the Borda count method, which is a data fusion technique, a single ranking was obtained by integrating the rankings obtained under different scenarios. According to this result, Albania was the first, Georgia was the second and Armenia was the third. The last place was taken by Türkiye. Thus, MCDM techniques can provide effective and comprehensive results in this kind of problems. It can be observed that the unbiased results are objective measures of the criteria used.

Keywords: Energy Indicators, Performance Evaluation, BSECO, CRITIC Method, COPRAS Method, Borda Count Method

1. INTRODUCTION

This study uses Multi-Criteria Decision Making (MCDM) to rank the member countries of the Black Sea Economic Cooperation Organization (BSECO) on a basic energy indicator. Energy demand is one of the most important issues in the world today [1]. Energy efficiency indicators are a popular topic for developed and developing countries in the world. However, some countries are striving to consume less energy and reduce their carbon dioxide emissions [1].

The term energy balance consists of supply, transformation and final consumption. Industry, transportation and other sectors are the final consumers of energy. Housing, communications and public services, agriculture/forestry and fisheries are the other sectors.

Energy consumption divided by activity is the energy efficiency indicator. Energy consumption divided by production is the industry indicator. Production consists of value added and physical production (paper, chemicals, other non-metallic mineral products and basic metals). Figure 1 shows the energy indicator pyramid.

*Corresponding Author: Ahmet SARUCAN, asarucan@ktun.edu.tr
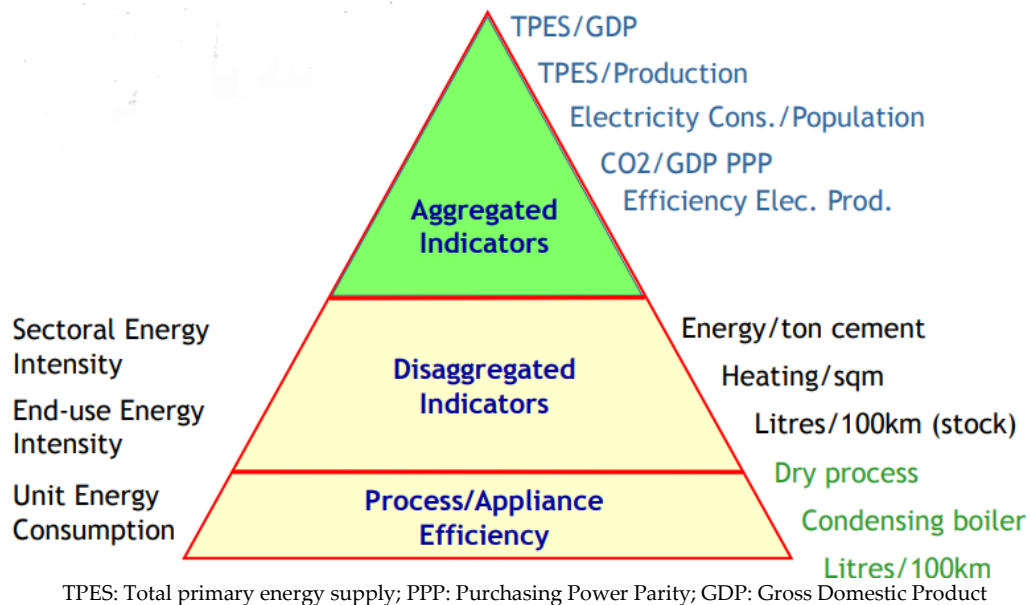
TPES: Total primary energy supply; PPP: Purchasing Power Parity; GDP: Gross Domestic Product
Figure 1. Pyramid of Energy Indicators [1]

The service indicator is the ratio of energy consumption to activity. Activity is the sum of value added, floor space and number of employees [1]. Section 3 explains the indicators used in the study.

The climate correction is based on heating degree-days. The heating correction is equal to the heating energy divided by the heating degree-days. Similarly, the residential energy efficiency indicator is equal to the energy consumption divided by the activity. The activity consists of the number of dwellings and the floor area. Residential energy consumption consists of space heating, space cooling, water heating, cooking, lighting, and appliances (energy use, inventory, diffusion) such as refrigerators, freezers, dishwashers, washers, dryers, televisions, and computers [1]. Energy efficient transportation is defined as moving more and farther with less fuel consumption. It is also defined as using public transportation instead of the private automobile.

There are a few studies in the literature on energy indicators for countries. The study by Unander [2] was based on the IEA energy indicator approach. The author presented examples of IEA work with indicators and an overview of the methodology used. The author also provided an example of a simplified indicator analysis in the case of India. Ramanathan [3] mentioned that some research articles on climate change examine the relationships between economic growth and carbon dioxide emissions or energy consumption separately to analyze the impact of economic growth and energy consumption on global carbon dioxide emissions. The relationships among CO_2 emissions, GDP growth, and energy consumption are examined simultaneously using data envelopment analysis. Sözen and Nalbant [4] mentioned that Turkey should make significant future plans about the strategy of consumption and production of basic energy sources. The energy indicators for Turkey have been identified. The energy indicators of EUROSTAT and Turkish Statistical Institute were taken and basic energy and economic indicators such as gross production, installed capacity, net energy consumption per person, import, export, consumption of coal, lignite, fuel oil, natural gas and hydropower were used. The study has shown the energy situation of Turkey among the EU countries.

Liu [5] mentioned that sustainability indicators are necessary to reflect various aspects of sustainability; the development of a general sustainability indicator including many basic sustainability indicators becomes critical. The method of selecting, quantifying, evaluating and weighting the basic indicators as well as the methods of the general sustainability indicator are reviewed. The study discusses the advantages and disadvantages of each method. Based on this discussion and the analysis of uncertainties in sustainability assessment, an effective framework and its procedures for the development of a global sustainability indicator for renewable energy systems are presented. What has been proposed

to constitute energy access and energy access indicators has been reviewed by Mensah et al [6]. There was also a brief review of the different types of energy access indicators and an analysis of access to modern energy in Ghana as measured by the energy access indicators used in Ghana. Iddrisu and Bhattacharyya [7] mentioned that energy plays a vital role in the modern lifestyle of any country. Understanding the sustainability of a country's energy system remains an important policy issue. It has been reviewed the comprehensiveness of existing metrics in tracking and tracing energy sustainability and the authors proposed a composite index, the Sustainable Energy Development Index. It is stated that the Sustainable Energy Development Index focuses on determining the level of sustainability of both intra- and inter-generational needs. The methodology, data availability and first country comparisons were discussed. It was found that the Sustainable Energy Development Index has a positive correlation with both the Human Development Index and the Energy Development Index, but provides a better understanding of the different dimensions of energy sustainability. Alvarez et al [8] mentioned that sustainable development is one of the main guiding principles of European Union policies. It was said that sustainable development is based on a framework of three pillars - economic development, social development and environmental protection, and argued that energy seems to be the cornerstone of economic growth; the Europe 2020 strategy emphasizes the importance of making the European Union more sustainable by establishing a long-term approach with clear guidelines on climate change. A synthetic index of sustainable energy development for the European Union (EU)-15 is proposed. It is based on 33 variables. Ogonowski [9] analyzed the development of renewable energy among the countries of the European Union for ten selected indicators in the field of climate change, environment, and energy for the years 2011-2019. Renewable energy data from 28 EU countries were analyzed using the vector measure construction method. Saraji et al. [10] ranked Energy Union members using the Pythagorean Fuzzy SWARA TOPSIS framework to assess the EU's progress towards sustainable energy. Ten experts working in different fields were selected to identify the criteria. A sensitivity analysis was performed based on twenty scenarios. Hasheminasab et al. [11] presented a detailed framework to assess energy poverty by considering energy demand, clean energy production, strategic location and energy equity between countries. Energy poverty is evaluated in three categories. The first is society's energy demand, access, and affordability; the second is ensuring access to energy resources and harmonizing energy markets with import policies; and the third is sustainability and emissions from energy production. By addressing these three categories, energy will be accessible, affordable and sustainable for future generations. The comprehensive EP framework has been applied in a case study of 27 EU countries with real data based on the EU database. The Threshold Based Feature Ratio Analysis method was used to weight the criteria.

This study measures the performance of BSECO member countries using MCDM methods. The MCDM approach is used for decision problems with a large number of conflicting criteria [12, 13]. MCDM is the most widely used method for energy problems in the literature in recent years. Some of the papers on MCDM for energy problems have been briefly summarized. Ertay et al. [14] used MACBETH and AHP based multi-criteria methods to evaluate renewable energy alternatives under fuzziness in Turkey. There are 4 main attributes and 15 sub-attributes used in the evaluation. Wang [15] developed a robust multi-criteria technique for order preference by similarity to an ideal solution based building energy efficiency benchmarking approach. Malkawi et al [16] evaluated energy options and ranked them with respect to several clusters of criteria including financial, technical, environmental, ecological, social and risk assessment. Ervural et al [17] studied the problem of energy planning and formulated this problem with a multiobjective decision model under a set of realistic constraints. Vasic [18] applied multi-criteria analysis to energy policy design and used preference ranking method for evaluation enrichment. Sarucan et al. [19] tested the ranking of BSECO countries for only one scenario with MCDM according to the basic energy indicator. Engin et al. [20] analyzed the alternatives of renewable energy sources with the MCDM methods for Turkey. Rao et al. [21] measured energy poverty with a multidimensional and comprehensive set of indicators by combining GRA- SRA method and did a case study of N11 countries with data from 2001 to 2017. Onifade [22] examined the environmental impact of energy indicators on the ecological footprint of African economies, mainly oil exporters, for the period between 1990 and 2016. To the best of

our knowledge, this is the first study in the literature to measure the performance of BSECO member countries in terms of basic energy indicators for two scenarios (base and active) and different four years using an MCDM approach. It is also the first study to rank countries on basic energy indicators using CRITIC's MCDM, COPRAS and Borda Count Methods.

The paper is organized as follows: Section 2, presents the material and methods. The material is the level of development and the actual energy indicators of the BSECO member countries. The method is the proposed MCDM approach consists of CRITIC, COPRAS method and the Borda Count method. Section 3, is the application of the proposed MCDM approach to measure the performance of BSECO member countries in terms of basic energy indicators. Section 4 is the discussion of the results and future research.

2. MATERIAL AND METHOD

2.1. Material

A model of multilateral political and economic initiative is the BSECO [23]. BSECO was first established on June 25, 1992, when Turkish President Turgut Özal and the leaders of the ten other countries of the region met in Istanbul. They signed the Istanbul Summit Declaration and the Bosphorus Declaration. The Permanent International Secretariat (Headquarters) of BSECO was established in Istanbul in March 1994. BSECO was given an international legal identity. It was transformed into a full-fledged regional economic organization with the entry into force of its Charter on May 1, 1999 [23]. The member countries of BSECO are as follows [24].

- The Republic of Albania,
- The Republic of Armenia,
- The Republic of Azerbaijan,
- Bulgaria,
- Georgia,
- Greece,
- The Republic of Moldova,
- Romania,
- Russian Federation,
- The Serbia,
- The Republic of Türkiye,
- Ukraine.

The objective of BSECO is to promote interaction and harmony among its members, to ensure peace and to promote friendly and good-neighbourly relations in the Black Sea region [23]. The main areas of cooperation of BSECO are energy, agriculture and agro-industry, banking and finance, fight against organized crime, culture, customs, education, emergency assistance, environmental protection, exchange of statistical data and economic information, health care and pharmaceuticals, information and communication technologies, institutional renewal and good governance, science and technology, SMEs, tourism, trade and economic development, and transport. BSECO's mission is summarized as follows [23];

- To strengthen dialogue and cooperation among Member Countries,
- To further develop and diversify bilateral and multilateral cooperation among Member Countries,
- To improve the business environment in the Member Countries,
- To develop economic cooperation among Member Countries.

The BSECO region spans two continents. It covers an area of nearly 20 million square kilometers and represents a region of nearly 335 million people. BSECO covers a geographical area that includes the territories of the countries bordering the Black Sea, the Balkans and the Caucasus. The annual volume of intra-community trade in BSECO is almost USD 187 billion [23]. The BSECO region is the world's second largest source of oil and natural gas after the Persian Gulf region. It is also rich in proven reserves of minerals, metals and other natural resources. BSECO is becoming Europe's most important corridor for

the transportation and transfer of energy [23]. BSECO Member Countries and Observers & Sectorial Dialogue Partners are shown in Figure 2.

Figure 2. The member countries of BSECO and Observers & Sectorial Dialogue Partners [23]

2.2. MCDM Methods

2.2.1. CRITIC Method

Diakoulaki et al [25] developed the CRITIC method. In this method, the weights of the criteria are determined taking into account both the standard deviation of the criteria and the correlation between the criteria [26]. The method consists of four steps [27], [28]. These steps are described below:

Step 1: Normalization of the decision matrix

In this step, the decision matrix (D=(d$_{ij}$)$_{mxn}$) consisting of m alternative and n criteria is normalized (x$_{ij}$) with the help of the Eq. 1 and 2. If the criterion is utility-oriented, the Eq. 1; if the criterion is cost direction, the Eq. 2 is used. Where:

d_j^{min}: The alternative with the lowest value according to the jth criterion

d_j^{max}: The alternative with the highest value according to the jth criterion

d_{ij}: Elements of the decision matrix

$$x_{ij} = \frac{d_{ij} - d_j^{min}}{d_j^{max} - d_j^{min}} \quad i = 1,2,\dots,m; j = 1,2,\dots,n \tag{1}$$

$$x_{ij} = \frac{d_j^{max} - d_{ij}}{d_j^{max} - d_j^{min}} \quad i = 1,2,\dots,m; j = 1,2,\dots,n \tag{2}$$

Step 2: Calculation of correlation coefficients

The linear correlation coefficients (ρ_{jk}) are calculated with the help of the Eq. 3 to measure the degree of correlation between the criteria. Correlation coefficients in the study are calculated by the "correlation" function of Microsoft Excel.

$$\rho_{jk} = \frac{\sum_{i=1}^{m}(x_{ij} - \overline{x_j})(x_{ik} - \overline{x_k})}{\sqrt{\sum_{i=1}^{m}(x_{ij} - \overline{x_j})^2 \sum_{i=1}^{m}(x_{ij} - \overline{x_k})^2}} \quad j,k = 1,\dots,n \tag{3}$$

Step 3: Calculation of the amount of information and standard deviation

The cumulative information of the criterion (T_j) is calculated according to the Eq. 4 and the standard deviation (σ_j) according to the Eq. 5.

$$T_j = \sigma_j \sum_{k=1}^{n}\left(1 - \rho_{jk}\right) \qquad (j = 1, \dots, n) \qquad (4)$$

$$\sigma_j = \sqrt{\frac{\sum_{i=1}^{m}(x_{ij}-\overline{x_j})^2}{m-1}} \qquad (j = 1, \dots, n) \qquad (5)$$

where m denotes alternatives, i.e. countries in Eq. 5.

Step 4: Calculation of criteria weights

The Eq. 6 determines the weights of the criteria.

$$w_j = \frac{T_j}{\sum_{j=1}^{n} T_j} \qquad (6)$$

2.2.2. COPRAS Method

Zavadskas and Kaklauskas developed the COPRAS method in 1996. This method ranks the alternatives by classifying the criteria in terms of costs and benefits. It is used for evaluation of criteria, maximization of benefit-based criteria and minimization of cost-based criteria [29]. The COPRAS method consists of seven steps [28], [30], [31], [32].

These steps are as follows:

Step 1: Decision matrix formation

The decision matrix produced in the first step of the CRITIC method is used.

Step 2: Normalization of the decision matrix

The Eq. 7 is used to normalize the decision matrix. In this equation, d_{ij} denotes the elements of the decision matrix.

$$d_{ij}^* = \frac{d_{ij}}{\sum_{i=1}^{m} d_{ij}} \quad j = 1,2, \dots, n \qquad (7)$$

Step 3: Calculation of weighted decision matrix (B)

The columns of the normalized decision matrix and the weight values of the criteria (w_j) multiplied. The weighted decision matrix is thus calculated (Eq. 8).

$$B = b_{ij} = d_{ij}^* * w_j \quad (i = 1,2, \dots, m; \; j = 1,2, \dots, n) \qquad (8)$$

Step 4: Calculation of useful and useless criteria

The sum of the values in the weighted normalized decision matrix for useful criteria (maximized) is denoted by $U_{i+} (Eq.\,9)$, and the sum of the values in the weighted normalized decision matrix for useless criteria (minimized) is denoted by $U_{i-} (Eq.\,10)$.

$$U_{i+} = \sum_{j=1}^{k} b_{ij} \quad (i = 1,2, \dots, m; \; j = 1,2, \dots, k; k \; is \; useful \; criteria) \qquad (9)$$

$$U_{i-} = \sum_{j=k+1}^{n} b_{ij} \quad (i = 1,2, \dots, m; \; j = k+1, k+2, \dots, n; n \; is \; useless \; criteria) \qquad (10)$$

Step 5: Calculation of relative importance values (Q_i)

The relative importance values (Q_i) are calculated by the Eq. 11.

$$Q_i = U_{i+} + \frac{\sum_{i=1}^{m} U_{i-}}{(U_{i-}) \sum_{i=1}^{m} \frac{1}{U_{i-}}} \qquad (11)$$

Step 6: Calculation of the highest relative importance values

The highest relative importance values (Q_{max}) are calculated by the Eq. 12.

$$Q_{max} = max\ \{Q_i\}, i = 12, \dots, m \qquad (12)$$

Step 7: Calculation of performance index

For each alternative, the performance index indicated by P_i is calculated using the Eq. (13).

$$P_i = \frac{Q_i}{Q_{max}} \%100 \qquad (13)$$

The performance index is expressed in terms of Pi. Among the alternatives, the alternative with a Pi index equal to 100 is considered the best alternative. In addition, the performance index values are sorted in descending order when ranking the preferred alternatives.

2.2.3. The Borda Count Method

The Borda counting method was introduced as a voting technique by Jean-Charles de Borda in 1784 [33]. The Borda counting method is a data combining technique that reduces two or more sequences to a single sequence [34]. In this method, voters choose from n alternatives. The least preferred alternatives by the voters are assigned a score of zero, the most preferred alternative is assigned a score of 1, and the most preferred alternative is assigned a score of (n-1). Using Eq. 14, the Borda scores of each alternative are calculated. The alternatives are then ranked according to their Borda scores [33].

$$A_i = \sum_{j=1}^{n} B_{ij} , \qquad (i = 1, \cdots, m) \tag{14}$$

where;

A_i : Borda score of each decision alternative,

B_{ij} : Borda point of different orders of the ith alternative

3. IMPLEMENTATION

Many studies have been conducted to measure the relationship between basic energy indicators and economic parameters. These studies show that there is a linear relationship between the level of development of countries and the actual energy indicators. It is also possible to evaluate countries in terms of basic variables such as energy production, consumption and emissions. Indicators such as electricity consumption, GDP, economic growth, energy prices, primary energy produced and consumed are considered in the studies [35], [36], [37], [38].

In this study, the performance of the 12 BSECO countries was ranked according to two scenarios in terms of basic proportional energy indicators using the COPRAS method. COPRAS is one of the multi-criteria decision making methods. The first scenario is the base scenario. The second is the active scenario.

Base scenario: The performance of countries in different years to be ranked according to the criterion weight values in the base year 2000. Criteria weight value to be found by the CRITIC method to calculate the performance of the countries in the desired years. It is a ranking of the performance of the BSECO countries in the study according to the periods of five years (i.e. 2000, 2005, 2010 and 2015).

Active scenario: The active scenario is defined as the ranking of the performance of the countries according to the weight values of the criteria in the year to be measured. This means that the weight values of the criteria are calculated separately for the mentioned years using the CRITIC method, taking into account the data of the years 2000, 2005, 2010 and 2015. The weight values of the respective year are taken into account when sorting the performance of the countries.

One of the main objectives of the study is to monitor the performance of Turkey, which is among the member countries of the BSECO organization in terms of basic energy indicators. In this context, Turkey, Ukraine, Moldova, Russia, Romania, Serbia, Greece, Georgia, Bulgaria, Azerbaijan, Armenia and Albania is composed of 12 member countries to decide. The aim of the meeting of BSECO member countries is to discuss and work on the main issues such as stabilization of relations between the countries and increase of economic cooperation. The study covers the energy data of the member countries for the years 2000, 2005, 2010 and 2015.

A comprehensive view of energy production, transformation, factors' influencing energy choices and the impact of energy use on CO_2 emissions is provided by the International Energy Agency (IEA) [39]. The study uses the IEA indicators. These indicators are total primary energy supply (TPES), electricity consumption and CO_2 emissions.

The energy statistics published by the IEA [39] provide the data to be used in the study and the basic energy indicator ratios. Analyzing the statistics, it can be seen that the data are published according to the following indicators: population, GDP, GDP (Purchasing Power Parity - PPP), electricity generation, net import, TPES, electricity consumption, amount of CO_2 emissions, TPES/Population, TPES/GDP, TPES/GDP(PPP), electricity consumption/Population, CO_2/TPES, CO_2/Population, CO_2/GDP, CO_2/GDP(PPP). The criteria to be used in the study have been determined according to the proportional

indicators with regard to the significance of the performance of BSECO member countries. The following codes are used for eight proportional indicators:

- C1: TPES/Population
- C2: TPES/GDP
- C3: TPES/GDP (PPP)
- C4: Electricity Consumption/Population
- C5: CO_2/TPES
- C6: CO_2/Population
- C7: CO_2/GDP
- C8: CO_2/GDP (PPP)

3.**1. Assignment of weights by CRITIC method**

The methods of weight assignment have been studied under three main headings: subjective methods, objective methods, and integrated methods [40]. Subjective methods weight criteria based on the preferences and judgments of decision makers. Examples include Delphi, Analytical Hierarchy Process (AHP), Weighted Least Squares, and LINMAP (Linear Programming Techniques for Multidimensional Analysis of Preferences). Objective methods are those that do not take into account the judgment of the decision maker. They were developed by researchers to minimize the effects of subjective weighting. They include entropy, standard deviation, and equal weighting. In integrated methods, weighting is done by using both the judgments of the decision makers and the numerical data of the decision matrix in an integrated manner. The subjective and objective integrated approaches developed and named by different researchers can be found in the literature [40]. In a study in which the criteria were determined on a proportional basis, the weight values were determined using the CRTIC method [41]. In this study, the CRITIC method was preferred. This is because the energy indicators were considered on a proportional basis and their weighting should be objective. The CRITIC method, which is one of the objective weighting methods, was chosen so that expert opinion would not be used in the study. It's important to use subjective weighting methods when the expertise and experience of the decision maker on an issue is needed. However, in cases where the decision maker or ideas change, problems arise regarding the reliability of the solution to the problem. In such negative situations, objective methods are preferred to subjective weighting methods. More realistic results are obtained by using objective methods that do not consider the decision maker's judgments in weighting the criteria [28]. Building the decision matrix is the first step in this method. The decision matrix for the base and active scenarios for the year 2000 is shown in Table 1. The IEA website [39] provided the data in Table 1.

Table 2 was obtained after the criteria C1, C2, C3 and C4 in this matrix were normalized by Eq. 1 and the rest of the criteria were normalized by Eq. 2.

Table 1. The basic energy indicator decision matrix for 2000

Alternatives	Criteria							
	C1	C2	C3	C4	C5	C6	C7	C8
Turkey	1.18	0.15	0.09	1.63	2.65	3.14	0.39	0.24
Ukraine	2.72	1.50	0.58	2.78	2.20	6.00	3.30	1.27
Moldova	0.79	0.82	0.35	1.64	2.27	1.80	1.85	0.79
Russia	4.22	0.61	0.34	5.20	2.38	10.06	1.45	0.81
Romania	1.61	0.33	0.16	1.99	2.38	3.84	0.78	0.39
Serbia	1.69	0.54	0.25	3.89	3.13	5.30	1.68	0.77
Greece	2.51	0.11	0.10	4.59	3.25	8.14	0.35	0.33
Georgia	0.65	0.45	0.20	1.45	1.61	1.05	0.73	0.33
Bulgaria	2.28	0.57	0.26	3.67	2.27	5.16	1.29	0.58
Azerbaijan	1.40	0.86	0.32	2.04	2.42	3.39	2.08	0.78
Armenia	0.65	0.47	0.23	1.29	1.70	1.11	0.79	0.39
Albania	0.58	0.26	0.11	1.45	1.72	1.00	0.44	0.19

Table 2. Normalized decision matrix

Alternatives	Criteria							
	C1	C2	C3	C4	C5	C6	C7	C8
Turkey	0.165	0.029	0.000	0.087	0.366	0.764	0.986	0.954
Ukraine	0.588	1.000	1.000	0.381	0.640	0.448	0.000	0.000
Moldova	0.058	0.511	0.531	0.090	0.598	0.912	0.492	0.444
Russia	1.000	0.360	0.510	1.000	0.530	0.000	0.627	0.426
Romania	0.283	0.158	0.143	0.179	0.530	0.687	0.854	0.815
Serbia	0.305	0.309	0.327	0.665	0.073	0.525	0.549	0.463
Greece	0.530	0.000	0.020	0.844	0.000	0.212	1.000	0.870
Georgia	0.019	0.245	0.224	0.041	1.000	0.994	0.871	0.870
Bulgaria	0.467	0.331	0.347	0.609	0.598	0.541	0.681	0.639
Azerbaijan	0.225	0.540	0.469	0.192	0.506	0.736	0.414	0.454
Armenia	0.019	0.259	0.286	0.000	0.945	0.988	0.851	0.815
Albania	0.000	0.108	0.041	0.041	0.933	1.000	0.969	1.000

The correlation coefficients of the criteria are calculated according to Eq. 3 using the data from Table 2. Table 3 shows the obtained correlation values.

Table 3. Correlation matrix of criteria

	C1	C2	C3	C4	C5	C6	C7	C8
C1	1.000	0.260	0.397	**0.884**	-0.431	-0.964	-0.336	-0.504
C2		1.000	**0.980**	0.018	0.169	-0.119	-0.974	-0.926
C3			1.000	0.157	0.126	-0.252	-0.960	-0.956
C4				1.000	-0.638	-0.947	-0.145	-0.333
C5					1.000	0.632	0.031	0.413
C6						1.000	0.232	0.413
C7							1.000	**0.974**
C8								1.000

A high correlation coefficient indicates that there is a direct relationship between the criteria and that the criteria are interdependent, according to [27], [40]. Ramík and Perzina [42] stated that it would be misleading to evaluate the criteria without considering the interdependence. This is because the weights of the interdependent criteria are calculated. One of the two interdependent criteria was removed from the study because it would have a greater impact on the decision to be made.

If the value of the correlation is negative and close to zero, then the criteria are independent of each other; if it is one and close to one, then we can say that the criteria are interdependent. Looking at the values in Table 3, we can see that C1 and C4, C2 and C3, and C7 and C8 are interdependent. This is the most important characteristic of the desired criteria. Since they do not influence each other, criteria C1, C3, and C8 were omitted from the study. This reduces the number of criteria to five. Table 4 shows the criteria and notations, the units and the optimization status of the criteria to be used in the later part of the work. When the transactions for the years 2000, 2005, 2010 and 2015 were carried out, eight criteria were reduced to five.

Table 4. Energy indicator criteria

Energy indicator ratios	Measurement unit	Optimization status
C2: TPES/GDP	toe/1000 $	Max
C4: Electricity Consumption/Population	MWh/Per person	Max
C5: CO_2/TPES	tCO_2/toe	Min
C6: CO_2/Population	tCO_2/Per person	Min
C7: CO_2/GDP	kg CO_2/$	Min

Table 5 shows the results of steps 2, 3 and 4 of the method for the year 2000.

In the step of generating the weighted decision matrix of the COPRAS method, the weight values obtained according to the CRITIC method are used.

The decision matrices for the basic energy indicators for the years 2005, 2010 and 2015 are shown in Tables 6, 7 and 8.

A Ranking of Member Countries in Black Sea Economic Cooperation Organization with Multi-Criteria Decision Making Methods

335

Table 5. Correlation coefficients, total information, standard deviation and weight values for 2000

	C2	C4	C5	C6	C7
C2	1.000	0.018	0.169	-0.119	-0.974
C4	0.018	1.000	-0.638	-0.947	-0.145
C5	0.169	-0.638	1.000	0.632	0.031
C6	-0.119	-0.947	0.632	1.000	0.232
C7	-0.974	-0.145	0.031	0.232	1.000
T_j	1.280	1.908	1.142	1.290	1.374
$\varnothing_j$	0.261	0.334	0.300	0.307	0.283
w_j	0.183	0.273	0.163	0.184	0.196

Table 6. The basic energy indicator decision matrix for 2005

	Criteria				
Alternatives	**C2**	**C4**	**C5**	**C6**	**C7**
Turkey	0.13	1.99	2.57	3.16	0.33
Ukraine	1.10	3.25	2.06	6.24	2.27
Moldova	0.70	2.05	2.20	2.14	1.55
Russia	0.48	5.77	2.27	10.32	1.08
Romania	0.27	2.37	2.40	4.35	0.64
Serbia	0.46	3.92	3.08	6.66	1.43
Greece	0.10	5.30	3.15	8.67	0.31
Georgia	0.31	1.78	1.43	0.97	0.45
Bulgaria	0.46	4.17	2.34	6.07	1.07
Azerbaijan	0.54	2.39	2.16	3.46	1.17
Armenia	0.33	1.50	1.64	1.37	0.54
Albania	0.23	1.72	1.76	1.27	0.41

Table 7. The basic energy indicator decision matrix for 2010

	Criteria				
Alternatives	**C2**	**C4**	**C5**	**C6**	**C7**
Turkey	0.14	2.47	2.49	3.64	0.34
Ukraine	0.97	3.56	2.01	5.80	1.96
Moldova	0.60	1.72	2.24	2.20	1.35
Russia	0.42	6.41	2.22	10.70	0.94
Romania	0.21	2.55	2.13	3.69	0.44
Serbia	0.40	4.36	2.94	6.29	1.16
Greece	0.09	5.33	3.02	7.50	0.28
Georgia	0.27	1.98	1.60	1.27	0.43
Bulgaria	0.35	4.56	2.48	6.00	0.88
Azerbaijan	0.22	1.60	2.03	2.60	0.44
Armenia	0.27	1.68	1.63	1.37	0.44
Albania	0.18	1.94	1.85	1.35	0.33

Table 8. The basic energy indicator decision matrix for 2015

	Criteria				
Alternatives	**C2**	**C4**	**C5**	**C6**	**C7**
Turkey	0.12	2.96	2.46	4.10	0.29
Ukraine	0.74	3.21	2.10	4.20	1.56
Moldova	0.48	1.40	2.24	2.13	1.08
Russia	0.41	6.59	2.07	10.19	0.85
Romania	0.17	2.64	2.18	3.51	0.37
Serbia	0.37	4.54	3.02	6.27	1.11
Greece	0.09	5.21	2.79	5.95	0.26
Georgia	0.31	2.73	1.81	2.26	0.57
Bulgaria	0.34	4.86	2.35	6.10	0.80
Azerbaijan	0.24	2.24	2.15	3.19	0.52
Armenia	0.27	1.90	1.53	1.56	0.41
Albania	0.17	2.09	1.75	1.32	0.29

Tables 9, 10, and 11 show the correlation coefficients, total information, standard deviation, and weight values for 2005, 2010, and 2015, respectively.

Table 9. Correlation coefficients, total information, standard deviation and weight values for 2005

	C2	C4	C5	C6	C7
C2	1.000	0.055	0.180	-0.136	-0.961
C4	0.055	1.000	-0.622	-0.970	-0.190
C5	0.180	-0.622	1.000	0.666	0.063
C6	-0.136	-0.970	0.666	1.000	0.278
C7	-0.961	-0.190	0.063	0.278	1.000
T_j	1.279	1.867	1.073	1.303	1.419
σ_j	0.263	0.326	0.289	0.313	0.295
w_j	0.184	0.269	0.155	0.188	0.204

Table 10. Correlation coefficients, total information, standard deviation and weight values for 2010

	C2	C4	C5	C6	C7
C2	1.000	0.107	0.130	-0.198	-0.970
C4	0.107	1.000	-0.624	-0.970	-0.234
C5	0.130	-0.624	1.000	0.614	0.086
C6	-0.198	-0.970	0.614	1.000	0.321
C7	-0.970	-0.234	0.086	0.321	1.000
T_j	1.297	1.859	1.157	1.261	1.430
σ_j	0.263	0.325	0.305	0.298	0.298
w_j	0.185	0.265	0.165	0.180	0.204

Table 11. Correlation coefficients, total information, standard deviation and weight values for 2015

	C2	C4	C5	C6	C7
C2	1.000	0.040	0.094	-0.146	-0.957
C4	0.040	1.000	-0.488	-0.955	-0.149
C5	0.094	-0.488	1.000	0.509	0.180
C6	-0.146	-0.955	0.509	1.000	0.264
C7	-0.957	-0.149	0.180	0.264	1.000
T_j	1.322	1.616	1.000	1.190	1.408
σ_j	0.266	0.291	0.270	0.275	0.302
w_j	0.202	0.247	0.153	0.182	0.215

3.**2. Ordering the alternatives by Implementation of COPRAS Method**

The COPRAS method is used to evaluate by maximizing benefit criteria and minimizing cost criteria [29]. In order to achieve this goal in the selected energy indicators or criteria, the COPRAS method was preferred. The COPRAS method is applied at this stage according to two defined scenarios. In each scenario, the problem is solved according to the years 2000, 2005, 2010 and 2015. In total, seven different solutions are obtained. For the year 2000 dataset, the implementation steps of the COPRAS method are carried out. For both the base scenario and the active scenario, the solution obtained after the year 2000 dataset is a common solution. This is because the weight values of the criteria in the base scenario are obtained with reference to the year 2000 data and are used in other years. In the active scenario, the weight values are calculated separately for each year. Therefore, the year 2000 is common to both scenarios.
Step1: Formation of the decision matrix

In the first step of the CRITIC method, the decision matrix generated in Table 1 is used by removing

the columns C1, C3, and C8.

Step2: Normalization of the decision matrix

The decision matrix is normalized by the Eq. 7. The normalized decision matrix is shown in Table 12.

Table 12. The normalized decision matrix for the year 2000

Alternatives	Criteria				
	C2	C4	C5	C6	C7
Turkey	0.022	0.052	0.095	0.063	0.026
Ukraine	0.225	0.088	0.079	0.120	0.218
Moldova	0.123	0.052	0.081	0.036	0.122
Russia	0.091	0.164	0.085	0.201	0.096
Romania	0.049	0.063	0.085	0.077	0.052
Serbia	0.081	0.123	0.112	0.106	0.111
Greece	0.016	0.145	0.116	0.163	0.023
Georgia	0.067	0.046	0.058	0.021	0.048
Bulgaria	0.085	0.116	0.081	0.103	0.085
Azerbaijan	0.129	0.065	0.086	0.068	0.137
Armenia	0.070	0.041	0.061	0.022	0.052
Albania	0.039	0.046	0.061	0.020	0.029

Step 3: Calculation of weighted decision matrix

The weighted decision matrix is found by multiplying each column of the normalized decision matrix by the weight values of 0.183, 0.273, 0.163, 0.184 and 0.196, respectively (Table 13). These weight values be also used when the base scenario results for 2005, 2010 and 2015 are being calculated. The weight values to be used in the active scenario are given in Table 14 as of years. The weight values in this table are taken from Tables 5, 9, 10, and 11.

Table 13. Weighted decision matrix for 2000

Alternatives	Criteria				
	C2	C4	C5	C6	C7
Turkey	0.004	0.014	0.015	0.012	0.005
Ukraine	0.041	0.024	0.013	0.022	0.043
Moldova	0.022	0.014	0.013	0.007	0.024
Russia	0.017	0.045	0.014	0.037	0.019
Romania	0.009	0.017	0.014	0.014	0.010
Serbia	0.015	0.034	0.018	0.020	0.022
Greece	0.003	0.040	0.019	0.030	0.005
Georgia	0.012	0.013	0.009	0.004	0.009
Bulgaria	0.016	0.032	0.013	0.019	0.017
Azerbaijan	0.024	0.018	0.014	0.012	0.027
Armenia	0.013	0.011	0.010	0.004	0.010
Albania	0.007	0.013	0.010	0.004	0.006

Table 14. Weight values to be used in the active scenario

Years	C2	C4	C5	C6	C7
2000	0.183	0.273	0.163	0.184	0.196
2005	0.184	0.269	0.155	0.188	0.204
2010	0.185	0.265	0.165	0.180	0.204
2015	0.202	0.247	0.153	0.182	0.215

Step 4: Calculation of useful and useless criteria

The sum of the values in the weighted normalized decision matrix for the useful criteria (for C1 and C2 with maxima status of optimization) is denoted by U_i+, the sum of the values in the weighted normalized decision matrix for the useless criteria (for C3, C4 and C5 with minima status of optimization) is denoted by U_i- (Table 15).

Step 5: Calculation of relative importance values (Qi)

Relative importance values (Q_i) are calculated with the help of the Eq. 8. It is seen in the third column in Table 15.

Table 15. U_{i+}, U_{i-}, Q_i, P_i Values

	U_{i+}	U_{i-}	Q_i	P_i	Rank
Turkey	0.018	0.032	0.071	66.40	11
Ukraine	0.065	0.078	0.087	81.09	4
Moldova	0.037	0.044	0.076	70.31	8
Russia	0.062	0.070	0.086	80.14	5
Romania	0.026	0.038	0.071	66.03	12
Serbia	0.048	0.060	0.077	71.71	7
Greece	0.043	0.053	0.075	69.38	9
Georgia	0.025	0.023	0.100	92.98	2
Bulgaria	0.047	0.049	0.082	76.47	6
Azerbaijan	0.041	0.054	0.073	67.99	10
Armenia	0.024	0.024	0.094	87.81	3
Albania	0.020	0.019	0.107	100.00	1

Step 6: Calculation of the highest relative importance values

Using the Eq. 9, the highest relative importance value is calculated as 0.107.

Step 7: Calculation of performance index

The performance index calculated by the Eq. 10 is shown in the fourth column in Table 15. With this calculation, the steps of the method end. Thus, the performance rank of the countries is determined.

Table 15 ranks the proportional energy indicator performance of the BSECO countries in seven steps according to the COPRAS method for the base and active scenarios. The base year is 2000. The country performance index Pi was used for the ranking in descending order. The first three places are taken by Albania, Georgia and Armenia. Romania ranked last. Turkey was ranked 11th.

Table 16 shows the performance of the BSECO countries according to the COPRAS method under the base scenario.

The top three countries in Table 16 are Georgia, Albania and Armenia for 2005 and 2010, and Albania, Armenia and Russia for 2015. The bottoms three are Romania for 2005, Turkey for 2010 and Moldova for 2015.

Table 16. Result list of base scenario

BASE SCENARIO							
2000		**2005**		**2010**		**2015**	
Pi	**Order**	**Pi**	**Order**	**Pi**	**Order**	**Pi**	**Order**
100.0	Albania	100.0	Georgia	100.0	Georgia	100.0	Albania
92.98	Georgia	88.87	Albania	96.85	Albania	96.04	Armenia
87.81	Armenia	85.12	Armenia	95.56	Armenia	88.47	Russia
81.09	Ukraine	78.66	Ukraine	92.17	Ukraine	86.18	Georgia
80.14	Russia	77.57	Russia	89.31	Russia	83.69	Ukraine
76.47	Bulgaria	72.09	Bulgaria	79.94	Bulgaria	80.05	Bulgaria
71.71	Serbia	68.90	Moldova	77.24	Azerbaijan	77.91	Greece
70.31	Moldova	67.93	Greece	76.68	Romania	75.83	Romania
69.38	Greece	67.78	Azerbaijan	76.63	Greece	73.73	Serbia
67.99	Azerbaijan	65.92	Turkey	75.96	Serbia	73.50	Azerbaijan
66.40	Turkey	64.81	Serbia	73.47	Moldova	72.92	Turkey
66.03	Romania	62.99	Romania	73.18	Turkey	69.40	Moldova

The performance of the BSECO countries is shown in Table 17. This is done by applying the steps of the COPRAS method according to the active scenario.

Looking at Table 17, the first three ranks are held by Georgia, Albania and Armenia in 2005 and 2010, and by Albania, Armenia and Russia in 2015. The last rank is held by Romania in 2005 and Moldova in 2010 and 2015.

The Spearman correlation test was performed to measure the similarity of the different rankings presented by the results of the base and active scenarios. The correlation values over the years are shown in Table 18.

There is a very strong relationship between the active and base scenarios, as shown in Table 18.

Table 17. The result list of active scenario

ACTIVE SCENARIO							
2000		**2005**		**2010**		**2015**	
Pi	**Order**	**Pi**	**Order**	**Pi**	**Order**	**Pi**	**Order**
100.0	Albania	100.0	Georgia	100.0	Georgia	100.0	Albania
92.98	Georgia	89.18	Albania	97.05	Albania	95.53	Armenia
87.81	Armenia	85.01	Armenia	95.65	Armenia	85.51	Russia
81.09	Ukraine	77.74	Ukraine	91.84	Ukraine	85.12	Georgia
80.14	Russia	76.44	Russia	88.52	Russia	83.79	Ukraine
76.47	Bulgaria	71.22	Bulgaria	79.46	Bulgaria	77.93	Bulgaria
71.71	Serbia	68.21	Moldova	77.57	Azerbaijan	75.53	Greece
70.31	Moldova	67.24	Greece	76.89	Romania	75.24	Romania
69.38	Greece	67.13	Azerbaijan	76.29	Greece	72.98	Azerbaijan
67.99	Azerbaijan	66.17	Turkey	75.42	Serbia	72.27	Turkey
66.40	Turkey	64.04	Serbia	73.46	Turkey	71.88	Serbia
66.03	Romania	62.64	Romania	73.27	Moldova	69.57	Moldova

Table 18. Correlation relationship between scenarios

Years	Correlations Values
2000	1.000
2005	0.999
2010	0.999
2015	0.995

3.**3. Aggregation of Ranking, the Implementation of the Borda Count Method**

In the final phase of the study, the different rankings from the base and active scenarios were combined using the Borda count method to obtain a final ranking. The rank values of the alternatives were scored to obtain a single ranking from these rankings. The highest score alternative was ranked first. Table 19 shows the result of using this method.

The top three positions in Table 19 are held by Albania, Georgia, and Armenia. Turkey is ranked last. It can be seen that both scenarios have the same country rankings as a result of the Borda counting method. This result is consistent with the values of the correlation coefficients in Table 18.

Table 19. Last ranking by Borda Count Method

Borda Base Scenario			Borda Active Scenario		
Country	**Score**	**Rank**	**Country**	**Score**	**Rank**
Albania	42	1	Albania	42	1
Georgia	40	2	Georgia	40	2
Armenia	37	3	Armenia	37	3
Ukraine	31	4	Ukraine	31	4
Russia	30	5	Russia	30	5
Bulgaria	24	6	Bulgaria	24	6
Greece	15	7	Greece	15	7
Azerbaijan	12	8	Azerbaijan	13	8
Serbia	11	9	Serbia	9	9
Moldova	10	10	Moldova	9	10
Romania	8	11	Romania	8	11
Turkey	4	12	Turkey	6	12

These results show that there is no change in the performance ranking of the BSECO countries in the two base scenarios. They are based on the CRITIC objective scoring methodology. This methodology is used to determine the weights of the criteria. According to these results, only one scenario can be considered. For the sake of simplicity, those working on this issue can be advised to use the base scenario.

4. CONCLUSIONS

This study compares countries on energy indicators. The alternatives are ranked according to the criteria. It is clear that this ranking can vary according to the different methods used for evaluation. As a result of the study, it was seen that an MCDM method can be used to solve this problem to achieve ranking between countries using objective weights.

Two scenarios were constructed in the study and seven different solutions were found. The best performance was achieved in the year 2010 with an average of 83.92% based on the Pi values calculated in the base scenario. In second place was the year 2015 with an average of 81.48% and in third place was the year 2000 with an average of 77.53%. In last place was the year 2005 with an average of 75.05%. According to the pi values of the active scenario, 2010 ranks first with 83.78%, 2015 ranks second with 80.45%, 2000 ranks third with 77.53% and 2005 ranks last with 74.58%.

Albania ranks first, Georgia second and Armenia third in the final results of the Borda counting method. The fact that the emission rate is lower than in other countries is an important factor for the first place of Albania. This is because: Almost all of Albania's electricity comes from hydroelectric plants. This, in turn, has an impact on carbon dioxide emissions.

It cannot be said that our country performs well when the results of the study are examined in terms of the basic proportional energy indicators. It is in the last place in the Borda Count method. It has not moved up from the last three places according to both scenarios. This is due to our energy dependence, the high proportion of fossil fuels used to generate electricity and the low quality of our lignite. Our country ranks last in the performance ranking because of the high emission rates of fossil fuels. In order for our country to move up in the rankings, we need to increase the share of renewable energy in the amount of energy from primary energy sources. We also need to start using nuclear energy immediately and reduce our energy dependence. It is expected that in the next ten years our country will be at the top due to the investments made in the energy sector in recent years.

In future studies, the problem can be solved with different MCDM methods. The results can be compared. Moreover, this work, which is carried out using objective criteria, can be solved in a different scenario, taking into account the subjective judgments of the decision maker.

Declaration of Ethical Standards

Authors declare to comply with all ethical guidelines including authorship, citation, data reporting, and publishing original research.

Credit Authorship Contribution Statement

Ahmet SARUCAN: Methodology, Data curation, Writing original draft, Visualization, Investigation, Software.
Mehmet Emin BAYSAL: Writing original draft, Visualization, Investigation, Supervision.
Orhan ENGİN: Data curation, Writing original draft, Visualization, Investigation, Supervision.

Declaration of Competing Interest

The authors declare that they have no known competing financial interests or personal relationships

Data Availability

Research data has not been made available in a repository.

5. REFERENCES

[1]   International Energy Agency, "Energy Efficiency Indicators data collection." Available: https://www.iea.org/media/training/presentations/escoct2013/Presentation_Energy_Efficiency_I ndicators.pdf [Accessed: July 24, 2018].

[2]   F. Unander, "Energy indicators and sustainable development: The International Energy Agency approach," *Natural Resources Forum,* vol. 29, pp. 377–391, 2005.

[3]   R. Ramanathan, "A multi- factor efficiency perspective to the relationships among world GDP, energy consumption, and carbondioxide emissions," *Technological Forecasting and Social Change,* vol. 73, no. 5, pp. 483- 494, 2006.

[4]   A. Sözen, and M. Nalbant, "Situation of Turkey's energy indicators among the EU member states," *Energy Policy,* vol. 35, no. 10, pp. 4993- 5002, 2007.

[5]   G. Liu, "Development of a general sustainability indicator for renewable energy systems: A review," *Renewable and Sustainable Energy Reviews,* vol. 31, pp. 611-621, 2014.

[6]   G. S. Mensah, F. Kemausuor, and A. Brew-Hammond, "Energy access indicators and trends in Ghana," *Renewable and Sustainable Energy Reviews,* vol. 30, pp. 317- 323, 2014.

[7]   I. Iddrisu, and S. C. Bhattacharyya, "Sustainable energy development index: a multi-dimensional indicator for measuring sustainable energy development," *Renewable and Sustainable Energy Reviews,* vol. 50, pp. 513-530, 2015.

[8]   M. T. Garcia-Alvarez, B. Moreno, and I. Soares, "Analyzing the sustainable energy development in the EU-15 by an aggregated synthetic index," *Ecological Indicators,* vol. 60, pp. 996-1007, 2016.

[9]   P. Ogonowski, "Application of VMCM, to assess of renewable energy impact in European Union Countries," *Procedia Computer Science,* vol. 192, pp. 4762-4769, 2021.

[10]   M. Kamali Saraji, D. Streimikiene, and R. Ciegis, "A novel Pythagorean fuzzy-SWARA-TOPSIS framework for evaluating the EU progress towards sustainable energy development," *Environmental Monitoring and Assessment,* vol. 194, no. 42, pp. 1-19, 2022.

[11]   H. Hasheminasab, D. Streimikiene, and M. Pishahang, "A novel energy poverty evaluation: Study of the European Union countries," *Energy,* vol. 264, pp. 1-9, 2023.

[12]   A. Sarucan, M. E. Baysal, and O. Engin, "A spherical fuzzy TOPSIS method for solving the physician selection problem," *Journal of Intelligent & Fuzzy Systems,* vol. 42, pp. 181-194, 2022.

[13]   A. Sarucan, M. E. Baysal, and O. Engin, "Physician selection with a neutrosophic multi-criteria decision making method," Intelligent and Fuzzy Techniques: Smart and Innovative Solutions-Proceedings of the INFUS 2020 Conference, 2021, pp. 319-327.

[14]   T. Ertay, C. Kahraman, and I. Kaya, "Evaluation of renewable energy alternatives using MACBETH and fuzzy AHP multicriteria methods: the case of Turkey," *Technological and Economic Development of Economy,* vol. 19, no. 1, pp. 38- 62, 2013.

[15]   E. Wang, "Benchmarking whole-building energy performance with multi-criteria technique for order preference by similarity to ideal solution using a selective objective-weighting approach," *Applied Energy,* vol. 146, pp. 92- 103, 2015.

[16]   S. Malkawi, M. Al-Nimr, and D. Azizi, "A multi-criteria optimization analysis for Jordan's energy mix," *Energy,* vol. 127, pp. 680- 969, 2017.

[17]   B. Cayir Ervural, R. Evren, and D. Delen, "A multi-objective decision-making approach for sustainable energy investment planning," *Renewable Energy,* vol. 126, pp. 387- 402, 2018.

[18]   G. Vasic, "Application of multi criteria analysis in the design of energy policy: space and water heating in households-city Novi Sad, Serbia," *Energy Policy,* vol. 113, pp. 410-419, 2018.

[19]   A. Sarucan, M. E. Baysal, and O. Engin, "A comparison of member countries in black sea economic cooperation organization with COPRAS method in terms of basic energy ındicators,"

International GAP Renewable Energy and Energy Efficiency Congress-GAPYENEV, 2018, pp. 109-113.

[20]   O. Engin, A. Sarucan, and M. E. Baysal, "Analysis of renewable energy alternatives with the multi-criteria decision making methods for Turkey," *Journal of Social and Humanities Science Research*, vol. 5, no. 23, pp. 1223-1231, 2018.

[21]   F. Rao, Y. M. Tang, K. Y. Chau, W. Iqbal, and M. Abbas, "Assessment of energy poverty and key influencing factors in N11 countries," *Sustainable Production and Consumption*, vol. 30, pp. 1- 15, 2022.

[22]   S. T. Onifade, "Environmental impacts of energy indicators on ecological footprints of oil-exporting African countries: Perspectives on fossil resources abundance amidst sustainable development quests," *Resources Policy*, vol. 82, 103481, 2023.

[23]   Organization of the Black Sea Economic Cooperation, Available: http://www.bsec-organization.org/ [Accessed: March 09, 2023].

[24]   Republic of Turkey Ministry of Foreign Affairs, Available: http://www.mfa.gov.tr/the-black-sea-economic-cooperation-organization-_bsec_.en.mfa [Accessed: March 09, 2023].

[25]   D. Diakoulaki, G. Mavrotas, and L. Papayannakis, "Determining objective weights in multiple criteria problems: the CRITIC method," *Computers & Operations Research*, vol. 22, no. 7, pp. 763-770, 1995.

[26]   C. Guo, Y. Wang, and W. Jiang, "An empirical study of evaluation index system and measure method on city's soft power: 17 cities in Shandong Province," *Cross-Cultural Communication*, vol. 9, no. 6, pp. 27-31, 2013.

[27]   A. Jahan, F. Mustapha, S. M. Sapuan, M. Y. Ismail, and M. Bahraminasab, "A framework for weighting of criteria in ranking stage of material selection process," *The International Journal of Advanced Manufacturing Technology*, vol. 58, pp. 411–420, 2012.

[28]   N. Ersoy, "Measuring corporate sustainability performance in the rubber coating industry: an integrated multicriterion framework," *The Online Journal of Science and Technology*, vol. 7, no. 4, pp. 146-161, 2017.

[29]   V. Podvezko, "The comparative analysis of MCDA methods SAW and COPRAS," *Engineering Economics*, vol. 22, no. 2, pp. 134-146, 2011.

[30]   A. Bakhouyi, R. Dehbi, and M. Talea, "Multiple criteria comparative evaluation on the interoperability of LMS by applying COPRAS method," 2016 Future Technologies Conference (FTC), 2016, pp. 361-366.

[31]   N. Kundakçı, and A. Tuş Işık, "Integration of MACBETH and COPRAS methods to select air compressor for a textile company," *Decision Science Letters*, vol. 5, no. 3, pp. 381-394, 2016.

[32]   C. Şahin, and A. Öztel, "Comparative analysis of habitability levels of countries with COPRAS method: BRICS countries and Turkey," *International Journal of Western Black Sea Social and Humanities Sciences*, vol. 1, no. 1, pp. 75-84, 2017.

[33]   C. Lamboray, "A comparison between the prudent order and the ranking obtained with Borda's, Copeland's, Slater's and Kemeny's rules," *Mathematical Social Sciences*, vol. 54, pp. 1-16, 2007.

[34]   R. Nuray, and F. Can, "Automatic ranking of information retrieval systems using data fusion," *Information Processing and Management*, vol. 42, no. 3, pp. 595-614, 2006.

[35]   J. Asafu-Adjaye, "The relationship between energy consumption, energy prices, and economic growth: time series evidence from Asian developing countries," *Energy Economics*, vol. 22, no. 6, pp. 615-625, 2000.

[36]   P. Mozumder, and A. Marathe, "Causality relationship between electricity consumption and GDP in Bangladesh," *Energy Policy*, vol. 35, no. 1, pp. 395-402, 2007.

[37]   A. Belke, F. Dobnik, and C. Dreger, "Energy consumption and economic growth – new insights into the cointegration relationship," *Energy Economics*, vol. 33, no. 5, pp. 782-789, 2011.

[38]   M. Gök, "Ranking G20 countries with regard to energy indicators via multiple criteria decision making techniques," M. S. thesis, Ankara University, Ankara, 2015.

[39]   International Energy Agency, "Key world energy statistics, 2017." Available: http://www.iea.org/statistics/statisticssearch/report/?country=TURKEY&product=indicators&year=2010 [Accessed: July 26, 2018].

[40]   Y. M. Wang, and Y. Luo, "Integration of correlations with standard deviationsfor determining attribute weights in multiple attribute decision making," *Mathematical and Computer Modeling,* vol. 51, no. 12, pp. 1-12, 2010.

[41]   M. T. Sarımermer, "Girişim sermayesi yatırım ortaklıklarının finansal performanslarının CRITIC ve PROMETHEE yöntemleriyle değerlendirilmesi," M. S. thesis, Marmara University, İstanbul, 2022.

[42]   J. Ramík, and R. Perzina, "A method for solving fuzzy multicriteria decision problems with dependent criteria," *Fuzzy Optimization and Decision Making,* vol. 9 pp. 123–141, 2010.

FUZZY LOGIC APPROACH FOR PREDICTING STUDENT ACHIEVEMENT IN SCRATCH TRAINING

Ali ÇETİNKAYA 🆔

Konya Technical University, Engineering Faculty, Computer Engineering Department, Konya, TÜRKİYE
ali.cetinkaya@gmail.com

Highlights

- Predictions were made about students' programming skills using fuzzy logic.
- It was investigated whether students' interest in learning algorithms and coding would increase by creating games with the visual programming tool.

*Corresponding Author: Ali ÇETİNKAYA, ali.cetinkaya@gmail.com

FUZZY LOGIC APPROACH FOR PREDICTING STUDENT ACHIEVEMENT IN SCRATCH TRAINING

Ali ÇETİNKAYA [iD]

Konya Technical University, Engineering Faculty, Computer Engineering Department, Konya, TÜRKİYE
ali.cetinkaya@gmail.com

ABSTRACT: 21st-century skills such as critical thinking, problem-solving, and analytical thinking gained importance to survive in today's world. There is growing research mostly focus on the prediction of students in higher education using machine learning and statistical models. However, predicting primary and middle school student's performance also becomes important especially in learning computer programming. In this study, it was primarily proposed to a fuzzy logic system to predict student performance during the experiment then compare fuzzy logic prediction results to the experts' results. Secondly, to test the theory that students' interest in learning algorithms and coding can be increased using the creation of games in a visual programming tool for beginners. The fuzzy logic inference system has been employed to predict middle school student's performance in the programming experiment which has been carried out using the Scratch environment with the participation of three different middle school students in Turkey. The success rate of three different middle school group success rates is estimated regarding task completion times, and the regression results with respect to the groups are %80, %97, %84.

Keywords: Predicting Student Achievement, Scratch Training, Fuzzy Logic

1. INTRODUCTION

Today, as advanced technologies emerge especially in computer-related technologies, it is imperative for students to gain 21st-century skills such as critical thinking, problem-solving, and analytical thinking. In order to acquire these skills, computer, and coding, which is also a part of everyday life, education has become crucial. Therefore, coding ability should be given to every student as a basic educational right of this century [1].

The young generation is so fluent with the Internet and other digital technologies that they can be called "digital natives" [2]. As seen, being a digital native requires not just browsing or interacting via social media but demands the skill to imagine, design, and invent using new media. To do so, it requires to learn some form of coding [3]. Visual programming techniques are becoming increasingly important when teaching programming concepts. Visual programming applications provide an environment that makes programming easy and fun [4]. The main applications of these applications are Scratch [3] and Alice [4].

Using Scratch-like visual block programming languages gives students more opportunity to concentrate on the semantics of programming languages instead of syntax issues. In addition to that, primary school pupils have not achieved a suitable level of conceptual thinking necessary to code up until now, which makes learning coding harder [5]. Learning coding with the help of a visual coding language tool could supply a concrete understanding to conceptual thinking. [4], and could hence be used as a mechanism for a suitable mindset shift [6] to "real" coding. Coding in Scratch environment switches the coding framework from solving math problems creating stories, games etc. which is more fun to do [5].

Students with under the average math skills could grasp programming and problem-solving easier if given suitable tools and the employing of less complicated visual environments before shifting to integrated development environments (IDEs) which are commonly used in the software industry and

*Corresponding Author: Ali ÇETİNKAYA, ali.cetinkaya@gmail.com

are seen as more complicated [7].

In recent years, machine learning techniques, fuzzy logic and artificial intelligence methods have been frequently used in estimating the performance of the students. L.A. Zadeh introduced the fuzzy logic theory in 1965 [8]. Fuzzy logic allows for the inclusion of vague human assessments in computing problems. A lot of work has been done about fuzzy logic so far. Fuzzy logic can be used in the development of intelligent systems for decision making, prediction, identification, pattern recognition, optimization, and control [9].

It is important for educators to recognize students' performance during training time. Therefore, this paper presents a fuzzy model approach to predicting student performance during Scratch programming training. In the proposed method, the completion of the tasks and mathematics grades were taken into consideration to test students' achievement of completing the given Scratch tasks. the high correlation coefficient between the real values and Fuzzy values indicates that the system works successfully. The proposed method can be used automatically to measure students' performance without expert supervision.

This paper is organized as follows. Section 2 presents the related work. Section 3 describes the material and methods employed in this paper. Section 4 presents our proposed method. Finally, Section 5 presents our conclusions.

2. RELATED WORK

There was huge excitement to educate children on how to code when personal computers were presented to the public. Most schools trained millions of pupils to code in Logo or Basic [3]. Seymour Papert's 1980 book Mindstorms [10] presented Logo as a keystone for rethinking approaches to education and learning. Recently, fresh efforts have been put forward to introduce programming to the younger generation, especially primary and middle school children using visual programming environments such as: Scratch [10] and Alice [4].

Predicting students' performance gets a lot of attention with the help of dizzying advancements in machine learning, fuzzy logic and statistical methods. Fuzzy logic techniques have been used in prediction in recent years. Yildiz et al. developed three types of fuzzy (classical fuzzy, gene-fuzzy, expert fuzzy) models to predict the student's year-end performance using the first eight weeks' data as a result the gene-fuzzy and the expert fuzzy models performed better than the classical fuzzy model [11]. Ingoley et al. proposed the multiple node fuzzy logic method, which takes into consideration the ambiguity of students' question paper beside certainty rate, complexity, and importance during the evaluation process, to provide more clear and objective results to all students [12]. Jamsandekar et al. proposed the fuzzy inference technique to evaluate student performance using grades as input data to the system and the proposed approach is further compared with traditional methods for evaluating the difference [13]. Yildiz et al. introduced a new approach using the fuzzy decision support system to evaluate student performance in laboratory applications and the results showed the proposed model performed better than the classical systems in terms of the reliability and the actuality of educational assessment [14]. Jyothi et al. proposed a fuzzy expert system for assessing teachers' overall performance in terms of an optimization evolution model for evaluating teachers' academic performance based on teaching activities [15]. In [16], the authors developed an intelligent tutoring system using Bayesian networks and fuzzy logic to assist students in educational settings and improve their academic performance. The system adhered to the conventional architecture of intelligent tutoring systems and used a fuzzy logic system to evaluate student performance in a particular topic by considering two factors: the pre-test grade and the topic test grade. They used three fuzzy sets for each input variable to characterise the students' grades as poor, good or excellent, and two fuzzy sets to describe the output (low and high). Doz et al., introduced a novel assessment model using fuzzy logic, combining teacher-assigned grades with results from the Italian National Assessment of Mathematical Knowledge (INVALSI). Applied to over 90,000 students across different grades, the fuzzy logic model yielded lower scores compared to traditional grading. However, its consistent results across educational levels suggest

its suitability for diverse contexts [17]. Jan et al., utilized fuzzy logic-based artificial intelligence for monitoring student academic performance in engineering education. The study introduces stress as an additional factor and employs both Mamdani and Sugeno inferencing methods. Results show promise, highlighting the potential for automated intelligent systems to contribute to achieving quality education goals [18]. Dhokare et al., proposed a fuzzy logic-based model to address the complexities in evaluating students' performance during the COVID-19 pandemic, considering the evolving teaching methods and the need for a comprehensive assessment approach [19]. In recent years, the combination of artificial intelligence and fuzzy logic has become popular in student performance prediction [20-23].

The classification technique is also one of the important areas in the prediction of teachers or pupil's performance. Agaoglu employs classification techniques, which are decision tree algorithms, support vector machines, artificial neural network, and discriminant analysis to determine a teacher's accomplishment instead of a student's accomplishment [24]. Lye et al. tried to predict pre-university pupils' math performance using several types of neural network models (the Back-propagation Neural Network, Classification and Regression Tree, and Generalized Regression Neural Network) which achieved moderate success in prediction rate [25].

It has become crucial for educators to teach younger age students programming skills and realize students' skills and accomplishments during training time. This study focuses on students' performance prediction using fuzzy logic approach.

3. MATERIAL AND METHODS

3.1. Fuzzy Logic

L.A. Zadeh introduced fuzzy logic theory in 1965 [8]. Fuzzy logic is used when conventional logic does not work properly. What makes fuzzy logic powerful is the concept of the linguistic variable whose values are not numbers but words or sentences in a natural or artificial language [26].

A fuzzy logic system (FLS) can be described as the nonlinear mapping of an input data set to a scalar output data [10]. An FLS is based on four essential sections: fuzzifier, rules, an inference engine, and defuzzifier (Fig. 1).

The fuzzifier maps crisp numbers into fuzzy sets. The defuzzifier maps output sets into crisp numbers.
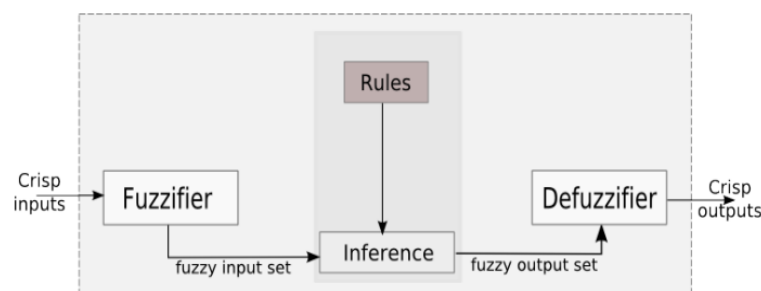
Fig. 1. A Fuzzy Logic System.

Fuzzy inference system (FIS) is the heart of FLS which consists of rules and inference. Two FISs are popular. First one is Mamdani FIS was introduced by Ebrahim Mamdani [27] and second is Takagi–Sugeno–Kang (TSK-FIS) was proposed in 1985 [28]. The main difference between Mamdani FIS and TSK-FIS is that the TSK-FIS output membership functions are either linear or constant [29]. The membership functions (MFs) are the key concept in fuzzy logic. MFs can be defined on input and output data sets. As shown in Fig. 2 several types of MFs can be used.
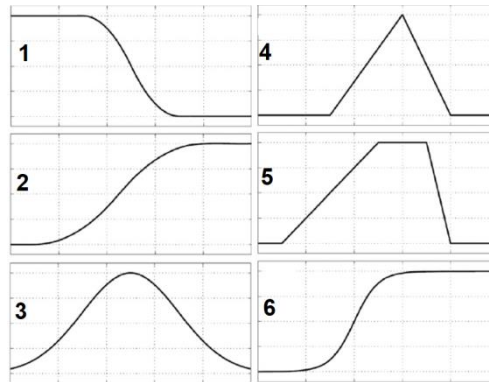
Fig. 2. Membership functions [29]: 1- z-shape, 2-s-shape, 3-gaussian, 4-triangular, 5- trapezoidal, 6-sigmoid.

3.2   Scratch

Scratch is a graphical programming language environment which developed by the Lifelong Kindergarten research group at the MIT Media Lab [30]. The Scratch environment which allows users to create interactive stories, games etc. easily is more than a visual block programming tool. It is open source and free and also an active learning community which so far has over 29 million registered users and almost 30 million projects shared [30]. Because of this easy to use graphical block style, any child who knows how to read or write, or who is just beginning to learn, can easily learn and use Scratch. The classical programming environment mostly uses text-based commands. However, The Scratch-like visual programming environments are founded on blocks which are a component of the language. Instead of test-based commands blocks are used to define a function, a variable, a control structure etc. during programming. A view of the comparison between Scratch and traditional programming language in Fig. 3. Scratch and similar visual programming applications are thought to improve the user's computer thinking skills [31].
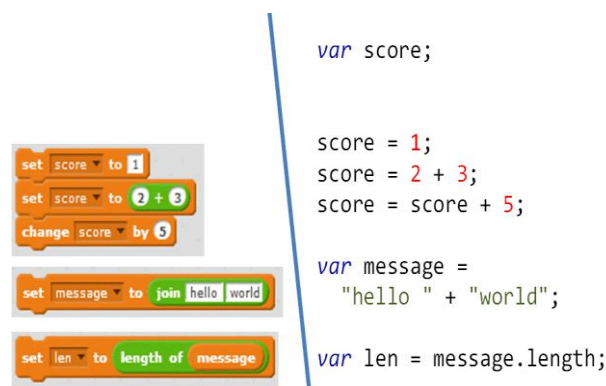
Fig. 3. Scratch vs. text based programming language

3.3   Participants

This experiment had been conducted in the 2016-2017 academic year with three groups of a randomly selected total of 61 sixth grade students of three different middle schools in the city of Konya, Turkey as shown in Table 1.

The students from each group received 3-hour Scratch training which was offered by Konya Science Center instructors. The students were asked to complete the tasks from simple to complex during the training session.

The students who were primarily trained for Scratch activities and who did not have a lot of computer training, in general, were preferred. Thus, it has been tested that a student who has never used a computer can easily learn to code with Scratch.

Table 1. Group characteristics

Group 1	Group 2	Group 3
17 students	22 students	22 students
12 male, 5 female	11 male, 11 female	13 male, 9 female
Public School	Public School (village)	Private School

To determine students programming level, the survey which consists of demographic backgrounds and math grades questions was hand out to all pupils before beginning to introduce the Scratch environment. During the training, firstly presented basic information about Scratch environment then students were given three different tasks, which is shown in Table 2, were from simple to the complex. Each student's the completion times of given task, which can be seen in Table 3, were noted by the instructor.

Table 2. Tasks

Tasks	Description
Task 1	To implement sound effect on the Scratch's main character
Task 2	To implement small fish which is chased by a shark
Task 3	To implement a prince and a princess who walk to each other and say "hello".

3.4 Method

In this study, A Mamdani-type FIS [27] and Scratch environment [30] have been used for building for the proposed model.

The Mamdani type FIS model given in Fig. 4, has been developed to predict participants' success during the Scratch training sessions. The fuzzification with four linguistic variables (i.e., very slow, slow, average, fast) is applied to each of the input and output attributes.
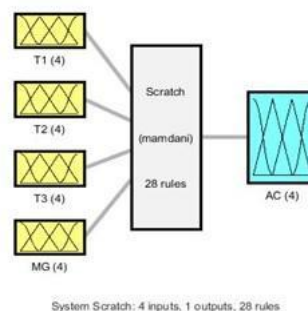
System Scratch: 4 inputs, 1 outputs, 28 rules
Fig. 4. The proposed model of Mamdani-type FIS

Four input and one output parameters (Table 3) were used to determine the students' success in the Scratch training. The membership functions that will result in the best performance were selected (Figs. 6-10).

Table 3. Input and Output Parameters

Parameter	Input/Output	Description
T1	Input	The first task completion time
T2	Input	The second task completion time
T3	Input	The third task completion time
MG	Input	Mathematics grade
SR	Output	Success Rate

The fuzzy inference diagram shows all pieces of the fuzzy inference process (Fig. 5).
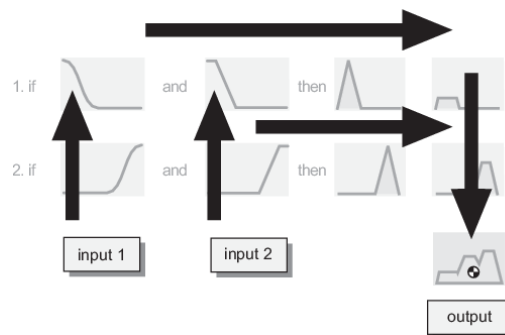
Fig. 5. Fuzzy Inference Diagram [29].

The fuzzy rule system, which is designed based on how the experts describe the attributes of the variables of the system, may vary from one expert to another. It is possible to write down a lot of "if-then" fuzzy rules. This study considers 28 if-then rules and some of the rules used in the model are as shown in Table 4.

Table 4. Subset of the if-then rules

										Input		Output
IF	T1	And	T2	And	T3	And	MG	Then	SR			
	Fast		Fast		Fast		High		Successful			
	Average		Average		Average		High		Average Successful			
	Slow		Slow		Slow		High		Low Successful			
	Very Slow		Very Slow		Very Slow		High		Unsuccessful			
	Fast		Very Slow		Very Slow		High		Unsuccessful			
	Fast		Slow		Slow		High		Low Successful			
	Fast		Average		Average		Very Low		Average Successful			
	Fast		Average		Average		Low		Average Successful			
	Fast		Average		Average		Average		Successful			
	Fast		Average		Average		High		Average Successful			

3.5   Fuzzification of Inputs

Input 1. The Input 1 is represented in the FIS as "T1: The first task completion time" (Fig. 6) and fuzzified with fast [0-33 second], average [0-66 second], slow [33-100 second], very slow [66+ second]. The triangular, s-shape and z-shape MF's were considered for the analysis (Fig. 6).
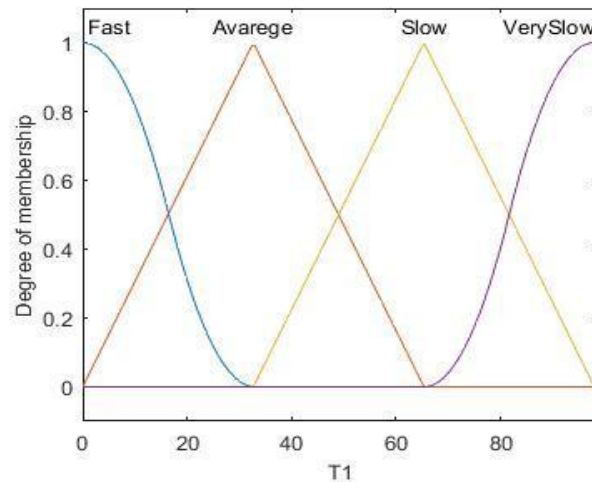
Fig. 6. MF's for Input T1

Input 2. The Input 2 is represented in the FIS as "T2: The second task completion time" (Fig. 7) and fuzzified with fast [0-150 second], average [0-300 second], slow [150-450 second], very slow [300+ second]. The triangular, s-shape and z-shape MF's were considered for the analysis (Fig. 7).
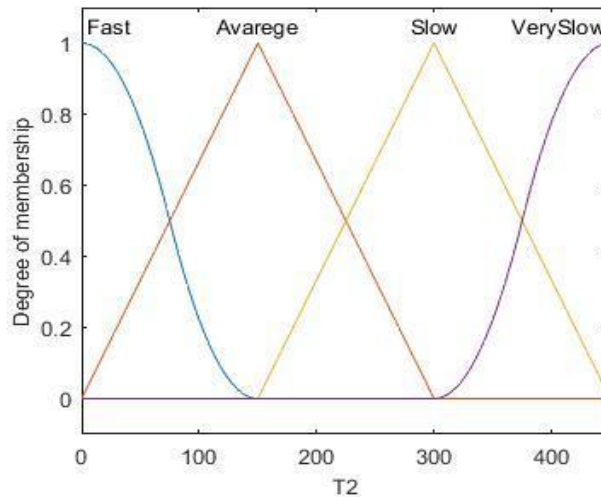
Fig. 7. MF's for Input T2

Input 3. The Input 3 is represented in the FIS as "T3: The third task completion time" (Fig. 8) and fuzzified with fast [0-330 second], average [0-660 second], slow [330-1000 second], very slow [660+ second]. The triangular, s-shape and z-shape MF's were considered for the analysis (Fig. 8).
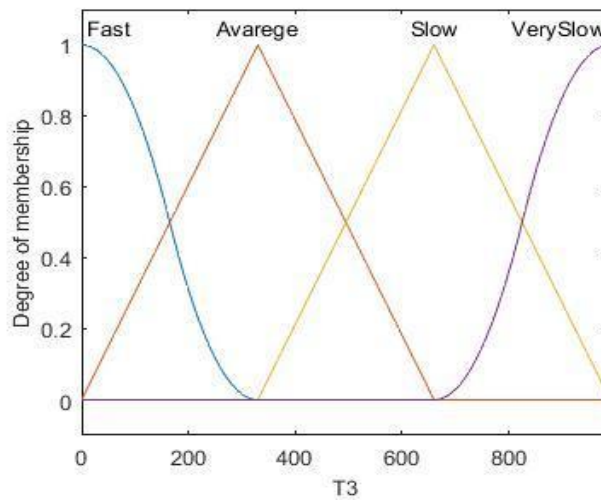
Fig. 8. MF's for Input T3

Input 4. Mathematics plays a very important role during the high school entrance exam and also in the university entrance exam in Turkey. If somebody wants to pursue his career in the engineering field, the mathematics' importance has remained quite constant so far. A number of studies by [32], [33], [34] confirmed that mathematical knowledge is a strong predictor of success in programming.

The Input 4 is represented in the FIS as "MG: Mathematics grade" (Fig. 9) and fuzzified with very low [0-33 point], low [0-66 point], average [33-100 point], high [66+ point]. The triangular, s-shape and z-shape MF's were considered for the analysis (Fig. 9).
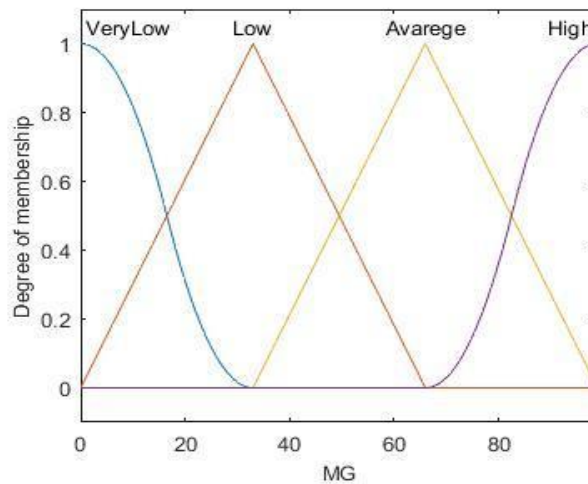
Fig. 9. MF's for Input MG

Defuzzification of Output. Centroid method was used for defuzzification. The Output is represented in the FIS as "SR: Success Rate" (Fig. 10) and classified with unsuccessful [0-33 point], Lsuccess [0-65 point], Asuccess [33-100 point], successful [65+ point]. MF's considered for the analysis were of triangular, s and z shape.
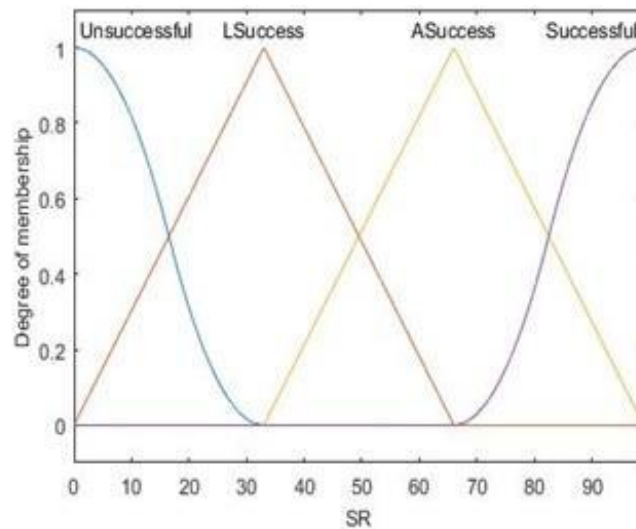
Fig. 10. MF's for Input SR (Success Rate)
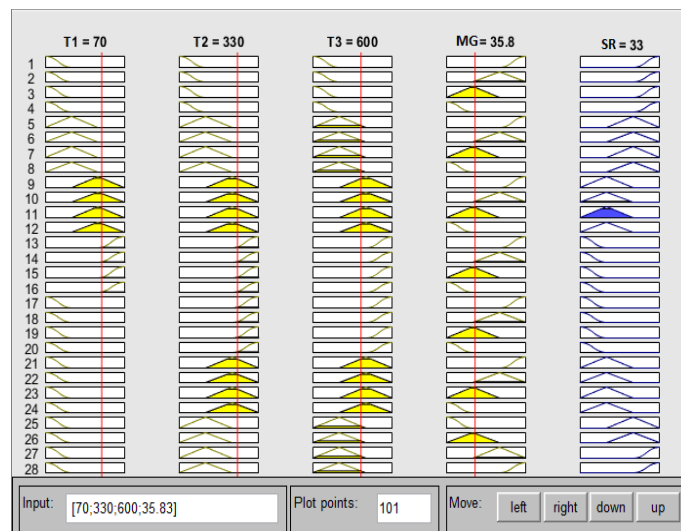
Fig. 11. Output for random input values

Fig. 11 shows the output for randomly selected input values. The inputs values, T1=70, T2=330, T3=600, MG=35.83, the system produced the output value as SR=33 which indicates the success of a student performance in the Scratch programming for the given T1, T2, T3 and MG values. The students are given an estimated success value by taking into consideration the task completion time and their course grades. If the given task's completion time is short and participant's course grade is high, then participant is rated with the highest success rate. If the given task's completion time is long and participant's course grade is low, then participant is rated with the lowest success rate. Then, the connection between the success rate (fuzzy value) and the real value obtained by experimental data was determined by regression analysis.

4. RESULTS AND DISCUSSION

A regression analysis was carried out between experimental and the predicted (fuzzy) values. The R^2 correlation coefficient shows the relationship between real values and fuzzy values. The relationship between values increases as the correlation coefficient approaches +1. As shown in Figs. 12-14, R^2 values for the success rates are 0,8023 for Group 1; 0,9704 for Group 2; 0,8446 for group 3

respectively. The R^2 values indicate that the predicted (fuzzy) value and the real value obtained by experimental data fairly close to each other. This shows the success of the fuzzy logic system.
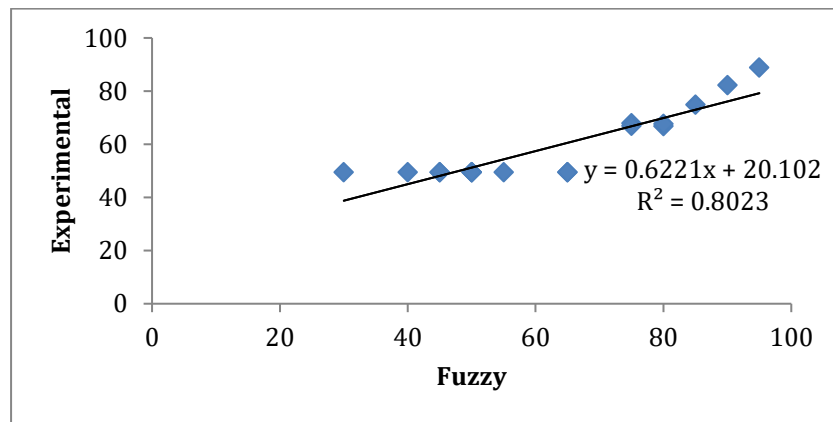
Fig. 12. R^2 value for group 1
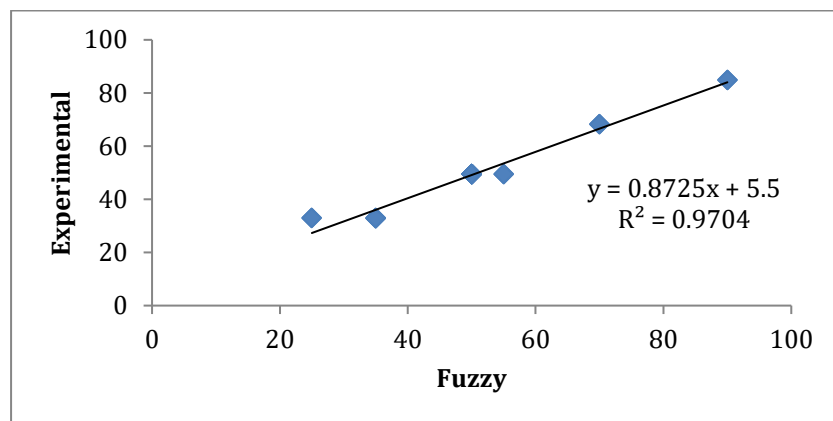
Fig. 13. R^2 value for group 2
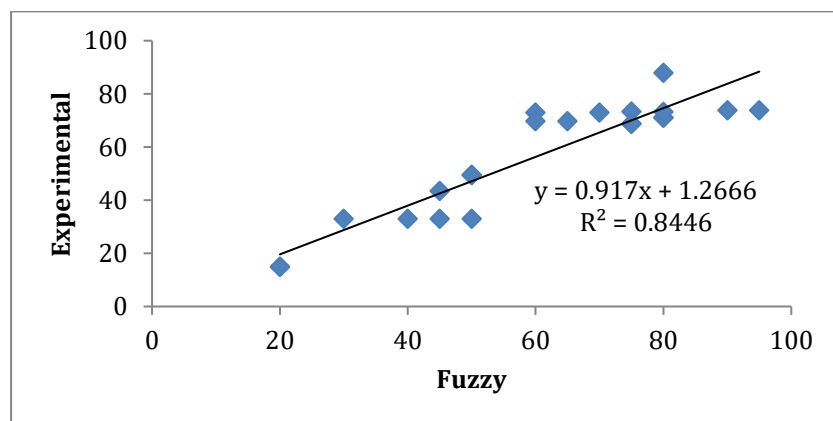
Fig. 14. R^2 value for group 3

Table 5. ANOVA analysis

	Sum of squares	DF	Mean Squares	F	P value
Factor1	10.801	1	10.801	0.041123	0.84028
Errror	11031	42	262.65		
Total	11042	43			

We have performed a one-way ANOVA with a single factor. According to Table 5 below considerations can be said: The F-statistic (0.041) is very small, indicating little difference between the variance explained by Factor1 and the residual (unexplained) variance.

The p-value (0.840) is much greater than the typical significance threshold of 0.05. This means we cannot reject the null hypothesis of no effect with enough confidence. In other words, there is no significant difference in means among the groups. It's important to note that when the p-value is high (above 0.05), it suggests that any observed differences could be due to random chance, and you do not have enough evidence to conclude that the factor has a significant effect.

Table 6. Each groups' task completion time (Min., Max., Avg., Std. Deviation)

	Group 1	Group 2	Group 3
Minimum duration	Task 1: 5 sec	Task 1: 5 sec	Task 1: 5 sec
	Task 2: 5 sec	Task 2: 60 sec	Task 2: 30 sec
	Task 3: 60 sec	Task 3: 90 sec	Task 3: 120 sec
Maximum duration	Task 1: 120 sec	Task 1: 90 sec	Task 1: 21 sec
	Task 2: 30 sec	Task 2: 410 sec	Task 2: 350 sec
	Task 3:1260 sec	Task 3: 990 sec	Task 3: 750 sec
Average duration	Task 1: 35,94 sec	Task 1: 57,36 sec	Task 1: 12,31 sec
	Task 2: 13,76 sec	Task 2: 222,27sec	Task 2: 115,68 sec
	Task 3: 377,64 sec	Task 3: 319.10 sec	Task 3: 332,72 sec
Standard deviation	Task 1: 43,12 sec	Task 1: 27,61 sec	Task 1: 5,40 sec
	Task 2: 6,74 sec	Task 2: 137,41 sec	Task 2: 116,23 sec
	Task 3: 401,80 sec	Task 3: 307,41 sec	Task 3: 235,95 sec

According to Table 6 below considerations can be said:

Evaluation of success according to the groups (schools): Given the average of the completion times of the assigned tasks of the groups, Group 2 can be considered to be more successful than the other groups. However, in Group 2, 10 students did not complete task 3. While the number of students who could not complete task 3 in Group 1 was 8, in Group 3, there were no failed students. Overall, it is possible to be considered that the students in Group 3 are more successful comparing to Group 2 and Group 1.

Evaluation of success according to the gender: Group 1: Among 17 students, 2 males and 1 female student seem to be over the average in terms of completion of the tasks. Group 2: 4 out of 22 students are over the average in terms of completion time of the task. No male students can be found over average. Group 3: Among 22 students, 8 males and 5 female students are above the average in terms of completion of the task. Since the standard deviations are low for all groups, we can say that the values for that task are close to the mean and suggest consistency.

According to the results, students in private schools were more successful than those who were in public schools. The private students' parent's education level, school facilities and financial opportunities have played an important role in their programming skills.

3. CONCLUSIONS

In this study, the programming experiment has been carried out using the Scratch environment. It was primarily proposed to a fuzzy logic system to predict student performance during the experiment then compare fuzzy logic prediction results to the experts' results. Secondly, to test the theory that students' interest in learning algorithms and coding can be increased using the creation of games in a visual programming tool for beginners.

During Scratch training, the students were tasked with three different gaming challenge. Instead of figuring out programming syntax, the Scratch environment allowed Pupils concentrate their attention on tackling problems. The tasks completion time and mathematics grades of students has been used as

input the Mamdani type fuzzy logic system and the success rate has been calculated.

While students were performing the given Scratch tasks there were no signs of boredom or distraction. On the contrary, it was observed that they try to complete the given tasks as if they were playing a game and without conscious effort, they were improving their analytical and problem-solving skills. In addition, it was observed that students who were coming from the village school and did not use computers before were able to use computers easily while trying to accomplish the given Scratch tasks.

With fuzzy logic, the success rate can be estimated for different task completion times. It is also possible to predict how long a student must perform a task in order to be successful.

In later studies, different factors can be used as inputs to measure the success of students in learning to code with Scratch environment.

Declaration of Ethical Standards

The authors of this article declare that the materials and methods used in this study do not require ethical committee permission and/or legal-special permission.

Declaration of Competing Interest

The authors declared that they have no conflict of interest.

Funding / Acknowledgements

The author(s) received no financial support for the research.

Data Availability

Data available on request from the author.

REFERENCES

[1]   J. H. Maloney, K. Peppler, Y. Kafai, M. Resnick, and N. Rusk, "Programming by choice: urban youth learning programming with scratch," in Proceedings of the 39th SIGCSE technical symposium on Computer science education, 2008, pp. 367-371.

[2]   M. Prensky, "Digital natives, digital immigrants part 2: Do they really think differently?," On the horizon, vol. 9, no. 6, pp. 1-6, 2001.

[3]   M. Resnick et al., "Scratch: programming for all," Communications of the ACM, vol. 52, no. 11, pp. 60-67, 2009.

[4]   W. Dann and S. Cooper, "Education Alice 3: concrete to abstract," Communications of the ACM, vol. 52, no. 8, pp. 27-29, 2009.

[5]   M. Mladenović, D. Krpan, and S. Mladenović, "Learning programming from Scratch," in International Conference on New Horizons in Education INTE, 2017.

[6]   W. Dann, D. Cosgrove, D. Slater, D. Culyba, and S. Cooper, "Mediated transfer: Alice 3 to java," in Proceedings of the 43rd ACM technical symposium on Computer Science Education, 2012, pp. 141-146.

[7]   A. K. Whitfield, S. Blakeway, G. E. Herterich, and C. Beaumont, "Programming, disciplines and methods adopted at Liverpool Hope University," Innovation in Teaching and Learning in Information and Computer Sciences, vol. 6, no. 4, pp. 145-168, 2007.

[8]   L. A. Zadeh, "Fuzzy sets," Information and control, vol. 8, no. 3, pp. 338-353, 1965.

[9]   H. Singh et al., "Real-life applications of fuzzy logic," Advances in Fuzzy Systems, vol. 2013, pp. 3-3, 2013.

[10]   S. A. Papert, Mindstorms: Children, computers, and powerful ideas. Basic books, 2020.

[11]   O. Yildiz, A. Bal, and S. Gulsecen, "Improved fuzzy modelling to predict the academic performance of distance education students," International Review of Research in Open and Distributed Learning, vol. 14, no. 5, pp. 144-165, 2013.

[12]   S. Ingoley and J. Bakal, "Use of fuzzy logic in evaluating students' learning achievement," International Journal on Advanced Computer Engineering and Communication Technology (IJACECT), vol. 1, no. 2, pp. 47-54, 2012.

[13]   S. S. Jamsandekar and R. Mudholkar, "Performance evaluation by fuzzy inference technique," International Journal of Soft Computing and Engineering, vol. 3, no. 2, pp. 158-164, 2013.

[14]   Z. Yıldız and A. F. Baba, "Evaluation of student performance in laboratory applications using fuzzy decision support system model," in 2014 IEEE Global Engineering Education Conference (EDUCON), 2014: IEEE, pp. 1023-1027.

[15]   G. Jyothi, C. Parvathi, P. Srinivas, and S. Althaf, "Fuzzy expert model for evaluation of faculty performance in Technical educational Institutions," International Journal of Engineering Research and Applications, vol. 4, no. 5, pp. 41-50, 2014.

[16]   M. Eryılmaz and A. Adabashi, "Development of an intelligent tutoring system using bayesian networks and fuzzy logic for a higher student academic performance," Applied Sciences, vol. 10, no. 19, p. 6638, 2020.

[17]   D. Doz, D. Felda, and M. Cotič, "Combining Students' Grades and Achievements on the National Assessment of Knowledge: A Fuzzy Logic Approach," Axioms, vol. 11, no. 8, p. 359, 2022.

[18]   N. U. Jan, S. Naqvi, and Q. Ali, "Using Fuzzy Logic for Monitoring Students Academic Performance in Higher Education," Engineering Proceedings, vol. 46, no. 1, p. 21, 2023.

[19]   M. Dhokare, S. Teje, S. Jambukar, and V. Wangikar, "Evaluation of academic performance of students using fuzzy logic," in 2021 International Conference on Advancements in Electrical, Electronics, Communication, Computing and Automation (ICAECA), 2021: IEEE, pp. 1-5.

[20]   J. A. Rojas, H. E. Espitia, and L. A. Bejarano, "Design and optimization of a fuzzy logic system for academic performance prediction," Symmetry, vol. 13, no. 1, p. 133, 2021.

[21]   M. Abou Naaj, R. Mehdi, E. A. Mohamed, and M. Nachouki, "Analysis of the Factors Affecting Student Performance Using a Neuro-Fuzzy Approach," Education Sciences, vol. 13, no. 3, p. 313, 2023.

[22]   R. Mehdi and M. Nachouki, "A neuro-fuzzy model for predicting and analyzing student graduation performance in computing programs," Education and Information Technologies, vol. 28, no. 3, pp. 2455-2484, 2023.

[23]   R. Parkavi and P. Karthikeyan, "Predicting academic performance of learners with the three domains of learning data using neuro-fuzzy model and machine learning algorithms," Journal of Engineering Research, 2023.

[24]   M. Agaoglu, "Predicting instructor performance using data mining techniques in higher education," IEEE Access, vol. 4, pp. 2379-2387, 2016.

[25]   C.-T. Lye, L.-N. Ng, M. D. Hassan, W.-W. Goh, C.-Y. Law, and N. Ismail, "Predicting Pre-university student's Mathematics achievement," Procedia-Social and Behavioral Sciences, vol. 8, pp. 299-306, 2010.

[26]   L. A. Zadeh, "The concept of a linguistic variable and its application to approximate reasoning—I," Information sciences, vol. 8, no. 3, pp. 199-249, 1975.

[27]   E. H. Mamdani and S. Assilian, "An experiment in linguistic synthesis with a fuzzy logic controller," International journal of man-machine studies, vol. 7, no. 1, pp. 1-13, 1975.

[28]   M. Sugeno, Industrial applications of fuzzy control. Elsevier Science Inc., 1985.

[29]   J. R. Jang, MATLAB: Fuzzy logic toolbox user's guide: Version 1. Math Works, 1997.

[30]   J. Yuan and R. T. Bowen, "Lifelong Kindergarten: Cultivating Creativity Through Projects, Passion, Peers, and Play," Interdisciplinary Journal of Problem-Based Learning, vol. 12, no. 2, p. 6, 2018.

[31]   K. Brennan and M. Resnick, "New frameworks for studying and assessing the development of computational thinking," in Proceedings of the 2012 annual meeting of the American educational research association, Vancouver, Canada, 2012, vol. 1, p. 25.

[32]   P. Byrne and G. Lyons, "The effect of student attributes on success in programming," in Proceedings of the 6th annual conference on Innovation and technology in computer science education, 2001, pp. 49-52.

[33]   G. White and M. Sivitanides, "An empirical investigation of the relationship between success in mathematics and visual programming courses," Journal of information systems education, vol. 14, no. 4, p. 409, 2003.

[34]   J. Bennedsen and M. E. Caspersen, "An investigation of potential success factors for an introductory model-driven programming course," in Proceedings of the first international workshop on Computing education research, 2005, pp. 155-163.

U2-NET SEGMENTATION AND MULTI-LABEL CNN CLASSIFICATION OF WHEAT VARIETIES

[1,*] **Mustafa Şamil ARGUN** [iD], [2] **Fuat TÜRK** [iD], [3] **Zafer CİVELEK** [iD]

[1] *Selçuk University, Akşehir Engineering and Architecture Faculty, Food Engineering Department, Akşehir, Konya, TÜRKİYE*
[2] *Kırıkkale University, Engineering Faculty, Computer Engineering Department, Kırıkkale, TÜRKİYE*
[3] *Çankırı Karatekin University, Engineering Faculty, Electrical and Electronics Engineering Department, Çankırı, TÜRKİYE*
[1] msargun@selcuk.edu.tr, [2] fturk@kku.edu.tr, [3] zafercivelek@karatekin.edu.tr

Highlights

- The two-stage system has been successfully tested in wheat classification and this is a prelude to more staged systems.

- Wheats have been successfully classified according to both their vitreous/yellow berry status and their varieties.

- Experimental results showed that the accuracy for binary classification was 98.71% and the multi-label classification average accuracy was 89.5%.

- This proposed system can be successfully used in wheat trade and breeding studies to help experts.

- The proposed U2-Net architecture is an example that can be easily used in all grain groups, especially wheat images.

*Corresponding Author: Mustafa Şamil ARGUN, msargun@selcuk.edu.tr

U2-NET SEGMENTATION AND MULTI-LABEL CNN CLASSIFICATION OF WHEAT VARIETIES

1, * Mustafa Şamil ARGUN iD **, 2 Fuat TÜRK** iD **, 3 Zafer CİVELEK** iD

1 *Selçuk University, Akşehir Engineering and Architecture Faculty, Food Engineering Department, Akşehir, Konya, TÜRKİYE*
2 *Kırıkkale University, Engineering Faculty, Computer Engineering Department, Kırıkkale, TÜRKİYE*
3 *Çankırı Karatekin University, Engineering Faculty, Electrical and Electronics Engineering Department, Çankırı, TÜRKİYE*
1msargun@selcuk.edu.tr, 2fturk@kku.edu.tr, 3zafercivelek@karatekin.edu.tr

ABSTRACT: There are many varieties of wheat grown around the world. In addition, they have different physiological states such as vitreous and yellow berry. These reasons make it difficult to classify wheat by experts. In this study, a workflow was carried out for both segmentation of wheat according to its vitreous/yellow berry grain status and classification according to variety. Unlike previous studies, automatic segmentation of wheat images was carried out with the U2-NET architecture. Thus, roughness and shadows on the image are minimized. This increased the level of success in classification. The newly proposed CNN architecture is run in two stages. In the first stage, wheat was sorted as vitreous-yellow berry. In the second stage, these separated wheats were grouped by multi-label classification. Experimental results showed that the accuracy for binary classification was 98.71% and the multi-label classification average accuracy was 89.5%. The results showed that the proposed study has the potential to contribute to making the wheat classification process more reliable, effective, and objective by helping the experts.

1. INTRODUCTION

Wheat ranks second after corn with a production of around 780 million tons worldwide [1]. A large number of wheat varieties are produced in the world. Feldman [2] reports that there are 25,000 different forms of cultivated bread wheat worldwide and the total number available is likely to be at least twice this estimate [3]. In Türkiye alone, there are hundreds of local wheat varieties and as of 2016, there are 198 registered varieties for bread and 61 for durum [4]. In the buying and selling transactions of wheat, which has so many varieties, only the experts make a wheat classification. Of course, such a classification can be subjective and there is a possibility of personal errors.

Yellow berry is a physiological condition that affects the quality and commercialization of wheat. In the grain, this situation is characterized by starchy or floury spots [5, 6]. It is stated that yellow berry grains have higher moisture and lower protein content compared to vitreous grains. [7]. Presence of yellow berry grains in durum and bread wheat is an important factor in terms of pasta cooking quality, grinding and baking quality [8]. Compared to non- vitreous grains, vitreous grains generally have better cooking quality, better pasta color, coarser granulation, higher protein content, higher hardness, and are sold at a higher price [9, 10]. For these reasons, it is important to detect the yellow berry grains in bread and durum wheat.

U2-NET is an architecture used in image processing. This architecture is a deep learning network used to obtain high quality and accurately parsed images. U2-NET is designed for salient object detection. The U2-NET architecture is specifically optimized for parsing high resolution images. U2-NET, unlike previous U-NET architectures, has more depth and expansion paths. It also has a dual-output architecture, meaning the same network is used to obtain detailed and extended outputs [11, 12].

*Corresponding Author: Mustafa Şamil ARGUN, msargun@selcuk.edu.tr

Classification processes are carried out successfully in agriculture with artificial intelligence models. Classical CNN models from artificial intelligence models, architectures such as DenseNet, NasNet Mobile, VGG16, VGG19 are widely used in classification problems [13, 14]. In the literature, applications such as the recognition of plant diseases [15], classification and grading of fruits [16, 17], classification of flowers [18], classification of hazelnut varieties [19], classification of green coffee beans [20], classification of cherry varieties [21], classification of lemons [22], weed detection in wheat fields [23], image-based quality analysis of strawberries [24], detection of impurities in wheat [25] and image-based wheat grain classification using CNN [26] have been carried out successfully. Shen et al. [25] using terahertz spectral imaging and CNN, classified straw from impurities in wheat with 96-97% precision, weed with 95-96% precision, wheat leaf with 96-98% precision, wheat grain with 97-99% precision, ladybug with 97-98% precision, and wheat husk with 95-97% precision. Lingwal et al. [26] classified 15 different wheat varieties with 98% accuracy with their proposed model based on CNN. In their studies, they stated that the image resolution over 256*256 reduces the system performance. Yasar [27] classified 5 varieties of wheat using Inception-V3, Mobilenet-V2 and Resnet18 CNN models with an accuracy of 97.37%, 97.07% and 97.67%, respectively.

In the literature, no study has been found in which wheat grains are distinguished according to both vitreous/yellow berry grain status and cultivar differences. In our study, it is aimed to create a two-stage CNN architecture that will classify wheat according to both variety and vitreous/yellow berry grain status. Thus, a reliable, effective, and objective system will be obtained to assist experts in wheat classification.

2. MATERIAL AND METHODS

2.1. Dataset Description

In our study, the varieties of Bayraktar 2000, Bezostaja-1, Delabrad, Ekiz, Esperia, Lucilla, Odeska, Rumeli and Selimiye, which are the most produced bread wheats in Konya Akşehir region, and the durum wheat variety Kızıltan were used (Figure 1). Wheats were obtained from Turkish Grain Board in Akşehir (Konya/Türkiye). The collected wheat images were first positioned in 224*224 dimensions and with the objects in the center. At this stage, the images were first cropped and then the resize process was applied. Then, blurring and sharpening errors in existing images were minimized. Finally, the Contrast, Brightness and Color parameters of the images were arranged with the image enhance class, and the image preprocessing steps were completed. At these stages, the PILLOW library in the Python programming language was used. Some examples of original and image preprocessing of images are shown in Figure 1.

Figure 1. Vitreous and yellow berry grain images of the wheat varieties used and the first image processing stage.

2.2. U2-Net Architecture with Wheat Segmentation

The U2-Net model was proposed by Qin and its structure is shown in Figure 2 [27]. In this study, the U2-Net architecture was arranged for a clear detection of wheat images. In addition, the U2-Net architecture can analyze the curves of the image edges better than a classical segmentation. In this way, the separation of wheat varieties will be more successful. In general, U2-Net model consists of a total of 11 layers including encoder and decoder.

This study, sigmoid function was used in the merging phase, and Adam optimizer was prefered in the other layers. In the proposed U2-Net architecture, batch-size: 4, mask-size: 600, threshold:140, trimap-dilation:4 and trimap-erosion-iters are set to :10 for segmentation. These hyperparameters given are the result of the training process until the best results are obtained. The values given in the tables are an average of 10-fold cross validation. Figure 3 shows the wheat images obtained as a result of the U2-Net segmentation process.
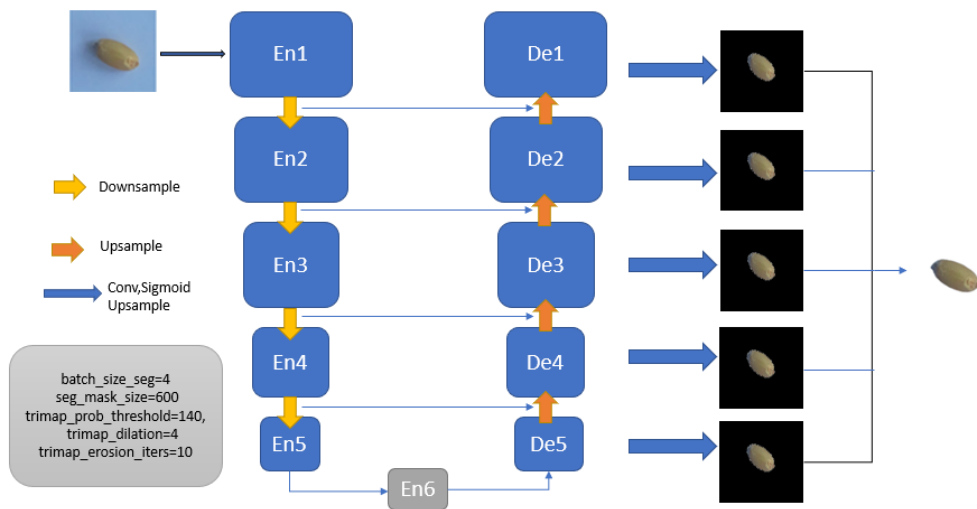
Figure 2. Proposed U2-Net architecture.
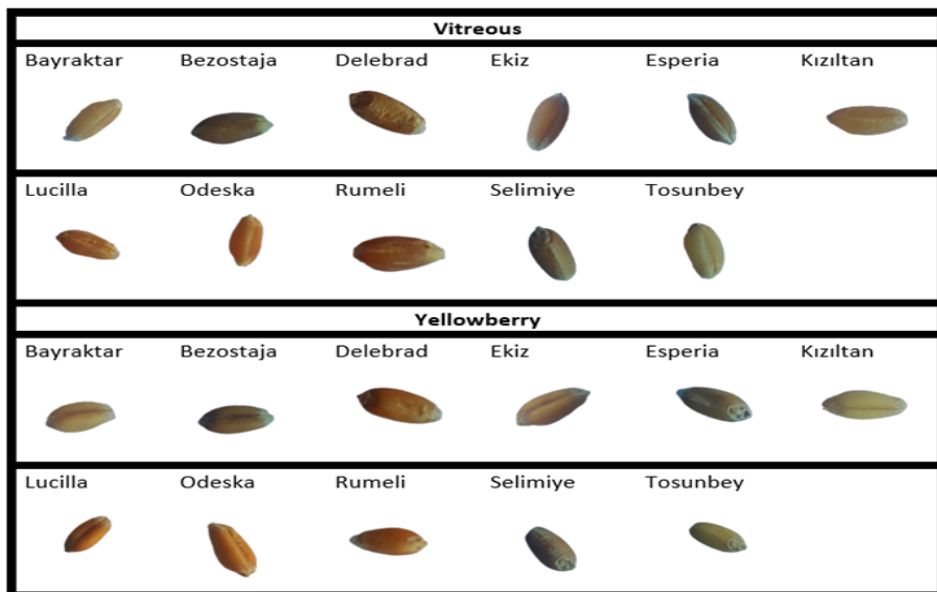
Figure 3. Images of wheat after U2-Net segmentation

While the images are being pre-processed, 196 images collected from each of the vitreous and yellow berry groups in the first place have been increased to a total of 1160 pieces, with the number of each subclass being equal, with the data augmentation process (Table 1). Finally, the train, validation, and test processes were randomly divided into 80%, 10%, and 10%, respectively. Figure 4 shows the train, validation, and test stages for the data set. Here, it is aimed to increase the accuracy of the training process with the cross-validation application. In order to evaluate the model success more effectively and to measure the accuracy of the results they gave; it was preferred to use the cross-validation technique. Thus, it is aimed to increase the success of the test data. The values given in the tables are an average of 10-fold cross validation.
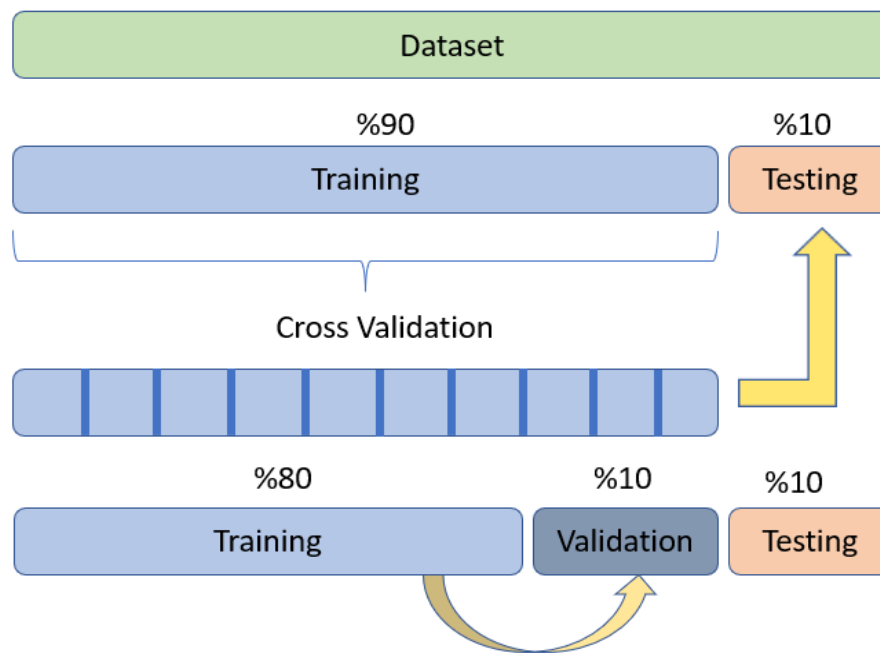
Figure 4. The train, validation, and test stages for the data set

In Table 1, the number of images obtained because of data augmentation is given. During data augmentation, the images were rotated by 45 degrees angles, but no shift (left/right) operation was applied. During the data augmentation phase, the zoom range ratio was set to 0.25. While rotation was applied on the horizontal axis, rotation on the vertical axis was not preferred.

Table 1. Total number of images before and after data augmentation

	Vitreous image	Yellow berry image
Total image	196	196
Total image after data augmentation	1160	1160
Train/Val/Test image	928/116/116	928/116/116

2.3. Proposed CNN Architecture

In the proposed CNN architecture, the input image size is set to 224×224 and then it is aimed to determine the features of the images in the feature extraction stage. At this stage, 4 convolutional layers were used in CNN architecture. The image was scanned with a 3×3 filter around the image. In the decoder phase, max pooling layer, ReLU as activation function and Adam optimizer as optimization method were chosen. At the binary classification stage, the vitreous/yellow berry separation of wheat was made. A multi classification pipeline was then executed with the same subclass names. The proposed CNN model

is shown in Figure 5.

The tensorflow 2.0 library was used during the training of the CNN network. In addition, the training and testing processes of the proposed architectural structure were carried out with Nvidia GTX 1060 graphics card.
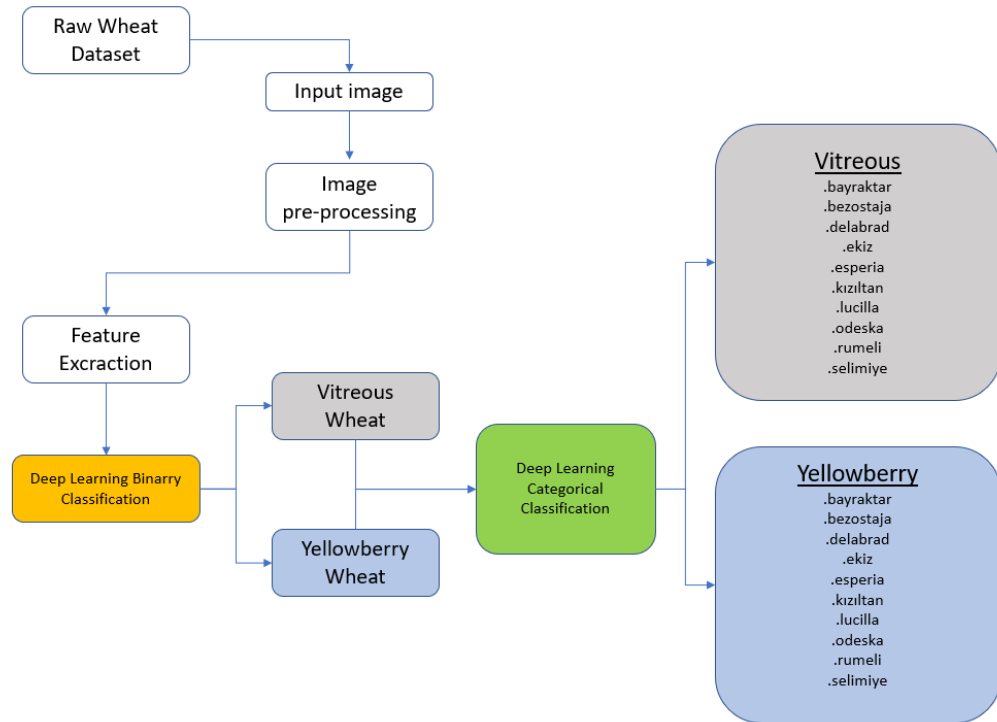
Figure 5. Proposed CNN architecture.

The artificial intelligence model used in our study was designed in two stages and operated differently from previous wheat classification studies. Accordingly, in the first stage, a binary classification output system was implemented that detects the vitreous/yellow berry state of the wheat images. In the second stage, the vitreous/yellow berry labeled data were determined by the multi-label classification output system. Even though the architectural structures used are similar to previous studies, there are differences in terms of choices such as the selection of hyperparameters, the use of activation functions, and filter sizes.

2.4. Performance Evaluation Criteria

Precision, Recall, Accuracy, and F1 score are the main criteria for evaluating the performance of classification algorithms. Precision refers to how many of the values predicted as Positive actually turn out to be Positive. Recall shows how many of the transactions that should have been predicted as Positive were predicted as Positive. Accuracy value is calculated by the ratio of the areas we predict correctly in the model to the total data set. The F1 Score value shows the harmonic mean of the Precision and Recall values. True Positive and True Negative are areas that the model predicts correctly, while False Positive and False Negative are areas that the model predicts incorrectly [13, 28].

The calculations of these metrics were made with the following Equations, respectively;

$$Accuracy = (TN + TP)/(TP + FP + TN + FN) \tag{1}$$
$$Precision = TP / (TP + FP) \tag{2}$$
$$Recall = TP/(TP + FN) \tag{3}$$
$$F1 - Score = 2 \times (Recall \times Precision) / (Recall + Precision) \tag{4}$$

3. RESULTS AND DISCUSSION

3.1. Binary Classification

In the first stage, the accuracy and loss values obtained as a result of the training process are shown in Figure 6. In Figure 6, the vertical axes correspond to the accuracy and loss values for train/validation operations, while the horizontal axes represent the number of epochs. When the graph is examined in detail, it is observed that the train and validation curves are close to each other. This showed us that the training was successful, and that there was no overfitting or memorization. In addition, the training and test results were found to be very close to each other.
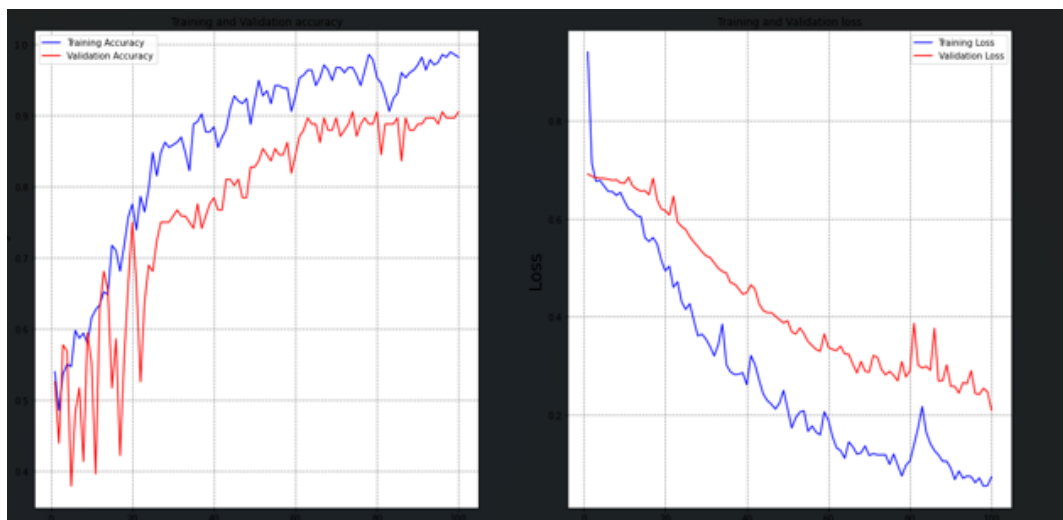
Figure 6. Train/validation accuracy/loss graph for binary classification

The confusion matrix graph calculated because of the test process in determining the vitreous and yellow berry classes is shown in Figure 7. Here, only 2 of the vitreous class and 1 of the yellow berry class were mislabeled, and the average accuracy was calculated as 98.71%.
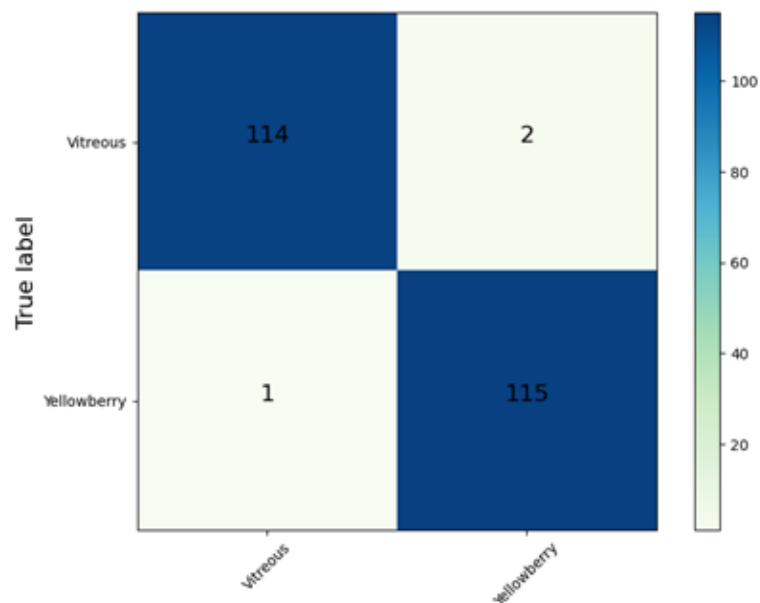
Figure 7. Confusion matrix graph for vitreous and yellow berry classes

The calculated performance metrics of the vitreous/yellow berry groups as the last step of the first phase are shown in Table 2. Looking at the confusion matrix in Figure 7, the accuracy for the vitreous class was calculated as 98.28% and the accuracy for the yellow berry class was calculated as 99.14%.

Table 2. Performance metrics of vitreous/ yellow berry groups

n(classified)	Accuracy(%)	Precision(%)	Recall(%)	F1-Score(%)
Vitreous:116	98.28	99.13	98.28	98.71
Yellow berry:116	99.14	98.29	99.14	98.71
Avg. Acc.	98.71			

3.2. Multi-Label Group Classification

In the Yellow berry/Vitreous group training, after the incorrectly labeled data was detected in the binary classification phase and transferred to the correct groups, the training process was started.

3.2.1. Yellow berry group class

The second stage was run separately for yellow berry and vitreous classes. The accuracy and loss values obtained because of the multi-class training process for the yellow berry class are given in Figure 8. Unlike the first stage, it is an acceptable situation that the validation/loss curves show a fluctuating state in the initial stage but are compatible with the train curve in the advancing epochs. Towards the end of the training, the curves again converged and there were no overfitting events or non-learning cases in the network.

Table 3. Yellow berry group multi-label classification evaluation results

Group No	Wheat variety	Precision (%)	Recall (%)	F1-Score (%)	Support (%)
0	Bayraktar2000	100	100	100	14
1	Bezostaja1	100	86.03	92.21	14
2	Delabrad2	80.13	86.34	83.34	14
3	Ekiz	100	100	100	14
4	Esperia	60.21	86.26	71.44	14
5	Kızıltan	100	100	100	14
6	Lucilla	100	100	100	14
7	Odeska	100	100	100	14
8	Rumeli	85.08	79.27	81.47	14
9	Selimiye	64.11	50.11	56.15	14
10	Tosunbey	100	93.28	96.37	14
	Accuracy (avg): 88.96%				154

The evaluation results of the yellow berry group are shown in Table 3 together with the class label names. Although some images were confused in Selimiye yellow berry classes due to its close resemblance to Esperia yellow berry, other class evaluation criteria were found to be quite good.

The confusion matrix graph calculated because of the yellow berry multi-class test process is shown in Figure 9. When the confusion matrix table is examined, it is observed that there is an acceptable level of mislabeling in a few classes where the test process was successful for most classes. In addition, we can say that performance metrics and average accuracy are very successful for a group of 11 classes.
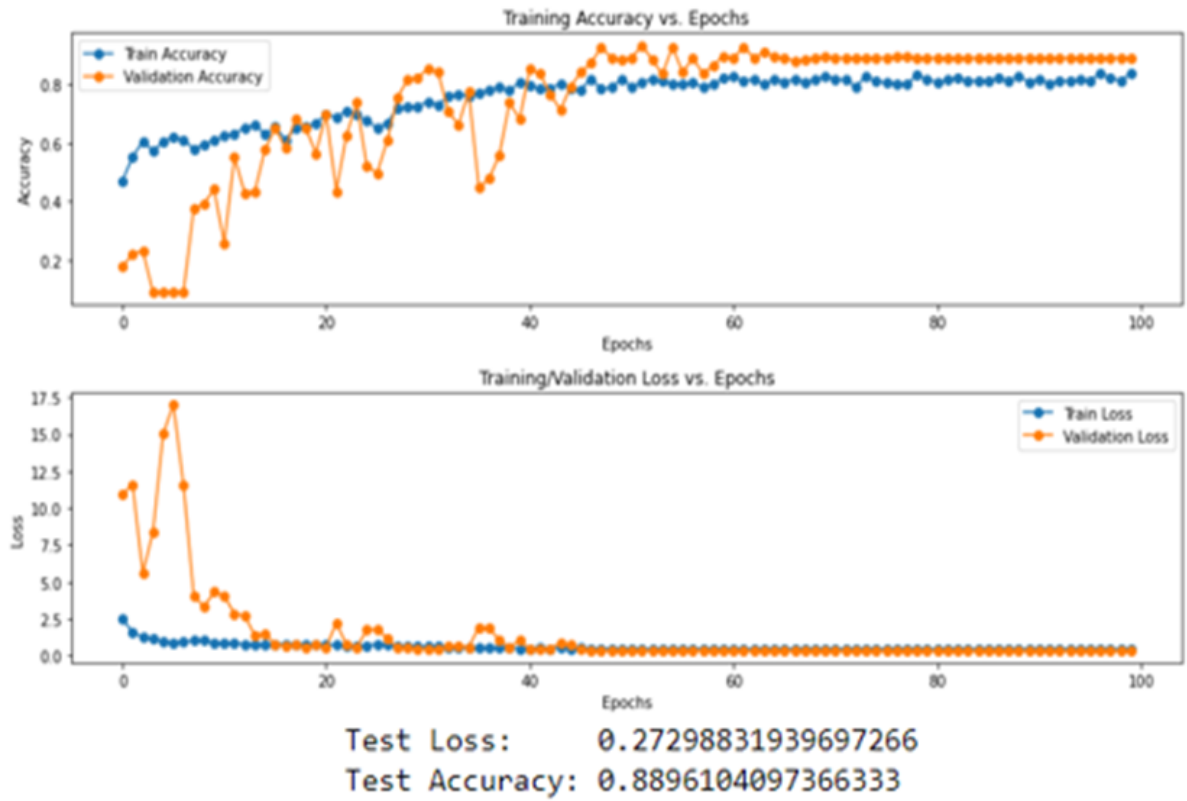
Figure 8. Train/validation accuracy/loss graph for yellow berry group multi-label classification
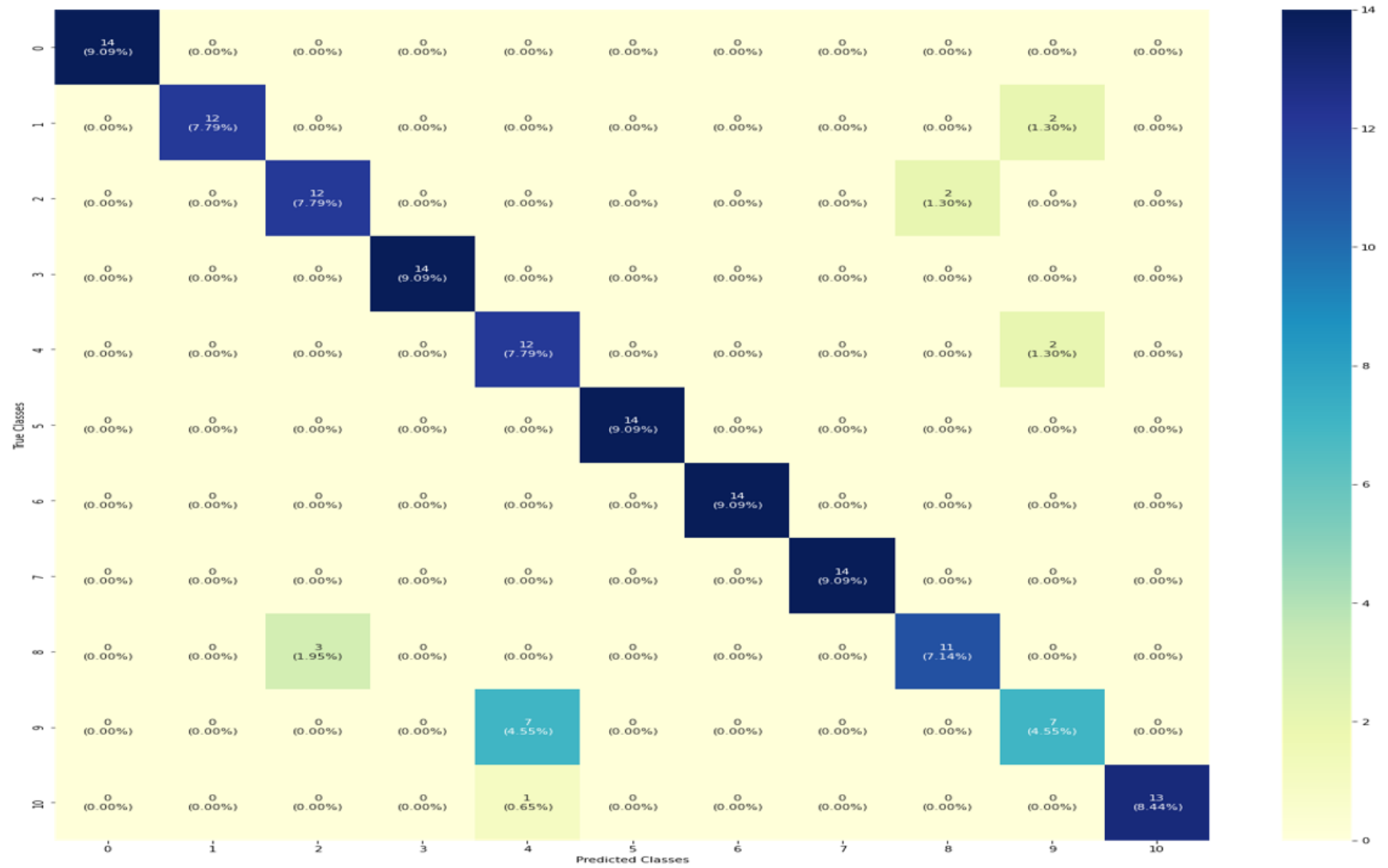
Figure 9. Yellow berry group confusion matrix and evaluation metric

3.2.2. Vitreous class

The accuracy and loss values obtained because of the multi-class training process for the vitreous class are given in Figure 10. It is an acceptable situation that validation/loss curves show a fluctuating state in the initial phase but are compatible with the train curve in the advancing epochs, as in the yellow berry multi-class. As a result of the training, yellow berry was slightly more successful than the classes and no over fitting was observed.

Test Loss: 0.30131110548973083
Test Accuracy: 0.9034090638160706
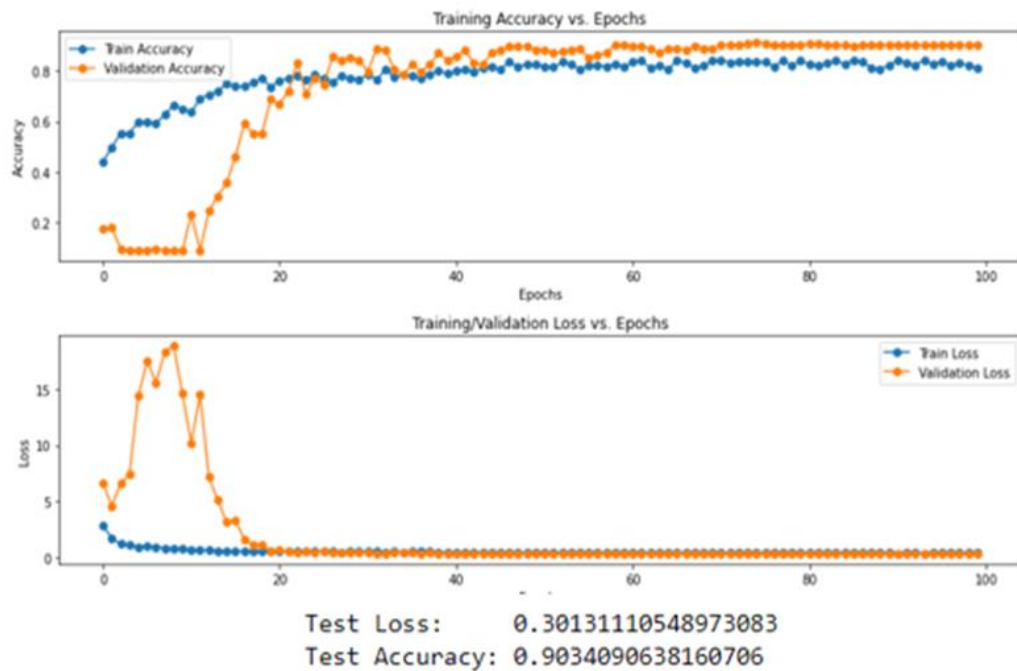
Figure 10. Train/validation accuracy/loss graph for vitreous group multi-label classification

The evaluation results of the vitreous group are shown in Table 4 together with the class label names. As in the yellow berry group, although the Selimiye and Esperia classes were somewhat confused due to their close similarity, the other class evaluation criteria were determined at a very good level.

Table 4. For vitreous group multi-label classification evaluation results

Group No	Wheat variety	Precision (%)	Recall (%)	F1-Score (%)	Support
0	Bayraktar2000	100	100	100	16
1	Bezostaja1	100	69.17	81.03	16
2	Delabrad2	100	100	100	16
3	Ekiz	100	100	100	16
4	Esperia	73.27	100	84.14	16
5	Kızıltan	100	100	100	16
6	Lucilla	76.05	94.33	84.41	17
7	Odeska	92.16	71.07	80.00	17
8	Rumeli	100	100	100	17
9	Selimiye	67.32	62.21	65.23	16
10	Tosunbey	100	100	100	13
		Accuracy (avg): 90.34%			176

The confusion matrix graph calculated because of the vitreous multi-class test process is shown in Figure 11. When the confusion matrix table is examined, it can be easily said that the test process was successful, as in the yellow berry group. Performance metrics were calculated slightly higher than the yellow berry group.
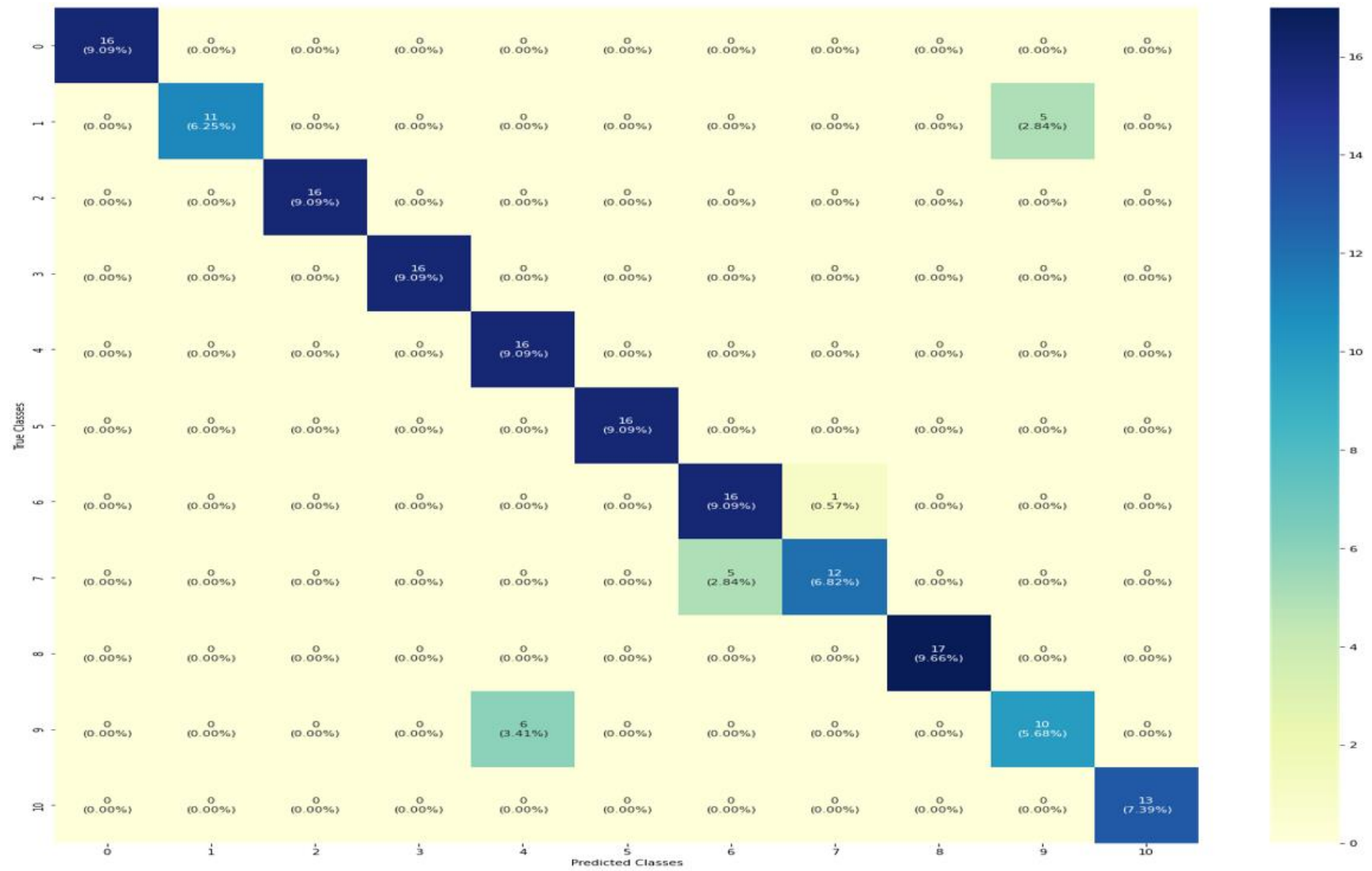
Figure 11. Vitreous group confusion matrix graph

Some results in which our proposed model mislabeled the vitreous and yellow berry groups in the test process are shown in Figure12. Looking at the results, we can say that this error is acceptable due to the close similarities between the images.

Vitreous Group
True Label: Epreria   True Label: Lucilla
Predict Label: Selimiye   Predict Label: Odeska

Yellowberry Group
True Label: Selimiye   True Label: Bezostaja1
Predict Label : Esperia   Predict Label: Selimiye

Figure 12. Mislabeled Vitreous/Yellow berry group image samples

As in our study, a two-stage classification was not found in the literature. When compared with other studies (Table 5), we can say that our results are in a reliable range, because the image classes used in our study are different and the margin of error may be slightly higher especially in multiple classes. An accuracy value of 98.71% was achieved in the separation into 2 different groups as Vitreous/Yellow berry class. Then, the images separated into vitreous and yellow berry were classified for the 11 wheat varieties mentioned in the study. Thus, it was possible to classify a total of 22 different classes of images and the accuracy value was calculated as 89.5%.

Considering the number of images in the data set, we can say that our study was quite successful.

Table 5. Comparison of techniques used for food classification.

Varieties	Number of classes	Number of images	Classification techniques	Accuracy (%)	References
Wheat	15	15000	CNN	98	[26]
Wheat	2	200	ANN	99.9	[29]
Rice	30	1500	Sparse-representation-based classification (SRC)	89.1	[30]
Pistachio nuts	4	600	CNN	95-98	[31]
Strawberry	4	4211	Swin-MLP-CNN	98	[24]
Wheat Yellow Rust Infection	4	1640	Embedded AI (A pre-trained U2 Net model)	96	[32]
Wheat	2	840	CNN	98.71	Proposed CNN architecture
Wheat	22	2320	CNN	89.5	Proposed CNN architecture

4. CONCLUSIONS

For companies that process or trade wheat, it is of great importance to determine the variety of wheat and its vitreous/yellow berry status. Extraction of wheat images by U2-Net architecture segmentation and preprocessing of images played an important role in increasing success. After, process is carried out with a two-stage classification system. With the CNN model we proposed, we performed the wheat multi-class detection process in two stages. In the first stage, the average accuracy for binary classification was calculated as 98.71%. In the second stage, the average accuracy value for the multiclass results (yellow berry, vitreous) was found to be 88.96% and 90.34%, respectively.   This developed classification system

has the potential to help experts in both seed producers, farmers and wheat processing factories and contribute to minimizing personal errors. In line with the results, it was seen that first, small, and difficult to distinguish grain groups, and then the use of segmentation and classification problems together were successfully carried out. In future studies, we plan to work on segmentation of the U2-Net model on different datasets with existing hyperparameters, and then on classification with CNN networks.

Declaration of Ethical Standards

The authors declare that the materials and methods used in this study do not require ethical committee permission.

Credit Authorship Contribution Statement

Mustafa Şamil ARGUN: Conceptualization, Methodology, Formal analysis, Writing- Reviewing and Editing. **Fuat TÜRK:** Methodology, Data curation, Writing- Original draft preparation, Writing- Reviewing and Editing. **Zafer CİVELEK:** Visualization, Investigation.

Declaration of Competing Interest

The authors declare that there is no conflict of interest concerning publication of this article.

Funding / Acknowledgements

No financial support was received from any institution or organization during the conduct of this study.

Data Availability

The datasets generated and/or analyzed during the current study are available from the corresponding author on reasonable request.

REFERENCES

[1]   I. G. C. (IGC). International Grain Council Grain Market Report [Online] Available: https://www.igc.int/ [Accessed Sept.21, 2023].

[2]   M. Feldman, "Origin of cultivated wheat," *The World Wheat Book, A history of wheat breeding,* 2000.

[3]   P. R. Shewry, "Do ancient types of wheat have health benefits compared with modern bread wheat?," *Journal of Cereal Science,* vol. 79, pp. 469-476, 2018/01/01/ 2018, doi: https://doi.org/10.1016/j.jcs.2017.11.010.

[4]   F. Özberk, A. Karagöz, İ. Özberk, and A. Ayhan, "Buğday genetik kaynaklarından yerel ve kültür çeşitlerine; Türkiye'de buğday ve ekmek," *Tarla Bitkileri Merkez Araştırma Enstitüsü Dergisi,* vol. 25, no. 2, pp. 218-233, 2016.

[5]   J. Ammiraju *et al.*, "Inheritance and identification of DNA markers associated with yellow berry tolerance in wheat (Triticum aestivum L.)," *Euphytica,* vol. 123, no. 2, pp. 229-233, 2002.

[6]   G. A. López-Ahumada *et al.*, "Physicochemical characteristics of starch from bread wheat (Triticum aestivum) with "yellow berry"," *Starch-Stärke,* vol. 62, no. 10, pp. 517-523, 2010.

[7]   J. Dexter, B. Marchylo, A. MacGregor, and R. Tkachuk, "The structure and protein composition of vitreous, piebald and starchy durum wheat kernels," *Journal of Cereal Science,* vol. 10, no. 1, pp. 19-32, 1989.

[8]   J. Dexter, P. Williams, N. Edwards, and D. Martin, "The relationships between durum wheat vitreousness, kernel hardness and processing quality," *Journal of Cereal Science,* vol. 7, no. 2, pp. 169-181, 1988.

[9]   R. C. Hoseney, *Principles of cereal science and technology. A general reference on cereal foods*. American Association of Cereal Chemists, Inc., 1986.

[10]   F. Dowell, "Differentiating vitreous and nonvitreous durum wheat kernels by using near-infrared spectroscopy," *Cereal Chem.,* vol. 77, no. 2, pp. 155-158, 2000.

[11]   X. Qin, Z. Zhang, C. Huang, M. Dehghan, O. R. Zaiane, and M. Jagersand, "U2-Net: Going deeper with nested U-structure for salient object detection," *Pattern Recognition,* vol. 106, p. 107404, 2020/10/01/ 2020, doi: https://doi.org/10.1016/j.patcog.2020.107404.

[12]   M. Lüy, F. Türk, M. Ş. Argun, and T. Polat, "Investigation of the effect of hectoliter and thousand grain weight on variety identification in wheat using deep learning method," *Journal of Stored Products Research,* vol. 102, p. 102116, 2023/05/01/ 2023, doi: https://doi.org/10.1016/j.jspr.2023.102116.

[13]   T. Fuat and Y. Kökver, "Application with deep learning models for COVID-19 diagnosis," *Sakarya University Journal of Computer and Information Sciences,* vol. 5, no. 2, pp. 169-180, 2022.

[14]   M. Gour, S. Jain, and T. Sunil Kumar, "Residual learning based CNN for breast cancer histopathological image classification," *International Journal of Imaging Systems and Technology,* vol. 30, no. 3, pp. 621-635, 2020.

[15]   G. Madhulatha and O. Ramadevi, "Recognition of plant diseases using convolutional neural network," in *2020 fourth international conference on I-SMAC (IoT in social, mobile, analytics and cloud)(I-SMAC)*, 2020: IEEE, pp. 738-743.

[16]   A. Pande, M. Munot, R. Sreeemathy, and R. Bakare, "An efficient approach to fruit classification and grading using deep convolutional neural network," in *2019 IEEE 5th International Conference for Convergence in Technology (I2CT)*, 2019: IEEE, pp. 1-7.

[17]   A. Kausar, M. Sharif, J. Park, and D. R. Shin, "Pure-cnn: A framework for fruit images classification," in *2018 International Conference on Computational Science and Computational Intelligence (CSCI)*, 2018: IEEE, pp. 404-408.

[18]   C. Narvekar and M. Rao, "Flower classification using CNN and transfer learning in CNN-Agriculture Perspective," in *2020 3rd International Conference on Intelligent Sustainable Systems (ICISS)*, 2020: IEEE, pp. 660-664.

[19]   A. Taner, Y. B. Öztekin, and H. Duran, "Performance analysis of deep learning CNN models for variety classification in hazelnut," *Sustainability,* vol. 13, no. 12, p. 6527, 2021.

[20]   N.-F. Huang, D.-L. Chou, and C.-A. Lee, "Real-time classification of green coffee beans by using a convolutional neural network," in *2019 3rd International Conference on Imaging, Signal Processing and Communication (ICISPC)*, 2019: IEEE, pp. 107-111.

[21]   M. Momeny, A. Jahanbakhshi, K. Jafarnezhad, and Y.-D. Zhang, "Accurate classification of cherry fruit using deep CNN based on hybrid pooling approach," *Postharvest Biol. Technol.,* vol. 166, p. 111204, 2020.

[22]   A. Jahanbakhshi, M. Momeny, M. Mahmoudi, and Y.-D. Zhang, "Classification of sour lemons based on apparent defects using stochastic pooling mechanism in deep convolutional neural networks," *Scientia Horticulturae,* vol. 263, p. 109133, 2020.

[23]   B. Jabir and N. Falih, "Deep learning-based decision support system for weeds detection in wheat fields," *International Journal of Electrical and Computer Engineering,* vol. 12, no. 1, p. 816, 2022.

[24]   H. Zheng, G. Wang, and X. Li, "Swin-MLP: a strawberry appearance quality identification method by Swin Transformer and multi-layer perceptron," *Journal of Food Measurement and Characterization,* pp. 1-12, 2022.

[25]   Y. Shen, Y. Yin, B. Li, C. Zhao, and G. Li, "Detection of impurities in wheat using terahertz spectral imaging and convolutional neural networks," *Comput. Electron. Agric.,* vol. 181, p. 105931, 2021.

[26]   S. Lingwal, K. K. Bhatia, and M. S. Tomer, "Image-based wheat grain classification using convolutional neural network," *Multimedia Tools and Applications,* vol. 80, no. 28, pp. 35441-35465, 2021.

[27]   A. Yasar, "Benchmarking analysis of CNN models for bread wheat varieties," *Eur. Food Res. Technol.*, pp. 1-10, 2022.

[28]   K. Hacıefendioğlu, A. F. Genc, S. Nayır, S. Ayas, and A. C. Altunışık, "Automatic Estimation of Post-fire Compressive Strength Reduction of Masonry Structures Using Deep Convolutional Neural Network," *Fire Technology*, vol. 58, no. 5, pp. 2779-2809, 2022.

[29]   K. Sabanci, A. Toktas, and A. Kayabasi, "Grain classifier with computer vision using adaptive neuro-fuzzy inference system," *Journal of the Science of Food and Agriculture*, vol. 97, no. 12, pp. 3994-4000, 2017.

[30]   T.-Y. Kuo, C.-L. Chung, S.-Y. Chen, H.-A. Lin, and Y.-F. Kuo, "Identifying rice grains using image analysis and sparse-representation-based classification," *Comput. Electron. Agric.*, vol. 127, pp. 716-725, 2016.

[31]   A. Soleimanipour, M. Azadbakht, and A. Rezaei Asl, "Cultivar identification of pistachio nuts in bulk mode through EfficientNet deep learning model," *Journal of Food Measurement and Characterization*, pp. 1-11, 2022.

[32]   U. Shafi *et al.*, "Embedded AI for Wheat Yellow Rust Infection Type Classification," *IEEE Access*, vol. 11, pp. 23726-23738, 2023.

HEAT TRANSFER EXAMINATION OF OSCILLATING NANOFLUID FLOW IN A RECTANGULAR CORRUGATED CHANNEL WITH VERTICAL PLATES: A NUMERICAL STUDY

Selma AKÇAY [iD]

Çankırı Karatekin University, Engineering Faculty, Mechanical Engineering Department, Çankırı, TÜRKİYE
selmaakcay@karatekin.edu.tr

Highlights

- The heat transfer of pulsating nanofluid flow in a rectangular corrugated duct with vertical plates.

- Effects of pulsating flow, vertical plates, Al_2O_3-water nanofluid, and Reynolds number.

- Nu increased by 1.57 times for the oscillating nanofluid flow at a Re = 800 in the duct with plates.

Graphical abstract

(a) 3D, and (b) 2D geometric schematics of the numerical model

*Corresponding Author: Selma AKÇAY, selmaakcay@karatekin.edu.tr

HEAT TRANSFER EXAMINATION OF OSCILLATING NANOFLUID FLOW IN A RECTANGULAR CORRUGATED CHANNEL WITH VERTICAL PLATES: A NUMERICAL STUDY
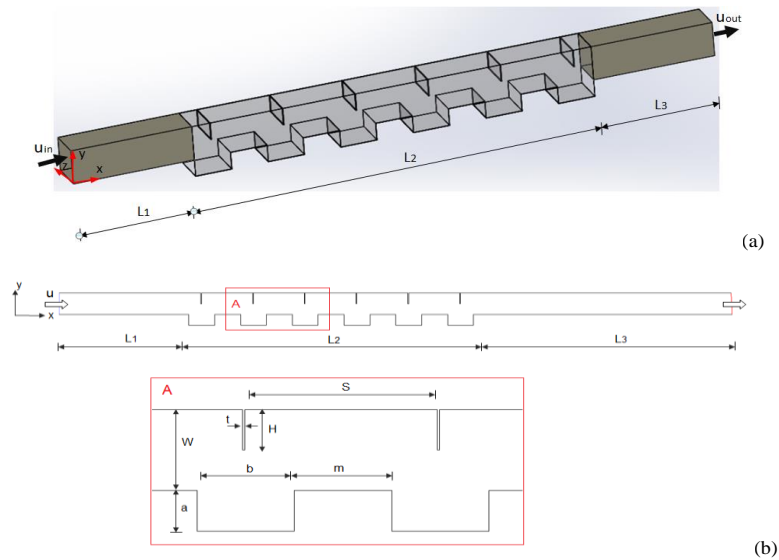
Selma AKÇAY iD

Çankırı Karatekin University, Engineering Faculty, Mechanical Engineering Department, Çankırı, TÜRKİYE
selmaakcay@karatekin.edu.tr

ABSTRACT: This study numerically focused investigating the thermal performance of flow oscillations in a rectangular corrugated channel with vertical plates on top wall. The numerical study was performed with the ANSYS Fluent software, and the SIMPLE algorithm was utilized to solve the pressure-velocity coupling. The top wall of the channel was adiabatic and included vertical plates. The bottom wall of the channel was rectangular grooved and kept at T_w=360 K. Suspension of Al_2O_3 nanoparticles into water was used as the fluid. The particle volume fraction in the suspension was kept constant at φ = 5%. Oscillating amplitude (A) and Strouhal number (St) were maintained constant at A = 1 and St = 2, respectively. In the presented study, the effects of vertical plates, Al_2O_3-water nanofluid and pulsating flow on flow and heat transfer were analyzed separately at different Reynolds numbers (200 ≤ Re ≤ 800). The Nusselt number (Nu), relative friction factor (f_{rel}) and performance evaluation criteria (PEC) were obtained for different Reynolds numbers. The temperature and velocity fields were acquired for varying parameters. The results demonstrated that the flow and temperature structures were significantly influenced by the channel geometry and oscillating flow. Heat transfer considerably enhanced with the oscillating flow at the high Re. At Re = 800, thermal improvement for oscillating flow of the nanofluid in the channel with plates increased by nearly 1.57 times relative to the steady case of the basic fluid in the channel without plates.

Keywords: Heat transfer, Nanofluids, Oscillating flow, Rectangular corrugated channel, Vertical plate

1. INTRODUCTION

Corrugated channels are a widely used passive heat transfer improvement method. Since these channel geometries increase the surface area and create an oscillating motion in the flow, they have significant potential for heat transfer improvement. This method does not contain any mechanical parts, so it is more economical and quite safe. Therefore, it is usually preferred in many engineering implementations such as thermal devices, heat exchangers, and chemistry processes [1-3]. In many experimental and numerical studies, the hydraulic and heat transfer enhancement has investigated in the corrugated channels, and the results of these studies demonstrated that wavy surface geometries significantly improve heat transfer when compared to straight channels [4-6]. Kurtulmus and Sahin [7] actualized a review study investigating the hydraulic and thermal characteristics on corrugated surfaces. In experimental and numerical work, Brodnianská and Kotśmíd [8] examined the thermal improvement in a duct with various wave forms and demonstrated that the thermal enhanced with the increasing Re and decreasing channel height. Mehta et al. [9] computationally examined the impacts of the wall wave amplitude on flow and thermal improvement in asymmetrical corrugated channels and declared that the Nu increased with Re and wall wave amplitude.

Another passive heat transfer improvement techniques are the use of extended surface modifications, such as twist tape, winglets, ribs, fins, barriers, and plates within the channel. These modifications added into the channel completely disrupt the flow structure and help with the flow mix and thermal improvement, but an increase in pressure loss occurs relative to straight ducts. Many experimental and numerical works have examined the flow and thermal enhancement in grooved and

---

*Corresponding Author: Selma AKÇAY, selmaakcay@karatekin.edu.tr

straight channels with different barriers [10-11]. Barriers with different shapes in different channel geometries have been investigated in previous studies. Lei et al. [12] examined the inclination angle of the baffles on thermal efficiency in a heat exchanger with helical turbulators. Sripattanapipat and Promvonge [13] numerically investigated the heat transfer of a duct with diamond-type barriers. Kwankaomeng and Promvonge [14] executed a numerical study investigating thermo-hydraulic behavior in a square duct with 30° inclined barriers on one surface. Sriromreun [15] performed a numerical work on the thermo-hydraulic behavior of inclined barriers in a rectangular channel. Li and Gao [16] numerically studied thermal enhancement in a triangular-shaped grooved duct with delta-type baffles. Karabulut [17] realized a CFD (Computational Fluid Dynamics) work studying the heat transfer at different slope angles of the baffles in a triangular corrugated duct, including triangular barriers on the upper wall. In a computational and experimental research, Bensaci et al. [18] studied the thermal efficiency of solar air channels with varying baffle configurations. These study results showed that corrugated/wavy ducts and surface arrangements considerably enhanced the thermal performance. In an experimental study, Promvonge et al. [19] researched the heat transfer in a duct with inclined horseshoe-type barriers and noticed that the heat transfer improved by nearly 208% and the pump power increased about 6.37 times, according to the flat duct. Kumar et al. [20] experimentally examined the thermal improvement of the solar duct with multiple V-shaped baffles. They declared that the thermal enhancement exceedingly increased with the baffles. In another experimental work conducted by Sahel et al. [21] was reported the rectangular channel flow with a different arrangement of the barriers increased the heat transfer about 65%.

On the other hand, the thermo-physical features of many traditional liquids utilized in heat transfer implementations are low. Particles with nano-sized are added to enhance these features of a basic fluid. Many researchers have examined nanofluids together with corrugated ducts [22-24]. Manca et al. [25] examined the thermal characteristics of water based Al_2O_3 nanofluid for different particle volume fractions ($0 \leq \varphi \leq 0.04$) in a duct with varying rib heights and declared that thermal performance improved with increasing the Re and φ. They also observed a rise in the pump power. Heshmati et al. [26] investigated the heat transfer efficiency of nanofluids in a duct with different geometries of the barriers. Their study examined the effects of nanofluid type, particle volume fraction ($0.01 \leq \varphi \leq 0.04$), particle diameter, and Reynolds number ($40 \leq Re \leq 400$). They found that the nanofluids with high particle volume ratio and small particle size enhanced thermal performance. In a review study, Huminic and Huminic [27] analyzed the thermal behavior of nanofluids and basic fluids in the grooved channel. Qi et al. [28] numerically and experimentally researched the thermal behavior of the nanofluids (TiO_2-water) in a grooved channel. Pordanjani et al. [29] presented review work that examined the impacts of nanoparticles on energy savings in heat exchangers. Mei et al. [30] theoretically studied the thermohydraulic performance of Fe_3O_4-water nanofluid using a magnetic field in a wavy channel. Kaood and Hassan [31] presented a theoretical work that analyzed the thermal improvement and energy analysis of varying nanofluids in different geometries of the wavy duct. They indicated that nanofluids enhanced the thermal performance according to the straight channel, and all the performance improvement decreased at $Re \geq 10000$ for all the fluids and channel configurations. Tian et al. [32] analyzed the energy, exergy analysis, and pump power of the triangular turbulators in different duct geometries. In their study, they examined the effects of different fluid types (CuO-water, Al_2O_3-water, water, and air). As a result of their study, they declared that the heat transfer was considerably enhanced in nanofluid flow in circular channels with turbulators. However, the nanofluids increased exergy destruction. Ajeel et al. [33] performed a numerical study that examined the thermal behavior of ZnO-water nanofluid in a curved wavy duct with L-type barriers. They indicated that the nanofluids and barriers had an important influence on thermal improvement. Akcay [34] evaluated the heat transfer of pulsating flow in a duct with inclined baffles for different Reynolds numbers, pulsating frequency, and pulsating amplitude. The result of the study indicated that the thermal performance improved by about 47% with increasing Reynolds number and pulsating parameters. Menni et al. [35] evaluated the thermal characteristics of baffles at varying angles in a channel under nanofluid flow. Their study results

indicated that the heat transfer enhanced at a high Re, and the highest thermal enhancement was obtained for the vertical baffles.

Although extended surfaces added to the channel and corrugated channel geometry increase heat transfer under steady flow conditions, these applications are insufficient in cases where higher thermal performance is required. For this reason, in these cases, a pulsating/oscillating flow is preferred over a steady regime. An oscillating flow enhances thermal performance by improving the flow mixing. Many experimental and numerical works have investigated the thermo-hydraulic efficiency in the wavy ducts under oscillating flow. The results of these studies indicated that the heat transfer enhanced depending on the geometry of the duct, the velocity of fluid, and oscillating parameters [36-38]. In two different numerical studies, Akdag et al. examined the thermal enhancement of the oscillating nanofluid flow in a triangular [39], and trapezoidal [40] corrugated channels. They indicated that the thermal enhancement increased with a rising oscillating frequency, oscillating amplitude, and particle volume ratio. Esfe et al. [41] executed a review work investigating the oscillating flow for heat transfer and non-heat transfer conditions. Munoz-Camara et al. [42] experimentally examined the thermal efficiency in the oscillating flow in a circular duct with barriers and declared that the heat transfer increased nearly five times with the oscillating flow. Akcay [43] presented a CFD work to investigate the heat transfer of the flow oscillations in a grooved duct with V-shaped winglets and found that the winglets and pulsating flow significantly increased thermal enhancement with rising in pump power. In another numerical study, Akcay [44] examined the pulsating flow of CuO-water nanofluid in a circular corrugated channel with barriers on the top wall. The results were compared with the steady case of the basic fluid in the non-barriers corrugated channel. The work's findings indicated the pulsating nanofluid flow improved the Nu by 2.6 times in the presence of baffles.

According to the above research, extended surfaces added to corrugated channels increase the thermal enhancement. Even if the heat transfer with these modifications is enhanced, the pressure loss rises due to the nanoparticles and obstruction of the flow area. A definite criterion has not been reported for determining the optimum nanofluids and corrugated channel geometries with plates in the existing literature. Thermal and hydraulic behavior in corrugated channels with plates were mostly studied under steady flow conditions, and it was found that very little study was realized under oscillating flow conditions. In studies carried out so far, it has been observed that thermal and hydraulic performance in oscillating nanofluid flow in a rectangular corrugated channel with vertical plates has not been examined. In the study, the impacts of vertical plates, nanofluids, and oscillation parameters on thermal enhancement and pressure drop in rectangular corrugated channels were analyzed separately.

2. MATERIAL AND METHODS

2.1. Numerical Geometry

Figure 1 indicates the geometry of the rectangular corrugated channel with vertical plates on the top surface. The height of the channel (W) is 12 mm. The channel width (Z) is equal to channel height. The lengths of flat parts at the inlet and exit of the channel are considered as $L_1 = 5\ W$ and $L_3 = 10\ W$, respectively. The distance between plates is $S = 3\ H$. The thickness and the length of plates are $t = 0.05\ W$ and $H = 0.5\ W$, respectively. The distance between corrugated parts is $m = 0.5\ W$. The dimensions of the corrugated part are $a = 0.5\ W$ and $b = W$. The corrugated channel contains a total of six wavy parts.

(a)

(b)
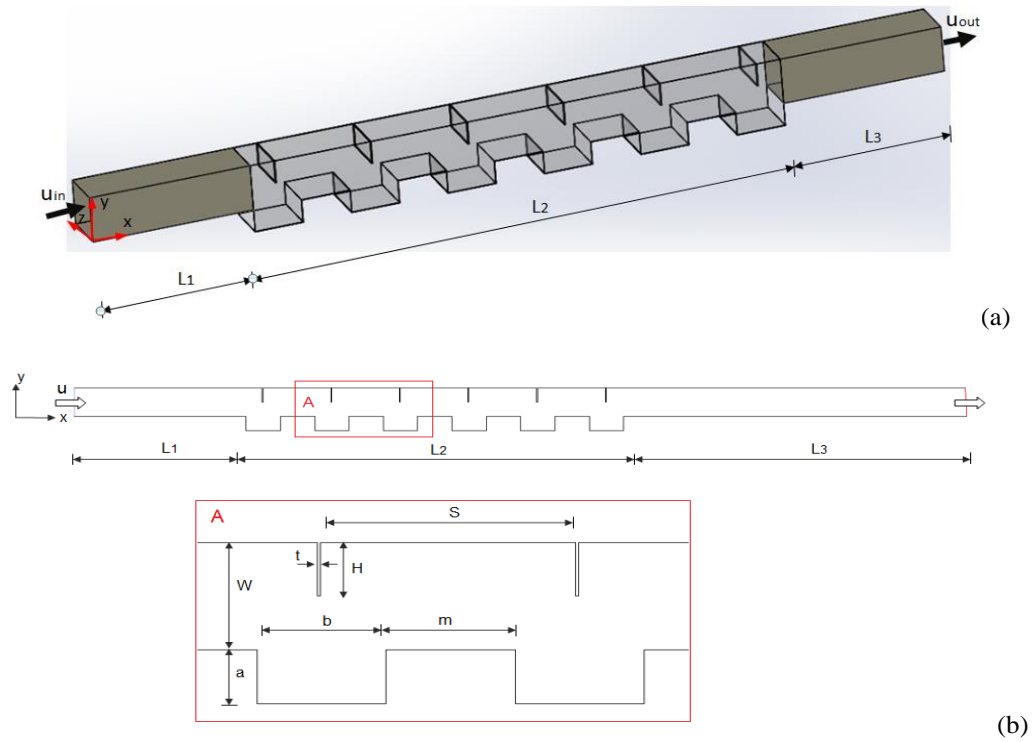
Figure 1. (a) 3D, and (b) 2D geometric schematics of the numerical model

2.2. Mathematical Model

In the numerical solutions, the flow field is laminar, time-depended for oscillating flow, steady for the other cases, two-dimensional (2D). The fluid is incompressible and Newtonian type. The impacts of thermal radiation and body forces are ignored. For these conditions, the continuity equation conservation, momentum, and energy equations are given as [36]:

$$\frac{\partial u_i}{\partial t} + \nabla(\rho u) = 0 \tag{1}$$

$$\frac{\partial u_i}{\partial t} + \frac{\partial(u_i u_j)}{\partial x_i} = -\frac{\partial P}{\partial x_i} + \frac{1}{Re}\nabla^2 u_j \tag{2}$$

$$\frac{\partial T}{\partial t} + u_i \frac{\partial T}{\partial x_i} = \frac{1}{RePr}\nabla^2 T \tag{3}$$

Reynolds number (Re) is given by [43]:

$$Re = \frac{\rho u D_h}{\mu} \tag{4}$$

Hydraulic diameter (D_h) is calculated as follows (Eq. 5) [44]:

$$D_h = \frac{4A_c}{P} = \frac{4WZ}{2(W+Z)} \tag{5}$$

where A_c denotes the cross-sectional area and P denotes the wetted perimeter.

Heat Transfer Examination of Oscillating Nanofluid Flow in a Rectangular Corrugated Channel with Vertical Plates: a Numerical Study

377

The oscillating frequency (Strouhal number, St) is given by [36]:

$$St = \frac{\omega D_h}{u} \tag{6}$$

2.3. Description of Boundary Conditions

The fluid enters the channel at T_i = 300 K. The rectangular corrugated lower wall of the channel is preserved at 360 K. The "velocity inlet" and "pressure outlet" boundary conditions are identified at the inlet and outlet of the channel, respectively. The oscillating inlet velocity defined at the channel inlet is given by Eq. (7) [36, 43].

$$u_{in} = u[1 + Asin(\omega t)] \tag{7}$$

where, ω (= $2\pi f$) is defined as the angular velocity and is used to obtain the Strouhal number (St), which describes the dimensionless oscillating frequency, A represents the dimensionless oscillating amplitude, and u indicates the mean velocity at the channel inlet. L_1 and L_3 lengths have adiabatic and no-slip conditions. Also, the vertical plates have adiabatic and no-slip conditions. The simulations are applied for different Reynolds numbers (Re: 200, 500, and 800). The study is carried out under laminar flow conditions. It was reported that the transition from laminar to turbulent flow in pulsating flow begins at Re=1100. Therefore, in this study, Reynolds numbers in the range of 200<Re<800 were used to maintain the validity of laminar flow conditions (for detailed information, see [34]).

2.4. Data Reduction

In this study, heat transfer is expressed with the Nusselt number (Nu). The overall Nusselt number for steady conditions is written as [34]:

$$Nu = \frac{hD_h}{k_f} \tag{8}$$

$$h = \frac{Q_{conv}}{A_L \Delta T_{lm}} \tag{9}$$

$$Q_{conv} = mC(T_{o,b} - T_{i,b}) \tag{10}$$

$$\Delta T_{lm} = \frac{(T_{i,b} - T_{o,b})}{ln\left(\frac{T_w - T_{o,b}}{T_w - T_{i,b}}\right)} \tag{11}$$

where, k is the heat conductivity, h is the heat convective coefficient, and ΔT_{lm} is logarithmic temperature difference. $T_{i,b}$ and $T_{i,o}$ represent the bulk temperature of the fluid at inlet and outlet of the channel, respectively. T_w shows the wall temperature of the corrugated channel. C, A_L, Q_{conv}, and m are the specific heat, surface area, heat transfer with convection, and, mass flow rate, respectively.

The overall Nusselt number (Nu_p) for oscillating flow conditions can be written as [36]:

$$Nu_p = \frac{1}{\tau L} \int_{x_o}^{L} \int_{0}^{\tau} Nu(x,t)dtdx \tag{12}$$

where, τ indicates a period time in oscillating flow, L is the length of the heated corrugated channel.

The thermal enhancement ratio (Nu_{rel}) is found as [34]:

$$Nu_{rel} = \frac{Nu_p}{Nu_s} \tag{13}$$

where, Nu_p and Nu_s represent the cycle-averaged Nu for oscillating conditions, and the Nu for a steady condition, respectively.

The friction factor (f) is calculated by [43]:

$$f = \frac{2\Delta P D_h}{\rho u^2 L} \tag{14}$$

where, ΔP shows the pressure difference.

The relative friction factor (f_{rel}) is computed as [44]:

$$f_{rel} = \frac{f_p}{f_s} \tag{15}$$

where, f_s is the average friction factor for steady flow and f_p is the average friction factor for oscillating flow.

The performance evaluation criteria (PEC) is given by [43]:

$$PEC = \frac{(Nu_p/Nu_s)}{(f_p/f_s)^{1/3}} \tag{16}$$

2.5. Nanofluid Properties

In the study, Al$_2$O$_3$-water nanofluid was used as the fluid and the nanoparticle volume ratio was kept constant ($\varphi = 5\%$). The diameter of the nanoparticles was accepted to be 20 nm. The thermodynamic features of the Al$_2$O$_3$-water nanofluid were calculated using the following equations [32, 45]:

$$\rho_{nf} = (1 - \varphi)\rho_{bf} + \varphi\rho_{pt} \tag{17}$$

$$C_{nf} = \frac{(1-\varphi)\rho_{bf}C_{bf} + \varphi\rho_{pt}C_{pt}}{\rho_{nf}} \tag{18}$$

$$k_{nf} = k_{bf} \frac{[k_{pt} + 2k_{bf} - 2\varphi(k_{bf} - k_{pt})]}{[k_{pt} + 2k_{bf} + \varphi(k_{bf} - k_{pt})]} \tag{19}$$

$$\mu_{nf} = \mu_{bf}[123\varphi^2 + 7.3\varphi + 1] \tag{20}$$

where the subscript *bf, pt and nf* show the basic fluid, the nanoparticle and the nanofluid, respectively. Water is used the basic fluid. Table 1 indicates the thermophysical properties of the basic fluid (water) and Al$_2$O$_3$ nanoparticle at 300 K [32].

Table 1 . Thermal and physical features of Al$_2$O$_3$ nanoparticle and H$_2$O at 300 K

	ϱ [kg/m³]	C [J/kgK]	k [W/mK]	μ [kg/ms]
H$_2$O	998.2	4182	0.6	0.001003
Al$_2$O$_3$	3950	765	36	-

2.6. Numerical Procedure and Validation

The 2D drawing of the channel geometry and the formation of the grid structure were generated with

Heat Transfer Examination of Oscillating Nanofluid Flow in a Rectangular Corrugated Channel with Vertical Plates: a Numerical Study

379

the help of the Gambit software. The mesh quality for triangular elements of the numerical model was obtained as 0.94. Therefore, the triangular elements were preferred to both channels (with and without plates). The mesh structures of both channels are given in Figure 2 with their details. To determine whether the solution results were independent of the grid numbers, the Nu was obtained for different grid numbers, namely 34258, 54162, 77652, 105058, and 131604. Since the change in the Nu was very small after the 77652-element number, this element number was adapted to the geometry. Figure 3 illustrates the variations of the Nu with the grid numbers at different Re for the steady case in the rectangular corrugated channel without plates.
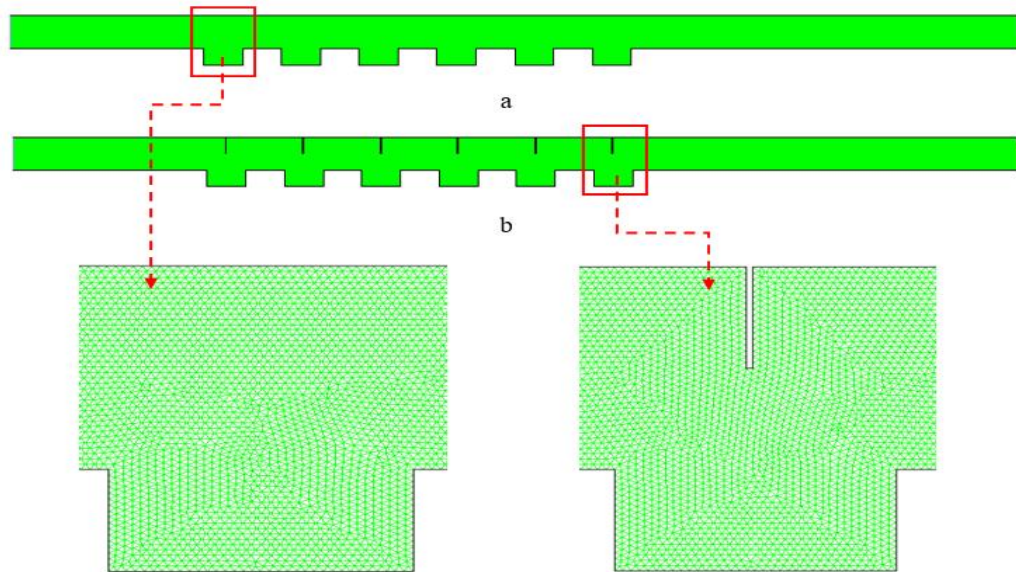
Figure 2. Mesh formations of the model: (a) without plates and (b) with plates
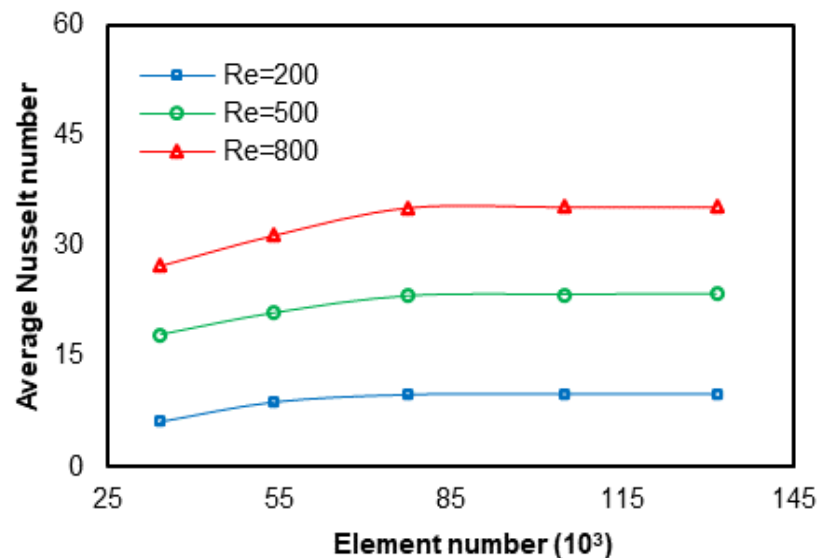
Figure 3. Nusselt numbers versus the element numbers for the steady case of the base fluid

The numerical simulations were realized by using the ANSYS Fluent [46] software. In the discretization of the relevant equations were used the second order upwind scheme. The velocity-pressure coupling in the discretized equations was solved with the SIMPLE algorithm. Convergence criteria were 10^{-8} for all the residuals. In oscillating flow, iterations were completed in 3000 s and then heat transfer and pressure drop calculations were performed.

Boukhadia et al. [47] studied the heat transfer and pressure drop for laminar flow in a straight channel with a hydraulic diameter of 12 mm. On the other hand, Ameur et al. [48] investigated convective heat transfer at Reynolds numbers in the range of $0.1 \leq Re \leq 300$ in a straight channel with the same hydraulic diameter. To validate the present simulation results, this work was checked with the results of the previous studies [47, 48]. The comparison of the numerical solutions of this study with the results of the previous studies was given detail in [43] and [44].

Time step independence test was carried out for three different time steps: $\Delta t=0.1s$, $0.01s$, and $0.001s$, and the test results were shown in Figure 4. Nusselt numbers were obtained very close to each other at time steps $\Delta t=0.01s$ and $\Delta t=0.001s$. Therefore, the time step for oscillatory flow solutions was set to $\Delta t=0.01$ s.
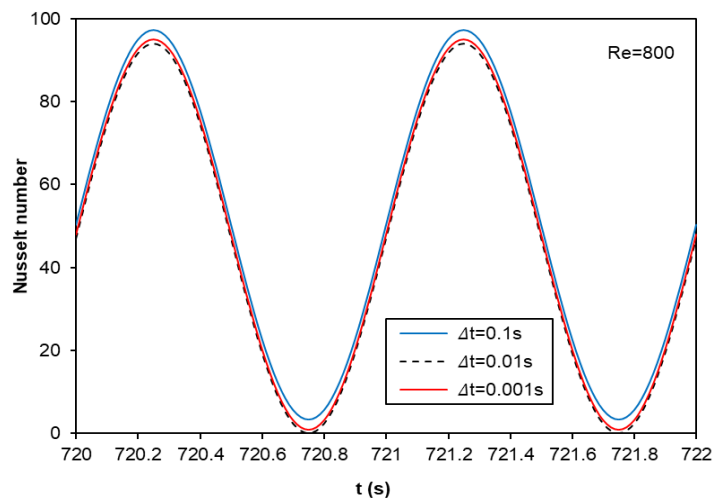
Figure 4. Time step independence test for Re=800

3. RESULTS AND DISCUSSION

In this section, the effects of vertical plates, Al$_2$O$_3$-water nanofluid and pulsating flow on flow and heat transfer were discussed for different Reynolds numbers $(200 \leq Re \leq 800)$**.** In oscillating flow, the temperature and flow fields in the channel change with time and therefore, the pressure drop, and heat transfer will also change periodically. One oscillation period was utilized to compute the friction factor and Nu. One oscillating period was accepted to be completed in $\omega t= 360°$, or 2π radians. Moreover, the temperature and flow fields for the steady and oscillating cases of the flow in the channel with and without plates were presented. In the paper, color scale values for all velocity contours are given in m/s, and color scale values for all temperature contours are given in Kelvin (K).

Figure 5 indicates the velocity (a) and temperature contours (b) in the steady flow of the water in a rectangular corrugated channel without the plates for different Re. The velocity fields for the water in the channel without plates are like each other at all the tested Re. The fluid generally flows parallel to the channel walls and is canalized towards the rectangular cavities on the bottom wall (Fig. 5a). In the channel without plates, cold fluid flows in the upper parts of the channel. The length of corrugated channel is kept at a constant temperature, and the rectangular cavities were completely covered with hot fluid. The wall temperatures of the rectangular cavities near the inlet of the channel are relatively lower (first two rectangular cavities in the flow direction) while the temperature of the rectangular cavities towards the end of the channel was relatively higher (last four rectangular cavities in the flow direction). As the Re increased, the surface temperature of the rectangular corrugated channel reduced (Fig. 5b).
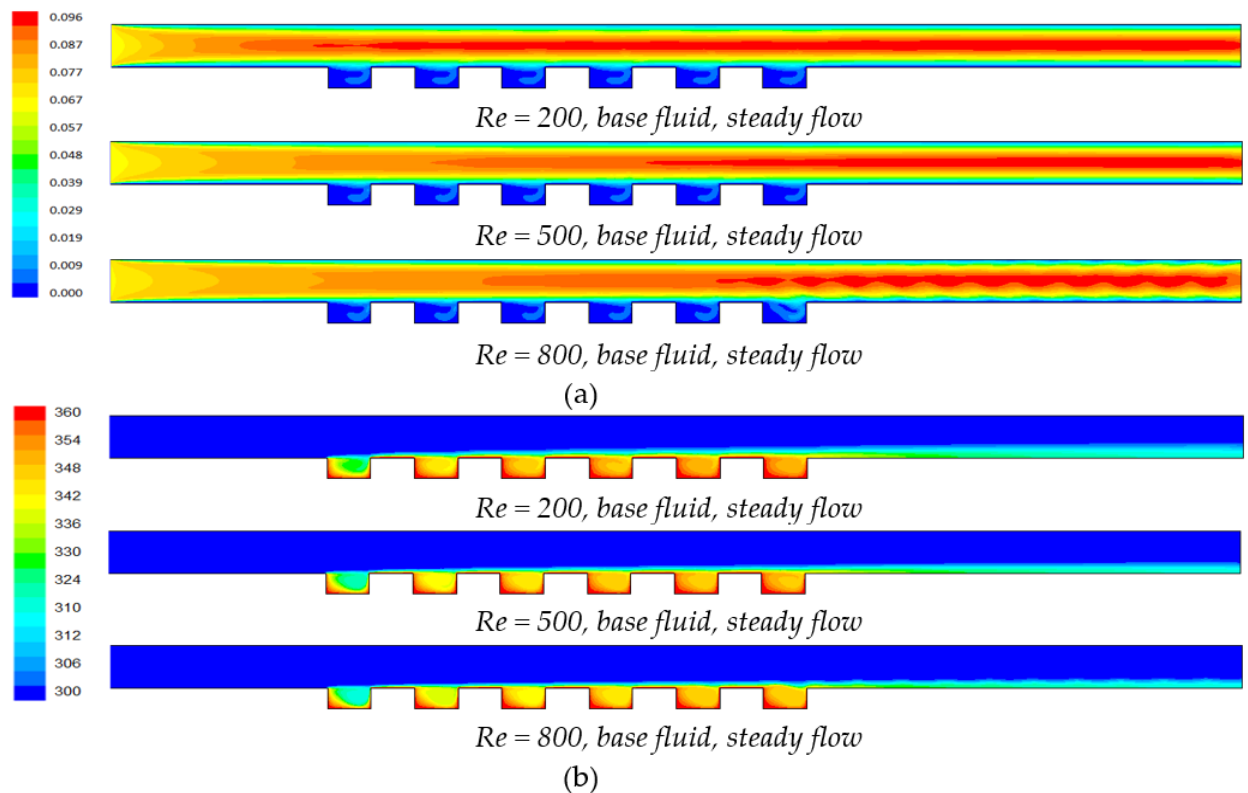
Figure 5. Velocity fields (a) and temperature fields (b) at different Re for the steady case of water in the corrugated channel without plates

Figure 6 indicates, the velocity contours (a) and temperature distributions (b) of the Al$_2$O$_3$-water nanofluid with $\varphi = 0.05$ particle volume fraction in the channel with plates for different Re in the steady case. The velocity and temperature contours significantly changed with the Re depending on the plates. The vertical plates significantly affected the flow field within the channel. These plates canalized the flow toward the rectangular corrugated surfaces, causing flow oscillation. With the oscillation movement, the cold fluid contacted the hot corrugated surfaces. The temperature of the corrugated walls in contact with the colder fluid decreased and the heat transfer improved. After each plate, the velocity and thermal boundary layer broke down and these structures helped to create flow cycles. The plates disrupted the flow structure, caused a diminish in thermal resistance, thus improving the heat transfer. At a low Re, it was seen that the flow cycles occurred between the vertical plates, while the mainstream flowed as a whole. With the increasing Re, flow breaks occurred and too many flow cycles were formed in the channel. The wall temperature decreased with the increasing Re.
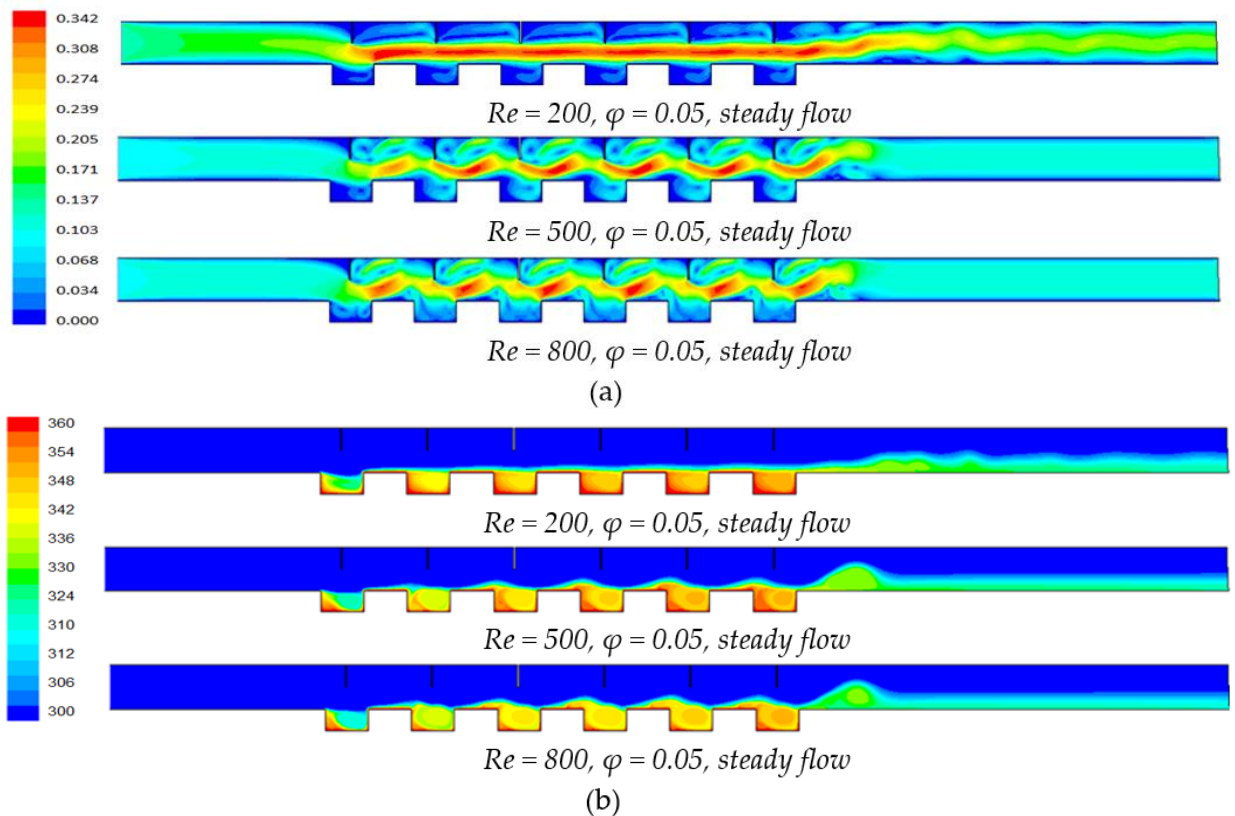
Figure 6. Velocity fields (a) and temperature fields (b) at different Re for the steady case of the nanofluid in the corrugated channel with plates

Figure 7 indicates the velocity vectors for different Re in the steady flow of nanofluid in the channel with plates. At a Re = 200, the velocity vectors for the main flow were downstream. It was seen that the velocity vectors between each plate were quite small and were positioned in different directions. In the rectangular cavities, the flow vectors were still small, and turbulence started in the flow. At a Re = 500, the oscillations occurred in the main flow due to the plates. Major and minor flow cycles were formed between each vertical plate. It was observed that a large flow cycle was formed near the right wall of each rectangular cavity. These cycles improved the flow mixing by mobilizing the more stagnant fluid between the plates and in the rectangular cavities. At a Re = 800, the increase in flow rate increased the flow oscillations because the vertical plates directed the main flow toward the rectangular cavities. The flow cycles seen between each plate at a Re = 500 grew even greater at a Re = 800. Smaller velocity vectors leaving the lower part of the main flow were directed to the right and left surfaces of the rectangular cavities, creating flow fluctuations.

Heat Transfer Examination of Oscillating Nanofluid Flow in a Rectangular Corrugated Channel with Vertical Plates: a Numerical Study

383
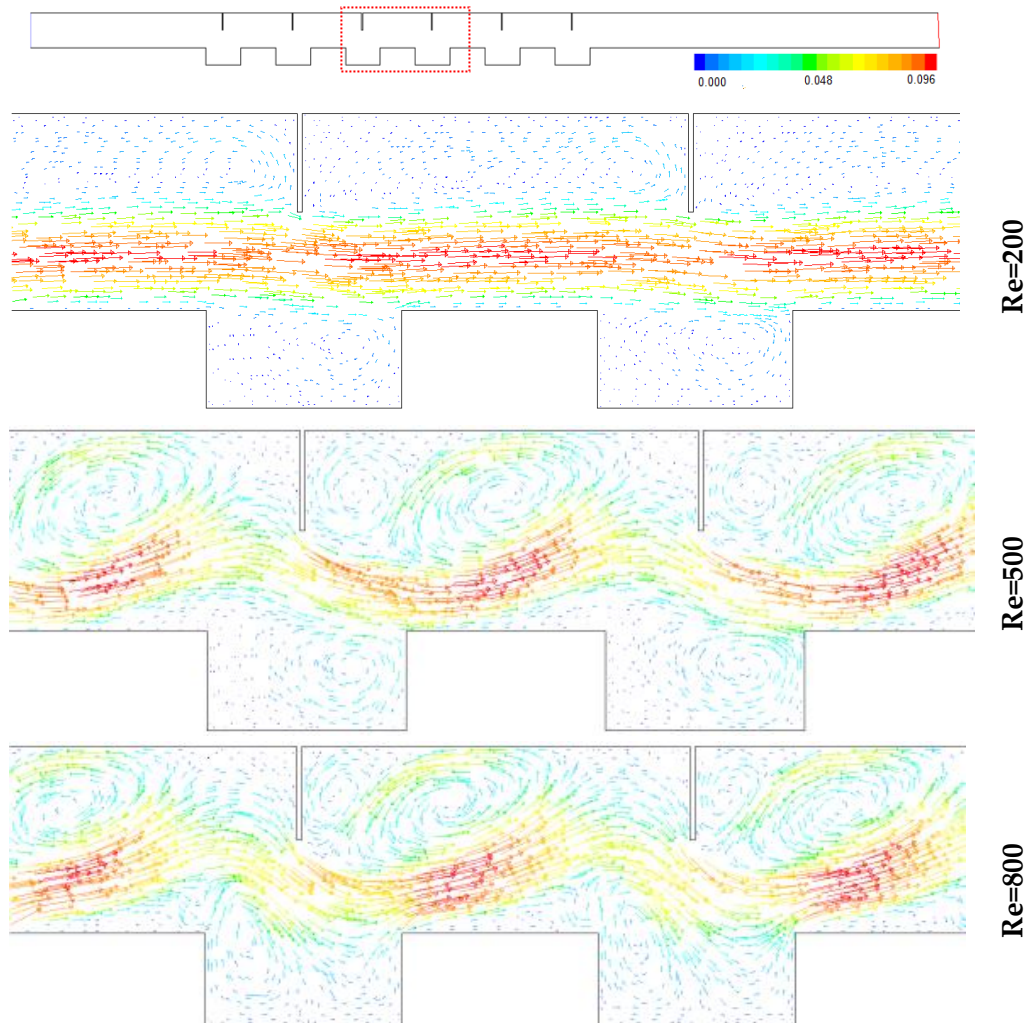
Figure 7. Velocity vectors for varying Re at the steady case of the nanofluid in the channel with plates

Figure 8 displays the velocity fields (a) and temperature contours (b) at varying phase angles in the channel without plates at the Re = 500, A = 1, St = 2, φ = 0.05. It was seen that the velocity and thermal fields changed remarkably by the oscillating parameters and the geometry of the channel. At ωt = 90°, the flow moved downstream and slightly directed into the rectangular cavities due to the oscillating components. At ωt = 180°, the flow began to change direction, and the low velocity fluid particles rotated upstream (in the opposite direction). The flow cycles that occurred in the rectangular cavities became larger. At ωt = 270°, the flow moved completely upstream. Growing flow cycles due to the opposite flow filled the rectangular cavities. At ωt = 360°, the flow began to flow downstream again and the flow cycles in the rectangular cavities got smaller. Thus, one oscillating period was terminated. This case is repeated in each oscillating cycle. The flow cycles that occurred in each periodic cycle carried the hot fluid in the rectangular cavity to the upper sections of the channel. The cold fluid displaced by the hot fluid caused the temperature of the channel walls to diminish. It was observed that the temperature of the channel walls in the oscillating nanofluid flow diminished significantly when compared to the channel wall temperatures in Figure 5b (Fig. 8b).
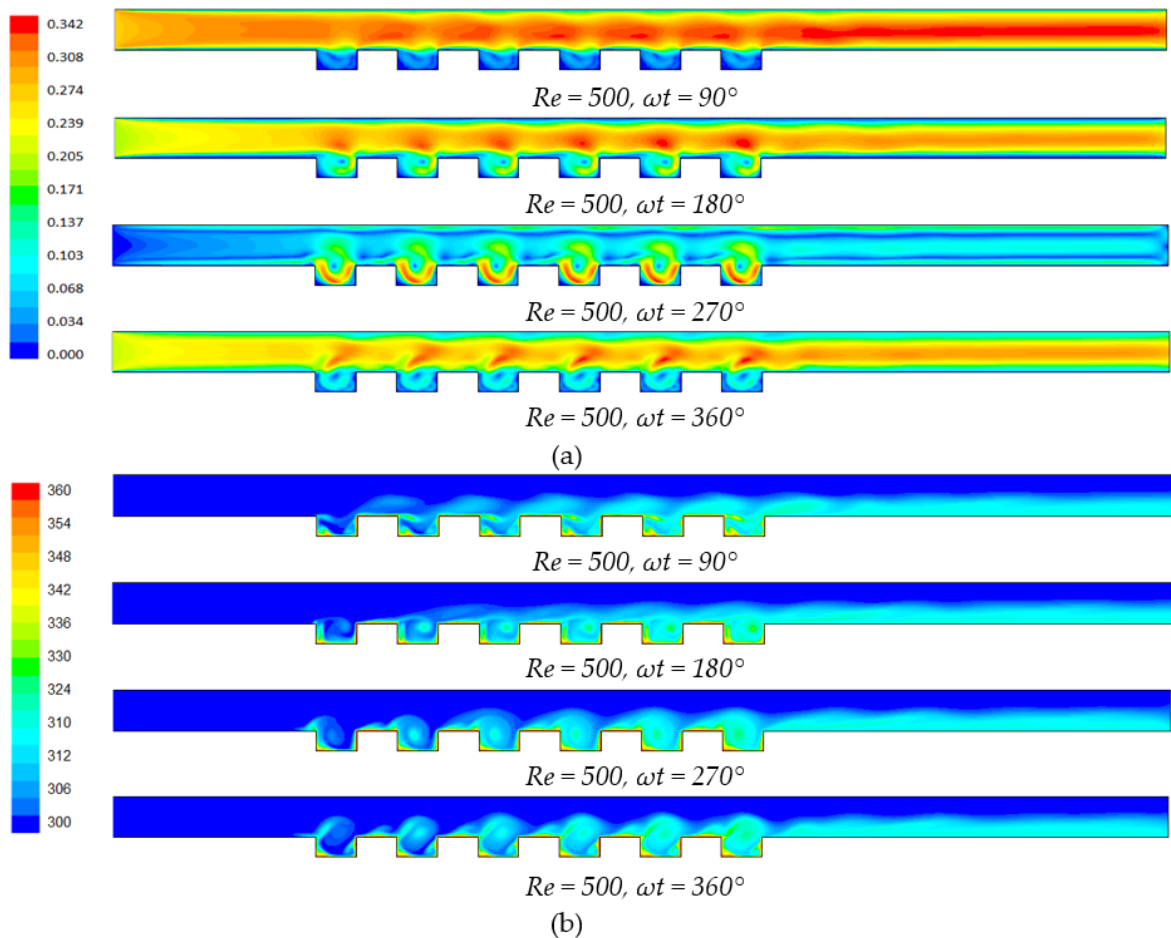
Figure 8. Velocity fields (a) and temperature fields (b) at varying phase angles in the channel without plates (Re = 500, A = 1, St = 2, φ = 0.05)

Figure 9 indicates the velocity fields (a) and temperature structures (b) for an oscillating period in the channel with plates at a Re = 500, A = 1, St = 2, φ = 0.05. The flow and temperature fields varied considerably during one oscillating cycle. The flow flowed downstream at ωt = 90°. The flow was directed into the rectangular cavities due to the vertical plates on the upper wall of the channel. At ωt = 180°, the direction of the flow changed, the fluid particles rotated upstream, and the structure of the flow was completely changed. Wide circulation zones were seen between the plates. Flow cycles also began to form in the rectangular cavities. At ωt = 270°, the flow moved completely upstream. Circular flow cycles were seen all over the channel. The flow began to flow downstream at a phase angle of ωt = 360°. Thus, one oscillating cycle was terminated. The oscillation parameters increased the flow oscillations and flow cycles. This case, which was reiterated in each oscillating cycle, was reflected in the temperature fields and heat transfer enhanced due to the better flow mixture.
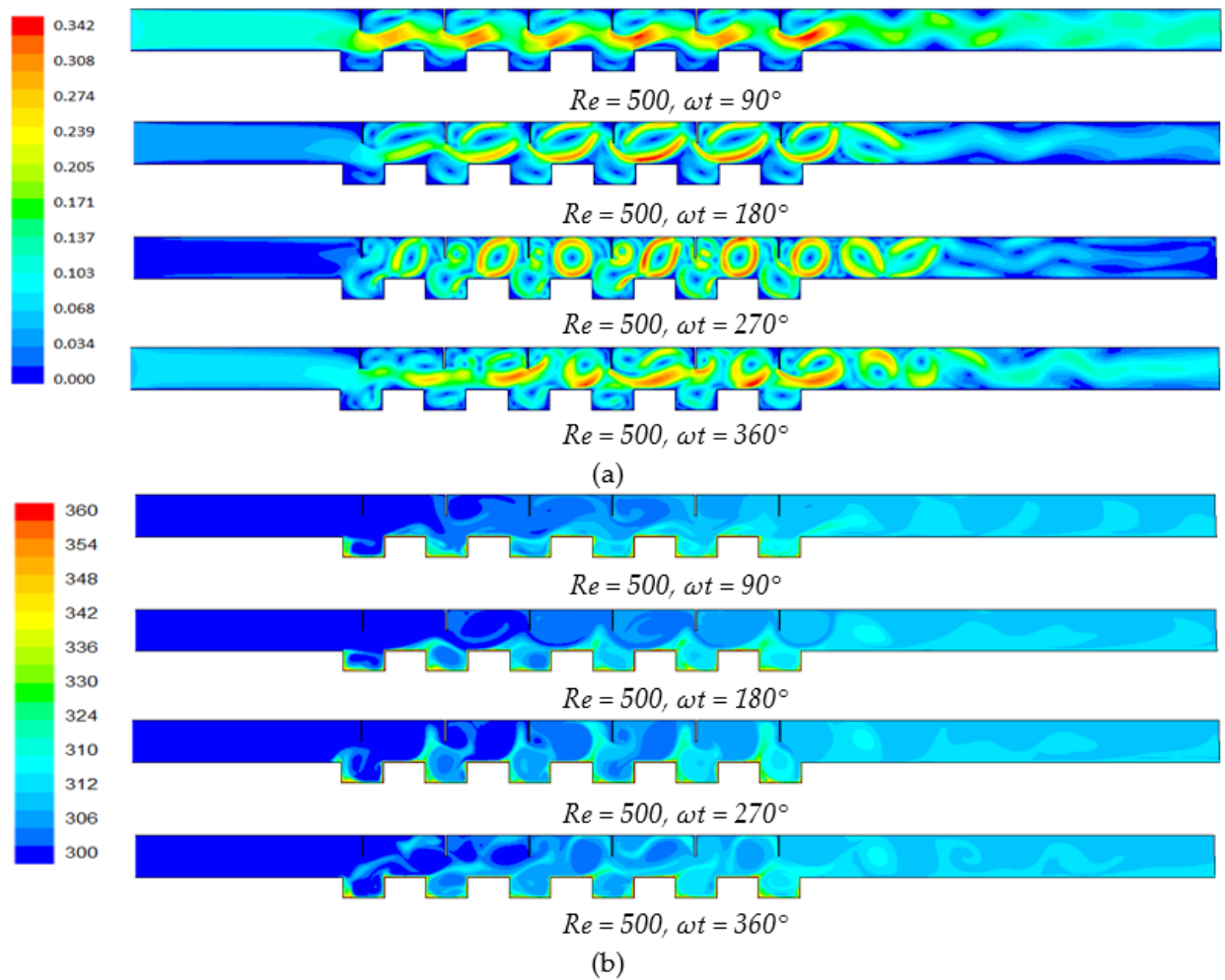
Figure 9. Velocity fields (a) and temperature fields (b) at varying phase angles in the channel with plates (Re = 500, A = 1, St = 2, φ = 0.05)

Figure 10 illustrates the velocity fields (a) and temperature structures (b) of the oscillating nanofluid flow at ωt = 180° for varying Re in the channel without plates. In the upper surfaces of the channel, the flow generally flowed parallel to the surface. Due to the oscillating components, this parallelism was disrupted in the center of the channel and the rectangular cavities on the lower surface, and recirculation zones were formed. With an increasing Re, the recirculation zones enlarged and filled the cavity. These cycles carried the cold fluid from the upper parts of the channel to the hot lower surfaces, thus reducing the temperature of the heated channel surfaces.
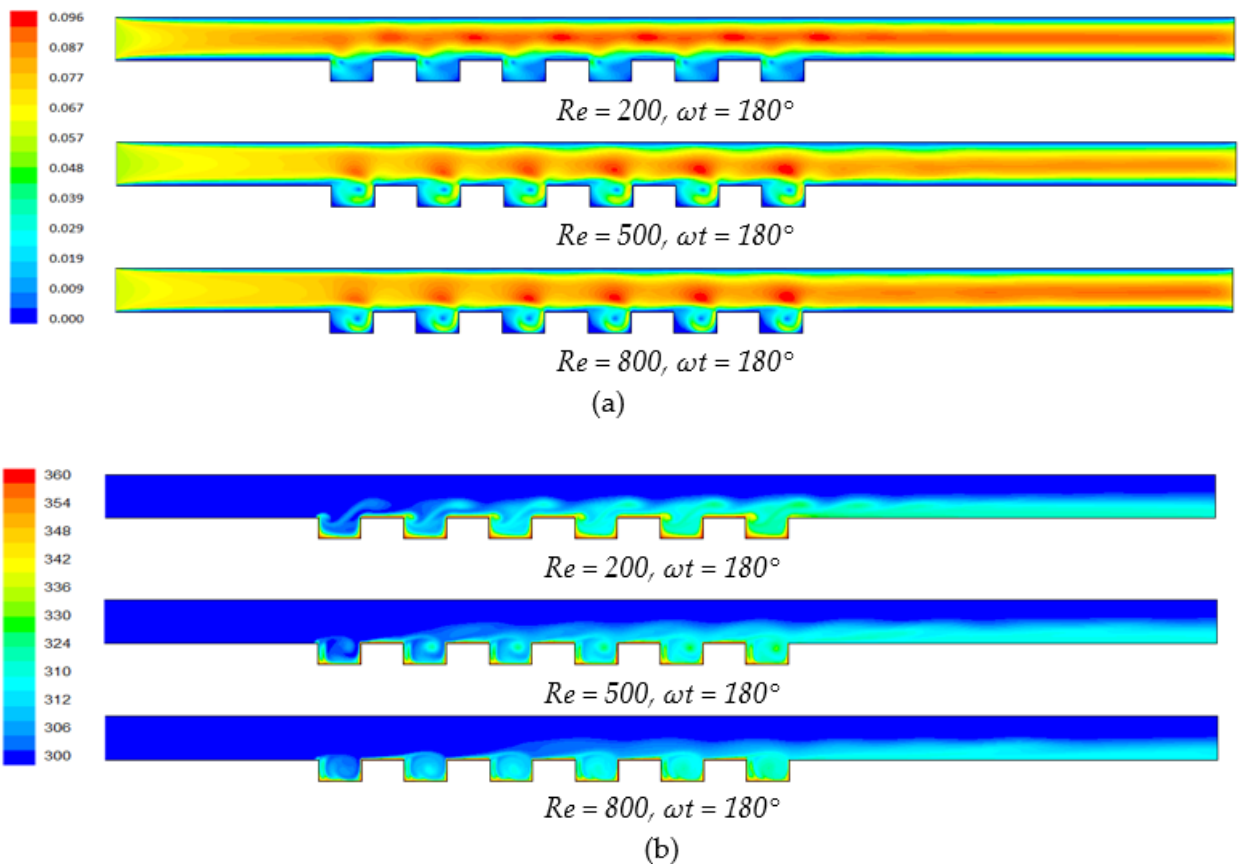
Figure 10. Velocity fields (a), temperature fields (b) at varying Re for oscillating nanofluid flow in the channel without plates (A = 1, St = 2, φ = 0.05, ωt = 180°)

Figure 11 shows the velocity fields (a) and temperature structures (b) of oscillating nanofluid flow at ωt = 180° for different Re in the channel with plates. The vertical plates completely altered the flow fields. The fluid flowed upstream at the ωt = 180° phase angle. Recirculation zones were formed in the channel due to plates and reverse flow. Vortex structures are formed between each plate and in rectangular spaces due to oscillating components. Increasing Re causes an increase in these structures in the channel. The flow cycles that were longitudinal at low Re become circular at high Re. These cycles help move the cold fluid from the top sections of the channel to the heated walls at the lower surface of the channel. Thus, the temperature of the heated walls in contact with the colder fluid diminishes, and heat transfer increases.

Heat Transfer Examination of Oscillating Nanofluid Flow in a Rectangular Corrugated Channel with Vertical Plates: a Numerical Study

387
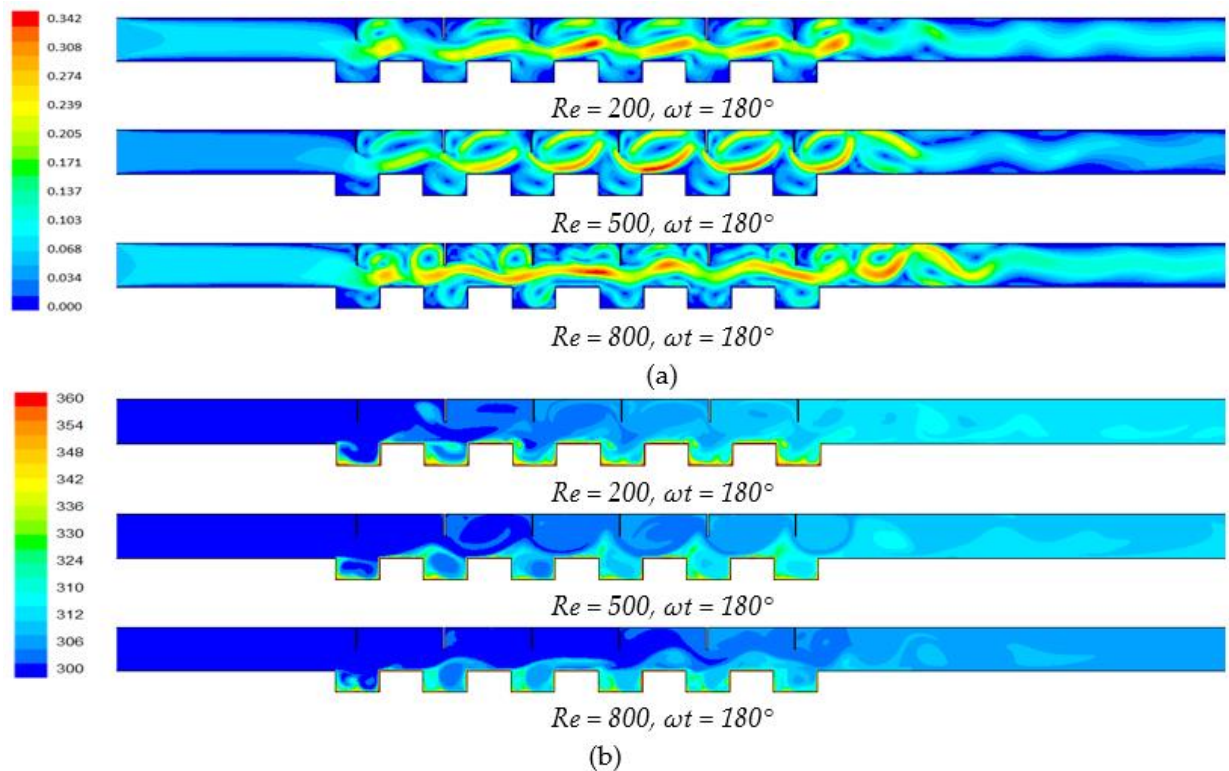
Figure 11. Velocity fields (a) and temperature fields (b) at different Re for the oscillating nanofluid flow in the channel with plates (A = 1, St = 2, φ = 0.05, ωt = 180°)

Figure 12 presents velocity vectors for an oscillating cycle in the channel without plates for Re = 800. At ωt = 90°, the vector directions are downstream. The flow moves parallel to the top surfaces of the channel, and the flow structure is disturbed near the bottom walls. In the corrugated parts of the channel, the vectors are quite small and move freely. At ωt = 180°, the flow starts to reverse direction and only the integrity of the flow is preserved. Flow cycles occurs in rectangular corrugated sections. At ωt = 270°, the direction of the vectors is upstream, and the flow cycles formed in the corrugated sections become larger and wider toward the center of the channel. At ωt = 360°, the vectors begin to flow downstream as a whole, and one cycle is completed.
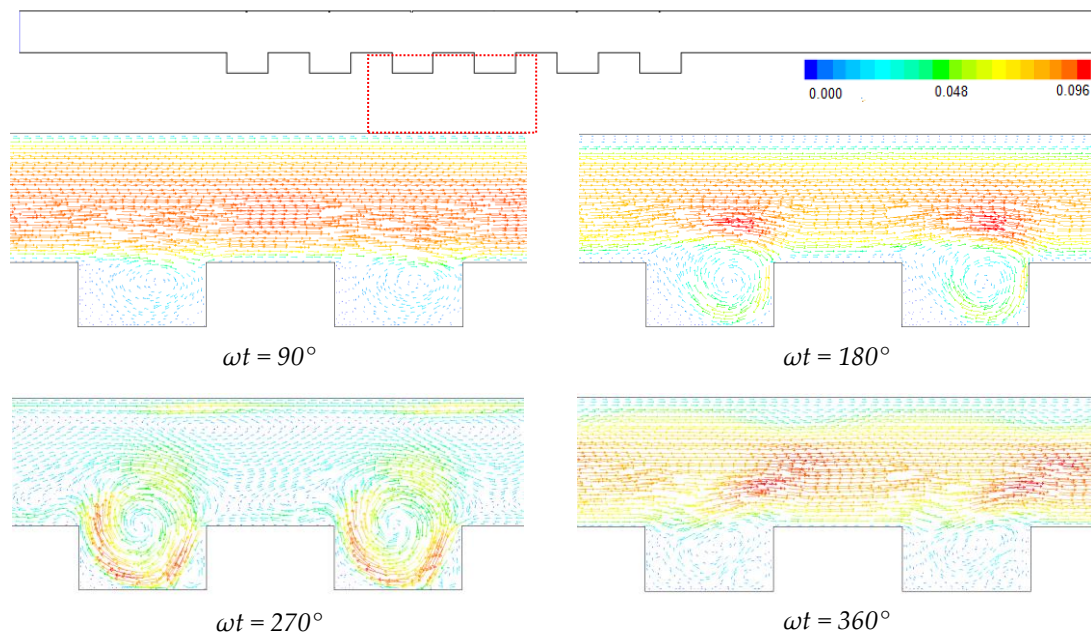
Figure 12. Velocity vectors for one period in the channel without plates at a Re = 800 (A = 1, St = 2, φ = 0.05)

Figure 13 shows the variation of the velocity vectors over one period in the channel with plates. The structure of velocity vectors is quite different from the channel without plates. At ωt = 90°, the main flow is considerably thinner than the channel without plates and flows downstream. The plates and oscillating parameters create flow oscillation. Flow cycles are seen between each plate and in the corrugated parts. At ωt = 180°, the main flow is quite thin, and the velocity vectors rotate upstream. Flow cycles enlarge between the plates and in the corrugated spaces. At ωt = 270°, the direction of the vectors is upstream, and the flow fields are completely disrupted. The recirculation zones grow considerably and spread all over the channel. At ωt = 360°, the flow cycles are lost, and the direction of the vectors is downstream. Thus, one oscillating cycle is completed for the channel with plates.
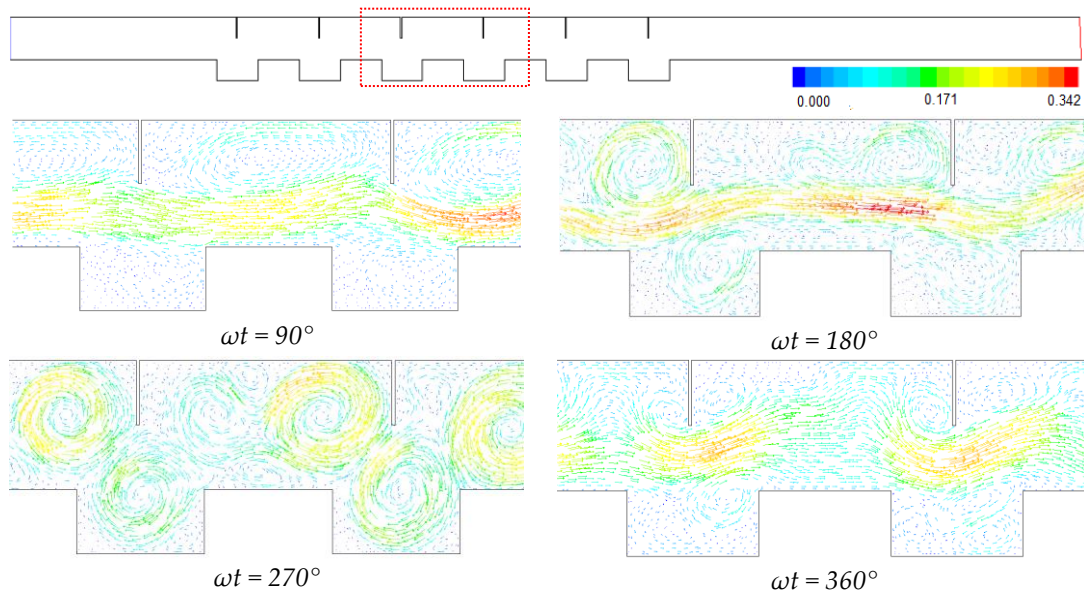
Figure 13. Velocity vectors for one oscillating period in the channel with plates at a Re = 800 (A = 1, St = 2, φ = 0.05)

Figure 14 indicates the variations of the Nu (a), Nu_{rel} (b), f_{rel} (c), and PEC (d) with varying Re for the steady flow. In the Figure, (w), (n), (b, w) and (b, n) subscripts represent the steady flow of the water in the channel without plates, the steady flow of the nanofluid in the channel without plates, the steady flow of water in the channel with plates, and the steady flow of the nanofluid in the channel with plates, respectively. The Nu increased with the rise in the Re for all channel cases. The maximum Nu was obtained as approximately Nu = 39.61 in the steady nanofluid case in the channel with plates at a Re = 800. Nu for the steady case of the nanofluid in the channel with plates increased by about 11% according to the water in the channel without plates.

Figure 14b shows the relative Nusselt number with the Re for oscillating flow of the nanofluid in the channel with/without plates. The Nu_{rel} is compared to the oscillating flow of the nanofluid in the channel with and without plates. (p) and (p, b) subscripts show the oscillating flow of the nanofluid in the channel without plates and with plates, respectively. The Nu_{rel} obtained for the steady state of the water in the channel without plates was considered as a reference. It is seen that the Nu_{rel} increased with the Re. The Nu_{rel} was found to be about 1.39 at the Re = 800 in the channel without plates. The highest Nu_{rel} was acquired at about 1.57 in the channel with plates at the Re = 800.

Figure 14c presents the relative friction factor with the Re for the oscillating flow of the nanofluid in the channel with and without plates. Since the plates added into the channel prevent the flow, the pressure loss in the channel increases. In addition, since the viscosity values of nanofluids is high than the basic fluid, it causes an increase in the pressure drop. Therefore, an important pressure loss occurred in the channel due to the plates, nanoparticles, and oscillating parameters. In Figure 14c, (p, b), (p) and (w) subscripts indicate the oscillating flow of the nanofluid in the channel with plates, the oscillating flow of the nanofluid in the channel without plates, and the steady flow of water in the channel without plates, respectively. The relative friction factor obtained in the steady flow of the water in the channel without plates was considered as a reference. It is seen that the f_{rel} increased with the Re. The relative friction factor was achieved at about 2.53 in the channel without plates at a Re = 800. The highest f_{rel} was acquired at nearly 3.82 in the channel with plates at a Re = 800.

Figure 14d indicates the variation of the PEC with the Re for the oscillating flow of the nanofluid in the channel with and without plates. In Figure 14d, PEC (p, b), PEC (p) and PEC (w) indicate performance evaluation criteria for the oscillating flow of the nanofluid in the channel with plates, for the oscillating flow of the nanofluid in the channel without plates, and for the steady flow of water in the channel without plates, respectively. The PEC obtained in the steady case of the water in the channel without plates was considered as a reference. Depending on the Nu_{rel} and f_{rel}, PEC was calculated in Eq. (16). PEC value higher than 1 show that the heat transfer in the channel is higher than the pressure drop. The PEC values were found very close to each other in all the tested Re. Although the Nu_{rel} was high in the channel with plates, the PEC values were almost the same for all the Re due to the increased the f_{rel}. The best PEC was achieved as 1.046 at a Re = 200 in the channel without plates. At the Re =200, the f_{rel} was very low in the channel without plates.
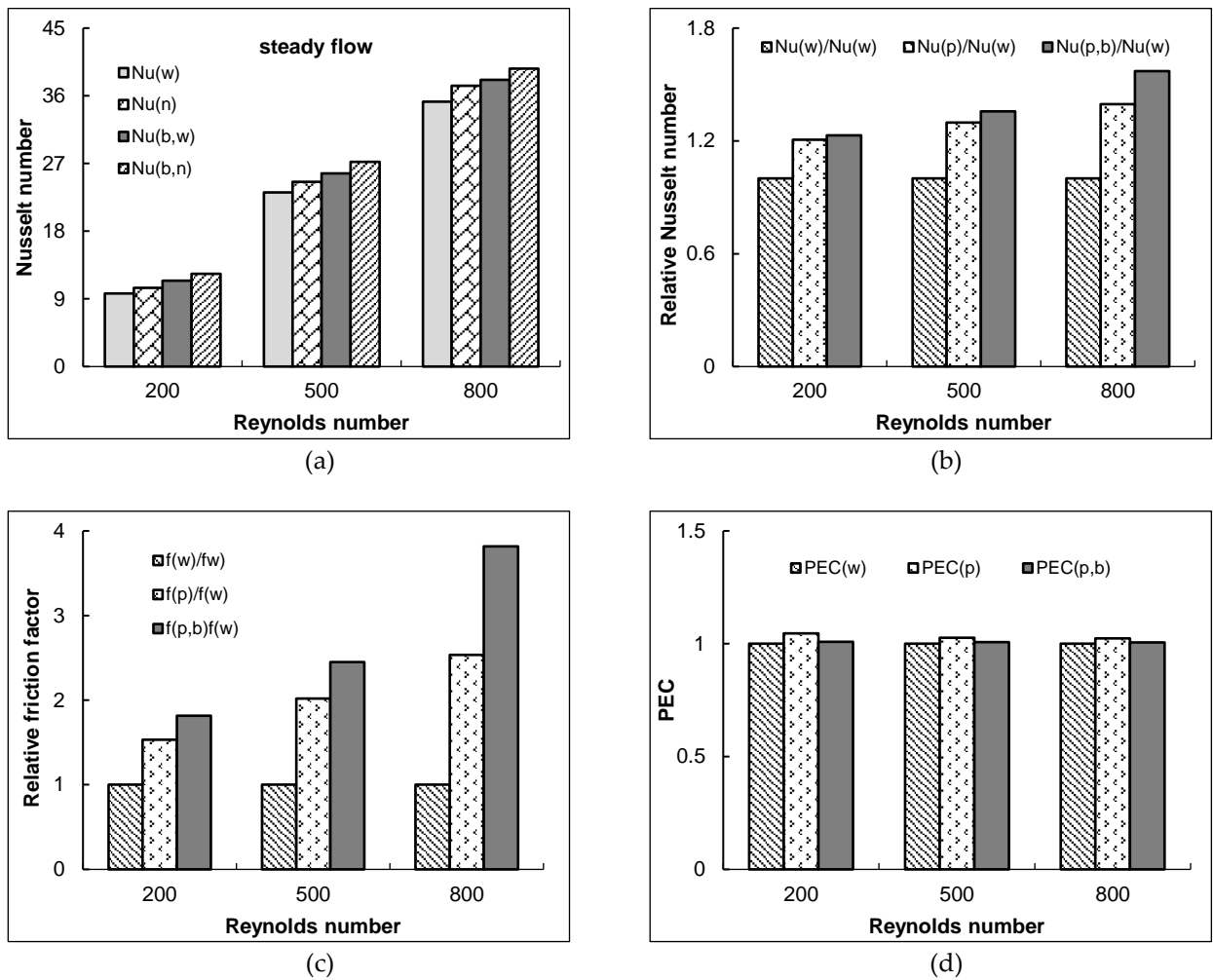
Figure 14. Nu for the steady flow (a), Nu_rel (b), f_rel (c), and PEC (d) with the Re

Figure 15 indicates the variation of the Nu with one oscillating cycle for the nanofluid flow at varying Re, in the channel without plates (a) and in the channel with plates (b). As can be seen from both figures, the Nu changed into sinusoidal form for one oscillating cycle in all the studied Re. As the Re increased, the Nu also increased. Moreover, the range of variation of the Nu was small at a low Re and larger at a high Re. It was seen that the Nu achieved in the channel with plates was higher than without plates. One pulsating cycle is completed at $\omega t = 2\pi = 360°$. The curve of the Nusselt number changes sinusoidally over the course of one cycle due to the pulsating velocity input. The pulsating flow mechanism throughout one cycle is explained in detail in the Figures 8 and 9. While the flow moves in the downstream direction until the phase angle $\omega t = 180°$, after $\omega t = 180°$ the direction of the flow changes and it starts to flow in the upward direction. At $\omega t = 270°$, the flow direction is towards the channel entrance. A decrease in the Nusselt number is observed at this phase angle due to the movement of the hotter fluid at the channel exit towards the channel entrance. After the phase angle $\omega t = 270°$, the flow changes direction again and starts to flow towards the channel exit. As the colder fluid at the channel entrance joins the pulsating cycle, the Nusselt number begins to increase.

(a) without plates   (b) with plates
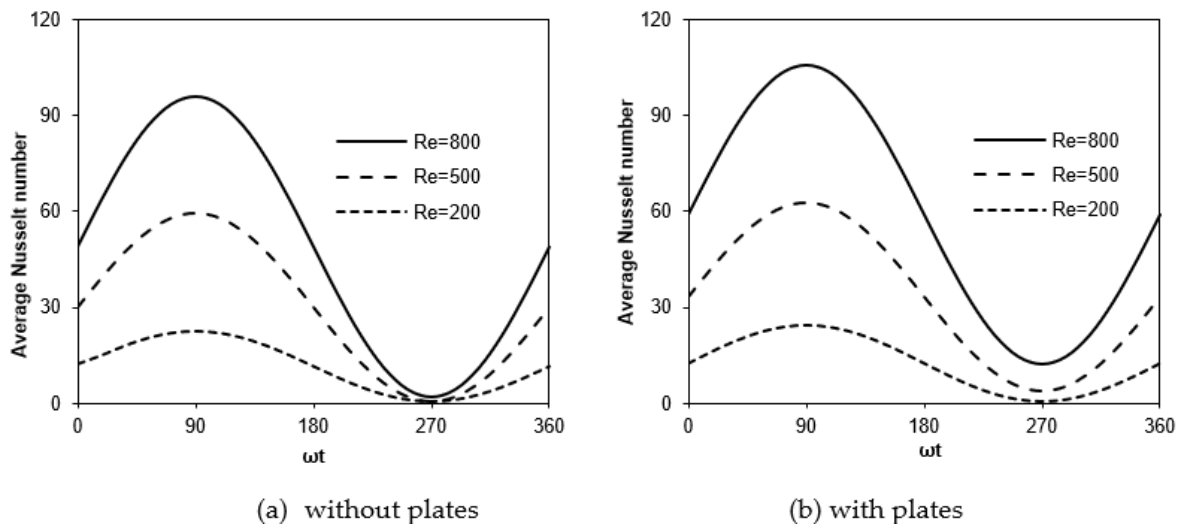
Figure 15. Nu with phase angles for the oscillating nanofluid flow at varying Re

The findings obtained from this study were compared with previous studies [44] to support them with literature studies. The parameters used in both studies are given in Table 2. In both studies, Nu_{rel}, f_{rel} and PEC values obtained under pulsating nanofluid flow conditions in the channel with vertical plates were presented in Table 3. f_{rel} values obtained in this study were found to be lower than [44]. It is seen that Nu_{rel} and PEC values were obtained higher in [44] than in this study. The reason for this may be due to differences between the parameters used in both studies.

Table 2 . Comparison of the parameters used in this study and [44]

Reference	Wave type	D_h	Re	A	St	T_i	T_w	Fluid	φ
Ref. [44]	Circular	12mm	200, 500, 800	1	2	293K	350K	CuO-water	3%
Present study	Rectangular	12mm	200, 500, 800	1	2	300K	360K	Al_2O_3-water	5%

Table 3 . Comparison of the results obtained from this study and [44]

Reference	Re	Nu_{rel}	f_{rel}	PEC
	200	2.624	3.014	1.817
Ref. [44]	500	2.581	3.185	1.752
	800	2.640	3.467	1.744
	200	1.230	1.816	1.008
Present study	500	1.358	2.451	1.007
	800	1.572	3.818	1.006

Present study indicates that the use of plates in the grooved channels significantly influences the flow behavior and heat transfer. Furthermore, preferring nanofluids as the working fluid increases the thermal enhancement relative to the base fluid. Additionally, the oscillating flow, when compared to the steady flow, considerably raises the heat transfer as it creates better flow mixing. Flow oscillations keep the nanoparticles in continuous motion in the channel and prevent the particles from collapsing. Therefore, it is very advantageous to use oscillating flow in nanofluid flows. However, the pump power in the channel slightly increases due to the plates, nanoparticles, and oscillating flow.

4. CONCLUSIONS

This numerical work examined the effects of the oscillating flow of the Al_2O_3-water nanofluid on the thermohydraulic performance in a rectangular corrugated channel with/without plate. The results

compared to steady case of the water in the channel with/without plates. The thermal performance and hydraulic behaviors of the vertical plates, Al_2O_3-water nanofluid, oscillating components, and Re were investigated. The temperature and flow fields in the channel were obtained for varying parameters. The pronounced consequences of the present work were presented by:

- The temperature and flow fields were significantly changed by the channel geometry, vertical plates, and oscillating components. The oscillating flow occurred due to the vertical plates and oscillating parameters, creating circulation zones between the plates and in the rectangular corrugated parts.
- Al_2O_3-water nanofluid increased Nusselt number compared to base fluid (water).
- The oscillating parameters provided important thermal enhancement in comparison with steady cases. The highest thermal enhancement was about 1.57 for the oscillating nanofluid flow at a Re = 800 in the channel with plates.
- The heat transfer increased with Re for all the cases. The Nu varied sinusoidally during one oscillating cycle, and the changing range of Nu increased with an increasing Re.
- The PEC values were obtained close to each other for all the tested Re.
- The pressure loss increased in the channel due to the plates, nanoparticles, oscillating amplitude, and oscillating frequency. The highest f_{rel} was found as about 3.82 in the channel with plates for the oscillating nanofluid flow at the Re = 800.
- Present study proved that the combinations of plates, nanofluids, and oscillating flow in the corrugated channels have important potential for thermal improvement.
- In future studies, the effects of different nanoparticle types and different nanoparticle volume ratios on flow and heat transfer can be investigated by changing the lengths and angles of the plates.

Declaration of Ethical Standards

Declaration of Competing Interest

Funding / Acknowledgements

REFERENCES

[1]   T. Alam, R. P. Saini, and J. S. Saini, "Use of turbulators for heat transfer augmentation in an air duct–A Review," *Renew. Energy*, vol. 62, pp. 689-715, 2014. https://doi.org/10.1016/j.renene.2013.08.024

[2]   F. Menasria, M. Zedairia, and A. Moummi, "Numerical study of thermohydraulic performance of solar air heater duct equipped with novel continuous rectangular plates with high aspect ratio," *Energy*, vol. 133, pp. 593-608, 2017. https://doi.org/10.1016/j.energy.2017.05.002

[3]   X. Gu, Z. Zheng, X. Xiong, E Jiang, T. Wang, D. Zhang, "Heat transfer and flow resistance characteristics of helical baffle heat exchangers with twisted oval tube," *Journal of Thermal Science*, vol. 31, no. 2, pp. 370–378, 2022. https://doi.org/10.1007/s11630-022-1581-1

[4]   P. Naphon, and K. Kornkumjayrit, "Numerical analysis on the fluid flow and heat transfer in the channel with V-shaped wavy lower plate," *Int. Commun. Heat Mass Transfer*, vol. 35, pp. 839-843, 2008. https://doi.org/10.1016/j.icheatmasstransfer.2008.03.010

Heat Transfer Examination of Oscillating Nanofluid Flow in a Rectangular Corrugated Channel with Vertical Plates: a Numerical Study

393

[5] N. E. Davkhar, and N. K. Deshmukh, "Review on analysis of heat transfer and fluid flow characteristics in corrugated duct," *International Journal of Research Publication and Reviews*, vol. 2, no. 1, pp. 262-268, 2021.

[6] H. Zontul, H. Hamzah, N. Kurtulmus, B. Sahin, "Investigation of convective heat transfer and flow hydrodynamics in rectangular grooved channels, *Int. Commun. Heat Mass Transfer*, vol. 126, no. 105366, 2021. https://doi.org/10.1016/j.icheatmasstransfer.2021.105366

[7] N. Kurtulmus, and B. Sahin, "A Review of hydrodynamics and heat transfer through corrugated channels," *Int. Commun. Heat Mass Transfer*, vol. 108, p. 104307, 2019. https://doi.org/10.1016/j.icheatmasstransfer.2019.104307

[8] Z. Brodnianská, and S. Kotśmíd, "Intensification of convective heat transfer in new shaped wavy channel configurations," *Int. J. Therm. Sci.*, vol. 162, p. 106794, 2021. https://doi.org/10.1016/j.ijthermalsci.2020.106794

[9] S. K. Mehta, S. Pati, and L. Baranyi, "Effect of amplitude of walls on thermal and hydrodynamic characteristics of laminar flow through an asymmetric wavy channel," *Case Stud. Therm. Eng.*, vol. 31, p. 101796, 2022. https://doi.org/10.1016/j.csite.2022.101796

[10] S. Skullong, P. Promvonge, C. Thianpong, M. Pimsarn, "Thermal performance in solar air heater channel with combined wavy-groove and perforated-delta wing vortex generators," *Appl. Therm. Eng.*, vol. 100, pp. 611–620, 2016. https://doi.org/10.1016/j.applthermaleng.2016.01.107

[11] M. A. El-Habet, S. A. Ahmed, and M. A. Saleh, "The effect of using staggered and partially tilted perforated baffles on heat transfer and flow characteristics in a rectangular channel," *Int. J. Therm. Sci.*, vol. 174, p. 107422, 2022. https://doi.org/10.1016/j.ijthermalsci.2021.107422

[12] Y. G. Lei, Y. L. He, and R. Li, "Effects of baffle inclination angle on flow and heat transfer of a heat exchanger with helical baffles," *Chem. Eng. Process. Process. Intensif.*, vol. 47, no. 12, pp. 2336–2345, 2008. https://doi.org/10.1016/j.cep.2008.01.012

[13] S. Sripattanapipat, and P. Promvonge, "Numerical analysis of laminar heat transfer in a channel with diamond-shaped baffles," *Int. Commun. Heat Mass Transfer*., vol. 36, no. 1, pp. 32-38, 2009. https://doi.org/10.1016/j.icheatmasstransfer.2008.09.008

[14] S. Kwankaomeng, and P. Promvonge, "Numerical prediction on laminar heat transfer in square duct with 30° angled baffle on one wall," *Int. Commun. Heat Mass Transfer*, vol. 37, pp. 857-866, 2010. https://doi.org/10.1016/j.icheatmasstransfer.2010.05.005

[15] P. Sriromreun, "Numerical study on heat transfer enhancement in a rectangular duct with incline shaped baffles," *Chem. Eng. Transfer*, vol. 57, pp. 1243–1248, 2017. https://doi.org/10.3303/CET1757208

[16] Z. Li, and Y. Gao, "Numerical study of turbulent flow and heat transfer in cross corrugated triangular ducts with delta-shaped baffles," *Int. J. Heat Mass Transfer*, vol. 108, pp. 658–670, 2017. https://doi.org/10.1016/j.ijheatmasstransfer.2016.12.054

[17] K. Karabulut, "Heat transfer and pressure drop evaluation of different triangular baffle placement angles in cross-corrugated triangular channels," *Therm. Sci*., 2020, vol. 24, pp. 355-365. https://doi.org/10.2298/TSCI190813466K

[18] C. E. Bensaci, A. Moummi, F.J. Sanchez de la Flor, E.A. Rodriguez Jara, A. Rincon-Casado, A. Ruiz-Pardo, "Numerical and experimental study of the heat transfer and hydraulic performance of solar air heaters with different baffle positions," *Renew. Energy*, vol. 155, pp. 1231–1244, 2020. https://doi.org/10.1016/j.renene.2020.04.017

[19] P. Promvonge, S. Tamna, M. Pimsarn, C. Thianpong, "Thermal characterization in a circular tube fitted with inclined horseshoe baffles," *Appl. Therm. Eng.*, vol. 75, pp. 1147–1155, 2015. https://doi.org/10.1016/j.applthermaleng.2014.10.045

[20] R. Kumar, A. Kumar, R. Chauhan, M. Sethi, "Heat transfer enhancement in solar air channel with broken multiple V-type baffle," *Case Stud. Therm. Eng*. vol. 8, pp. 187–197, 2016. https://doi.org/10.1016/j.csite.2016.07.001

[21] D. Sahel, H. Ameur, R. Benzeguir, Y. Kamla, "Enhancement of heat transfer in a rectangular

channel with perforated baffles," *Appl. Therm. Eng.*, vol. 101, pp. 156–164, 2016. https://doi.org/10.1016/j.applthermaleng.2016.02.136

[22] A. M. Abed, M. A. Alghoul, K. Sopian, H.A. Mohammed, H. Majdi, A.N. Alshamani, "Design characteristics of corrugated trapezoidal plate heat exchangers using nanofluids," *Chem. Eng. Process. Process. Intensif.*, vol. 87, pp. 88–103. 2015. https://doi.org/10.1016/j.cep.2014.11.005

[23] H. Fazeli, S. Madani, and P. R. Mashaei, "Nanofluid forced convection in entrance region of a baffled channel considering nanoparticle migration," *Appl. Therm. Eng.*, vol. 106, pp. 293–306, 2016. https://doi.org/10.1016/j.applthermaleng.2016.06.010

[24] O. A. Alawi , H. M. Kamar , O. A. Hussein, A. R. Mallah, H. A. Mohammed, M. Khiadani, A. B. Roomi, S. N. Kazi , Z. M. Yaseen, "Effects of binary hybrid nanofluid on heat transfer and fluid flow in a triangular-corrugated channel: An experimental and numerical study," *Powder Technology,* vol. 395, pp. 267-279, 2022. https://doi.org/10.1016/j.powtec.2021.09.046

[25] O. Manca, S. Nardini, and D. Ricci, "A Numerical study of nanofluid forced convection in ribbed channels," *Appl. Therm. Eng.,* vol. 37, pp. 280-297, 2012. https://doi.org/10.1016/j.applthermaleng.2011.11.030

[26] A. Heshmati, H. A. Mohammed, and A. N. Darus, "Mixed convection heat transfer of nanofluids over backward facing step with a slotted baffle," *Applied Mathematics and Computation*, vol. 240, pp. 368–386, 2014. https://doi.org/10.1016/j.amc.2014.04.058

[27] G. Huminic, and A. Huminic. "Heat transfer and flow characteristics of conventional fluids and nanofluids in curved tubes: A review," *Renewable and Sustainable Energy Reviews*. vol. 58, pp. 1327–1347, 2016. https://doi.org/10.1016/j.rser.2015.12.230

[28] C. Qi, Y. L. Wan, C. Y. Li, D.T. Han, Z.H. Rao, "Experimental and numerical research on the flow and heat transfer characteristics of TiO$_2$-water nanofluids in a corrugated tube," *Int. J. Heat Mass Transfer*, vol. 115, pp. 1072–1084, 2017. https://doi.org/10.1016/j.ijheatmasstransfer.2017.08.098

[29] A. H. Pordanjani, S. Aghakhani, M. Afrand, B. Mahmoudi, O. Mahian, S. Wongwises, "An updated review on application of nanofluids in heat exchangers for saving energy," *Energy Conversion Management*, vol. 198, p. 111886, 2019. https://doi.org/10.1016/j.enconman.2019.111886

[30] S. Mei, C. Qi, T. Luo, X. Zhai, Y. Yan, "Effects of magnetic field on thermo-hydraulic performance of Fe$_3$O$_4$-water nanofluids in a corrugated tube," *Int. J. Heat Mass Transfer*, vol. 128, pp. 24–45, 2019. https://doi.org/10.1016/j.ijheatmasstransfer.2018.08.071

[31] A. Kaood, and M. A. Hassan, "Thermo-hydraulic performance of nanofluids flow in various internally corrugated tubes," *Chem. Eng. Process. Process. Intensif.,* vol. 154, p. 08043, 2020. https://doi.org/10.1016/j.cep.2020.108043

[32] M-W. Tian, S. Khorasani, H. Moria, S, Pourhedayat, H.S. Dizaji, "Profit and efficiency boost of triangular vortex-generators by novel techniques," *Int. J. Heat Mass Transfer*, vol. 156, p. 19842, 2020. https://doi.org/10.1016/j.ijheatmasstransfer.2020.119842

[33] R. K. Ajeel, K. Sopian, and R. Zulkifli, "Thermal-hydraulic performance and design parameters in a curved-corrugated channel with L-shaped baffles and nanofluid," *Journal of Energy Storage*, vol. 34, p. 101996, 2021. https://doi.org/10.1016/j.est.2020.101996

[34] S. Akcay, and U. Akdag, "Heat transfer enhancement in a channel with inclined baffles under pulsating flow: A CFD study," *Journal of Enhanced Heat Transfer*, vol. 30, no. 5, pp. 61-79, 2023. https://doi.org/10.1615/JEnhHeatTransf.2023047227

[35] Y. Menni, A. J. Chamkha, M. Ghazvini, M.H. Ahmadi, H. Ameur, A. Issakhov, M. Inc, "Enhancement of the turbulent convective heat transfer in channels through the baffling technique and oil/multiwalled carbon nanotube nanofluids," *Numerical Heat Transfer, Part A: Applications*, vol. 79, no. 4, pp. 311-351, 2021. https://doi.org/10.1080/10407782.2020.1842846

[36] U. Akdag, S. Akcay, and D. Demiral, "Heat transfer enhancement with laminar pulsating nanofluid flow in a wavy channel," *Int. Commun. Heat Mass Transfer*, vol. 59, pp. 17–23, 2014. https://doi.org/10.1016/j.icheatmasstransfer.2014.10.008

[37]　S. W. Chang, and T. H. Cheng, "Thermal performance of channel flow with detached and attached pin-fins of hybrid shapes under inlet flow pulsation," *Int. J. Heat Mass Transfer*, vol. 164, p. 20554, 2021. https://doi.org/10.1016/j.ijheatmasstransfer.2020.120554

[38]　Akcay, S. "Numerical analysis of hydraulic and thermal performance of Al_2O_3-water nanofluid in a zigzag channel with central winglets," *Gazi University Journal of Science*, vol. 36, pp. 383-397, 2023. https://doi.org/10.35378/gujs.1012201

[39]　U. Akdag, S. Akcay, and D. Demiral, "Heat transfer in a triangular wavy channel with CuO-water nanofluids under pulsating flow," *Therm. Sci.*, vol. 23, no. 1, pp. 191-205, 2019. https://doi.org/10.2298/TSCI161018015A

[40]　U. Akdag, S. Akcay, and D. Demiral, "Heat transfer enhancement with nanofluids under laminar pulsating flow in a trapezoidal-corrugated channel," *Progress in Computational Fluid Dynamics*, vol. 17, no. 5, pp. 302-312, 2017. https://doi.org/10.1504/PCFD.2017.086322

[41]　M.H. Esfe, M. Bahiraei, A. Torabi, M. Valadkhani, "A critical review on pulsating flow in conventional fluids and nanofluids: thermo-hydraulic characteristics," *Int. Commun. Heat Mass Transfer.*, vol. 120, p. 104859, 2021. https://doi.org/10.1016/j.icheatmasstransfer.2020.104859

[42]　J. Munoz-Camara, D. Crespí-Llorens, J.P. Solano, P. Vicente, "Baffled tubes with superimposed oscillatory flow: Experimental study of the fluid mixing and heat transfer at low net Reynolds numbers," *Experimental Thermal and Fluid Science*, vol. 123, p. 110324, 2021. https://doi.org/10.1016/j.expthermflusci.2020.110324

[43]　S. Akcay, "Numerical analysis of heat transfer ımprovement for pulsating flow in a periodic corrugated channel with discrete V-type winglets," *Int. Commun. Heat Mass Transfer*, vol. 134, p. 105991, 2022. https://doi.org/10.1016/j.icheatmasstransfer.2022.105991

[44]　S. Akcay, "Heat transfer analysis of pulsating nanofluid flow in a semicircular wavy channel with baffles," *Sādhanā*, vol. 48, no. 2, pp. 57, 2023. https://doi.org/10.1007/s12046-023-02119-x

[45]　S. Kakac, and A. Pramuanjaroenkij, "Review of convective heat transfer enhancement with nanofluids," *Int. J. Heat Mass Transfer*, vol. 52, pp. 3187–3196, 2009. https://doi.org/10.1016/j.ijheatmasstransfer.2009.02.006

[46]　ANSYS Inc. ANSYS Fluent User Guide & Theory Guide-Release 15.0 USA, 2015.

[47]　K. Boukhadia, H. Ameur, D. Sahel, M. Bozit, "Effect of the perforation design on the fluid flow and heat transfer characteristics of a plate fin heat exchanger," *Int. J. Therm. Sci.*, vol. 126, pp. 172-180, 2018. https://doi.org/10.1016/j.ijthermalsci.2017.12.025

[48]　H. Ameur, D. Sahel, and Y. Menni, "Numerical investigation of the performance of perforated baffles in a plate-fin heat exchanger," *Therm. Sci.*, vol. 25, no. 5B, pp. 3629-3641, 2021. https://doi.org/10.2298/TSCI190316090A

SOLAR-POWERED UAV: A NOVEL APPROACH TO CONCEPTUAL DESIGN

[1, *] Caner İLHAN Ⓘ, [2] Zeynep ÇALIK Ⓘ

[1] *Istanbul Technical University, Energy Institute, Energy Science and Technology, Istanbul, TÜRKİYE*
[2] *Darmstadt Technical University, Mechanical Engineering Department, Darmstadt, GERMANY*
[1] ilhan22@itu.edu.tr, [2] zeynep.calik@stud.tu-darmstadt.de

Highlights

- A UAV system was designed to enhance the performance of a solar-powered UAV system by integrating the solar cells inside the wing

- Reduction of equipment weight used in solar-powered UAV to optimize performance and lead an increase in operational efficiency and flight ranges.

- Developing a conceptual design according to the duration of the UAV's stay in the air depending on the solar irradiation

*Corresponding Author: Caner İLHAN, ilhan22@itu.edu.tr

SOLAR-POWERED UAV: A NOVEL APPROACH TO CONCEPTUAL DESIGN

1, * Caner İLHAN [iD], **2 Zeynep ÇALIK** [iD]

1 Istanbul Technical University, Energy Institute, Energy Science and Technology, Istanbul, TÜRKİYE
2 Darmstadt Technical University, Mechanical Engineering Department, Darmstadt, GERMANY
1 ilhan22@itu.edu.tr, 2 zeynep.calik@stud.tu-darmstadt.de

ABSTRACT: The increasing environmental impact of fossil fuel usage has propelled a sense of urgency to address depletion concerns and environmental consequences. This article explores the potential of solar-powered unmanned aerial vehicles (UAVs) as a sustainable alternative in the aviation sector. Originating from advancements in photovoltaic (PV) technology, the integration of solar cells onto aircraft structures has led to innovations in electric aircraft, with a focus on UAVs. The study searchs the conceptual design methodology, emphasizing the complex interplay of factors such as aerodynamics, structural analysis, and performance requirements in solar UAV design. The selection and analysis of solar cells, energy storage systems, and their integration into the UAV are detailed. The study further discusses the crucial aspects of solar irradiation, weight analysis, and aerodynamic parameters in the design process. The proposed UAV design incorporates monocrystalline silicon solar cells, lithium batteries, and Maximum Power Point Tracking (MPPT) technology. A constraint analysis aids in optimizing power-to-weight ratios, thrust-to-weight ratios, and wing loading. The article concludes with a detailed weight estimation, aerodynamic parameters, and a conceptual design that envisions a solar-powered UAV capable of sustained flight. The outlined approach provides insights for future enhancements in solar-powered UAV technology, addressing challenges and contributing to the evolution of eco-friendly aviation solutions.

Keywords: Conceptual Design, Solar Energy, Solar Powered UAV

1. INTRODUCTION

The undeniable environmental impact resulting from the utilization of fossil fuels underscores the urgency of addressing their depletion, given the alarming rate at which reserves are diminishing [1]. As a result, a considerable transition toward renewable energy sources is expected in the coming years**.**

The arrival of photovoltaic (PV) technology, pioneered by Bell Laboratories in the mid-twentieth century, marked a substantial leap in the development of electric aircraft, which had initially emerged alongside the Wright brothers' pioneering invention [2]. As PV technology advanced, it was used in both unmanned and manned aerial vehicles, as shown by Astro Flight Inc's Sunrise I. Over time, significant progress has been achieved in enhancing the efficiency of solar cells. While laboratory research into solar cell efficiency continues, this study looks into the best technique to use solar cells in unmanned aerial vehicles [2].

Renewable energy has gained a great deal of interest in the aviation sector, particularly in the twenty-first century, due to its potential to supply the energy needs of spacecraft. Furthermore, considering the adverse environmental effects of fossil fuels, solar cells have emerged as a viable option for meeting energy requirements in this industry [3].

The sun's limitless energy supply, combined with the ability to store such energy in batteries, enables the building of aircraft capable of sustained flight. Additionally, solar energy production is emissions-free, supporting ongoing ecological initiatives [4] and is expected to reduce maintenance and repair costs [5]. Nevertheless, solar-powered aircraft face challenges due to the inherent fluctuations of weather conditions, leading to fluctuating solar availability throughout the year, which affects aircraft performance [6].

*Corresponding Author: Caner İLHAN, ilhan22@itu.edu.tr

The integration of Unmanned Aerial Vehicles (UAVs) into the aviation sector occurred shortly after the flight experiments conducted by the Wright Brothers. Consequently, the timeline of UAVs aligns with the year 1916, which is close to that period [7]. The emergence of UAVs has led to their significant utilization across various sectors, particularly in agriculture, defense, and reconnaissance. As the frequency of UAV deployment continues to rise, there is a growing emphasis on addressing current climate issues and adopting energy transformation strategies. Consequently, numerous configurations have been developed for powering these aircraft, with solar energy serving as a prominent option among them [8].

The solar-powered UAV employs a technologically innovative approach, integrating solar panels onto the aircraft structure [9]. This integration functions as a basis for the generation of electricity through photovoltaic processes, thereby enabling propulsion. The underlying principle involves utilizing solar panels as energy converters, harnessing solar radiation, and converting it into electrical energy.

During daylight hours, the solar panels directly absorb sunlight, converting it into usable electrical energy. This energy powers various UAV components, including the propulsion system, avionics, and communication systems. Excess energy generated during this phase is stored in onboard batteries or capacitors, ensuring continuous power supply for UAV operations even in the absence of sunlight.

This research aims to conceptualize a solar-powered UAV and explore potential enhancements to maximize its efficiency. The initial phase involves detailing the fundamental processes in the conceptual design of the solar-powered UAV. Subsequently, an assessment and selection process will identify the materials needed to meet the required power parameters based on sizing factors.

2. DESIGN METHODOLOGY

The planning of an aircraft is a highly complex and diverse task that demands a methodical strategy, utilizing extensive expertise and experience acquired over time. The process involves the integration of numerous factors, such as aerodynamics, structural analysis, performance requirements, and operational constraints. By combining these elements, engineers strive to create an aircraft that meets the desired objectives and specifications while ensuring safety, efficiency, and reliability [10].

Throughout the development of aviation, various design philosophies and methodologies have emerged, influenced by historical avhievements, technological advancements, and insights gained from previous aircraft designs. These varied approaches, along with the continual advancements in aeronautical industry, have shaped the contemporary practices of aircraft design [11, 12].

The assumptions made during the presizing phase are pivotal in the initial phases of aircraft design. These assumptions encompass preliminary estimations of the aircraft's dimensions, weights, and performance characteristics, relying on initial requirements and a predefined set of assumptionsassumptions [11]. Presizing allows designers to establish a starting point and evaluate the feasibility of the design concept before delving into more detailed analyses and refinements. To capture and share the knowledge and methodologies integral to aircraft design, extensive documentation has been created, serving as a valuable reference for engineers and designers [10].

The UAV design process shares similarities with that of traditional aircraft. However, in the case of solar-powered UAV systems, there are distinctions from conventional systems. The integration of energy derived from sustainable sources into the aviation industry is a relatively recent concept, and the limited number of experimental applications constrains the design possibilities of such systems, particularly in the pre-sizing phase of solar-powered aircraft.

Despite these limitations and challenges, there have been numerous studies on this topic. Solar energy, being a sustainable and boundless source, is regarded as a promising technology for UAV systems in aviation [13, 14, 15]. These studies include calculations of the required solar panel area to provide the requisite power along with a general solar-powered UAV design.

Variable factors such as weather conditions, the amount of solar intake depending on duration and latitude all have an impact on how a solar-powered UAV is designed [10]. This is due to the fluctuations

in energy intake, the number of solar cells to be used, the battery, and other equipment to be utilized all vary depending on the amount of energy to be stored. Consequently, these studies involve assessments of the required solar panel area to meet the specified power output, alongside a comprehensive design framework for solar-powered UAVs.

Due to a lack of extensive studies on solar-powered UAVs in the literature, the initial data of the UAV, whose mission profile was developed, was derived from a survey of the literature [13]. The design of the UAV will be conducted independently, utilizing calculations performed at various stages of the ongoing procedure. As the design process is incremental, each stage must be individually planned and executed.

2.1. Solar Cells and Energy Storage Systems

In the subsequent stage of the design process, the most crucial decision revolves around the selection of solar cells to be utilized. During this selection process, market research was conducted with a focus on the fact that spacecraft and satellites meet their energy requirements using solar panels as a standard. Upon reviewing the existing solar cell types available in the market and considering the findings from NCEL's studies [16], monocrystalline silicon (monoSi) solar cells emerged as the most efficient option, achieving efficiencies of up to 23% [17]. These monocrystalline solar cells are considered a viable alternative due to their lightweight nature, excellent structural properties, and high reliability, as evidenced by their usage in similar studies.

It is worth noting that solar cells generate heat; however, the planned UAV is expected to operate at altitudes of up to 5 km, where the prevailing weather conditions (-17.5 °C at 5 km) will aid in natural cooling [18]. Despite this, a more comprehensive investigation into the temperature distribution of the solar cells is necessary to ensure accurate calculations.

The selection of solar cells is an important part of solar aircraft design. Solar cell technologies are continuously evolving, witnessing ongoing advancements in efficiency. Consequently, each component used inevitably impacts the overall efficiency of the system. A crucial component in this regard is the battery, necessary for storing and utilizing the collected energy for the aircraft. Considering battery performance, the decision was made for Lithium due to their superior charging capabilities and minimal impact on system efficiency. Lithium batteries are widely preferred in various sectors, including electric vehicles, UAVs, and electric aircraft, owing to their extended service life and low volumetric energy densities [19]

In this specific case, similar studies were explored, and after evaluating various options, a Li-ion battery with an energy density of 300 Wh/kg was chosen as the most suitable option for the calculations. This choice ensures an efficient energy storage solution for solar-powered aircraft [20].

MPPT (Maximum Power Point Tracking) technology is essential for efficiently harvesting and reliably transferring solar energy to the battery [21]. However, due to the limited availability of lightweight MPPT systems, especially tailored for solar-powered aircraft, selecting suitable options becomes challenging. Weight plays a critical role in aircraft, making it advantageous to **opt for** choices that minimize the overall weight.

Considering these factors, it was found that in the context of using MPPT in studies, designs for systems to be integrated into compact structures, such as UAVs, had to be custom-made from the ground up. This approach ensured that the MPPT systems met the specific size constraints and weight limitations of solar-powered aircraft, allowing for optimal performance in the given applications. [13].

Another critical factor to consider is the Electronic Speed Control (ESC). This component must be selected in alignment with the chosen battery, and several factors need to be considered during the selection process. These criteria encompass the specifications provided by the battery, along with weight-related considerations.

2.2. Solar Irradiation

For this study, a comprehensive analysis of available solar irradiation was conducted, taking into account factors such as flight altitude, latitude, day of the year, and time of day. It's worth noting that altitude plays a crucial role in optimizing solar energy absorption [10]. Additionally, an examination of Turkey's annual solar consumption map, depicted in Figure 2.1, indicates that a significant portion of the region experiences solar potential exceeding 1600 kWh/m². Utilizing the data from Figure 1, considering that the majority of Turkey's average solar radiation falls within the range of 1600-1700 kWh/m², a value within this range was used as a reference in the relevant portion of the study.
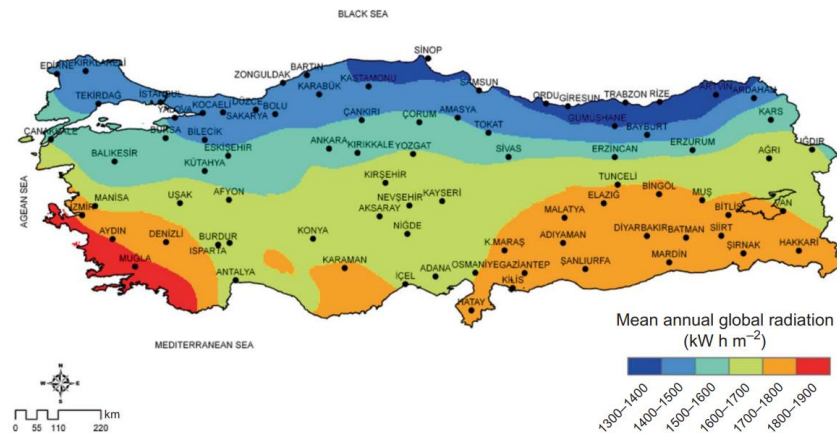
Figure 1. Geographical annual solar irradiation map of Türkiye [22]

2.3. Conceptual Design

Before proceeding with the conceptual design, it is essential to establish specific design criteria for the aircraft under consideration, a step common to nearly all aircraft design projects. While the construction of solar-powered aircraft may vary slightly, the design phase employs methods similar to those outlined in [11], which provide insights into the properties of solar-powered aircraft developed up to this point.

Designing a solar-powered UAV presents unique challenges distinct from other types of aircraft, particularly in the process of generating thrust to meet power requirements. Until reaching this iteration stage, the design follows the conventional steps employed in traditional aircraft design, which are widely preferred in the field [11]. Despite the limited research on solar-powered UAV design, key studies in this area are encompassed in [13].

2.3.1 Weight analysis

The weight of an aircraft is an important factor to consider. Given that the necessary power will be derived from solar radiation and considering the relatively low efficiency of solar cells, minimizing the weight of the unmanned aerial vehicle is essential. A lighter aircraft is paramount to conserving power for the solar-powered UAV under design. With an increase in the system's weight, the corresponding power consumption also rises.

$$P_{level} = Tv \tag{1}$$

When examining the P_{level} equation provided in Eq. (1), the required power value dependent on velocity and thrust is derived. By making this equation under the necessary assumptions and extending it accordingly, Eq. (2) is obtained according to [11].

$$P_{level} = \left(\frac{C_D}{C_L}\right)^{\frac{3}{2}} \cdot \sqrt{\frac{(mg)^2}{S}} \sqrt{\frac{2}{\rho}}$$

(2)

This formula requires the total weight of the aircraft. Solar-powered aircraft do not have varying weights based on flight phases, as do liquid-fueled aircraft. As a result, the total weight of the system is early constant, and the system's power consumption is calculated accordingly.

The weight value after design is determined by the weight of the chosen equipment and the materials utilized after production. Since these weight values were not precisely specified initially, the reference weight of the planned aircraft was calculated using the weight calculations detailed in [13]. On the basis of this value, MATLAB computes the average weight range for each component.
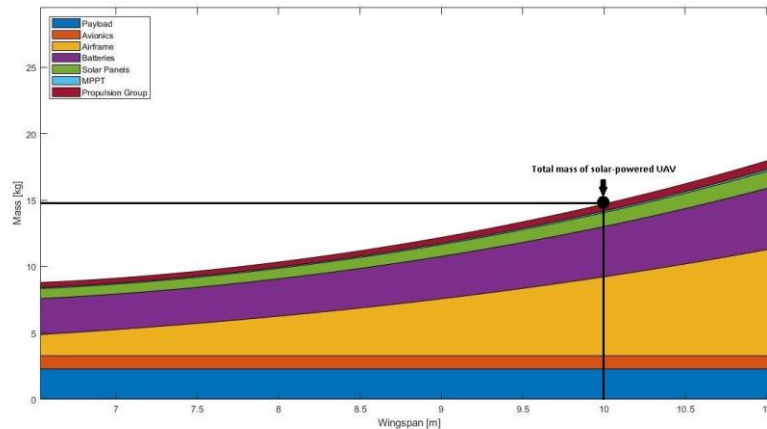
Figure 2. Total mass distribution of the designed solar-powered UAV

2.3.2 Design phase

A constraint analysis is a graph illustrating the variations in power-to-weight (P/W) or thrust-to-weight (T/W) ratios, as well as wing loading (W/S) values during the preliminary design phase [23]. This graph provides insights into the aircraft's capabilities and identifies areas where enhancements can be implemented.

In Figure 3, the constraint analysis in this study is represented by a graph generated using MATLAB Code, a method uncommon in most research studies. The estimated wing sizing parameters are computed utilizing other code outputs with an R-value of 0.65.
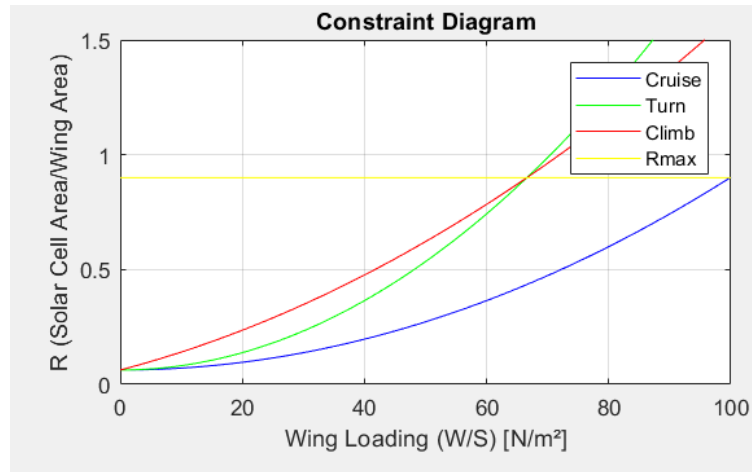
Figure 3. Constraint diagram for solar-powered UAV

In the consideration of other aspects of wing construction, no taper was applied to facilitate cell placement, and it was kept at a value of 1 for this purpose. The wing incidence angle, which is usually predetermined based on the type of aircraft being designed, was set to 0 in this case. This decision aimed to eliminate shadow effects and optimize cell usage. As for the dihedral angle, it was agreed upon to be zero. This choice was made because the weight, which increased with the number of pins used in the fuselage assembly, held greater significance for the solar-powered UAV.

The R-value, determined by selecting a point on the graph as depicted in Figure 3, represents the ratio of the solar cell area to the wing area. Utilizing the calculated wing dimensions, the area covered by the cells on the wing is computed to be 2,86 m².

At this point, to determine the power produced by the solar cells, it is imperative to conduct a power assessment for each individual solar cell. Subsequently, the total power provided by the number of cells that can be accommodated within the calculated wing area must be calculated.

To calculate the electrical power output, an analysis of solar cells available in the market and those used in comparable studies was conducted to select the solar cells suitable for mounting on the wings. The calculation was performed using Eq. (3). During this calculation, data from the manufacturer of the QJ Solar Cell 4G32C series was utilized. It was determined that 894 cells could fit within the calculated wing area. The power output for a single cell was calculated and extrapolated to the entire system, resulting in a total power output of 1172.3 W.

$$P_{mp} = V_{mp} \times I_{mp} \tag{3}$$

This value represents the maximum power output and was determined without factoring in efficiency. When calculating the power output from the solar cells, it is essential to consider their efficiency. The selected solar cell falls within an efficiency class of approximately 32%. Additionally, a 10% risk factor is incorporated in the calculations to account for other potential losses, resulting in an assumed efficiency of 28%. Consequently, the recalculated power output is represented in Eq. (4). "The efficiency values, or in other words the potential losses taken into account, result in a calculated new power value of 328.24W from solar cells.

$$P_{sc} = P_{mp} \times \eta_{sc} \tag{4}$$

The next step involves calculating the power needed for the intended aircraft to achieve flight and evaluating whether this power matches the power generated by the solar cells. If there is surplus power, it should be directed to the batteries. Conversely, if there is a shortfall in power, adjustments should be

made to the design or alternative methods should be devised to compensate for the power deficiency from different systems.

When Figure 3 is re-evaluated, the power required can be calculated from the intersection point of the curves. In this determined value, the efficiency losses of the electric motor, propeller, and other components will be analyzed, leading to the determination of the power needed for the system. Evaluating the power required from Figure 3 as 65 W and factoring in the efficiency of the electric motor and propeller, the required power value is calculated to be 95.6 W.

There exists a power surplus of up to 232.64 W when comparing the power output generated by the solar system, computed using Eq. (4), and the power requirements determined from Figure 3. This surplus power will be stored in the batteries and utilized in situations where power cannot be supplied by solar cells or during high-power consumption phases, such as take-off and climb. During a cruise, the energy stored in the batteries will not be consumed as long as the aircraft can gain energy from the sun.
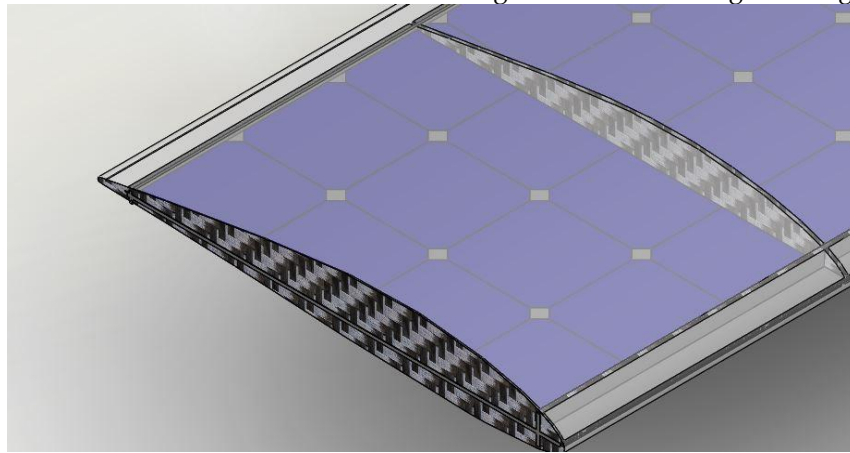
Figure 4. Detailed view of the designed wing for the solar-powered UAV

2.3.3 Detailed weight estimation

Up to this point, the computed weight has included weight estimates for designing and determining the required power. It is now requested that a final weight study be conducted, referencing the weight of all the equipment to be utilized in the system, as part of the ultimate weight calculation process.

After determining the weight generated by the required number of solar cells in the previous section, along with the weight of the battery to be used, other systems, and the UAV's empty weight, the fuselage design and sizing are calculated based on the total weight. Therefore, it is crucial to finalize the weight calculation once the conceptual design has been clarified to a certain extent.

In the context of weight analysis, there will be no variation in weight during flight phases, as observed in liquid-fueled systems. The weight change resulting from the chemical reactions occurring during the usage of energy stored in the battery is negligible. Consequently, Table 1 presents a comprehensive value table, including the total weight and the weights of all components contributing to this extent.

Table 1. Total Weight Estimation

Component	Weight in kilogram
Batteries	3.196
Solar cells	2.579
MPPT	0.22
Motor controller	0.020
Motor	0.34
Propeller	0.034
Other	1.5
TOTAL	7.889

2.3.4 Aerodynamic and performance parameters

Afterward, the fundamental aerodynamic properties of the aerial vehicle, including the airfoil characteristics and geometric parameters of the wing, are specified. These selections were made taking into account the trends and limitations pertinent to the design of solar aircraft.

When evaluating the design requirements, selecting the appropriate airfoil for integrating the solar cells into the wing is essential. The choice of airfoil holds significant importance as it directly influences the aerodynamic characteristics. When picking an airfoil, careful consideration must be given to features such as camber and thickness. Given that the solar cells will be housed within the airfoil, it was decided to opt for airfoils with minimal camber, striving to design wings that are as symmetrical and thick as possible. The selected thickness is crucial when accounting for the surface area covered by solar panels and other equipment placed on the wing. A balance must be struck, as greater thickness leads to increased weight and reduced aerodynamic efficiency due to higher air resistance.

As a result, analyses have been conducted on these airfoils. To assess the aerodynamic performance of the airfoils under low altitude and low-velocity conditions, the plan involves utilizing XFLR5 software [24]. This software will be used to analyze the airfoils, allowing for the selection of the most suitable one under the desired conditions. The wing will then be designed around the chosen airfoil. In the study, after evaluating the required performance, installation procedure E197 was chosen. This choice was made due to the projection of a thicker wing profile to accommodate equipment and solar cell positioning. Table 2 displays the aerodynamic parameters determined at an altitude of 2000 meters, utilizing the outputs from the batch analysis conducted on XFLR5.

Table 2. Analysis results obtained for 2000 m.

Parameter	Value
$C_{L, max}$	1.2
$C_{D, min}$	0.02
C_m	-0.062
α_{stall}	10°

2.3.4 Configuration layout

After establishing the fundamental aerodynamic performance parameters, the factors necessary for configuration creation can be determined. The design of the UAV's fuselage structure and other layouts should be executed in a manner that does not disturb the overall design, avoids incurring aerodynamic penalties, and minimizes additional weight. Consequently, the fuselage structure is shaped to mirror the airfoil profile, aiming to minimize fuselage-induced drag. This approach not only reduces drag but also enhances lift, aiding the aircraft in maintaining its stability.

If the winglet structure is used, it is used as a structure that prevents lift loss due to fuel use, reduction of sound emission, and vortex formation [12]. However, since there is no high altitude or high speed for the solar-powered UAV designed and since there will not be much of a situation such as sound emission due to the use of an electric motor and this structure will create unnecessary weight, it was decided not to add winglets. However, in hybrid designs, it will be useful to have this add-on.

2.3.4 Fuselage configuration

The design and dimensioning of the fuselage for aircraft using solar energy is one of the simplest steps in the design phase as there is no need to add fuel to the body and no positioning is required. If there is a need to study the equipment that will be attached to the body; The two most important elements are the battery and the motor.

The fuselage configurations of solar-powered aircraft vary. To disperse wing load, some utilize two fuselages and tail booms, while others use a single fuselage and tail boom for structural continuity. A single-engine application example in this study implies that a single fuselage and tail boom combination might be more appropriate, providing a lighter construction and less surface friction drag.

The dimensions of the diameter of the body must be in the smallest dimensions, and the maximum value of this size must be determined so that the maximum size of the equipment used in it will fit. Hence, it was decided that it would be more accurate to show the measurements of the detailed sizing as a final CAD drawing after the full aircraft design was completed. At this stage, this length is given as a dependent function of the weight in [11], since the length of the body must be used as a parameter for the size of the tail.

$$L_{fuselage} = AW_0^c \tag{5}$$

The calulcation can be performed using the equation above for the fuselage length accordingto Eq (5) from [11]. In the Eq. (5), A and c are constant and, based on experimental studies, have been given a certain standard for different types of aircraft. The values of these constants are given in [11] and for this study, these values are chosen 1.48 and 0.23, respectively.

In solar-powered aircraft, fuselage design and sizing are critical considerations in determining the optimum dimensions and positioning of the empennage (tail section). When sizing and situating the empennage, proportional consideration of body size is vital, with special care paid to moment arm length, a critical element in tail sizing. The fuselage length is used as a criterion, by the guideline provided in reference [11], which indicates that the moment arm length is 60% of the fuselage length. Following that, the dimensions of the empennage are computed using the equations (Eq (6) and Eq (7)) stated in [11]'s relevant section.

$$S_{VT} = \frac{c_{VT} bS}{L_{VT}} \tag{6}$$

$$S_{HT} = \frac{c_{HT} bS}{L_{HT}} \tag{7}$$

Examining Eq. (6) and Eq. (7) reveal that tail volume coefficients are necessary for both equations. These coefficients are calculated using specific assumptions and aircraft types, which is a standard approach in the entire aircraft design process. However, because solar-powered UAV design is a unique method, no standard parameters for this specific aircraft type are supplied in reference [11]. As a result, the essential data for these calculations can be obtained by using an aircraft with similar characteristics or by conducting experimental trials with various sizes to determine the appropriate empennage type.

Since the V-tail will be developed as the tail type in this study, the angle between the V-tail must be determined in addition to the measurements. [11] states that the formula in Eq. (8) can be used to

compute this angle and the CAD drawing of the V-tail design created based on the values obtained from the calculations is shown in Figure 5.

$$\theta_T = arctan\left(\sqrt{\frac{S_{VT}}{S_{HT}}}\right) \tag{8}$$

Figure 5. CAD drawing of the computed V-tail

3. RESULTS AND DISCUSSION

The design approach results in a solar-powered UAV concept capable of completing its intended missions and achieving the initial requirements by utilizing both solar and stored energy sources. Figure 6 represents a 3D Computer-Aided Design (CAD) model of the envisioned UAV, whereas Table 3 displays the primary geometric, performance, and aerodynamic properties of the intended solar-powered UAV. It should be noted that the solar-powered UAV is far from an optimum concept since only the conceptual design phase has been completed. There is still a tremendous possibility for improvement in the latter design phases, including extensive structural analysis.
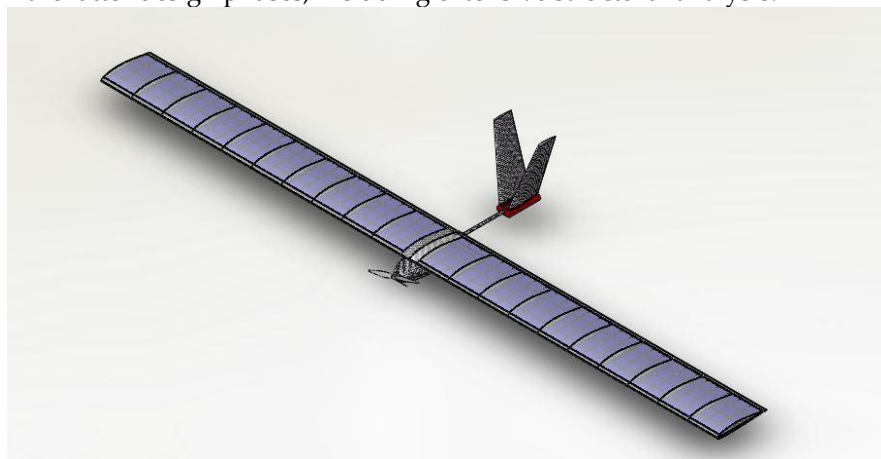
Figure 6. The final 3D CAD model of the completed solar-powered UAV design

Table 3 includes a comparison between this concept and various solar-powered UAVs to provide information about the concept's validity. Specifically, the Sunrise 2 and the The Solar Challenger, are two separate solar-powered UAVs powered only with solar energy and energy storage technology that supply electrical power to the UAV.

Table 3. Technical characteristics and comparison of the conceptual designed solar UAV and other solar UAVS

	Solar-powered UAV concept	Sunrise 2	The Solar Challenger
Gross Weight	7.889 kg	10.21 kg	153.77 kg
Wing Span	7.162 m	9.75 m	14.26 m
Wing Area	5.9283 m²	8.36 m²	21.83 m²
Aspect Ratio	8,65	11,4	9
Wing Loading	1.33 kg/m²	1.22 kg/m²	7.03 kg/m²
Length	2.38 m	14.4 m	9.27 m
Solar Array	894 cells	4480 cells	16128 cells
Airfoil	Eppler 197	Eppler 387	Lissaman
Cruise Speed	10 m/s	24.9 m/s	20.56 ml/h
Maximum Altitude	5000 m	22000 m	9100 m

Batch analysis with XFLR5 was used to determine aerodynamic performance parameters influencing the flight performance of the planned solar-powered UAV at 2000 meters altitude. The UAV had the wing properties and cruise speed listed in Table 1 at the time of analysis. Table 2 displays the acquired results, which include aerodynamic performance metrics.
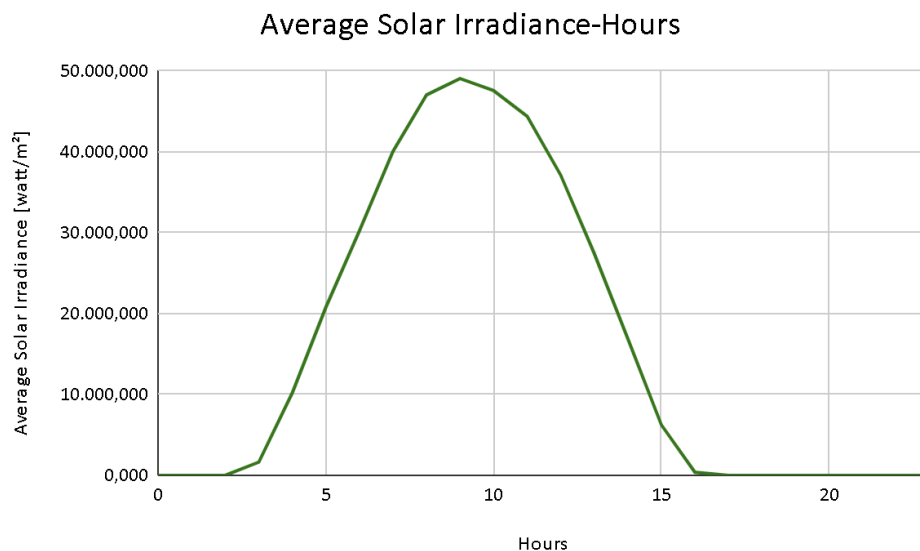
Figure 7. Solar irradiance for each hour in April 2018

As can be seen from Figure 7, it is almost impossible to benefit directly from the sun after 5 pm. Solar irradiance reaches its maximum value at 9 am. In this scenario, the designed UAV should initiate its flight before the specified hour to capitalize on sunlight optimally, storing surplus energy in the battery to extend the total flight duration. The irradiance model exhibits regional variations; hence, flight predictions for the selected region should be made to achieve maximum efficiency. Efficiency extends beyond such factors and is closely associated with system performance, including the characteristics of

the utilized equipment and considerations such as weight. Particularly, the efficiency of the solar cells employed must be maximized, and the system weight should be reduced through ongoing studies.

4. CONCLUSIONS

In conclusion, the exploration of solar-powered unmanned aerial vehicles (UAVs) through the lens of a conceptual design methodology has unveiled promising prospects for the integration of renewable energy in aviation. The comprehensive analysis presented in this article highlights the feasibility and potential benefits of utilizing photovoltaic technology to power UAVs. As a result of this study, it was recognized that solar-powered manned/unmanned aerial vehicle design is a very complex area due to the lack of studies on the subject and the limited number of studies in this area.

The classic design approach relies heavily on statistics and assumptions. This design approach does not have enough information on the design methodology for battery-powered and electric aircraft, as the design applies primarily to fueled manned aircraft. Therefore, as in the classical aircraft design approach, the maximum number of solar cells that can be placed was calculated after determining the required power of the aircraft with the help of the constraint diagram, according to the design criteria determined by first proceeding from the wing design. As a result of this calculation, it was calculated that the integration of 894 cells was possible.

Depending on the number of 894 cells integrated and considering the efficiency coefficient, it was concluded that there is an excess power of 232.64 W, based on the ratio between the amount of power that can be transmitted to the aircraft by the cells and the amount of power required by the engine. In order to prevent the waste of this excess energy and increase the flight time, it is planned to use a Li-ion battery and store the excess energy there.

In addition to the fact that analyses and calculations are made considering the altitude as 5000 meters within the scope of the design, the value of $C_{l,max}$ of 1.2 indicates that the aircraft's ability to hold in the air is good and that the stall angle is 10 degrees, which is not a serious obstacle to performing a controlled flight.

The detailed results obtained as a result of the calculations and analyses made within the scope of this study can be found in Table 3.

When economic issues are examined, the composite materials used in the airframe, including solar cells, the high cost depending on the amount of battery, the cost of production and equipment, and the cost of an aircraft that runs on renewable energy can be examined. It can cost high prices, and with technological progress, this situation will no longer be a problem in the next few years, this assumption arises from the result when the costs of solar cells when they are launched on the market are compared with their current values.

Considering the aspects for improvement, most of the parameters that affect the aerodynamic properties of the wing geometry have not been assessed in order to increase the maximum number of cells that can be used. Because the UAV is designed to be a non-aerodynamic performance UAV that flies at low speeds, however, these properties were not a problem in the context of this project, as the preference for solar energy in aircraft with different properties can lead to changes in the properties of the wing design can be discussed in more detail.

The body size has been designed so that only the necessary equipment can be mounted to keep drag and weight as low as possible, and to use in the fuselage geometry, it is necessary to change types of equipment and geometry to add other equipment to the body geometry. In this context, a new design of the fuselage size can be created through flow analysis and an evaluation of the weight, which is influenced by the material to be used.

Finally, the collaborative efforts of researchers, engineers, and environmental advocates will play a pivotal role in realizing the full potential of solar-powered UAVs. For instance, advancements such as the development of higher-efficiency cells for integration into UAVs, the improvement of energy storage equipment with high energy density, and studies aimed at reducing the weight of equipment used in solar-powered UAVs and aircraft will make progress easier in this field. Hence, these endeavours will

open up avenues for research, enabling the use of solar energy as the main energy source across all types of aircraft, thereby fostering the evolution of the entire aviation sector.

Declaration of Ethical Standards

Authors declare to comply with all ethical guidelines including authorship, citation, data reporting, and original research publication.

Declaration of Competing Interest

The authors declare that they have no known competing financial interests or personal relationships that could have appeared to influence the work reported in this paper.

Funding / Acknowledgements

The authors declare that they have not received any funding or research grants during the review, research of the article.

Data Availability

Not applicable.

REFERENCES

[1]   "The Energy Report ǀ Publications ǀ WWF", World Wildlife Fund. [Online]. Available: https://www.worldwildlife.org/publications/the-energy-report [Accessed Oct. 18, 2023]

[2]   R. Boucher, "History of solar flight", içinde *20th Joint Propulsion Conference*, Cincinnati,OH,U.S.A.: American Institute of Aeronautics and Astronautics, June 1984. doi: 10.2514/6.1984-1429.

[3]   W. Ni, Y. Bi, D. Wu, ve X. Ma, "Energy-optimal trajectory planning for solar-powered aircraft using soft actor-critic", *Chin. J. Aeronaut.*, c. 35, sy 10, ss. 337-353, Oct. 2022, doi: 10.1016/j.cja.2021.11.009.

[4]   W. Jamshed, K. S. Nisar, R. W. Ibrahim, F. Shahzad, ve M. R. Eid, "Thermal expansion optimization in solar aircraft using tangent hyperbolic hybrid nanofluid: a solar thermal application", *J. Mater. Res. Technol.*, c. 14, ss. 985-1006, Sept. 2021, doi: 10.1016/j.jmrt.2021.06.031.

[5]   K. Milidonis, A. Eliades, V. Grigoriev, ve M. J. Blanco, "Unmanned Aerial Vehicles (UAVs) in the planning, operation and maintenance of concentrating solar thermal systems: A review", *Sol. Energy*, c. 254, ss. 182-194, Nis. 2023, doi: 10.1016/j.solener.2023.03.005.

[6]   J. Ge ve L. Liu, "Electromagnetic interference modeling and elimination for a solar/hydrogen hybrid powered small-scale UAV", *Chin. J. Aeronaut.*, c. 36, sy 10, ss. 293-308, Oct. 2023, doi: 10.1016/j.cja.2023.03.044.

[7]   K. L. B. Cook, "The Silent Force Multiplier: The History and Role of UAVs in Warfare", içinde *2007 IEEE Aerospace Conference*, Mar. 2007, ss. 1-7. doi: 10.1109/AERO.2007.352737.

[8]   P. Radoglou-Grammatikis, P. Sarigiannidis, T. Lagkas, ve I. Moscholios, "A compilation of UAV applications for precision agriculture", *Comput. Netw.*, c. 172, s. 107148, May. 2020, doi: 10.1016/j.comnet.2020.107148.

[9]   Y. Chu, C. Ho, Y. Lee, ve B. Li, "Development of a Solar-Powered Unmanned Aerial Vehicle for Extended Flight Endurance", *Drones*, c. 5, sy 2, Art. sy 2, June 2021, doi: 10.3390/drones5020044.

[10]   P. Panagiotou, I. Tsavlidis, ve K. Yakinthos, "Conceptual design of a hybrid solar MALE UAV", *Aerosp. Sci. Technol.*, c. 53, ss. 207-219, June 2016, doi: 10.1016/j.ast.2016.03.023.

[11]   "Aircraft Design: A Conceptual Approach, Sixth Edition ǀ AIAA Education Series" [E-book]. https://arc.aiaa.org/doi/book/10.2514/4.104909

[12]   J. Roskam, *Airplane Design, Part II : Preliminary Configuration Design and Integration of the Propulsion System*. Lawrence: DARcorporation, 1999. [Online]. Available: https://www.biblio.com/book/airplane-design-part-ii-preliminary-configuration/d/1568943846 [Accessed Oct. 30, 2023]

[13]   A. Noth, R. Siegwart, ve W. Engel, "Design of Solar Powered Airplanes for Continuous Flight", *Env. Res*, Oca. 2007.

[14]   G. Romeo, G. Frulla, ve E. Cestino, "Design of a High-Altitude Long-Endurance Solar-Powered Unmanned Air Vehicle for Multi-Payload and Operations", *Proc. Inst. Mech. Eng. Part G J. Aerosp. Eng.*, c. 221, sy 2, ss. 199-216, Şub. 2007, doi: 10.1243/09544100JAERO119.

[15]   S. Jashnani, T. R. Nada, M. Ishfaq, A. Khamker, ve P. Shaholia, "Sizing and preliminary hardware testing of solar powered UAV", *Egypt. J. Remote Sens. Space Sci.*, c. 16, sy 2, ss. 189-198, Ara. 2013, doi: 10.1016/j.ejrs.2013.05.002.

[16]   "Best Research-Cell Efficiency Chart | Photovoltaic Research | NREL". [Online]. Available: https://www.nrel.gov/pv/cell-efficiency.html [Accessed Oct. 30, 2023].

[17]   "Solar Impulse - Around the World to Promote Clean Technologies". [Online]. Available: https://aroundtheworld.solarimpulse.com/adventure [Accessed Oct. 30 2023].

[18]   "Getting to Grips with Aircraft Performance - February 2002 | SKYbrary Aviation Safety". [Online]. Available: https://skybrary.aero/bookshelf/getting-grips-aircraft-performance-february-2002 [Accessed Oct. 30, 2023].

[19]   S. Afroze *vd.*, "Emerging and Recycling of Li-Ion Batteries to Aid in Energy Storage, A Review", *Recycling*, c. 8, sy 3, Art. sy 3, June 2023, doi: 10.3390/recycling8030048.

[20]   C. Xiao, B. Wang, D. Zhao, ve C. Wang, "Comprehensive Investigation on Lithium Batteries for Electric and Hybrid-Electric Unmanned Aerial Vehicle Applications", *Therm. Sci. Eng. Prog.*, c. 38, s. 101677, Feb. 2023, doi: 10.1016/j.tsep.2023.101677.

[21]   H. Suryoatmojo *vd.*, "Design of MPPT Based Fuzzy Logic for Solar-Powered Unmanned Aerial Vehicle Application", içinde *2018 International Conference on Engineering, Applied Sciences, and Technology (ICEAST)*, Tem. 2018, ss. 1-4. doi: 10.1109/ICEAST.2018.8434430.

[22]   "Solar radiation over Turkey and its analysis: International Journal of Remote Sensing: Vol 32, No 21". [Online]. Available: https://www.tandfonline.com/doi/full/10.1080/01431161.2010.508056 [Accessed Oct. 30, 2023].

[23]   S. Gudmundsson, "Chapter 3 - Initial Sizing", içinde *General Aviation Aircraft Design (Second Edition)*, S. Gudmundsson, Ed., Butterworth-Heinemann, 2022, ss. 57-91. doi: 10.1016/B978-0-12-818465-3.00027-6.

[24]   XFLR5. [CD-ROM]. Available: https://www.xflr5.tech/xflr5.html [Accessed Oct. 30, 2023].

AN INVESTIGATION ON UTILIZATION OF DOĞANHİSAR/KONYA CLAYS IN GLAZED PORCELAIN TILE BODIES

[1,*] Volkan KALEM [iD], [2] Gülay SARIKAYA [iD]

[1] *Konya Technical University, Faculty of Engineering and Natural Sciences, Department of Metallurgical and Materials Engineering, Konya, TÜRKİYE*
[2] *Research & Development Center, Yurtbay Seramik, Eskişehir, TÜRKİYE*
[1] vkalem@ktun.edu.tr, [2] gulay.sarikaya@yurtbay.com.tr

Highlights

- Technical properties of 3 different clays from Doğanhisar/Konya region were determined in order to investigate their usage potential in glazed porcelain tile production.

- Use of Konya clays instead of Ukrainian clay in tile body recipes increased the strength of fired bodies.

- Konya based clays could be used in bodies up to 6 wt.% of tile recipes.

*Corresponding Author: Volkan KALEM, vkalem@ktun.edu.tr

AN INVESTIGATION ON UTILIZATION OF DOĞANHİSAR/KONYA CLAYS IN GLAZED PORCELAIN TILE BODIES

1, * Volkan KALEM [ID], **2 Gülay SARIKAYA** [ID]

1 Konya Technical University, Engineering and Natural Sciences Faculty, Metallurgical and Materials Engineering Department, Konya, TÜRKİYE
2 Research & Development Center, Yurtbay Seramik, Eskişehir, TÜRKİYE
1 vkalem@ktun.edu.tr, 2 gulay.sarikaya@yurtbay.com.tr

ABSTRACT: In this study, technical properties of 3 different clays from Doğanhisar/Konya region were determined to investigate their usage potential in glazed porcelain tile production of Yurtbay Seramik Company. For this purpose, mineralogical, chemical, and thermal characterization of the clays was performed using XRD, XRF, and dilatometric analyses. Furthermore, the use of Konya clays instead of Ukrainian clay in the porcelain tile compositions was studied. Ukrainian clay was substituted gradually by Konya clays in different tile body recipes. Samples, having these new compositions, were prepared by uniaxial pressing, and exposing to a firing regime at 1190 °C for 55 min. Fired samples were then characterized based on their dry strength, fired strength, water absorption, color, and firing shrinkage properties. Experimental results proved that the use of Konya clays instead of Ukrainian clay increased the strength of fired bodies. It would be possible to use Konya clays in tile bodies up to 6 wt.% with some modifications in the body compositions and firing regime.

Keywords: Ceramic, Konya Clay, Tile, Ukrainian Clay

1. INTRODUCTION

Porcelain tiles are produced using naturally occurred raw materials in nature such as quartz, clay, and feldspar. Among these raw materials, clay is widely abundant in the world and is one of the oldest crafting and building materials [1]. On the other hand, clay minerals used in the production of porcelain tiles can vary in structure and chemical content since they are natural materials having different origins. As an example, Ukrainian clays were characterized with their low iron content, good sintering properties, and high plasticity whereas eastern and central Europe-based clays were characterized with their medium plasticity and weak sintering properties [2]. Hence, mostly Ukrainian clays are preferred by the ceramic industry in Turkey. Porcelain tile body compositions generally consist of 25-40 wt.% plastic clay. So, the high price of the Ukrainian clays and of their transportation has a significant effect on the manufacturing cost of porcelain tile products. In addition, the production quantities of ceramic tile industry grow year by year, and as a result the need for raw materials also increases at the same rate.

Due to the decrease in raw material reserves, the supply of quality raw materials in the ceramic tile industry is becoming increasingly difficult. Therefore, ceramic tile industry in Turkey is in a search of local clay sources to minimize their dependency on foreign raw material import, to decrease raw material and product costs, and to secure their clay sources for prudential reasons. But the recent geopolitical uncertainties in the supply of Ukrainian clays as well as the decrease in the quantity of local clays and environmental problems related to their mining lead the ceramic industry to search for alternative clay sources.

There are some research studies for the alternative clay sources that can be utilized in the production of ceramic products, such as Nevşehir- [3, 4], Afyon- [5, 6], Çanakkale- [7], Denizli- [8], and Konya-based clays [9]. Apart from the tile products, Konya-based clays were also tested for ceramic primer applications in artistic ceramics [10]. Usage of waste materials as alternative raw materials in ceramic products was also studied in literature [11, 12]. Ceramic tile manufacturers supply clay mainly from Şile (İstanbul) and

*Corresponding Author: Volkan KALEM, vkalem@ktun.edu.tr

Söğüt (Bilecik) regions, which are the two largest clay fields of Turkey. Apart from these regions, the regions with secondary clay potential are Afyon, Kütahya, Çanakkale, and Konya. Konya-based clays are generally used in the production of bricks, pottery, and tiles. Aim of this study was to investigate the possibility and suitability of regional clays (Doğanhisar/Konya, Turkey) for fabrication of porcelain tile products by replacing the currently used Ukrainian clay in the tile recipes. 3 different Konya-based clays were added to the standard porcelain tile body recipe of Yurtbay Seramik (Eskişehir) instead of Ukrainian clay. Physical, chemical, mechanical, and thermal properties of both the clays and the tile bodies were investigated. Tarhan also studied the use of a Doğanhisar region clay in porcelain tile body compositions [9]. But the clay used had a different chemical composition and physical properties compared to the clays used in this study.

2. MATERIAL AND METHODS

2.1. Characterization of Clay Samples

In this section, mineralogical, thermal, and physical analyses were performed on 3 different clays (K1, K2, and K3) collected from Doğanhisar region of Konya. X-ray diffraction (XRD) was used for the phase identification of clay samples. Prior to measurement, samples were ground in an agate mortar and sieved through 125-micron (120 mesh) sieve. A Europe-Gnr model diffractometer was used with Cu-Kα radiation; the diffraction data were collected over the 2θ range from 5° to 70° with a scanning rate of 2°/min. Quantitative analysis of the phases detected by XRD was performed using the MDI JADE software package. It was assumed that the phase content of the clays was entirely accounted for by the XRD patterns. In addition to XRD, chemical analysis was also performed to identify the mineralogical content of clay samples. Bulk chemical composition was determined using a Panalytical/Axios MAX model wavelength dispersive X-ray fluorescence spectrometry (WD-XRF). Loss on ignition (LOI) values were obtained via mass data monitored before and after a calcination process performed at ~1000 °C.

Physical properties of fired clays were investigated by preparing disc samples pressed at 40.79 kg/cm² in a cylindrical die with 50 mm diameter. Then, these discs were fired at 1190 °C for 39 min in a roller kiln at Yurtbay Seramik Company. Water absorption of the fired samples was tested using water impregnation method (ISO 10545-3) in immersion under vacuum (Essepienne VSVD/120) [13]. Firing shrinkage values were calculated by measuring sample dimensions before and after the firing process. An X-rite Ci62 model spectrophotometer was used to measure the chromatic coordinates (L*, a*, and b* values) of the fired clay samples. Thermal expansion coefficient (TEC, α) of clays were determined using a Toledo SDTA841 model thermomechanical analyzer. Measurement was performed by heating the pressed clay samples from 20 °C to 600 °C with a heating rate of 10 °C/min, and calculating the TEC value at 400 °C.

2.2. Characterization of Ceramic Bodies

New porcelain tile body formulations were prepared to determine the effect of Konya clays on the technical properties of ceramic bodies. Using these new formulations, suitability of Konya clays instead of Ukrainian clay was also investigated. For this purpose, Konya clays were added in different ratio instead of Ukrainian clay in the standard tile recipes of Yurtbay Seramik. Ratio of raw materials (in weight percentage) in the standard (Std) and modified recipes were listed in Table 1.

Ceramic slurries were prepared according to the body recipes by wet milling. Then, they were dried, ground, sieved to <63 μm, and moisturized with 5-6 wt.% water to obtain granulated powders. Samples were formed by pressing the powders in a 100 x 50 x 5 mm rectangular die under 50.99 kg/cm² using a Gabrielli brand press. Some of these samples were used to determine the sintering behavior and dry (green) strength values. Other samples were fired at 1190 °C for 55 min in the industrial roller kiln. Fired samples were tested with respect to their phase content, fired strength, and thermal expansion. 3 samples were prepared for each recipe for the strength and thermal expansion tests to increase the reliability of the data.

Table 1. Raw material fractions (wt.%) of the tile body recipes.
(*Other Raw Materials: clays & feldspars (from different regions in Turkey), kaolinite, silica sand, magnesite, and Na_2SiO_4)

Recipes	Ukrainian Clay	K1	K2	K3	Other raw materials*
Std	17	-	-	-	83
R1	11	-	-	6	83
R2	6	-	-	11	83
R3	-	-	-	17	83
R4	11	6	-	-	83
R5	6	11	-	-	83
R6	-	17	-	-	83
R7	11	-	6	-	83
R8	6	-	11	-	83
R9	-	-	17	-	83

Granulated powders were also pressed in a 50 mm die at 40.79 kg/cm² to obtain disc shaped samples, to be used for the investigation of physical properties such as water absorption, firing shrinkage, and color developed after firing. Phase content of fired bodies were analyzed using a Europe-Gnr model XRD with Cu-Kα radiation; the diffraction data were collected over the 2θ range from 10° to 70° with a scanning rate of 2°/min. Quantitative analysis of the phases detected in the fired bodies was performed using the MDI JADE software package. Dry strength tests were performed with a 3-point bend testing machine in Yurtbay Seramik (Gabrielli Flexi 150). A Shimadzu AGS-X model universal testing machine was used for the fired strength measurements. Water absorption, firing shrinkage, and color of fired samples were determined using the same methods mentioned in Section 2.1 (Characterization of Clay Samples). TEC values were measured with a mechanical dilatometer (DIL 402 PC Netzsch) using cylindrical samples with 6 mm diameter and 25 mm length. Sintering behavior of ceramic bodies were investigated via an optical dilatometer (Misura 3 ODHT). For the measurements, samples were heated from room temperature to 1300 °C using 50 °C/min heating rate.

3. RESULTS AND DISCUSSION

3.1. Clay Samples

XRD patterns of Konya clays as well as Ukrainian clay are presented in Figure 1. They prove that the main phases of Konya clays are quartz (JCPDS no:05-0490), illite (JCPDS no:26-0911), and kaolinite (JCPDS no:06-0221). On the other hand, Ukrainian clay is rich in kaolinite and poor in illite content.

Contrary to the similar XRD patterns of Konya clays, their appearances are significantly different from each other as seen in the photograph given in Figure 2. Especially K1 clay has a darker color than the other 2 clays. A similar color formation is also observed in subclays at coal fields. In a research study on Ilgın/Konya region coal fields, a similar XRD pattern (to the pattern of K1 clay) was obtained for the lower clays formed underneath the coal level and named as "black subclay" [14]. The pattern mainly contained quartz, illite, and kaolinite as well as pyrite mineral (FeS_2). Black color was due to the existence of pyrite mineral in the subclay. Phase content of K1 clay (collected from Doğanhisar) and subclays (in Ilgın) might be similar since these two regions are very close to each other (~30 km). However, a clear peak of pyrite phase cannot be observed in the XRD pattern of K1 clay. This may be due to the pyrite content in K1 clay probably being lower than the XRD detection limit. Elemental compositions of clays were measured by XRF, and the results are shown as oxides in Table 2. K1 clay has higher amount of sulfite, compared to

other 2 clays. This proves the possible existence of compounds, such as pyrite, in K1 clay causing a darker appearance.
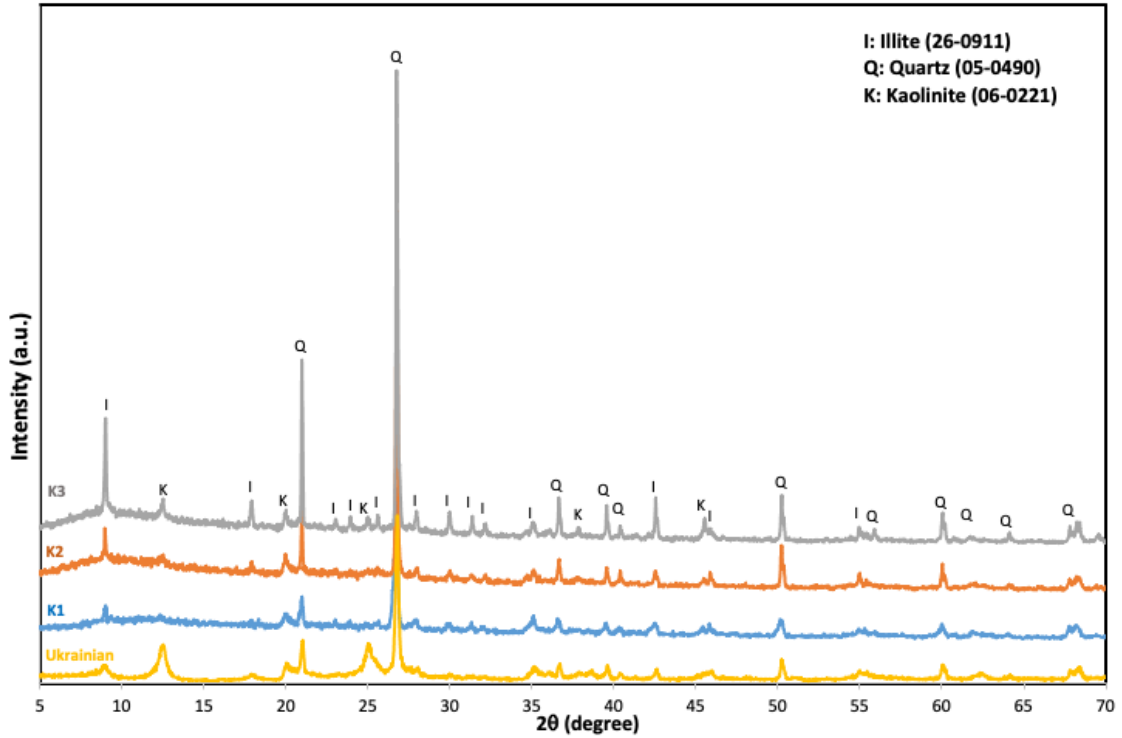
Figure 1. XRD patterns of clay samples.
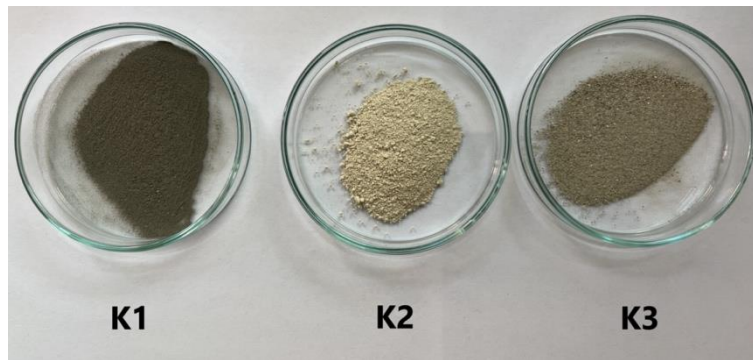
Figure 2. Clay samples collected from Doğanhisar/Konya region.

Physical properties of clay samples after firing are listed in Table 3. Water absorption value for Ukrainian clays in literature is given as a range between 0.2% and 2.0% [15]. Konya clays exhibit higher water absorption than the Ukrainian clay used in this study. This is due to the differences between Konya clays and Ukrainian clay in their phase content and structure. Clays are classified as layer- and chain-structured based on the arrangement of silica and alumina layers. In layer-structured clays, this arrangement can be either in an order or disorder. In the latter case, mixed-layer clay minerals are formed. Ukrainian clays exhibit a mixed-layer formation [16]. As shown in Figure 1, Konya clays are rich in illite mineral which has a 3-layered structure (2:1 type) and a theoretical chemical formula of $K_{1-1.5}Al_{4-3.5}(Si_{7-6.5}Al_{1-1.5})O_{20}(OH)_4$ [17]. On the other hand, kaolinite, the main constituent of Ukrainian clays, is a 2-layered (1:1 type) mineral. Compared to 2-layered minerals, clays with 3-layered structure can hold more water between these layers. Among the 3 Konya clays investigated in this study, K1 clay has a higher water absorption value than that of other 2 clays.

Table 2. Oxide content and loss on ignition (wt.%) of Ukrainian and Konya clays.

	K1	K2	K3	Ukrainian Clay
SiO_2	65.49	68.75	77.62	59.68
Al_2O_3	21.20	18.81	13.17	26.56
K_2O	2.98	2.41	1.65	2.00
TiO_2	1.00	0.99	0.65	1.25
Na_2O	0.97	0.31	0.24	0.57
Fe_2O_3	0.84	1.52	0.82	1.09
MgO	0.54	0.63	0.42	0.39
P_2O_5	0.16	0.40	0.12	-
CaO	0.11	0.32	0.09	0.62
ZrO_2	0.06	0.08	0.04	-
SO_3	0.09	0.04	0.02	-
LOI	6.56	5.69	5.13	7.84

Table 3. Physical properties of fired clay samples.

	Ukrainian Clay	K1	K2	K3
Water Absorption (%)	1.0-1.5	8.5-9.0	7.2-7.9	7.0-7.5
Firing Shrinkage (%)	7.5-8.0	3.4-3.7	3.3-3.9	3.0-3.5
Chromatic Coordinates (L*-a*-b*)	82.00-2.20-13.00	82.36-0.88-12.71	78.49-2.75-21.65	78.00-3.20-20.00
TEC (α_{400}x10^{-7} °C^{-1})	61.80	78.25	80.08	78.80

Firing shrinkage value for 3 clays are in a range of 3-4% and it fits well with the standard value desired for the clay raw materials used in the ceramic tile industry. Chromatic coordinates are also given in Table 3. K1 clay has lower a* and b* values than that of other 2 clays. Therefore, a different color development can be expected for the fired K1 clay sample, compared to the color of other 2 clay samples. Besides, K2 clay has the highest b* value (more yellowish appearance). Both conditions are also in good agreement with the clay appearances shown in Figure 2. According to the quantitative analysis of the phases in XRD patterns in Figure 1, amount of quartz in clays is in order of K2>K3>K1>Ukrainian. Since crystalline quartz has a very high thermal expansion coefficient [18], Konya clays have higher TEC values than that of Ukrainian clay as given in Table 3.

3.2. Ceramic Bodies

Among the ceramic body recipes prepared in this study, R2, R5, and R8 (recipes with a mixture in which the amount of Konya clay is higher than Ukrainian clay) were selected for the phase analysis of ceramic bodies. XRD patterns of these mentioned recipes and the standard recipe are shown in Figure 3.

Microstructure of a porcelain-ware mainly consists of newly formed phases after firing (e.g., mullite) as well as residual phases (quartz and feldspars) dispersed in a glassy (vitreous) phase [19]. There is an obvious increase in the intensity of mullite peaks with the addition of Konya clays in the bodies instead of Ukrainian clay. This increase is more significant for R2 (K3 clay) and R8 (K2 clay) bodies. In addition, there is also an increase in the intensity of peaks belonging to residue feldspars after firing. McConville et al also observed a much higher proportion of fluid amorphous phases for 2:1 type clays (e.g., illite) than the kaolinite based clays. This result was related to the existence of feldspars and the fluxing action of the cations located between 2:1 layers. This caused the formation of larger mullite crystals than the mullite in kaolinite samples, at temperatures above 1000 °C [20].
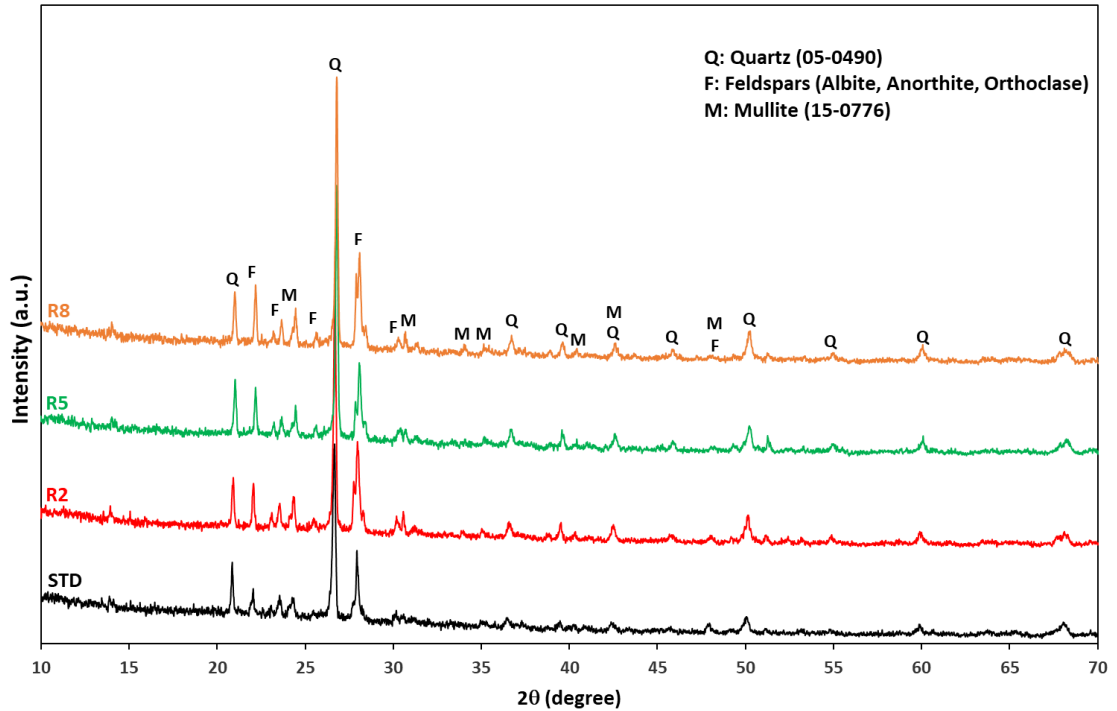
Figure 3. XRD patterns of fired ceramic bodies belonging to Std, R2, R5, and R8 recipes.

Mechanical and physical properties of ceramic bodies prepared according to the standard and modified recipes are given in Table 4. Dry strength values decrease with the increase in clay amounts compared to the standard recipe. The dry strength values of the recipes coded as R1 and R7 are close to the standard recipe value and are within the tolerance range of floor tile standards. Dry strength acceptance standard of the company is in the range of 15-16 kg/cm^2.

Firing shrinkage values increase with the increase in amount of Konya clays. This increase can be interpreted as an improvement in the sintering properties of the bodies. However, considering all recipes, firing shrinkage values ranging between 8.21-9.27% did not show any negative deviation from that of the standard body. Firing shrinkage acceptance standard of the company is around 8.5-9.0%. According to the firing color results, although there is a decrease in lightness (L*) values as the amount of Konya clays increase, the L*-a*-b* values of all 9 recipes are generally similar to that of the standard recipe.

The fired strength values of the bodies obtained using K3 (R1-R3) and K2 (R7-R9) clays are higher than that of the standard recipe. This increase can be associated with the amount of mullite phase formed during firing. Mechanical strength of a porcelain body is directly related to the interlocking mechanism of the fine mullite needles in its microstructure. Therefore, as the amount of mullite in the body decreases, the bending strength is expected to decrease. According to the results of the quantitative analysis performed on the XRD patterns in Figure 3, the lowest amount of mullite was determined in the body containing K1 clay (R5). As a result, the lowest fired strength values were obtained for recipes containing K1 clay in Table 4. In addition, the increase in fired strength values can also be related to vitrification period during firing. As already stated for XRD patterns in Figure 3, amount of residue feldspars increased for bodies containing Konya clays. High amount of residue feldspars implies the high alkali content of starting raw materials. Alkali oxide and alkaline earth oxide based raw materials decrease the viscosity in the order $MgO < CaO < SrO < BaO < K_2O < Na_2O < Li_2O$ [21]. The decrease in the viscosity of the liquid phase with the increasing alkali content increases the rate of condensation during firing and contributes to the increase in the amount of mullite crystals, and as a result, provides denser and high strength structures [22].

Water absorption is one of the most important physical properties of ceramic tile products. Water

absorption value mainly depends on the raw materials used in the production of tiles. Especially for floor tiles used at outdoor surfaces, a water absorption value lower than 3% is desired. Higher absorption values can cause breaking and cracking of outdoor floor tiles [5]. Furthermore, ISO 10545-3 standard for porcelain tiles imposes a water absorption value of ≤0.5%. All the recipes used in this study exhibit water absorption values lower than 0.1% (not given in Table 4) and they have been evaluated to comply with the standards.

Table 4. Mechanical and physical properties of ceramic bodies.

Recipes	Dry Strength (kg/cm²)	Firing Shrinkage (%)	Chromatic Coordinates (L*-a*-b*)	Fired Strength (kg/cm²)
Std	17.30	8.45	64.3-3.4-11.1	512.63
R1	15.54	8.25	64.2-3.3-11.2	533.69
R2	10.24	8.45	63.8-3.3-11.4	579.10
R3	6.84	9.17	61.9-3.6-11.5	569.48
R4	13.60	8.35	65.1-3.3-11.4	469.61
R5	10.47	8.71	63.2-3.5-10.3	428.77
R6	6.57	9.27	65.2-3.1-10.7	416.74
R7	14.96	8.21	63.0-3.6-11.4	517.54
R8	13.06	8.45	62.7-3.5-11.5	566.39
R9	10.80	8.83	61.2-3.4-11.5	615.11

Thermal expansion coefficients of fired ceramic bodies are listed in Table 5. Thermal expansion values increase -compared to the standard recipe- with the increase in the amount of all 3 clays. The quartz phase content of Ukrainian clays is less compared to Konya clays. It is well known that the thermal expansion coefficient of crystalline quartz is higher than that of amorphous quartz [18]. As the amount of Konya clay increases instead of Ukrainian clay in the bodies, the amount of crystalline quartz increases, and this causes the coefficient of thermal expansion to increase.

Table 5. Thermal expansion coefficients of fired ceramic bodies.

Recipes	TEC (α_{400}x10^{-7} °C^{-1})
Std	74.00
R1	76.04
R2	78.02
R3	78.10
R4	75.85
R5	76.49
R6	76.83
R7	73.63
R8	78.42
R9	78.77

"Flex point" temperatures at which the highest dimensional change is achieved during rapid sintering were determined using the optical dilatometer analysis data. Flex point of standard, R2, R5, and R8 bodies are 1220, 1222, 1223, and 1194 °C, respectively. In the bodies (R2 and R5) where K3 and K1 clays are used, the flex point temperature is close to the standard body. There is a decrease in the flex point value in the R8 body where K2 clay is used. According to this result, it can be concluded that the body containing K2

clay is rich in terms of alkaline-earth content compared to other bodies. It has also been stated in similar studies in the literature that raw materials containing Fe_2O_3 and alkaline-earth oxides such as CaO and MgO, with their fluidizing (fluxing) effects, improve vitrification in ceramic bodies and the liquid phase is formed at lower temperatures [11, 23].

4. CONCLUSIONS

In this study, the suitability of 3 different clays from Doğanhisar region of Konya (K1, K2, and K3 clays) for porcelain tile production was investigated. When Konya clay is added instead of Ukrainian clay in tile body recipes, the packing (compressibility) feature of green bodies is negatively affected, and dry strength values decrease. Ukrainian clays, with their high plasticity property, enable easier pressing and thus enable a body with high green density to be obtained. Dry strength acceptance standard for porcelain tiles is in the range of 15-16 kg/cm^2, and the use of K2 and K3 clays up to 6 wt.% instead of Ukrainian clay can provide the desired dry strength standard.

An increase in firing shrinkage and thermal expansion values was observed with the use of Konya clays. Crystalline quartz has a higher coefficient of thermal expansion compared to amorphous quartz. Hence, the coefficient of thermal expansion increases with the addition of Konya clays (especially K3 clay with high SiO_2 content) in the recipes. On the other hand, the use of Konya clay (K2 and K3) instead of Ukrainian clay has a positive effect on the fired strength of the bodies. This result is related to the increase in the amount of mullite phase formed after firing, with the use of Konya clays.

Konya clays (since they are illite-based clays) cannot be used as a complete replacement for Ukrainian clay in the recipe. However, with optimizations in the recipes and firing regime to keep the firing shrinkage and thermal expansion values at the desired standard values, it is possible to partially use Konya clay (especially K3 clay) instead of Ukrainian clay.

Declaration of Competing Interest

The author(s) stated that there are no conflicts of interest regarding the publication of this article.

REFERENCES

[1]   F. Bergaya, G. Lagaly, "General introduction: clays, clay minerals, and clay science", *Handbook of Clay Science,* vol. 1, pp. 1–18, 2006.

[2]   G. Krzysztof, "Composition and ceramic properties of ball clays for porcelain stoneware tiles manufacture in Poland", *Applied Clay Science*, vol. 51, pp. 74–85, 2011.

[3]   Z. B. Ozturk, "Microstructural characterization of mullite and anorthite-based porcelain tile using regional clay", *Journal of Ceramic Processing Research*, vol. 17, pp. 555-559, 2016.

[4]   Z. B. Ozturk, "Effect of addition of Avanos's (Nevsehir) clays on the physical and microstructure properties of ceramic tile", *Journal of the Australian Ceramic Society*, vol. 53, pp. 101-107, 2017.

[5]   A. E. Kurt, "Use of Local Clay on behalf of Russian Clay in Granite Production (dissertation in Turkish with an abstract in English)" MSc, Afyon Kocatepe University, Afyonkarahisar, Turkey, 2007.

[6]   M. Tarhan, B. Tarhan, "Investigation of the usage of Afyon Clay in Porcelain Tile Bodies (article in Turkish with an abstract in English)", *International Journal of Engineering Research and Development*, vol. 11, pp. 275-281, 2019.

[7]   K. Kayacı, "Investigation of the use of Rheological Problemed Clays of Çanakkale Region (TURKEY) in Porcelain Tile Bodies (article in Turkish with an abstract in English)", *Afyon Kocatepe University Journal of Sciences and Engineering,* vol. 19, pp. 321-325, 2019.

[8]   B. Semiz, "Characteristics of clays from Pamukkale (Denizli) region and their usability in ceramic sector (article in Turkish with an abstract in English)", *Pamukkale University Journal of Engineering Sciences*, vol. 24, pp. 1237-1244, 2018.

[9]   M. Tarhan, "Use of Konya Clay for Porcelain Tile Productions (article in Turkish with an abstract in English)", *International Journal of Engineering Research and Development*, vol. 11, pp. 705-712, 2019.

[10]   ME. Avşar, AM Önder, "Investigation of Using Different Take Three Clay Ceramic Primer Making Such from Konya (article in Turkish with an abstract in English)" *Kalemişi,* vol. 4, pp. 141-166, 2016.

[11]   K. Köseoğlu, H. Cengizler, L. İ. İsrail, "Production of Wall Tiles Containing Ulexite Waste at Different Sintering Temperatures", *Gümüşhane University Journal of Science and Technology*, vol. 10, pp. 463-473, 2020.

[12]   G. Sarıkaya, B. C. Makkak, "The Usage of Industrial Filter Press Waste in Glazed Porcelain Tile (article in Turkish with an abstract in English)", *Journal of the Turkish Ceramics Society,* in press, 2024.

[13]   Ceramic tiles- Part 3. Determination of water absorption, apparent porosity, apparent relative density, and bulk density, TS EN ISO 10545-3, 2018.

[14]   M. Kuşçu, Ş. Yıldırımlar, "Investigation of Geological and Economical Properties of Clays Under Ilgın Coal Deposite (Ilgın, Konya) (article in Turkish with an abstract in English)", *Afyon Kocatepe University Journal of Sciences and Engineering*, vol. 16, pp. 368-383, 2016.

[15]   C. Zanelli, C. Iglesias, E. Dominguez, D. Gardini, M. Raimondo, G. Guarini, M. Dondi, "Mineralogical composition, and particle size distribution as a key to understand the technological properties of Ukrainian ball clays", *Applied Clay Science*, vol. 108, pp. 102-110, 2015.

[16]   H. Sazcı, "Seramikte Kullanılan Killerin Tanımı (proceeding in Turkish with an abstract in English)", In: 4th Industrial Raw Materials Symposium, İzmir, Turkey, pp. 28-42, 18-19 October 2001.

[17]   T. Yeşilkaya, "Improvement of Pyroplastic Behavior and Semi-Finished Strength In Ceramic Sanitary Ware (dissertation in Turkish with an abstract in English)", MSc, Zonguldak Bülent Ecevit University, Zonguldak, Turkey, 2019.

[18]   W. D. Kingery, H. K. Bowen, D. R. Uhlmann, "Introduction to Ceramics", 2nd ed. New York, NY, USA: Wiley, 1976.

[19]   C. Zanelli, M. Raimondo, G. Guarini, M. Dondi, "The vitreous phase of porcelain stoneware: Composition, evolution during sintering and physical properties", *Journal of Non-Crystalline Solids,* vol. 357, pp. 3251-3260, 2011.

[20]   C. J. McConville, W. E. Lee, "Microstructural Development on Firing Illite and Smectite Clays Compared with that in Kaolinite", *Journal of the American Ceramic Society*, vol. 88, pp. 2267–2276, 2005.

[21]   A. Fluegel, "Glass viscosity calculation based on a global statistical modelling approach", *Glass Technology - European Journal of Glass Science and Technology Part A,* vol. 48, pp. 13–30, 2007.

[22]   T. Aydın, O. Bican, R. Gümrük, "Investigation of wear resistance of the porcelain tile bodies by solid particle impingement using alumina particles", *Journal of the Australian Ceramic Society*, vol. 56, pp. 525-531, 2020.

[23]   Ö. Cengiz, A. Kara, "Effect of alkaline-earth oxides on firing behaviour of monoporosa wall tile bodies", *Journal of Ceramic Processing Research*, vol. 19, pp. 189-197, 2018.

EXPLORING MIL-53 (Al) ADSORPTION EFFICIENCY FOR INDIGO CARMINE DYE

1, * Duygu YANARDAĞ KOLA (ID) **, 2 Serpil EDEBALİ** (ID)

Konya Technical University, Engineering and Natural Sciences Faculty, Chemical Engineering Department,
Konya, TÜRKİYE
1 dyanardag@ktun.edu.tr, 2 sedebali@ktun.edu.tr

Highlights

- This study focuses on addressing the environmental issue by utilizing MIL-53 (Al) as an adsorbent for removing indigo carmine dye, particularly from textile industries.

- MIL-53 (Al) was synthesized through the hydrothermal method, and different conditions were explored to optimize its effectiveness as an adsorbent for indigo carmine.

- The adsorption study revealed that the Langmuir isotherm model and pseudo-second-order kinetic model provided the best fit to the data.

- The highest adsorption capacity reached 145 mg/g, showcasing the efficiency of MIL-53 (Al) in removing indigo carmine.

*Corresponding Author: Duygu YANARDAĞ KOLA, dyanardag@ktun.edu.tr

EXPLORING MIL-53 (Al) ADSORPTION EFFICIENCY FOR INDIGO CARMINE DYE

1, * Duygu YANARDAĞ KOLA , **2 Serpil EDEBALİ**

Konya Technical University, Engineering and Natural Sciences Faculty, Chemical Engineering Department, Konya, TÜRKİYE

1 dyanardag@ktun.edu.tr, 2 sedebali@ktun.edu.tr

ABSTRACT: Synthetic dyes are extensively used in industrial areas, including plastic, textile, and food. However, they are a major environmental problem due to their negative effects on water quality and living organisms. To address one of these problems, MIL-53 (Al) is served as an adsorbent for removing indigo carmine dye, being widely used in textile industries. The synthesis of MIL-53 (Al) was carried through the hydrothermal method and different synthesis conditions were studied to find the best adsorbent to remove indigo carmine. FTIR, XRD, SEM, and EDS were used to assess materials. Isotherm models and kinetic models were investigated for indigo carmine adsorption, revealing that the Langmuir isotherm model and pseudo-second-order kinetic model provided best fit to data. The highest adsorption capacity was calculated as 145 mg/g. The study contributes valuable insights into the adsorption of indigo carmine by MIL-53 (Al).

Keywords: Adsorption, Indigo Carmine, Isotherms, Metal Organic Frameworks, MIL-53

1. INTRODUCTION

Wastewater containing various pollutants is a significant issue today, particularly with the rising population density and the corresponding increase in water consumption rates. As water demand becomes a growing threat daily, it is crucial to transition towards the efficient use of water through wastewater treatment. Industrial waste encompasses numerous pollutants, such as heavy metals, antibiotics, organic chemicals, and dyes. One of the biggest environmental challenges is purification wastewater from dyes, which is growing concern in the textile, food, and leather industries [1].

Metal-organic frames (MOFs) represent a category of porous materials that have garnered a great interest owing to their substantial surface area, adjustable chemical functionality, and structural diversity [2, 3]. In the last three decades, researchers have used MOFs across various applications, such as separation, storage, catalysis, drug delivery, and purification [4]. The suitable properties of MOFs make them well-suited for addressing environmental challenges, particularly in the treatment of organic matter from wastewater.

Indigo Carmine (I.C.), a synthetic dye, is commonly used in dyeing processes especially for silk, wool, and protein fibers [5]. Like many other synthetic dyes, I.C. has adverse impacts on the environment and life forms [6]. The uncontrolled release of I.C. into the environment decreases the quality of water, damages aquatic life and causes permanent damage to human health. Treatment of wastewater is essential before releasing it into nature. In literature, there are different treatment methods for removing I.C. dye, including photocatalytic degradation [7], electrocoagulation [8], membrane filtration [9], and adsorption [10, 11]. Among these methods, adsorption has been worked more since it has many advantages such as easy processing, high efficiency, easy handling, and environmentally friendliness [12]. The selection of an adsorbent is the most important point of the adsorption process due to achieving high removal capacity.

MIL-53 (Al) is a metal organic framework that consist of aluminium metal connected by benzene-1,4-dicarboxylate linkers [13]. MIL-53 (Al) possesses a specific breathing effect, as well as water and thermal stability, making it a suitable for use as an adsorbent [14]. It has been examined for removing specific dyes

---

*Corresponding Author: Duygu YANARDAĞ KOLA, dyanardag@ktun.edu.tr

from wastewater. Adsorption of dye by utilizing MOFs is an increasing trend and many researchers have been examined different MOFs to remove various dyes [15-17].

This study aims to examine the indigo carmine adsorption by using MIL-53 (Al), providing valuable information on potential of MOFs as an adsorbent for obtaining clean water. FTIR, XRD, SEM, and EDS were used to characterize MIL-53 (Al). the effects of different synthesis conditions of MIL-53 (Al) on adsorption capacity were studied. Moreover, the typical adsorption parameters such as the effect of adsorbent amount, the effect of initial dye concentrations, the effect of time, and the effect of temperature were examined. Different isotherm and kinetic adsorption models were employed to understand adsorption behavior of indigo carmine dye by MIL-53 (Al).

2. MATERIALS AND METHOD

2.1. Chemicals

Aluminium nitrate nanohydrate (Sigma-Aldrich), 1,4-benzenedicarboxylic acid (Merck), N,N-dimethylformamide (Merck) and methanol (Merck) were used for the MIL-53 (Al) synthesis. Hydrochloric acid (Sigma-Aldrich) and sodium hydroxide (Sigma-Aldrich) were used to arrange the pH of the solutions. Indigo carmine ($C_{16}H_8N_2Na_2O_8S_2$, Sigma-Aldrich) was utilized as a dye.

2.2. MIL-53 (Al) Synthesis

Solvothermal method was used synthesis MIL-53 (Al). Firstly, 0.0023 mol $Al(NO_3)_3\cdot9H_2O$ and 0.0023 mol 1,4-benzenedicarboxylic acid was dissolved in 45 ml DMF solvent at separate beakers for 15 minutes. After that solutions were mixed for 15 minutes. Solution was added to stainless steel Teflon autoclave and kept at 120 °C for 24 hours [18, 19]. Then, the resulting white solution were centrifuged and washed with DMF and methanol. Lastly, obtained material was dried at 60 °C overnight. Further syntheses were conducted with different metal:organic ligand:solvent ratios (1:1:84.6, 1:1:169.2, 1:1:253.8, and 1:1:338.4), temperatures (120, 150, and 220 °C), and times (24h, 48h, and 72h).

2.3. Characterization

X-ray diffraction (XRD) analysis was carried out GNR EUROPE 600. Fourier transform infrared (FTIR) analysis was obtained from Thermo Scientific Nicolet iS20 spectrometer. Scanning electron microscopy (SEM) images and Energy dispersive spectrometer (EDS) results were acquired with SM Zeiss LS10.

3. RESULTS AND DISCUSSION

3.1. Synthesis conditions

To see the effect of solvent amount on the synthesized MIL-53 (Al) structure and adsorption capacity, the synthesis was carried out using different ratios of methanol. The molar ratios of metal, organic ligand and methanol were determined as 1:1:84.6, 1:1:169.2, 1:1:253.8, 1:1:338.4. Indigo carmine removal was carried out using MIL-53 (Al) obtained from these syntheses. It was aimed to determine the synthesis conditions for MIL-53 (Al) that show the best adsorption rate. Adsorption experiments were executed a 0.5 g/L adsorbent amount and a 50 mg/L indigo carmine dye solution. The highest adsorption efficiency of 94.6% was acquired with MIL-53(Al) at a molar ratio of 1:1:253.8 (Table 1). Therefore, the next parameter studies will be carried out using this ratio.

Table 1. The adsorption results of MIL-53 (Al) for indigo carmine dye at various solvent amounts

Molar ratio of Al(III)/BDC/metanol	1:1:84.6	1:1:169.2	1:1:253.8	1:1:338.4
% Adsorption	57	85.6	94.6	93.9
q_t (mg/g)	56	84	93.4	92

After investigating the solvent effect, the temperature effect was investigated for the synthesis of MIL-53 (Al). For this purpose, the experiments were performed at temperatures of 120, 150, and 220 °C. The indigo carmine removal efficiencies and adsorption capacities of MIL-53 (Al) that obtained from these experimental conditions are given in Table 2. According to these results, the highest efficiency of 88.7% was obtained with MIL-53 (Al) synthesized at 120 °C. Therefore, the temperature value will be 120 °C in the next steps.

Table 2. The adsorption results of MIL-53 (Al) for indigo carmine dye at various temperatures

Temperature (°C)	120	150	220
% Adsorption	88.7	75.1	48.9
q_t (mg/g)	76.7	61.5	44

Finally, the effect of synthesis time on the structure and adsorption capacity of MIL-53 (Al) was investigated. 24 h, 48 h, and 72 h were selected for synthesis. The highest adsorption capacity was obtained with MIL-53 (Al) synthesized in 24 h, achieving 93% removal (Table 3). When comparing results of all parameters in terms of yields, the experimental conditions were determined as follows; metal, ligand and solvent ratio of 1:1:253.8, temperature of 120 °C as and synthesis time of 24 h.

Table 3. The adsorption results of MIL-53 (Al) for indigo carmine dye at various synthesis times

Time (hours)	24	48	72
% Adsorption	93.0	88.8	92.6
q_t (mg/g)	86.0	79.1	84.0

3.2. Characterization of MOFs

To understand effect of synthesis conditions on material structure, XRD analysis was used. XRD patterns of MIL-53 (Al) samples obtained by manipulating different metal-to-organic ligand ratios, solvent amounts, and reaction times are presented in Figures 1.a, 1.b, and 1.c. All XRD results of MIL-53 (Al) samples show characteristic peaks at 2θ = 9.6, 10.2, 15.8, and 19.0 with diffraction (101), (200), (011), and (211), respectively [20-22]. As seen from the XRD results, the obtained MIL-53 (Al) samples have sharp intensity and show high crystallinity. However, some samples have lower intensity compared to others, this is due to the lower crystallinity of the samples. The MIL-53 (Al) structure obtained from the synthesis at 150° shows less crystallinity compared to other conditions (Figure 1).

Figure 2. shows FTIR results for MIL-53 (Al) before and after indigo carmine adsorption. The FTIR spectrum of MIL-53 (Al) did not change significantly after adsorption (Figure 2). The strong absorption band at 1603 cm^{-1} is attributed to C=C stretching band in the aromatic group [20]. The peak at 1676 cm^{-1} is ascribed to the stretching vibration of C=O group in terephthalic acid molecules, which are stucked within the pores of MOFs [23]. This peak shifted to 1690 cm^{-1} after indigo carmine adsorption, likely due to interactions between MIL-53 (Al) and indigo carmine dye. The broad peak appeared at 3400 cm^{-1} is belong to the O-H stretching vibration [20], while the peak at 590 cm^{-1} is ascribed to the Al-O group [23], indicating its presence in MIL-53 (Al). Indigo carmine contains C-N bond in its structure and its peak occurs in the

1350-1000 cm^{-1} range. As seen in the FTIR graph, it is thought to form a broad peak around 1320 after adsorption, overlapping with the adjacent peak due to the C-N peak.

SEM images of MIL-53 (Al) for before indigo carmine adsorption (a,c) and after indigo carmine adsorption (b,d) at various magnifications are showed in Figure 3. As depicted in Figure 3, no significant differences were observed between surfaces of MIL-53 (Al) before and after indigo carmine adsorption. The surface of MIL-53 (Al) appears smoother compared to neat MIL-53 (Al) (Figure 3.d). This may be associated to the adsorption of indigo carmine on the surfaces of MIL-53 (Al).
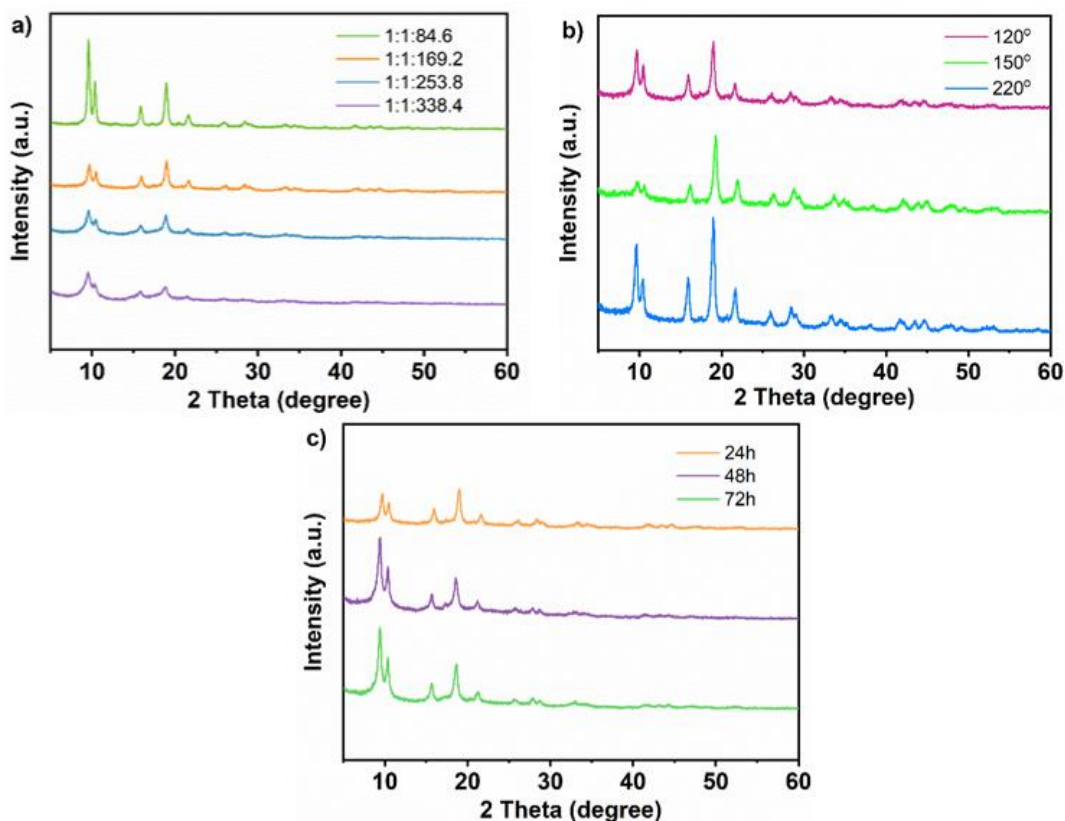
Figure 1. XRD patterns of the MIL-53 (Al) at various solvent amounts (a), temperatures (b), and times (c)
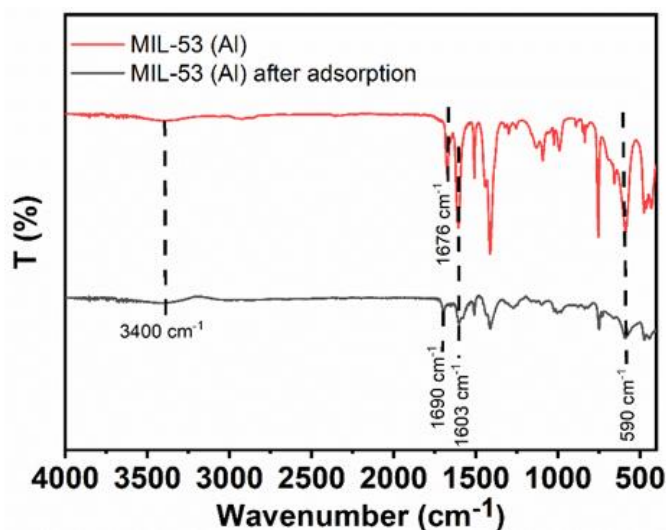
Figure 2. FTIR spectra of MIL-53 (Al).
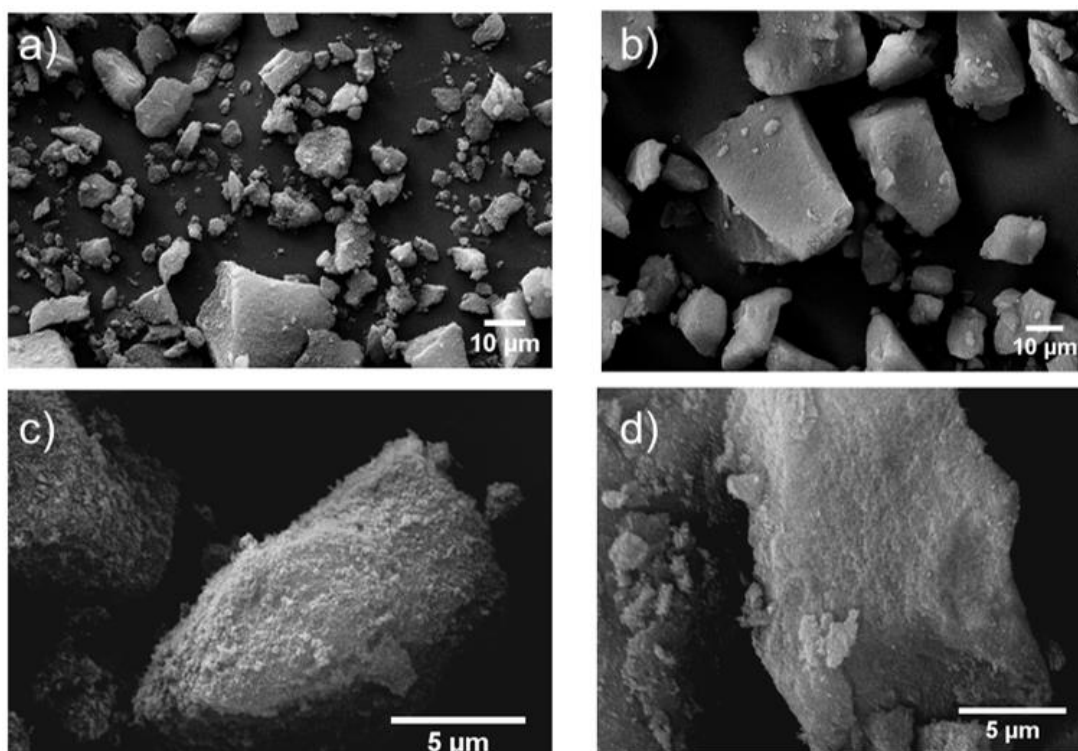
Figure 3. Morphological structure of the MIL-53 (Al) before I.C adsorption (a,c) and after I.C adsorption (b,d).
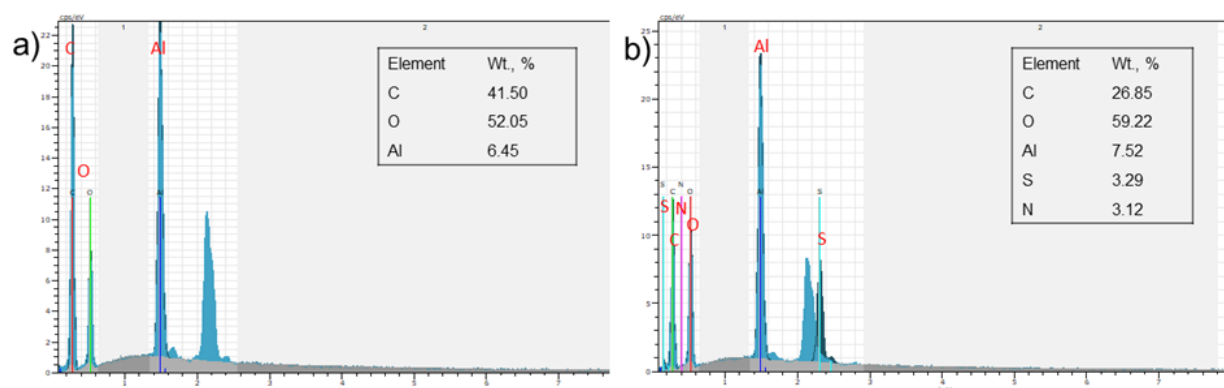
Figure 4. EDS spectrum of the MIL-53 (Al) before I.C adsorption (a) and after I.C adsorption (b).

EDS spectrum of the MIL-53 (Al) before (a) and after (b) indigo carmine adsorption is indicated in Figure 4. As expected, carbon, oxygen, and aluminum peaks (Fig. 4a) were observed at neat MIL-53 (Al). After indigo carmine adsorption, in addition to these peaks, sulfur and nitrogen peaks (Fig. 4b). were also observed since indigo carmine dye includes these elements in its structure. This result clearly shows that indigo carmine dye is adsorbed by MIL-53 (Al).

3.3. Batch adsorption studies

Indigo carmine adsorption by MIL-53 (Al) as adsorbent were conducted with batch studies. Removal percentage of indigo carmine (R, %) and adsorption capacity (q_e, mg g^{-1}) were specified with Equations (1) and (2), respectively.

$$R = \frac{C_0 - C_e}{C_0} \, x \, 100 \tag{1}$$

$$q_e = \frac{(C_0 - C_e) \, x \, V}{m} \, x \, 100 \tag{2}$$

Langmuir isotherm (Equation 3) and Freundlich isotherm equations (Equation 4) are as shown below. In this equations, q_m (mg g^{-1}), K_L (L mg^{-1}), K_F (mg g^{-1}), and n (L mg^{-1}) represent maximum adsorption capacity, Langmuir isotherm constant, Freundlich isotherm constant related to adsorption capacity, and Freundlich isotherm constant associated with adsorption intensity, respectively.

$$\frac{C_e}{q_e} = \frac{C_e}{q_m} + \frac{1}{K_L q_m} \tag{3}$$

$$\log q_e = \log K_F + \frac{1}{n} \log C_e \tag{4}$$

Pseudo-first-order (Equation 5) and pseudo-second-order (Equation 6) models were used to examine indigo carmine adsorption kinetics. In these models, q_t (mg g-1) represents adsorption capacity at time t (min). k_1 (min-1) and k_2 (g mg-1 min-1) are pseudo-first-order and pseudo-second-order rate constants, respectively.

$$\log(q_e - q_t) = \log q_e - \frac{k_1}{2.303} t \tag{5}$$

$$\frac{t}{q_t} = \frac{1}{k_2 \, q_e{}^2} + \frac{t}{q_e} \tag{6}$$

Various factors affect the adsorption process, and pH effect is being one of the most crucial ones. In order to find the optimum pH value for indigo carmine removal with MIL-53 (Al), several studies were conducted from pH 2 to 10. The acidity of the dye solutions for pH studies were set up with 0.1 M HCl and NaOH. In these experimental studies, a 50 mg/L, 10 mL I.C dye solution was used for the optimum dosage of adsorbent.

The percentage of I.C adsorption with MIL-53(Al) varied between pH 2 and 10 (Figure 5.a). The pH optimum adsorption efficiency was acquired at pH 3.2, and the adsorption efficiency decreased after this point. In the adsorption process, the pH value of the medium changes the surface charges, providing better information about adsorption. The point of zero charge (pHpzc) value of adsorbent is also studied and given in Figure 5.b. As depicted in the figure, the pHpzc value for MIL-53 (Al) was calculated as 4.1. If the pH of the medium is below 4.1, the net adsorbent charge is positive, while above it is negative [24]. In this case, at the optimum pH value (pH=3.2) the adsorbent charge is positive. Indigo carmine is an anionic dye, and the best adsorption efficiency is achieved at the pH where the adsorbent surface charge is positive. This suggest that effective mechanism can be electrostatic attraction at this point [25]. The reason for decrease in adsorption percentage after after pH 4 can be attributed to surface charges. The adsorbent surface are becomes negatively charged above pHpzc which is 4.1. Since dye is anionic surface interaction between dye and adsorbent are repulsive above pH 4.1 [26].
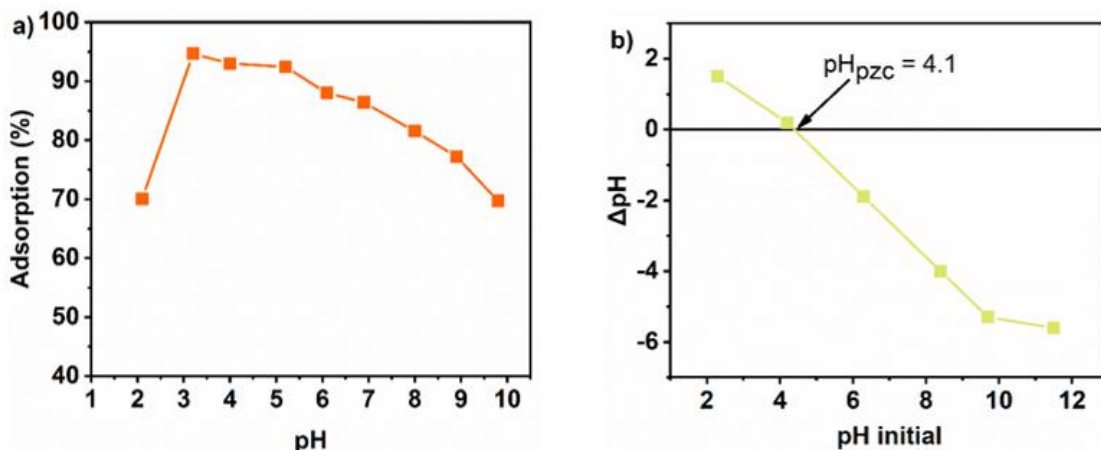
Figure 3. pH effect on the indigo carmine adsorption (a), and pHpzc of the MIL-53 (Al).
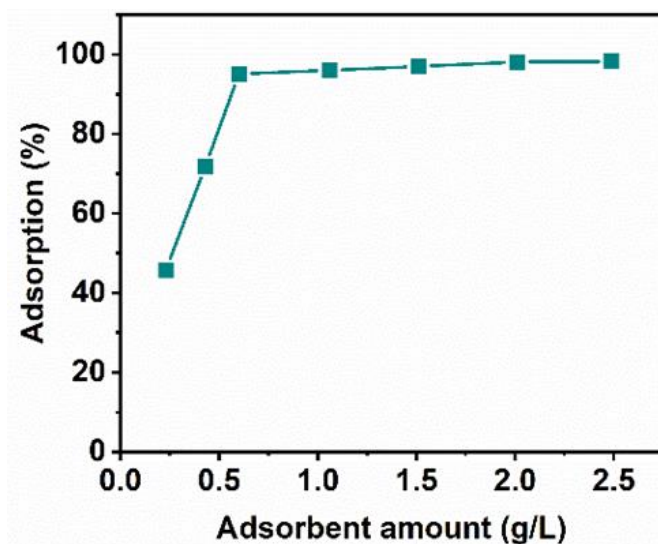
Figure 6. MIL-53 (Al) amount effect on I.C adsorption.

In the study to find the optimum adsorbent amount, experiments were performed with various adsorbent amounts between 0.2 and 2.5 g/L. In the experiments, a 50 mg/L, 10 mL I.C. dye solution was used and carried out at room temperature. The adsorption efficiency increased up to a 0.6 g/L adsorbent dosage and remained constant after this value (Figure 6). The adsorption efficiency increases until the adsorbent amount reaches 0.6 g/L because the adsorbent amount increases the surface area (active sites). However, the adsorption efficiency remains constant after this value since all I.C dye molecules in the medium adsorbed by MIL-53 (Al).

The effect of contact time for I.C dye removal with MIL-53 (Al) was also examined and displayed in Figure 7a. This study was operated at room temperature, employing a 50 mg/L dye solution and an optimum adsorbent amount. As seen in the figure, adsorption efficiency increased up to 120 minutes, and it remained constant after this point. With this study, the optimum contact time was determined as 120 minutes.
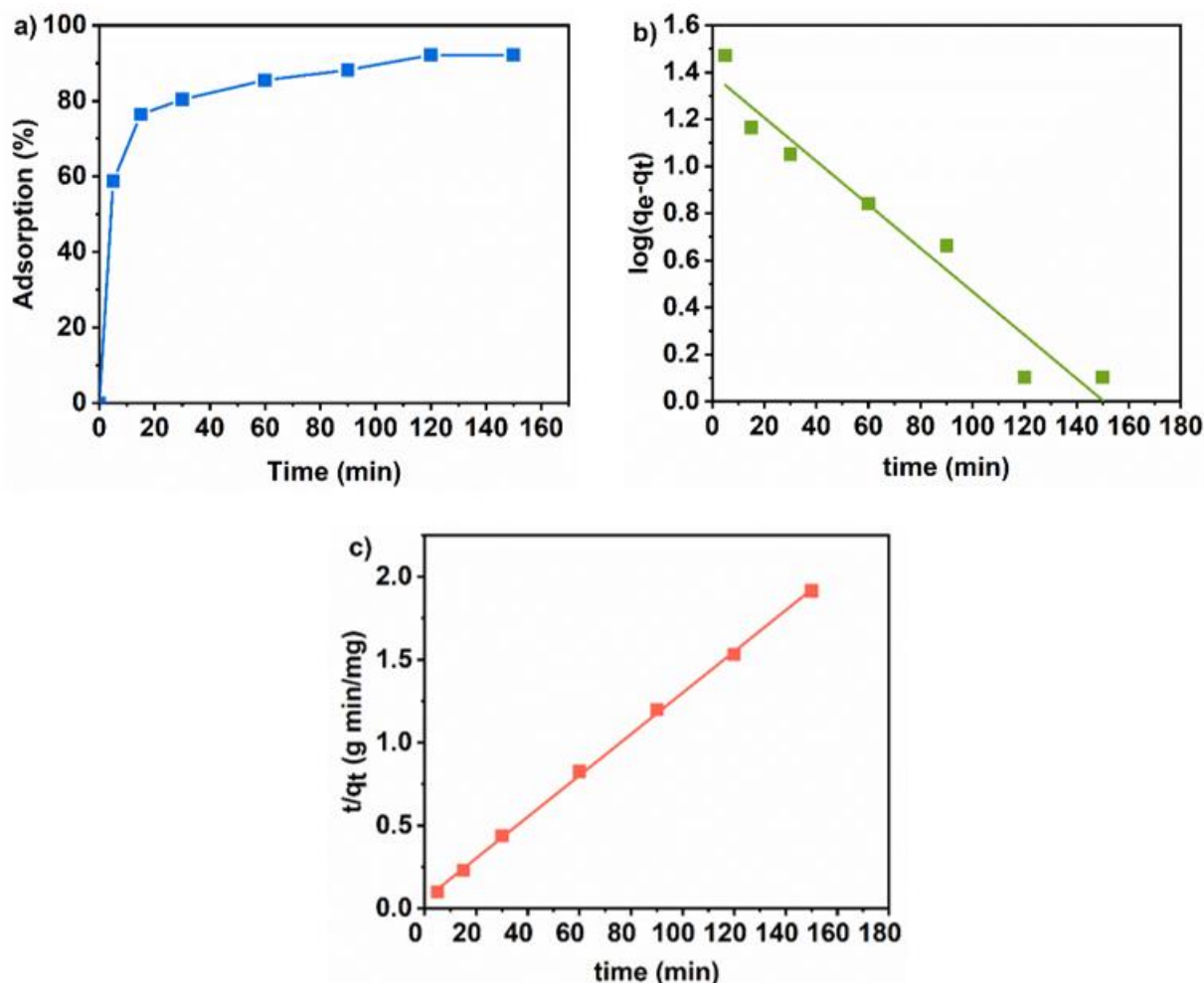
Figure 7. Contact time effect on I.C adsorption (a), pseudo-first-order kinetic (b), and pseudo-second-order kinetic (c) models for I.C adsorption.

The indigo carmine dye adsorption kinetics were examined using both the pseudo-first-order and pseudo-second-order kinetic models [27] (Figure 7b-c). The parameters for these kinetic models for indigo carmine are given in Table 4. The pseudo-second order kinetic model exhibits a superior correlation coefficient (R^2 = 0.999) in comparison to the pseudo-first order kinetic model (R^2 = 0.932). Thus, the pseudo-second order kinetic model better fits the adsorption data of this work. The assumption of pseudo-second order kinetic model is that rate-limiting step in the process is chemical adsorption [28].

The effect of initial dye concentration is also studied. Different dye solutions varying between 25 and 200 mg/L were used in the study. The studies were performed at the optimum amount of adsorbent at room temperature. The indigo carmine adsorption capacity of MIL-53 (Al) increased with increasing indigo carmine dye concentration (Figure 8.a). The concentration increase provides more chances for the dye molecules to interact with adsorbent. Furthermore, these higher interactions increased adsorption capacity of MIL-53 (Al).

Table 4 displays the capacity of adsorption for the adsorption of indigo carmine dye on various adsorbents. The literature has several research on the adsorption of I.C dye on various adsorbents, and MIL-53 (Al) has a comparatively high adsorption capacity.
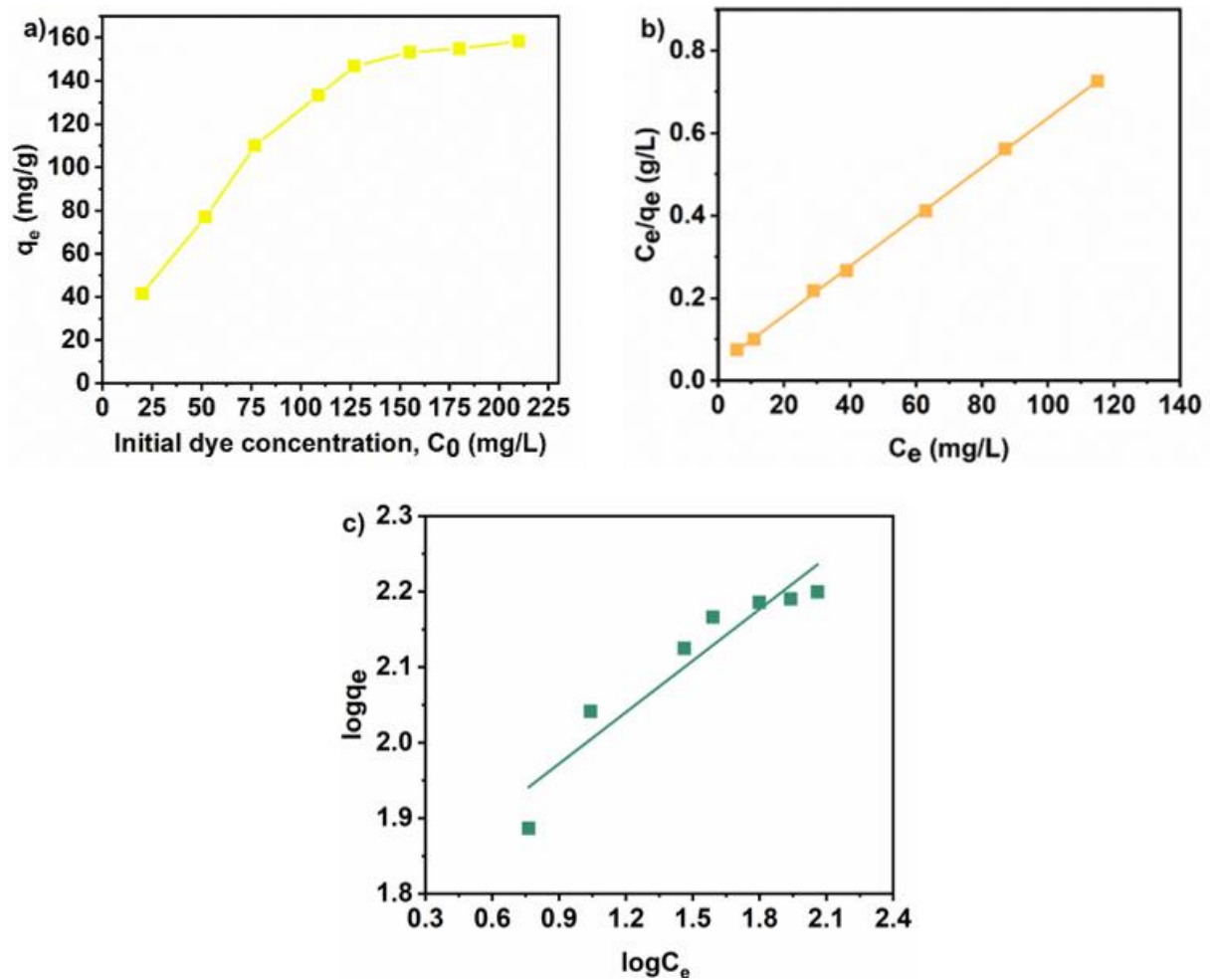
Figure 8. Initial I.C dye concentration effect on adsorption capacity (a), Langmuir (b), and Freundlich (c) isotherm models for I.C adsorption.

Table 4. Comparison of indigo carmine dye adsorption by different adsorbents

No.	Adsorbents	Adsorption capacity (mg/g)	Ref.
1	Activated carbon	79.49	[5]
2	Water treatment residuals (WTR)	30.86	[6]
3	Moringa oleifera seeds	60.0	[10]
4	Chitosan-FAS composite	76.64	[29]
5	Acacia nilotica sawdust activated carbon	24.67	[11]
6	UiO-66	87.2	[30]
7	Maize cob carbon (MCC)	118.48	[31]
8	Pistia stratiotes biosorbent	41.2	[32]
9	Terminalia catappa	106.98	[33]
10	MIL-53 (Al)	156	This work

Table 5. The kinetic models and isotherm models parameters for I.C adsorption.

Models	Parameter	MIL-53 (Al)
Pseudo-first order kinetic	q_e (mg g^{-1})	24.6
	R^2	0.951
	k_1 (min^{-1})	0.021
Pseudo-second order kinetic	q_e (mg g^{-1})	80
	R^2	0.999
	k_2 (g mg^{-1} min^{-1})	0.0028
Langmuir isotherm	q_m (mg g^{-1})	156
	K_L (L mg^{-1})	4156
	R^2	1
Freundlich isotherm	K_F (mg g^{-1})	58.5
	n (L mg^{-1})	4.41
	R^2	0.897

Isotherm mechanism for indigo carmine adsorption by MIL-53 (Al) were investigated, utilizing Langmuir and Freundlich isotherm models (Figure 8.b and 8.c). Moreover, adsorption isotherms parameters are presented in Table 5. High correlation coefficient (R^2) value of Langmuir isotherm model ($R^2 = 1$) was shown that this isotherm model was more suitable compared to Freundlich isotherm model. According to Langmuir isotherm model, every point on the adsorbent surface exhibits equivalent adsorption. Furthermore, monolayer, and homogeneous adsorption is observed if data fit to Langmuir isotherm model [34]. The maximum adsorption capacity of MIL-53 (Al) was calculated as 156 mg/g.

4. CONCLUSION

In conclusion, this study demonstrated the effective removal of indigo carmine synthetic dye from water through utilization of MIL-53 (Al). As a result of the adsorption studies, the optimum removal parameters were determined and they are pH: 3.2, adsorbent amount: 0.6 g/L, time: 120 min. In kinetic and isothermal studies, it was observed that the experimental data conformed well to the Langmuir isotherm model ($R^2 = 1$) and pseudo-second-order kinetic model ($R^2 = 0.999$), both of which gave a high correlation value. The Langmuir isotherm indicates equal and equivalent adsorption in all regions. The pseudo second-order kinetic model shows the adsorbate binds rapidly to a specified number of adsorption sites on a surface. The maximum adsorption capacity was determined as 156 mg/g. Detailed characterizations and systematic adsorption studies and removal studies of indigo carmine dye using MIL-53 (Al) will contribute to further studies in this field.

Declaration of Ethical Standards

Authors declare to comply with all ethical guidelines including authorship, citation, data reporting, and publishing original research.

Credit Authorship Contribution Statement

D. YANARDAĞ KOLA: Conceptualization, Methodology, Investigation, Writing - Original Draft

S. EDEBALİ: Investigation, Resources, Writing - Review & Editing, Supervision, Project administration, Funding acquisition

Declaration of Competing Interest

The authors declared that they have no conflict of interest.

Funding / Acknowledgements

Data Availability

Data will be made available on request.

REFERENCES

[1]   K. Sharma, A. K. Dalai, and R. K. Vyas, "Removal of synthetic dyes from multicomponent industrial wastewaters," Reviews in Chemical Engineering, vol. 34, no. 1, pp. 107-134, 2017.

[2]   L. Jiao, J. Y. R. Seow, W. S. Skinner, Z. U. Wang, and H.-L. Jiang, "Metal–organic frameworks: Structures and functional applications," Materials Today, vol. 27, pp. 43-68, 2019.

[3]   M. Ding, R. W. Flaig, H.-L. Jiang, and O. M. Yaghi, "Carbon capture and conversion using metal–organic frameworks and MOF-based materials," Chemical Society Reviews, vol. 48, no. 10, pp. 2783-2828, 2019.

[4]   P. Kumar, K. Vellingiri, K.-H. Kim, R. J. Brown, and M. J. Manos, "Modern progress in metal-organic frameworks and their composites for diverse applications," Microporous and Mesoporous Materials, vol. 253, pp. 251-265, 2017.

[5]   Z. Harrache, M. Abbas, T. Aksil, and M. Trari, "Thermodynamic and kinetics studies on adsorption of Indigo Carmine from aqueous solution by activated carbon," Microchemical Journal, vol. 144, pp. 180-189, 2019.

[6]   M. El-Kammah, E. Elkhatib, S. Gouveia, C. Cameselle, and E. Aboukila, "Cost-effective ecofriendly nanoparticles for rapid and efficient indigo carmine dye removal from wastewater: Adsorption equilibrium, kinetics and mechanism," Environmental Technology & Innovation, vol. 28, p. 102595, 2022.

[7]   N. AbouSeada, M. Ahmed, and M. G. Elmahgary, "Synthesis and characterization of novel magnetic nanoparticles for photocatalytic degradation of indigo carmine dye," Materials Science for Energy Technologies, vol. 5, pp. 116-124, 2022.

[8]   M. Oliveira, L. F. Garcia, A. Siqueira, V. Somerset, and E. Gil, "Electrocoagulation of the indigo carmine dye using electrodes produced from the compression of metallurgical filing wastes," International Journal of Environmental Science and Technology, vol. 17, pp. 1657-1662, 2020.

[9]   S. Gopi, P. Balakrishnan, A. Pius, and S. Thomas, "Chitin nanowhisker (ChNW)-functionalized electrospun PVDF membrane for enhanced removal of Indigo carmine," Carbohydrate polymers, vol. 165, pp. 115-122, 2017.

[10]   M. El-Kammah, E. Elkhatib, S. Gouveia, C. Cameselle, and E. Aboukila, "Enhanced removal of Indigo Carmine dye from textile effluent using green cost-efficient nanomaterial: Adsorption, kinetics, thermodynamics and mechanisms," Sustainable Chemistry and Pharmacy, vol. 29, p. 100753, 2022.

[11]   T. Gupta et al., "Adsorption of Indigo Carmine Dye by Acacia nilotica sawdust activated carbon in fixed bed column," Scientific Reports, vol. 12, no. 1, p. 15522, 2022.

[12]   R. Rashid, I. Shafiq, P. Akhter, M. J. Iqbal, and M. Hussain, "A state-of-the-art review on wastewater treatment techniques: the effectiveness of adsorption method," Environmental Science and Pollution Research, vol. 28, pp. 9050-9066, 2021.

[13]   L. Xie, K.-Y. Chan, and V. C.-Y. Li, "Molecular dynamics simulation of hydration and free energy of ions in nanochannels of polyelectrolyte threaded metal organic framework and the impacts on selective ion transport," Journal of Molecular Liquids, vol. 367, p. 120553, 2022.

[14]   Y. Gao, R. Kang, J. Xia, G. Yu, and S. Deng, "Understanding the adsorption of sulfonamide

antibiotics on MIL-53s: Metal dependence of breathing effect and adsorptive performance in aqueous solution," Journal of colloid and interface science, vol. 535, pp. 159-168, 2019.

[15]   M. Al Sharabati and R. Sabouni, "Selective removal of dual dyes from aqueous solutions using a metal organic framework (MIL-53 (Al))," Polyhedron, vol. 190, p. 114762, 2020.

[16]   X. Ma et al., "Fabrication of stable MIL-53 (Al) for excellent removal of rhodamine B," Langmuir, vol. 38, no. 3, pp. 1158-1169, 2022.

[17]   X.-D. Du et al., "Extensive and selective adsorption of ZIF-67 towards organic dyes: Performance and mechanism," Journal of Colloid and Interface Science, vol. 506, pp. 437-441, 2017.

[18]   X. Cheng et al., "Size-and morphology-controlled NH 2-MIL-53 (Al) prepared in DMF–water mixed solvents," Dalton Transactions, vol. 42, no. 37, pp. 13698-13705, 2013.

[19]   L. Silvester et al., "Fine tuning of the physico-chemical properties of a MIL-53 (Al) type-Mesoporous alumina composite using a facile sacrificial-template synthesis approach," Microporous and Mesoporous Materials, vol. 306, p. 110443, 2020.

[20]   M. S. Rostami and M. M. Khodaei, "Effect of incorporated hybrid MIL-53 (Al) and MWCNT into PES membrane for CO2/CH4 and CO2/N2 separation," Fuel, vol. 356, p. 129598, 2024.

[21]   C. Li, Z. Xiong, J. Zhang, and C. Wu, "The strengthening role of the amino group in metal–organic framework MIL-53 (Al) for methylene blue and malachite green dye adsorption," Journal of Chemical & Engineering Data, vol. 60, no. 11, pp. 3414-3422, 2015.

[22]   F. Ahmadijokani, S. Ahmadipouya, H. Molavi, and M. Arjmand, "Amino-silane-grafted NH 2-MIL-53 (Al)/polyethersulfone mixed matrix membranes for CO 2/CH 4 separation," Dalton Transactions, vol. 48, no. 36, pp. 13555-13566, 2019.

[23]   W. W. Lestari et al., "Fabrication of hybrid membranes based on poly (ether-sulfone)/Materials Institute Lavoisier (MIL-53)(Al) and its enhanced CO2 gas separation performance," Chemical Papers, vol. 75, no. 12, pp. 6519-6530, 2021.

[24]   G. Guzel Kaya, E. Yilmaz, and H. Deveci, "A novel silica xerogel synthesized from volcanic tuff as an adsorbent for high-efficient removal of methylene blue: parameter optimization using Taguchi experimental design," Journal of Chemical Technology & Biotechnology, vol. 94, no. 8, pp. 2729-2737, 2019.

[25]   D. Yanardag, G. G. Kaya, and S. Edebali, "Ciprofloxacin adsorption performance of Co-doped UiO-66," Applied Organometallic Chemistry, p. e7311, 2023.

[26]   A. Stavrinou, C. Aggelopoulos, and C. Tsakiroglou, "Exploring the adsorption mechanisms of cationic and anionic dyes onto agricultural waste peels of banana, cucumber and potato: Adsorption kinetics and equilibrium isotherms as a tool," Journal of environmental chemical engineering, vol. 6, no. 6, pp. 6958-6970, 2018.

[27]   F. Çengel and F. Temel, "p-NİTRO FENOLÜN KALİKSAREN TEMELLİ GRAFEN OKSİT İLE SULU ÇÖZELTİLERDEN UZAKLAŞTIRILMASI," Konya Journal of Engineering Sciences, vol. 9, pp. 79-90, 2021.

[28]   P. S. Kumar, S. Ramalingam, S. D. Kirupha, A. Murugesan, T. Vidhyadevi, and S. Sivanesan, "Adsorption behavior of nickel (II) onto cashew nut shell: Equilibrium, thermodynamics, kinetics, mechanism and process design," Chemical Engineering Journal, vol. 167, no. 1, pp. 122-131, 2011.

[29]   S. Korde, S. Deshmukh, S. Tandekar, and R. Jugade, "Implementation of response surface methodology in physi-chemisorption of Indigo carmine dye using modified chitosan composite," Carbohydrate Polymer Technologies and Applications, vol. 2, p. 100081, 2021.

[30]   R. S. Salama, E.-S. M. El-Sayed, S. M. El-Bahy, and F. S. Awad, "Silver nanoparticles supported on UiO-66 (Zr): as an efficient and recyclable heterogeneous catalyst and efficient adsorbent for removal of Indigo Carmine," Colloids and Surfaces A: Physicochemical and Engineering Aspects, vol. 626, p. 127089, 2021.

[31]   J. Zhang, P. Zhang, S. Zhang, and Q. Zhou, "Comparative study on the adsorption of tartrazine and indigo carmine onto maize cob carbon," Separation Science and Technology, vol. 49, no. 6, pp. 877-886, 2014.

[32]   R. M. Ferreira, N. M. de Oliveira, L. L. Lima, A. L. D. Campista, and D. M. Stapelfeldt, "Adsorption of indigo carmine on Pistia stratiotes dry biomass chemically modified," Environmental Science and Pollution Research, vol. 26, pp. 28614-28621, 2019.

[33]   R. Zein, L. Hevira, Zilfa, Rahmayeni, S. Fauzia, and J. O. Ighalo, "The improvement of indigo carmine dye adsorption by Terminalia catappa shell modified with broiler egg white," Biomass Conversion and Biorefinery, vol. 13, no. 15, pp. 13795-13812, 2023.

[34]   O. Pezoti et al., "NaOH-activated carbon of high surface area produced from guava seeds as a high-efficiency adsorbent for amoxicillin removal: Kinetic, isotherm and thermodynamic studies," Chemical Engineering Journal, vol. 288, pp. 778-788, 2016.

EXAMINATION OF THE SEISMIC BEHAVIOR OF THE HISTORICAL YEŞILDERE BRIDGE

[1] Pınar USTA EVCİ ⁱᴰ , [2,*] Ali Ekber SEVER ⁱᴰ , [3] Elifnur ŞAKALAK ⁱᴰ, [4] Cemile ÜNVEREN ⁱᴰ

Isparta University of Applied Sciences, Technology Faculty, Civil Engineering Department, Isparta, TÜRKİYE
[1] pinarusta@isparta.edu.tr, [2] alisever@isparta.edu.tr, [3] elifnursakalak@isparta.edu.tr, [4]
unverencemile@gmail.com

Highlights

- Historical buildings serve as a link between the past and the present. Historical arch bridges, which are common in Turkey, have an important place as cultural heritage. In order to preserve these historical buildings, it is necessary to know their structural behavior

- In this study, the seismic behavior of a historical masonry arch bridge was investigated.

- The finite element model of the historical bridge was created in SAP2000 program

- Modal analysis was performed to obtain the natural periods and mode shapes of this bridge.

- Response spectrum and time history analyzes were performed to examine the seismic behavior of the bridge.

- Acceleration records of the Pazarcık and Elbistan earthquakes that occurred in Turkey on February 6, 2023 were used in time history analyses.

- The values of displacements and stresses obtained as a result of response spectrum and time history analyzes and the regions where they are concentrated were determined and evaluated.

*Corresponding Author: Ali Ekber SEVER, alisever@isparta.edu.tr

EXAMINATION OF THE SEISMIC BEHAVIOR OF THE HISTORICAL YEŞILDERE BRIDGE

[1] **Pınar USTA EVCİ** (ID) , [2, *] **Ali Ekber SEVER** (ID) , [3] **Elifnur ŞAKALAK** (ID) , [4] **Cemile ÜNVEREN** (ID)

Isparta University of Applied Sciences, Technology Faculty, Civil Engineering Department, Isparta, TÜRKİYE
[1] pinarusta@isparta.edu.tr, [2] alisever@isparta.edu.tr, [3] elifnursakalak@isparta.edu.tr, [4] unverencemile@gmail.com

ABSTRACT: Historical buildings serve as a connection between the present and the past. Historical arch bridges, which are widespread in Turkey, hold significant cultural value. To preserve these structures, it is essential to understand their structural behavior. This study discusses the seismic behavior of historical masonry arch bridges, focusing on the Yeşildere Bridge located in Yeşildere Village on the Ulaş-Kangal-Hekimhan highway route in Sivas province. The historical bridge was modelled using the finite element method (FEM) with SAP2000 software. Modal analysis, response spectrum analysis, and linear time history analysis were conducted on the model using earthquake ground motion levels defined in TBDY 2018. The acceleration records of the Elbistan Earthquake and Pazarcık Earthquake that occurred in Turkey on February 6, 2023 were used for the time history analysis. The results of the modal analysis provided the mode shapes and period values of the bridge. The stress and displacement values on the bridge and the regions where they reached the highest values were determined as a result of the time history and response spectrum analysis.

Keywords: Arch Bridge, Modal Analysis, Time History Analysis, Response Spectrum Analysis, Masonry

1. INTRODUCTION

Historic masonry arch bridges are an important aspect of cultural heritage. They are vulnerable to damage or destruction from earthquakes, wind, and traffic loads, particularly in areas with moderate to high seismic activity. Due to their weight and rigidity, they are particularly susceptible to significant earthquake forces. Therefore, it is essential to evaluate their seismic behavior to preserve their structural integrity.

Historical masonry arch bridges typically comprise arches, basic gusset filling, and wall materials. These historical structures are susceptible to damage or destruction from natural disasters, such as earthquakes and floods. Therefore, it is essential to assess the seismic performance of these bridges to ensure their structural integrity [1].

Numerous studies have been conducted in the literature on the dynamic response of masonry arch bridges. Karaton et al. [1] modeled the Malabadi Bridge using FEM in the ANSYS [2] computer software to examine the bridge's behavior under synthetic acceleration records produced for different earthquake levels. The researchers concluded that the bridge is at risk of collapsing during an earthquake with a probability of 2% over the next 50 years. Therefore, it is recommended that the bridge be reinforced to withstand seismic activity.

Brencich and Sabia [3] analysed the Tanaro Bridge, a masonry arch bridge. They conducted tests to obtain the bridge's mode shapes and natural periods, and used this data to construct an FEM model of the bridge. The model was analysed at different stages of the bridge's service life and demolition.

Özmen and Sayın [4] analysed the Dutpınar Bridge, a historical masonry arch bridge, using acceleration records from the Bingöl earthquake that occurred in 2003. The bridge was modelled using FEM, and the authors obtained the largest and smallest shear stresses and shape changes as a result of their analysis.

Özmen and Sayın [5] conducted a study to compare the influence of far and near fault lines on the seismic response of a masonry arch bridge. They analyzed the arch bridge, which they modeled with FEM,

Corresponding Author: Ali Ekber SEVER, alisever@isparta.edu.tr

using the acceleration records of different earthquakes. The study concluded that earthquakes occurring on distant fault lines are equally significant as those occurring on close fault lines.

Yılmaz et al. [6] examined the Murat Bey Bridge, a single-span historical masonry bridge. They created a three-dimensional FEM model of the bridge using the SAP2000 [7] program and analyzed it statically, modally, and through time history. The bridge was analyzed under different earthquake acceleration records. The study evaluated the stress and displacement values obtained.

In their study, Nemutlu et al. [8] examined the earthquake behavior of a historical masonry bridge. They performed a nonlinear analysis of the bridge using five different ground motion recordings. The analysis revealed that tensile cracks occurred in both the middle and heel area of the arch.

Gönen and Soyöz [9] analysed the seismic response of a masonry arch bridge using three different methods and compared them.

Altunışık et al. [10] analyzed the effect of arch thickness on the structural response of a historical masonry arch bridge under dead and moving loads. Their study revealed a correlation between arch thickness and structural behavior.

In their study, Güllü [11] analysed the dynamic behaviour of the Cendere bridge, a masonry arch bridge, using modal analysis and linear time history analysis. Time history analyses were performed using acceleration records from various earthquakes, while modal analysis was used to obtain the period values of the bridge. The study identified regions with the highest tensile stresses.

Sakcalı et al. [12] examined the Irgandı Bridge in Bursa using a FEM model. The bridge is a masonry arch bridge, and modal and linear analysis were performed under different earthquake acceleration records. The study found that the upper part of the arch bridge experienced the greatest displacements, while the support area experienced the largest shear stresses.

In their study, Milana and Lourenço [13] created models of two masonry arch bridges in 3D and analysed their non-linear behaviour.

Kumbasaroglu et al. [14] conducted a study to evaluate the seismic performance of a masonry arch bridge. The bridge was modeled using FEM and analyzed under its own weight and acceleration records of past earthquakes. The stress and displacement values obtained from the analysis were evaluated.

Harapin et al. [15] conducted a dynamic and static analysis of a masonry arch bridge. The study investigated the effects of vertical load, seismic activity, and temperature changes. The authors found that the deformation and crack regions obtained from the computer model were consistent with the real model.

Karalar and Yeşil [16] investigated the impact of arch altitude on the dynamic and static behavior of single-span masonry arch bridges. The study examined a bridge in Karabük under far and near fault ground motions. The results showed that the arch height of the bridge increased while the maximum movements decreased as a result of the far fault and near fault ground motions.

Özodabaş and Artan [17] examined the Muş Murat Bridge, which is a masonry arch bridge. They analyzed the bridge under traffic, flood and earthquake loads. To investigate the bridge's dynamic behaviour, modal and earthquake analyses were conducted in the frequency domain. The modal analysis yielded the bridge's period and mode shapes, while the earthquake load analysis evaluated the displacements and stresses experienced by the bridge.

Akin et al. [18] analysed the dynamic behaviour of the historic Tağar Bridge, a masonry bridge, using different damping rates. The bridge was modelled with FEM in the SAP 2000 software and its behaviour was analysed with earthquake acceleration records. The study evaluated the stresses and displacements obtained.

Laterza et al. [19] conducted a study on the seismic performance of an existing historical arch bridge. They created a finite element model of the multi-span bridge and performed a pushover analysis. The analysis showed that the bridge provided the displacement values required by the capacity spectrum method.

Oztürk et al. [20] modelled the historical Sultan Hamit I-II and III bridges in Erzurum using the SAP2000 program. They conducted static, modal, and dynamic analyses on the models, considering only their own weights. For dynamic analysis, they utilised the acceleration records of the 1992 Erzincan

Earthquake and the 2020 Elazig Earthquake. The results of the analysis showed that the maximum displacement occurred during the 1992 Erzincan Earthquake.

Saydan et al. [21] conducted a study on the behaviour of Mısırlıoğlu Bridge, a historical masonry arch bridge in Konya, under the effects of freezing and thawing. The mechanical properties of the building materials that make up the bridge were determined through experimental studies. Subsequently, a finite element model of the bridge was created using the ANSYS program. Modal analysis was conducted to investigate the impact of freeze-thaw cycles on the period and mode shapes of the bridge. The results showed an increase in the period values after the rotation-dissolution event.

This paper examines the seismic behavior of historical masonry arch bridges by discussing the Yeşildere Bridge. The bridge was modeled in the SAP2000 program and four different EGML defined in the Turkish Building Earthquake Code 2018 (TBDY 2018)[22] were applied. Response spectrum analysis was performed, and modal analysis was carried out to determine the mode shapes and period values of the historical bridge. To investigate the seismic behaviour of the historical masonry arch bridge, we conducted a linear time history analysis on the bridge model using the acceleration records of the Elbistan and Pazarcık earthquakes that occurred in Kahramanamaraş on February 6, 2023. The analysis yielded results for the structure's period, mode deformations, maximum stress and displacement values in both the x and y directions for each level of earthquake ground motion. Additionally, stress and displacement values obtained from the time history analysis were also obtained.

2. MATERIAL AND METHODS

This section discusses the historical Yeşildere Bridge, located within the borders of Yeşildere Village on the Ulaş-Kangal-Hekimhan highway route in Sivas province. The bridge is introduced and its modeling is explained. Additionally, information is provided about EGML and earthquake acceleration records to be used for dynamic analysis.

2.1. Yeşildere Bridge and its modeling in SAP2000 program

The Yeşildere Bridge, which will be analysed, is 26 metres long and 3 metres wide. It features an arch pier in the middle, fixed with inlays on the sides. The bridge has two wide arches with a span of 7 metres. The distance from the keystone to the ground is 3.5 metres. Please refer to Figure 1 for the location and appearance of the bridge.

Figure 1. Location and appearance of Yeşildere Bridge

Figure 2 presents the geometric characteristics of the building, which were determined through interviews and measurements conducted with the 16th Regional Directorate of Highways [23] to assess the bridge's earthquake performance.
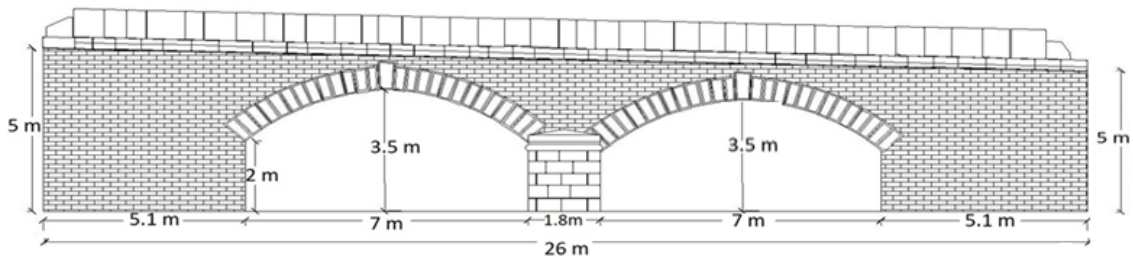
Figure 2. Geometric features of Yeşildere Bridge

Three separate methods are commonly used for numerical modeling of masonry structures: simplified micro-modeling, detailed micro-modeling, and macro-modeling. The choice of method depends on the size and accuracy level of the structural system [24]. In detailed micro-modeling, the material properties of the masonry units and the mortar are evaluated separately. Simplified micro-modeling expands the masonry units by half of the mortar layer, neglecting the mortar and separating the units from each other by interface lines. On the other hand, macro modeling considers masonry as a composite material without distinguishing between the unit and mortar. The macro modeling method is commonly used to examine large building systems due to its significantly shorter solution time. This method neglects the relationship between the mortar and the masonry unit. The material is considered a composite [25]. Figure 3 demonstrates the modeling methods used. This study employed the macro modeling method.
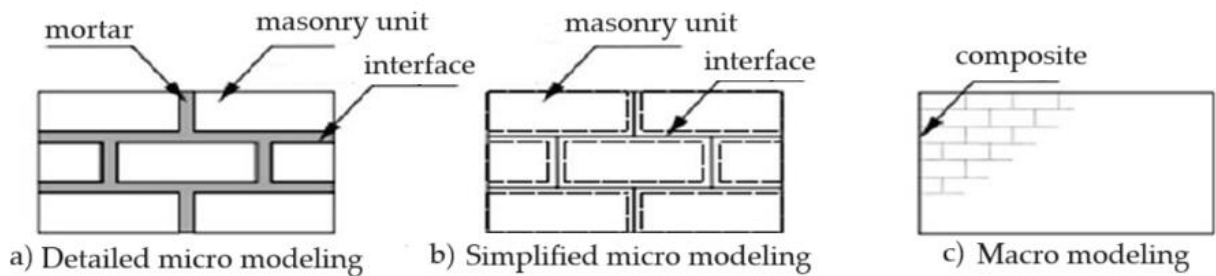
Figure 3. Modeling methods for masonry structures [24]

The Yeşildere Bridge was modelled using solid elements in the SAP2000 computer program. Response spectrum analysis, modal analysis, and linear time history analysis were conducted. Solid elements are eight-node objects used to model three-dimensional structural systems. In the solid element, S11 indicates the stress in the x direction, while S22 defines the stress in the y direction [7]. Figure 4 shows the axes, stresses, and solid element defined in the solid element.
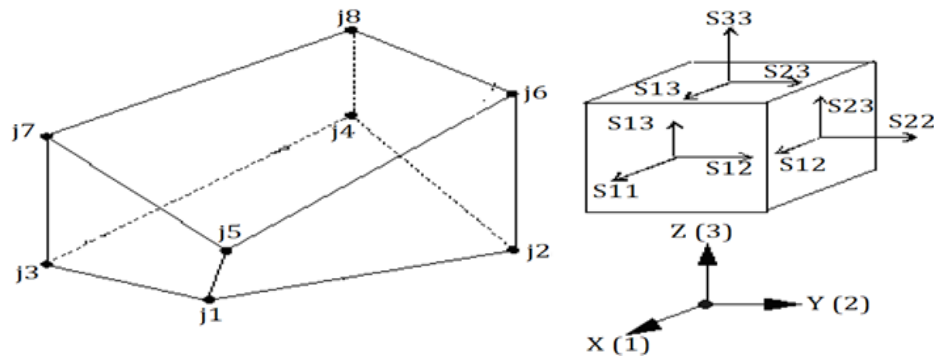
Figure 4. Solid member and stresses in solid member [7]

The Yeşildere Bridge comprises a load-bearing arch, filling material, and spandrel walls. Material properties are crucial in analysing structural behaviour. The properties of the materials used in this study

were obtained from similar studies in the literature and are listed in Table 1.   Figure 5 displays the SAP2000 model of the Yeşildere Bridge.

Table 1. Characteristics of the materials used in the bridge [26, 27]

Material	Modulus of elasticity (MPa)	Poisson's ratio	Compressive strength (MPa)	Tensile Strength (MPa)
Stone arch	3000	0.2	5	0.5
Spandrel wall	2500	0.2	5	0.5
Filling	1500	0.05	1	0.05
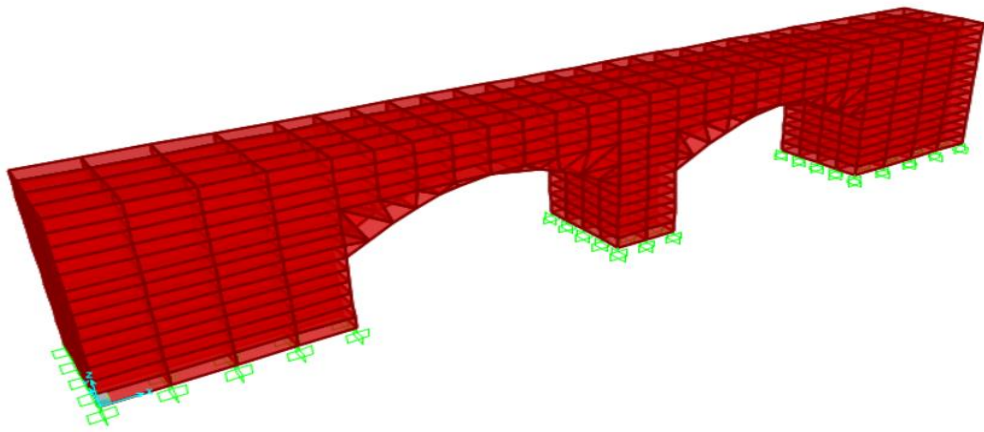
Figure 5. SAP2000 modeling of Yeşildere Bridge

2.2. Response spectrum analysis

The seismic response of the bridge was analysed using response spectrum analysis in both the x and y directions. Four earthquake ground motion levels, as defined in TBDY 2018, were used for this purpose. Table 2 displays the parameters associated with the earthquake ground motion levels used in the response spectrum analysis.

Table 2. Earthquake ground motions given in TBDY 2018 [22]

Earthquake ground motion level	Probability of exceedance in 50 years	Recurrence period (year)	Frequency
DD1	%2	2475	very rare
DD2	%10	475	rare
DD3	%50	72	often
DD4	%68	43	very often

Earthquake data for four levels of ground motion, as shown in Table 2, were obtained from the Turkey Earthquake Hazard Map (TEHM) using an interactive web application, using the effective ground motion level (EGML), building location and local soil class as key parameters. These data are presented in Table 3, which shows the local soil class ZC for each EGML, with the specified building location at 38.901445° latitude and 37.508398° longitude. The local ground class ZC, according to the TBDY 2018 standards, comprises of conditions such as very tight sand, hard clay layers, gravel, or decomposed and highly

fractured weak rocks. Additionally, SS is defined as the dimensionless short-period map spectral acceleration coefficient, and S1 as the dimensionless map spectral acceleration coefficient for a period of 1.0 second [22, 28].

Table 3. Data obtained from TEHM

Earthquake ground motion level	Local soil class	Ss	S1
DD1	ZC	0.721	0.232
DD2	ZC	0.341	0.131
DD3	ZC	0.128	0.056
DD4	ZC	0.094	0.040

2.3. Time History analysis

The process of examining the structure's response to dynamic loads on a second-by-second basis is known as time history analysis. For this study, a finite element model was created in the SAP2000 computer program and subjected to linear time history analysis. The analysis employed acceleration records from two major earthquakes that occurred in Kahramanmaraş on February 6, 2023. Analysis was only conducted for the DD2 level as it was given as the standard design earthquake ground motion in TBDY 2018.

The earthquake behavior of the bridge in Kahramanmaraş during two major earthquakes on February 6, 2023 was investigated using acceleration records obtained from the Turkish Acceleration Database and Archive System (TADAS) [29]. Table 4 provides information on the earthquakes used.

Table 4. Earthquakes used in the analysis

Earthquake	Station	Mw
6 February 2023 Pazarcik	Pazarcık	7.7
6 February 2023 Elbistan	Nurhak	7.6

To determine the earthquake behaviour of the modelled historical bridge, we obtained the earthquake parameters for the region where the Yeşildere Bridge is located from the TEHM interactive web application through AFAD (Disaster and Emergency Management Presidency) according to TBDY 2018. The earthquake parameters found for earthquake ground motion level 2 (DD2) are presented in Table 3.

The seismicity of the area where the bridge is located was matched with the acceleration time graphs of the earthquakes given in Table 4 using the Seismomatch [30] program. Figure 6 shows the original and paired states of the horizontal elastic design spectra, while Figure 7 shows the original and paired acceleration time graphs of the earthquakes. For all earthquake loadings, the east component was used.
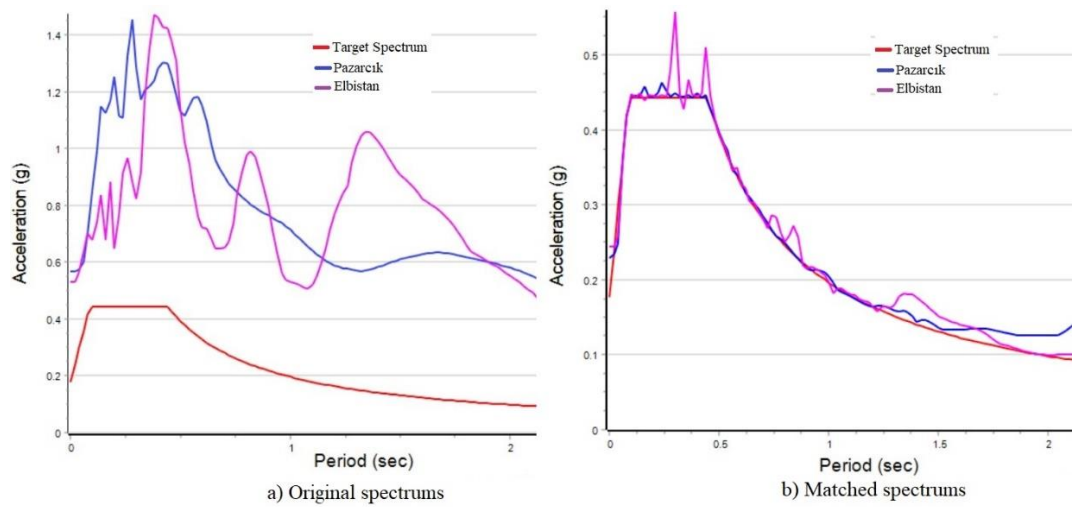
Figure 6. Spectrum of original and matched horizontal elastic design [30]
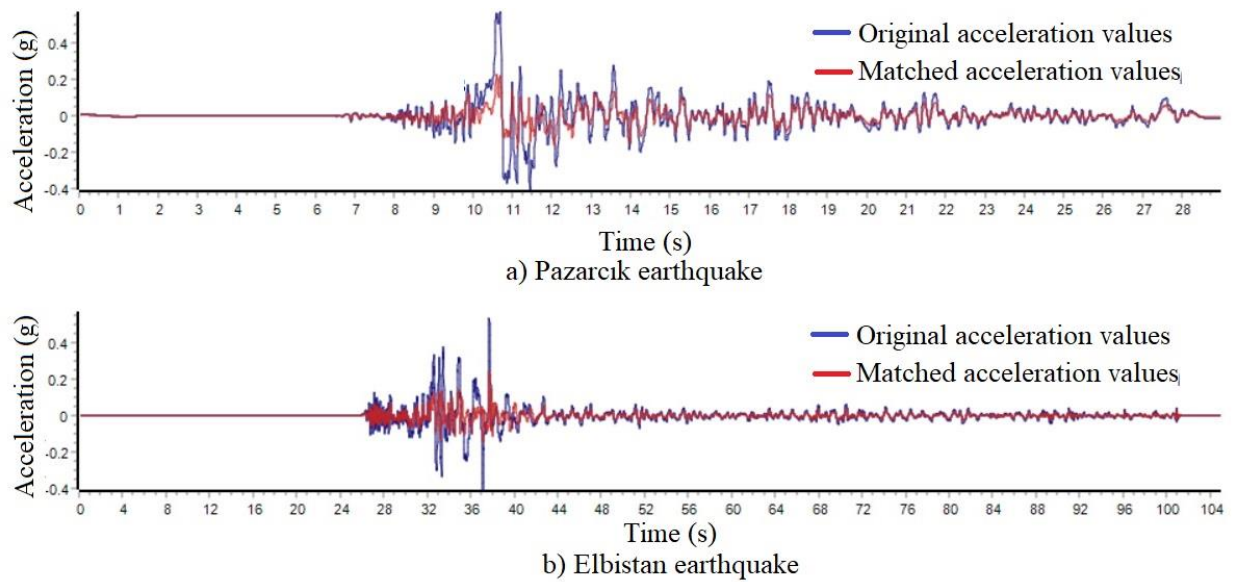
Figure 7. Original and matched acceleration time graphs of earthquakes [30]

2.4. Wall characteristic shear strength

The characteristic shear strength of masonry walls can be calculated with the help of Equation (1) as specified in TBDY-2018 [22].

$$f_{vk} = f_{vko} + 0.4\,\sigma \leq 0.10\,f_b \tag{1}$$

In this equation;

f_{vk}: Characteristic shear strength of masonry wall,

σ: Earthquake loads multiplied by load coefficients and vertical compressive stress calculated under the influence of vertical loads,

f_b: It is the average compressive strength of the masonry unit.

3. RESULTS AND DISCUSSION

The Yeşildere Bridge's FEM model, which was constructed using masonry, was simulated using the SAP2000 program. Modal analysis, response spectrum analysis, and linear time history analysis were conducted in accordance with TBDY 2018.

3.1. Modal Analysis

Mode shapes play a crucial role in understanding the overall behaviour of stone arch bridges. Table 5 presents the first 5 mode shapes obtained from the modal analysis. The first mode has a period of 0.03214 seconds.

Table 5. The first 5 mode shapes of the model

Mode	Mode shape	Period (s)	Frequency (Hz)
1		0.03214	31.110
2		0.02431	41.141
3		0.01853	53.959
4		0.01851	54.032
5		0.01562	64.007
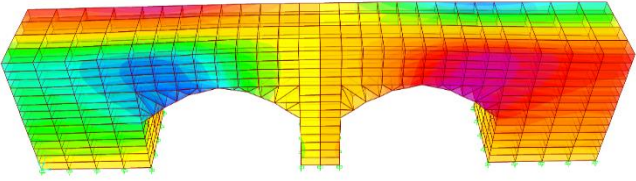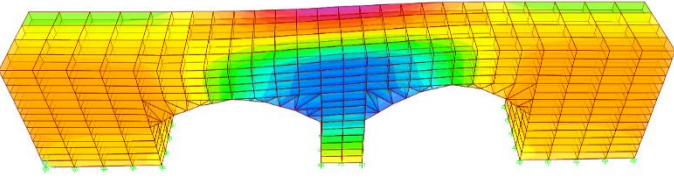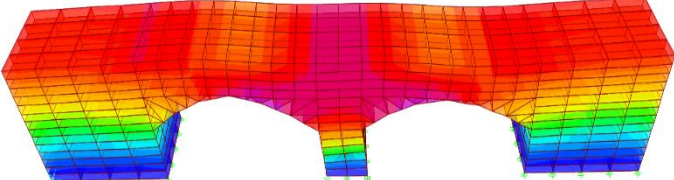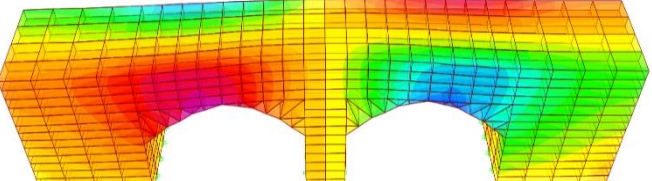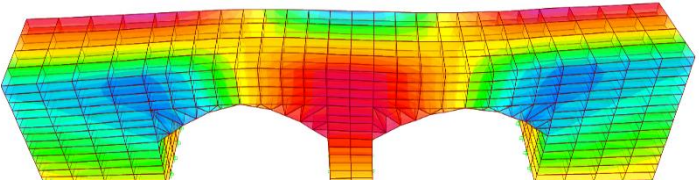
As per TBDY 2018, the effective masses should constitute at least 95% of the total mass of the structure. The analysis of Yeşildere Bridge modeling resulted in obtaining 100 mode shapes and free vibration periods. Table 6 presents the first, third, sixty-third, and sixty-sixth modes out of the 100 obtained. The mass participation ratio of the 3rd mode, which represents the lateral displacement motion of the main mass in the x direction of the bridge, is approximately 70%. The mass participation rate of the first mode, which corresponds to the lateral displacement in the Y direction, was approximately 54%.

<div align="center">Table 6. Mass participation ratios and period values of some modes</div>

Mode	Period (s)	Mass participation ratio	
		X direction	Y direction
1	0.032	0.000	0.537
3	0.019	0.698	0.537
63	0.003	0.94	0.95
66	0.003	0.95	0.95

The effective mass ratios obtained from the modal analysis are provided as a percentage of the total building mass. The structure model has achieved 95% in the sixty-sixth mode for the x direction and 95% in the sixty-third mode for the y direction.

3.2. Response Spectrum Analysis

The TEHM data was inputted into the SAP2000 program and response spectrum analysis was conducted in both the x and y directions. The analysis yielded stress and displacement values for each EGML applied to the bridge model in both directions.

Figure 8 displays the highest displacement values for EGMLs DD1, DD2, DD3, and DD4 in both the x and y directions. Figure 9 shows the locations with the greatest displacements in the x and y directions resulting from earthquake ground motions.
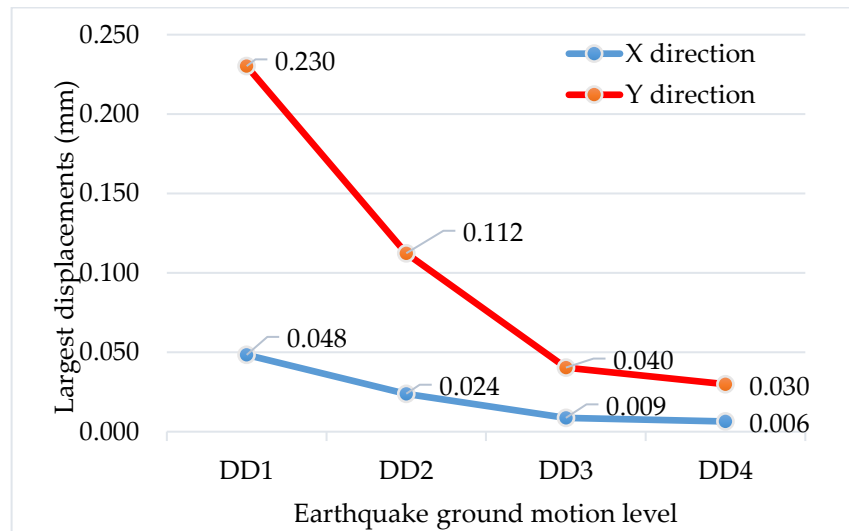
Figure 8. Maximum displacements obtained for earthquake ground motion levels
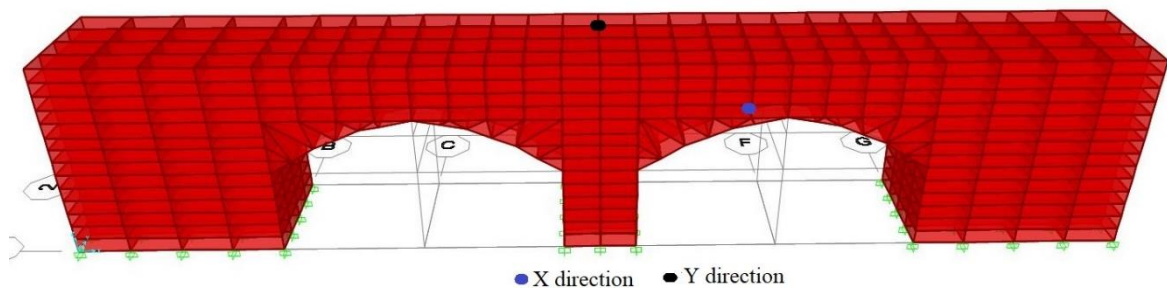
Figure 9. The points where the greatest displacements occur

Figure 8 shows that the largest displacements for all EGML were greater in the y direction than in the x direction.

Figure 10 displays the largest normal stresses obtained in both the y and x directions for the DD1, DD2, DD3, and DD4 EGML. Figure 11 shows the largest shear stresses obtained for the same EGMLs.
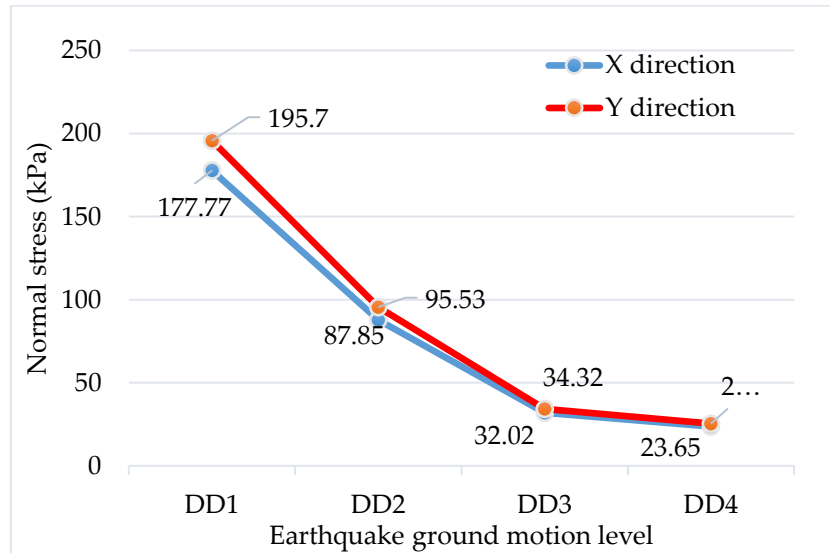
Figure 10. Maximum normal stresses obtained for EGML
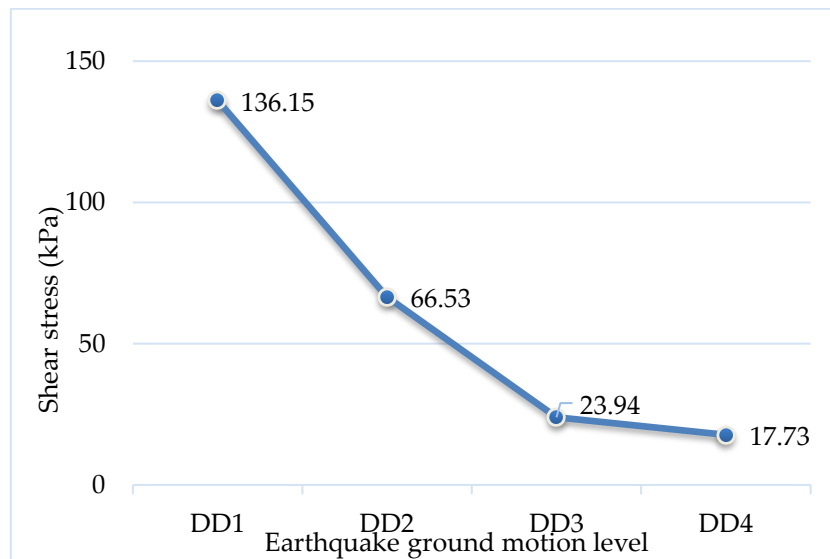
Figure 11. Maximum shear stresses obtained for EGML

Upon examining Figure 10 and Figure 11, it can be observed that normal and shear stresses decrease non-linearly from DD1 to DD4, in accordance with the decreasing values of parameters Ss and S1 as shown in Table 3. Similarly, the analysis of Figure 8 reveals that this trend also applies to displacements.

Table 7 displays the shear stresses obtained from the FEM model analysis conducted in the SAP2000 computer program for EGML.

Table 7. Shear stresses obtained for EGML

Definition	Shear stresses resulting from response spectrum analysis
DD1	
DD2	
DD3	
DD4	
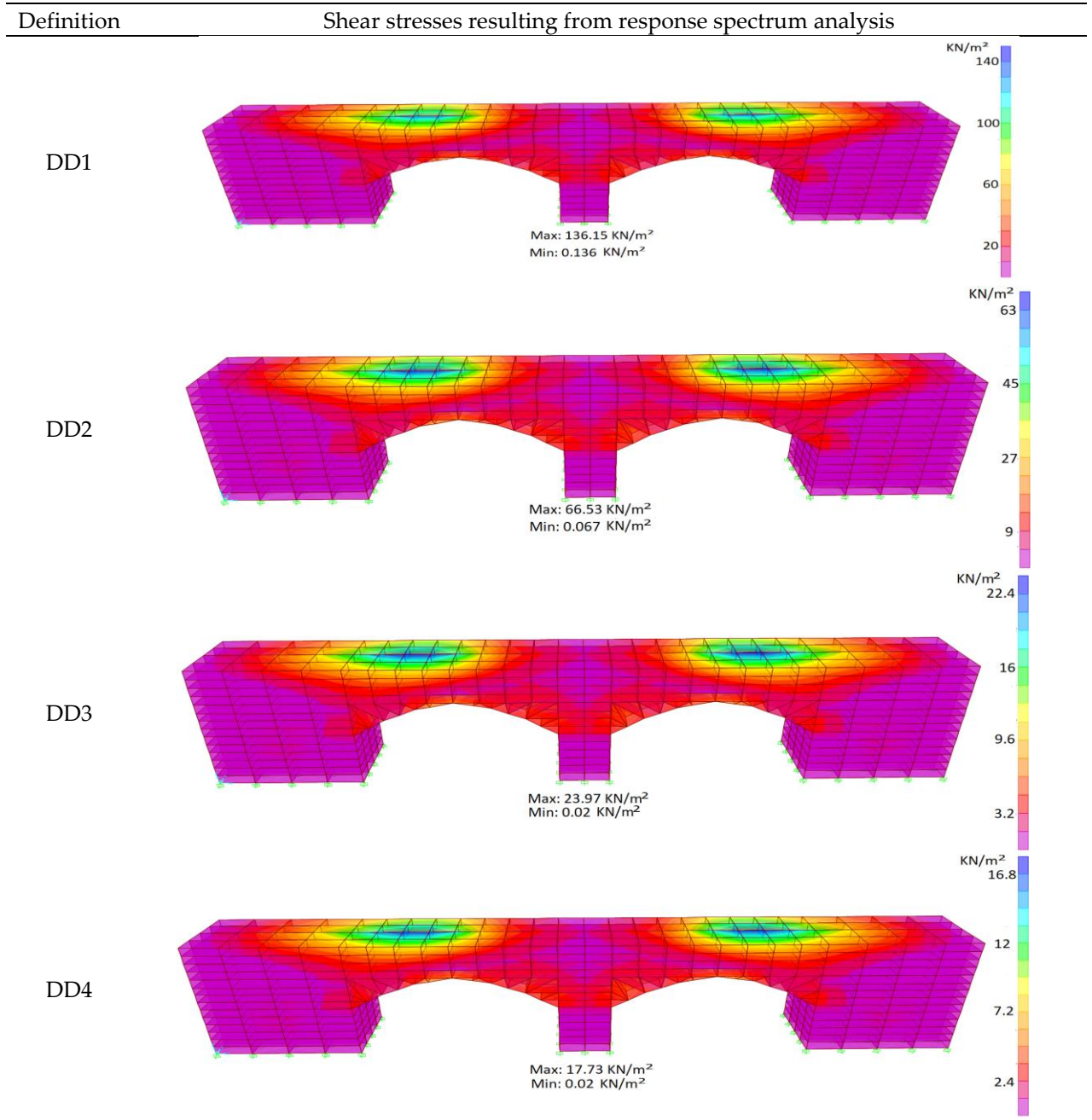
Equation (1) is used to calculate the characteristic shear strength of the wall. The equation provides a value of 100 kPa for the characteristic initial shear strength (fvko) of natural or artificial stones in TBDY 2018. The static analysis determined that the wall is subjected to a vertical load of 6159.663 kN, resulting in a vertical compressive stress of 171 kPa. Using Equation (1), the characteristic shear strength fvk is calculated as 168 kPa. Upon examining Figure 11, it can be seen that the maximum shear stress caused by earthquake ground movements in the bridge is 136.15 kPa. This result indicates that the bridge is safe in terms of shear stress.

3.3. Time History Analysis

The arch bridge underwent modal analysis, which revealed that the 1st mode shape occurred in the y

direction. Additionally, response spectrum analysis indicated larger stresses and displacements in the same direction. Therefore, time history analysis was conducted solely in the y direction (stream flow direction). The historical bridge underwent time history analyses, which yielded the largest relative displacement and stress results for the Pazarcık and Elbistan earthquakes.

3.4. Largest relative displacement results

Table 8 shows the largest relative displacement results obtained from the linear time history analysis. The largest relative displacement for the Pazarcik and Elbistan Earthquakes occurred in the y direction at 10.6 and 37.7 seconds, respectively. The largest relative displacement was 0.085 mm in the Pazarcık Earthquake, while approximately 0.06 mm was obtained in the Elbistan Earthquake. Upon comparing the displacement results obtained from time history and response spectrum analysis, it was observed that the displacements obtained from time history were similar to those obtained from DD2 and DD3 earthquake ground motion levels. Table 8 shows that the largest relative displacements for both earthquake loadings occurred at the same point. In both earthquake loadings, the displacements increased from the ground to the top of the bridge and reached their maximum value at the top of the bridge.

Figure 12 shows the displacement time graphs resulting from the time history analysis for both earthquake loadings. The point with the highest displacements was selected, and the changes in displacement over time were examined.

Table 8. The largest displacements that occur as a consequence of the time history analysis (mm)

a) Pazarcık Earthquake (10.6 s)   b) Elbistan Earthquake (37.7 s)
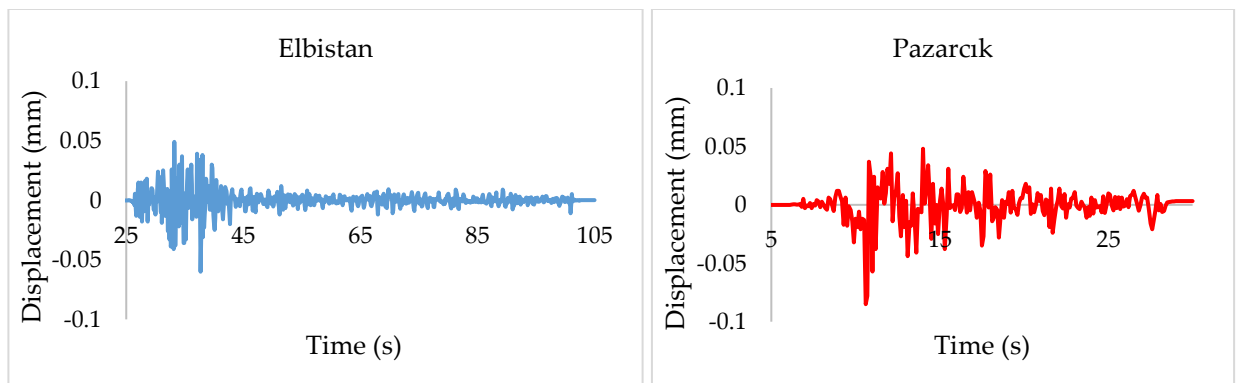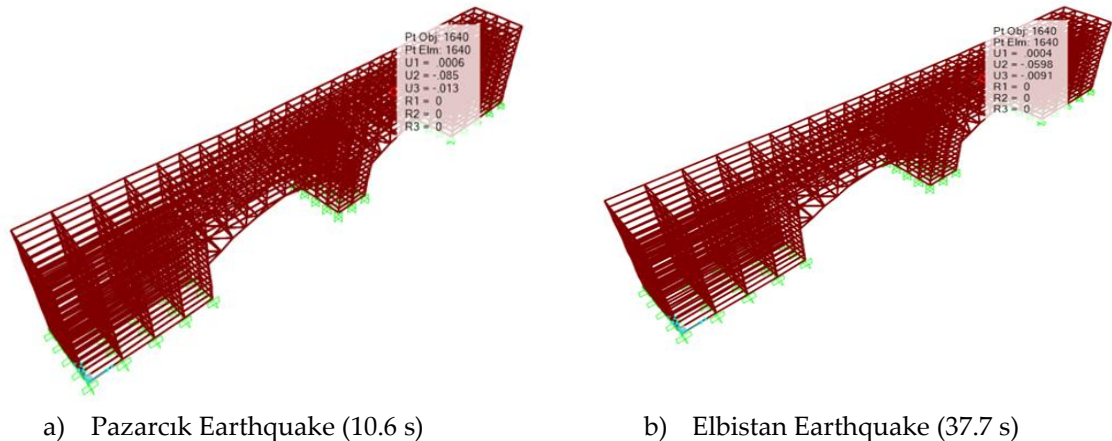
Figure 12. Time – displacement diagrams

3.5. Stress results

As per the SAP2000 program format, compressive or tensile stresses resulting from time history analysis are denoted as S11 or S22, while shear stresses are denoted as S12. Table 9 presents the stress

graphs obtained at the moment of maximum displacement for both earthquake loadings (10.6 s for Pazarcık Earthquake and 37.7 s for Elbistan Earthquake) on the Historical Yeşildere Bridge.

Table 9. Stresses as a result of seismic analysis

Stress	Stresses as a result of seismic analysis
S11	Max: 99.492 kN/m² Min: -99.492 kN/m²
S22	Max: 74.668 kN/m² Min: -74.668 kN/m²
S12	Max: 33.265 kN/m² Min: - 32.875 kN/m²

Pazarcık Earthquake
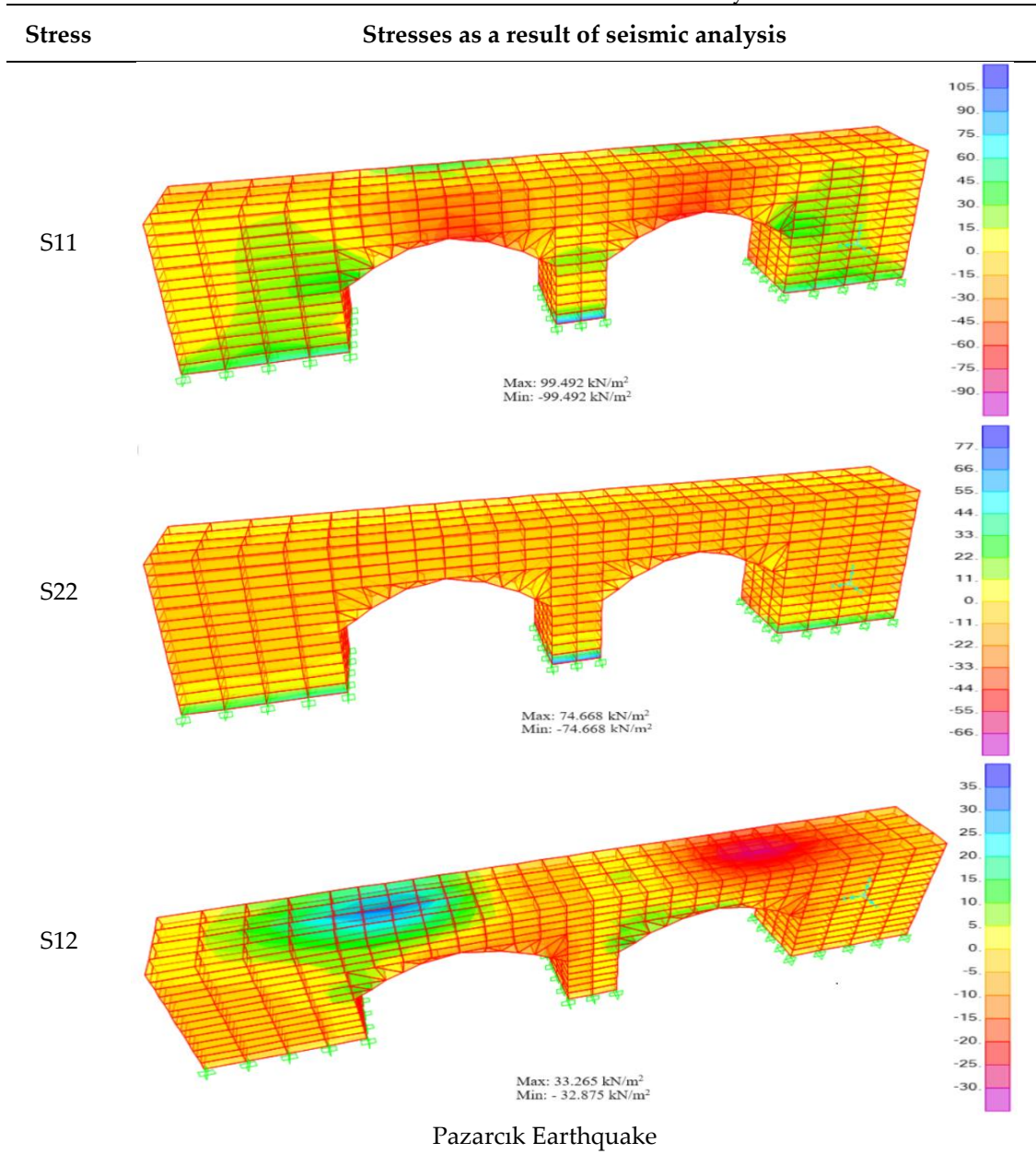
Table 9. Stresses as a result of seismic analysis (continued)

Stress	Stresses as a result of seismic analysis
S11	Max: 69.933 kN/m² Min: -69.933 kN/m²
S22	Max: 52.488 kN/m² Min: -52.488 kN/m²
S12	Max: 23.398 kN/m² Min: -23.125 kN/m²
	Elbistan Earthquake
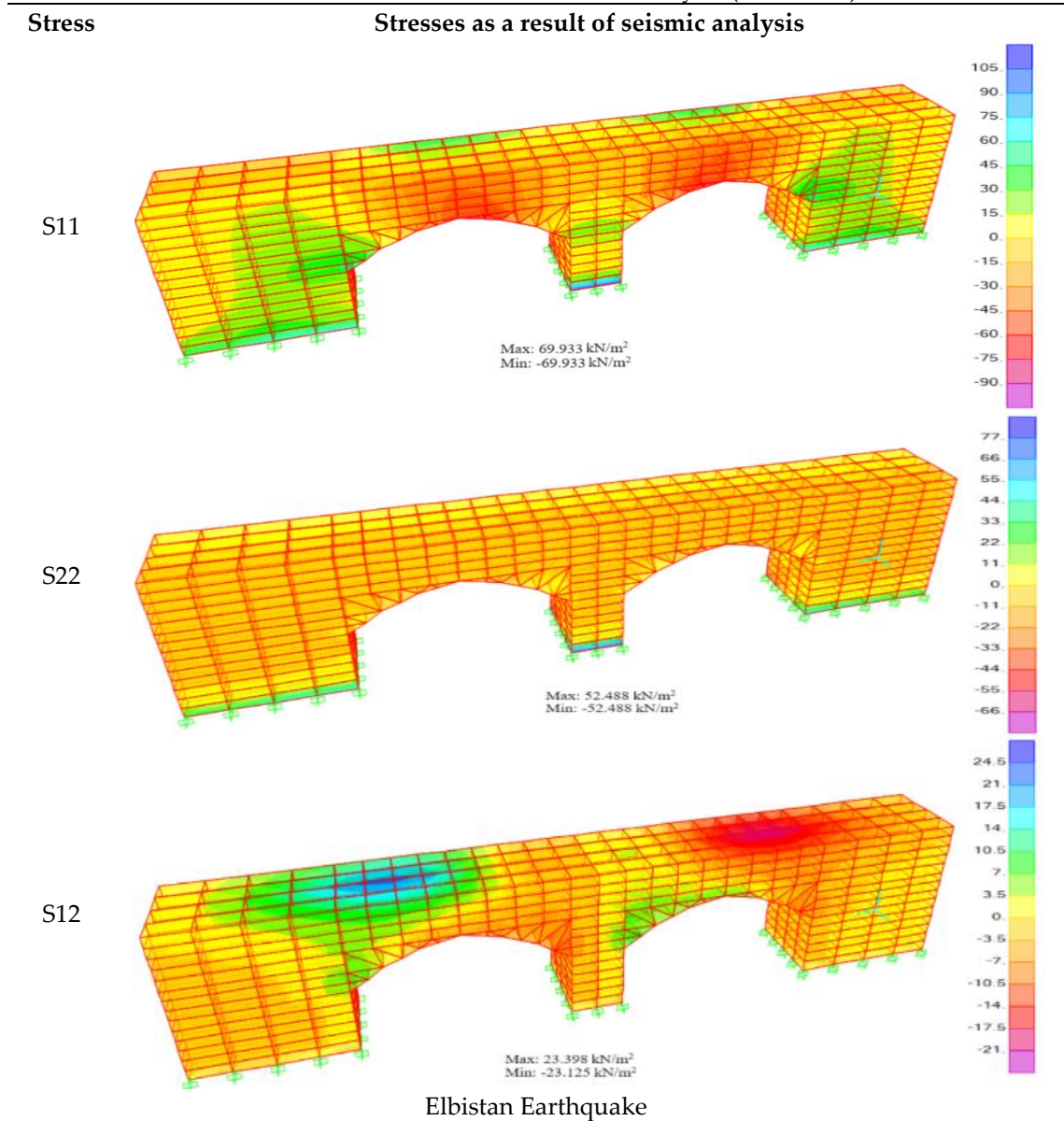
Upon examining Table 9, it was observed that both earthquake loadings resulted in the accumulation of tensile/compressive stresses and shear stress in the same regions of the model. Tensile/compressive stress build-ups were observed at the heel parts of the bridge model for S11 and S22, while S12 shear stress accumulations were observed at the middle upper parts of the model.

The results of the time history analysis show that the tensile/compressive stresses in the model were higher during the Pazarcık Earthquake compared to the Elbistan Earthquake. Specifically, the absolute values of S11 and S22 stresses were approximately 42.3% larger in the Pazarcık Earthquake. Similarly, the S12 shear stress was 42.2% greater in the Pazarcık Earthquake than in the Elbistan Earthquake.

Upon examination of the effects of earthquakes on the bridge, it was discovered that shear stresses concentrate in the upper middle regions of the structure, which could result in shear damage in those areas. Additionally, normal stresses under seismic loads indicate that compressive damage may occur in the upper part of the arch, while tensile damage could occur in the areas where the structure is supported on the ground. Figure 13 displays the contours of the minimum and maximum principal stresses resulting from the time history analysis.

a)   Pazarcık Smax

b)   Pazarcık Smin

c)   Elbistan Smax

d)   Elbistan Smin
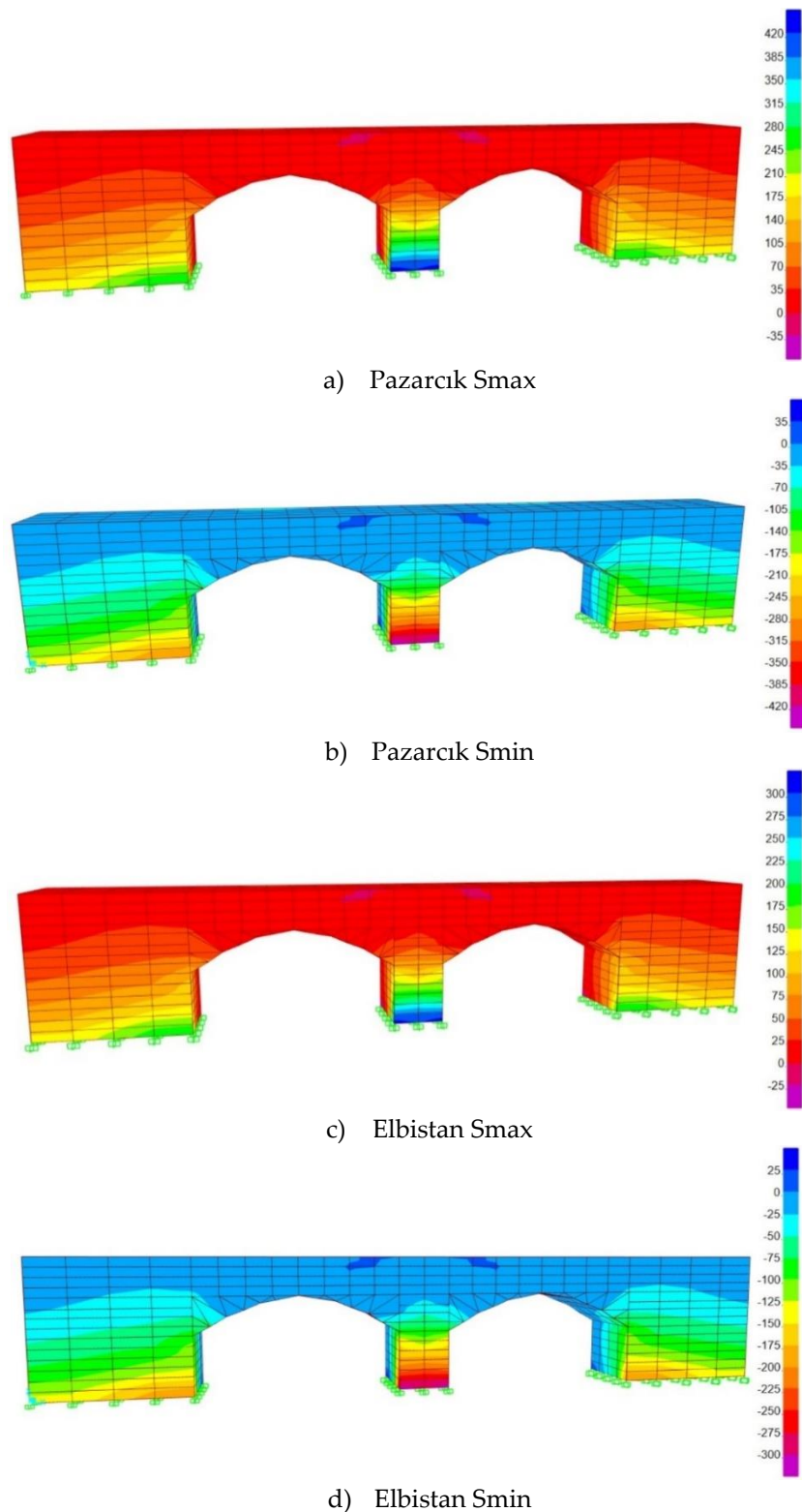
Figure 13. Maximum and minimum principal stresses (kPa)

Figure 13 shows that in both models, the minimum and maximum principal stresses reached their highest values in the support regions. This is consistent with previous studies on masonry arch bridges [5, 12, 25, 31].

Figure 14 displays the time-dependent graphs of the maximum and minimum principal stresses. This section discusses the time periods with the highest earthquake accelerations. Figures 13 and 14 show that the Pazarcık earthquake resulted in higher minimum and maximum principal stresses compared to the Elbistan earthquake.
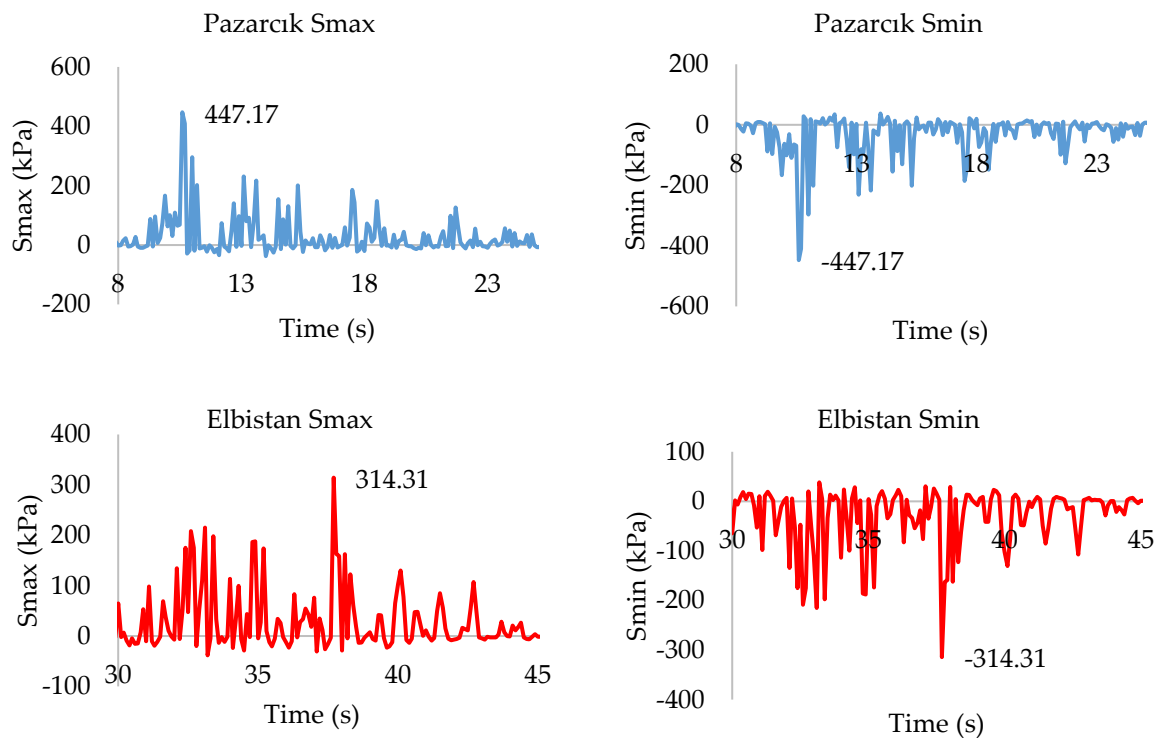
Figure 14. Time-dependent representation of minimum and maximum principal stresses

4. CONCLUSIONS

This study examines the seismic behavior of historical masonry arch bridges by discussing Yeşildere Bridge. To achieve this, the bridge was modelled using solid elements in the SAP2000 computer program. Modal analysis and response spectrum analysis were performed on the historical bridge using 4 different EGML, DD1, DD2, DD3, and DD4 defined in TDBY 2018. To examine the seismic performance of the building, linear time history analysis was conducted using the acceleration records of the Pazarcık Earthquake and the Elbistan Earthquake that occurred on February 6, 2023.

The findings of modal analysis, response spectrum analysis, and linear time history analysis of the FEM model were used to summarize the results obtained for the Historical Yeşildere Bridge.

- The modal analysis resulted in a period of 0.03214 seconds for the structure's first mode.
- The mass participation ratio of the third mode, which represents the lateral displacement of the main mass in the x direction of the bridge, is approximately 70%. The mass participation ratio of the first mode, which represents the lateral displacement movement in the y direction, is approximately 54%.
- The effective mass ratios of the building reached 95% in mode 66 for the x direction and 95% in the 63rd mode for the y direction.
- The response spectrum analysis showed that the largest displacement for the four EGML was in the y direction.
- There was a non-linear decrease in normal and shear stresses as we progressed from DD1 to DD4 to the ground motion level.
- The arch bridge's wall shear strength was found to be greater than the largest shear stress caused

by earthquake ground movements, indicating that it is safe in terms of shear stresses. As a consequence of the linear time history analysis, the largest relative displacement value was obtained from the Pazarcık earthquake. The largest relative displacement value obtained from the Pazarcik earthquake is approximately 41.67% larger than the Elbistan earthquake.

- As a result of the time history analysis, the heel parts of the bridge model experienced accumulations of tensile/compressive stress in S11 and S22, while the middle upper parts of the model experienced accumulations of shear stress in S12.
- The absolute values of the tensile/compressive stresses S11 and S22 in the Pazarcık Earthquake were approximately 42.3% higher than those in the Elbistan Earthquake.
- When examining the shear stresses obtained, it was found that the S12 stress obtained in the Pazarcık Earthquake was 42.2% higher than that in the Elbistan Earthquake.
- The time history analysis revealed that the minimum and maximum principal stresses in both earthquake loadings reached their highest values in the region where the middle bridge pier is supported on the ground. Therefore, it is recommended to strengthen the bridge piers in this region.

To enhance the study's outcomes, nonlinear methods can be used to analyze the bridge.

Historically constructed masonry structures are crucial for maintaining cultural continuity. These structures are susceptible to damage from natural disasters, such as earthquakes and floods. Therefore, preserving these structures is vital to pass them on to future generations. The study evaluated the historical Yeşildere Bridge from a seismic perspective to better understand its seismic behavior. The sentences are grammatically correct and free from errors. No changes in content were made. The study evaluated the historical Yeşildere Bridge from a seismic perspective to better understand its seismic behavior. The text adheres to conventional structure, clear and objective language, formal register, and precise word choice.

Declaration of Ethical Standards

Declaration of Competing Interest

Funding / Acknowledgements

5. REFERENCES

[1]   M. Karaton, H. S. Aksoy, E. Sayın, Y. Calayır, "Nonlinear seismic performance of a 12th century historical masonry bridge under different earthquake levels," *Engineering Failure Analysis*, vol. 79, pp. 408-421, 2017.

[2]   ANSYS, 2008. Swanson Analysis System, US.

[3]   A. Brencich, D. Sabia, "Experimental identification of a multi-span masonry bridge: The Tanaro Bridge," *Construction and Building Materials*, vol. 22, no. 10, pp. 2087-2099, 2008.

[4]   A. Özmen, E. Sayın, "Seismic assessment of a historical masonry arch bridge," *Journal of Structural Engineering & Applied Mechanics*, vol. 1, no. 2, pp. 95-104, 2018.

[5]   A. Özmen, E. Sayın, "Seismic response of a historical masonry bridge under near and far-fault ground motions," *Periodica Polytechnica Civil Engineering*, vol. 65, no. 3, pp. 946-958, 2021.

[6] E. G. Yılmaz, E. Sayın, A. Özmen, "A dynamic analysis of historical masonry arch bridges under different earthquakes: The Case of Murat Bey Bridge," *Turkish Journal of Science and Technology*, vol. 17, no. 2, pp. 461-473, 2022.

[7] SAP2000. "Integrated Finite Element Analysis and Design of Structures Basic Analysis Reference Manual". Berkeley, California, Computer and Structres Inc.

[8] Ö. F. Nemutlu, İ. Güzel, B. Balun, M. Öztürk, A. Sarı, "Nonlinear seismic assessment of historical Masonry Karaz Bridge under different ground motion records," *Bitlis Eren University Journal of Science*, vol. 12 no. 1, pp. 247-260, 2023.

[9] S. Gönen, S. Soyöz, "Seismic analysis of a masonry arch bridge using multiple methodologies," *Engineering Structures,* vol. 226, 111354, 2021.

[10] A. C. Altunışık, B. Kanbur, A. F. Genc, "The effect of arch geometry on the structural behavior of masonry bridges," *Smart Struct.* Syst, vol. 16, no. 6, pp. 1069-1089, 2015.

[11] H. Güllü, "Investigation of earthquake effect of historical masonry cendere bridge," *Nigde Omer Halisdemir University Journal of Engineering Sciences*, vol. 7 no. 1, pp. 245-259, 2018.

[12] G. B. Sakcalı, A. Gönül, İ. Yüksel, "Seismic behavior of historical masonry bridges: The case study of Irgandi Bridge," *International Journal*, vol. 6, pp. 24-32, 2019.

[13] G. Milani, P. B. Lourenço. "3D non-linear behavior of masonry arch bridges," *Computers & Structures*, vol. 110, pp. 133-150, 2012.

[14] A. Kumbasaroglu , A. Celik, O. Demir, A. I. Turan, H. Yalciner, "An assessment of the seismic performance of the historic Tigris Bridge," *Open Journal of Civil Engineering*, vol. 9 no. 3, pp. 230-239, 2019.

[15] A. Harapin, M. Smilović, N. Grgić, M. Glibić, J. Radnić, "Static and dynamic analysis of the old stone bridge in Mostar," *Gradevinar* vol. 64, pp. 655-655, 2013.

[16] M. Karalar, M. Yeşil, "implications of arch warp altitudes on an ancient masonry bridge under ground movements," *Applied Sciences*, vol. 13, no. 13, 7395, 2023.

[17] A. Özodabaş, C. Artan, "Determination of stress and deformation zones of historical Mus Murat Bridge," *Bilecik Seyh Edebali University Journal of Science,* vol. 8, no. 1, pp. 413-429, 2021.

[18] K. Akın, E. Sayın, A. Özmen, "Evaluation of seismic responses of historical masonry bridges under different damping types," *Fırat University Journal of Engineering Science*, vol. 34, no. 1, pp. 45-59, 2021.

[19] M. Laterza, M. D'Amato, V. M. Casamassima, "Seismic performance evaluation of multi-span existing masonry arch bridge," In AIP Conference Proceedings. 1863, no. 1, pp. 450010, 2017.

[20] Ç. O. Öztürk, S. Y. Çetin, S. E. Sayın, "Dynamic analysis of historical Sultan Hamit Masonry Arch Bridges," *Dicle Üniversitesi Mühendislik Fakültesi Mühendislik Dergisi*, vol. 14, no. 3, pp. 499-506, 2023.

[21] M. Saydan, A. Unal, U. S. Keskin, & G. Kansun, "An investigation of the current situation of the Mısırlıoğlu bridge and possible damages after freeze-thaw by using finite elements analysis, Sille–Konya (Central Anatolia, Turkey)," *Engineering Failure Analysis*, vol. 117, 104788, 2020.

[22] Disaster and Emergency Management Presidency. "Türkiye Building Earthquake Regulation". Ankara, Türkiye, 2018.

[23] 16th Regional Directorate of Highways, Sivas, Türkiye, 2023.

[24] P. B. Lourenco "Computational strategy for masonry structures," *Delft University of Technology and DIANA Research*, 1996.

[25] A. Özmen, E. Sayın, "Evaluation of earthquake behavior of a historical masonry bridge," *Nigde Omer Halisdemir University Journal of Engineering Sciences*, vol. 9 no. 2, pp. 956-965, 2020.

[26] E. Hokelekli, & B. N. Yilmaz, "Effect of cohesive contact of backfill with arch and spandrel walls of a historical masonry arch bridge on seismic," *Periodica Polytechnica Civil Engineering,* vol. 63, no. 3, pp. 926–937, 2019.

[27] P. Usta., & Ö. Bozdağ, "Earthquake analysis of the historical Başdurak mosque," *Pamukkale University Journal of Engineering Sciences,* vol. 27, no. 3, pp. 244-250, 2021.

[28]   Disaster and Emergency Management Presidency. "Türkiye Earthquake Hazard Maps Interactive Web Application," *Disaster and Emergency Management Presidency*, Available: https://tdth.afad.gov.tr/TDTH/main.xhtml. [Accessed: Oct. 27, 2023].

[29]   Disaster and Emergency Management Presidency. ''Earthquake,'' *Disaster and Emergency Management Presidency*, Available: https://tadas.afad.gov.tr/. [Accessed: Mar. 2, 2023].

[30]   Seismosoft, SeismoMatch 2023-A Computer Program for Spectrum Matching of Earthquake Records, 2023.

[31]   A. E. Sever, ''Investigation of the effects of strengthening with frp sheet on earthquake behavior of a masonry arch structure,'' *International Journal of Sustainable Engineering and Technology*, vol. 7, no. 1, pp. 7-19, 2023.

THE INFLUENCE OF FUSED FILAMENT FABRICATION PARAMETERS ON THE FRACTURE BEHAVIOR OF PLA SPECIMENS CONSIDERING ENERGY CONSUMPTION

[1, *]Osman ÖZTÜRK [iD], [2]Muhammed Arif ŞEN [iD], [3]Mevlüt AYDIN [iD]

Konya Technical University, Engineering and Natural Sciences Faculty, Mechanical Engineering Department, Konya, TÜRKİYE
[1] osmanozturk@ktun.edu.tr, [2] masen@ktun.edu.tr, [3] maydin@ktun.edu.tr

Highlights

- Quasi-static penetration test of the 3D printed polylactic acid (PLA) specimens.

- Exploration of role of the printing parameters on the fracture behavior.

- CPA optimization algorithm was used for maximum fracture force and reasonable power usage.

Graphical Abstract
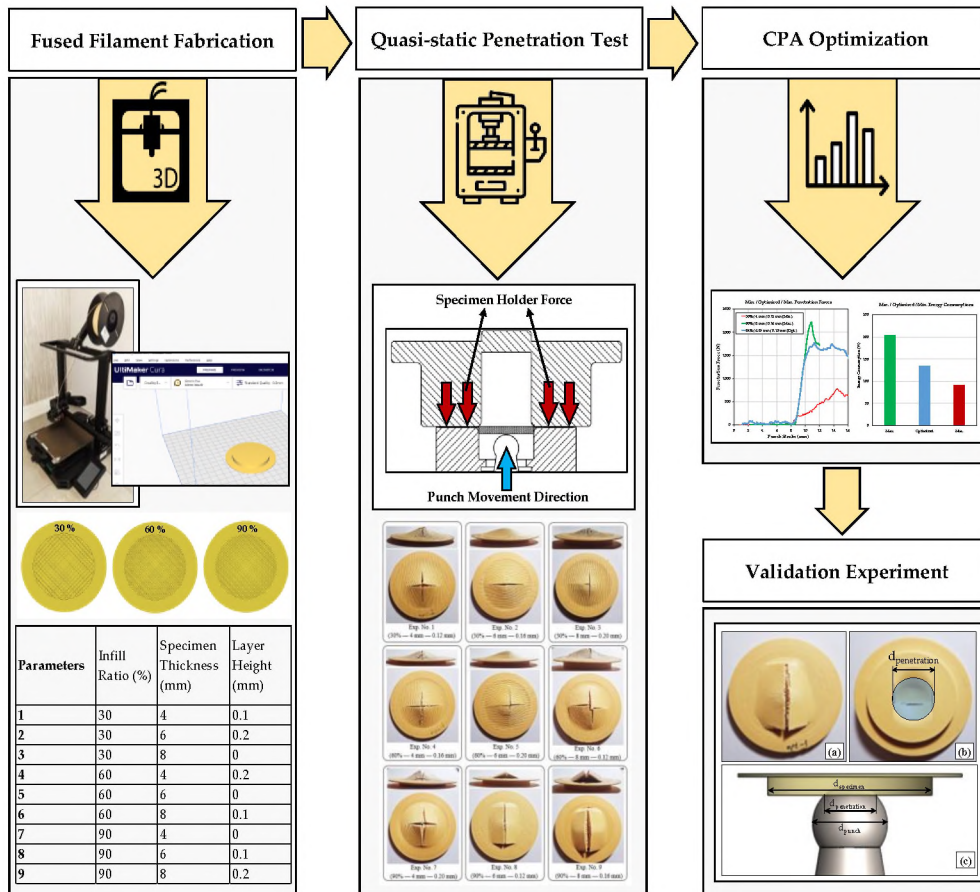
*Corresponding Author: Osman ÖZTÜRK, osmanozturk@ktun.edu.tr

THE INFLUENCE OF FUSED FILAMENT FABRICATION PARAMETERS ON THE FRACTURE BEHAVIOR OF PLA SPECIMENS CONSIDERING ENERGY CONSUMPTION

[1, *] Osman ÖZTÜRK (ID), [2] Muhammed Arif ŞEN (ID), [3] Mevlüt AYDIN (ID)

Konya Technical University, Engineering and Natural Sciences Faculty, Mechanical Engineering Department, Konya, TÜRKİYE
[1] osmanozturk@ktun.edu.tr, [2] masen@ktun.edu.tr, [3] maydin@ktun.edu.tr

ABSTRACT: Fused Filament Fabrication (FFF) is a 3D (three-dimensional) printing technology that allows the production of polymers with a wide range of infill densities and unlimited geometric variations. Because of this flexibility, mechanical properties can be optimized by tuning printing parameters. However, the energy consumption during fabrication varies significantly for different printing settings. In the present study, both maximum fracture force and minimum energy consumption of 3D printed PLA (Polylactic Acid) are achieved together by optimizing the printing parameters using CPA (Cyclical Parthenogenesis Algorithm) optimization algorithm. Firstly, a quasi-static penetration test is performed to measure the maximum fracture force. The energy consumption of each specimen is also calculated. Then, maximum fracture force and energy consumption are modeled and integrated into the optimization algorithm. As a result, the three most convenient parameter levels are 84%, 6.83 mm, and 0.19 mm for infill ratio, specimen thickness, and layer height, respectively. While high infill ratio values and specimen thickness increase mechanical performance, these parameter levels are disadvantageous for energy consumption. As a result of optimization, parameters that provide balanced strength and energy consumption were obtained. Fracture force and energy consumption are 1829.87 N and 134.56 W, respectively for the validation experiment of the optimal solution.

Keywords: *3D Printing, Additive Manufacturing, Fused Filament Fabrication, PLA, Quasi-Static Penetration, Optimization*

1. INTRODUCTION

Additive manufacturing processes enable the manufacture of complex parts more easily compared to traditional forming and manufacturing techniques [1]. Additive manufacturing is used in industry with various techniques such as stereolithography [2], selective laser melting [3], and fused filament fabrication [4]. Among these methods, Fused Filament Fabrication (FFF), is an additive manufacturing method primarily based on the deposition of extruded filament layers for a complex 3D geometry. FFF printers have recently become the most popular machines for the printing of polymers because the printed complex parts can be produced and revised easily with a considerably low-cost printing machine [5]. There are many parameters in FFF, and parameter selection affects mechanical properties such as tensile or compressive strength. The influence of parameters is not limited to mechanical properties. Printing parameters also highly influenced the dimensional accuracy [6] and surface quality [7]. In addition to product quality, the energy consumption of FFF printers significantly depends on the printing settings. Therefore, various printing settings such as layer height, infill ratio, infill pattern, build orientation, printing temperature, and printing speed are investigated in the literature [8]. The influence of these parameters on the process was investigated for commonly used thermoplastic materials such as Polylactic acid (PLA), Acrylonitrile butadiene styrene (ABS), and Polyethylene terephthalate-glycol (PETG). Among these alternatives, PLA is a biodegradable filament material because PLA is obtained from crops such as corn and sugar beet. ABS is more durable but less eco-friendly. PETG is suitable for products in contact with food and beverages, but PETG is the least durable material among other alternatives. Because PLA

---

*Corresponding Author: Osman ÖZTÜRK, osmanozturk@ktun.edu.tr

is biodegradable and ideal for prototype manufacturing, automotive, packaging, and prosthesis applications; PLA is the most popular material, which is an alternative to petroleum-based polymer materials [9]. The studies related to influence of parameters are focused on effect of layer thickness [10, 11], infill ratio [12] and raster orientation [13] etc.

Optimization of 3D printing parameters is widely investigated in academic and industrial studies. In a study aiming to minimize printing time and to optimize printing parameters, the most suitable infill type, infill ratio and layer height for PLA material was determined [14]. The best parameters for the minimum printing time are found as grid, 300 μm and 10% for the infill type, layer height and infill ratio respectively. In a study conducted by Korkut et al. [15], the effect of bed temperature, layer height, printing speed and nozzle temperature are found as the most significant variables considering reasonable printing time and lower energy consumption. The results indicate a decrease of 6.91% in energy usage and a considerable shortening in printing time. Kamer et al. [16] compared two different printers and two filaments with different thicknesses (1.75 mm and 2.85 mm) were compared in terms of energy consumption before, during and after printing a standard tensile test specimen. The most important result was that the power usage per specimen was considerably reduced when multiple test specimens were printed instead of printing specimens one by one. Şirin et al. [17] investigated the wear behavior of the 3D printed PLA materials with different infill densities. The results indicate that the wear performance of the middle level of infill density (50%) is better than high and low-level infill densities (70% and 30%, respectively). Akıncıoğlu et al. [18] performed friction tests of Acrylonitrile Styrene Acrylate (ASA) filament by using pin on disc test setup. One of the most significant results of this study is that the wear characteristic of the ASA depends highly on the surface quality and contact area, which also depends on infill density. The effect of different infill ratios on the wear properties of ABS was studied by Akıncıoğlu et al. by using a pin-on-disc device [19]. It was clearly emphasized that higher the infill density higher the coefficient of friction and friction temperature. The wear characteristics of cylindrical and flexible 3D printed scaffolds are also investigated by researchers [20]. As an overall result, studies on the mechanical and wear properties of 3D printed polymeric materials remain up-to-date and continue intensively.

In this study, the fracture forces of PLA samples produced by FFF were determined by quasi-static penetration test. The different printing parameters are investigated and optimized using CPA. These parameters are three various infill ratios (30%, 60%, 90%), specimen thickness (4 mm, 6 mm, and 8 mm), and layer height (0.12 mm, 0.16 mm, and 0.20 mm) which were used when manufacturing the test specimens. The fractured specimens were pictured prior to and after the test to illustrate the fracture patterns. The novelty of the current work is using quasi-static penetration test to reveal fracture behavior considering energy consumption in the 3D printing phase. The secondary purpose is to optimize the printing parameters for higher fracture force and lower energy consumption using CPA.

2. MATERIAL AND METHODS

2.1. Experimental Method

This study aims to reveal the effect of infill ratio, specimen thickness, and layer height on the fracture behavior of PLA material. The specimen was printed by Creality Ender3 S1 Pro printing machine using a 1.75 mm wood colored Esun PLA+ filament. The technical specifications of Creality Ender3 S1 Pro and Esun PLA+ filament are given in Table 1 [21, 22]. The melting point of the commercial Esun PLA+ filament is stated generally as 170-180 °C for PLA in the literature where some of the results are supported by DSC (Differential Scanning Calorimetryanalyses) [23, 24]. To avoid the other influencing factors; the built orientation, printing position, infill pattern, printing temperature, and printing speed were set as constant for all specimens. These fixed parameters are given in Table 2 with their values. Infill pattern was chosen as grid, a commonly used pattern for general applications. Infill ratio is crucial for strength, and layer height significantly reduces printing time. While the total thickness of the specimen is irrelevant from 3D printing settings, thickness affects the fracture force of the PLA material. Therefore, infill ratio (30%, 60%, 90%), specimen thickness (4 mm, 6 mm, 8 mm), and layer height (0.12 mm, 0.16 mm, 0.20 mm) are chosen

The Influence of Fused Filament Fabrication Parameters on the Fracture Behavior of PLA Specimens Considering
Energy Consumption

453

as the input parameters of this study. The printing machine and parameters intended to be optimized are given in Figure 1. The filament in this study is a wood colored filament which is a thermoplastic material used in 3D printing.

Table 1. The technical specifications of Creality Ender 3 S1 Pro 3D printing machine
and Esun PLA+ filament

Creality Ender 3 S1 Pro			Esun PLA+		
Parameter	Value	Unit	Parameter	Value	Unit
Build Volume	220x220x270	mm	Tensile Strength	63	MPa
Printing Speed	Up to 160	mm·s^{-1}	Elongation at break	20	%
Printing Precision	±0.1	mm	Density	1.23	g/cm^3
Layer Height	0.1-0.35	mm	Melting Point	170-180	°C
Filament Diameter	1.75	mm	Diameter	1.75	mm
Nozzle Diameter	0.4	mm			
Nozzle Temperature	Up to 300	°C			
Bed Temperature	Up to 110	°C			
Rated Power	350	W			
Supported Filament	PLA, ABS, TPU, PETG, PA	—			

Table 2. Fixed 3D printing parameters

Parameter	Value	Unit
Printing Speed	70	mm·s$^-$
Nozzle Temperature	210	°C
Bed Temperature	60	°C
Top Layer Thickness	1	mm
Bottom Layer Thickness	1	mm
Infill Pattern	GRID	—
Wall Thickness	0.8	mm
Wall Line Count	2	—

A systematic approach was preferred to reduce the number of experiments. Instead of a full factorial design, the Taguchi design of experiment by L9 orthogonal array, which is given in Table 3, was used in this study. Taguchi L9 design is generally used in the literature to estimate the factors that influence the mechanical performance of the printed part and which factors are more significant than others [25]. The CAD (Computer Aided Design) model of the test specimen was designed considering its thickness, as the specimen thickness is one of the parameters in this study. After that, the designed models were imported to slicing software Ultimaker Cura (version 5.3.1) so that the infill ratio and layer height were set to the required values in Table 3. In the next step, the G-code of the sliced models were uploaded to the 3D-printer and the test samples were ready to be printed. The printing stages of the samples are given in Figure 2.
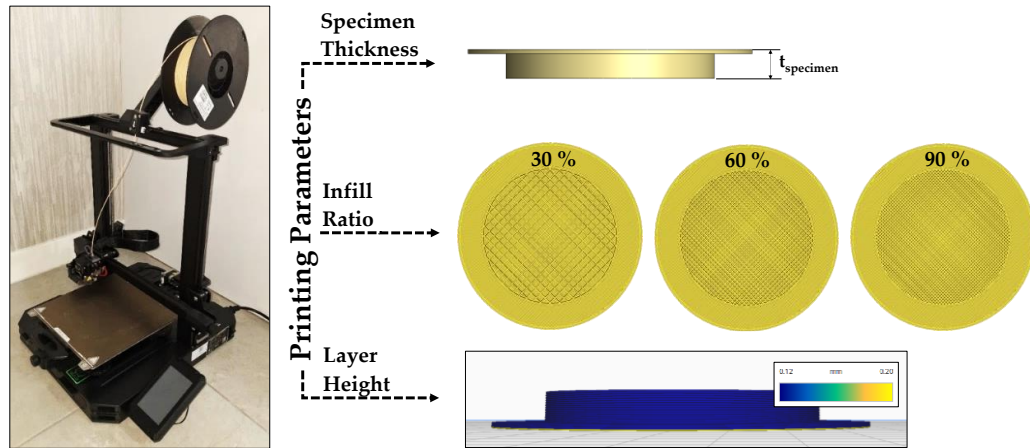
Figure 1. Creality Ender 3 S1 Pro 3D Printer and printing parameters
(specimen thickness, infill ratio, layer height)
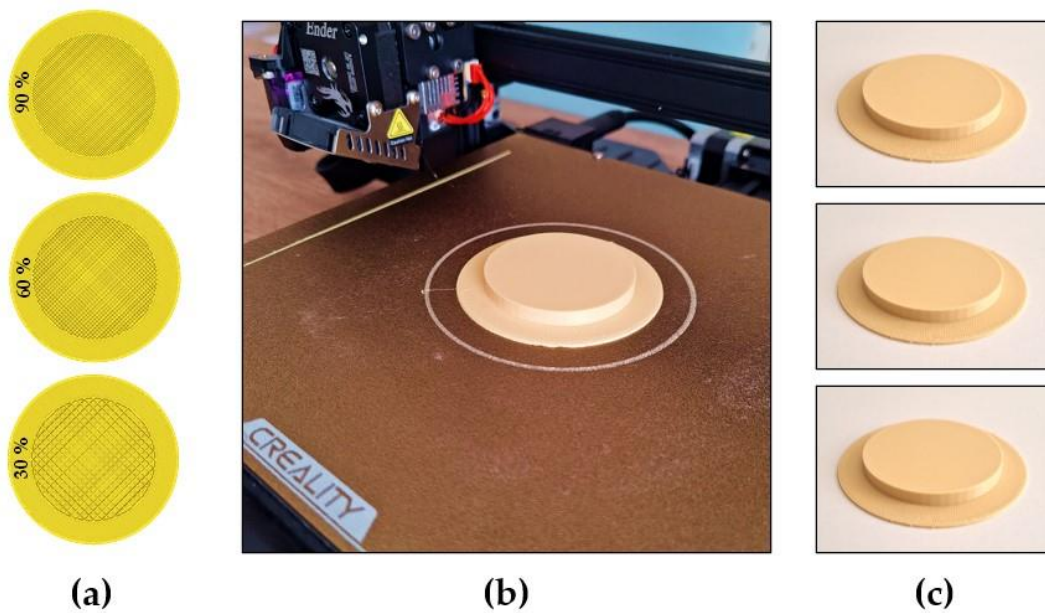
Figure 2. (a) Sliced specimen models in Ultimaker Cura 5.3.1, (b) printing one specimen at a time,
(c) final printed specimens

Table 3. The experimental design according to Taguchi L9 and the variables
(specimen thickness and printing parameters)

Parameters	1	2	3	4	5	6	7	8	9
Infill Ratio (%)	30	30	30	60	60	60	90	90	90
Specimen Thickness (mm)	4	6	8	4	6	8	4	6	8
Layer Height (mm)	0.1	0.2	0	0.2	0	0.1	0	0.1	0.2

After all specimens were printed, quasi-static penetration tests were performed in a four-column hydraulic press. In the penetration test, two dies were used. The diameters of the upper and lower dies are 50 mm and 55 mm, respectively. The dimensions of the specimen were chosen to be compatible with

standard quasi-static testing. In the literature, the ratio between the die cavity diameter and the punch head diameter (D_{cavity}/D_{punch}) is defined as 'SPR', a value which must be in the range of 1.01<SPR<13.33 [26]. In this study, the diameter of the semi-spherical punch is 24 mm, and the diameter of the die cavity is 50 mm. Therefore, SPR of this study is 2.08 which is acceptable for the quasi-static penetration test. The specimen was designed with a 1 mm brim at the bottom so the specimen holder force could be applied without damaging the main specimen. During each penetration experiment, penetration forces in response to punch stroke were recorded with WinView software. The exploded, sectional, and literal views of the test are given in Figure 3a, 3b and 3c respectively. The working principle of the test is given in sectional view in Figure 3b. The fracture force of the specimen was determined by the first significant drop in the penetration force. In addition, the energy consumption was determined using a smart watt-meter during the 3D printing process. Total printing time and instantaneous energy utilization were used to measure each specimen's energy consumption.

(a)   **(b)**   **(c)**
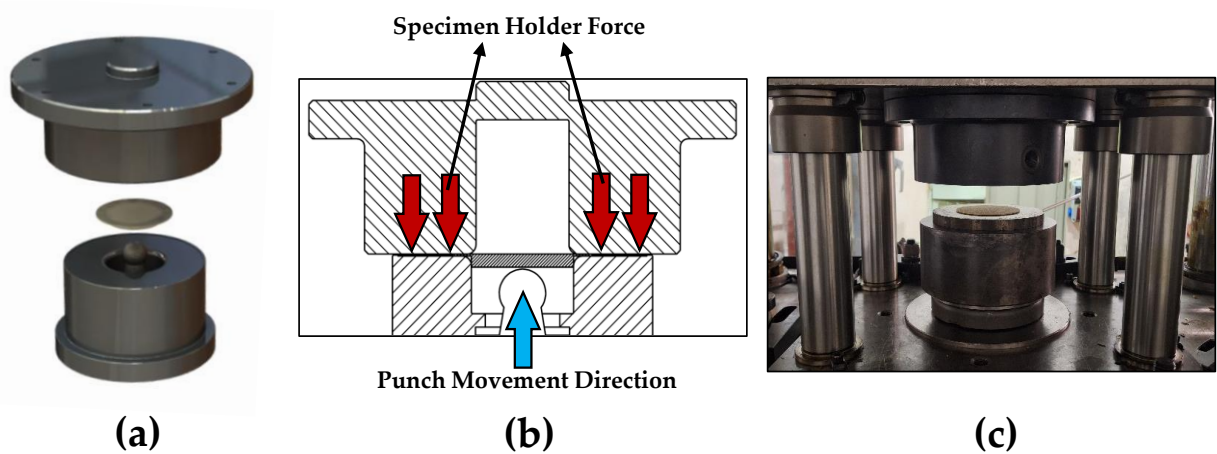
Figure 3. (a) Exploded view, (b) sectional view and
(c) literal view of the experimental setup for Quasi-static Penetration Test

2.2. Modeling and Optimization

This section describes the obtaining of mathematical modeling by the experimental dataset and later tuned printing parameters using a metaheuristic algorithm via the model. Generating a mathematical expression of all FFF parameters can be challenging and possibly impossible. However, it is a very efficient and effective method to develop mathematical formulations that can accurately represent the process with sufficient experimental data.

As can be seen in the below equations, the quasi-static penetration test data of samples produced with the FFF were modeled in Minitab software where the inputs are three main parameters (infill ratio, specimen thickness, and layer height), and the outputs are fracture force and energy consumption, separately. The second-degree polynomial equations giving the mathematical relationship between the printing parameters and fracture force (Eq.1) and energy consumption (Eq. 2) are obtained as follows.

$$y_1 = -2178 - [65.20 \cdot x_1] + [955 \cdot x_2] + [23416 \cdot x_3] + [0.3293 \cdot x_1{}^2] - [56.01 \cdot x_2{}^2] \\ - [120792 \cdot x_3{}^2] - [0.099 \cdot x_1 \cdot x_2] + [221.2 \cdot x_1 \cdot x_3] \tag{1}$$

$$y_2 = 509.7 + [1.308 \cdot x_1] + [28 \cdot x_2] - [6115 \cdot x_3] - [0.00623 \cdot x_1{}^2] - [1.402 \cdot x_2{}^2] + [16207 \cdot x_3{}^2] \tag{2}$$

In these equations; x_1, x_2, and x_3 are infill ratio, specimen thickness, and layer height, respectively. All coded variables and parameter ranges are given in Table 4. Table 4 is an explanation of how input and output variables are expressed in the objective function. For example, the parameter "infill ratio" is

represented as x_1 in the objective function. Additionally, the range in which these parameters will be optimized must be defined as a constraint in the CPA. For this reason, the most used range in the literature was chosen for the input parameters and is given in Table 4. For example, the parameter range for infill ratio is $30 \geq x_1 \geq 90$, so the optimization will be performed within this range. Using these mathematical formulations, the optimal infill ratio, specimen thickness, and layer height values that can provide the highest strength, maximum fracture force, despite as less energy consuming as possible in the FFF process, are tunned with the CPA.

Table 4. Coded variables and preferred parameter ranges in 3D printing

Input Parameters	Coded Variables	Unit	Parameter Range
Infill Ratio	x_1	%	$30 \geq x_1 \geq 90$
Specimen Thickness	x_2	mm	$4 \geq x_2 \geq 8$
Layer Height	x_3	mm	$0.12 \geq x_3 \geq 0.2$
Output Parameters	**Coded Variables**	**Unit**	
Fracture Force	y_1	N	
Power Consumption	y_2	W	

CPA optimization method is one of the newly introduced heuristic optimization methods. Firstly, proposed by Kaveh and Zolghadr in 2017, Cyclical Parthenogenesis Algorithm (CPA) is a population-based metaheuristic search algorithm [27]. CPA is developed by inspiring social behavior and the reproduction of aphids which is a kind of zoological organism. The sexual and asexual reproduction abilities of aphids, named cyclical parthenogenesis, and some unique aspects of their life are exciting for many optimization approaches. CPA is successfully applied to solve many optimization problems. As with all population-based algorithms, CPA starts with a randomly generated aphid population, which includes candidate solutions. Each iteration runs along a five-step and evaluates the objective function according to the newly generated candidate solutions. Detailed descriptions and pseudocode of CPA are available in the literature [28, 29, 30].

The objective function (J) that is determined to maximize the Fracture Force (F_f) while minimizing the energy consumption (E_C) is given in Equation 3. Here, c_1 and c_2 are used to weigh the components in the objective function because fracture force and energy consumption are different physical values with dissimilar units. The constant gains c_1 and c_2 are determined as 112.14 and 1693.07, respectively.

$$J = (c_1 \, F_f) * (c_2 \, E_C)^{-1} \tag{3}$$

3. RESULTS AND DISCUSSION

3.1. Experimental Results

The results of the penetration test are given in Figure 4. According to the test results, the fracture directions were generally in two directions, and these directions were perpendicular to each other. The fracture characteristic is brittle, similar to the literature [31]. As expected, as the specimen thickness and infill ratio increased, the force at which the fracture started also increased. The penetration force was measured instantly throughout the test, and the force value at which the fracture started was taken as fracture force. Penetration and fracture forces are given in Figure 5.

The Influence of Fused Filament Fabrication Parameters on the Fracture Behavior of PLA Specimens Considering Energy Consumption

457
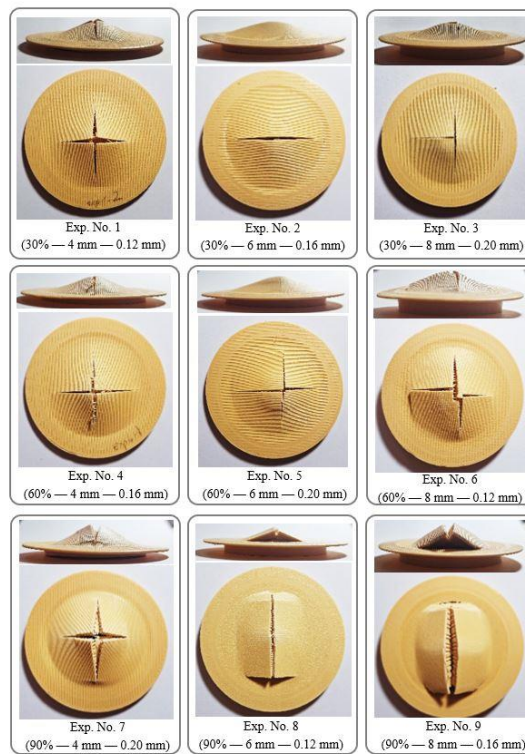
Figure 4. Experimental results of the quasi-static penetration test
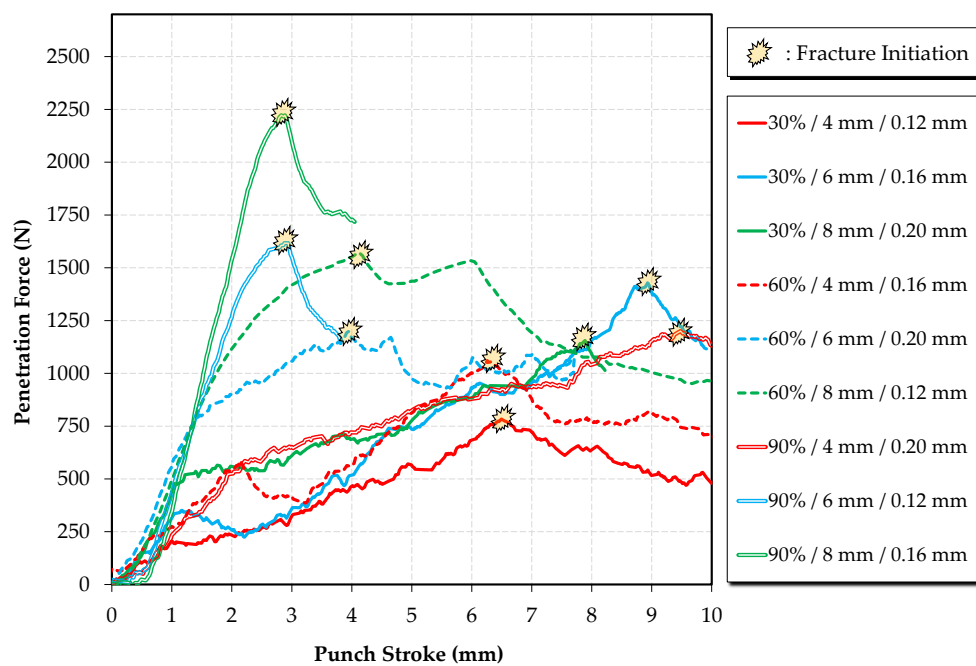
Figure 5. The results of the penetration force versus punch stroke and fracture initiation points

3.2. Optimization Results

The ideal CPA parameters were assigned as 20, 2, 0.02, 0.03, and 0.7 for nA, nC, step size (α_1), step size (α_2), and Fr, respectively, using a trial-and-error method. As it can be clearly understood in Table 5, to define every CPA parameter, each parameter value was defined as minimizing the objective function by

keeping the others constant.

After constructing the mathematical equations, objective function, and CPA in MATLAB R2022b, the algorithm was run to search for optimal infill ratio, specimen thickness, and layer height values, which ensure the best fit of the transfer function. The printing parameters, which could ensure that the maximum fracture force with reasonable energy consumption, were optimized. These are given in Table 5 in bold.

The optimum algorithm parameters of the CPA were found using the trial-and-error method, as explained in detail before. Using these parameters, the algorithm has been run more than once. Printing parameters that minimize the fit function are given in the first row of Table 6, which is the best run in this case. The convergence graph for minimum, maximum, and mean values is given in Figure 6.

Table 5. Finding the best optimization parameter by ranking the value of the fit function

No.	nA	x_1 (Infill Ratio)	x_2 (Specimen Thickness)	x_3 (Layer Height)	Fit	Rank
1-1	10	86.990	7.922	0.192	0.853	5
1-2	15	89.529	5.886	0.184	0.833	2
1-3	**20**	**90.000**	**6.659**	**0.180**	**0.817**	**1**
1-4	25	89.869	7.216	0.174	0.833	3
1-5	30	87.306	6.539	0.191	0.848	4
	nC					
2-1	**2**	**90.000**	**7.114**	**0.180**	**0.82**	**1**
2-2	3	78.751	6.284	0.171	0.97	5
2-3	4	80.052	7.561	0.174	0.92	4
2-4	5	87.192	5.961	0.182	0.86	3
2-5	6	90.000	7.699	0.191	0.82	2
	Stepsize					
3-1	α_1:0.01 α_2:0.01	86.831	7.643	0.191	0.85	7
3-2	α_1:0.01 α_2:0.02	86.429	7.148	0.181	0.85	6
3-3	α_1:0.01 α_2:0.03	87.404	5.566	0.172	0.9	9
3-4	α_1:0.02 α_2:0.01	88.508	6.961	0.189	0.83	4
3-5	α_1:0.02 α_2:0.02	86.514	7.197	0.192	0.85	8
3-6	**α_1:0.02 α_2:0.03**	**90.000**	**7.322**	**0.187**	**0.81**	**1**
3-7	α_1:0.03 α_2:0.01	90.000	6.543	0.186	0.81	2
3-8	α_1:0.03 α_2:0.02	90.000	5.975	0.187	0.82	3
3-9	α_1:0.03 α_2:0.03	88.918	7.951	0.189	0.83	5
	Fr					
4-1	0.2	90.000	7.733	0.165	0.878	6
4-2	0.3	90.000	5.529	0.181	0.843	5
4-3	0.4	90.000	6.349	0.185	0.816	4
4-4	0.5	78.492	6.266	0.172	0.965	7
4-5	0.6	90.000	6.399	0.187	0.815	3
4-6	**0.7**	**90.000**	**7.009**	**0.184**	**0.810**	**1**
4-7	0.8	90.000	7.167	0.188	0.810	2
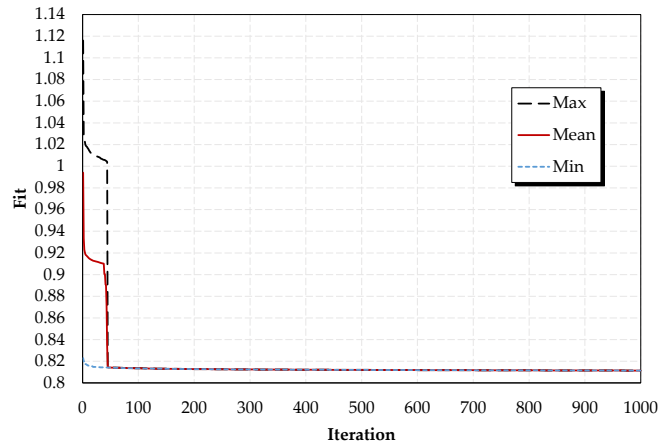
Figure 6. Convergence graph of the best optimization run

Table 6. The optimization algorithm was run several times for optimized printing parameters. Optimized parameters for the best fit (given bold in first row) are; 84%, 6.83 mm, 0.19 mm for x_1, x_2 and x_3 respectively

x_1 (Infill Ratio)	x_2 (Specimen Thickness)	x_3 (Layer Height)	Fit	Rank
83.77	**6.83**	**0.19**	**0.812**	**1**
87.54	6.22	0.18	0.861	4
88.85	7.62	0.19	0.828	2
88.64	5.29	0.17	0.912	6
89.22	7.37	0.16	0.858	3
90.00	6.84	0.19	0.884	5

The outputs obtained from the polynomial model and experimental outputs are given in Table 7. Both polynomial models developed for force and energy showed excellent agreement with the experimental results. The 10th row in Table 7 indicates the validation experiment results, which is the optimized solution for this study. The mathematical models are also good enough to predict the optimized output responses. The graphical representations of the fracture force and energy consumption are given in Figure 7 and Figure 8, respectively. As the graph implies, the fracture force is very close to the maximum value within the response space, while the energy consumption is near the average value. As a result, CPA can predict one of the optimal printing parameters with the aim of maximum fracture force and minimum energy consumption.
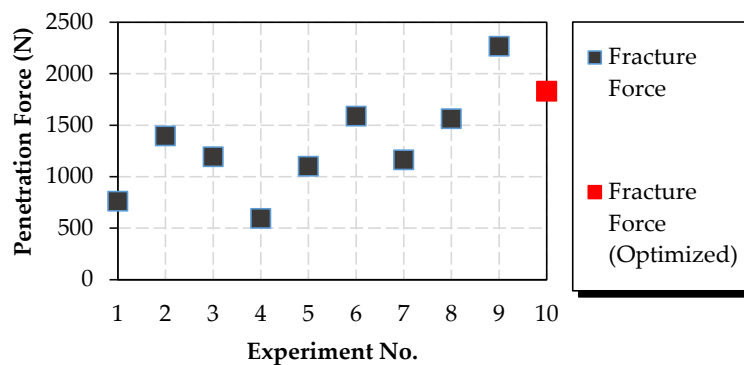
Figure 7. Comparison of optimized fracture force and corresponding Taguchi experiments

Table 7. The results of the Taguchi L9 orthogonal array and optimal solution. The results of the optimal solution (validation experiment) is given in 10th row in bold

Exp. No	Input Parameters			Output Responses (intended to be optimized)		Output Responses		Mathematical Model	
	Infill Ratio (%)	Specimen Thickness (mm)	Layer Height (mm)	Fracture Force (N)	Total energy consumption (Watt)	Printing Time (min)	Filament Consumption (g)	Fracture Force (N)	Total energy consumption (Watt)
1	30	4	0.12	763.25	130.36	93	11	761.17	132.48
2	30	6	0.16	1397.15	100.92	72	13	1394.23	97.36
3	30	8	0.2	1196.40	102.32	73	15	1192.69	102.89
4	60	4	0.16	595.65	91.11	65	12	593.36	91.82
5	60	6	0.2	1102.55	106.53	76	16	1099.40	108.56
6	60	8	0.12	1590.40	203.24	145	20	1586.48	199.60
7	90	4	0.2	1165.15	95.31	68	14	1162.65	91.81
8	90	6	0.12	1564.30	193.43	138	19	1560.99	194.07
9	90	8	0.16	2269.15	145.77	104	24	2264.97	147.73
10	**84**	**6.83**	**0.19**	**1829.87**	**134.56**	**96**	**21**	**1960.59**	**124.67**
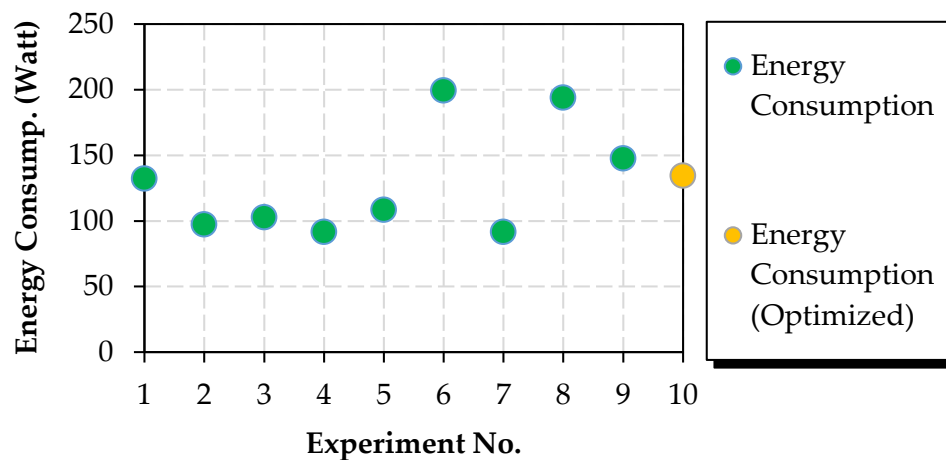
Figure 8. Comparison of optimized energy consumption and corresponding Taguchi experiments

Finally, the graphs of penetration force versus punch stroke are given in Figure 9a. These graphs compare the minimum and maximum fracture forces of Taguchi experiments with the optimal solution. The corresponding energy utilizations are also provided in Figure 9b. Judging by the result, the fracture force improved significantly, while the energy consumption of the optimal specimen remained approximately in the middle of Taguchi experiments.
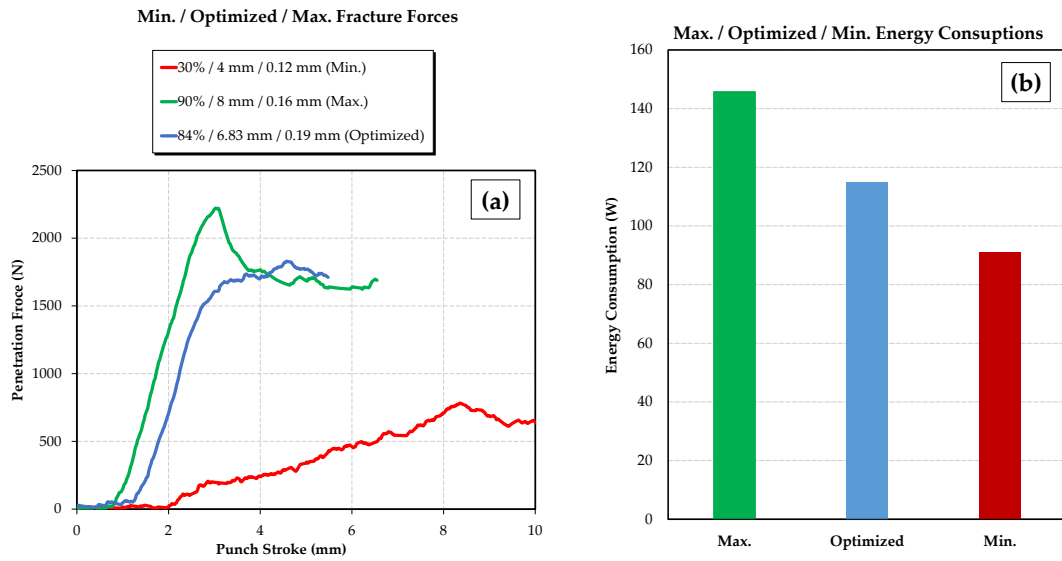
Figure 9. (a) Minimum, maximum, and optimal fracture forces,
(b) maximum, minimum and optimal energy consumptions

3.3. Validation Experiment

A validation experiment was performed after optimization. A characteristic penetration behavior is given in Figure 10a, 10b and 10c. As the figures imply, the material appears to fail before full penetration of the material. The reason behind this phenomenon is the damage mechanism by penetration consists of various damage shapes as stated in previous studies in the literature [32]. The damage mechanism began with small sized cracks near the area that is in contact with the spherical punch. The damage proceeded with either cross shaped or linear shaped larger cracks. Eventually the material was completely damaged. Both the linear and the cross shaped cracks were mainly the result of excessive shear stresses in the grid structure of the PLA.
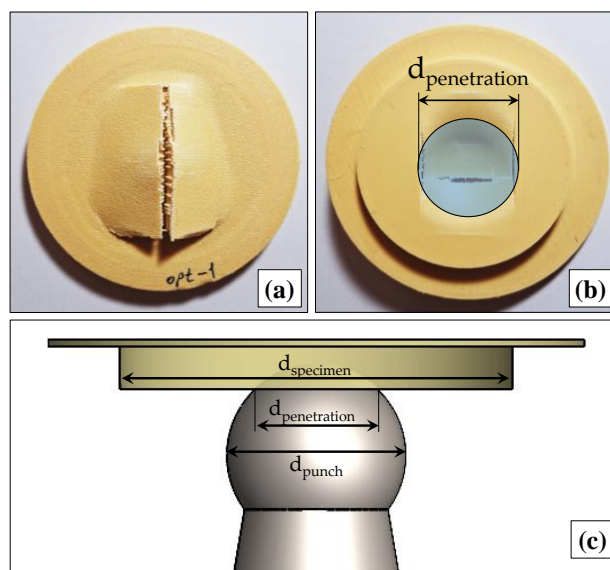
Figure 10. (a) Front view, (b) back view of the fractured specimen and
(c) comparison of the penetration and punch diameters at failure

4. CONCLUSIONS

In this study, to improve the maximum fracture of 3D printed PLA materials with minimum energy consumption on Fused Filament Fabrication, which is a current and developing manufacturing method, the optimal printing parameters (infill ratio, specimen thickness, and layer height) are adjusted using metaheuristic CPA.

When the results obtained from modeling and experimental studies were examined, it was understood that the proposed method could successfully adjust the printer parameters to provide the desired objective function. The optimum parameters of the CPA were obtained by trial-and-error method. The CPA has performed well in providing 3D printing parameters that provide the highest fracture force and lowest energy consumption when producing the part. It was observed that the sample produced with optimal parameters (84%, 6.83 mm and 0.19 mm for infill ratio, specimen thickness and layer height) could provide an energy consumption of 134.56 watts at an average value despite an above-average breaking force of 1829.87 N. This result indicates that an unlimited number of geometries can potentially be optimized for better impact performance while maintaining minimum energy usage. To gain a deeper and systematic understanding of fracture behavior of optimized polymer materials, the Essential Work of Failure (EWF) method should be used in future studies [33].

Declaration of Ethical Standards

The authors followed all ethical guidelines, including authorship, citation, data reporting, and publishing original research.

Declaration of Competing Interest

The authors declare that they have no known competing financial interests or personal relationships that could have appeared to influence the work reported in this paper.

Funding / Acknowledgements

This study is not funded by any institution or council.

Data Availability

The data that support the finding of this study are available from the corresponding author.

REFERENCES

[1]   I. J. Solomon, P. Sevvel, and J. Gunasekaran, "A review on the various processing parameters in FDM," *Mater. Today Proc.*, vol. 37, no. Part 2, pp. 509–514, 2020, doi: 10.1016/j.matpr.2020.05.484.

[2]   C. Liu, B. Qian, X. Liu, L. Tong, and J. Qiu, "Additive manufacturing of silica glass using laser stereolithography with a top-down approach and fast debinding," *RSC Adv.*, vol. 8, no. 29, pp. 16344–16348, 2018, doi: 10.1039/c8ra02428f.

[3]   E. Aydoğan Güngör, "Production of Oxide Dispersion Strengthened Inconel 718 Alloys Using Conventional Powder Metallurgy and Additive Manufacturing Methods," *Konya J. Eng. Sci.*, vol. 8055, pp. 678–692, 2023, doi: 10.36306/konjes.1254946.

[4]   S. Singh, G. Singh, C. Prakash, and S. Ramakrishna, "Current status and future directions of fused filament fabrication," *J. Manuf. Process.*, vol. 55, no. April, pp. 288–306, 2020, doi: 10.1016/j.jmapro.2020.04.049.

[5]   C. Fonda, E. Canessa, and M. Zennaro, *Low-Cost 3D Printing for Science, Education and Sustainable Development*. 2013. [Online]. Available: http://sdu.ictp.it/3d/book.html [Accessed: Dec. 8, 2023]

[6]   R. Mendricky and D. Fris, "Analysis of the accuracy and the surface roughness of fdm/fff

technology and optimisation of process parameters," *Teh. Vjesn.*, vol. 27, no. 4, pp. 1166–1173, 2020, doi: 10.17559/TV-20190320142210.

[7]   J. Kechagias, D. Chaidas, N. Vidakis, K. Salonitis, and N. M. Vaxevanidis, "Key parameters controlling surface quality and dimensional accuracy: a critical review of FFF process," *Mater. Manuf. Process.*, vol. 37, no. 9, pp. 963–984, 2022, doi: 10.1080/10426914.2022.2032144.

[8]   V. Cojocaru, D. Frunzaverde, C. O. Miclosina, and G. Marginean, "The Influence of the Process Parameters on the Mechanical Properties of PLA Specimens Produced by Fused Filament Fabrication—A Review," *Polymers (Basel).*, vol. 14, no. 5, pp. 886-909, 2022, doi: 10.3390/polym14050886.

[9]   A. Pandzic, D. Hodzic, and A. Milovanovic, "Influence of carbon fibers on mechanical properties of materials in FDM technology," *Ann. DAAAM Proc. Int. DAAAM Symp.*, vol. 30, no. 1, pp. 545–554, 2019, doi: 10.2507/30th.daaam.proceedings.074.

[10]   O. Luzanin, D. Movrin, V. Stathopoulos, P. Pandis, T. Radusin, and V. Guduric, "Impact of processing parameters on tensile strength, in-process crystallinity and mesostructure in FDM-fabricated PLA specimens," *Rapid Prototyp. J.*, vol. 25, no. 8, pp. 1398–1410, 2019, doi: 10.1108/RPJ-12-2018-0316.

[11]   J. Giri, A. Chiwande, Y. Gupta, C. Mahatme, and P. Giri, "Effect of process parameters on mechanical properties of 3d printed samples using FDM process," *Mater. Today Proc.*, vol. 47, pp. 5856–5861, 2021, doi: 10.1016/j.matpr.2021.04.283.

[12]   A. Alafaghani and A. Qattawi, "Investigating the effect of fused deposition modeling processing parameters using Taguchi design of experiment method," *J. Manuf. Process.*, vol. 36, no. October, pp. 164–174, 2018, doi: 10.1016/j.jmapro.2018.09.025.

[13]   Ö. Bayraktar, G. Uzun, R. Çakiroğlu, and A. Guldas, "Experimental study on the 3D-printed plastic parts and predicting the mechanical properties using artificial neural networks," *Polym. Adv. Technol.*, vol. 28, no. 8, pp. 1044–1051, 2017, doi: 10.1002/pat.3960.

[14]   F. Kartal, C. Nazlı, Z. Yerlikaya, F. Şimşek, and M. H. Çetin, "Yapım Zamanı için Erimiş Birikim Modelleme İşlem Parametrelerinin Optimizasyonu". *Int. J. 3D Print. Tech. Dig. Ind.*, vol. 2, no. 1, pp. 97-104, 2018, https://dergipark.org.tr/en/pub/ij3dptdi/issue/36075/404817

[15]   V. Korkut, and H. Yavuz, "Açık-Kaynaklı 3B Yazıcılarda Enerji ve Zaman Gereksinimini Azaltmada Etkili Parametrelerin İncelenmesi." *J. Ins. Sci. Technol.*, vol. 12, no. 1, pp. 403-411, 2022, doi: 10.21597/jist.903159.

[16]   M. S. Kamer, Ş. Temiz, and A. Kaya, "Determination of Energy Consumption During The Tensile Test Sample Production in 3D Printer Working with The Fused Deposition Modeling Method. *J. Inst. of Sci. Technol.*, vol. 13, no. 3, pp. 1998-2007, 2023, doi: 10.21597/jist.1198510.

[17]   Ş. Şirin, E. Aslan, and & G. Akincioğlu, "Effects of 3D-printed PLA material with different filling densities on coefficient of friction performance,". *Rapid Prototyp. J.*, vol. 29, no. 1, pp. 157-165, 2023, doi: 10.1108/RPJ-03-2022-0081.

[18]   G. Akıncıoğlu, and E. Aslan, "Investigation of tribological properties of amorphous thermoplastic samples with different filling densities produced by an additive manufacturing method," *Gazi Mühendislik Bilimleri Dergisi*, vol. 8, no. 3, pp. 540-546, 2021, doi: 10.30855/gmbd.0705041.

[19]   G. Akıncıoğlu, E. Şirin, and E. Aslan, "Tribological characteristics of ABS structures with different infill densities tested by pin-on-disc," *Proc. Inst. Mech. Eng. J: J. Eng. Tribol.*, vol. 237, no. 5, pp. 1224-1234, 2023, doi: 10.1177/13506501231153521.

[20]   E. Aslan, and G. Akincioğlu, "Tribological Characterization of Two Different Elastic Polymers Produced via FDM," *International Symposium on Lightweight and Sustainable Polymeric Materials*, pp. 189-200, 2023, doi: 10.1007/978-981-99-5567-1_14.

[21]   "Ender 3 S1 Pro 3D Printer" [Online] Available: https://www.creality.com/products/creality-ender-3-s1-pro-fdm-3d-printer [Accessed Jan. 31, 2024]

[22]   "ESUN PLA+ Technical Data Sheet" [Online] Available:
         https://www.esun3d.com/uploads/eSUN_PLA+-Filament_TDS_V4.0.pdf [Accessed Feb. 15, 2024]

[23]   S. Yilmaz, B. Eyri, O. Gul, N.G. Karsli, and T. Yilmaz, (2024). "Investigation of the influence of salt remelting process on the mechanical, tribological, and thermal properties of 3D-printed poly (lactic acid) materials," *Polym. Eng. Sci.*, vol. 64, no.1, pp. 17-30, 2024, doi: 10.1002/pen.26526.

[24]   H. Lara-Padilla, C. Mendoza-Buenrostro, D. Cardenas, A. Rodriguez-Garcia, and C.A. Rodriguez, "Influence of controlled cooling in bimodal scaffold fabrication using polymers with different melting temperatures," *Mater.*, vol. 10, no. 6, pp. 640, 2017, doi:10.3390/ma10060640.

[25]   N. Lokesh, B. A. Praveena, J. Sudheer Reddy, V. K. Vasu, and S. Vijaykumar, "Evaluation on effect of printing process parameter through Taguchi approach on mechanical properties of 3D printed PLA specimens using FDM at constant printing temperature," *Mater. Today Proc.*, vol. 52, pp. 1288–1293, 2022, doi: 10.1016/j.matpr.2021.11.054.

[26]   Ö.F. Erkendirci, and B.Z.G. Haque, "Quasi-static penetration resistance behavior of glass fiber reinforced thermoplastic composites," *Compos. B. Eng.*, vol. 43, no. 8, pp. 3391-3405, 2012, doi: 10.1016/j.compositesb.2012.01.053.

[27]   A. Kaveh and A. Zolghadr, "Cyclical Parthenogenesis Algorithm: A new meta-heuristic algorithm," *Asian J. Civ. Eng.*, vol. 18, no. 5, pp. 673–701, 2017.

[28]   A. Kaveh and A. Zolghadr, "Cyclical Parthenogenesis Algorithm for guided modal strain energy based structural damage detection," *Appl. Soft Comput. J.*, vol. 57, pp. 250–264, 2017, doi: 10.1016/j.asoc.2017.04.010.

[29]   A. Kaveh and A. Zolghadr, "Optimal design of cyclically symmetric trusses with frequency constraints using cyclical parthenogenesis algorithm," *Adv. Struct. Eng.*, vol. 21, no. 5, pp. 739–755, 2018, doi: 10.1177/1369433217732492.

[30]   A. Kaveh and A. Zolghadr, "Cyclical parthenogenesis algorithm for layout optimization of truss structures with frequency constraints," *Eng. Optim.*, vol. 49, no. 8, pp. 1317–1334, 2017, doi: 10.1080/0305215X.2016.1245730.

[31]   S. Cicero, V. Martínez-Mata, L. Castanon-Jano, A. Alonso-Estebanez, and B. Arroyo, "Analysis of notch effect in the fracture behaviour of additively manufactured PLA and graphene reinforced PLA," *Theor. Appl. Fract. Mech.*, vol. 114, no. May, pp. 103032, 2021, doi: 10.1016/j.tafmec.2021.103032.

[32]   P. Cheng, Y. Peng, K. Wang, A. Le Duigou, S. Yao, and C. Chen, "Quasi-static penetration property of 3D printed woven-like ramie fiber reinforced biocomposites". *Compos. Struct.*, vol. 303, 116313, 2023, doi: 10.1016/j.compstruct.2022.116313.

[33]   I. I. Cuesta, E. Martinez-Pañeda, A. Díaz, and J. M. Alegre, (2019). "The Essential Work of Fracture parameters for 3D printed polymer sheets". *Mater. & Des.*, vol. 181, 107968, 2019, doi: 10.1016/j.matdes.2019.107968.

PERFORMANCE EVALUATION OF DIFFERENT DEEP LEARNING MODELS FOR CLASSIFYING ISCHEMIC, HEMORRHAGIC, AND NORMAL COMPUTED TOMOGRAPHY IMAGES: TRANSFER LEARNING APPROACHES

[1] **Mustafa ALTINTAŞ** , [2, *] **Muhammet Üsame ÖZİÇ**

[1] *Konya City Hospital, Department of Neurology, Konya, TÜRKİYE*
[2] *Pamukkale University, Faculty of Technology, Department of Biomedical Engineering, Denizli, TÜRKİYE*
[1] altintas20@gmail.com, [2] muozic@pau.edu.tr

Highlights

- Classification results with different deep-learning models of ischemic stroke, hemorrhagic stroke, and normal computed tomography images are presented.

- Pre-trained deep learning networks have been adjusted for fine-tuning and transfer learning.

- The results have been compared with performance evaluation metrics.

- The result of the study gave promising results in the classification of stroke types and normal images in computed tomography images.

*Corresponding Author: Muhammet Üsame ÖZİÇ, muozic@pau.edu.tr

PERFORMANCE EVALUATION OF DIFFERENT DEEP LEARNING MODELS FOR CLASSIFYING ISCHEMIC, HEMORRHAGIC, AND NORMAL COMPUTED TOMOGRAPHY IMAGES: TRANSFER LEARNING APPROACHES

[1] **Mustafa ALTINTAŞ** , [2, *] **Muhammet Üsame ÖZİÇ**

[1] *Konya City Hospital, Department of Neurology, Konya, TÜRKİYE*
[2] *Pamukkale University, Faculty of Technology, Department of Biomedical Engineering, Denizli, TÜRKİYE*
[1] altintas20@gmail.com, [2] muozic@pau.edu.tr

ABSTRACT: A stroke is a case of damage to a brain area due to a sudden decrease or complete cessation of blood flow to the brain. The interruption or reduction of the transportation of oxygen and nutrients through the bloodstream causes damage to brain tissues. Thus, motor or sensory impairments occur in the body part controlled by the affected area of the brain. There are primarily two main types of strokes: ischemic and hemorrhagic. When a patient is suspected of having a stroke, a computed tomography scan is performed to identify any tissue damage and facilitate prompt intervention quickly. Early intervention can prevent the patient from being permanently disabled throughout their lifetime. This study classified ischemic, hemorrhage, and normal computed tomography images taken from international databases as open source with AlexNet, ResNet50, GoogleNet, InceptionV3, ShuffleNet, and SqueezeNet deep learning models using transfer learning approach. The data were divided into 80% training and 20% testing, and evaluation metrics were calculated by five-fold cross-validation. The best performance results for the three-class output were obtained with AlexNet as 0.9086 ± 0.02 precision, 0.9097 ± 0.02 sensitivity, 0.9091 ± 0.02 F1 score, 0.9089 ± 0.02 accuracy. The average area under curve values was obtained with AlexNet 0.9920 ± 0.005 for ischemia, 0.9828 ± 0.008 for hemorrhage, and 0.9686 ± 0.012 for normal.

Keywords: *Computed Tomography, Deep Learning, Hemorrhagic Stroke, Ischemic Stroke, Transfer Learning*

1. INTRODUCTION

Stroke, the most common cause of disability in the world, is also the third leading cause of death. Stroke, a disease that affects the brain vessels, accounts for more than half of the neurological disorders that require hospitalization. The majority of strokes are of ischemic origin (85%-87%), while the remainder are hemorrhagic strokes (15%-13%). It has been reported that more than 795,000 people have a stroke each year in the United States. In Turkey, cerebrovascular diseases include ischemic strokes with a rate of 72% and hemorrhagic strokes with a rate of 28%. When this disease occurs in different parts of the brain, it causes paralysis in different body parts, which increases the loss of labor and the cost of care. Rapid intervention at the time of stroke is critical in reducing the level of disability as well as prolonging the patient's life expectancy. Therefore, when the disease is diagnosed and the stroke site is quickly identified, the patient's quality of life will improve significantly. Computed tomography (CT) and magnetic resonance (MR) imaging methods are of great importance for the clinical diagnosis of stroke. In the diagnosis of stroke, CT and MR images are interpreted by a specialist radiologist. Because CT images can be obtained more quickly than MR images, they are primarily preferred for early diagnosis. Depending on the test results, the hemorrhage protocol is applied if the bleeding is caused. If the cause is ischemia, the thrombolytic protocol is activated. However, in cases of ischemic stroke, it is important to intervene within the first 3 hours after the onset of symptoms. The new findings show that this time could be extended to 4.5 hours. The rapid diagnosis process helps to save brain tissues with minimal damage with early intervention [1-3].

Medical image analyses are performed by specialist radiologists in hospitals. In radiological image

*Corresponding Author: Muhammet Üsame ÖZİÇ, muozic@pau.edu.tr

analysis, difficulties such as the necessity of intervention in a short time, problems in accessing specialists who need to interpret images, limitations of facilities in hospitals in small regions, and shortages in the number of radiologists can be encountered. Considering all the disadvantages mentioned, to overcome these shortcomings, the number of studies on image processing and artificial intelligence-based radiological image analysis has been increasing recently and continues to be a hot topic in the literature [4, 5]. Deep learning models have recently been used frequently in the literature for the classification, segmentation, and object detection of medical images [5-7]. In medical studies, where classical machine-learning methods were used for a period, deep-learning models began to be used over time. In classical machine learning methods, features are extracted and classification is performed on the image with different methods. However, there are many different feature extraction methods for this process. Since not every feature is important for classification, then the appropriate feature selection method should be used. Many feature selections can be used for this process as well. There are many feature extraction, feature selection, and machine learning algorithms in this process for the classification application of medical images. Hence, numerous trials are required to determine the most suitable methodology to be applied In deep learning models, the features on medical images are selected by extracting them along the layers. Therefore, less costly and higher accuracy results can be obtained compared to classical machine learning methods [8]. In the future, it is anticipated that analyzing images on high-speed computers, by pre-processing them and offering doctors preliminary information about the diseases in the images, will become a standard technology in the field of medicine [9]. It may not be predicted whether the cause of stroke is ischemia or hemorrhage in the patient who comes to the emergency room. Because of this, deep learning-based clinical decision support systems can be used as auxiliary tools for the identification of stroke types. In the literature, some studies classify stroke using deep learning algorithms on CT images. However, many of these studies are focused on classifying either ischemic or hemorrhagic strokes [9-28]. Fewer studies simultaneously classify normal, ischemic, and hemorrhagic stroke images [9, 12, 14, 23]. In this study, ischemia, hemorrhage, and normal CT images taken from two different databases were classified using deep learning models. 300 ischemic brain CT images, 300 hemorrhagic brain CT images, and 300 normal brain CT images were used from the databases of the Ischemic Stroke Lesion Segmentation Competition 2018 (ISLES 2018) [29] and the North American Society of Radiology (RSNA) [30]. Data augmentation was applied by performing certain pre-processing steps on the images. The images were randomly divided into 80% training and 20% test data, and validation was performed with 5-fold cross-validation. AlexNet [31], ResNet50 [32], GoogleNet [33], InceptionV3 [34], ShuffleNet [35], and SqueezeNet [36] deep learning models were trained with the transfer learning strategy. The successful performances of the networks were compared with the criteria of precision, recall (sensitivity), F1 score, accuracy, receiver operating characteristic (ROC) curve, the area under the ROC curve (AUC), and training time. As a result of the study, the disease classification performances of the models were compared.

2. MATERIAL AND METHODS

2.1. Dataset

In this study, 300 ischemia and 18 normal CT images obtained from the ISLES 2018 (Ischemic Stroke Lesion Segmentation) database [29, 37], 300 hemorrhage and 282 normal CT images obtained from the open source RSNA Intracranial Hemorrhage Detection database published by the Radiological Society of North America were used [30]. The data in DICOM (Digital Imaging and Communications in Medicine) and NIfTI (The Neuroimaging Informatics Technology Initiative) formats were saved as a PNG (Portable Network Graphics) image with a contrast value of 120 and a brightness value of 60 using the MRIcro program [38]. Hemorrhage and ischemia CT slices were determined according to the label information in the databases. Data other than these two labels were filed as normal CT slices. Thus, 300 normal, 300 hemorrhage and 300 ischemia images were collected using multi-center data. Each class was created in equal numbers to avoid an unbalanced data set. Figure 1a shows the ischemic stroke CT slice from the

ISLES dataset, and Figure 1b shows the normal CT slice from the ISLES dataset. Figure 2a shows the hemorrhagic CT slice from the RSNA dataset, and Figure 2b shows the normal CT slice from the RSNA dataset.
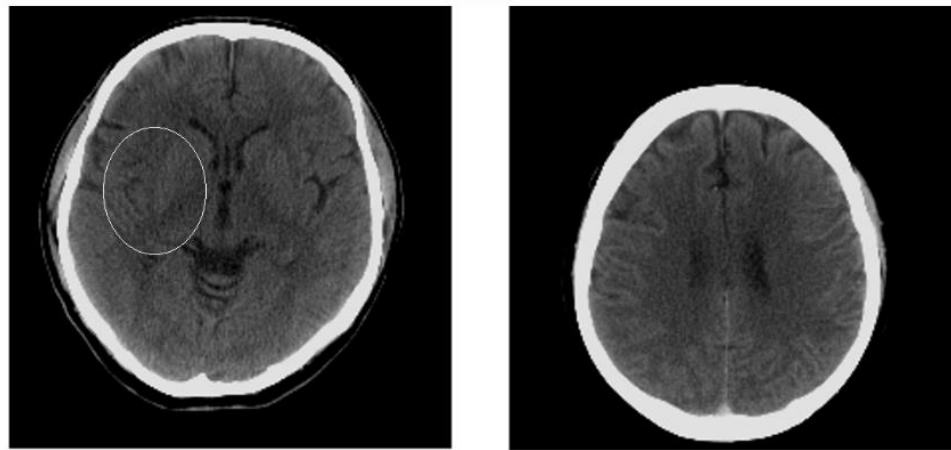
(a)   (b)

Figure 1. ISLES dataset (a) Ischemic stroke CT slice (b) Normal CT slice [29, 39]
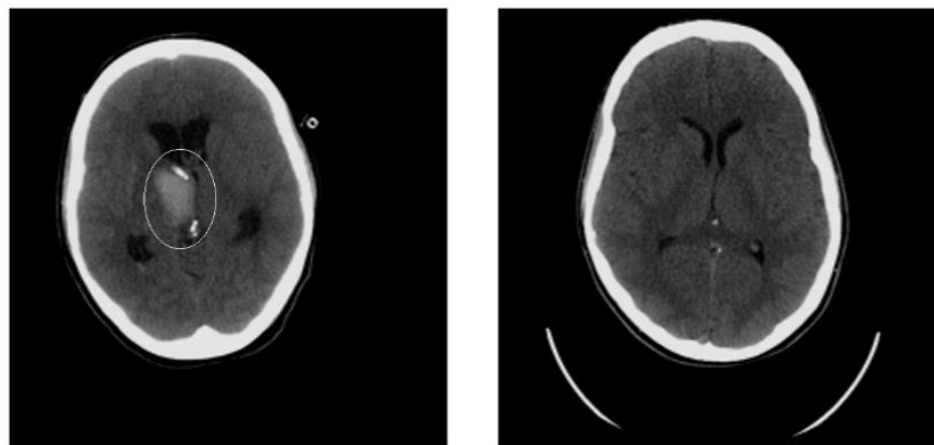
(b)   (b)

Figure 2. RSNA dataset (a) Hemorrhagic stroke CT slice (b) Normal CT slice [30, 39]

2.2. Deep Learning Models and Transfer Learning

In this study, CT images were classified and the performance of the AlexNet [31], ResNet-50 [32], GoogleNet [33], InceptionV3 [34], ShuffleNet [35], SqueezeNet [36] deep learning models were investigated. All experiments were conducted using the Matlab R2021a program running on a 64-bit Windows operating system with an Intel Core i7-7700HQ CPU 2.80 GHz, 16 GB RAM, and an NVIDIA GeForce GTX 1050 Ti graphics card with 8 GB of memory. The deep learning models in the MATLAB program are already trained with the IMAGENET dataset and produce 1000-class outputs. By using these pre-trained networks, classification can be performed without the need for new training. However, when training with a new dataset, some parameters in the network need to be changed. Thus, pre-trained networks can be used as a starting point for learning a new task. This process, called transfer learning, allows training with the new data set by using pre-trained model weights. In this process, instead of training the network with random weights from scratch by fine-tuning, it becomes quick and easy to perform the training process using the existing pre-trained weights. Fine-tuning a network with transfer learning is often much quicker and more straightforward compared to training a network with

randomly initialized weights from scratch [40]. Transfer learning and fine-tuning processes were carried out by changing the last layers of the six deep learning models used in this study to give three classes of output. These models train according to standard input image size and three-channel color images. CT image sizes should be normalized to 227-by-227 for AlexNet, ShuffleNet, and SqueezeNet, 224-by-224 for GoogleNet and ResNet-50, and 229-by-229 for InceptionV3. CT images were automatically normalized to these dimensions by MATLAB during the training process. Necessary parameter settings were arranged so that the images entered the model inputs as a three-channel color image. In this process, the images were added one after the other, and they acted as if they were colored images. The image contents did not change, they were only converted to the format accepted by the models. Data augmentation was carried out using projection methods and random rotation in the x-direction and y-direction up to 30 pixels. The necessary hyperparameters for measuring the performance results of the models under the same conditions were set as given in Table 1.

Table 1. Hyper-parameters for deep learning models [39]

Hyper-parameters	Values
Momentum	0.9
InitialLearnRate	1.00E-04
LearnRateDropFactor	0.2
LearnRateDropPeriod	5
L2Regularization	1.00E-04
GradientThresholdMethod	l2norm
MaxEpochs	7
MiniBatchSize	20
Shuffle	every-epoch
ExecutionEnvironment	GPU
BatchNormalizationStatistics	population

2.3. Performance Evaluation Metrics

The training process was performed under equal hyper-parameters for each model and the performance evaluation metrics were calculated. The data used were randomly divided into five parts 80% training and 20% test, one part in each fold was used as test data, and the other four were used as training data. Thus, the images in all data were used in the training and testing process, and the average of the performance values obtained as a result of five-fold cross-validation was calculated. Table 2 shows the five-fold cross-validation strategy for splitting data.

Table 2. Five-fold cross-validation strategy

	Data-1 (20%)	Data-2 (20%)	Data-3 (20%)	Data-4 (20%)	Data-5 (20%)
1. Fold	Test	Train	Train	Train	Train
2. Fold	Train	Test	Train	Train	Train
3. Fold	Train	Train	Test	Train	Train
4. Fold	Train	Train	Train	Test	Train
5. Fold	Train	Train	Train	Train	Test

True Positive (TP), True Negative (TN), False Positive (FP), and False Negative (FN) values were determined by creating a confusion matrix for each fold. The values determined as actual and predicted were placed in the confusion matrix as shown in Figure 3 according to the abbreviations expressed below. (I: Ischemic, H: Hemorrhagic, N: Normal)

CT_{II} : Number of correctly classified ischemic images

CT_{HH} : Number of correctly classified hemorrhagic images

CT_{NN} : Number of correctly classified normal brain images

CT_{IH} : Number of images misclassified as hemorrhagic while ischemic image

CT_{IN} : Number of images misclassified as normal brain, while ischemic image

CT_{HI} : Number of images misclassified as ischemic while images of hemorrhagic

CT_{HN} : Number of images misclassified as normal brain, while hemorrhagic image

CT_{NI} : Number of images misclassified as ischemic, while normal image

CT_{NH} : Number of images misclassified as hemorrhagic, while normal brain image

		Predicted		
		Ischemic	Hemorrhagic	Normal
Actual	Ischemic	CT_{II}	CT_{IH}	CT_{IN}
	Hemorrhagic	CT_{HI}	CT_{HH}	CT_{HN}
	Normal	CT_{NI}	CT_{NH}	CT_{NN}

Figure 3. Confusion Matrix

Performance metrics calculated using TP, TN, FP, and FN values are given in precision Equation 1, recall Equation 2, accuracy Equation 3, and F1-score Equation 4. Cumulative results were obtained for each model by taking the average and standard deviation of the performance values calculated separately for the five folds. Another performance criterion used in this study was the AUC value, which indicates the ROC. ROC curve is one of the graphs used in performance reviews. An AUC value of 1 indicates that the performance is 100% and the classification has been performed fully. The graph is drawn with the false positive rate value corresponding to the true positive rate value of each class. ROC is a probability curve and AUC shows the extent of decomposition. Figure 4 shows the confusion matrix and ROC graph obtained after the first fold of the AlexNet model. These graphs and matrices were created after each fold. Therefore, a total of 30 confusion matrices and 30 ROC graphs were obtained for six deep-learning models. In Figure 5, the flow diagram of the application carried out in this study is given.

$$Precision = \frac{TP}{TP+FP} \tag{1}$$

$$Recall = \frac{TP}{TP+FN} \tag{2}$$

$$F1-score = 2*\frac{Precision*Recall}{Precision+Recall} \tag{3}$$

$$Accuracy = \frac{TP+TN}{TP+FN+TN+FP} \tag{4}$$

(a)

(b)
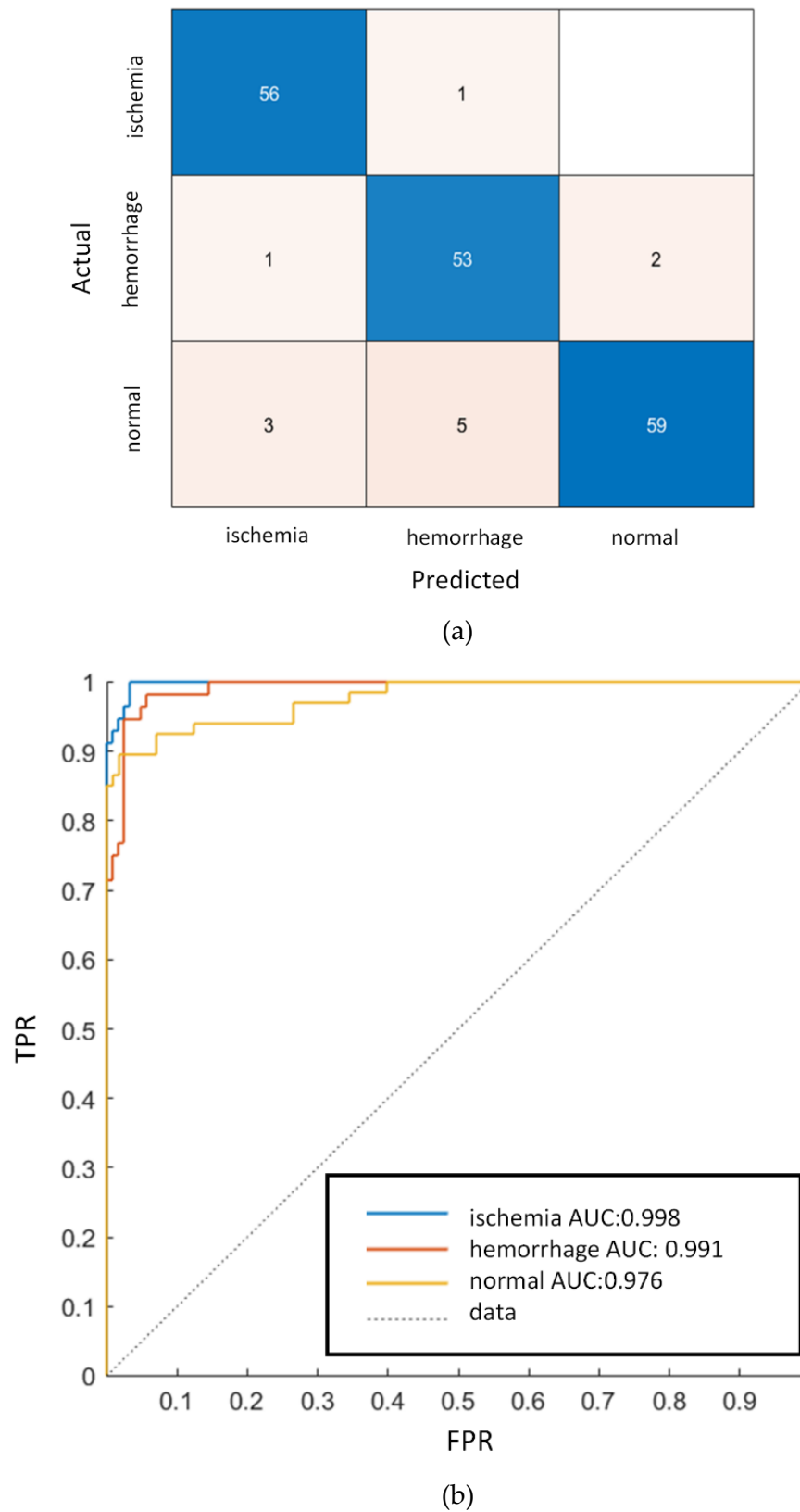
Figure 4. (a) Confusion matrix for first fold AlexNet (b) ROC graph for first fold AlexNet [39]
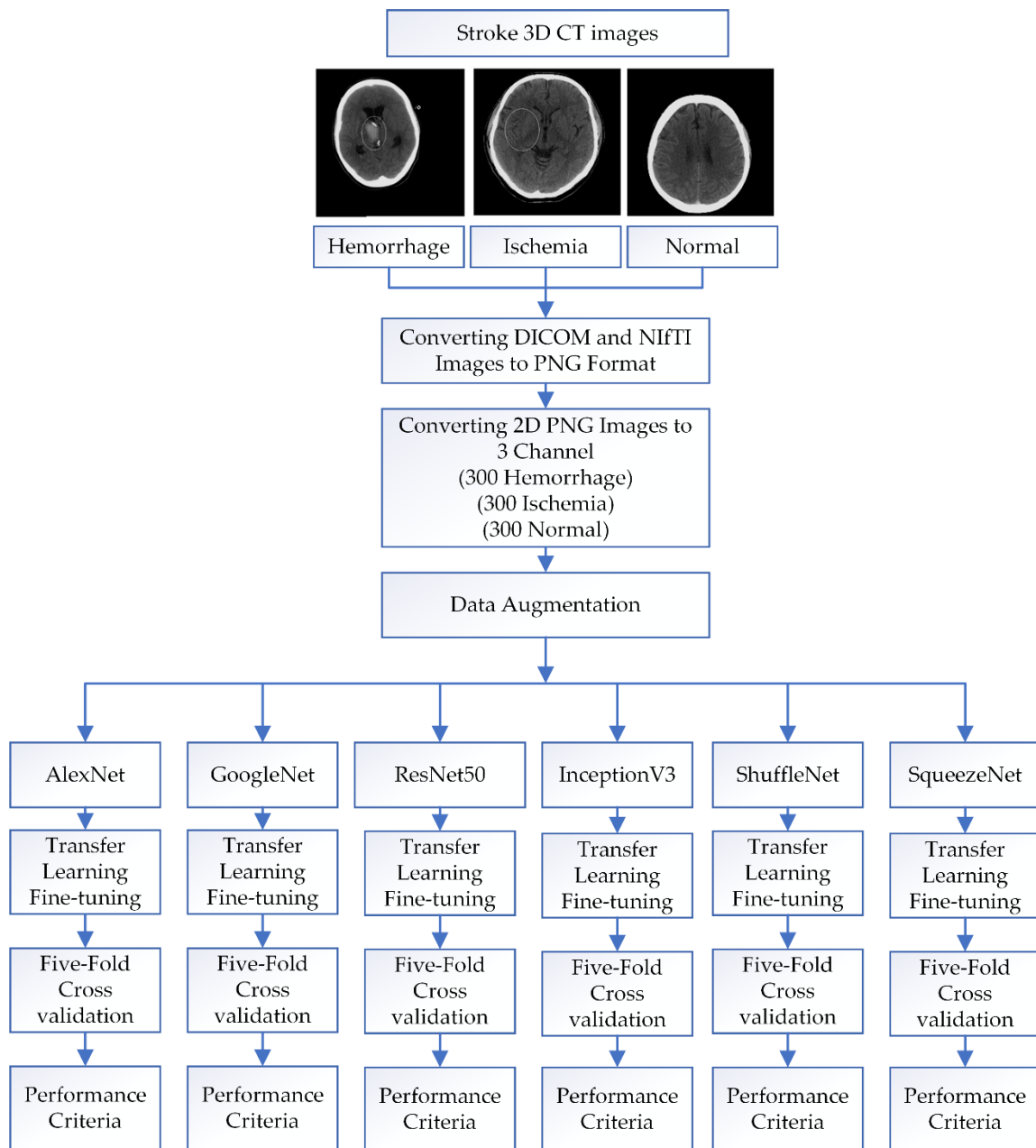
Figure 5. Flow chart of the application performed in this study.

3. RESULTS AND DISCUSSION

The average and standard deviation values of the performance criteria obtained as a result of the classification of ischemia, hemorrhage, and normal CT images using six deep learning (DL) models and five-fold cross-validation are given in Table 3.1. At the same time, the average training period is given in the table. In Table 3.2, the average AUC values of all deep learning models obtained according to classes are given.

Table 3.1. Performance criteria obtained as a result of the classification of six DL models [39]

DL Models	Precision	Recall	F1-Score	Accuracy	Training Time (hh:mm:ss)
AlexNet	0.9086±0.02	0.9097±0.02	0.9091±0.02	0.9089±0.02	00:21:37
ResNet50	0.9092±0.01	0.9081±0.01	0.9086±0.01	0.9067±0.01	02:33:23
GoogleNet	0.9058±0.019	0.9001±0.024	0.9029±0.021	0.9033±0.019	00:36:10
InceptionV3	0.8772±0.026	0.8781±0.021	0.8777±0.023	0.8778±0.026	00:56:38
ShuffleNet	0.9017±0.014	0.8982±0.018	0.9000±0.016	0.9000±0.015	00:36:27
SqueezeNet	0.8493±0.041	0.8374±0.052	0.8433±0.046	0.8411±0.044	00:16:44

Table 3.2. The average AUC values of all DL models [39]

DL Models	Ischemia	Hemorrhage	Normal
AlexNet	0.9920±0.005	0.9828±0.008	0.9686±0.012
ResNet50	0.9918±0.003	0.9856±0.003	0.9688±0.009
GoogleNet	0.9900±0.005	0.9794±0.004	0.9628±0.011
InceptionV3	0.9872±0.007	0.971±0.012	0.9432±0.025
ShuffleNet	0.9882±0.006	0.9784±0.003	0.9558±0.017
SqueezeNet	0.9874±0.005	0.9488±0.020	0.9358±0.027

When examining Table 3.1, the lowest average training time was 00:21:37 (hh:mm:ss), and the highest average accuracy result was 0.9089±0.02 from the AlexNet deep learning model. Although the classification performance values were generally close to each other, AlexNet yielded slightly higher results with fewer layers and a shorter training time. Although SqueezeNet had the shortest training time, it achieved the lowest result with an accuracy value of 0.8411±0.044. In general, it was observed that successful results were obtained in the classification of CT images using the transfer learning method of deep learning models. The average values of the area under the curve were calculated as 0.9920±0.005 for ischemia, 0.9828±0.008 for hemorrhage, and 0.9686±0.012 for normal using AlexNet. There are studies in the literature for the detection and classification of stroke with deep learning models and CT images [9-28]. However, many studies classify either hemorrhage or ischemia. In some studies, CT segmentation applications of the stroke-related region are carried out with different deep-learning models [13, 17, 41-44]. There are also studies that use MR images, which are acquired over a longer duration compared to CT images, to perform stroke classification [45-52]. The number of studies classifying normal, ischemia, and hemorrhage CT images is limited[9, 12, 14, 23]. Although studies have shown successful results in detecting only ischemia or hemorrhage, a person who arrives at the hospital with a suspected stroke cannot have only hemorrhage or ischemia. A patient who arrives with a suspected stroke can have one of three possibilities on the CT image: normal, ischemia, or hemorrhage. Therefore, deep learning-based clinical decision support systems capable of predicting and detecting these three classes can generate quick results for diagnosis. The applications and experiments conducted in this study have been carried out with this motivation. Dourado et al. developed an IoT system using deep learning for feature extraction and classical machine learning algorithms for classification. They used CT images of 140 normal cases, 140 hemorrhagic cases, and 140 ischemic cases. The dataset consisted of DICOM and grayscale images from two different databases, but no information about the data collection centers was provided. The data was split into 80% for training and 20% for testing, and classification experiments were performed using 10-fold cross-validation. For DICOM images, combining all convolutional neural network (CNN) architectures with various machine learning classifiers resulted in 100% accuracy, F1-score, recall, and precision. The highest accuracy rates were obtained when the classifiers were combined with InceptionV3, MobileNet, and VGG16 architectures. Similarly, for grayscale images, combining CNN architectures with different classifiers resulted in 100%

accuracy, F1-score, recall, and precision. The experiments showed that the highest accuracies were observed when different classifiers were combined with the NASNet Large architecture. The study used a transfer learning approach but did not mention data augmentation and the AUC metric [9]. Gautam and Raman created two different data sets in their study (Himalayan Institute of Medical Sciences (HIMS) in Dehradun, India). The first dataset consists of 192 brain images of two different classes: hemorrhagic stroke and ischemic stroke. The second data set is a data set containing three categories of brain CT scans (hemorrhagic stroke, ischemic stroke, and normal). This data set consists of a total of 900 brain images and includes 300 images for each category. Pre-processing techniques and image fusion were applied to enhance image quality. In this study, the approaches of transfer learning and data augmentation were not mentioned. Performance metrics including precision, TPR, FPR, F-measure, and accuracy were calculated. For the experiments to be performed on the first data set, the data set was divided into 70% training and 30% testing, and for the experiments on the second data set, the data set was divided into 80% training and 20% testing. Additionally, 10-fold cross-validation was applied in both experiments. In the first data set, the highest accuracy rate was obtained by the proposed CNN model called P_CNN with 98.33%. In the second data set, the highest accuracy rate was again obtained by the P_CNN model with 92.22%. [14]. Neethi et al. collected 3D CT images of 70 ischemic, 68 hemorrhagic, and 96 normal cases from the Sree Chitra Tirunal Institute for Medical Sciences and Technology (Trivandrum, India). A three-output classification study was carried out by developing a 3D CNN model with 3D CT images. The data was divided into 60% for training, 20% for validation, and 20% for testing to perform the model's performance. Data augmentation, cross-validation, and transfer learning approach were not used. The model performance result was 0.88 F1-score, 0.84 recall, 0.94 precision, and 0.92 accuracy. ROC and AUC values were not calculated. A voxel-based evaluation was made because it was a study using a 3D CNN model [23]. Pereira et al., with support from Clinical Trajano Almeida, collected a total of 100 normal, 100 ischemic, and 100 hemorrhagic CT images. Using the Particle Swarm Optimization method, a CNN model was optimized and utilized for classification. As a result of the study, a classification rate close to 99% was achieved. However, the study did not mention the utilization of transfer learning, cross-validation, or the AUC approach [12]. As observed in the studies, different deep learning models, images from various centers, varying data quantities, distinct performance criteria, diverse transfer learning, and data augmentation strategies, all contribute to significantly complexify result comparisons. Generally, high accuracy rates have been reported for three-class outputs. The differences in data quantities introduce uncertainties regarding how the diagnosis would perform across the entire stroke population. In this study, promising outcomes were achieved on data obtained from distinct centers and protocols. Especially the AUC values being very close to 100% indicate the substantial separability of one group from the others.

4. CONCLUSIONS

In this study, ischemia, hemorrhage, and normal CT images were classified using the transfer learning method in six different deep-learning models. The AlexNet model gave higher classification results than other models. Rapid diagnosis of hemorrhage and ischemia in CT images of patients suspected of having a stroke is essential. However, several factors can complicate stroke diagnosis, including time constraints, lack of experience, variations in interpretation based on experience, approximate pixel tone distributions in the images, confusion between hemorrhage and ischemia, a large number of images requiring evaluation in hospitals, and challenges in accessing doctors or radiologists in smaller cities. Because of this, deep learning-based clinical decision support systems can provide the opportunity for rapid diagnosis and early treatment. In advanced applications, the size, localization, and three-dimensional models of strokes can be developed using deep learning segmentation models. By developing mobile and desktop applications and embedding deep learning models that perform predictive tasks in the background, assistant diagnostic tools for doctors can be expected as a future technology in the field of medicine. In this study, it is clear that clinical decision support systems based on deep learning show significant potential in distinguishing and categorizing stroke types. However,

further research is needed in this area, which requires the use of comprehensive datasets covering various stroke subtypes, as well as the inclusion of standard assessment methodologies.

Acknowledgments

Declaration of Ethical Standards

The authors declare that there are no ethical standards.

Credit Authorship Contribution Statement

MA contributed to data processing, creation and running of models, calculation of performance evaluation metrics, and article writing. MÜÖ contributed to article writing and literature review.

Declaration of Competing Interest

There is no conflict of interest.

Funding / Acknowledgements

Data Availability

The authors used ISLES 2018 and RSNA datasets. These datasets are available to researchers and free of charge.

REFERENCES

[1]   M. Şahan, S. Satar, A. F. Koç, and A. Sebe, "İskemik İnme ve Akut Faz Reaktanları," *Arşiv Kaynak Tarama Dergisi,* vol. 19, no. 2, pp. 85-140, 2010.

[2]   M. Emre, "Nöroloji Temel Kitabı," Ankara: Güneş Tıp Kitapevleri, ch. 669-792, p. 1616, 2013.

[3]   C. W. Tsao *et al.*, "Heart disease and stroke statistics—2023 update: a report from the American Heart Association," *Circulation,* vol. 147, no. 8, pp. e93-e621, 2023.

[4]   R. Karthik, R. Menaka, A. Johnson, and S. Anand, "Neuroimaging and deep learning for brain stroke detection-A review of recent advancements and future prospects," *Computer Methods and Programs in Biomedicine,* p. 105728, 2020.

[5]   F. Yuce, M. Ü. Öziç, and M. Tassoker, "Detection of pulpal calcifications on bite-wing radiographs using deep learning," *Clinical Oral Investigations,* vol. 27, no. 6, pp. 2679-2689, 2023.

[6]   H. P. Chan, L. M. Hadjiiski, and R. K. Samala, "Computer-aided diagnosis in the era of deep learning," *Medical Physics,* vol. 47, no. 5, pp. e218-e227, 2020.

[7]   H. Fujita and technology, "AI-based computer-aided diagnosis (AI-CAD): the latest review to read first," *Radiological Physics,* vol. 13, no. 1, pp. 6-19, 2020.

[8]   C. Park, C. C. Took, and J.-K. Seong, "Machine learning in biomedical engineering," *Biomedical Engineering Letters,* vol. 8, pp. 1-3, 2018.

[9]   C. M. Dourado Jr, S. P. P. da Silva, R. V. M. da Nobrega, A. C. d. S. Barros, P. P. Reboucas Filho, and V. H. C. J. C. N. de Albuquerque, "Deep learning IoT system for online stroke detection in skull computed tomography images," *Computer Networks*, vol. 152, pp. 25-39, 2019.

[10]   T. D. Phong *et al.*, "Brain hemorrhage diagnosis by using deep learning," in *Proceedings of the 2017 International Conference on Machine Learning and Soft Computing*, 2017, pp. 34-39.

[11]   C.-L. Chin *et al.*, "An automated early ischemic stroke detection system using CNN deep learning algorithm," in *2017 IEEE 8th International Conference on Awareness Science and Technology (iCAST)*, Taiwan, 2017: IEEE, pp. 368-372.

[12]   D. R. Pereira, P. P. Reboucas Filho, G. H. de Rosa, J. P. Papa, and V. H. C. de Albuquerque, "Stroke lesion detection using convolutional neural networks," in *2018 International Joint Conference on Neural Networks (IJCNN)*, 2018: IEEE, pp. 1-6.

[13]   A. Majumdar, L. Brattain, B. Telfer, C. Farris, and J. Scalera, "Detecting intracranial hemorrhage with deep learning," in *2018 40th Annual International Conference of the IEEE Engineering in Medicine and Biology Society (EMBC)*, 2018: IEEE, pp. 583-587.

[14]   A. Gautam and B. Raman, "Towards effective classification of brain hemorrhagic and ischemic stroke using CNN," *Biomedical Signal Processing Control,* vol. 63, p. 102178, 2021.

[15]   J. Pan, G. Wu, J. Yu, D. Geng, J. Zhang, and Y. Wang, "Detecting the Early Infarct Core on Non-Contrast CT Images with a Deep Learning Residual Network," *Journal of Stroke Cerebrovascular Diseases,* vol. 30, no. 6, p. 105752, 2021.

[16]   C.-M. Lo, P.-H. Hung, and D.-T. Lin, "Rapid Assessment of Acute Ischemic Stroke by Computed Tomography Using Deep Convolutional Neural Networks," *Journal of Digital Imaging,* pp. 1-10, 2021.

[17]   Y. Watanabe *et al.*, "Improvement of the diagnostic accuracy for intracranial haemorrhage using deep learning–based computer-assisted detection," *Neuroradiology,* vol. 63, no. 5, pp. 713-720, 2021.

[18]   K. L. Gia *et al.*, "A Computer-Aided Detection to Intracranial Hemorrhage by Using Deep Learning: A Case Study," presented at the Green Technology and Sustainable Development 2020, Da Nang Eyaleti, Vietnam, 2020.

[19]   A. M. Dawud, K. Yurtkan, and H. Oztoprak, "Application of deep learning in neuroradiology: Brain haemorrhage classification using transfer learning," *Computational Intelligence Neuroscience,* vol. 2019, 2019.

[20]   S.-M. Jung and T.-K. Whangbo, "A Deep Learning System for Diagnosing Ischemic Stroke by Applying Adaptive Transfer Learning," *Journal of Internet Technology,* vol. 21, no. 7, pp. 1957-1968, 2020.

[21]   O. Öman, T. Mäkelä, E. Salli, S. Savolainen, and M. Kangasniemi, "3D convolutional neural networks applied to CT angiography in the detection of acute ischemic stroke," *European Radiology Experimental,* vol. 3, no. 1, pp. 1-11, 2019.

[22]   Y. Shinohara, N. Takahashi, Y. Lee, T. Ohmura, and T. Kinoshita, "Development of a deep learning model to identify hyperdense MCA sign in patients with acute ischemic stroke," *Japanese Journal of Radiology,* vol. 38, no. 2, pp. 112-117, 2020.

[23]   A. Neethi, S. Niyas, S. K. Kannath, J. Mathew, A. M. Anzar, and J. Rajan, "Stroke classification from computed tomography scans using 3d convolutional neural network," *Biomedical Signal Processing and Control,* vol. 76, p. 103720, 2022.

[24]   O. Ozaltin, O. Coskun, O. Yeniay, and A. Subasi, "A Deep Learning Approach for Detecting Stroke from Brain CT Images Using OzNet," *Bioengineering,* vol. 9, no. 12, p. 783, 2022.

[25]   S. Korra, R. Mamidi, N. R. Soora, K. V. Kumar, and N. C. S. Kumar, "Intracranial hemorrhage subtype classification using learned fully connected separable convolutional network," *Concurrency and Computation: Practice and Experience,* vol. 34, no. 24, p. e7218, 2022.

[26]   A. A. M. Suberi, W. N. W. Zakaria, R. Tomari, A. Nazari, M. N. H. Mohd, and N. F. N. Fuad, "Deep transfer learning application for automated ischemic classification in posterior fossa CT images," *International Journal of Advanced Computer Science and Applications,* vol. 10, no. 8, 2019.

[27]   B. A. Mohammed *et al.*, "Multi-method diagnosis of CT images for rapid detection of intracranial hemorrhages based on deep and hybrid learning," *Electronics,* vol. 11, no. 15, p. 2460, 2022.

[28]   T. H. Gençtürk, F. K. Gülağiz, and K. İsmail, "Derin Öğrenme Yöntemleri Kullanılarak BT Taramalarında Beyin Kanaması Teşhisinin Karşılaştırmalı Bir Analizi," *Journal of Intelligent Systems: Theory and Applications,* vol. 6, no. 1, pp. 75-84, 2023.

[29]   A. Hakim *et al.* "Ischemic Stroke Lesion Segmentation." Available: http://www.isles challenge.org/ [Accessed: May 7, 2020].

[30]   RSNA. "Intracranial Hemorrhage Detection." Radiological Society of North America. Available: https://www.kaggle.com/c/rsna-intracranial-hemorrhage-detection/rules [Accessed: Oct. 30, 2020].

[31]   A. Krizhevsky, I. Sutskever, and G. E. Hinton, "Imagenet classification with deep convolutional neural networks," *Advances in neural information processing systems,* vol. 25, pp. 1097-1105, 2012.

[32]   K. He, X. Zhang, S. Ren, and J. Sun, "Deep residual learning for image recognition," in *Proceedings of the IEEE Conference on Computer Vision and Pattern Recognition*, 2016, pp. 770-778.

[33]   C. Szegedy *et al.*, "Going deeper with convolutions," in *Proceedings of the IEEE Conference on Computer Vision and Pattern Recognition*, 2015, pp. 1-9.

[34]   C. Szegedy, V. Vanhoucke, S. Ioffe, J. Shlens, and Z. Wojna, "Rethinking the inception architecture for computer vision," in *Proceedings of the IEEE Conference on Computer Vision and Pattern Recognition*, 2016, pp. 2818-2826.

[35]   X. Zhang, X. Zhou, M. Lin, and J. Sun, "Shufflenet: An extremely efficient convolutional neural network for mobile devices," in *Proceedings of the IEEE Conference on Computer Vision and Pattern Recognition*, 2018, pp. 6848-6856.

[36]   F. N. Iandola, S. Han, M. W. Moskewicz, K. Ashraf, W. J. Dally, and K. Keutzer, "SqueezeNet: AlexNet-level accuracy with 50x fewer parameters and < 0.5 MB model size," *arXiv preprint arXiv:1602.07360,* 2016.

[37]   C. W. Cereda *et al.*, "A benchmarking tool to evaluate computer tomography perfusion infarct core predictions against a DWI standard," *Journal of Cerebral Blood Flow & Metabolism,* vol. 36, no. 10, pp. 1780-1789, 2016.

[38]   Neuroimaging Informatics Tools and Resources Clearinghouse. "MRIcro." McCausland Brain Imaging Center. Available: https://www.nitrc.org/projects/mricro/ [Accessed: Oct. 20, 2020].

[39]   M. Altıntaş, "Classification of Stroke with Different Deep Learning Models in Computerized Tomography Images," Master's Thesis, Department of Biomedical Engineering, Graduate School of Natural and Applied Sciences, Necmettin Erbakan University, Türkiye, 2021.

[40]   Z. N. K. Swati *et al.*, "Brain tumor classification for MR images using transfer learning and fine-tuning," *Computerized Medical Imaging and Graphics,* vol. 75, pp. 34-46, 2019.

[41]   M. Soltanpour, R. Greiner, P. Boulanger, and B. Buck, "Ischemic Stroke Lesion Prediction in CT Perfusion Scans Using Multiple Parallel U-Nets Following by a Pixel-Level Classifier," in *2019 IEEE 19th International Conference on Bioinformatics and Bioengineering (BIBE)*, 2019: IEEE, pp. 957-963.

[42]   S. Yalçın and H. Vural, "Brain stroke classification and segmentation using encoder-decoder based deep convolutional neural networks," *Computers in Biology and Medicine,* vol. 149, p. 105941, 2022.

[43]   I. Guerrón, N. Peréz, D. Benítez, F. Grijalva, D. Riofrío, and M. Baldeon-Calisto, "Extending the U-Net Architecture for Strokes Segmentation on CT Scan Images," in *2023 IEEE 13th International Conference on Pattern Recognition Systems (ICPRS)*, 2023: IEEE, pp. 1-7.

[44]   S. Yalcin, "Hybrid Convolutional Neural Network Method for Robust Brain Stroke Diagnosis and Segmentation," *Balkan Journal of Electrical and Computer Engineering,* vol. 10, no. 4, pp. 410-418, 2022.

[45]   Z. Liu, C. Cao, S. Ding, Z. Liu, T. Han, and S. J. I. A. Liu, "Towards clinical diagnosis: Automated stroke lesion segmentation on multi-spectral MR image using convolutional neural network," *IEEE Access*, vol. 6, pp. 57006-57016, 2018.

[46]   L. Chen, P. Bentley, and D. Rueckert, "Fully automatic acute ischemic lesion segmentation in DWI using convolutional neural networks," *NeuroImage: Clinical,* vol. 15, pp. 633-643, 2017.

[47]   A. Clèrigues *et al.*, "Acute and sub-acute stroke lesion segmentation from multimodal MRI," *Computer Methods and Programs in Biomedicine,* vol. 194, p. 105521, 2020.

[48]   J. Hong, H. Cheng, Y.-D. Zhang, and J. Liu, "Detecting cerebral microbleeds with transfer learning," *Machine Vision Applications,* vol. 30, no. 7, pp. 1123-1133, 2019.

[49]   Y. Yu *et al.*, "Use of deep learning to predict final ischemic stroke lesions from initial magnetic resonance imaging," *JAMA Network Open,* vol. 3, no. 3, pp. e200772-e200772, 2020.

[50]   L. Zhang *et al.*, "Ischemic Stroke Lesion Segmentation Using Multi-Plane Information Fusion," *IEEE Access,* vol. 8, pp. 45715-45725, 2020.

[51]   R. Zhang *et al.*, "Automatic segmentation of acute ischemic stroke from DWI using 3-D fully convolutional DenseNets," *IEEE Transactions on Medical Imaging,* vol. 37, no. 9, pp. 2149-2160, 2018.

[52]   C. U. Perez Malla, M. d. C. Valdes Hernandez, M. F. Rachmadi, and T. Komura, "Evaluation of enhanced learning techniques for segmenting ischaemic stroke lesions in brain magnetic resonance perfusion images using a convolutional neural network scheme," *Frontiers in Neuroinformatics,* vol. 13, p. 33, 2019.

MACHINE LEARNING AS A POWERFUL TOOL FOR PERFORMANCE PREDICTION AND OPTIMIZATION OF CONCENTRATED PHOTOVOLTAIC-THERMOELECTRIC SYSTEM

[1] **Aminu YUSUF** [iD], [2, *] **Nevra BAYHAN** [iD], [3] **Hasan TİRYAKİ** [iD], [4] **Sedat BALLIKAYA** [iD]

[1,4] *Istanbul University-Cerrahpaşa, Engineering Faculty, Engineering Sciences Department, Istanbul, TÜRKİYE*
[2,3] *Istanbul University-Cerrahpaşa, Engineering Faculty, Electrical and Electronics Engineering Department, Istanbul, TÜRKİYE*
[1] aminu.yusuf@iuc.edu.tr, [2] nevra@iuc.edu.tr, [3] hasan.tiryaki@iuc.edu.tr, [4] ballikaya@iuc.edu.tr

Highlights

- PS, MOGA, and GOAL-MOGA optimizations were used to optimize a CPV-TE system.

- Machine learning algorithms were trained using datasets of MOGA and GOAL-MOGA.

- ANN-based ML algorithm has an average prediction error of 0.0692%.

- The ANN-based ML also has a correlation coefficient of $R^2 \approx 1$ on the test data.

- ANN-based optimization can accurately predict the performance of the CPV-TE system.

*Corresponding Author: Nevra BAYHAN, nevra@iuc.edu.tr

MACHINE LEARNING AS A POWERFUL TOOL FOR PERFORMANCE PREDICTION AND OPTIMIZATION OF CONCENTRATED PHOTOVOLTAIC-THERMOELECTRIC SYSTEM

[1] Aminu YUSUF [ID], [2,*] Nevra BAYHAN [ID], [3] Hasan TİRYAKİ [ID], [4] Sedat BALLIKAYA [ID]

[1,4] *Istanbul University-Cerrahpaşa, Engineering Faculty, Engineering Sciences Department, Istanbul, TÜRKİYE*
[2,3] *Istanbul University-Cerrahpaşa, Engineering Faculty, Electrical and Electronics Engineering Department, Istanbul, TÜRKİYE*
[1] aminu.yusuf@iuc.edu.tr, [2] nevra@iuc.edu.tr, [3] hasan.tiryaki@iuc.edu.tr, [4] ballikaya@iuc.edu.tr

ABSTRACT: Because there is a critical necessity to ensure the optimal operation of concentrated photovoltaic-thermoelectric (CPV-TE) systems, various optimization methods such as Paretosearch (PS), Multi-objective genetic algorithm (MOGA), and the hybrid Goal Attainment – Multi-objective genetic algorithm (GOAL-MOGA) are commonly employed. These approaches aim to enhance both the output power and energy efficiency of CPV-TE systems. By combining the Pareto fronts generated by MOGA and GOAL-MOGA, 19 distinct machine learning (ML) algorithms were trained. The findings demonstrate that the Artificial Neural Network (ANN) ML algorithm outperforms others, displaying an average prediction error of 0.0692% on the test dataset. In addition to its prediction capability, the ANN-based ML model can be viewed as an optimization model since it produces optimized outputs similar to those from MOGA and GOAL-MOGA. The ANN-based ML algorithm performs better when trained on a combined dataset from both MOGA and GOAL-MOGA compared to using either MOGA or GOAL-MOGA alone. To enhance the optimization capability of the ANN-based ML algorithm further, more Pareto fronts from other optimization techniques can be added.

Keywords: Concentrated Photovoltaic, Thermoelectric Module, Machine Learning, Optimization, Prediction

1. INTRODUCTION

Solar energy is a crucial green energy source with diverse applications, including domestic heating, crop drying, and electrical energy generation. Photovoltaic (PV) and thermoelectric (TE) devices are technologies used for converting solar energy into electrical energy. However, these technologies utilize different solar energy spectrums, resulting in each device's ability to convert only a portion of solar energy into electricity [1]. Combining these devices allows for full utilization of the solar spectrum, potentially enhancing energy output. Nonetheless, this integration doesn't always guarantee increased efficiency due to the PV's operational principles being nearly opposite to those of the thermoelectric generator (TEG). While PV performance declines with rising temperatures [2], TEG's performance improves under the same conditions [3]. Consequently, optimizing the combined concentrated photovoltaic-thermoelectric (CPV-TEG) system becomes essential to ascertain its optimal parameters.

For instance, the influence of TE leg geometry [4], load resistance [5], thermal resistance, Thomson coefficient [6], cooling fluid [7], and system configurations [8] on the CPV-TE system's performance has been studied. Many optimization studies concentrate on single-parameter optimization, which is time-consuming. This method often fails to identify the optimal operational point due to the system's dependency on numerous parameters. Conversely, multi-objective multi-parameter optimization is rapid and can identify the global optimum of the CPV-TE system [9, 10]. This approach yields non-dominative optimal solutions that strike the best balance between multiple system outputs. However, it is important to note that modelling complexity escalates with an increase in the number of parameters, and finding a global optimum is not guaranteed.

Concentrated PV systems are typically integrated with maximum power point tracking (MMPT) algorithms to harvest maximum output power throughout the day. Traditional methods like Perturb &

*Corresponding Author: Nevra BAYHAN, nevra@iuc.edu.tr

Observe (PO) and incremental conductance lack accuracy and response time, often causing oscillations around the maximum power point in a steady state [11]. To address these limitations, advanced control methods, including artificial intelligence such as fuzzy logic, neural networks, and genetic algorithms, have been introduced [12]. Experimental results demonstrate that using a fuzzy logic controller in a solar tracking system increases the efficiency of energy conversion of the PV panels [13]. In another study [14], an adaptive fuzzy logic MPPT controller outperforms conventional techniques in terms of efficiency, tracking ability, and harmonic reduction. It exhibits a faster response to the PV system, even without knowledge of the actual model, and ensures the optimal operating point remains stable without oscillation around the MPP.

Incorporating machine learning (ML) into multi-objective multi-parameter optimization could significantly advance research in mathematical programming. ML is a system employing complex algorithms and statistical models to discern patterns and trends in data [15]. Recent advancements have made ML an increasingly indispensable tool in various sectors. One notable application is predicting short-term and long-term output performance of stand-alone PVs [16-18], TEGs [19, 20], and CPV-TE systems [21]. Such predictions aid in preventing partial or total power blackouts by enabling strategic planning during energy system operations. Moreover, ML implementation has led to considerable reductions in computational time and modelling complexity [22-24].

Aligned with the aforementioned studies, this work aims to demonstrate ML's ability to predict and optimize a CPV-TE system. By amalgamating the Pareto front from various optimization techniques, a robust ML model can be developed. This study endeavours to bridge the existing research gap between ML, energy systems, and optimization techniques.

2. MATERIAL AND METHODS

2.1. Concentrated Photovoltaic-Thermoelectric System (CPV-TE)

The depicted system in Figure 1 comprises a linear solar concentrator, PV, TEG, and heat sink. While the PV can convert a portion of the concentrated solar energy into electrical power, the remaining energy takes the form of thermal energy used by the TEG. A heat sink is affixed to the TEG's cold side to establish a substantial temperature gradient. Additionally, thermal grease (8 Wm^{-1}K^{-1}) is assumed to be placed between the PV, TEG, and heat sink to mitigate thermal resistance among these components.
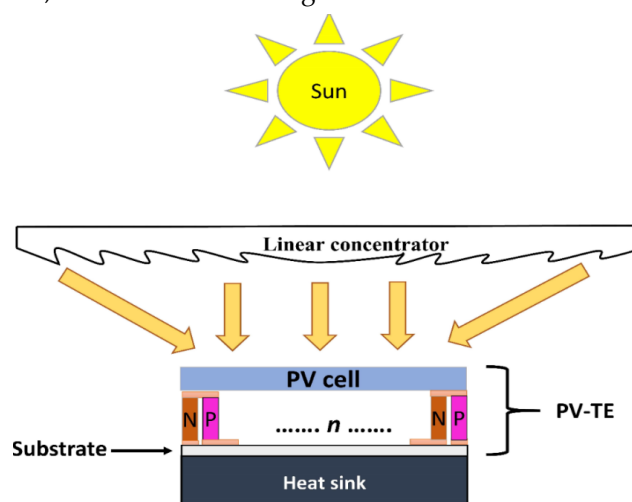
Figure 1. Proposed CPV-TE System

Should the upper ceramic plate of the TEG be eliminated, the temperatures of both the hot side of the TEG and the rear side of the PV become nearly identical. Consequently, the temperature of the hot side can be approximated as [25]:

$$T_h = T_a + Ge^{a+bv} \tag{1}$$

where G is the solar irradiance, T is the ambient temperature, and v is the wind speed measured at a height of 10 m. For a linear concentrator of 22, a and b are empirically determined to be -3.23 and -0.13, respectively. The temperature of the PV can be computed in relation to the temperature of the hot side as [25]:

$$T_{pv} = T_a + Ge^{a+bv} + \frac{G\,\Delta T}{G_s} \tag{2}$$

where G_s is the solar irradiance measured at a standard test condition, $\Delta T = T_{pv} - T_h$ is measured at a standard test condition of 1000 Wm^{-2}. For a solar concentration ratio of 22, the ΔT is empirically found to be 13.

From Equation 2, the electrical output of the PV can be given by:

$$P_{pv} = CGA_{pv}\tau_g\eta_r\left(1 - \beta(T_{pv} - 25)\right) \tag{3}$$

where A_{pv} is the surface area of the PV, β is the temperature coefficient of the PV, η_r is the reference efficiency of the PV, and τ_g is the transmissivity of glass.

A fraction of the thermal energy absorbed by the TEG gets transformed into electrical energy, whereas the remaining portion is dissipated through the cold side. Therefore, the electrical output of the TEG is calculated as follows:

$$P_{te} = NI[(S_hT_h - S_cT_c) - \tau(T_h - T_c) - IR] \tag{4}$$

where I is the electric current of one pair of thermoelement, $N = 127$ is the number of pairs of thermoelements, τ is the Thomson coefficient, R is the internal resistance of one pair of thermoelement, S_h and S_c are the Seebeck coefficients of the hot and cold sides of the TEG, respectively.

The internal resistance in Equation 4 is computed as:

$$R = \frac{L}{\sigma_p A_p} + \frac{L}{\sigma_n A_n} \tag{5}$$

where L is the length of thermoelements, A_p and A_n are the cross-sectional areas of the thermoelements, σ_p and σ_n are the electrical conductivities of the p- and n-type TE materials.

While the temperature of the cold side in Equation 4 depends on both the temperature of the hot side and the parameters of the heat sink as given by Equation 6:

$$T_c = \frac{T_h + hT_a A_{te} R_{kt}}{1 + h A_{te} R_{kt}} \tag{6}$$

where A_{te} is the surface area of the TEG, R_{kt} is the thermal resistance of the TEG, and h is the heat transfer coefficient. Similarly, the thermal resistance of the TEG is given as:

$$R_{kt} = \frac{L}{N\left(A_n k_n + A_p k_p\right)} \tag{7}$$

where k_n and k_p are the thermal conductivities of the n- and p-type TE materials. The TE materials are temperature dependent and are given in Table 1 while the parameters of the PV are given in Table 2.

Table 1. Temperature dependent TE materials

Variable	Bi_2Te_3 [26]
$S = Sp–(–Sn)$	$(44448 + 1861.2T_m − 1.981T_m^2) \times 10^{-9}$ V/K
$\sigma_p = \sigma_n$	$[(5112 + 163.4Tm + 0.6279T_m^2) \times 10 − 10 \, (\Omega m)]^{-1}$
$k_p = k_n$	$(62605 − 277.7T_m + 0.4131T_m^2) \times 10^{-4}$ W/(m K)
$\tau = \tau_p - (-\tau_n)$	$(1861.2T_m − 3.962T_m^2) \times 10^{-9}$ V/K

Table 2. Parameters of the PV [27]

Parameter	Symbol	Value
Area of PV/TEG	A_{pv}	$16 \times 10^{-4} \, m^2$
Reference efficiency of PV	η_r	15.6%
Transmissivity of glass	τ_g	0.95
Efficiency temperature coefficient of PV	β	$45 \times 10^{-3} \, K^{-1}$

The electrical output and energy efficiency of the system are respectively given as:

$$P_{sys} = P_{pv} + P_{te} \tag{8}$$

$$\eta_{sys} = \frac{P_{pv} + P_{te}}{CGA} \tag{9}$$

The above equations are then used in the optimization process.

2.2. Optimization of the CPV-TE System

Due to the conflicting operational principles of photovoltaics and thermoelectric generators, the hybrid system consistently requires optimization to achieve peak performance. Furthermore, optimization efforts can contribute to material cost reduction and an extension of the hybrid system's lifespan. Regrettably, there exists no assurance that a specific algorithm will excel across all optimization problem types. To address this issue, researchers frequently compare multiple algorithms' performances on a particular optimization problem, selecting the algorithm that demonstrates the most favorable performance. In this context, three well-established algorithms—namely, the multi-objective genetic algorithm (MOGA) [28], Paretosearch (PS) [29, 30], and hybrid Goal Attainment – Genetic Algorithm (GOAL – MOGA) [31, 32] are employed to optimize the CPV-TE system using the MATLAB optimization toolbox. While MOGA and PS are individual optimization techniques, GOAL – MOGA represents a hybrid algorithm combining the strengths of both, thereby exhibiting greater potency than a single algorithm. The optimization variables considered in this study are given in Table 3.

Table 3. Optimization variables

Parameter	Symbol	Range
Solar irradiance	G	$200 – 1000$ Wm^{-2}
Wind speed	v	$2 – 11$ ms^{-1}
Ambient temperature	T_a	$15 – 40$ °C
Temperature between top and back surfaces of PV	ΔT	$3 – 20$ °C
Electric current	I	$1 – 100$ mA
Length of thermoelement	L	$0.5 – 4 \times 10^{-3}$ m
Cross-sectional area of thermoelement	$A_{n/p}$	$1 – 5 \times 10^{-6} \, m^2$
Heat transfer coefficient	h	$100 – 2000$ Wm^{-2}K^{-1}

The optimization process involves two primary objectives: maximizing output power and

maximizing energy efficiency of the system, as represented by Equations 8 and 9, respectively. The variables subject to optimization encompass both the system's parameters and prevailing weather conditions. Traditionally, system parameters are optimized under fixed weather conditions. However, since weather conditions fluctuate throughout the day and across seasons, optimal performance is achieved only when these conditions align with those during optimization. For instance, if the system is optimized based on summer weather, its performance will be suboptimal during winter, spring, and fall. To address this, our study incorporates weather conditions as dynamic optimization variables. This approach allows us to identify both the system parameters and weather conditions that yield maximum output. By revealing the Pareto optimal solution, our optimization results provide insights into the system's performance throughout the year. The Subset of the optimization outputs for the three algorithms is given in Appendix A.

2.3. Machine Learning Method

Each algorithm used for optimization in this study encompasses two objective functions, aiming to maximize the system's output power and energy efficiency. As these objectives cannot simultaneously reach their maximum values, the result is a collection of non-dominating solutions forming a Pareto front. These solutions represent optimal trade-offs between the two objective functions. To ensure a broad exploration of the search space and generate substantial data suitable for machine learning (ML), a large population size is selected for each algorithm. Moreover, running the three algorithms multiple times prevents them from getting stuck in local minima. Upon completion of the algorithms, both MOGA and the GOAL – MOGA hybrid produce 1400 datasets each, which are then merged to create a comprehensive dataset for ML. Consequently, the ML model acquires optimization capabilities akin to both the MOGA and GOAL-MOGA hybrid algorithms. This combined dataset of 2800 entries are employed to train various ML methods within the WEKA 3.8.5 program. The primary objective is to identify the ML method exhibiting superior predictive and optimization performance. In this scenario, only the optimized output power is predicted, considering that energy efficiency can be straightforwardly derived from the output power. The combined dataset undergoes classification into training (90% of the data) and testing (10% of the data) subsets. It is important to highlight that the ML algorithms are exclusively trained using the training data to predict outcomes on the test data accurately. To ensure an objective evaluation, the obtained training results from diverse ML methods are compared using performance criteria such as Mean Absolute Error (MAE), Root Mean Square Error (RMSE), and Correlation Coefficient (R^2), whose formulae are detailed in Table 4.

Table 4. Performance criteria

R^2	RMSE	**MAE**
$1 - \dfrac{\sum_{l=1}^{n}(y_i - \widehat{y_l})^2}{\sum_{l=1}^{n}(y_i - \widehat{y_{avg}})^2}$	$\sqrt{\dfrac{1}{n}\sum_{i=1}^{n}(y_i - \widehat{y_l})^2}$	$\dfrac{1}{n}\sum_{i=1}^{n}|y_i - \widehat{y_l}|$

where y_i, $\widehat{y_l}$, and $\widehat{y_{avg}}$ are the desired output, the predicted output, and the average of the desired output, respectively, and n represents each sample in the dataset [33].

2.3.1 Training phase

Table 5 showcases a random subset extracted from the complete training dataset, which comprises 2520 samples utilized to train 19 distinct ML algorithms. Each dataset within this subset comprises 8 input parameters and 1 output (representing output power), aligning with the optimization variables and objective function employed in the optimization algorithms.

Table 5. Sample training data

Parameter	Training Data 1	Training Data 2520
G (W/m^2)	200.0100902	999.9998231
v (m/s)	0.753583	0.500053
Ta (^{o}C)	29.99898876	29.99972218
I (mA)	99.96031788	1.054309357
L (mm)	3.999981986	0.583339642
Ap/n (mm^2)	1.000123794	4.999859674
h (W/(m^2 K))	656.4862416	573.603443
Delta T (^{o}C)	19.99098467	19.99995895
Output Power (W)	0.921398994	3.759967994

Table 6 presents the performance of the ML algorithms in respect to the prediction of the optimized output power on the training data. The success of ML algorithms is usually based on the R^2, RMSE, MAE, and computational time. For high prediction accuracy, it is desired that the R^2 approaches unity, while the RMSE and MAE should approach zero. Moreover, the computational time should be small.

Table 6. Training results

ML Algorithm	Duration (seconds)	R^2	RMSE	MAE
Artificial Neural Networks	**48.22**	**1.0000**	**0.0019**	**0.0012**
M5P	0.04	1.0000	0.0049	0.0027
M5Rules	0.55	1.0000	0.0055	0.0035
Random Committee	0.50	1.0000	0.0067	0.0052
Random Forest	0.93	0.9999	0.0095	0.0065
Bagging	0.43	0.9999	0.0087	0.0069
KStar	29.83	0.9998	0.0142	0.0036
Random Tree (RT)	0.01	0.9997	0.0171	0.0139
REPTree	0.01	0.9997	0.0187	0.0155
Linear Regression	0.09	0.9971	0.0557	0.0456
Support Vector Machines	10.88	0.9970	0.0602	0.0428
Simple Linear Regression	0.03	0.9969	0.0578	0.0477
Gaussian Process	54.42	0.9968	0.0594	0.4740
Regression by Discretization	5.60	0.9940	0.0804	0.6920
Decision Table	0.13	0.9937	0.0826	0.0707
Additive Regression	0.04	0.9796	0.1494	0.1220
Random Sub Space	0.38	0.9690	0.2168	0.1780
LWL	10.38	0.8840	0.3447	0.2935
Decision Stump	0.03	0.8571	0.3798	0.3233

In Table 6, it is worth observing that as the correlation coefficient of most of the ML algorithms approach unity, while concurrently, both RMSE and MAE tend towards zero. Remarkably, despite completing training in 48.22 seconds, the Artificial Neural Networks (ANN-Multilayer Perceptron) exhibit the most outstanding performance concerning the correlation coefficient, RMSE, and MAE. Figure 2 illustrates the prediction performance of the ANN-based ML concerning the actual training data, while Figure 3 depicts the correlation between the actual training data and the predicted data. Due to the high prediction accuracy of the ANN-based ML on the training data, the actual training and predicted output power remain indistinguishable. This performance is further solidified with Figure 3, where a very good agreement can be seen between the training and the predicted dataset because the correlation coefficient is $R^2 = 1$.
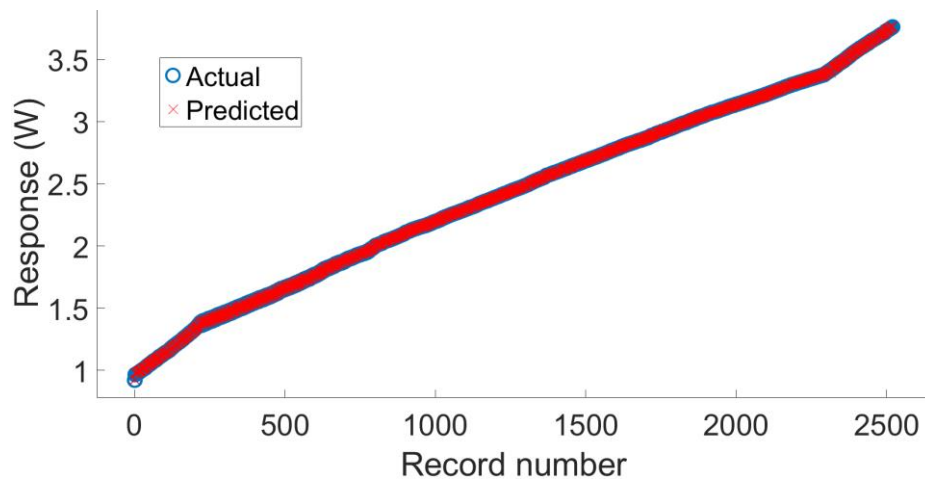
Figure 2. Actual and predicted training data
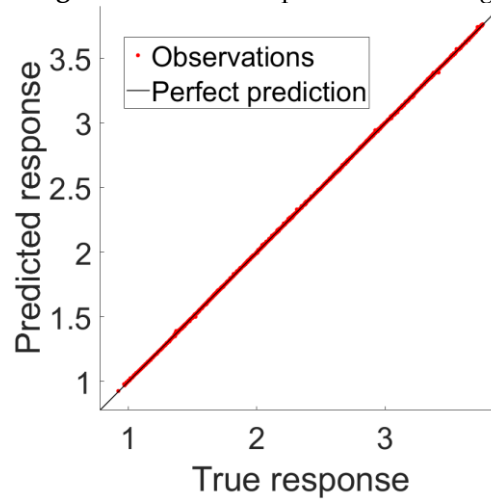
Figure 3. Correlation between the actual training data and the predicted data

2.3.1 Testing and prediction phase

All the ML methods used during training are also used during the testing phase. Table 7 presents a sample of the test data.

Table 7. Actual test data

Parameter	Test Data 1	Test Data 280
G (W/m²)	200.0003864	994.103292
v (m/s)	0.501314	0.500595
Ta (°C)	29.99990794	29.99981498
I (mA)	1.804981179	1.09343441
L (mm)	0.507706014	0.64921773
Ap/n (mm²)	4.933844599	4.91306995
h (W/(m² K))	285.2222814	567.3205518
Delta T (°C)	19.99887316	19.99919087
Output Power (W)	0.966334315	3.745774637

As previously stated, the test data (comprising 280 samples) remains entirely separate from the training and validation processes. Therefore, this test data is entirely new to the ML algorithms. During the testing phase, the ML methods predict the output power since the actual output of the test dataset is

not provided.

3. RESULTS AND DISCUSSION

Reiterating the two primary objectives of maximizing the output power and energy efficiency of the CPV-TE system, it is important to note that achieving the optimal value for both objectives simultaneously is unfeasible. Hence, a Pareto optimal solution needs to be identified. Each point situated on the Pareto front signifies a trade-off between the two objective functions. Figure 4 illustrates the Pareto front generated by the PS, MOGA, and GOAL-MOGA algorithms. Comparing the optimization performance of MOGA and PS reveals that MOGA tends to find higher energy efficiency, whereas PS excels in finding higher output power. This highlights the varying strengths of different optimization algorithms when applied to the same problem. The extreme values of the energy efficiency and output power for the MOGA were 13.8% and 3.35 W, respectively. Likewise, the extreme values of the energy efficiency and output power for the PS were 12.9% and 3.75 W, respectively. To enhance the optimization performance, MOGA was integrated with the Goal Attainment algorithm. The optimization process begins with Goal attainment, and upon its completion, MOGA takes over. This hybrid approach improves the output power in comparison with the output power searched by the MOGA alone, while maintaining higher energy efficiency than that of the PS. Thus, the hybrid algorithm has the highest energy efficiency of 13.15% and highest output power of 3.75 W. This indicates 11.9% power enhancement of the hybrid algorithm in comparison with MOGA alone and 1.9% energy efficiency enhancement in comparison with the energy efficiency of PS.
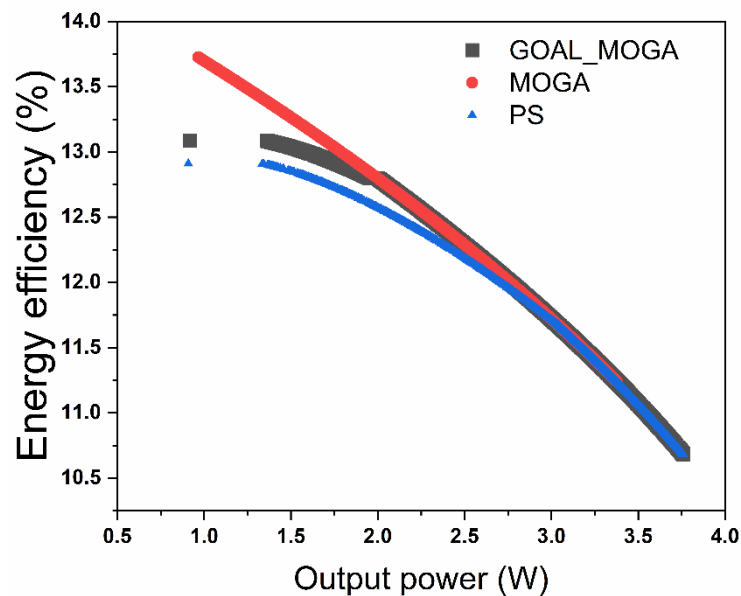
Figure 4. Pareto front: three algorithms

Figure 5 mirrors Figure 4, with the exclusion of the PS algorithm due to its inferior performance, hence not utilized in training the ML algorithms. The rationale behind combining the datasets from MOGA and GOAL-MOGA is to develop an ML model that surpasses any single optimization algorithm. This implies that the ML algorithm can predict the highest optimized energy efficiency similar to MOGA and the highest optimized output power similar to the GOAL-MOGA algorithm. This capability of the ML model can be improved by incorporating data from other optimization algorithms with varying performance levels.
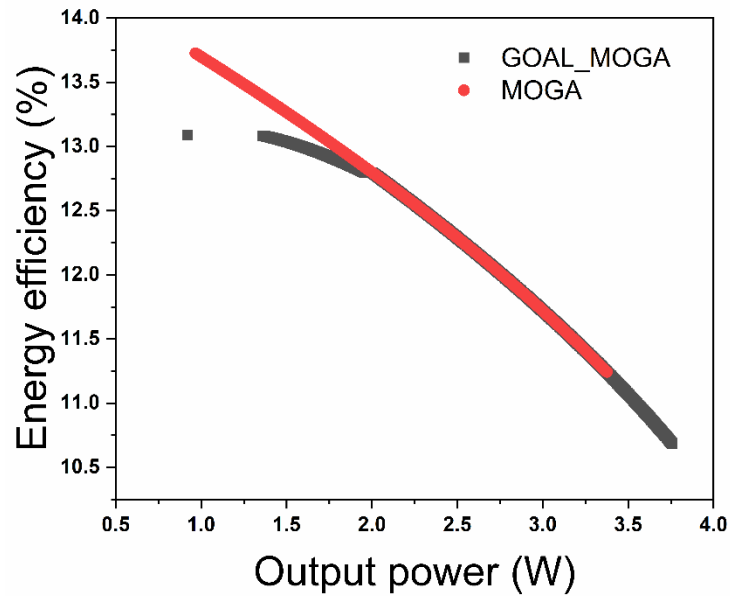
Figure 5. Pareto front: two algorithms

Table 8 presents the prediction performance of the ML algorithms on the test dataset in descending order from the top to the bottom of the Table. For each algorithm, maximum, minimum, and average prediction errors were determined. The performance of the ML algorithms on the test data is similar to their performance on the training data as presented in Table 6. As can be seen in Table 8, the ANN-based ML has the lowest percentage of errors, indicating the highest prediction accuracy. On the other hand, the Decision Stump ML algorithm has the highest percentage of errors, indicating the least prediction accuracy. Due to its lowest prediction percentage error, the ANN is chosen for the prediction of the optimized output power.

Table 8. Prediction performance on the test dataset

ML Algorithm	Duration (seconds)	Max % Error	Min % Error	Average % Error
Artificial Neural Networks	**7.15**	**0.6898**	**0.0006**	**0.0692**
M5P	0.39	1.2589	0.0002	0.1873
M5Rules	0.22	1.2589	0.0011	0.1536
Random Committee	0.33	1.7246	0.0002	0.3580
Random Forest	0.17	2.6211	0.0048	0.7230
Bagging	0.23	12.3335	0.0040	3.2334
KStar	0.27	13.4517	0.0099	2.2435
Random Tree (RT)	0.22	13.7288	0.0157	2.3196
REPTree	24.11	15.7732	0.0103	2.3351
Linear Regression	10.74	16.9845	0.0210	2.2625
Support Vector Machines	0.25	17.7646	0.0103	3.4466
Simple Linear Regression	0.35	18.8024	0.0040	1.1230
Gaussian Process	0.24	19.1380	0.0058	5.6337
Regression by Discretization	0.17	22.2515	0.0024	1.1994
Decision Table	0.74	27.2764	0.0020	0.6261
Additive Regression	0.32	47.8816	0.0977	9.5229
Random Sub Space	4.42	50.5384	0.0039	5.9131
LWL	2.67	74.6807	0.0898	14.3199
Decision Stump	0.17	81.0967	0.0804	15.7659

Figure 6 illustrates the ANN-based ML model's prediction of the optimized output power on the test data. The high prediction accuracy results in the actual and predicted output power being nearly identical. The test data was randomly selected from the combined dataset as shown in Figure 5, leading to predicted optimized output power ranging from 1 W to 3.75 W.
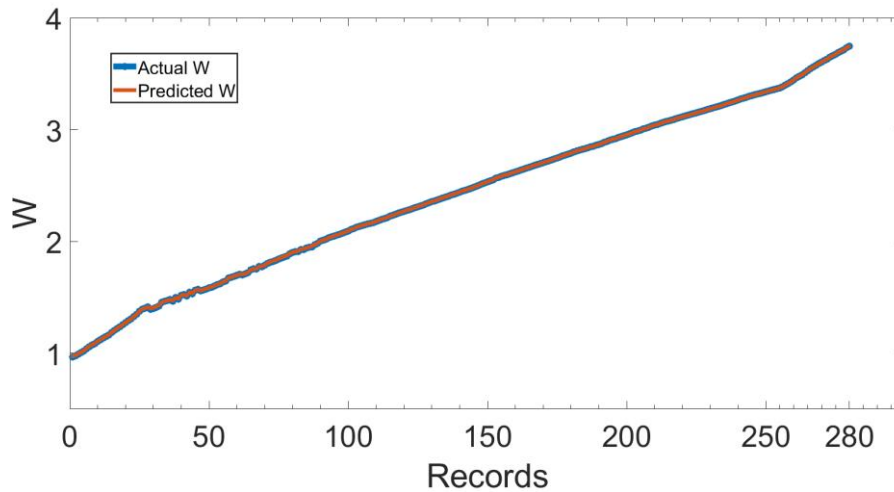
Figure 6. Actual and predicted test data

Figure 7 presents the correlation between the actual test data and the predicted optimized output power using the ANN-based ML model. As the correlation coefficient of the ANN-based ML stands at $R^2 = 1$, a strong agreement between the two responses is obtained. Consequently, a well-trained ANN-based ML algorithm can accurately predict the optimized output power of the CPV-TE system. This outcome is expected to match or potentially surpass that achieved by MOGA or GOAL-MOGA algorithms. Furthermore, the optimization process using the ANN-based ML will be notably swifter than the aforementioned metaheuristic optimizations. While enhancing the performance of a single optimization algorithm is typically challenging, augmenting the optimization capability of the ANN-based ML algorithm can be accomplished by integrating additional datasets from various optimization techniques. This study underscores the substantial value of ML in engineering applications.
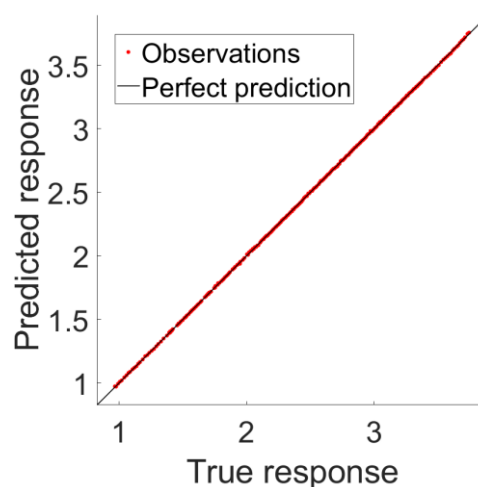
Figure 7. Correlation between the actual response and the prediction response

4. CONCLUSIONS

This study delves into the design and optimization of a concentrated photovoltaic-thermoelectric

hybrid system. Despite previous studies highlighting the potential for improved output performance by integrating photovoltaic and thermoelectric systems compared to standalone configurations, the conflicting operational characteristics of these subsystems necessitate the optimization of the hybrid system. Herein, PS, MOGA, and GOAL-MOGA metaheuristic optimizations are employed to optimize the output power and energy efficiency of the hybrid system. The optimization performance of PS was inferior to that of the MOGA and GOAL-MOGA algorithms, leading to its exclusion from further analysis.

Subsequently, the combined dataset from MOGA and GOAL-MOGA optimizations were utilized to train 19 distinct machine learning algorithms. Among these, an ANN-based ML algorithm trained in 48.22 seconds, exhibiting a correlation coefficient of $R^2 \approx 1$, an RMSE of 0.0019, and an MAE of 0.0012, emerges as the superior option. This ANN-based ML algorithm showcases an average prediction error of 0.0692% and a correlation coefficient $R^2 \approx 1$ on the test dataset, signifying its potential in predicting the optimized output power of the hybrid system. The ANN-based ML model performs better when trained on a combined dataset from both MOGA and GOAL-MOGA compared to using either MOGA or GOAL-MOGA alone. Furthermore, the optimization capability of the ANN-based ML algorithm can be further enhanced by incorporating additional datasets from other optimization techniques.

Declaration of Ethical Standards

Authors complied with all ethical guidelines including authorship, citation, data reporting, and publishing original research.

Credit Authorship Contribution Statement

AUTHOR1: Conceptualization, Methodology, Data collection, Validation, Writing- original draft.
AUTHOR2: Data curation, Visualization, Review, Investigation.
AUTHOR3: Data mining of training and testing phases, Software, Writing- original draft.
AUTHOR4: Supervision, Writing- review, and editing.

Declaration of Competing Interest

The authors declare that they have no known competing financial interests or personal relationships that could have appeared to influence the work reported in this paper.

REFERENCES

[1]   A. Yusuf, S. Ballikaya, and H. Tiryaki, "Thermoelectric material transport properties-based performance analysis of a concentrated photovoltaic–thermoelectric system," *Journal of Electronic Materials*, vol. 51, no. 12, pp. 7198-7210, 2022.

[2]   K. Teffah and Y. Zhang, "Modeling and experimental research of hybrid PV-thermoelectric system for high concentrated solar energy conversion," *Solar Energy*, vol. 57, pp. 10-19, 2017.

[3]   A. Yusuf and S. Ballikaya, "Electrical, thermomechanical and cost analyses of a low-cost thermoelectric generator," *Energy*, Feb., vol. 241, p. 122934, 2022.

[4]   C. Maduabuchi, R. Lamba, H. Njoku, M. Eke, and C. Mgbemene, "Effects of leg geometry and multistaging of thermoelectric modules on the performance of a photovoltaic-thermoelectric system using different photovoltaic cells," *International Journal of Energy Research*, vol. 45, no. 12, pp. 17888-17902, 2021.

[5]   E. Yin, Q. Li, and Y. Xuan, "Experimental optimization of operating conditions for concentrating photovoltaic-thermoelectric hybrid system," *Journal of Power Sources*, Mar., vol. 422, pp. 25-32, 2019.

[6]   A. Yusuf and S. Ballikaya, "Thermal resistance analysis of trapezoidal concentrated photovoltaic–Thermoelectric systems," *Energy Conversion and Management*, Dec., vol. 250, p. 114908, 2021.

[7]   F. Rajaee, M. A. V. Rad, A. Kasaeian, O. Mahian, and W. M. Yan, "Experimental analysis of a photovoltaic/thermoelectric generator using cobalt oxide nanofluid and phase change material heat sink," *Energy Conversion and Management,* vol. 212, p. 112780, 2020.

[8]   A. Yusuf and S. Ballikaya, "Performance analysis of concentrated photovoltaic systems using thermoelectric module with phase change material," *Journal of Energy Storage*, vol.59, p. 106544, 2023.

[9]   E. Yin and Q. Li, "Device performance matching and optimization of photovoltaic-thermoelectric hybrid system," *Energy Conversion and Management: X*, vol. 12, p. 100115, 2021.

[10]   A. Yusuf, N. Bayhan, H. Tiryaki, B. Hamawandi, M.S. Toprak, and S. Ballikaya, "Multi-objective optimization of concentrated Photovoltaic-Thermoelectric hybrid system via non-dominated sorting genetic algorithm (NSGA II)," *Energy Conversion and Management*, vol. 236, p. 114065, 2021.

[11]   A. Menadi, S. Abdeddaim, A. Betka, and M. T. Benchouia, "Real Time Implementation of A Fuzzy Logic Based Mppt Controller for Grid Connected Photovoltaic System", *International journal of renewable energy research* Vol. 5, no. 1, 2015.

[12]   L. Suganthi, S. Iniyan, and A. A. Samuel, "Applications of fuzzy logic in renewable energy systems – A review", *Renewable and Sustainable Energy Reviews*, vol. 48, pp. 585–607, 2015,

[13]   H. Toylan, "Performance of Dual Axis Solar Tracking System Using Fuzzy Logic Control: A Case Study in Pinarhisar, Turkey", *European Journal of Engineering and Natural Sciences*, vol. 2, no. 1, 2017.

[14]   S.Choudhury, and P.K.Rout, "Adaptive Fuzzy Logic based MPPT Control for PV System Under Partial Shading Condition", *IJRER*, Vol. 5, no. 4, 2015.

[15]   C. Maduabuchi, "Thermo-mechanical optimization of thermoelectric generators using deep learning artificial intelligence algorithms fed with verified finite element simulation data," *Applied Energy*, vol. 315, p. 118943, 2022.

[16]   Z. He, M. Yang, L. Wang, E. Bao, and H. Zhang, "Concentrated photovoltaic thermoelectric hybrid system: an experimental and machine learning study," *Engineered Science*, vol. 15, pp. 47-56, 2021.

[17]   K. S. Garud, S. Jayaraj, and M.Y. Lee, "A review on modeling of solar photovoltaic systems using artificial neural networks, fuzzy logic, genetic algorithm and hybrid models," *International Journal of Energy Research*, vol. 45, no. 1, pp. 6-35, 2021.

[18]   J. H. Yousif and H. A. Kazem, "Prediction and evaluation of photovoltaic-thermal energy systems production using artificial neural network and experimental dataset," *Case Studies in Thermal Engineering*, vol. 27, p. 101297, 2021.

[19]   K. S. Garud, J. H. Seo, C. P. Cho, and M. Y. Lee, "Artificial neural network and adaptive neuro-fuzzy interface system modelling to predict thermal performances of thermoelectric generator for waste heat recovery," *Symmetry*, vol. 12, no. 2, p. 259, 2022.

[20]   I. S. Ameenuddin, K. Irshad, A. Algahtani, B. Azeem, V. Tirth, S. Algarni, and M. A. Abdelmohimen, "Machine learning-based modeling of thermoelectric materials and air-cooling system developed for a humid environment," *Materials Express*, vol. 11, no. 2, pp. 153-165, 2021.

[21]   H. Alghamdi, C. Maduabuchi, A. Yusuf, S. Al-Dahidi, A. Albaker, I. Alatawi, and M. Alkhedher, "Multiobjective Optimization and Machine Learning Algorithms for Forecasting the 3E Performance of a Concentrated Photovoltaic-Thermoelectric System," *International Journal of Energy Research*, vol. 2023, pp. 1-22, 2023.

[22]   R. A. Kishore, R. L. Mahajan, and S. Priya, "Combinatory finite element and artificial neural network model for predicting performance of thermoelectric generator," *Energies*, vol. 11, no. 9, p. 2216, 2018.

[23]   A. A. Angeline, L. G. Asirvatham, D. J. Hemanth, J. Jayakumar, and S. Wongwises, "Performance prediction of hybrid thermoelectric generator with high accuracy using artificial neural networks," *Sustainable Energy Technologies and Assessments*, vol. 33, pp. 53-60, 2019.

[24]   P. Wang, K. Wang, L. Xi, R. Gao, and B. Wang, "Fast and accurate performance prediction and optimization of thermoelectric generators with deep neural networks," *Advanced Materials Technologies*, vol. 6, no. 7, p. 2100011, 2021.

[25]   D. L. King, J. A. Kratochvil, and W. E. Boyson, "Photovoltaic array performance model, SANDIA Report," *Department of Energy (US)*, Dec., p. Report No.: SAND2004-3535, 2004.

[26]   R. Lamba and S. C. Kaushik, "Solar driven concentrated photovoltaic-thermoelectric hybrid system: Numerical analysis and optimization," *Energy Conversion and Management*, vol. 170, pp. 34-49, 2018.

[27]   P. Motiei, M. Yaghoubi, E. GoshtashbiRad, and A. Vadiee, "Two-dimensional unsteady state performance analysis of a hybrid photovoltaic-thermoelectric generator," *Renewable Energy*, vol. 119, pp. 551-565, 2018.

[28]   K. Deb, *Multi-objective optimisation using evolutionary algorithms: an introduction In: Multi-objective evolutionary optimisation for product design and manufacturing*. 1st ed., New York: John Wiley & Sons, 2011, pp. 3-34.

[29]   MATLAB & Simulink-MathWorks, "Paretosearch Algorithm," [Online]. Available: https://uk.mathworks.com/help/gads/paretosearch-algorithm.html. [Accessed September 14, 2023].

[30]   MATLAB & Simulink-MathWorks, "Find points in Pareto set," [Online]: https://uk.mathworks.com/help/gads/paretosearch.html. [Accessed September 22, 2023].

[31]   MATLAB & Simulink-MathWorks, "Effects of Multiobjective Genetic Algorithm Options," [Online]. Available: https://www.mathworks.com/help/gads/gamultiobj-options-effects.html. [Accessed September 22, 2023].

[32]   MATLAB & Simulink-MathWorks, "When to Use a Hybrid Function," [Online]. Available: https://www.mathworks.com/help/gads/when-to-use-hybrid-function.html. [Accessed September 22, 2023].

[33]   M. T. Akçay, A. Akgundogdu, and H. Tiryaki, "Prediction of travel time for railway traffic management by using the AdaBoost algorithm," *Balıkesir Üniversitesi Fen Bilimleri Enstitüsü Dergisi*, vol. 24, no. 1, pp. 300-312, 2022.

APPENDIX A

Table A1: Sample optimization output of the MOGA.

G (W/m²)	v (m/s)	Ta (°C)	I (mA)	L (mm)	A$_{n/p}$ (mm²)	h (WK^{-1} m^{-2})	ΔT (°C)	P (W)	Eff (%)
200.000386	0.5013	29.99991	1.80498	0.50771	4.933846	285.222281	19.998873	0.966334	13.726313
848.013699	0.5013	29.99924	1.41919	0.63165	4.852545	282.134138	19.997093	3.361266	11.260490
843.439852	0.5012	29.99876	1.79998	0.91075	4.862054	282.252476	19.997537	3.348482	11.278495
852.141534	0.5016	29.99814	1.92321	0.85974	4.826997	282.342032	19.995078	3.373186	11.245685
211.114279	0.5025	29.99791	1.62313	0.65108	4.810399	283.259538	19.988916	1.016926	13.684499
844.193420	0.5012	29.99883	1.70337	0.68983	4.603974	282.408527	19.998209	3.350511	11.275256
203.740383	0.5004	29.98741	1.64914	0.54866	4.814525	283.953076	19.981623	0.983456	13.713087
204.872787	0.5019	29.99917	1.48108	0.56830	4.804085	283.720155	19.976610	0.988563	13.708105
213.646280	0.5013	29.99945	1.52868	0.57289	4.791397	283.149118	19.995959	1.028365	13.674431
849.483425	0.5017	29.99122	1.90443	0.54373	4.923843	281.996238	19.995775	3.365675	11.255755
393.063516	0.5021	29.99864	1.52785	0.59747	4.764583	282.947521	19.996756	1.797536	12.991889
487.055165	0.5018	29.99905	1.55586	0.57390	4.776474	282.856822	19.993667	2.166057	12.634238
227.547113	0.5037	29.99904	1.78371	0.58734	4.792177	283.271018	19.996324	1.091067	13.621887
210.206866	0.5023	29.99421	1.68224	0.59594	4.791652	283.475314	19.992676	1.01282	13.688090
827.454683	0.5013	29.99917	1.68226	0.63185	4.840436	282.921384	19.997646	3.302599	11.338849
204.204056	0.5026	29.99921	1.50795	0.52660	4.850762	283.745195	19.997963	0.985498	13.710358
217.119467	0.5013	29.99911	1.90186	0.62686	4.682009	283.232852	19.996883	1.044096	13.661525
805.971713	0.5019	29.9983	1.62445	0.66246	4.815351	282.356393	19.994432	3.240161	11.420998
852.750068	0.5016	29.99813	2.50820	1.28033	4.867599	282.280735	19.997811	3.375201	11.244372
816.118559	0.5025	29.9978	1.60988	0.63171	4.770346	282.516046	19.998265	3.269847	11.382339
830.213961	0.5016	29.99899	1.75287	0.65546	4.808196	282.611144	19.997284	3.310606	11.328561
245.859458	0.5015	29.99902	1.39935	0.63212	4.779866	282.868678	19.995307	1.172816	13.551909
411.782129	0.5020	29.99871	1.42370	0.62363	4.799575	282.634199	19.996793	1.872808	12.920611
238.247811	0.5034	29.99879	1.39908	0.60337	4.7805135	282.874929	19.994354	1.138948	13.581016

Table A2: Sample optimization output of the Paretosearch.

G (W/m²)	v (m/s)	Ta (⁰C)	I (mA)	L (mm)	$A_{n/p}$ (mm²)	h (WK⁻¹ m⁻²)	ΔT (⁰C)	P (W)	Eff (%)
866.9499512	0.5	30	1	0.5	5	100	20	3.413964	11.187221
978.9499512	0.5	30	1	0.5	5	100	20	3.708125	10.760964
751.8813477	0.5	30	1	0.5	5	100	20	3.07674	11.625157
738.3613281	0.5	30	1	0.5	5	100	20	3.034789	11.676612
942.378418	0.5	30	1	0.5	5	100	20	3.615767	10.90015
845.4499512	0.5	30	1	0.5	5	100	20	3.35365	11.269047
753.8613281	0.5	30	1	0.5	5	100	20	3.082843	11.617621
949.6210938	0.5	30	1	0.5	5	100	20	3.634342	10.872586
751.8881836	0.5	30	1	0.5	5	100	20	3.076761	11.625131
817.8613281	0.5	30	1	0.5	5	100	20	3.274442	11.374046
879.8881836	0.5	30	1	0.5	5	100	20	3.449662	11.13798
585	0.5	30	100	4	1	100	20	2.508172	12.180323
805.5820313	0.5	30	1	0.5	5	100	20	3.238532	11.420779
737.8598633	0.5	30	1	0.5	5	100	20	3.033223	11.678521
949.628418	0.5	30	1	0.5	5	100	20	3.634361	10.872558
849.8613281	0.5	30	1	0.5	5	100	20	3.366126	11.252258
773.5820313	0.5	30	1	0.5	5	100	20	3.143051	11.542567
946.9499512	0.5	30	1	0.5	5	100	20	3.627508	10.882752
903.878418	0.5	30	1	0.5	5	100	20	3.514668	11.046676
825.8813477	0.5	30	1	0.5	5	100	20	3.297678	11.343523
849.8813477	0.5	30	1	0.5	5	100	20	3.366183	11.252182
882.8110352	0.5	30	1	0.5	5	100	20	3.457665	11.126856
745.9135742	0.5	30	1	0.5	5	100	20	3.058283	11.647869
946.8305664	0.5	30	1	0.5	5	100	20	3.627202	10.883206
785.8813477	0.5	30	1	0.5	5	100	20	3.180074	11.495757
753.8813477	0.5	30	1	0.5	5	100	20	3.082904	11.617545

Table A3: Sample optimization output of the GOAL-MOGA.

G (W/m²)	v (m/s)	Ta (⁰C)	I (mA)	L (mm)	$A_{n/p}$ (mm²)	h (WK⁻¹ m⁻²)	ΔT (ºC)	P (W)	Eff (%)
360.871689	0.5077	29.99864	99.90044	3.99988	1.000282	625.866164	19.991230	1.647717	12.971411
297.968850	0.5198	29.99789	99.91607	3.99992	1.000063	641.151626	19.994881	1.372038	13.081355
310.217479	0.5128	29.99897	99.89149	3.99976	1.000062	626.451889	19.988589	1.426465	13.063276
966.859799	0.5004	29.99998	1.14896	0.64442	4.842421	568.170675	19.999821	3.678387	10.808146
470.015757	0.5018	29.99993	1.129458	0.64991	4.816721	566.007426	19.972198	2.101173	12.700086
429.168312	0.5090	29.99842	99.85233	3.99992	1.000315	626.862322	19.988118	1.935272	12.810663
297.349445	0.5245	29.99895	99.84141	3.99995	1.000276	630.252947	19.996356	1.369279	13.082236
344.413708	0.5135	29.99871	99.98328	3.99999	1.000148	626.810153	19.991762	1.576522	13.003999
298.667001	0.5086	29.99893	99.8912	3.99995	1.000392	629.731606	19.984575	1.375086	13.079766
295.832371	0.5147	29.99932	99.92162	3.99992	1.000181	632.171377	19.989962	1.362393	13.083198
308.529584	0.5062	29.99918	99.88103	3.99990	1.000246	626.863755	19.984508	1.418979	13.065817
324.074627	0.5132	29.99878	99.96889	3.99976	1.000109	626.635429	19.990582	1.487608	13.040700
331.722227	0.5054	29.99899	99.86777	3.99983	1.000279	626.240193	19.993239	1.521237	13.028053
393.990425	0.5046	29.99973	99.86743	3.99989	1.000472	627.116501	19.991165	1.788697	12.897586
420.964817	0.5092	29.99952	99.8517	3.99980	1.000442	627.869491	19.994003	1.901391	12.831667
995.647940	0.5013	29.99992	1.095738	0.65418	4.921296	569.789844	19.999608	3.749608	10.698858
952.070853	0.5009	29.99985	1.135866	0.63580	4.935311	570.002570	19.999601	3.64103	10.864565
445.617767	0.5006	29.99968	1.093316	0.65274	4.794118	567.037360	19.998832	2.006505	12.791899
420.780858	0.5096	29.999	99.88572	3.99996	1.000372	626.248573	19.990103	1.900599	12.831925
444.988961	0.5051	29.99969	1.127076	0.63524	4.759751	563.825234	19.999653	2.004148	12.794927
429.807035	0.5011	29.99895	99.83445	3.99986	1.000528	627.248351	19.991078	1.937828	12.808523
355.394880	0.5083	29.99952	99.89478	3.99986	1.000233	626.838490	19.993045	1.624126	12.982722
461.675030	0.5005	29.9997	1.082932	0.65799	4.790491	570.236830	19.991772	2.068908	12.730991
303.478657	0.5052	29.99853	99.88477	3.99992	1.000311	627.653728	19.987631	1.396517	13.073002

PARAMETER OPTIMIZATION OF LQR CONTROLLER APPLIED TO THREE DEGREES OF FREEDOM SYSTEM WITH HYBRID APPROACH

[1,*] **Yasin BÜYÜKER** [iD], [2] **İlhan İLHAN** [iD]

[1] *KTO Karatay University, Vocational School of Trade and Industry, Electronics and Automation Department, Konya, TÜRKİYE*
[2] *Necmettin Erbakan University, Engineering Faculty, Mechatronic Engineering Department, Konya, TÜRKİYE*
[1] yasin.buyuker@karatay.edu.tr, [2] ilhan@erbakan.edu.tr

Highlights

- Hybrid Algorithm Development: Introduction of a novel hybrid algorithm (hSA-GWO) combining Simulated Annealing (SA) and Gray Wolf Optimization (GWO).

- Optimization Efficiency: Enhanced optimization of complex control parameters for the Linear-Quadratic Regulator (LQR) using advanced algorithms.

- Algorithm Performance Comparison: Comprehensive comparison with traditional optimization algorithms, demonstrating the effectiveness of the proposed method.

- Quadcopter Control Improvement: Significant improvement in controlling quadcopter flight behaviors with the proposed hSA-GWO algorithm.

- Simulation-Based Analysis: Effective application of optimization techniques to the 3-DOF Hover system in simulation for detailed flight behavior analysis.

*Corresponding Author: Yasin BÜYÜKER, yasin.buyuker@karatay.edu.tr

PARAMETER OPTIMIZATION OF LQR CONTROLLER APPLIED TO THREE DEGREES OF FREEDOM SYSTEM WITH HYBRID APPROACH

1, * Yasin BÜYÜKER [ID] , **2 İlhan İLHAN** [ID]

1 KTO Karatay University, Vocational School of Trade and Industry, Electronics and Automation Department, Konya, TÜRKİYE
2 Necmettin Erbakan University, Engineering Faculty, Mechatronic Engineering Department, Konya, TÜRKİYE
1 yasin.buyuker@karatay.edu.tr, 2 ilhan@erbakan.edu.tr

ABSTRACT: There have been numerous studies on the control of quadcopters. These studies mainly aim to control the flight behavior of quadcopters. To achieve this, researchers have been developing new tools and testing new methods. One of the developed tools is the 3-DOF Hover system, which enables researchers to analyze the flight behaviors of quadcopters, such as roll, pitch, and yaw, even in a physically limited area or only in a computer environment. The control method applied in the control of the 3-DOF Hover system has been determined by the manufacturer as Linear-Quadratic Regulator (LQR). LQR has control parameters that are complex to calculate. This complex calculation process creates an optimization problem. Beyond controlling the 3-DOF Hover system using LQR, this study focuses on calculating the complex control parameters of LQR using optimization algorithms when controlling a dynamic system with LQR.

This study includes well-known algorithms such as Genetic Algorithm (GA), Particle Swarm Optimization (PSO), and Simulated Annealing (SA), as well as an innovative approach known Gray Wolf Optimization (GWO). These algorithms were selected due to their proven effectiveness in various studies. Based on the results obtained from these algorithms, a hybrid algorithm incorporating SA and GWO is proposed. The aim of this hybrid algorithm is to combine the advantages of different methods and achieve a more effective and efficient optimization process. The mentioned hybrid algorithm, obtained by combining SA and GWO, is named hSA-GWO. This hSA-GWO is compared with traditional algorithms, and the comparison results show that the proposed hybrid algorithm can be used as an alternative and competitive method for controlling the flight behaviors of quadcopters.

Keywords: Hybrid Algorithm, LQR Control, Optimization Algorithms, Quadcopter

1. INTRODUCTION

Unmanned aerial vehicles with four rotors are called quadcopters. Unlike fixed-wing aircraft, they are difficult to control. However, they offer advantages such as maneuverability, portability, runway-free takeoff, and landing, to their users. Despite the difficulties in controlling them, quadcopters are used in many fields due to the advantages they offer. Control methods are used to maximize the benefits of quadcopters and minimize their disadvantages [1]–[4].

Linear and nonlinear control systems exist, and both approaches are evaluated for quadcopters. However, quadcopters are nonlinear systems, unlike fixed-wing aircraft, making linear control methods inadequate for controlling them. Therefore, the handicap caused by using linear control methods in nonlinear systems needs to be overcome. Researchers have turned to nonlinear control methods for this purpose [1]–[13]. One of the control methods considered in this context is LQR control. LQR control is a control method that can be applied to both linear and nonlinear systems. Due to difficulties in calculating controller parameters, LQR control has not been preferred until recently [1], [8].

The optimization of controller parameters in LQR control is a complex optimization process. Initially, this optimization process was conducted using numerical methods. However, difficulties are encountered in reaching the ideal solution using numerical methods. When it is realized that the solution

---

*Corresponding Author: Yasin BÜYÜKER, yasin.buyuker@karatay.edu.tr

obtained by the numerical method is not suitable for the system, minor changes are made to the obtained solution using a trial-and-error method to try to reach the ideal solution. In other words, the fate of the developed system depended on both the large computational cost caused by numerical methods and the luck of the researcher. With the development of high-capacity computers, the computational cost of numerical methods is transferred to optimization algorithms. With the help of these processes, complex optimization problems can be solved in an applicable time and in a way that is close to being correct [14]–[17]. As it can be understood, optimizing the controller parameters of LQR is also a complex optimization process. Therefore, it is a reasonable solution to use optimization algorithms in optimizing the controller parameters of LQR. In addition, many researchers today are optimizing LQR parameters using optimization algorithms [1], [8], [9].

In this study, a simulation model of the 3-DOF Hover test environment, produced by Quanser which is a company developing test systems in various fields, was used [2]. Currently, LQR is applied to this system. LQR parameters were optimized using the hSA-GWO algorithm, which is a hybridization of SA and GWO, to obtain a better system response. The results obtained were compared with traditional methods.

2. DESCRIPTION OF THE PROBLEM

In Figure 1, a block diagram representing the optimization processes to be performed in this study is given. It can be seen that control will be applied to the 3-DOF Hover system in this diagram. The control method used for the system is LQR, which is represented by the K block in the diagram. The K block is not only a block but also a matrix that is the root of the Ricatti Equation. The Q and R matrices, which are the control matrices of LQR and are optimized using optimization algorithms, are used in the Ricatti Equation to obtain the K matrix [18].
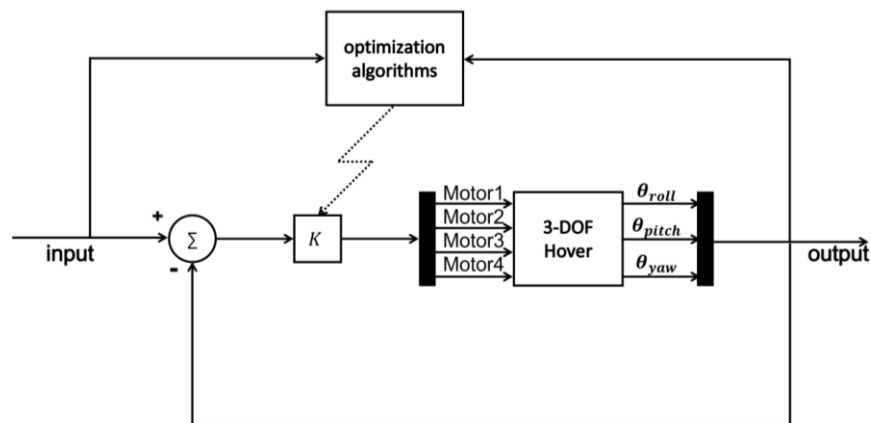
Figure 1. Block diagram of the optimization process.

2.1. 3-DOF Hover

Figure 2 shows the 3-DOF Hover environment developed by the Quanser company. From the image, it can be understood that 3-DOF Hover is a system that can be fixed to the ground and does not have the ability to fly. Because it cannot fly, unlike quadcopters, it has three degrees of freedom instead of six. With this system, the roll, pitch, and yaw movements of quadcopters can be examined in a narrow area. There are two different uses of the system. In the first use, the 3-DOF Hover system and a computer are required. In this way of using the system, the data generated from the behavior of the real-world system is transferred to the computer through a software called Quarc. The second method, which is also preferred in this study, focuses only on the model of the system designed in the computer environment. The data

obtained in the second method is based on the physical laws and system dynamics defined in the model. [1], [2].

The preference for the second method in this study leads to some disadvantages due to the absence of real-world data. For instance, real-world conditions such as wind disturbances are present, which are not considered in the simulation environment. Additionally, even though the motors used in the system are assumed to be identical, there may be slight differences. These mentioned disadvantages result in a greater emphasis on the theoretical aspect of the study. However, simulations allow for a more controlled examination of the system's behavior and enable work on various scenarios. In situations where obtaining difficult or costly real-world data is challenging, simulations offer a valuable alternative. This study aims to focus on model-based analysis of the system, contributing to a general understanding and interpretation of theoretical results.

Figure 2. 3-DOF Hover [2].

The model of the 3-DOF Hover system has been designed in MATLAB/Simulink, which is an accepted program by the researchers. Additionally, the 3-DOF Hover system has been the subject of many studies [1], [2], [8]. The state-space matrices used in the modeling of the system in MATLAB/Simulink program are given in Eqs. (1) – (4) as [1]. The meanings and values of symbols used in these equations are presented in Table 1.

$$A = \begin{bmatrix} 0 & 0 & 0 & 1 & 0 & 0 \\ 0 & 0 & 0 & 0 & 1 & 0 \\ 0 & 0 & 0 & 0 & 0 & 1 \\ 0 & 0 & 0 & 0 & 0 & 0 \\ 0 & 0 & 0 & 0 & 0 & 0 \\ 0 & 0 & 0 & 0 & 0 & 0 \end{bmatrix} \tag{1}$$

$$B = \begin{bmatrix} 0 & 0 & 0 & 0 \\ 0 & 0 & 0 & 0 \\ 0 & 0 & 0 & 0 \\ -\dfrac{K_t}{J_y} & -\dfrac{K_t}{J_y} & \dfrac{K_t}{J_y} & \dfrac{K_t}{J_y} \\ \dfrac{L \times K_f}{J_p} & \dfrac{L \times K_f}{J_p} & 0 & 0 \\ 0 & 0 & \dfrac{L \times K_f}{J_r} & \dfrac{L \times K_f}{J_r} \end{bmatrix} \tag{2}$$

$$C = \begin{bmatrix} 1 & 0 & 0 & 0 & 0 & 0 \\ 0 & 1 & 0 & 0 & 0 & 0 \\ 0 & 0 & 1 & 0 & 0 & 0 \end{bmatrix} \tag{3}$$

$$D = \begin{bmatrix} 0 & 0 & 0 & 0 \\ 0 & 0 & 0 & 0 \\ 0 & 0 & 0 & 0 \end{bmatrix} \tag{4}$$

Symbol	Description	Value	Unit
$K_{t,n}$	Counter rotation propeller torque-thrust constant	0.0036	Nm/V
$K_{t,c}$	Normal rotation propeller torque-thrust constant	0.0036	Nm/V
K_f	Propeller force-thrust constant	0.1188	N/V
l	Distance between pivot to each motor	0.197	m
J_y	Equivalent moment of inertia about the yaw axis	0.110	kgm²
J_p	Equivalent moment of inertia about the pitch axis	0.0552	kgm²
J_r	Equivalent moment of inertia about the roll axis	0.0552	kgm²

2.2. Linear-Quadratic Regulator (LQR)

LQR is used in the control of 3-DOF Hover. Besides being a control method that can be applied to both linear and nonlinear systems, LQR stands out as a state feedback control method. In contrast to output feedback control methods, all state space variables such as speed, acceleration, and angle can be controlled instead of a single output variable in LQR. For example, a linear control method such as PID control receives feedback from the output signal, but this is not the case in LQR. With LQR, it is possible to access and control all designated state variables of the system. A block diagram of the operation of LQR control is given in Figure 3. It is clearly seen here that LQR is a state feedback control method.
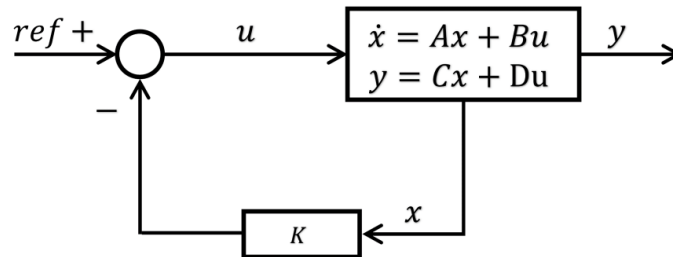
Figure 3. LQR diagram.

To apply LQR, it is necessary to obtain the mathematical model of the system. The state-space matrices formed in Eqs. (1) – (4) represent this mathematical model, and the model created is used in Eq. (5). The goal here is to express the time derivative of the system's state variables in terms of state variables, so that the state variables of the system can be controlled separately with LQR [18].

$$\dot{x} = Ax + Bu \tag{5}$$
$$u = -Kx \tag{6}$$

The cost function of LQR control is as shown in Eqs. (7) – (9). Here, x represents the time-varying state variable of the system, u represents the time-varying control signal, and Q and R represent the LQR controller parameters. LQR control aims to achieve maximum gain with minimum cost using these equations.

$$J = \int_0^\infty (x^T Q x + u^T R u) dt \tag{7}$$
$$x[k+1] = Ax[k] + Bu[k] \tag{8}$$
$$J = \sum_{k=0}^\infty (x^T Q x + u^T R u) \tag{9}$$

To minimize this cost function, the Ricatti Equation obtained in Eqs. (12) is used. Here, K represents the root of the equation. It should be noted that the control signal is generated using K and state variables in Eq. (6). Although the operations may seem complex, the LQR control can easily be applied to the system using the "lqr" function developed by MATLAB company.

$$0 = A^T P + PA - PBR^{-1}B^T P + Q \tag{10}$$
$$0 = A^T PA - PA^T PB(B^T PB + R)^{-1}B^T PA + Q \tag{11}$$
$$K = (B^T PB + R)^{-1}B^T PA \tag{12}$$

2.3. Preparing The System for Optimization

In this study, the hSA-GWO method is used to optimize the Q and R parameters of LQR. The Q and R parameters already provided by the manufacturer for the device are given in Eqs. (13) and (14) [3].

$$Q = \begin{bmatrix} 500 & 0 & 0 & 0 & 0 & 0 \\ 0 & 350 & 0 & 0 & 0 & 0 \\ 0 & 0 & 350 & 0 & 0 & 0 \\ 0 & 0 & 0 & 0 & 0 & 0 \\ 0 & 0 & 0 & 0 & 20 & 0 \\ 0 & 0 & 0 & 0 & 0 & 20 \end{bmatrix} \tag{13}$$

$$R = \begin{bmatrix} 0{,}01 & 0 & 0 & 0 \\ 0 & 0{,}01 & 0 & 0 \\ 0 & 0 & 0{,}01 & 0 \\ 0 & 0 & 0 & 0{,}01 \end{bmatrix} \tag{14}$$

Q and R parameters are matrices with positive real numbers in their diagonal elements (except for the fourth row and fourth column of the Q matrix, which can be zero). The other elements of the matrices have zero values and do not need to be optimized. In summary, there are ten parameters that need to be calculated by optimization algorithms. The parameters to be optimized are named in Eqs. (15) and (16).

$$Q = \begin{bmatrix} q_{11} & 0 & 0 & 0 & 0 & 0 \\ 0 & q_{22} & 0 & 0 & 0 & 0 \\ 0 & 0 & q_{33} & 0 & 0 & 0 \\ 0 & 0 & 0 & q_{44} & 0 & 0 \\ 0 & 0 & 0 & 0 & q_{55} & 0 \\ 0 & 0 & 0 & 0 & 0 & q_{66} \end{bmatrix} \tag{15}$$

$$R = \begin{bmatrix} r_{11} & 0 & 0 & 0 \\ 0 & r_{22} & 0 & 0 \\ 0 & 0 & r_{33} & 0 \\ 0 & 0 & 0 & r_{44} \end{bmatrix} \tag{16}$$

2.3.1. Formation of Search Space

Optimization algorithms perform a search operation on a search space. The search space to be used in this study was determined based on the values provided by the Quanser company for the device in Eqs. (13) and (14). The search space is given in Table 2. Default Quanser parameters and the created search space.. System parameters are very important in any control system. If the system parameters are incorrectly determined in control systems, the systems can easily fail. To cope with this situation, control system designers use saturation blocks in the control system they design. In the "3-DOF Hover" system whose simulation files are used in this study, saturation blocks are also used by the system designer. Therefore, in this study, the search space was kept large and parameters that would cause the system to exhibit undefined behavior, such as division by zero error, were excluded from the search space.

Table 2. Default Quanser parameters and the created search space.

	q_{11}	q_{22}	q_{33}	q_{44}	q_{55}	q_{66}	r_{11}	r_{22}	r_{33}	r_{44}
Qua [2]	500	350	350	0	20	20	0.01	0.01	0.01	0.01
Max	700	500	500	20	50	50	2	2	2	2
Min	1	1	1	0	0.01	0.01	0.01	0.01	0.01	0.01

The lower and upper limits are sufficient due to the parametric proportionality of the LQR controller. The proportionality mentioned here can be explained with a simple example as follows. The current control parameters of the system are [500 350 350 0 20 20 20 0.01 0.01 0.01 0.01 0.01]. If these parameters were applied to the system by multiplying them by a coefficient - for example, if the coefficient were 2, then the control parameters would be [1000 700 700 0 40 40 0.02 0.02 0.02 0.02] - there would be no change in the control response of the system.

Finally, the algorithms will be run for 200 iterations and a population size of 50, as described in the following pages. Therefore, in order to determine the final parameter, 10000 solution sets will be applied to the system and simulated. Here, very bad parameters can also be generated for the control of the system. However, in this study, such parameters are also needed to remove the system from local minima. For example, this provides genetic diversity in the genetic algorithm.

Optimization algorithms try to find the most suitable solution for the system in the created search space by means of metaheuristics. To be able to perform this process, it is necessary to express the problem appropriately. The expressed problem must be in a form that the algorithm can understand. In short, a problem descriptor is required. This problem descriptor is called the objective function.

2.3.2.   Formation of Objective Function

A properly constructed objective function will aid in the metaheuristics of the algorithm, enabling the evaluation of better solutions instead of poor solutions in the search space. The objective function created for this problem is given in Eq.(17). The objective function created includes some parameters that are important for dynamic systems [19]. The meanings of these parameters used in the equation are explained in Table 3.

$$Je = (\theta_{Rrt} + \theta_{Prt} + \theta_{Yrt} + \theta_{Rst} + \theta_{Pst} + \theta_{Yst} + \theta_{Rpt} + \theta_{Ppt} + \theta_{Ypt} + \theta_{Ros} + \theta_{Pos} + \theta_{Yos} \\ + \theta_{Rp} + \theta_{Pp} + \theta_{Yp} + \theta_{Rn} + \theta_{Pn} + \theta_{Yn}) \tag{17}$$

Table 3. The meanings of the expressions in the objective function.

Roll			Pitch			Yaw		
Rise time (sec)	Settling time (sec)	Peak time (sec)	Rise time (sec)	Settling time (sec)	Peak time (sec)	Rise time (sec)	Settling time (sec)	Peak time (sec)
θ_{Rrt}	θ_{Rst}	θ_{Rpt}	θ_{Prt}	θ_{Pst}	θ_{Ppt}	θ_{Yrt}	θ_{Yst}	θ_{Ypt}
Over shot (degree)	Peak (degree)	Norm	Over shot (degree)	Peak (degree)	Norm	Over shot (degree)	Peak (degree)	Norm
θ_{Ros}	θ_{Rp}	θ_{Rn}	θ_{Pos}	θ_{Pp}	θ_{Pn}	θ_{Yos}	θ_{Yp}	θ_{Yn}

The fitness value is calculated using the objective function. In this study, the aim is to achieve the fastest rise time of the system response without maximum overshoot and steady-state error. This can be achieved by minimizing the fitness value. The term 'minimization' is used in optimization processes of this kind.

System response obtained when the default Q and R parameters are applied to the system by the manufacturer are shown in Figure 4. These system responses are obtained without any optimization process. The objective function created will try to make these system responses more optimum.
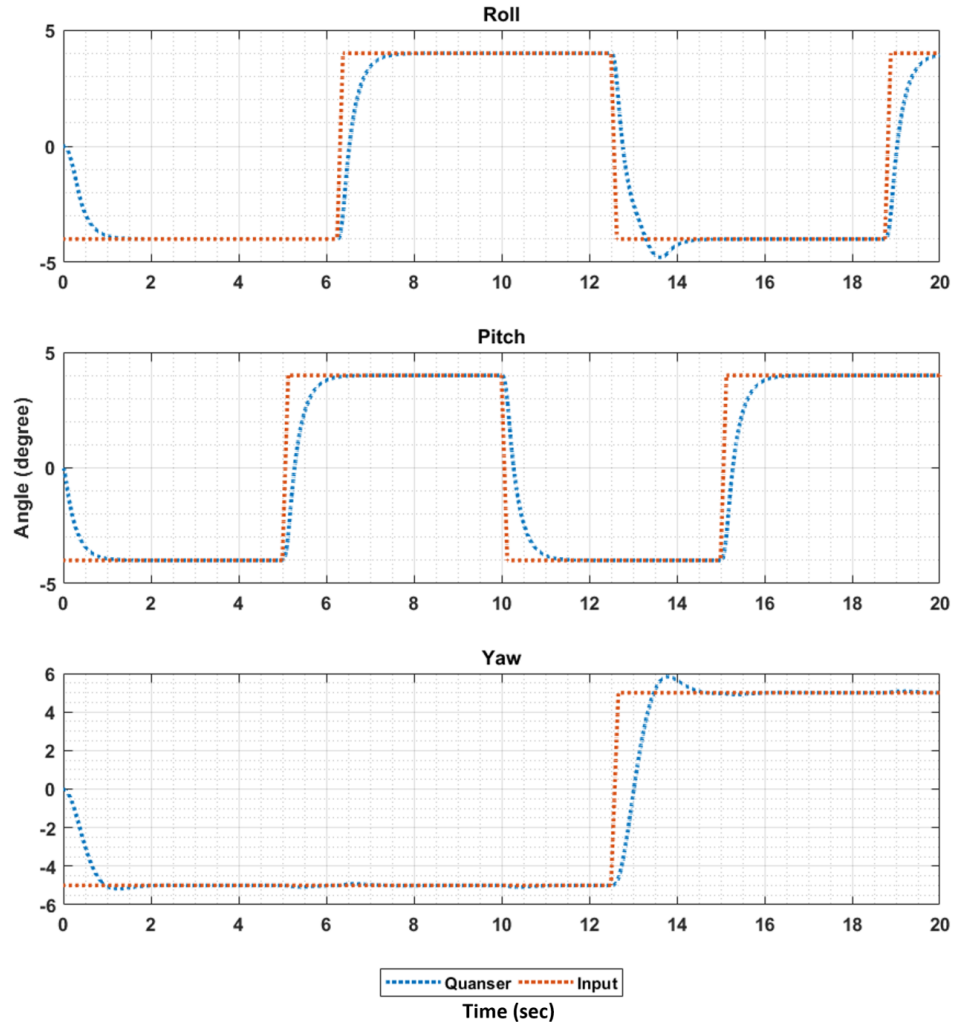
Figure 4. System responses obtained using default Quanser parameters [2].

A dynamically optimum system will try to produce the most ideal output signal against the input signal given to it. For optimum conditions, the output signal must closely follow the input signal. In other words, the better the input signal covers the output signal, the more controlled the system is operating.

3. THE PROPOSED HYBRID ALGORITHM

In this study, a hybrid algorithm (hSA-GWO) containing SA and GWO has been developed for solving the problem under investigation. Hybrid algorithms arise from the combination of two algorithms that solve the same problem. The aim of this process is to simultaneously benefit from the unique advantages of both algorithms. With the performed hybridization process, both SA's ability to overcome local optimal solutions and GWO's early generation of satisfactory solution sets are aimed to be utilized at the same time [20], [21].

The pseudocode of the developed hSA-GWO algorithm along with some abbreviations is provided in Algorithm 1. The developed hSA-GWO works as follows: The population size and iteration number are determined for the GWO section of the hSA-GWO. Starting temperature, ending temperature, and the number of trials parameters are determined for the SA section of hSA-GWO. Similar to GWO, hSA-GWO

also starts with a randomly generated population and the fitness value of the solutions in the population is calculated. Additionally, the positions of the alpha, beta, and delta wolves are determined as in GWO.

Algorithm 1. HSA-GWO algorithm pseudocode.

/*
Abbreviations:
dimention of problem = d, number of iteration = gn, number of population = pn,
number of trial = tn, start temperature = t_s, end temprature = t_e,
alpha candidate wolf = acw, beta candidate wolf = bcw,
delta candidate wolf = dcw, annealed alpha wolf = aaw,
annealed beta wolf = abw, annealed delta wolf = adw,
real alpha wolf = raw, real beta wolf = rbw,
real delta wolf = rdw, alpha wolf fitness = awf,
beta wolf fitness = bwf, delta wolf fitness = dwf
*/
Input: The parameters d, a, gn, pn, tn, ts, te
Output: The best solution set, The best fitness value

1	**Begin**
2	initialize_parameters ()
3	define (search_space)
4	$t_{GWO} = t_s$
5	$frac_{GWO} = (t_e / t_s) \wedge (1 / (gn - 1))$
6	p = generate_initial_wolf_position ()
7	p = limitation_search_space (p)
8	$f(p_i)$ = calculate_fitness_value (p_i)
9	determination (awc, bwc, dwc)
10	[aaw, abw, adw] = apply_sa (awc, bwc, dwc)
11	[raw, rbw, rdw] = sort (aaw, abw, adw)
12	**while (ts < te)**
13	p = generate_gwo_population (raw, rbw, rdw)
14	p = limitation_search_space (p)
16	$f(p_i)$ = calculate_fitness_value (p_i)
17	determination (awc, bwc, dwc)
18	[aaw, abw, adw] = apply_sa (awc, bwc, dwc)
19	$t_{GWO} = t_{GWO} * frac_{GWO}$
20	[raw, rbw, rdw] = sort (aaw, abw, adw)
21	**end while**
22	**Finish**

The determined wolf positions here, however, are not directly used. Therefore, the determined wolf positions are expressed as "candidate wolf positions" in this study. For example, the alpha wolf position obtained as a result of this process is referred to as the "alpha candidate wolf position – (acw)". The best position set is determined as the acw, the second-best position set as the beta candidate wolf's position (bcw) and the third-best position set as the delta candidate wolf's position (dcw). First, SA is applied separately for each of the determined candidate wolf positions. To apply SA to the candidate wolf positions, a variable named t is created to represent the current temperature value. The start temperature is assigned to this t variable. The cooling coefficient created in Eq. (18) is used with Eq. (19) to reduce the value of t temperature during the defined number of trials. Here, $frac_{SA}$ represents the cooling coefficient

used for the SA section of the hSA-GWO, t_e represents the ending temperature, t represents the current temperature, and tn represents the number of trials.

$$frac_{SA} = \left(\frac{t_e}{t}\right)^{\frac{1}{tn-1}} \tag{18}$$

$$t = t \times frac_{SA} \tag{19}$$

A loop is created for a predetermined number of trials. Within this loop, the SA procedure, respectively, are applied to candidate wolf positions. The loop will end when the number of trials is reached. Additionally, the equations used ensure that the current temperature is lower than the finishing temperature when the specified number of trials is reached. In other words, the loop can be terminated when the calculated current temperature is less than the finishing temperature. Following the operation, alpha, beta, and delta wolves with SA applied are obtained. These SA-applied positions obtained are named as "annealed wolf" in this study. For example, the SA-applied alpha candidate wolf position is named "annealed alpha wolf – (aaw)". At the end of the SA section, aaw is obtained by applying SA to acw. The start temperature is assigned to the variable t again. The same process is applied for bcw and dcw, as a result, "annealed beta wolf – (abw)" and "annealed delta wolf – (adw)" are obtained.

The fitness values of the wolves that have undergone SA may have changed. Therefore, their fitness values should be reevaluated. Thus, the fitness values of the annealed wolves are sorted in ascending order. As a result of the sorting process, the best solution is determined, and it is named as "real alpha wolf – (raw)" in this study. Similarly, the second-best solution is determined as "real beta wolf – (rbw)" and the third best solution as "real delta wolf – (rdw)". The starting temperature is reduced using Eq. (20) by using the cooling coefficient given in Eq. (21). Here, $frac_{GWO}$ represents the cooling coefficient used for the GWO section of the hSA-GWO, t_e represents the ending temperature, t_s represents the starting temperature, and gn represents the number of iterations.

$$frac_{GWO} = \left(\frac{t_e}{t_s}\right)^{\frac{1}{gn-1}} \tag{20}$$

$$t_s = t_s \times frac_{GWO} \tag{21}$$

The wolf population for the new iteration is obtained using raw, rbw, and rdw. The hybridization process described above is applied to the newly generated wolf population, and the hybridization process is repeated for the number of iterations. In summary, there is one outer loop and three inner loops in the hSA-GWO. GWO operates in the outer loop, and SA operates in the inner loops, provided that the initial temperatures are equal.

4. EXPERIMENTAL STUDIES

4.1. Algorithms Used in the Comparison

The performance of the hSA-GWO algorithm was compared with the performances of the GA, PSO, SA, and GWO algorithms. The operators and parameter values used in these algorithms were explained below.

GA was created by modeling the natural selection, crossover, and mutation processes occurring in evolutionary processes [14]. In this implementation, the real-coded version of GA was used. A special multi-point crossover method was used for GA, different from its usage in the literature. The crossover method used is given in Eqs. (22) and (23).

$$chromosome1_{new} = chromosome_1 \times \alpha + (1 - \alpha) \times chromosome_2 \tag{22}$$

$$chromosome2_{new} = chromosome_2 \times \alpha + (1 - \alpha) \times chromosome_1 \tag{23}$$

As the problem involves ten elements, single-point and two-point crossover operations commonly used in the literature are insufficient. To overcome this limitation, A multi-point crossover method similar to the one described in the literature was utilized. The value denoted by α represents a randomly generated number between [-0.05, 0.05].

The crossover rate (cr) and mutation rate (mr) in GA are crucial parameters significantly affecting the quality of the search process. Both parameters theoretically can be selected from the range [0, 1]. Empirical studies indicate better results when the crossover rate exceeds 0.75 and the mutation rate is below 0.10 [22]. It is critical to select appropriate parameter values to ensure the effective functioning of GA for a given problem. Hence, A test scenario was established with the crossover rates set to 0.75, 0.85, and 0.95, and the mutation rates set to 0.03, 0.05, and 0.07, respectively. Nine scenarios were generated. Each scenario was run three times with 100 iterations and 50 populations. Table 4 shows the obtained results, with 'Best' and 'Worst' indicating the highest and lowest fitness values in all runs, respectively. 'Avg.' represents the average fitness value of all runs. As can be seen from the table, better results were obtained when the crossover rate was 0.85 and the mutation rate was 0.07.

Table 4. The results obtained for different cr and mr values of GA.

	scen.1 cr=0.75 mr=0.03	scen.2 cr=0.75 mr=0.05	scen.3 cr=0.75 mr=0.07	scen.4 cr=0.85 mr=0.03	scen.5 cr=0.85 mr=0.05	scen.6 cr=0.85 mr=0.07	scen.7 cr=0.95 mr=0.03	scen.8 cr=0.95 mr=0.05	scen.9 cr=0.95 mr=0.07
Avg.	43.1685	43.1460	40.5917	42.4631	40.7681	<u>40.4742</u>	41.5950	41.0700	41.3856
Best	40.0128	40.7031	40.3187	41.1961	38.2624	40.1983	38.8629	38.2745	39.4478
Worst	45.1583	44.4829	40.8501	44.1879	43.2103	40.9879	43.8623	44.3430	44.2344

PSO, a search method developed by taking inspiration from the social behaviors of living creatures that live in flocks. This algorithm uses a swarm intelligence-based approach [15]. In this study, PSO was applied as described in the literature. However, unlike the literature, only a limitation was imposed on the velocity value. According to this limitation, a particle's velocity will be between -20% and +20% of the maximum position value that the particle can take. For example, the maximum position value that the q_{11} element of the solution set can take is 700. Therefore, the maximum velocity that a q_{11} particle can reach is +140 units, and the minimum velocity value is -140 units. This means that, for example, a q_{11} particle with a current position of 250 can have a next position between the minimum value of 110 and the maximum value of 390.

In PSO, like in GA, there are parameters that directly affect the algorithm's performance. These parameters are the cognitive component (c_1), social component (c_2), and inertia weight (w). In the literature, various methods were used to optimize these parameters. In this study, c_1 and c_2 were chosen to be equal to each other, and their values are 1.50, 1.75, and 2.00, respectively. The w value was created geometrically to decrease from 1 to 0.5, from 0.9 to 0.4, and from 0.8 to 0.3, respectively. Nine different scenarios have been created in total. Each scenario was run three times with 100 iterations and 50 populations. The results are presented in Table 5. According to this table, scenario 1 works well for PSO.

Table 5. The results obtained for different c and w values of PSO.

	scen.1	scen.2	scen.3	scen.4	scen.5	scen.6	scen.7	scen.8	scen.9
	$c_{1,2}$ = 1.50 w = 0.8 to 0.3	$c_{1,2}$ = 1.50 w = 0.9 to 0.4	$c_{1,2}$ = 1.50 w = 1 to 0.5	$c_{1,2}$ = 1.75 w = 0.8 to 0.3	$c_{1,2}$ = 1.75 w = 0.9 to 0.4	$c_{1,2}$ = 1.75 w = 1 to 0.5	$c_{1,2}$ = 2.00 w = 0.8 to 0.3	$c_{1,2}$ = 2.00 w = 0.9 to 0.4	$c_{1,2}$ = 2.00 w = 1 to 0.5
Avg.	<u>27.8970</u>	36.3531	34.1600	28.1666	32.9110	30.4122	28.3296	32.5397	30.3248
Best	27.7259	34.1887	28.4640	27.9749	28.6407	27.9180	27.8047	29.9864	27.8553
Worst	27.9910	37.5576	41.7170	28.3460	36.6938	34.8586	29.2942	34.1673	34.7977

The annealing process of metals has been mimicked to develop SA and solve nonlinear problems. SA's most significant advantage lies in its structure, which prevents it from becoming trapped in local minima [16]. Various methods have been proposed to adjust the temperature reduction in SA [23]. In this study, a geometric cooling method is employed. Two cooling coefficients ($frac_1$ and $frac_2$) are utilized for SA. $frac_1$ is used in the main loop to decrease the initial temperature at the end of each iteration, while $frac_2$ is used in inner loop, known as the testing process, to reduce current temperature. Eqs. (24) - (27) describe how the cooling coefficients are calculated and utilized, where t_e represents the ending temperature, t_s represents the starting temperature, gn represents the iteration number, and tn represents the testing number.

$$frac_1 = \left(\frac{t_e}{t_s}\right)^{\frac{1}{gn-1}} \tag{24}$$

$$t_s = t_s \times frac_1 \tag{25}$$

$$frac_2 = \left(\frac{t_e}{t}\right)^{\frac{1}{tn-1}} \tag{26}$$

$$t = t \times frac_2 \tag{27}$$

In this study, trials were conducted using different values for the starting and ending temperatures, which are the parameters of SA, in order to optimize them. For example, various studies were conducted using values between 1000 and 100 for the starting temperature and between 0.01 and 0.001 for the ending temperature. However, no significant difference was observed in the results of the trials. Therefore, the starting temperature was set to 100 and the ending temperature to 0.01.

GWO is an optimization algorithm based on the hunting behavior of gray wolves in nature. This algorithm has been applied in this study as described in the literature [17]. All of the described algorithms were run ten times under equal conditions with the parameters outlined in Table 6.

Table 6. The parameters used in the algorithms.

Algorithms	Search Agents	Number of Iterations	Parameters
GA	50	200	crossover rate: 0.85, mutation rate: 0.07, crossover method: multi-point crossover, α: range of randomly generated numbers for multi-point crossover [-0.05 - 0.05]
PSO	50	200	cognitive component (c_1): 1.5, social component (c_2): 1.5, inertia weight: geometrically decreasing from 0.8 to 0.3
GWO	50	200	distance control parameter a: linearly decreasing from 2 to 0
SA	50	200	start temperature: 100, end temperature: 0.01, cooling factor: geometric reduction method (it was described)
hSA-GWO	50	200	distance control parameter a: linearly decreasing from 2 to 0, start temperature: 100, end temperature: 0.01, cooling factor: geometric reduction method (it was described), trial number: 10

4.2. Experimental Results

All tests conducted within the scope of this study were carried out on a computer equipped with an Intel Core i7 4510u processor and DDR3 8 GB RAM. Each algorithm was executed ten times using the parameters described earlier and listed in Table 6. As a result of these experiments, ten fitness values were obtained for each algorithm. The arithmetic mean, standard deviation, best fitness value, worst fitness value, and average elapsed time data associated with these fitness values are presented in Table 7. These data allowed for a superficial comparison of the performance of the algorithms.

For example, when GA was executed ten times, the best fitness value achieved was 33.8631, and no better fitness value was obtained. It is observed that the average fitness value obtained by GA is comparatively lower than that of the other algorithms, and its standard deviation is also lower. Therefore, it can be inferred that GA yielded poorer results in comparison to the other fitness values. Another example pertains to SA, where the best fitness value obtained was 27.7106, and the worst fitness value was 40.9759. Upon examining the average fitness values of SA, it achieved a value of 31.2066, and its standard deviation is relatively high. From this, it can be deduced that SA's performance is closer to the worst fitness value for only a few fitness values, while it is closer to the best for the others.

Table 7. The results obtained by algorithms.

	GA	PSO	SA	GWO	hSA-GWO
Avg. fitness	39.3906	33.2920	31.2066	29.5936	28.5446
Std. deviation.	2.1138	3.9054	4.9310	3.6637	2.2507
Best fitness	33.8631	27.6717	27.7106	27.5239	27.5006
Worst fitness	41.8453	38.0265	40.9759	37.9892	35.2547
Avg. elapsed time (sec.)	1682.0768	1651.0739	1699.7117	1583.6175	2098.8970

When evaluated based on their best results, the performance of the algorithms is in the following order from high to low: hSA-GWO, GWO, PSO, SA, and GA. Comparing the algorithms based on the average fitness value, the standard deviation value, and the best fitness values, it is observed that hSA-GWO yields the best results. On the other hand, when the average time taken is examined, it is seen that hSA-GWO gives a worse result than the others. The reason for hSA-GWO appearing to be poor in terms of time is due to simulating an additional thirty solutions compared to other algorithms in each iteration.

A superficial analysis of the fitness values achieved by the algorithms has been conducted up to this point. Now a more in-depth analysis will be performed using the optimal values obtained by the

algorithms. The third row of Table 7 provides the best fitness values achieved by the algorithms during these studies. The convergence curve for the iterations that produced these fitness values are shown in Figure 5. When comparing the convergence curves of the algorithms, it can be seen that hSA-GWO leads the race for the most part and wins the competition. The solution sets that resulted in the best fitness values reached by the algorithms during these studies are given in Table 8.
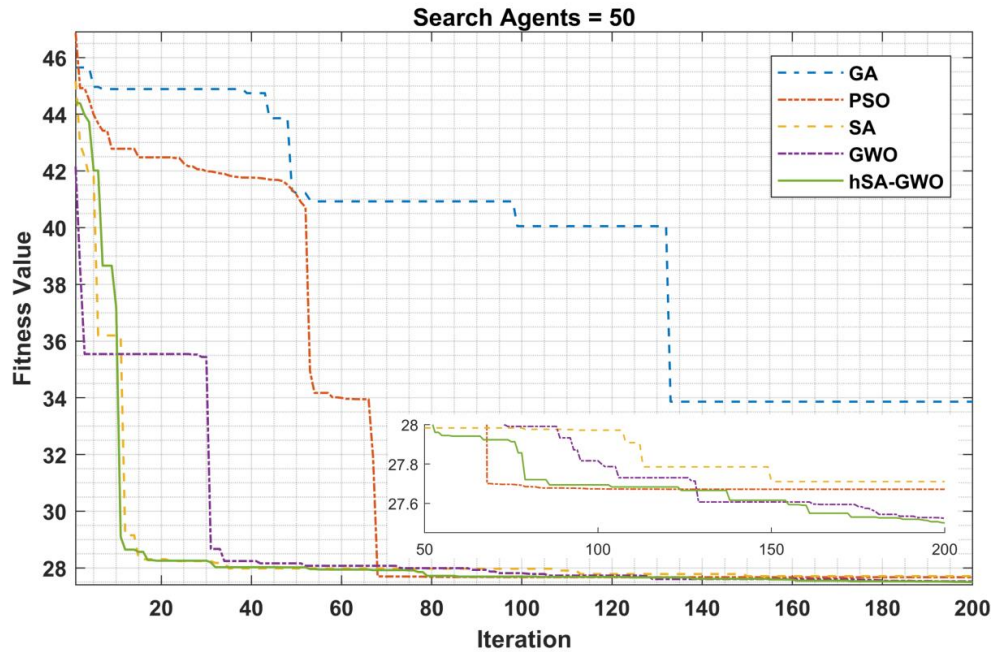
Figure 5. The convergence curves belong to the iterations where the best fitness values were achieved.

Table 8. The best solution sets reached by the algorithms.

	Quanser	GA	PSO	SA	GWO	hSA-GWO
q_{11}	500.0000	549.3473	677.3150	674.8986	696.1097	698.5897
q_{22}	350.0000	362.2833	472.9308	500.0000	498.2206	499.1072
q_{33}	350.0000	136.0409	371.8367	55.1683	166.0198	90.8695
q_{44}	0.0000	1.6330	3.7883	0.0000	3.0516	0.5257
q_{55}	20.0000	8.1317	10.7165	7.8515	8.9430	7.3262
q_{66}	20.0000	25.3702	4.6246	0.0475	2.0045	0.7627
r_{11}	0.0100	0.0100	0.0100	0.0102	0.0100	0.0100
r_{22}	0.0100	0.0196	0.0202	0.0131	0.0152	0.0128
r_{33}	0.0100	1.1162	0.0355	0.0100	0.0168	0.0109
r_{44}	0.0100	0.4970	0.1035	0.0569	0.0610	0.0476

The system response when applying these solution sets is shown in Figure 6. It can be seen that the system response obtained with hSA-GWO reaches the input value given for roll, pitch, and yaw angles earlier than the system responses attained with other algorithms, as shown in Figure 6. However, when the upper overshoots in roll and yaw angles are examined, it is observed that hSA-GWO exhibits a similar upper overshoot as other algorithms. Note that hSA-GWO only performs worse than the other algorithms only in the top overshoot. Overall, it is evident from Figure 6 that hSA-GWO demonstrates superiority over the others.
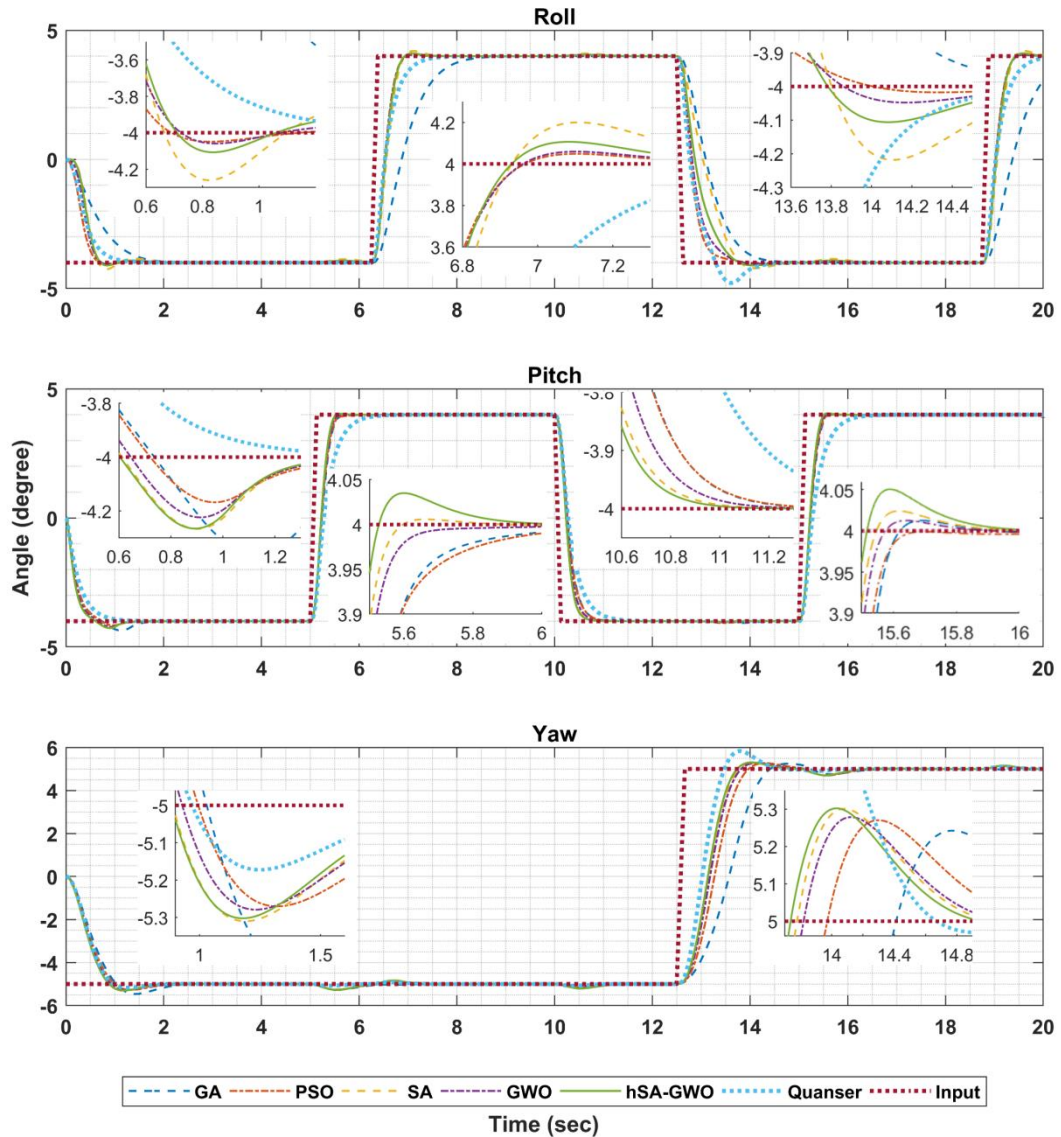
Figure 6. The response of the system to the application of the best obtained solutions.

Table 9 presents the numerical data supporting hSA-GWO superiority, explained in Figure 6 in the previous paragraph. Table 9 provides the settling time and overshoot values for Figure 6. These data are obtained using the stepinfo function in the MATLAB program, which evaluates the system response to a pulse input signal after the last pulse entry. The stepinfo function is a powerful tool used to assess and analyze the behavior of control systems, offering valuable insights into various performance metrics such as settling time, overshoot, rise time, and peak time. The settling time refers to the duration when the system output remains stable within a 2% range, indicating the stabilization duration of system. A low settling time means that the system rapidly approaches the desired setpoint. The stepinfo function also provides a significant measure, the overshoot value, representing the percentage by which the system response exceeds the desired setpoint. Overshoot occurs when the system output temporarily surpasses the target value. This information provides essential guidance for control engineers and system designers in optimizing the system and achieving the desired behavior [19].

For example, the frequency of the roll input signal is 0.08 hertz. One period consists of positive and negative pulses and these pulses last for 6.25 seconds. For the system response obtained with the GWO, the roll output signal reaches the settling time at the 0.6289th second after the last pulse (6.25 * 3 + 0.6289).

As mentioned in the previous sections, early settling time and low overshoot are targeted in this system. Therefore, the data in Table 9 should be evaluated from this perspective.

Table 9. System response data.

Algorithms	Settling time (sec.)			Overshoot (deg)		
	Roll	Pitch	Yaw	Roll	Pitch	Yaw
GA	1.1952	0.5264	3.3231	0.0085	0.3597	0.4649
PSO	0.6245	0.5145	3.3587	0.0487	0.1678	0.2702
SA	0.6427	0.4780	3.2918	0.2602	0.2664	0.3100
GWO	0.6289	0.4894	3.3073	0.0592	0.2238	0.2789
hSA-GWO	0.6228	0.4660	3.2838	0.1070	0.2654	0.3021

When considering settling time, hSA-GWO outperforms other algorithms shown in Table 9. In terms of overshoot, hSA-GWO never ranks last. This phenomenon stems from the nature of dynamic systems. When a dynamic system aims to reach the settling time as rapidly as possible, the overshoot of the system is likely to be higher. Multi-objective optimization problems arise when the desired data for attaining the optimum point conflict with each other. Therefore, it is crucial to consider all objectives and find a balance between them. The main aim is to identify the best parameters to improve the system's performance without compromising its current parameters. In other words, the aim is to strike a balance between different objectives within the system and determine the most suitable parameters.

5. CONCLUSION

This study addresses the problems that arise with the application of LQR to control a complex system with three degrees of freedom. The first and most important of these problems is the formation of ten different controller parameters arising from three degrees of freedom and the need to calculate them. The second difficulty is the impossibility of calculating ten-element optimum solution matrix containing control parameters using mathematical methods. For the system to work optimally, it needs to be tested in real-world conditions; This requires multiple iterations with different sets of ten solutions each, which can be a time-consuming process. This study offers an innovative solution to overcome the mentioned problems.

To make this process possible in a reasonable time, a computer model of the system was used. Within the scope of this study, the system was simulated using randomly generated solution sets within a certain range in the computer environment using optimization algorithms. Weak solution sets were intelligently filtered out and new solution sets were automatically regenerated under certain conditions. As a result, a comprehensive search was made within the specified range and the new solution sets created were repeatedly applied to the system. As a result of the experiments conducted in the simulation environment, it was concluded that the optimization algorithms were superior to each other in different subjects. These findings are shared in detail in the Experimental Results section.

This study, which focuses on the computability of controller parameters with optimization algorithms when LQR is applied to a complex system for control purposes, has shown that this is possible. In addition, considering the results obtained and the work of the algorithms, it was predicted that better results could be obtained by handling the SA and GWO algorithms with a hybrid approach. To test the accuracy of this prediction, the SA and GWO algorithms were hybridized. The resulting hSA-GWO algorithm was applied to the system under equal conditions with other algorithms and the results were presented impartially. As a result, it appears that hSA-GWO has superior performance compared to other algorithms in some aspects.

Declaration of Ethical Standards

This study was conducted in strict accordance with ethical standards and guidelines.

Credit Authorship Contribution Statement

Declaration of Competing Interest

Funding / Acknowledgements

Data Availability

The data that support the findings of this study are available from the corresponding author upon reasonable request.

REFERENCES

[1]   S. Mohanty and A. Misra, "3 DOF Autonomous Control Analysis of an Quadcopter Using Artificial Neural Network," *Studies in Computational Intelligence*, vol. 885, pp. 39–57, 2020, doi: 10.1007/978-3-030-38445-6_4/COVER.

[2]   "3 DOF Hover- Quanser." https://www.quanser.com/products/3-dof-hover/ (accessed Apr. 17, 2023).

[3]   M. K. Bayrakceken and A. Arisoy, "An Educational Setup for Nonlinear Control Systems: Enhancing the Motivation and Learning in a Targeted Curriculum by Experimental Practices [Focus on Education]," *IEEE Control Syst*, vol. 33, no. 2, pp. 64–81, Mar. 2013, doi: 10.1109/MCS.2012.2234971.

[4]   Ö. Bayraktar and A. Güldaş, "Quadrotor İtme ve Tork Katsayılarının Optimizasyonu ve Matlab/Simulink ile Simülasyonu," *Politeknik Dergisi*, vol. 23, no. 4, pp. 1197–1204, Dec. 2020, doi: 10.2339/POLITEKNIK.636950.

[5]   B. Alagoz, A. Ates, and C. Yeroglu, "Auto-tuning of PID Controller According to Fractional-order Reference Model Approximation for DC Rotor Control," *Mechatronics*, vol. 23, no. 7, pp. 789–797, Oct. 2013, doi: 10.1016/J.MECHATRONICS.2013.05.001.

[6]   R. Beard, *"Quadcopter Dynamics and Control Rev*, no. 1, p. 1325, 2008, Accessed: Apr. 17, 2023. [Online].   Available: https://scholarsarchive.byu.edu/facpubhttps://scholarsarchive.byu.edu/facpub/1325

[7]   T. Oktay and O. Köse, "Farklı Uçuş Durumları için Quadcopter Dinamik Modeli ve Simulasyonu," *European Journal of Science and Technology*, pp. 132–142, Mar. 2019, doi: 10.31590/EJOSAT.507222.

[8]   M. İçen, A. Ateş, and C. Yeroğlu, "Optimization of LQR Weight Matrix to Control Three Degree of Freedom Quadcopter," *IDAP 2017- International Artificial Intelligence and Data Processing Symposium*, Oct. 2017, doi: 10.1109/IDAP.2017.8090164.

[9]   V. E. Ömürlü, U. Büyükşahin, R. Artar, A. Kirli, and M. N. Turgut, "An Experimental Stationary Quadrotor with Variable DOF," *Sadhana- Academy Proceedings in Engineering Sciences*, vol. 38, no. 2, pp. 247–264, Apr. 2013, doi: 10.1007/S12046-013-0132-6.

[10]   H. K. Tran and T. N. Nguyen, "Flight Motion Controller Design Using Genetic Algorithm for a Quadcopter," *Measurement and Control (United Kingdom)*, vol. 51, no. 3–4, pp. 59–64, Apr. 2018, doi: 10.1177/0020294018768744/ASSET/IMAGES/LARGE/10.1177_0020294018768744-FIG7.JPEG.

[11]   A. Reizenstein, "Position and Trajectory Control of a Quadcopter Using PID and LQ Controllers," 2017, Accessed: Apr. 17, 2023. [Online]. Available: http://urn.kb.se/resolve?urn=urn:nbn:se:liu:diva-139498

[12]   Demiryurek A, "Modelıng and Control of a Quadrotor," Hacettepe University, Ankara, 2018.

[13]   M. Karakoyun and A. Özkış, "Transfer Fonksiyonları Kullanarak İkili Güve-Alev Optimizasyonu Algoritmalarının Geliştirilmesi ve Performanslarının Karşılaştırılması," *Necmettin Erbakan Üniversitesi Fen ve Mühendislik Bilimleri Dergisi,* vol. 3, no. 2, pp. 1–10, 2021.

[14]   D. E. Goldberg and J. H. Holland, "Genetic Algorithms and Machine Learning," *Mach Learn*, vol. 3, no. 2, pp. 95–99, 1988, doi: 10.1023/A:1022602019183/METRICS.

[15]   J. Kennedy and R. Eberhart, "Particle Swarm Optimization," *Proceedings of ICNN'95- International Conference on Neural Networks*, vol. 4, pp. 1942–1948, doi: 10.1109/ICNN.1995.488968.

[16]   S. Kirkpatrick, C. D. Gelatt, and M. P. Vecchi, "Optimization by Simulated Annealing," *Science (1979)*, vol. 220, no. 4598, pp. 671–680, May 1983, doi: 10.1126/SCIENCE.220.4598.671.

[17]   S. Mirjalili, S. M. Mirjalili, and A. Lewis, "Grey Wolf Optimizer," *Advances in Engineering Software*, vol. 69, pp. 46–61, Mar. 2014, doi: 10.1016/J.ADVENGSOFT.2013.12.007.

[18]   "Linear-Quadratic Regulator (LQR) design- MATLAB lqr." https://www.mathworks.com/help/control/ref/lti.lqr.html (accessed Apr. 18, 2023).

[19]   "Rise time, settling time, and other step-response characteristics- MATLAB stepinfo." https://www.mathworks.com/help/control/ref/dynamicsystem.stepinfo.html (accessed Apr. 17, 2023).

[20]   İ. İlhan, "An Improved Simulated Annealing Algorithm with Crossover Operator for Capacitated Vehicle Routing Problem," *Swarm Evol Comput*, vol. 64, p. 100911, Jul. 2021, doi: 10.1016/J.SWEVO.2021.100911.

[21]   A. Tabak and İ. İlhan, "An Effective Method Based on Simulated Annealing for Automatic Generation Control of Power Systems," *Appl Soft Comput*, vol. 126, p. 109277, Sep. 2022, doi: 10.1016/J.ASOC.2022.109277.

[22]   A. Hassanat, K. Almohammadi, E. Alkafaween, E. Abunawas, A. Hammouri, and V. B. S. Prasath, "Choosing Mutation and Crossover Ratios for Genetic Algorithms—A Review with a New Dynamic Approach," *Information 2019, Vol. 10, Page 390*, vol. 10, no. 12, p. 390, Dec. 2019, doi: 10.3390/INFO10120390.

[23]   A. K. Peprah, S. K. Appiah, and S. K. Amponsah, "An Optimal Cooling Schedule Using a Simulated Annealing Based Approach," *Appl Math (Irvine)*, vol. 08, no. 08, pp. 1195–1210, Aug. 2017, doi: 10.4236/AM.2017.88090.

ASSESSING THE IMPACTS OF TITANIUM DIOXIDE NANOPARTICLES ON SEED GERMINATION AND SEEDLING GROWTH IN WHEAT

[1, *] **Ozlem ATES SONMEZOGLU** [ID], [2]**Alaa KAMO** [ID], [3] **Busra BOZKAYA** [ID], [4] **Savas SONMEZOGLU** [ID]

[1,2,3] *Karamanoglu Mehmetbey University, Engineering Faculty, Bioengineering Department, Karaman, TÜRKİYE*
[4] *Karamanoglu Mehmetbey University, Engineering Faculty, Metallurgical and Materials Engineering Department, Karaman, TÜRKİYE*

[1] ozlemsonmezoglu@kmu.edu.tr, [2] alaakamow4@gmail.com, [3] bozkayabus@gmail.com, [4] svssonmezoglu@kmu.edu.tr

Highlights

- We evaluate the impact of TiO₂ nanoparticles not only on the germination of seeds but also on the growth of wheat (*Triticum aestivum* L.) through soil application.

- TiO₂ treatment at concentrations up to 2000 mg/L in seeds has a favorable effect on root and shoot length of wheat.

- TiO₂ treatment up to a dosage of 60 mg/kg in the soil treatment has a favorable effect on plant shoot length.

- The most significant stage in demonstrating the favorable impacts of TiO₂ NPs on plant germination rate and root and shoot growth in a dose-dependent way is to determine the optimal concentration.

- The beneficial effects of TiO₂ nanoparticles on seed germination and plant growth may have a big financial impact on horticulture, agriculture, and the energy industry—particularly on the manufacturing of biofuels.

Graphical Absract

*Corresponding Author: Özlem ATEŞ SÖNMEZOĞLU, ozlemsonmezoglu@kmu.edu.tr

ASSESSING THE IMPACTS OF TITANIUM DIOXIDE NANOPARTICLES ON SEED GERMINATION AND SEEDLING GROWTH IN WHEAT

[1,*] Ozlem ATES SONMEZOĞLU [ID], **[2]Alaa KAMO** [ID], **[3] Busra BOZKAYA** [ID], **[4] Savas SONMEZOGLU** [ID]

[1,2,3] Karamanoglu Mehmetbey University, Engineering Faculty, Bioengineering Department, Karaman, TÜRKİYE
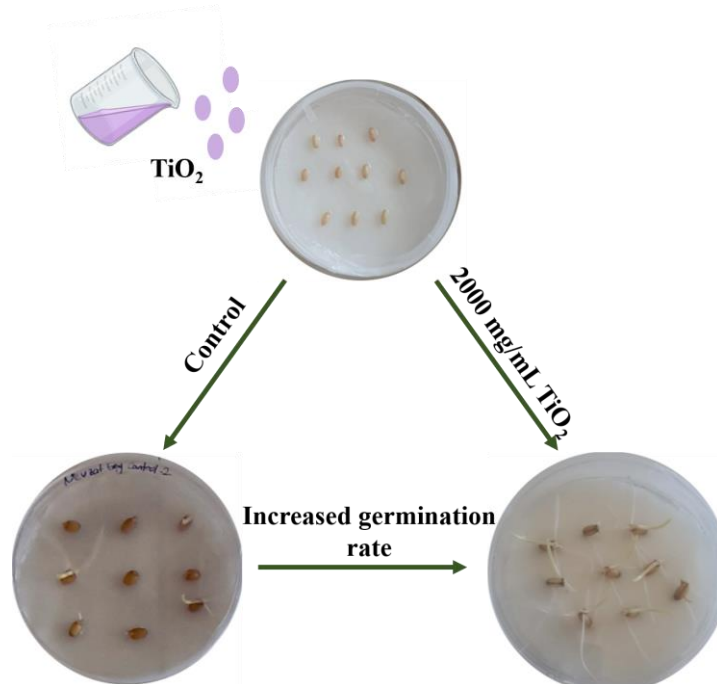*[4] Karamanoglu Mehmetbey University, Engineering Faculty, Metallurgical and Materials Engineering Department, Karaman, TÜRKİYE*
[1] ozlemsonmezoglu@kmu.edu.tr, [2] alaakamow4@gmail.com, [3] bozkayabus@gmail.com, [4] svssonmezoglu@kmu.edu.tr

ABSTRACT: Wheat is the main food source for key nutrients in humans, hence any new research into boosting wheat quality and yield is vital. Recent advances in nanotechnology have made nanoparticles appropriate for use in agriculture. Titanium dioxide (TiO_2) nanoparticles have a considerable impact on plants, but further research is required to make them commercially feasible. Herein, we evaluate the impact of TiO_2 nanoparticles not only on the germination of seeds but also on the growth of wheat (*Triticum aestivum* L.) through soil application. The experimental findings reveal that TiO_2 treatment at concentrations up to 2000 mg/L in seeds planted in Petri dishes has a favorable effect on wheat root and shoot length, whereas it has a suppressive effect at higher concentrations. As expected, a similar trend is observed for plant shoot length in the soil treatment with beneficial effects recorded up to a dosage of 60 mg/kg. In conclusion, the beneficial effects of TiO_2 nanoparticles on seed germination and plant growth may have a big financial impact on horticulture, agriculture, and the energy industry—particularly on the manufacturing of biofuels.

Keywords: Germination, Root Length, Shoot Length, TiO_2 Nanoparticles, Wheat, Triticum Aestivum L.

1. INTRODUCTION

The growing world population has raised the need for food, which has become a serious worldwide concern; boosting agricultural production and minimizing plant yield losses are required to address this issue. Wheat recognized as an essential ingredient in human nutrition, is critical in satisfying dietary requirements; hence, extensive breeding experiments are conducted to improve wheat quality and yield. Besides breeding research, nanotechnology has recently been employed to accelerate the germination and growth of wheat, minimize development time, and produce more efficient seeds [1-3]. Inorganic and organic nanoparticles are employed in a variety of agricultural applications, including the biosensors, nanopesticides and nanofertilizers, the genetic modification of plants and animals to incorporate desired traits, and the development of plant growth regulators through rapid advances in nanotechnology [4, 5]. TiO_2 has been shown in the literature to have greater beneficial impacts on plant growth and seed germination than other inorganic nanoparticles [6-11].

TiO_2 nanoparticles are not only one of the most attractive materials in agriculture and food technology but are also used commercially in a wide range of other industries, such as cosmetics, medicines, catalysts, solar cells and microelectronic devices [12-18]. TiO_2 usage in various sectors can lead to its accumulation in rivers and water treatment systems, meaning that the probability of reaching the plants during irrigation is high. Understanding the impact of TiO_2 on plants is therefore crucial for both the environment and human health.

A research in the literature reported that nano-anatase TiO_2 dramatically boosted spinach leaf biomass, total nitrogen, and oxygen, chlorophyll, and protein levels [19]. In another work, they discovered that TiO_2 NPs can mitigate the negative impacts of drought stress on plant physiological

*Corresponding Author: Ozlem ATES SONMEZOGLU, ozlemsonmezoglu@kmu.edu.tr

processes by lowering MDA and H_2O_2 levels and stabilizing photosynthetic pigments[6]. On the other hand, Amini et al. [20] revealed that TiO_2 NPs have an active role in signal transduction, defense, metabolism, and regulation under stress conditions. Badshah et al. [21] investigated the effects of green synthesized TiO_2 NPs (25, 50, 75, and 100 μg/mL) on wheat cultivars under salt stress. The results show that TiO2 NPs improved germination rates as well as morphological and metabolic characteristics in both salt-stressed and control environments. Specifically, 25 μg/mL and 50 μg/mL concentrations improved plant length, fresh and dry weight, leaf area, and chlorophyll content under stress conditions. However, 75 μg/mL and 100 μg/mL concentrations showed adverse effects on germination, agronomic, physiological, and biochemical attributes. Moreover, Faraji and Sepehri [22] explored the effects of TiO_2 NPs (0, 500, 1000, and 2000 mg/L) and sodium nitroprusside (SNP) (0 and 100 μM) on seed germination and seedling growth of wheat under drought stress caused by polyethylene glycol (PEG) (0, -0.4 and -0.8 MPa). They reported that drought stress induced by PEG decreased germination percentage (GP), germination rate (GR), germination energy (GE), fresh root weight (RFW), root length (RL), vigor index (VI), fresh shoot weight (SFW), shoot length (SL) and the germination time (MGT) increased in wheat seeds. It has been reported that MGT decreases significantly under severe drought stress. However, using TiO_2 NPs and SNP alone or in combination has significantly increased GP, GE, GR, RL, SL, RFW, SFW, and VI. After all these observations, they concluded that applying TiO_2 NPs and SNP alone or in combination could substantially reduce the adverse effects of PEG-induced drought stress on seed germination and early seedling growth of wheat. In another study, Feizi et al. [23] evaluated the effects of TiO_2 concentrations (in the range of 1-500 ppm) on seed germination and wheat seedling growth. Their results showed that only the TiO_2 NPs treatments affected the mean germination time among the wheat germination indices. The lowest and highest mean germination time was found at control and 10 ppm concentration, respectively. The authors reported that shoot length, seedling length, and root dry matter were positively affected by TiO_2 NPs, and plant seedling lengths were higher than control (without TiO_2) at 2 and 10 ppm concentrations of TiO_2. According to the EU's Scientific Committee on Emerging and Newly Identified Health Risks, NPs are not dangerous, but their safety is still debated.

The purpose of this study was to investigate the effects of TiO_2 NPs on morphological characteristics of wheat (*Triticum aestivum* L.) such as germination, root, and shoot length. To assess shoot and root development in two bread wheat varieties (Adana 99 and Nevzatbey), we evaluated the impact of four different concentrations (500, 1000, 2000, and 3000 mg/L) in a Petri dish and five variable concentrations (20, 40, 60, 80 and 100 mg/kg--TiO_2/soil) in the soil.

2. MATERIAL and METHOD

2.1. Plant Material and Sterilization

Two varieties of wheat, Adana 99 and Nevzatbey, were used in the study. Adana 99 and Nevzatbey wheat *seeds* were supplied by Prof. Dr. Nevzat AYDIN. Wheat seeds were sterilized with 70% Ethyl Alcohol (C_2H_5OH), distilled water, and 0.5 % sodium hypochlorite (NaClO), respectively. Then, the seeds were rinsed in pure water four times for 5 minutes.

2.2. Preparation of TiO_2 Solutions

The Nanosized TiO_2 powder was AEROXIDE® TiO_2 P25, supplied by Sigma Aldrich Company. The primary particle size of nanosized TiO_2 was 21 nm, and purity was > 99.5%. 500, 1000, 2000, and 3000 mg/L TiO_2 solutions were prepared from the main stock. 80 mL of ultrapure water was used to disperse 0.5 g of TiO_2 using sonication at 300 W and 40 kHz for 2 hours. Once the sonication process was complete, the solution was diluted with distilled water to a final volume of 100 mL.

2.3. Seed Germination

Experiments were carried out in two replications. After the seed sterilization, autoclaved filter papers were placed on the Petri dishes, and nine wheat seeds were placed at an equal distance. Then, 5 ml of the prepared TiO₂ solutions were added to each Petri dish at the determined concentrations with a micropipette. After sowing the seeds, the Petri dishes were closed by parafilm. The Petri dishes were kept in the dark for two days, then transferred to a plant growth cabinet and left to grow for 21 days at 24°C, under a 16-hour light and 8-hour darkness cycle [24]. During this period, the root and shoot lengths of the germinated wheat in the sterile cabinet on the 3rd, 7th, 15th, 18th, and 21st days were measured and noted. Seeds with a root of 2 mm were considered to have started to germinate, and the following formula was used to calculate the germination rate.

$$Germination\ Rate\ (\%) = \frac{\text{The Number of Germinated Seeds}}{\text{The Total Seeds Placed in Petri Dish}} \times 100$$

Under greenhouse conditions, an equal amount of soil was placed in the pots, and two seeds from Adana 99 and Nevzatbey varieties were planted and grown in each pot under equal conditions; for soil treatment five different concentrations of TiO₂ NPs (0, 20, 40, 60, 80 and 100 mg/kg – w(TiO₂)/w(Soil)) were applied. The pots were watered regularly in equal amounts at certain intervals. Plants were grown in the greenhouse and shoot length measurements were made at certain intervals during the 15th and 30th days.

2.4. Statistical Analysis

The obtained data were subjected to variance analysis with the "SPSS 16 for Windows" program, and the Duncan (DMRT) test was used to compare the means. P < 0.05 was accepted as significant in all statistical evaluations.

3. RESULTS and DISCUSSIONS

TiO₂ solutions were prepared at concentrations of control (0), 500, 1000, 2000, and 3000 mg/L to evaluate the effects of TiO₂ NPs on germination, root, and shoot length of wheat (*Triticum aestivum* L). Nine seeds were sown in each Petri dish in two replications and the sown seeds were treated with TiO₂ solutions prepared at different concentrations.

Germination rates of the wheat seeds planted in Petri dishes according to different days given in Table 1. According to Table 1, the germination rate of Adana 99 variety seeds planted in Petri dishes on the third day in the control group was 61.11%. Germination rates on the 7th, 10th, and 15th days were calculated as 66.67%. At 500 mg/L TiO₂ concentration, germination rates were calculated as 66.67% on the 3rd day and 77.78% on the other days. At 1000 mg/L TiO₂ concentration, the germination rate did not change from the 3rd day and gave 77.78%. The germination rate at 2000 mg/L gave the highest rate with 83.33%. The germination rate was 66.67% on the 3rd day at 3000 mg/L TiO₂ concentration and 72.22% on the other days. While the lowest germination rate result was observed in the control group, the highest germination rate was determined at 2000 mg/L concentration. According to the results obtained, it can be stated that TiO₂ NPs have a positive effect on the germination of the Adana 99 variety. The germination rate, which was calculated as 55.56% on the 3rd day in the control group, was calculated as 61.11% on the other days for Nevzatbey (Table 1). While the germination rates were calculated as 66.67% on the 3rd day at 500 mg/L TiO₂ concentration, it was 72.22% on the 7th, 10th, and 15th days. While the germination rate was 72.22% on the 3rd day at 1000 mg/L, it was calculated as 77.78% in subsequent days. The germination rate results of 2000 mg/L and 3000 mg/L TiO₂ concentrations were calculated as 72.22% and 66.67 respectively. While the highest germination rate was observed at 1000 mg/L, the lowest germination rate was observed in the control group.

Table 1. Germination rates of the wheat seeds with time-varying

Day	Adana 99		Nevzatbey	
	Concentration (mg/L)	Germination rate (%)	Concentration (mg/L)	Germination rate (%)
3	Control	61,11 a	Control	55,56 a
7	Control	66,67 a	Control	61,11 a
10	Control	66,67 a	Control	61,11 a
15	Control	66,67 a	Control	61,11 a
3	500	66,67 ab	500	66,67 ab
7	500	77,78 ab	500	72,22 ab
10	500	77,78 ab	500	72,22 ab
15	500	77,78 ab	500	72,22 ab
3	1000	77,78 bc	1000	72,22 b
7	1000	77,78 ab	1000	77,78 b
10	1000	77,78 ab	1000	77,78 b
15	1000	77,78 ab	1000	77,78 b
3	2000	83,33 c	2000	72,22 b
7	2000	83,33 b	2000	72,22 ab
10	2000	83,33 b	2000	72,22 ab
15	2000	83,33 b	2000	72,22 ab
3	3000	66,67 ab	3000	66,67 ab
7	3000	72,22 ab	3000	66,67 ab
10	3000	72,22 ab	3000	66,67 ab
15	3000	72,22 ab	3000	66,67 ab

**The difference between the means shown with different letters in the same column is significant at the $p \leq 0.05$ level.

The lowest germination rate of the two investigated wheat cultivars was observed in the control group. Since the calculated germination rate at different concentrations of TiO_2 is higher than the control group, it is determined that the TiO_2 NPs positively affect the germination rate. NPs can induce active oxygen owing to their photocatalytic activity. Thus, they can support the germination of the plant by increasing the stress resistance and water and oxygen uptake of the seed [25]. Feizi et al. [23] reported that an appropriate concentration of nano-TiO_2 can promote wheat seed germination but has an inhibitory effect at high concentrations. Similarly, in another study in which the effect of NPs on wheat germination under stress was observed, the positive role of TiO_2 NPs and SNP on wheat germ germination indices was stated. As a result of the study, it was reported that applying TiO_2 NPs and SNP could be a promising approach for reducing the effects of stress on wheat seed germination and early growth [24]. Shoot and root lengths of Adana 99 and Nevzatbey wheat varieties were measured at 7, 10, 15, and 21 days to evaluate the effects of TiO_2 NPs. The results of the effect of TiO_2 applied at different concentrations on plant shoot and root length of the wheat varieties are shown in Table 2. Accordingly, the Nevzatbey cultivar had the highest shoot and root length on the 21st day, with a concentration of 2000 mg/ml and values of 15.71 and 15.99, respectively. By increasing the concentration to 3000 mg/ml, shoot and root lengths generally decreased compared to other concentration ratios. Taking into consideration the assessment of shoot and root lengths in Table 2, both shoot and root lengths at 3000 mg/ml were much lower for the Adana 99 variety than the control. Low TiO_2 concentrations may not show any significant favorable benefits. It is clear that further increases in concentrations may result in toxicity, even if other research indicate the presence of beneficial benefits at high concentrations [26].

Table 2. The effect of TiO₂ application at different concentrations and days on shoot and root length of the wheat varieties

TiO₂ (mg/L)	Day	Adana 99		Nevzatbey	
		Shoot Length (cm)**	Root Length (cm)**	Shoot Length (cm)**	Root Length (cm)**
Control	7	7,00 a	6,82 a	6,23 a	5,68 a
	10	7,41 ab	6,67 a	10,68 a	10,71 a
	15	11,32 a	10,99 a	12,84 ab	12,08 a
	21	12,53 a	12,21 a	13,35 a	12,38 a
500	7	7,22 ab	6,95 a	6,55 a	5,95 ab
	10	7,71 bc	7,93 b	10,88 ab	11,08 ab
	15	12,04 ab	12,59 b	13,30 abc	13,88 b
	21	13,27 b	13,84 b	13,73 a	14,25 b
1000	7	7,52 ab	6,99 a	7,01 ab	6,36 ab
	10	7,96 cd	8,40 c	11,66 bc	11,83 bc
	15	12,36 b	12,86 b	13,75 bc	14,36 b
	21	14,18 c	14,87 c	15,22 b	15,70 c
2000	7	7,77 b	7,22 a	7,48 b	6,71 b
	10	8,26 d	8,75 c	12,14 c	12,49 c
	15	12,50 b	13,28 b	14,12 c	14,60 b
	21	14,59 c	15,08 c	15,71 b	15,99 c
3000	7	6,94 a	6,62 a	6,39 a	5,85 ab
	10	7,15 a	6,40 a	10,47 a	10,33 a
	15	11,20 a	10,64 a	12,40 a	11,96 a
	21	12,42 a	11,97 a	12,93 a	12,33 a

**The difference between the means shown with different letters in the same column is significant at the p≤0.05 level.

According to the Adana 99 variety shoot lengths at different TiO₂ concentrations (Figure 1a), a linear increase was observed in shoot lengths up to 2000 mg/L concentration on the 7th and 10th days, while a higher increase was observed on the 15th day compared to the other days. The lowest shoot length was determined at 3000 mg/L TiO₂ concentration. When the root lengths observed on the 7th, 10th, 15th, and 21st days of the Adana 99 cultivar were examined (Figure 1b), the same result was reached with the shoot length and the highest root length was observed at 2000 mg/L, while the lowest root length was found at 3000 mg/L. Song et al. [27] also found that low concentrations of titanium dioxide promoted plant growth, but high concentrations inhibited it. According to SPSS data results of the shoot and root lengths of the Nevzatbey variety, root and shoot measurements are shown in Figures 1c and 1d. A linear increase up to 2000 mg/L was observed in both graphs, while a decrease was observed at 3000 mg/L. The experimental findings suggest that TiO₂ NPs can increase plant water and nutrient uptake by expanding root pores due to heightened surface reactivity [28]. However, elevated concentrations of TiO₂ nanoparticles may cause NP aggregation, potentially leading to decreased water availability due to pore clogging in roots [29]. Higher organic matter concentration reduces the bioavailability and mobility of NPs. For this reason, high levels of TiO₂ NPs may also affect shoots and roots [30].
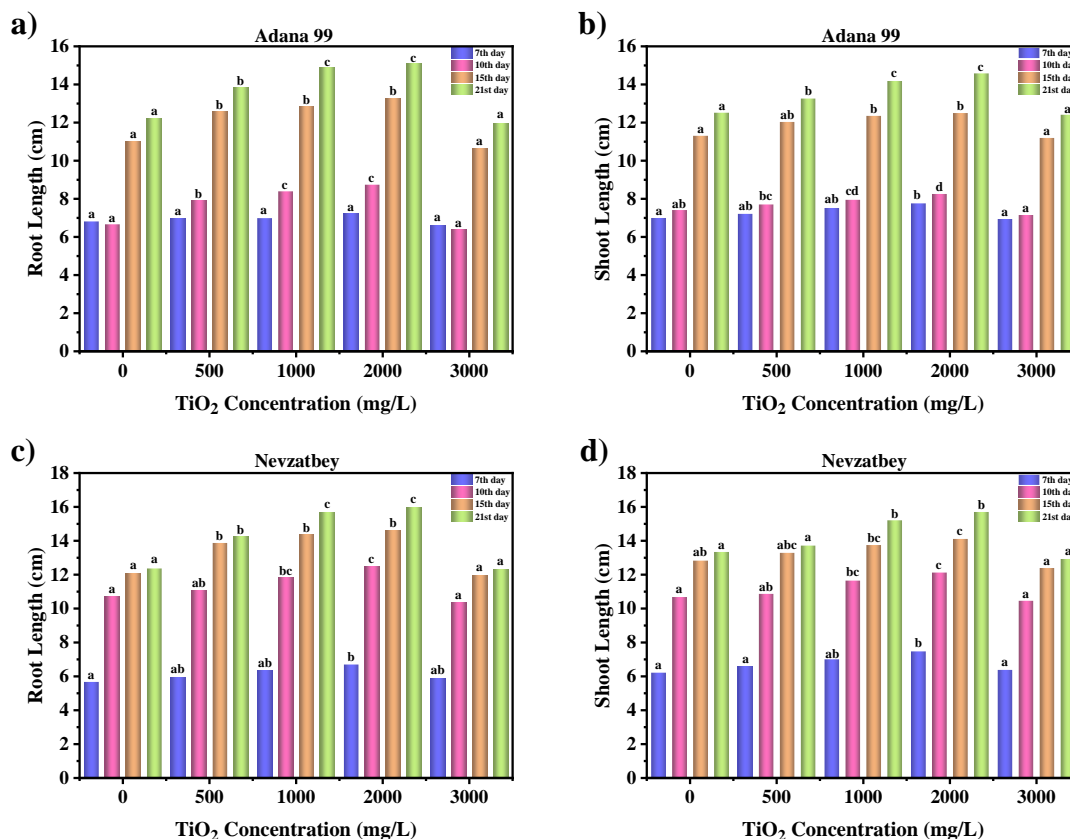
Figure 1. The effect of TiO$_2$ at different concentrations on the root (a,c) and shoot (b,d) length of Adana 99 and Nevzatbey varieties.

Aliabadi et al. [31] used both nano TiO$_2$ and nano aluminum in four different concentrations (0, 100, 1000, and 2000 mg/L). Their study shows that high doses of nano aluminum and TiO$_2$ have a negative and toxic effect on wheat. Generally, it was determined that high NP concentration decreased shoot and root length and showed a small positive effect at 100 mg/L concentration. Nano titanium dioxide application at a concentration of 100 mg/L positively affected growth parameters. It was reported that it could alleviate the negative effects of nano aluminum in combined effects. This study found no negative and toxic effects of TiO$_2$ on wheat. It has been observed that TiO$_2$ NPs up to a certain dose positively affect plant root and shoot length.

According to the 7th-day variance analysis results of the Adana 99 variety, there was no significant difference between shoot lengths but a considerable difference between root lengths. However, significant differences were found between the shoot and root lengths according to the analysis of variance on the 10th, 15th, and 21st days (Table S1). Considering the 7th-day variance analysis results of the Nevzatbey variety, there was no significant difference between shoot lengths but a significant difference in root lengths. Additionally, significant differences were found between the shoot and root lengths according to the analysis of variance on the 10th, 15th, and 21st days (Table S2). When the analysis results of the Adana 99 and Nevzatbey varieties are evaluated, it can be stated that TiO$_2$ concentrations up to 2000 mg/L increase wheat root and shoot length, while a concentration of 3000 mg/L negatively affects shoot and root length. The highest shoot and root lengths were observed in the 1000 and 2000 mg/L TiO$_2$ treatments.

Considering the experimental findings by applying different TiO$_2$ concentrations to wheat grown in pots at greenhouse conditions with equal treatments, at the end of the 15th day, the shoot length of the plant increased up to 60 mg/kg compared to the control, while it decreased at 80 and 100 mg/kg TiO$_2$ at Adana 99 variety grown in the soil (Figure 2a). As a result of the measurements made at the end of the 30th day in the Adana 99 variety, it was seen that TiO$_2$ application up to 60 mg/kg provided elongation

in shoot length. However, it was determined that TiO_2 caused a decrease in shoot length at the rates of 80 and 100 mg/kg. Also, for the Nevzatbey variety, the lowest shoot length (26.2 cm) was observed at the concentration of 100 mg/kg on the 15th day, followed by the lowest shoot length of 26.3 cm in the control group ((Figure 2b). The shoot length was highest at 60 mg/kg and 40 mg/kg TiO_2 concentrations, measuring 28.6 cm and 28.4 cm, respectively. At the end of the 30th day, the lowest shoot length was observed at 34.2 cm and 34.3 cm at 100 mg/kg and control group, while the highest shoot length was observed at 36.8 cm and 36.4 cm at concentrations of 60 mg/kg and 40 mg/kg.
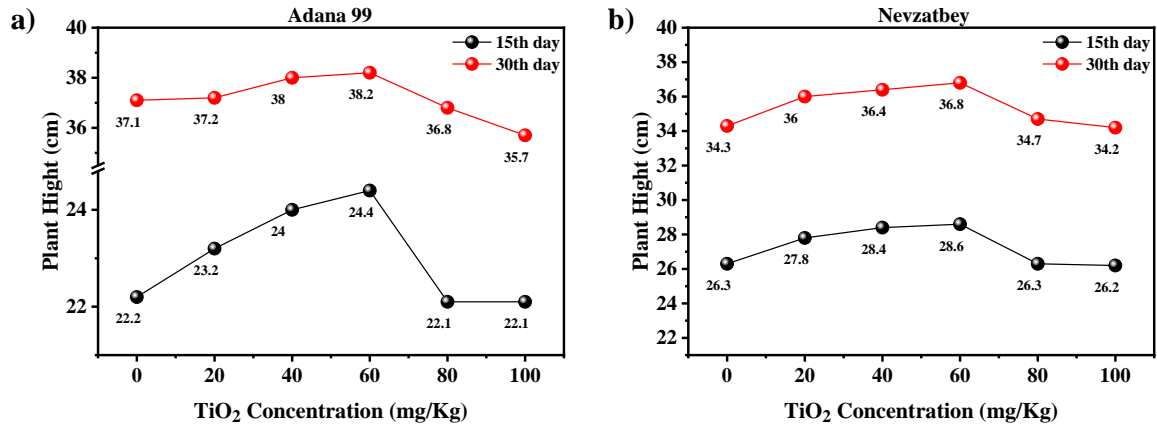
Figure 2. Plant height (cm) graph of a) Adana 99 and b) Nevzatbey variety planted in soil on the 15th and 30th days.

Rafique et al. [32] evaluated the effects of different concentrations of TiO_2 (0, 20, 40, 60, 80, 100 mg/kg) on morphological parameters such as root, shoot length, and biomass of wheat plants (*Triticum aestivum*). In general, TiO_2 NPs positively affected shoot length up to 60 mg/kg, while it negatively impacted 80 and 100 mg/kg TiO_2 treatments. These results concluded that while TiO_2 NPs positively affected plant growth up to a particular concentration, they had a negative effect at higher concentrations [32]. Our results are consistent with the study of Rafique et al. (2014). It was observed that root, shoot length, and biomass were significantly affected by TiO_2 NP treatment. It was determined that the root and shoot lengths of the plant increased up to 60 mg/kg TiO_2 NPs. However, it has been reported that high TiO_2 NP concentrations increase the root and shoot lengths of the plant while decreasing its biomass.

The effect of TiO_2 applications at different concentrations of both wheat varieties grown in the soil on the shoot length of the plant was analyzed by the SPSS program and given in Table 3. In Adana 99 wheat varieties, the highest shoot length was measured at 38.13 cm on the 30th day, while the lowest was 35.72 cm at a 100 mg/kg concentration. In the Nevzatbey variety, the highest shoot length was observed at 60 mg/kg TiO_2 treatment on the 30th day, while the lowest shoot length was determined at 100 mg/kg TiO_2 concentration on the 30th day.

Table 3. The effect of TiO$_2$ treatment at different concentrations and days on shoot length of Adana 99 and Nevzatbey cultivars

TiO$_2$ (mg/kg)	Wheat cultivar	Day	Shoot Length (cm)
Control	Adana 99	15	22,15 a
		30	37,08 a
20	Adana 99	15	23,18 a
		30	37,12 a
40	Adana 99	15	23,96 a
		30	38,03 a
60	Adana 99	15	24,16 a
		30	38,13 a
80	Adana 99	15	22,10 a
		30	36,78 a
100	Adana 99	15	22,05 a
		30	35,72 a
Control	Nevzatbey	15	26,33 a
		30	34,25 ab
20	Nevzatbey	15	27,81 a
		30	35,98 ab
40	Nevzatbey	15	28,41 a
		30	36,41 ab
60	Nevzatbey	15	28,55 a
		30	36,81 b
80	Nevzatbey	15	26,30 a
		30	34,66 ab
100	Nevzatbey	15	26,21 a
		30	34,15 a

It was determined that TiO$_2$ increased the shoot length of the plant up to a concentration of 80 mg/kg, caused a decrease in shoot length at 100 mg/kg, and adversely affected plant growth. Based on these results, it was stated that high concentrations of TiO$_2$ NPs might be inhibitory, and that further investigation is needed to determine the possible consequences and effects of applying NPs to crops (Table 3). The results we obtained in this study supported the study of Rafique et al. (2014).

4. CONCLUSION

In this study, we evaluated the effects of TiO$_2$ NPs on the growth and germination of wheat. For this point, cultivars of Adana 99 and Nevzatbey were treated with varying concentrations of TiO$_2$ (0, 500, 1000, 2000, and 3000 mg/L) in Petri dishes, and observations regarding germination and growth were recorded at 7, 10, 15, and 21 days. As a result of TiO$_2$ treatments, the same results were obtained in both wheat varieties. The highest root and shoot length was determined at 2000 mg/L and 1000 mg/L TiO$_2$ concentrations. Compared to the control group, it was observed that TiO$_2$ NPs up to 2000 mg/L had a positive effect on wheat root and shoot length, while it had a negative effect at 3000 mg/L TiO$_2$ concentration. At the same time, TiO$_2$ positively affected wheat germination rate up to 2000 mg/L, while a decrease was found at 3000 mg/L. Consequently, it was observed that TiO$_2$ NPs had a positive effect on the root growth of wheat up to a specific concentration. In both cultivars grown in soil, it was determined that the shoot lengths increased up to 60 mg/kg compared to the control and decreased at 80 and 100 mg/kg TiO$_2$ concentrations. This study suggested that the most significant stage in demonstrating the favorable impacts of TiO$_2$ NPs on plant germination rate and root and shoot growth in a dose-dependent way is to determine the optimal concentration. On the other hand, we may

conclude that further in-depth research under various environmental conditions, dosages, and durations should be conducted in the future to completely understand the mechanism of action of TiO$_2$ NPs on germination and growth of wheat.

Declaration of Ethical Standards

The authors declare that the study complies with all applicable laws and regulations and meets ethical standards.

Credit Authorship Contribution Statement

Ozlem ATES SONMEZOGLU: Conceptualization, Funding acquisition, Project administration, Supervision, Writing – review & editing. Alaa KAMO: Visualization, Writing-original draft. Busra BOZKAYA: Investigation, Methodology. Savas SONMEZOGLU: Conceptualization, Resources, Writing – review & editing.

Declaration of Competing Interest

The authors declare that they have no known competing financial interests or personal relationships that could have appeared to influence the work reported in this paper.

Data Availability

Research data will be made available on request.

REFERENCES

[1]   A. Staroń, O. Długosz, J. Pulit-Prociak, and M. Banach, "Analysis of the exposure of organisms to the action of nanomaterials," Materials, vol. 13, no. 2, pp. 349, 2020.

[2]   O. Ates Sonmezoglu and K. Ozkay, "A new organic dye-based staining for the detection of plant DNA in agarose gels," Nucleosides, Nucleotides and Nucleic Acids, vol. 34, no. 7, pp. 515-522, 2015.

[3]   E. Yavuzaslanoglu, M. Karaca, O. A. Sonmezoglu, O. Atilla, H. Elekcioglu, and M. Aydogdu, "Occurrence and abundance of cereal nematodes in Konya and Karaman Provinces in Turkey," Turkish Journal of Entomology, vol. 44, no. 2, pp. 223-236, 2020.

[4]   D. Singh and B. R. Gurjar, "Nanotechnology for agricultural applications: Facts, issues, knowledge gaps, and challenges in environmental risk assessment," Journal of Environmental Management, vol. 322, pp. 116033, 2022.

[5]   A. Kamo, A. Ozcan, O. A. Sonmezoglu, and S. Sonmezoglu, "Understanding antibacterial disinfection mechanisms of oxide-based photocatalytic materials," Nanocomposite and Nanohybrid Materials: Processing and Applications, vol. 17, pp. 195, 2023.

[6]   M. T. B. Aghdam, H. Mohammadi, and M. Ghorbanpour, "Effects of nanoparticulate anatase titanium dioxide on physiological and biochemical performance of Linum usitatissimum (Linaceae) under well-watered and drought stress conditions," Brazilian journal of botany, vol. 39, pp. 139-146, 2016.

[7]   H. Sun et al., "Uptake, transformation, and environmental impact of zinc oxide nanoparticles in a soil-wheat system," Science of The Total Environment, vol. 857, pp. 159307, 2023.

[8]   V. Kreslavski, A. Ivanov, A. Shmarev, A. Khudyakova, and A. Kosobryukhov, "Influence of iron nanoparticles (Fe3O4 and Fe2O3) on the growth, photosynthesis and antioxidant balance of wheat plants (Triticum aestivum)," in BIO Web of Conferences, 2022, vol. 42: EDP Sciences, pp. 01023.

[9]   A. S. Ibrahim, G. A. Ali, A. Hassanein, A. M. Attia, and E. R. Marzouk, "Toxicity and uptake of CuO nanoparticles: evaluation of an emerging nanofertilizer on wheat (Triticum aestivum L.) plant," Sustainability, vol. 14, no. 9, pp. 4914, 2022.

[10]   M. S. Khater, "Effect of titanium nanoparticles (TiO2) on growth, yield and chemical constituents of coriander plants," Arab Journal of Nuclear Science and Applications, vol. 48, no. 4, pp. 187-194, 2015.

[11]   M. Aasim, E. Korkmaz, A. Culu, B. Kahveci, and O. A. Sonmezoglu, "TiO2 nanoparticle synthesis, characterization and application to shoot regeneration of water hyssop (Bacopa monnieri L. Pennel) in vitro," Biotechnic & Histochemistry, vol. 98, no. 1, pp. 29-37, 2023.

[12]   T. Kaida, K. Kobayashi, M. Adachi, and F. Suzuki, "Optical characteristics of titanium oxide interference film and the film laminated with oxides and their applications for cosmetics," Journal of cosmetic science, vol. 55, no. 2, pp. 219-220, 2004.

[13]   M. Pourmadadi et al., "TiO2-based nanocomposites for cancer diagnosis and therapy: a comprehensive review," Journal of Drug Delivery Science and Technology, p. 104370, 2023.

[14]   S. Sonmezoglu, G. Çankaya, and N. Serin, "Influence of annealing temperature on structural, morphological and optical properties of nanostructured TiO2 thin films," Materials Technology, vol. 27, no. 3, pp. 251-256, 2012.

[15]   O. Ates Sonmezoglu, S. Akın, B. Terzi, S. Mutlu, and S. Sönmezoğlu, "An effective approach for high-efficiency photoelectrochemical solar cells by using bifunctional DNA molecules modified photoanode," Advanced Functional Materials, vol. 26, no. 47, pp. 8776-8783, 2016.

[16]   S. Sonmezoglu and S. Akın, "High performance GaAs metal-insulator–semiconductor devices using TiO2 as insulator layer," Current applied physics, vol. 12, no. 5, pp. 1372-1377, 2012.

[17]   E. Akman, S. Akın, G. Karanfil, and S. Sonmezoglu, "Organik güneş pilleri," Trakya Üniversitesi Mühendislik Bilimleri Dergisi, vol. 14, no. 1, pp. 1-30, 2013.

[18]   A. Culu, I. C. Kaya, and S. Sonmezoglu, "Spray-pyrolyzed tantalium-doped TiO2 compact electron transport layer for UV-photostable planar perovskite solar cells exceeding 20% efficiency," ACS Applied Energy Materials, vol. 5, no. 3, pp. 3454-3462, 2022.

[19]   F. Yang et al., "The improvement of spinach growth by nano-anatase TiO2 treatment is related to nitrogen photoreduction," Biological trace element research, vol. 119, pp. 77-88, 2007.

[20]   S. Amini, R. Maali-Amiri, R. Mohammadi, and S.-S. Kazemi-Shahandashti, "cDNA-AFLP analysis of transcripts induced in chickpea plants by TiO2 nanoparticles during cold stress," Plant physiology and biochemistry, vol. 111, pp. 39-49, 2017.

[21]   I. Badshah et al., "Biogenic titanium dioxide nanoparticles ameliorate the effect of salinity stress in wheat crop," Agronomy, vol. 13, no. 2, p. 352, 2023.

[22]   J. Faraji and A. Sepehri, "Ameliorative effects of TiO2 nanoparticles and sodium nitroprusside on seed germination and seedling growth of wheat under PEG-stimulated drought stress," Journal of Seed Science, vol. 41, pp. 309-317, 2019.

[23]   H. Feizi, P. Rezvani Moghaddam, N. Shahtahmassebi, and A. Fotovat, "Impact of bulk and nanosized titanium dioxide (TiO2) on wheat seed germination and seedling growth," Biological trace element research, vol. 146, pp. 101-106, 2012.

[24]   J. Faraji, A. Sepehri, and J. C. Salcedo-Reyes, "Titanium dioxide nanoparticles and sodium nitroprusside alleviate the adverse effects of cadmium stress on germination and seedling growth of wheat (Triticum aestivum L.)," Universitas Scientiarum, vol. 23, no. 1, pp. 61-87, 2018.

[25]   Y. Wang et al., "The application of nano-TiO2 photo semiconductors in agriculture," Nanoscale research letters, vol. 11, no. 1, pp. 1-7, 2016.

[26]   L. Kořenková et al., "Physiological response of culture media-grown barley (Hordeum vulgare L.) to titanium oxide nanoparticles," Acta Agriculturae Scandinavica, Section B—Soil & Plant Science, vol. 67, no. 4, pp. 285-291, 2017.

[27]   G. Song, Y. Gao, H. Wu, W. Hou, C. Zhang, and H. Ma, "Physiological effect of anatase TiO2 nanoparticles on Lemna minor," Environmental Toxicology and Chemistry, vol. 31, no. 9, pp. 2147-2152, 2012.

[28]   C. Larue et al., "Accumulation, translocation and impact of TiO2 nanoparticles in wheat (Triticum aestivum spp.): influence of diameter and crystal phase," Science of the total environment, vol. 431, pp. 197-208, 2012.

[29]   H. Feizi, S. Amirmoradi, F. Abdollahi, and S. J. Pour, "Comparative effects of nanosized and bulk titanium dioxide concentrations on medicinal plant Salvia officinalis L," Annual Research & Review in Biology, vol. 3, no. 4, pp. 814-824, 2013.

[30]   C. Larue et al., "Influence of soil type on TiO2 nanoparticle fate in an agro-ecosystem," Science of the total environment, vol. 630, pp. 609-617, 2018.

[31]   T. Aliabadi, A. Safipour Afshar, and F. Saeid Nematpour, "The effects of nano TiO2 and Nano aluminium on the growth and some physiological parameters of the wheat (Triticum aestivum)," Iranian Journal of Plant Physiology, vol. 6, no. 2, pp. 1627-1635, 2016.

[32]   R. Rafique, M. Arshad, M. Khokhar, I. Qazi, A. Hamza, and N. Virk, "Growth response of wheat to titania nanoparticles application," NUST Journal of Engineering Sciences, vol. 7, no. 1, pp. 42-46, 2014.

VIBRATION BEHAVIOR OF THERMOPLASTIC COMPOSITE WITH DIFFERENT GLASS FIBER CONTENTS UNDER LOW-TEMPERATURE CONDITIONS

[1] **Hayrettin ŞEN** [ID], [2,*] **Murat AKDAĞ** [ID], [3] **Gökçe Mehmet GENÇER** [ID], [4] **Nahit ÖZTOPRAK** [ID]

[1] *Izmir Katip Celebi University, Mechatronics Engineering, Izmir, TÜRKİYE*
[2, 3, 4] *Dokuz Eylul University, Mechanical Engineering Department, Izmir, TÜRKİYE*
[1] hayrettin.sen@ikcu.edu.tr, [2] murat.akdag@deu.edu.tr, [3] mehmet.gencer@deu.edu.tr, [4] nahit.oztoprak@deu.edu.tr

Highlights

- Free vibration responses of the thermoplastic composite beam were investigated.

- Effect of subzero temperature on the natural frequency and damping ratio was observed.

- The relation between the change of glass fiber content and vibration characteristics was revealed.

*Corresponding Author: Murat AKDAĞ, murat.akdag@deu.edu.tr

VIBRATION BEHAVIOR OF THERMOPLASTIC COMPOSITE WITH DIFFERENT GLASS FIBER CONTENTS UNDER LOW-TEMPERATURE CONDITIONS

[1] Hayrettin ŞEN, [2, *] Murat AKDAĞ, [3] Gökçe Mehmet GENÇER, [4] Nahit ÖZTOPRAK

[1] Izmir Katip Celebi University, Mechatronics Engineering, Izmir, TÜRKİYE
[2, 3, 4] Dokuz Eylul University, Mechanical Engineering Department, Izmir, TÜRKİYE
[1] hayrettin.sen@ikcu.edu.tr, [2] murat.akdag@deu.edu.tr, [3] mehmet.gencer@deu.edu.tr, [4] nahit.oztoprak@deu.edu.tr

ABSTRACT: Glass fiber-reinforced thermoplastic composites are continuously finding their application especially in the field of aerospace and marine due to their stiffness-to-weight advantages. Accordingly, it has gained prominence to evaluate the behavior of composites under diversified environmental conditions where vibration inputs are common. In this research, effect of various environments on the free vibration response of long glass fiber-reinforced polypropylene (PP) composites with different fiber ratios is investigated. Free vibration under an impulse response of thermoplastic composite samples is studied experimentally in a vibration test setup with fixed support. Numerical simulations are also performed through 3D FE models. The present study has revealed that the decrease in temperature increases the natural frequency of the PP composites by over 20%, exceeding 20 Hz. Moreover, whether the composites have 20 wt.% or 40 wt.% long glass fiber content, the damping factors of thermoplastic composites are highly dependent on temperature. The damping ratio distinctly decreases to below 0.008 at -70°C while it increases by over 50% at 0°C relative to the value at room temperature.

1. INTRODUCTION

Developing technology has triggered to substitution of conventional materials with modern engineered materials that can offer a variety of required qualities altogether. Especially, to ensure the low emission goal and efficient use of natural resources due to the increasing environmental restrictions, without sacrificing any mechanical property, the importance of the utilization of polymer-based composite materials that are lighter than traditional alloys has been growing rapidly in the designed structures [1]. In this regard, thermoplastic-based composites with remarkable characteristics, such as being light and having good recyclability, low cost, high ductility, and adequate damping strength; are commonly employed in the aviation, automotive, marine, and petroleum industries [2], [3], [4], [5], [6].

Fiber-reinforced composites are mostly preferred materials among the various composites in engineering applications [7]. While the fibers, having high strength and modulus, take the bearing role, the matrix material transfers the stress between fibers, performs a barrier role against unfavorable environmental conditions, and protects the fibers from wear by wrapping them [8]. Glass fiber as a reinforcement has a usage share of approximately 90% in the industry due to its notable qualities, which include being readily available in a variety of forms, inexpensively processable using various manufacturing techniques, and inert [9]. Considering the effect of glass fiber on improving the mechanical properties of the composite, its utilization as a reinforcement in polypropylene (PP), one of the thermoplastic-based matrixes now in use, is cost-effective and quite common [2], [3], [4], [5], [6], [8], [9], [10].

According to the application fields, engineering materials should continue to exhibit the expected qualities under various and variable conditions. For instance, while modern airplanes should endure varying temperatures between -55°C and 50°C [11], spacecraft and satellites operating in low-orbit conditions should withstand changing temperatures between -170°C and 200°C. Consequently, studies

__Corresponding Author__: Murat AKDAĞ, murat.akdag@deu.edu.tr

also have been carried out in aerospace engineering to investigate and optimize the properties of the composite materials used as wing, airframe, and structural elements of cryogenic fuel tanks under extreme circumstances [12], [13].

Exposing fiber-reinforced composite materials to low temperatures may result in the formation of internal stress-based micro-cracks between fibers and matrix due to the unequal thermal expansion coefficients. Therefore, it may be possible that the desired characteristics of a composite material may not be achieved as the ambient temperature drops or changes [2]. This becomes more critical in particular if an engineering material utilized in the aerospace/space industry is also required to resist dynamic loading or vibrations under this kind of extreme service conditions. To prevent any fracture or crack initiation, the structural component of a designed system should endure internal or external vibrations. Since the damping capability of the structure determines the stability of the system [14].

Several studies focus on the mechanical characteristics of polymer-based composites under sub-zero temperatures. However, in low temperatures, free vibration behaviors of the composites are still being investigated. To the best of authors' knowledge, there is no published study comparing the vibration performance of the long glass fiber-reinforced PP composites in room and sub-zero temperature regions. In this work, the damping and natural frequency responses of PP composites fabricated with a ratio of 20 wt.% and 40 wt.% long glass fiber reinforcement are investigated, especially at low temperatures. Thus, a significant contribution to the literature is made by determining the responses by vibrational phenomena that composites may exhibit under various temperatures during the service conditions.

2. EXPERIMENTAL STUDY

2.1. Preparation of Composites

20 wt.% and 40 wt.% long glass fiber (~12 mm) reinforced-homopolypropylene composite granules procured from Nuh Kompozit Inc. (Istanbul, Turkey) are used for the fabrication of thermoplastic composite panels in this research. The E-glass reinforced thermoplastic composites are manufactured through a Fontijne Presses - LabEcon60 Laboratory Platen Press as shown in Figure 1. Load sensitive rectangular platen having the dimension of 400 × 400 mm^2 is used to compress the granules and to fabricate the panels. The panel thickness, temperature, force, and length of processing time are 4 mm, 210 ℃, 100 kN, and 50 min, respectively. Between the press platens, the polytetrafluoroethylene (PTFE) films are utilized for easy removal of the panels and making the whole mold levelly heat. Accordingly, final composite panels with different glass fiber ratios in desired dimensions are obtained. Some technical properties of the PP composites extracted from datasheet of the supplier are shown in Table 1 [15].

2.2. Measurement of Vibration Characteristics

A Laser displacement sensor Keyence LK-G157 is used to measure the vibrations of the composite beam. Analog output of the displacement sensor is read and recorded with 3 kHz sampling rate by using a NI DAQPad-6015 data acquisition module in LabView. Laser displacement sensor, composite beam and the other equipment which are a PC, NI DAQPad-6015 and display panel Keyence LK-G3001 are shown in Figure 2. The composite beam is placed and fixed in an isolated foam box. Two thermocouples are placed inside of the composite beam to measure the temperature. The first thermocouple is inserted very close to the end point of the composite beam. The second one is also placed into a portion of composite in the fixed support region. The temperature of the composite beam is measured in every two seconds.
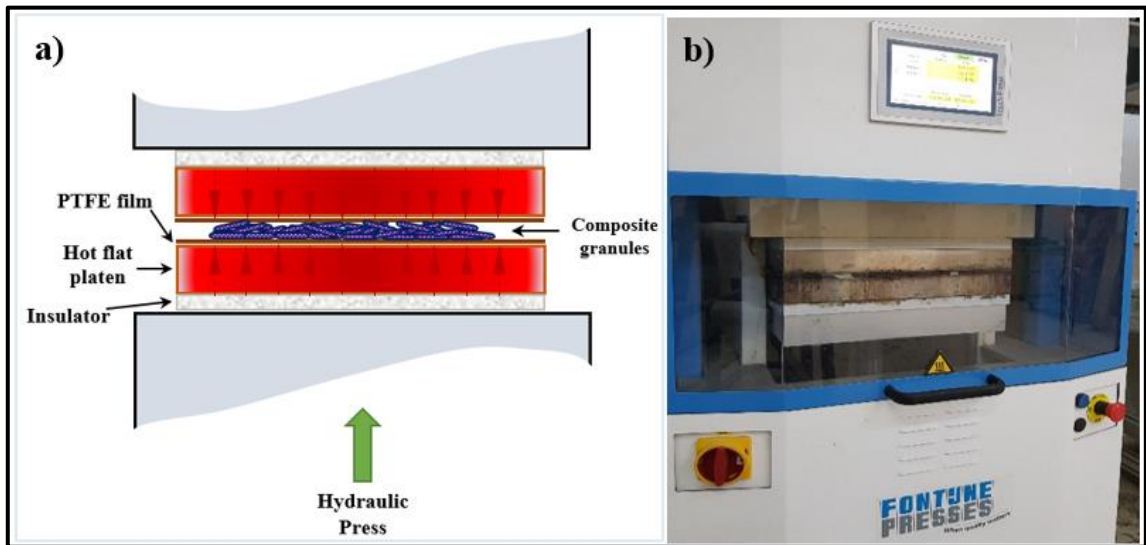
Figure 1. Hot pressing process; a) Schematic illustration, b) Hot-pressing machine

Table 1. Properties of the thermoplastic composites

Properties	Duramax LFT PP 40	Duramax LFT PP 20
Glass fiber percent (%)	40	20
Density (g/cm³)	1.20	1.03
Tensile strength (MPa)	119	92
Flexural strength (MPa)	190	125
Izod impact, unnotched (kJ/m²)	37.5	30
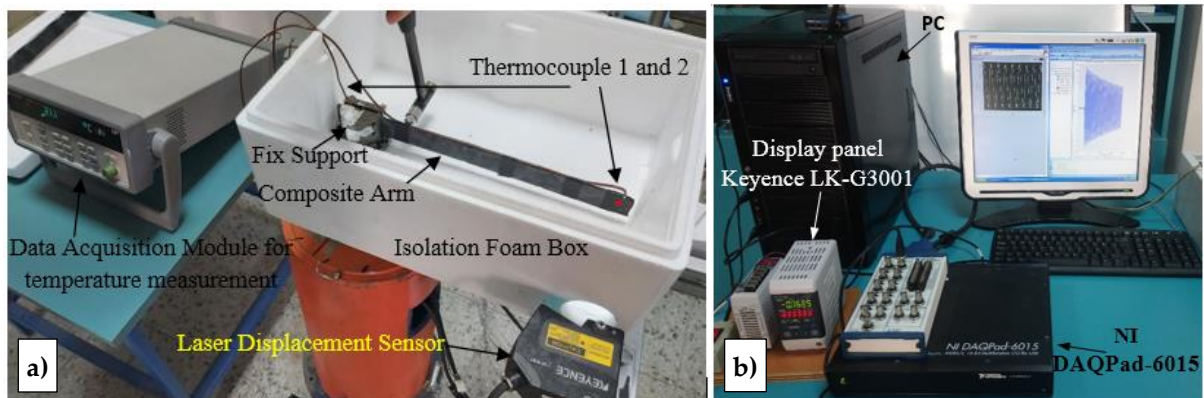
Figure 2. a) Measurement setup, b) Data logging setup of measured values

The solid CO_2 is placed inside the foam box and box lid is then closed. As shown in Figure 3-a, the composite beams are uniformly cooled to -75 °C with no regional variations. The temperatures of the thermocouple at the tip are observed. The temperature changes of the thermocouples at the tips of both 20 wt.% and 40 wt.% long glass fiber reinforced composite (GFRP) are demonstrated in Figure 3-b. The 40 wt.% GFRP has reached the lowest and highest temperatures in a shorter time than 20 wt.% GFRP as expected since the 40 wt.% GFRP has more glass fiber content. This is in line with the previous study showing that the effective thermal conductivity of polymer composite increases with the glass fiber volume fraction [16]. When the temperatures are reached up to -75°C, the lid is opened, and an impulse force is applied on the composite beam by using a hammer at the desired temperatures. Accordingly, the vibration of the composites is measured by the laser displacement sensor.

a)   b)
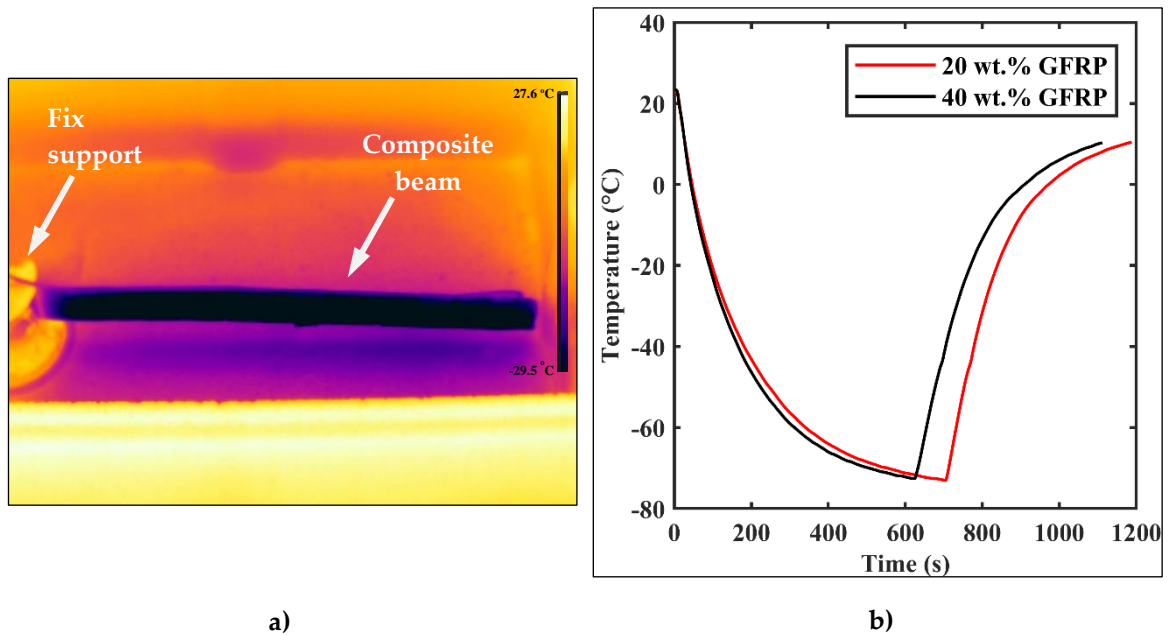
Figure 3. Details of cooling process; (a) Thermal image of the composite, (b) Temperature changes of the tip thermocouples

3. RESULTS AND DISCUSSION

The obtained natural frequencies and damping ratios for both 20 wt.% and 40 wt.% GFRP beams are given in Table 2. The vibration results for both 20 wt.% and 40 wt.% GFRP composites for different temperatures are also exhibited in Figure 4 and Figure 5, respectively. When considering the 40 wt.% GFRP, the natural frequency is higher than that of the 20 wt.% GFRP under the same temperature condition due the more glass fiber existence. This result is in line with the previous studies which emphasize that increasing the fiber fraction from 30% to 60% enhances the natural frequency (Hz) [17] and that the frequency of particle reinforced-composite changes in direct proportion to elastic modulus (E) of the composite [18]. The natural frequencies are increased for both type of GFRPs with the temperature decrease since the glass fiber and homopolypropylene become more brittle and stiffer. It is observed that the damping ratio of 20 wt.% GFRP is higher than that of the 40 wt.% GFRP under the same temperature condition since the homopolypropylene provides more damping than glass fiber. However, it is additionally discovered that the change of the damping does not show the same behavior as the variation of the natural frequency with temperature. The damping ratios of the GFRPs increase while the temperature decreases around 0°C, then the damping ratios are started to decrease exponentially as seen in Figure 6. In the report of a study conducted by NASA [19] it is seen that similar results were obtained for the damping behavior of stainless-steel. The reason for this behavior could not be explained in that report. This behavior may be attributed to the fact that the thermal expansion coefficient of homopolypropylene is higher than glass fiber. For this reason, it is thought that the matrix material shrinks more during cooling that making intermolecular energy transfer easier, and as a result, the damping rate decreases significantly. To summarize, these findings of the free vibration parameters can be associated with the modulus of elasticity of the polymeric matrix material, which changes depending on temperature.

Table 2. Obtained natural frequencies and damping ratios under various temperatures

Temperature (°C)	20 wt.% glass fiber reinforced		40 wt.% glass fiber reinforced	
	Natural Freq. (Hz)	Damping Ratio	Natural Freq. (Hz)	Damping Ratio
20	17.25	0.0126	18.26	0.0111
10	18.13	0.0185	18.94	0.0148
0	19.32	0.0197	19.87	0.0168
-10	20.27	0.0170	20.69	0.0136
-20	20.88	0.0131	21.22	0.0118
-30	21.37	0.0109	21.57	0.0099
-40	21.6	0.0099	21.87	0.0087
-50	21.95	0.0091	22.14	0.0078
-60	22.18	0.0079	22.34	0.0073
-70	22.28	0.0077	22.53	0.0056
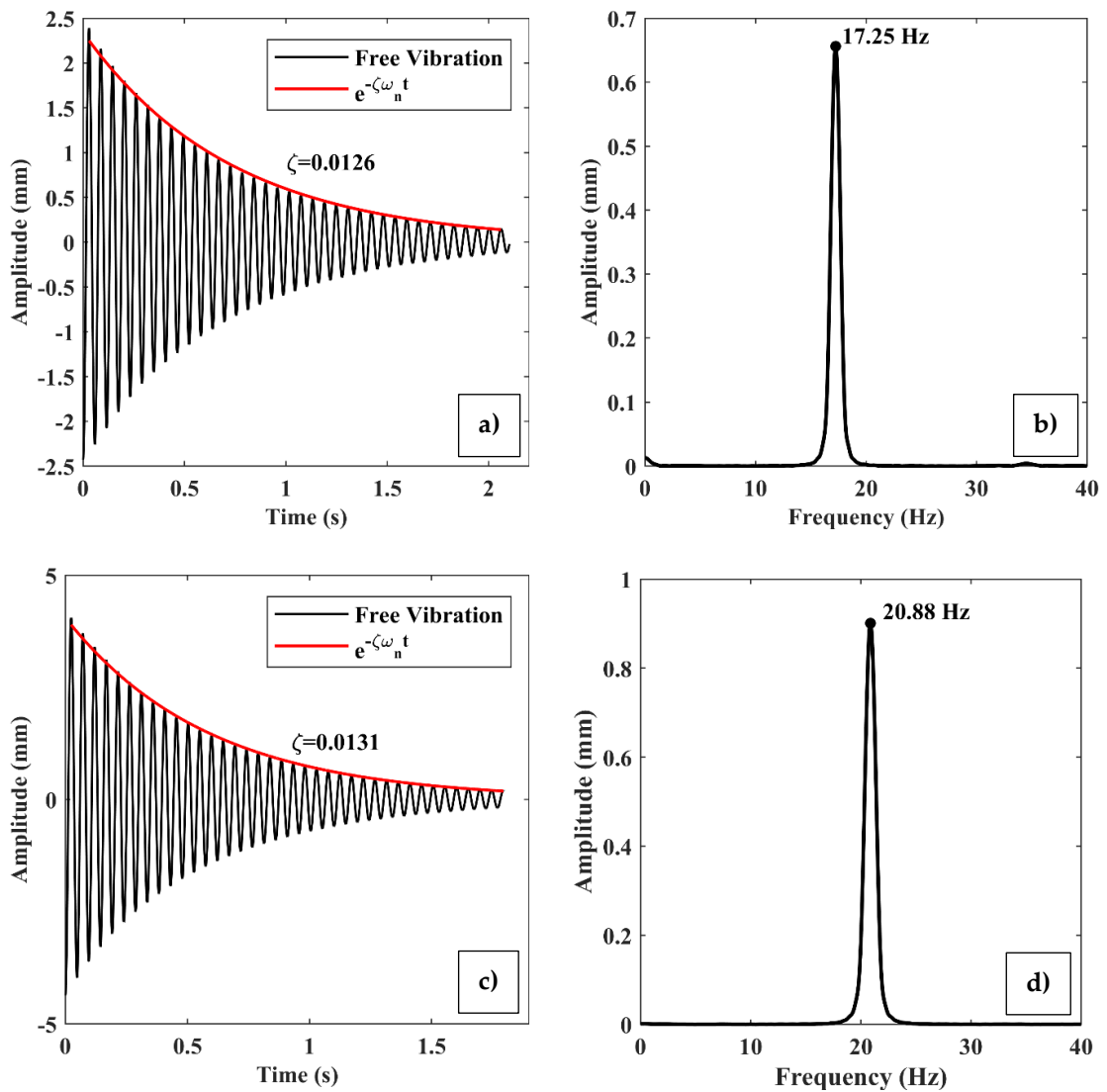
Figure 4. Vibration results of 20 wt.% GFRP; (a) and (b) @ 20°C, (c) and (d) @ -20°C
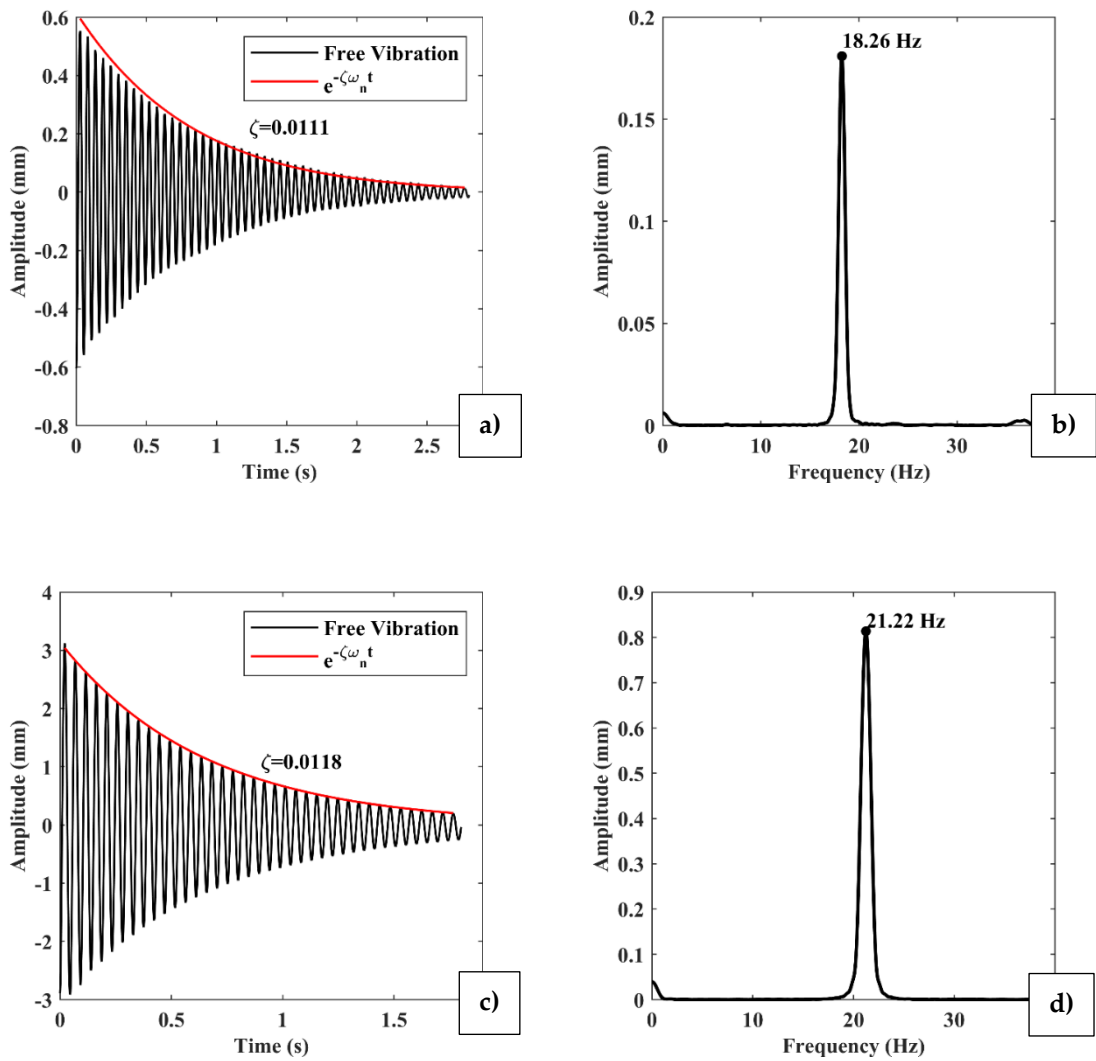
Figure 5. Vibration results of 40 wt.% GFRP; (a) and (b) @ 20°C, (c) and (d) @ -20°C
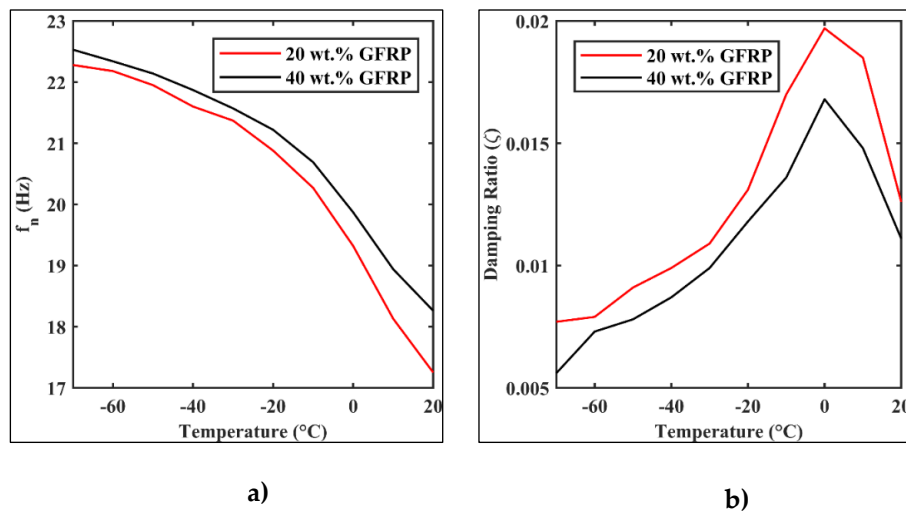
Figure 6. a) The variation of natural frequency with temperature b) The change of damping ratio according to temperature

The data obtained from the tensile tests of the thermoplastic composites used, both at room temperature and the test condition of ~ -40 °C, are given in Table 3. The results obtained are used to show a trend regarding the behavior of the material. As seen in Table 3, the elastic modulus of both materials increases as the material is cooled. The results of the frequency analysis performed by Solidworks using the values acquired from the tensile tests are also given in Table 3. Figure 7 also exhibits the results of numerical frequency analysis. It can be seen that the results derived from the analysis are compatible with the experimental results given in Table 2.

Table 3. Elastic modulus values obtained from tensile tests of thermoplastic composites at different temperatures and numerical frequency analysis results

	Room temperature		~ -40 °C	
	Elasticity modulus (GPa)	First natural frequency (Hz)	Elasticity modulus (GPa)	First natural frequency (Hz)
20 wt.% GFRP	2.235	15.473	3.595	19.623
40 wt.% GFRP	2.920	17.685	4.350	21.586
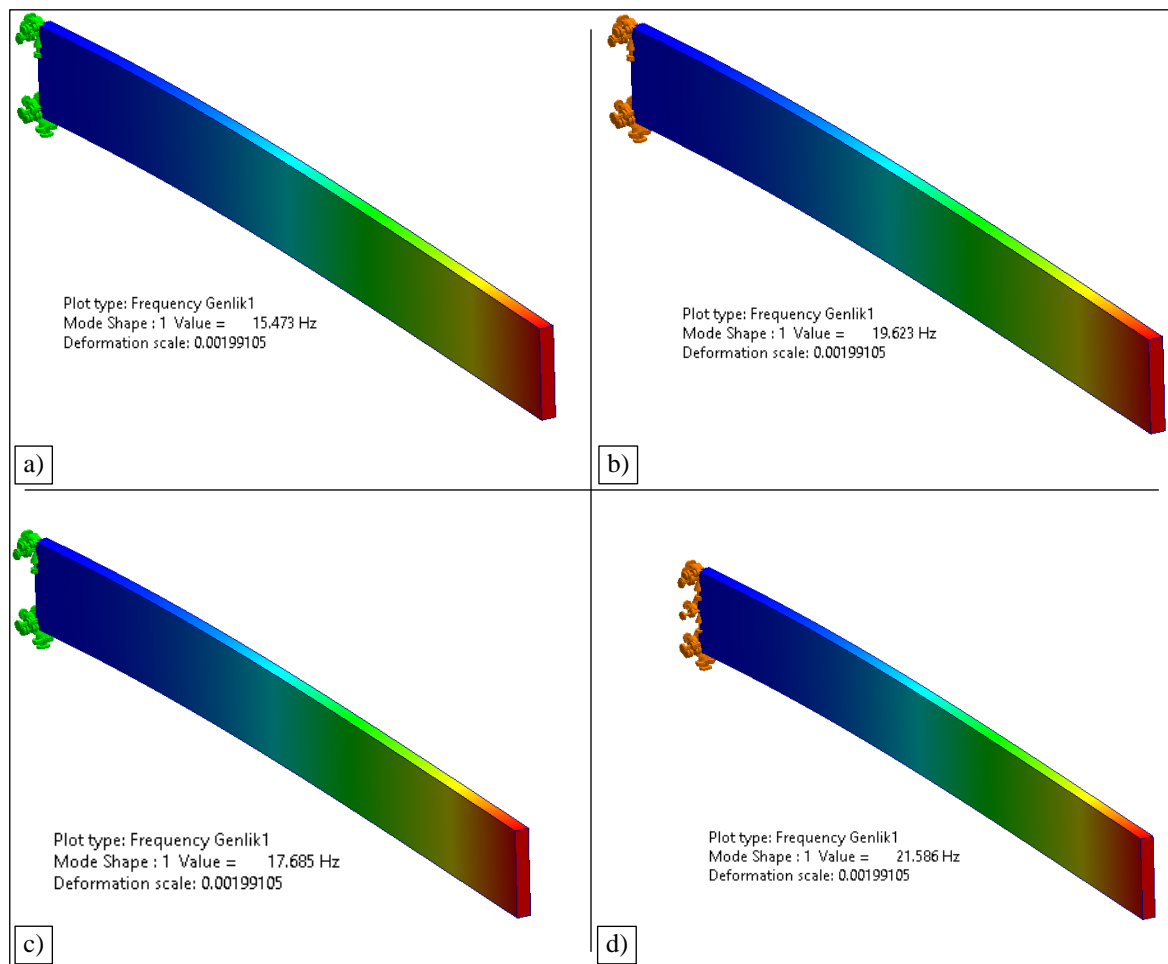
Figure 7. Numerical frequency analysis results; (a) PP20 at room temperature, (b) PP20 at ~ -40 °C, (c) PP40 at room temperature, (d) PP40 at ~ -40 °C

4. CONCLUSIONS

The goal of this research is to evaluate the vibration characteristics such as natural frequency and damping factor of the thermoplastic composites under a room temperature and low-temperature

environments, and try to broaden a kind of service condition selection in composites. The main conclusions are drawn as follows:

♦ It is noticed that the natural frequencies of free vibration of thermoplastic composites are improved with the increase in glass fiber content under all temperatures examined. GFRP with 40 wt.% glass fiber at -70°C gives the higher vibration result in terms of the natural frequency. While the increase rate in 40 wt.% GFRP composite is 23.38%, it is calculated as 29.16% for the composite with lower fiber ratio.

♦ The experimental modal analysis concludes an increasing trend in the natural frequency of the composites with the decrease in temperature. Thus, thermoplastic composites can be a promising alternative for parts subject to shock cooling since the natural frequency of the samples is improved, which leads to minimizing vibrations.

♦ Unlike the natural frequencies, damping factors of thermoplastic composites are declined with the increase in glass fiber content under all temperatures. While the damping ratio for both composites increase from a room temperature to 0°C, it tends to decrease at sub-zero temperatures. While this decrease in damping ratio is 38.89% for 20 wt.% GFRP, it is 49.55% for 40 wt.% GFRP.

♦ The created FE model and analysis results show a tight agreement with the experimentally determined natural frequency responses for both composites.

In this study, vibration performance of the thermoplastic composites with different glass fiber ratios under sub-zero temperatures demonstrates its potential from the point of natural frequency as an outstanding candidate for low-temperature applications. In future, vibration damping behavior of alternative engineering materials and polymer-metal hybrids can be explored under cryogenic temperature environments.

Declaration of Ethical Standards

Authors declare to comply with all ethical guidelines, including authorship, citation, data reporting and original research publication.

Declaration of Competing Interest

The authors declare that they have no known competing financial interests or personal relationships that could have appeared to influence the work reported in this paper.

Funding / Acknowledgements

Data Availability

Data will be made available on request.

REFERENCES

[1]   S. Maraş, M. Yaman, M. F. Şansveren, and S. K. Reyhan, "Free Vibration Analysis of Fiber Metal Laminated Straight Beam," *Open Chemistry*, vol. 16, no. 1, pp. 944-948, 2018.

[2]   J. Fitoussi, M. H. Nikooharf, A. Kallel, and M. Shirinbayan, "Mechanical Properties and Damage Behavior of Polypropylene Composite (GF50-PP) Plate Fabricated by Thermocompression Process Under High Strain Rate Loading at Room and Cryogenic Temperatures," *Applied Composite Materials*, vol. 29, no. 5, pp. 1959-1979, 2022.

[3]   M. Shayan Asenjan, S. A. R. Sabet, and M. Nekoomanesh, "Mechanical and high velocity impact performance of a hybrid long carbon/glass fiber/polypropylene thermoplastic composite," *Iranian Polymer Journal,* vol. 29, no. 4, pp. 301-307, 2020.

[4]   F. Hassani, P. J. Martin, and B. G. Falzon, "Progressive failure in interply hybrid composites of self-reinforced polypropylene and glass fibre," *Polymer,* vol. 195, p. 122411, 2020.

[5]   M. H. Nikooharf, M. Rezaei-Khamseh, M. Shirinbayan, J. Fitoussi, and A. Tcharkhtchi, "Comparison of the physicochemical, rheological, and mechanical properties of core and surface of polypropylene composite (GF50-PP) plate fabricated by thermocompression process," *Polymer Composites,* vol. 42, no. 7, pp. 3293-3306, 2021.

[6]   T. Gobikannan, A. Portela, A. K. Haldar, N. H. Nash, C. Bachour, I. Manolakis, *et al.*, "Flexural properties and failure mechanisms of infusible thermoplastic- and thermosetting based composite materials for marine applications," *Composite Structures,* vol. 273, p. 114276, 2021.

[7]   S. Maraş and M. Yaman, "Free vibration analysis of fiber-metal laminated composite plates using differential, generalized and harmonic quadrature methods: experimental and numerical studies," *Engineering Computations,* vol. 39, no. 6, pp. 2326-2349, 2022.

[8]   M. Etcheverry and S. E. Barbosa, "Glass Fiber Reinforced Polypropylene Mechanical Properties Enhancement by Adhesion Improvement," *Materials,* vol. 5, no. 6, pp. 1084-1113, 2012.

[9]   W. N. Ota, S. C. Amico, and K. G. Satyanarayana, "Studies on the combined effect of injection temperature and fiber content on the properties of polypropylene-glass fiber composites," *Composites Science and Technology,* vol. 65, no. 6, pp. 873-881, 2005.

[10]   J. Gómez-Monterde, M. Sánchez-Soto, and M. L. Maspoch, "Microcellular PP/GF composites: Morphological, mechanical and fracture characterization," *Composites Part A: Applied Science and Manufacturing,* vol. 104, pp. 1-13, 2018.

[11]   H. Keskın and C. T. Yücer, "Use of Vacuum Insulation Panels in Aircraft," *Pamukkale University Journal of Engineering Sciences,* vol. 26, no. 4, pp. 638-642, 2020.

[12]   M. Kara, M. Kırıcı, A. C. Tatar, and A. Avcı, "Impact behavior of carbon fiber/epoxy composite tubes reinforced with multi-walled carbon nanotubes at cryogenic environment," *Composites Part B: Engineering,* vol. 145, pp. 145-154, 2018.

[13]   X. Liu, L. Cheng, L. Zhang, N. Dong, S. Wu, and Z. Meng, "Tensile properties and damage evolution in a 3D C/SiC composite at cryogenic temperatures," *Materials Science and Engineering: A,* vol. 528, no. 25, pp. 7524-7528, 2011.

[14]   E. Sarlin, Y. Liu, M. Vippola, M. Zogg, P. Ermanni, J. Vuorinen, *et al.*, "Vibration damping properties of steel/rubber/composite hybrid structures," *Composite Structures,* vol. 94, no. 11, pp. 3327-3335, 2012.

[15]   Available: http://nuhkompozit.com.tr/en/. [Accessed August 29, 2023]

[16]   W.-Q. Lin, Y.-X. Zhang, and H. Wang, "Thermal conductivity of unidirectional composites consisting of randomly dispersed glass fibers and temperature-dependent polyethylene matrix," *Science and Engineering of Composite Materials,* vol. 26, no. 1, pp. 412-422, 2019.

[17]   M.A.M. Norman, M.R.M. Razean, M.H.H. Rosaidi, M.S. Ismail, J. Mahmud, "Effect of fibre volume on the natural frequencies of laminated composite plate," *Materials Today: Proceedings*, vol. 75, pp. 133-139, 2023.

[18]   G.H. Manjunatha Chary, K.S. Ahmed, "Evaluation of natural frequencies and damping ratios of coconut shell particles reinforced epoxy composites," *Materials Today: Proceedings,* vol. 5, no. 8, pp. 16199-16205, 2018.

[19]   C. P. Young Jr and R. D. Buehrle, "Structural damping studies at cryogenic temperatures," National Aeronautics and Space Administration, Langley Research Center, Hampton, Virginia, USA, Rep. NASA-TM-109073, May, 1994.

MODELING OF MALACHITE GREEN ADSORPTION ONTO AMBERLITE IRC-748 AND DIAION CR-11 COMMERCIAL RESINS BY ARTIFICIAL NEURAL NETWORK

[1] **Hüseyin ECEVİT** , [2, *] **Duygu YANARDAĞ KOLA** , [3] **Serpil EDEBALİ** , [4] **Türkan ALTUN**

[1,2,3,4] *Konya Technical University, Engineering and Natural Sciences Faculty, Chemical Engineering Department,*
Konya, TÜRKİYE
[1] hecevit@ktun.edu.tr, [2] dyanardag@ktun.edu.tr, [3] sedebali@ktun.edu.tr, [4] taltun@ktun.edu.tr

Highlights

- Amberlite IRC-748 and Diaion CR-11 are effective adsorbent materials for malachite green removal.

- The ANN model is developed using a three-layer feed forward back propagation network.

- Adsorbent dosage, initial malachite green concentration and contact time are studied for modeling.

- The effects of the training algorithm, the transfer function in the hidden layer and the number of hidden neurons on model accuracy were investigated.

*Corresponding Author: Duygu YANARDAĞ KOLA, dyanardag@ktun.edu.tr

MODELING OF MALACHITE GREEN ADSORPTION ONTO AMBERLITE IRC-748 AND DIAION CR-11 COMMERCIAL RESINS BY ARTIFICIAL NEURAL NETWORK

[1] **Hüseyin ECEVİT** ⓘD , [2, *] **Duygu YANARDAĞ KOLA** ⓘD , [3] **Serpil EDEBALİ** ⓘD , [4] **Türkan ALTUN** ⓘD

[1,2,3,4] *Konya Technical University, Engineering and Natural Sciences Faculty, Chemical Engineering Department, Konya, TURKIYE*
[1] hecevit@ktun.edu.tr, [2] dyanardag@ktun.edu.tr, [3] sedebali@ktun.edu.tr, [4] taltun@ktun.edu.tr

ABSTRACT: In this study, the malachite green adsorption process using Amberlite IRC-748 and Diaion CR-11 resins was modelled by artificial neural network method. In the model created for this study, adsorbent dosage, initial malachite green concentration and contact time parameters, which are the independent variables of the adsorption process, were used as input. Adsorption percentage values, which are the dependent variables of the adsorption process, were obtained as output. Mean squared error (MSE) and determination coefficient (R^2) values were obtained from the models created using thirty-one experimental data for adsorption of malachite green with Amberlite IRC-748 and thirty-eight experimental data for adsorption with Diaion CR-11. By evaluating these values together, the most appropriate training algorithm, transfer function in the hidden layer and the number of neurons in the hidden layer were defined. Accordingly, for both Amberlite IRC-748 and Diaion CR-11 resins, the optimum training algorithm was determined as Levenberg-Marquardt back-propagation and the optimum hidden layer transfer function as tan sigmoid. The optimum number of neurons in the hidden layer was identified as 13 for Amberlite IRC-748 and 12 for Diaion CR11. The MSE, R^2_{all} and R^2_{test} values of the models produced with the optimum parameters were obtained as 0.000261, 0.9972, 0.9903 for Amberlite IRC-748 and 0.000482, 0.9932, 0.9931 for Diaion CR11, respectively.

Keywords: *ANN, Dye, Simulation, Optimization, Wastewater, Algorithm*

1. INTRODUCTION

Artificial intelligence is frequently encountered in many fields such as intelligent search, autonomous driving, robotics, and data processing due to its usefulness in tasks such as learning, understanding, prediction, problem solving, suggestion and decision making in various disciplines [1], [2]. Artificial neural network (ANN) is a computational artificial intelligence and machine learning model that simulates the structure and functions of biological neural networks [1], [3], [4]. ANN learns linear, non-linear or complex relations between inputs and outputs from the presented data like the human brain, and the models created in this way can produce new results for different and unknown processes [5], [6].

In ANN, processing units called "neurons" process the input signals according to a specific algorithm and obtain an output signal. The operation of the neurons mentioned here is similar to the operation of biological neurons in the human brain. Accordingly, as schematised in Fig. 1, in the neuron receiving one or more input signals I_j, these inputs are weighted according to a $w_{i,j}$ value. The term weight here is similar to the synaptic strength between interconnected neurons in the human brain. The weighted signals sent to the neuron are summed to form a signal called activation, denoted by h, and sent to a transfer function "g". The resulting O_j output signal can then be sent to one or more neurons or utilized as the output of the ANN model [7], [8].

The human brain is filled with many interconnected neurons. Each neuron executes a simple task such as responding to an input signal. When these neurons are connected to each other like a network, they can execute complex functions such as speech or image recognition very quickly [9]. Similarly, ANN is formed by connecting artificial neurons to within a particular topology, interacting with each other, as

*Corresponding Author: Duygu YANARDAĞ KOLA, dyanardag@ktun.edu.tr

schematised in Fig. 1. Typically, an ANN contains of an input layer, a hidden layer and an output layer. There may also be more than one hidden layer in the ANN. Artificial neurons are contained within these layers. The input signals supplied to the neurons in the input layer are processed through the neurons across the input, hidden, and output layers to generate an output signal (Fig. 2) [7], [10]. This structure can be used in chemical processes, as in many other fields, to explain the effects of parameters on the outcome of the process and to model the process [1], [3], [6], [11].
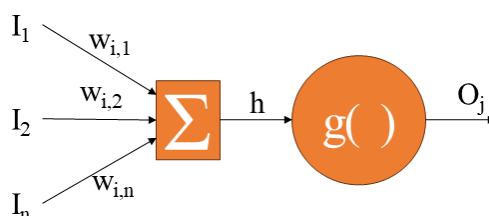
Figure. 1. Structure of a single processing neuron
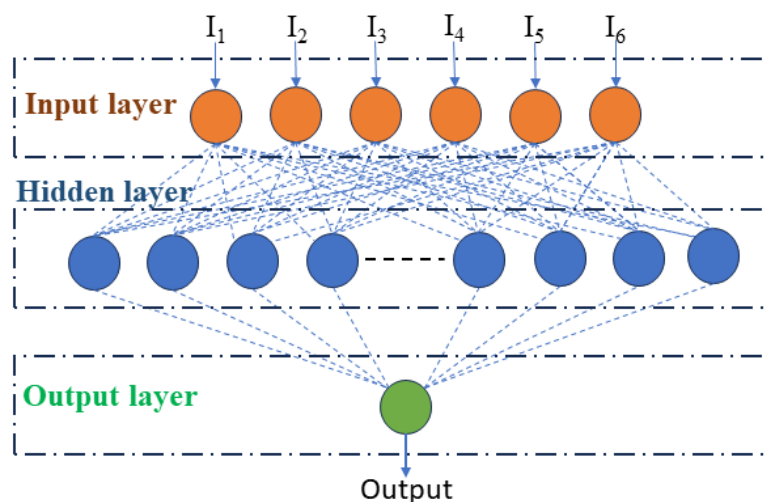
Figure 2. A typical ANN architecture with one hidden layer

In ANN, input signals are converted into output signals in accordance with its structure (Fig. 2). The dataset utilized for the model is divided into three components: training, validation, and test (for example 70% training, 15% validation and 15% test). With the data allocated for training, the network is trained through a training mechanism using the backpropagation algorithm depending on the output obtained. For this purpose, the ANN calculates the error difference between the predicted output and the experimental output (target) and feeds back via backpropagation so that the model readjusts the weights to decrease the error. This process is repeated until the weight changes no longer reduce the error, thus optimizing the model and training the network. Finally, validation and testing are performed with the optimized network [12].

Dyes are widely used in paper, rubber, textile, medical, cosmetic, and plastic production sectors, and are largely discharged into the environment [13], [14]. Since dyes cause colour formation even at low concentrations, they prevent the penetration of sunlight into water and reduce photosynthetic activity [15]. In addition, since their toxicity threatens living life, it is necessary to remove dyes from wastewater [16]. Numerous studies have investigated the removal of dyes using adsorption [17], [18], flocculation [19], chemical precipitation [20], membrane filtration [21], advanced oxidation processes [22], [23], reductive degradation processes [24] and electrochemical methods [25]. Of these methods, adsorption stands out as one of the most effective techniques in wastewater treatment [16].

Batch experiments and adsorption isotherm analyses are commonly employed to examine the removal behavior of different pollutants through adsorption. However, these methods are time-consuming and somewhat inefficient [26]. Since many chemical processes, such as adsorption are affected by many parameters, modelling or optimization of these processes using various statistical or machine learning methods, like ANN, instead of conventional experiments, is very useful [6], [26], [27], [28].

In this study, the adsorption process of malachite green (MG) dye using Diaion CR-11 and Amberlite IRC-748 resins, which were investigated with batch experiments in our previous publication [29] and the results were reported, was modelled by ANN method. The most appropriate ANN algorithm and parameters were determined. As a result, this process was modelled successfully.

2. MATERIALS AND METHODS

2.1. Chemicals

Amberlite IRC-748 and Diaion CR-11 used in the removal studies of MG dye are commercially available materials. Amberlite IRC-748 was purchased from Lenntech. Diaion CR-11 was supplied from Mitsubishi company. Malachite green dye was supplied from Acros Organics. Deionised water was used for preparing dye solution and washing resins before used.

Amberlite IRC-748 and Diaion CR-11 are iminodiacetic acid chelating ion exchange resins with a porous styrene-divinylbenzene matrix. Amberlite IRC-748 features opaque and beige spherical beads, while Diaion CR-11 has highly porous spherical beads. The bulk densities of Amberlite IRC-748 and Diaion CR-11 are 750 g/L and 730 g/L, respectively. The maximum operating temperatures for Amberlite IRC-748 and Diaion CR-11 are 90°C and 120°C, respectively. The suggested pH range for Amberlite IRC-748 is between 1.5 and 14, whereas for Diaion CR-11, it is between 2 and 6.

2.2. Adsorption Studies

MG adsorption by Amberlite IRC-748 and Diaion CR-11 was executed for batch adsorption studies, and experiments were carried out under different parameters. To assess the effect of adsorbent amount, different ratios of resins ranging from 0.1 to 2 g/L were used. Additionally, to investigate the effect of initial dye concentration, dye solutions with concentrations varying from 10 to 240 mg/L were prepared and studies were carried out accordingly. To investigate effect of contact time, experiments were carried out at times ranging from 0-400 min. All experiments were studied at room temperature and with 200 rpm mixer speed.

2.3. Artificial Neural Network

In this study, a neural network model consisting of an input, a hidden and an output layer was created using MATLAB 2022b software. Thirty-one experimental data were used for adsorption of MG with Amberlite IRC-748 resin and thirty-eight experimental data were used for adsorption with Diaion CR-11 resin. The parameters affecting adsorption are input and the removal efficiency obtained by adsorption constitutes the target/output values. Accordingly, three inputs are fed to the model as adsorbent dosage (g/L), MG concentration (mg/L) and contact time (min) and one output value is obtained as adsorption percentage (%). The model has a feed-forward back propagation algorithm. The adsorption percentage (%) value is calculated as in Equation 1.

$$\% \text{ adsorption} = \frac{C_0 - C_t}{C_0} \times 100 \tag{1}$$

C_0 is the initial MG concentration and C_t is the MG concentration after a certain contact time.

Before creating the model, all input and target values in the experimental data were normalised according to Equation 2 to prevent numerical overflow [6]. Then, these data were divided into 70% for training, 15% for validation and 15% for testing.

$$X_{normal} = \frac{X_i - X_{min}}{X_{max} - X_{min}}$$ (2)

X_i is the original data, X_{min} and X_{max} are the minimum and maximum values of the relevant input or target data series.

Subsequently, the learning algorithm of the model, the transfer function in the hidden layer and the number of neurons to be used in the hidden layer were optimized. All training trials for optimization were repeated 10 times, and the result with the lowest mean squared error (MSE) and the highest determination coefficient (R^2) values is presented in this paper. MSE and R^2 values were calculated as in Equations 3 and 4 [6], [30].

$$MSE = \frac{1}{N} \sum_1^n (Y_{exp,i} - Y_{prd,i})^2$$ (3)

$$R^2 = 1 - \frac{\sum_1^n (Y_{prd,i} - Y_{exp,i})^2}{\sum_{i=1}^n (Y_{prd,i} - Y_m)^2}$$ (4)

$Y_{prd,i}$ is the predicted data of ANN model, $Y_{exp,i}$ is the experimental data, Y_m is the average of the experimental data, and n is the number of data.

In order to determine the training algorithm and the optimum transfer function in the hidden layer, firstly 10 neurons are defined in the hidden layer. Then scaled conjugate gradient backpropagation (trainscg), Levenberg-Marquardt backpropagation (trainlm), gradient descent with momentum backpropagation (traingdm), conjugate gradient backpropagation (traincgp), resilient backpropagation (trainrp) algorithms were used as training algorithms. In the hidden layer, the network was trained using purelin, log sigmoid (logsig) and tan sigmoid (tansig) transfer functions. Purelin, logsig and tansig transfer functions are presented in Equations 5, 6 and 7, respectively [31]. Then, the optimum number of neurons was determined by changing the number of neurons used in the hidden layer from 1 to 20 by using the transfer function with the optimum result. Here, MSE values of the model and R^2 values (R^2_{all} and R^2_{test}) for the whole data set and test data were evaluated together in the selection of the optimum model parameters. Finally, the output and target values obtained in the test using the optimum number of neurons and transfer function were compared, and the accuracy of the model was demonstrated.

$$f(x) = x$$ (5)

$$f(x) = \frac{1}{1 + e^{-x}}$$ (6)

$$f(x) = \frac{e^x - e^{-x}}{e^x + e^{-x}}$$ (7)

3. RESULTS AND DISCUSSION

The ranges of the independent variables sent to the model as input in the creation of the ANN model are given in Table 1. The batch adsorption results presented in our previous study [29] were used to determine the ranges. According to these results, the experimental results in the range up to the parameter value where adsorption reaches equilibrium, and 100% adsorption efficiency is obtained were used in the modelling study. Therefore, for Amberlite IRC-748, the ranges of these parameters were set lower since adsorption reached equilibrium at lower adsorbent dosage and contact time. In addition to the

experiments presented in the publication [26], some new experiments were carried out in the ranges shown in Table 1 in order to provide more accurate modelling results.

Table 1. The ranges of data set

Parameters	Ranges	
	Amberlite IRC-748	**Diaion CR-11**
Input layer		
Adsorbent dosage (g/L)	0.03 – 0.42	0.05 – 3.00
MG initial concentration (mg/L)	10 – 240	10 – 240
Contact time (min)	5 – 180	5 – 300
Output layer		
Adsorption (%)	12.8 – 100.0	18.4 – 100.0

3.1. Optimization on ANNs

One of the primary steps to create a suitable ANN for a process is the optimization of model parameters. Model parameters significantly affect the accuracy of a model. For this purpose, the optimal training algorithm and transfer function for the hidden layer were identified by utilizing 10 neurons within the hidden layer. Then, the optimum number of neurons in the hidden layer was determined by using the optimum training algorithm and transfer function.

3.1.1.   ANN for MG adsorption with Amberlite IRC-748

The effect of training algorithm and hidden layer transfer functions on model accuracy with regard to MSE and R^2 for modelling MG adsorption data with Amberlite IRC-748 is given in Fig 3. Based on the results obtained, the algorithm and function with optimum accuracy were determined as trainlm and tansig. The MSE, R^2_{all} and R^2_{test} values of this algorithm and function are 0.000405, 0.9930 and 0.9849, respectively.
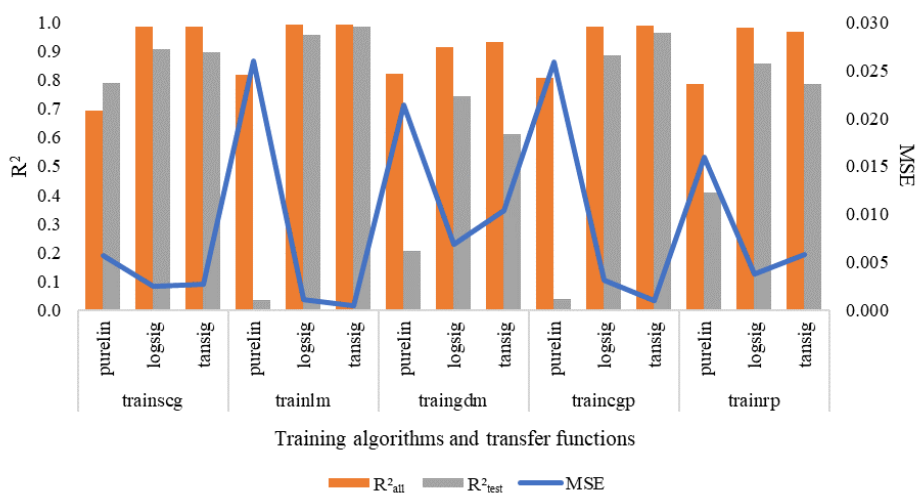
Figure 3. MSE, R^2_{all} and R^2_{test} values for modelling of MG adsorption with Amberlite IRC-748 using different training algorithms and transfer functions

The optimum number of hidden neurons for the ANN using the trainlm algorithm and the tansig transfer function is also analysed (Fig. 4). The figure reveals that the lowest MSE and the highest R^2 values are obtained for 13 neurons. When 13 neurons are used in the hidden layer, MSE, R^2_{all} and R^2_{test} values are 0.000261, 0.9972, 0.9903, respectively. For this reason, 13 was determined as the optimum number of hidden neurons.

The ANN model was constructed using trainlm as the training algorithm, tansig and 13 neurons as the transfer function and number of neurons in the hidden layer. Accordingly, the simulated (output) and experimental (target) adsorption percentage values in the test step are given in Fig. 5. It is understood from the fact that the simulated results and experimental results curves are very close to one to other in the graph that the model can predict the process results with a very high accuracy.
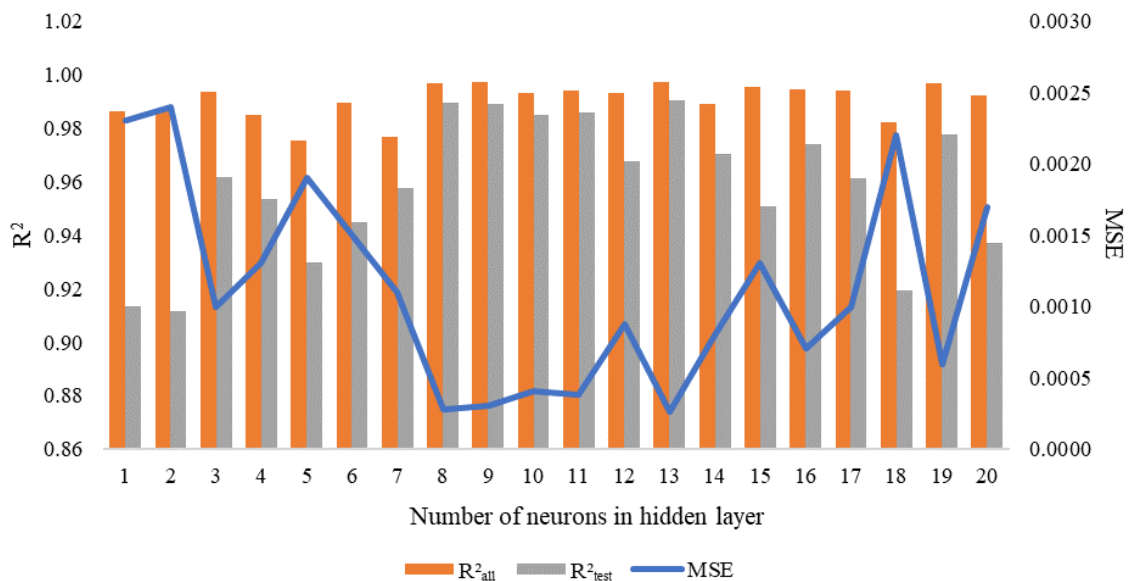
Figure 4. Comparison of ANN models of MG adsorption process with Amberlite IRC-748 according to the number of neurons in the hidden layer

3.1.2.   ANN for MG adsorption with Diaion CR-11

The effect of training algorithm and hidden layer transfer functions on model accuracy in terms of MSE and R^2 for modelling MG adsorption data with Diaion CR-11 is given in Fig 6. Based on the results obtained, the algorithm and function with optimum accuracy were determined as trainlm and tansig. The MSE, R^2_{all} and R^2_{test} values of this algorithm and function are 0.001100, 0.9949, 0.9845 respectively.

The optimum number of hidden neurons for the ANN using the trainlm algorithm and the tansig transfer function is also analysed and the results are presented in Fig. 7. The graph illustrates that the lowest MSE and the highest R^2 values are obtained for 12 neurons. When 12 neurons are used in the hidden layer, MSE, R^2_{all} and R^2_{test} values are obtained as 0.000482, 0.9932, 0.9931 respectively. For this reason, 12 was determined as the optimum number of hidden neurons.
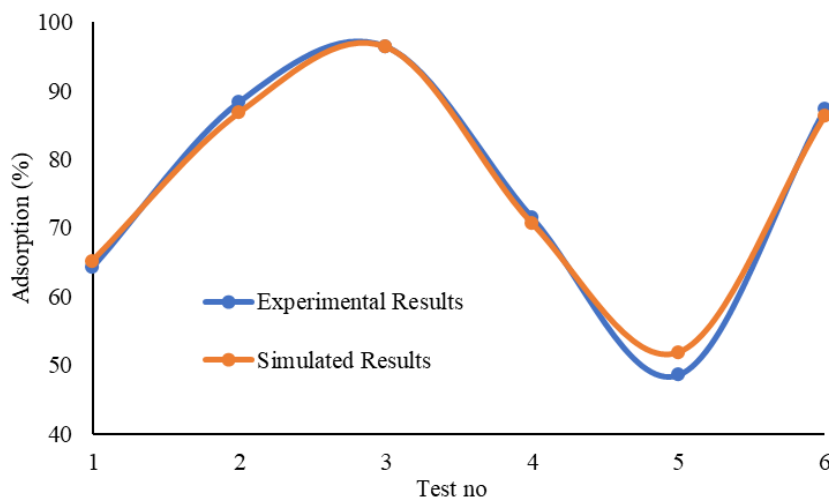
Figure 5. Experimental and simulated results for MG adsorption with Amberlite IRC-748
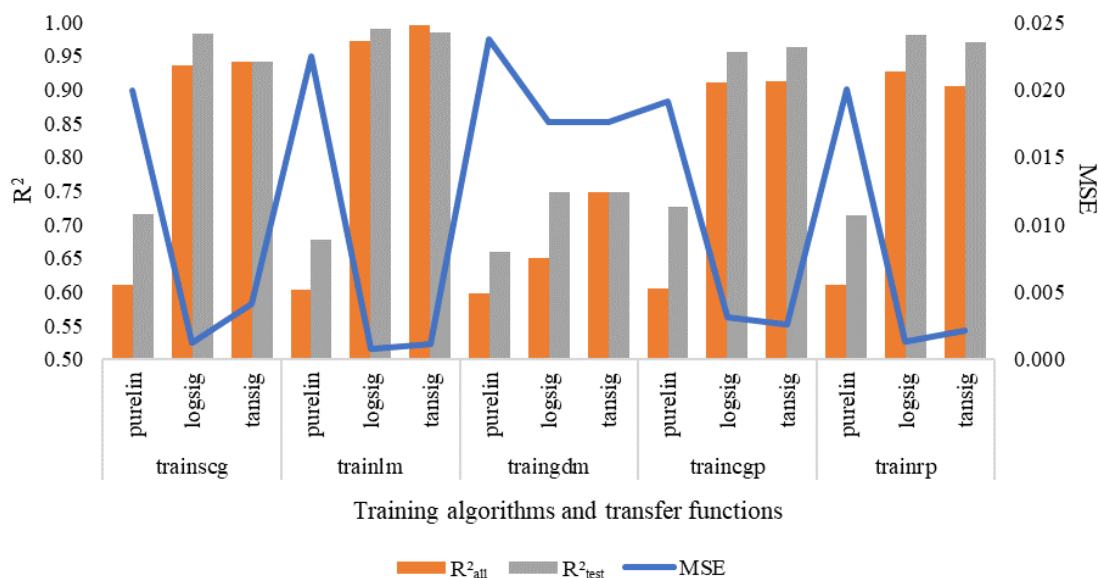
Figure 6. MSE, R^2_{all} and R^2_{test} values for the modelling of MG adsorption by Diaion CR-11 with different training algorithms and transfer functions

The ANN model was created using trainlm as the training algorithm, tansig as the transfer function in the hidden layer and tansig and 12 neurons as the number of neurons. accordingly, the output and target adsorption percentage values in the test step are shown in Fig. 8. This graph was similar to the graph generated for MG adsorption with Amberlite IRC-748. The fact that the simulated results and experimental results curves are very close to each other in Fig. 8 indicates that the model can predict the process results with a very high accuracy.
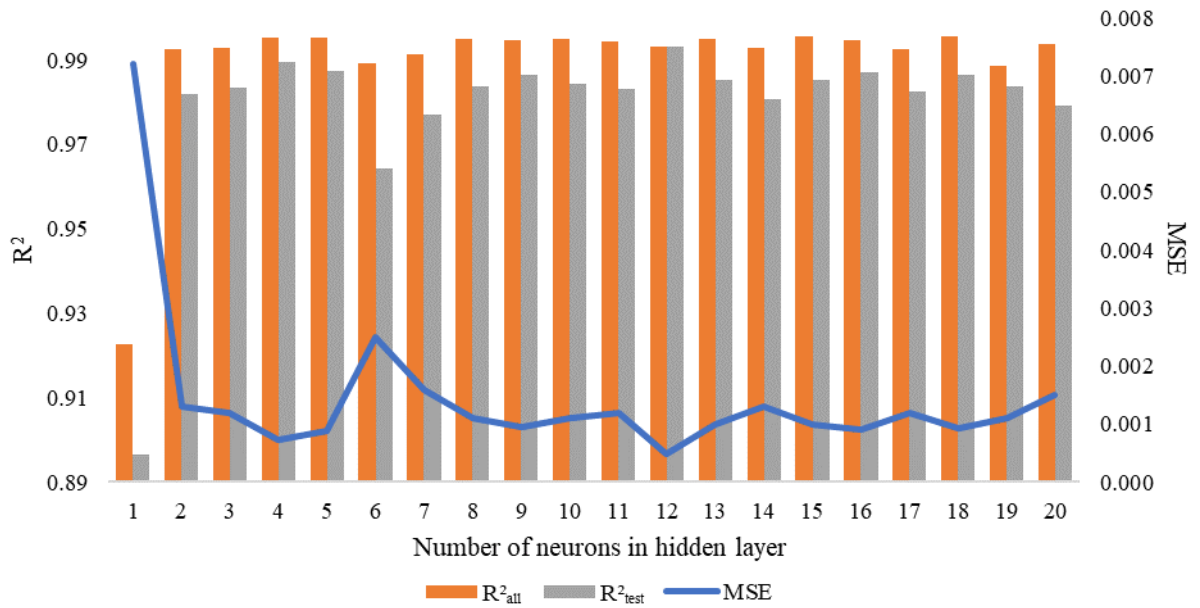
Figure 7. Comparison of ANN models of MG adsorption process with Diaion CR-11 according to the number of neurons in the hidden layer
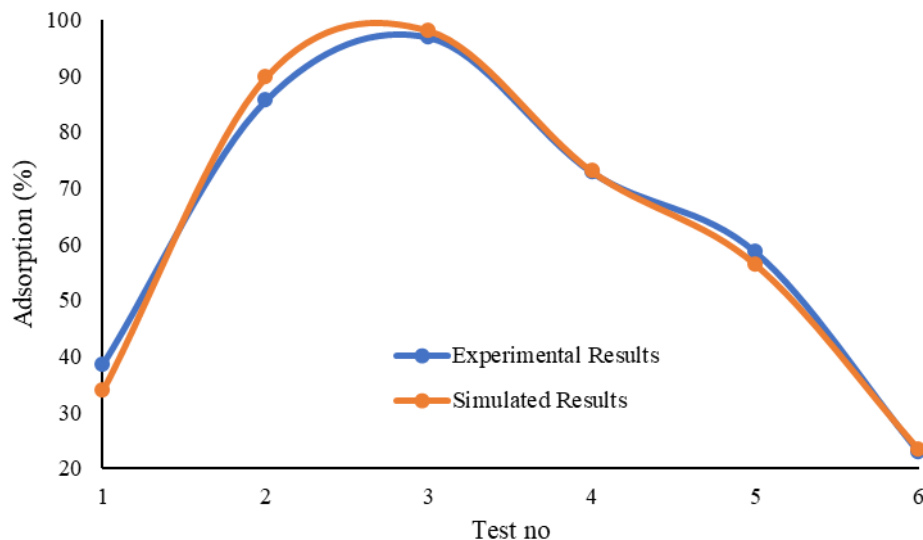
Figure 8. Experimental and simulated results for MG adsorption with Diaion CR-11

According to the studies, MG adsorption processes with Amberlite IRC-748 and Diaion CR-11 resins were modeled successfully and with high accuracy by ANN method. In addition, there is no study in the literature in which these processes are modelled with ANN. For this reason, this study brings an important innovation to the literature.

4.   CONCLUSIONS

In this study, the adsorption of malachite green dye by Amberlite IRC-748 and Diaion CR-11 resins, previously studied in batch experiments with published results, has been modelled using the artificial neural network method. Both resins exhibit high adsorption capacities and show significant potential for application in this field. Furthermore, these processes have been successfully modelled with high accuracy in the present study.

Models were created using Thirty-one experimental data for adsorption of malachite green with Amberlite IRC-748 and thirty-eight experimental data for adsorption with Diaion CR-11. In modelling of processes with artificial neural networks, model parameters significantly affect the accuracy of the model. For this reason, the parameters of the training algorithm, the transfer function in the hidden layer and the number of neurons in the hidden layer were optimized through network training experiments. Trainscg, trainlm, traingdm, traincgp and trainrp algorithms were used as training algorithms. Purelin, log sigmoid and tan sigmoid transfer functions were used as transfer functions in the hidden layer. After determining the optimum of these algorithms and functions, the number of neurons in the hidden layer was changed between 1 and 20 to determine the optimum number of neurons. Accordingly, for both Amberlite IRC-748 and Diaion CR-11 resins, the optimum training algorithm was determined as Levenberg-Marquardt backpropagation and the optimum hidden layer transfer function as tan sigmoid. The optimum number of neurons in the hidden layer was determined as 13 for Amberlite IRC-748 and 12 for Diaion CR-11. Modelling results were similar for both resins. MSE, R^2_{all} and R^2_{test} values of the models produced with optimum parameters were obtained as 0.000261, 0.9972, 0.9903 for Amberlite IRC-748 and 0.000482, 0.9932, 0.9931 for Diaion CR-11, respectively. According to these results, malachite green adsorption processes with both resins were successfully modelled using artificial neural network method.

Declaration of Ethical Standards

Authors declare to comply with all ethical guidelines including authorship, citation, data reporting, and publishing original research.

Credit Authorship Contribution Statement

H. ECEVİT: Conceptualization, Methodology, Software, Validation, Formal analysis, Writing - Original Draft, Visualization

D. YANARDAĞ KOLA: Conceptualization, Methodology, Formal analysis, Investigation, Resources, Writing - Original Draft

S. EDEBALİ: Investigation, Resources, Writing - Review & Editing, Supervision, Project administration, Funding acquisition

T. ALTUN: Conceptualization, Writing - Review & Editing, Supervision

Declaration of Competing Interest

The authors declared that they have no conflict of interest.

Funding / Acknowledgements

The authors received no financial support for the research.

Data Availability

The data that support the findings of this study are available from the corresponding author upon reasonable request.

REFERENCES

[1]   W. Ruan *et al.*, "Modeling of malachite green removal from aqueous solutions by nanoscale zerovalent zinc using artificial neural network," *Applied Sciences*, vol. 8, no. 1, p. 3, 2017.

[2]   N. Yüksel, H. R. Börklü, H. K. Sezer, and O. E. Canyurt, "Review of artificial intelligence applications in engineering design perspective," *Eng Appl Artif Intell*, vol. 118, p. 105697, 2023.

[3]   M. Mourabet, A. El Rhilassi, M. Bennani-Ziatni, and A. Taitai, "Comparative study of artificial neural network and response surface methodology for modelling and optimization the adsorption capacity of fluoride onto apatitic tricalcium phosphate," *Universal Journal of Applied Mathematics*, vol. 2, no. 2, pp. 84–91, 2014.

[4]   H. Yang, K. Huang, K. Zhang, Q. Weng, H. Zhang, and F. Wang, "Predicting heavy metal adsorption on soil with machine learning and mapping global distribution of soil adsorption capacities," *Environ Sci Technol*, vol. 55, no. 20, pp. 14316–14328, 2021.

[5]   A. G. Adeniyi, C. A. Igwegbe, and J. O. Ighalo, "ANN modelling of the adsorption of herbicides and pesticides based on sorbate-sorbent interphase," *Chemistry Africa*, vol. 4, no. 2, pp. 443–449, 2021.

[6]   A. E. Tümer and S. Edebali, "Modeling of trivalent chromium sorption onto commercial resins by artificial neural network," *Applied Artificial Intelligence*, vol. 33, no. 4, pp. 349–360, 2019.

[7]   D. M. Himmelblau, "Applications of artificial neural networks in chemical engineering," *Korean journal of chemical engineering*, vol. 17, pp. 373–392, 2000.

[8]   H. H. Bilgic, M. A. Guvenc, M. Cakir, and S. Mistikoglu, "A study on prediction of surface roughness and cutting tool temperature after turning for s235jr steel," *Konya Journal of Engineering Sciences*, vol. 7, pp. 966–974, 2019.

[9]   J. Zou, Y. Han, and S.-S. So, "Overview of artificial neural networks," *Artificial neural networks: methods and applications*, pp. 14–22, 2009.

[10]   A. Abraham, "Artificial neural networks," *Handbook of measuring system design*, 2005.

[11]   S. Beyhan and H. İşleroğlu, "Extraction of phenolic compounds from fenugreek seeds: modelling and analysis using artificial neural networks," *Konya Journal of Engineering Sciences*, vol. 11, no. 2, pp. 312–323, 2023.

[12]   A. Nighojkar *et al.*, "Application of neural network in metal adsorption using biomaterials (BMs): a review," *Environmental Science: Advances*, vol. 2, no. 1, pp. 11–38, 2023.

[13]   R. Liu, B. Zhang, D. Mei, H. Zhang, and J. Liu, "Adsorption of methyl violet from aqueous solution by halloysite nanotubes," *Desalination*, vol. 268, no. 1–3, pp. 111–116, Mar. 2011, doi: 10.1016/j.desal.2010.10.006.

[14]   J. Mittal, R. Ahmad, M. O. Ejaz, A. Mariyam, and A. Mittal, "A novel, eco-friendly bio-nanocomposite (Alg-Cst/Kal) for the adsorptive removal of crystal violet dye from its aqueous solutions," *Int J Phytoremediation*, pp. 1–12, Sep. 2021, doi: 10.1080/15226514.2021.1977778.

[15]   P. Geetha, M. S. Latha, and M. Koshy, "Biosorption of malachite green dye from aqueous solution by calcium alginate nanoparticles: Equilibrium study," *J Mol Liq*, vol. 212, pp. 723–730, Dec. 2015, doi: 10.1016/J.MOLLIQ.2015.10.035.

[16]   A. M. Ghaedi and A. Vafaei, "Applications of artificial neural networks for adsorption removal of dyes from aqueous solution: a review," *Adv Colloid Interface Sci*, vol. 245, pp. 20–39, 2017.

[17]   E. Altintig, A. Alsancak, H. Karaca, D. Angın, and H. Altundag, "The comparison of natural and magnetically modified zeolites as an adsorbent in methyl violet removal from aqueous solutions," *Chem Eng Commun*, pp. 1–15, Jan. 2021, doi: 10.1080/00986445.2021.1874368.

[18]   İ. Küçük and H. Biçici, "Adsorption of malachite green into potato peel: nonlinear isotherm and kinetic," *Konya Journal of Engineering Sciences*, vol. 12, no. 1, pp. 150–161, 2024.

[19]   Q. Feng, B. Gao, Q. Yue, and K. Guo, "Flocculation performance of papermaking sludge-based flocculants in different dye wastewater treatment: Comparison with commercial lignin and coagulants," *Chemosphere*, vol. 262, p. 128416, Jan. 2021, doi: 10.1016/j.chemosphere.2020.128416.

[20]   Q. Liu *et al.*, "An efficient chemical precipitation route to fabricate 3D flower-like CuO and 2D leaf-like CuO for degradation of methylene blue," *Advanced Powder Technology*, vol. 31, no. 4, pp. 1391–1401, Apr. 2020, doi: 10.1016/j.apt.2020.01.003.

[21]   P. Zhao, J. Wang, X. Han, J. Liu, Y. Zhang, and B. Van der Bruggen, "Zr-Porphyrin Metal–Organic Framework-Based Photocatalytic Self-Cleaning Membranes for Efficient Dye Removal," *Ind Eng Chem Res*, 2021, doi: 10.1021/acs.iecr.0c05583.

[22]   P. Chanikya, P. V. Nidheesh, D. Syam Babu, A. Gopinath, and M. Suresh Kumar, "Treatment of dyeing wastewater by combined sulfate radical based electrochemical advanced oxidation and electrocoagulation processes," *Sep Purif Technol*, vol. 254, p. 117570, Jan. 2021, doi: 10.1016/j.seppur.2020.117570.

[23]   M. Corona-Bautista, A. Picos-Benítez, D. Villaseñor-Basulto, E. Bandala, and J. M. Peralta-Hernández, "Discoloration of azo dye Brown HT using different advanced oxidation processes," *Chemosphere*, vol. 267, p. 129234, Mar. 2021, doi: 10.1016/j.chemosphere.2020.129234.

[24]   H. Veisi, P. Abassi, P. Mohammadi, T. Tamoradi, and B. Karmakar, "Gold nanoparticles decorated biguanidine modified mesoporous silica KIT-5 as recoverable heterogeneous catalyst for the reductive degradation of environmental contaminants," *Sci Rep*, vol. 11, no. 1, p. 2734, 2021, doi: 10.1038/s41598-021-82242-z.

[25]   J. Alagesan, M. Jaisankar, S. Muthuramalingam, E. Mousset, and P. V. Chellam, "Influence of number of azo bonds and mass transport limitations towards the elimination capacity of continuous electrochemical process for the removal of textile industrial dyes," *Chemosphere*, vol. 262, p. 128381, Jan. 2021, doi: 10.1016/j.chemosphere.2020.128381.

[26]   W. Zhang, W. Huang, J. Tan, D. Huang, J. Ma, and B. Wu, "Modeling, optimization and understanding of adsorption process for pollutant removal via machine learning: Recent progress and future perspectives," *Chemosphere*, vol. 311, p. 137044, 2023.

[27]   S. Ghafoori, M. Mehrvar, and P. Chan, "Optimisation of photo-Fenton-like degradation of aqueous polyacrylic acid using Box-Behnken experimental design," *Can J Chem Eng*, vol. 92, no. 1, pp. 97–108, 2014, doi: https://doi.org/10.1002/cjce.21849.

[28]   T. Altun and H. Ecevit, "Adsorption of malachite green and methyl violet 2B by halloysite nanotube: Batch adsorption experiments and Box-Behnken experimental design," *Mater Chem Phys*, vol. 291, p. 126612, 2022.

[29]   D. Yanardağ and S. Edebali, "Adsorptive removal of malachite green dye from aqueous solution by ion exchange resins," *Biomass Convers Biorefin*, pp. 1–12, 2023.

[30]   K. Yetilmezsoy and S. Demirel, "Artificial neural network (ANN) approach for modeling of Pb (II) adsorption from aqueous solution by Antep pistachio (Pistacia Vera L.) shells," *J Hazard Mater*, vol. 153, no. 3, pp. 1288–1300, 2008.

[31]   Y. Xu and A. T. Karunanithi, "Using Artificial Neural Network to Predict Speed of Sound and Heat Capacity of Pure Ionic Liquids," United States -- Colorado, 2017. [Online]. Available: https://www.proquest.com/dissertations-theses/using-artificial-neural-network-predict-speed/docview/2077621067/se-2?accountid=201746

LITHIUM EXTRACTION POTENTIAL OF HECTORITES FROM THE BIGADIÇ BORATE BASIN: MINERALOGICAL CHARACTERIZATION AND SELECTIVE CATION EXCHANGE EXPERIMENTS

***Hatice ÜNAL ERCAN** 🆔

Konya Technical University, Vocational School of Technical Sciences, Chemistry and Chemical Processing Technologies, Konya, TÜRKİYE
hunalercan@ktun.edu.tr

Highlights

- The mineralogical characteristics of the clays in the Bigadiç borate basin have been assessed.

- Selective cation exchange of hectorite with various cations was investigated.

- Mg and Li concentrations transferring from clay to acidic solution were ascertained.

- Experimental observations were conducted based on the ions' diameters and hydration enthalpy.

- Partition coefficient values were calculated from solutions and interpreted.

Graphical Abstract
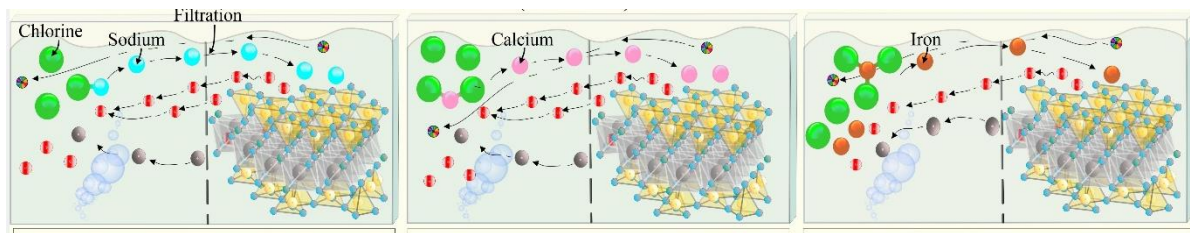
Model showing the process of Li extraction from hectorite with cations of different ionic charges.

*Corresponding Author: Hatice ÜNAL ERCAN, hunalercan@ktun.edu.tr

LITHIUM EXTRACTION POTENTIAL OF HECTORITES FROM THE BIGADIÇ BORATE BASIN: MINERALOGICAL CHARACTERIZATION AND SELECTIVE CATION EXCHANGE EXPERIMENTS

*Hatice ÜNAL ERCAN (ID)

Konya Technical University, Vocational School of Technical Sciences, Chemistry and Chemical Processing Technologies, Konya, TÜRKİYE
hunalercan@ktun.edu.tr

ABSTRACT: Although lithium is a common element worldwide, it is primarily concentrated in specific areas, including pegmatites, granites, and clays, as well as brine. Today, research in various countries is exploring experimental techniques for extracting Li from Li rich rocks and clays. The Bigadiç boron deposits form in a volcano-sedimentary environment in western Turkey, and their boron minerals interlayer with significant amounts of Li-rich hectorite. However, the clays' high Mg content presents a significant complication, increasing the cost of lithium processes and necessitating an intricate extraction process.

In this study, a solution with high Li and low Mg content was obtained by a two-step extraction process from raw Bigadiç clays with high Li content. Raw hectorite samples NaCl, $CaCl_2$ and $FeCl_3$ cation sources were mixed by the mechanical mixing method to provide cation absorption on the clay surface. The targeted ion, Li, was transferred from the clay to the solution by preferential displacement using acid treatment. The findings produced through $D_{Li} = [Li_{(clay)}]/[Li_{(aq)}]$ (ppm/ppm) and $\log D_{Li} = 1319/T_{(K)} + 5.5$ $([Li_{(aq)}])^{-0.0806}$ formulae were analyzed and interpreted. The investigation has demonstrated the viability of selective cation exchange procedures upon rich lithium clay reserves present in Bigadiç.

Keywords: Bigadiç Borate Deposit, Clay Minerals, Hectorite, Lithium Extraction, Selective Cation Exchange

1. INTRODUCTION

In recent years, the significance of lithium (Li) in the global market has risen due to advancements in technology that utilize Li's high electrochemical potential, leading to a corresponding rise in its price [1-3]. The utilization of rechargeable lithium batteries, particularly for eco-friendly electric/hybrid vehicles, is a significant factor in making lithium a reliable and useful material/source, therefore, as it produces no pollutants and meets the objectives of sustainable environmental policies. However, the demand for lithium is dramatically growing, and it is becoming crucial for the comprehensive investigation and utilization of all available natural and artificial sources [4].

Although clays are found in restricted regions on the Earth's surface such as Turkey, France, Morocco, Arizona and Nevada, they can possess large amounts of Li in their crystal structures, serving as a potential source of the Li element. However, understanding and predicting clay crystal systems poses a challenge due to the reactions of clay minerals which release cations by exchange or solution and the existence and diversity of exchangeable cations. Additionally, another difficulty is the existence of varying binding energies of these cations to different exchange sites located on clays [5-7].

Hectorite $(Na_{0.6}Mg_{2.7}Li_{0.3}Si_4O_{10}(OH)_2)$, widely recognized as an adsorbent, catalyst, and rheological additive, and its use has lately increased in fields such as optics, medical materials, and tissue engineering is a smectite group magnesium-lithium clay mineral. Hectorite with the chemical formula $Na_{0.6}Mg_{2.7}Li_{0.3}Si_4O_{10}(OH)_2$ has a Si-O-Mg(Li)-O-Si layered trioctahedral structure separated by interlayer cations, such as Na+, and Li+. The adjacent negatively charged 2:1 layer is fixed by interlayer cations and by hydrogen bonding between water molecules coordinated to interlayer cations and basal oxygen atoms of the tetrahedral sheets. The partial isomorphic substitution of Li+ for Mg^{2+} in the octahedral sheets is

*Corresponding Author: Hatice ÜNAL ERCAN, hunalercan@ktun.edu.tr

responsible for the negative charges of hectorite. These negative charges are compensated by the interlayer cations in the interlayer space and interlayer cations can also be exchanged with other cations. Additionally, hectorite nanolayers exhibit an anisotropic charge distribution, with negative charges on the basal faces and positive charges on the edges [8, 9]. In addition to these characteristics, hectorite can be defined as a highly functional nanoparticle that can be used in cation exchange reactions with a high cation exchange capacity (CEC) of 50-150 mmol/100 g in the pH range of 6-13 [8]. and a large specific surface area of about 350 m^2/g [10]. The positioning and quantity of lithium in the crystal site must be clearly defined in the extraction of the Li element from hectorite or Li-rich clays. This is because Li^+ can occupy two distinct sites in the clay: i) Li+ substituting for Mg^{2+} in the structural octahedral sites, and ii) exchanged Li^+, a cation that is primarily located in the interlayer sites and is exchangeable [11]. It is essential to ensure that these two sites are distinguished from each other. It is believed that the replacement of Mg^{2+} with Li^+ in the octahedral sites is a result of the element's position in the periodic table and their closely linked external geochemical cycles [12, 13].

Many studies have revealed that besides inorganic ions, organic cations can also be incorporated into the interlayer space of hectorite through an ion-exchange reaction [14-22]. Bivalent cations are much more likely to enter the exchange sites than monovalent cations [23]. The treatment of rare-earth element and Li rich clay group minerals to be exploited for these elements are based on the fact that the charge on clay minerals is predominantly negative, attracting cations from solutions to neutralize the said charge. Ion exchange in these minerals occurs through a reversible chemical reaction between the ions in the solutions and the ions positioned on the crystal surface due to the unbalanced electrical charges within the crystal framework. Ion exchange reactions follow the law of mass action; however, the reactions are constrained by the count of exchange sites on the mineral and the strength of the bond between the exchangeable cations and the mineral surface [7, 24-28]. Hectorite possesses several active sites utilized for cation exchange, including interlayer, surface, edge, and inter-particle sites for conducting the ion-exchange reaction as outlined above. These active sites enable the clay to interact with other substances readily, leading to diverse types of reactions. This unique property allows for the manipulation of the hectorite's structure and functionality [9].

The Borate Basin around Bigadiç in Western Anatolia is extensively recognized with its Miocene borate deposits attracting widespread interest. On-going explorations and exploitation activities in the basin revealed the clay layers of the deposits are Lithium-rich [29-36]. The initial investigation of Li leaching was conducted by [37] utilizing sulfuric acid solution from ulexite-clay samples sourced from the Kırka borate deposit, including dolomite, montmorillonite, and hectorite. Despite favorable leaching conditions, this study highlighted that acid leaching failed to exhibit discernible Li selectivity (99%) and led to significant dissolution of iron (42.97%), magnesium (58.10%), and calcium (35.04%). With the advancement of technology new research was conducted, including new processes to obtain a solution rich in the element Li, and a very rich Li solution was obtained, but the biggest technical problem was that the solution was enriched with elements such as Mg and Ca at the same time as Li [34, 35]. Regarding the usefulness of grain size reduction, [36] also conducted a study and found that when grinding samples of different grain sizes and compositions, the amount of Li increased with decreasing grain size, while the increase in the amount of Li was associated with clay minerals.

All of the above indicates that we have entered a period of significant investment in lithium mining and production worldwide and in Turkey. Furthermore, it seems inevitable that lithium will open new dimensions in the economic and political fields as a result of international trade predictions. The growing economic and geopolitical significance of this raw material has attracted global attention to the boron basins in Turkey. The principal challenge encountered during the extraction of lithium from clays in Boron basins in Turkey is the co-extraction of magnesium. This study aims to develop a lithium-rich magnesium-poor solution during the extraction of lithium from clays. The findings of this study demonstrate the feasibility of obtaining a Li-rich, Mg-poor solution in the preliminary stages of extracting this raw material. For this purpose, unlike previous research, the clay samples were mixed and ground with a cation source before being mixed with acid. Additionally, the focus of the research was on the extraction of lithium

between the layers rather than on the octahedral layer. NaCl, $CaCl_2$ and $FeCl_3$ salts were blended and grinded as cation sources with Li-rich clays. In addition, the partition coefficient values of the geochemical data were calculated, evaluated and interpreted to support the integrity of the data and the applicability of the study.

1.1 Geology of the Bigadiç Borate Basin

The NE-SW-trending Bigadiç Borate Basin is classified as among the boron-rich basins in Western Anatolia (Figure 1). It covers an area of approximately 50-90 km and deposited over an amalgamated basement consisting of tectonic units of the Menderes Massif, the Sakarya Zone, the Lycian Nappes, and the Bornova Flysch Zone. The area experienced extensional deformation starting from the latest Oligocene as being a part of the Aegean Extensional province [38-42]. Miocene is remarkable with the development of the NE- and SW-trending basins as manifestations of a highly attenuated lithosphere and accompanied volcanism [43, 44]. These basins were filled with deposits eroded from highlands and produced by the surrounding volcanoes (Figure 1). The Neogene volcano-sedimentary sequences from bottom to top; basement volcanic unit, basement limestone unit, lower tuff unit, lower borate unit, upper tuff unit, upper borate unit and basalt [38]. (Figure 1, stratigraphic section). Quaternary sediments cover all these Neogene units.

Within the Miocene units of the Bigadiç Basin lie four open pits that are renowned worldwide as containing the largest colemanite and ulexite deposits: Simav, Tülü, Acep, and Avşar quarry (Figure 1). These deposits were formed due to Tertiary-Quaternary volcanic activity and are distinguished by the presence of borate minerals [40, 41]. Borate minerals are operated from two distinct section, upper and lower. In the lower section, the units enriched in borate minerals consist of intercalations of clayey limestone, marl, claystone, mudstone and tuff. In the upper section, the lithological sequence is very closely similar to that of the lower section, where units such as limestone, claystone, clayey limestone, marl and tuff are intercalated [30, 41] (Figure 1, stratigraphic section, left). This study used samples from the upper borate zone of the Simav quarry. The Simav quarry represents the basin's deeper parts, with Ca- and Na-borates (colemanite + ulexite) being the predominant borate minerals present in Simav (Figure 1. stratigraphic section, right). Clays of the quarries intercalate with other sediments in borate-rich strata, and these clays indicate considerable quantities of the element Li. Li in borate deposits in the region is mostly confined to clay minerals, and studies of clays have shown that the clays in this region contain between 0.17 and 0.58% Li_2O [31].

2. MATERIAL AND METHODS

The experimental studies were carried out in two stages. The first process is based on the characterization and determination of clays. The second process involves mixing clays with a cation source in a high-energy mill and obtaining a lithium-rich solution with the addition of a solvent.

2.1 Characterization of Clays

The clay samples (BG1, BG2 and BG3) were first cleaned of coarse gravel and sand-sized materials and boron minerals to obtain a purer clay composition. Then, the decantation technique, also known as suspended particle gravity sedimentation, was used to separate silt and clay-sized materials. < 2 μm clays were obtained by centrifugation from the dispersion obtained after the decantation process. An oriented aggregate mount was prepared for each clay sample prior to X-Ray diffraction (XRD). The oriented aggregate mounts force the clay mineral particles, usually plate-shaped phyllosilicates, to lie flat, allowing the incident X-ray beam to be directed along the z-axis of the minerals and the diagnostic basal diffraction to be recorded. Oriented samples were air dried, then solvated with ethylene glycol (EG) at 60°C for 2 hours and thermally heated at 400°C and 550°C for 1/2 hour. All these steps are the basis for the

determination of the mineralogical composition of clays <2 μm. XRD analyses were performed at Konya Technical University, Central Laboratory Application and Research Center, Konya, Turkey, in GNR EUROPE 600 XRD model device, CuKα radiation, 40 mA, 40 kV operating conditions, 0.005° scanning speed, 0.250 mm slit interval. The 2θ range was preferred as 2.0–45.0° for EG-solvated and thermally treated samples.
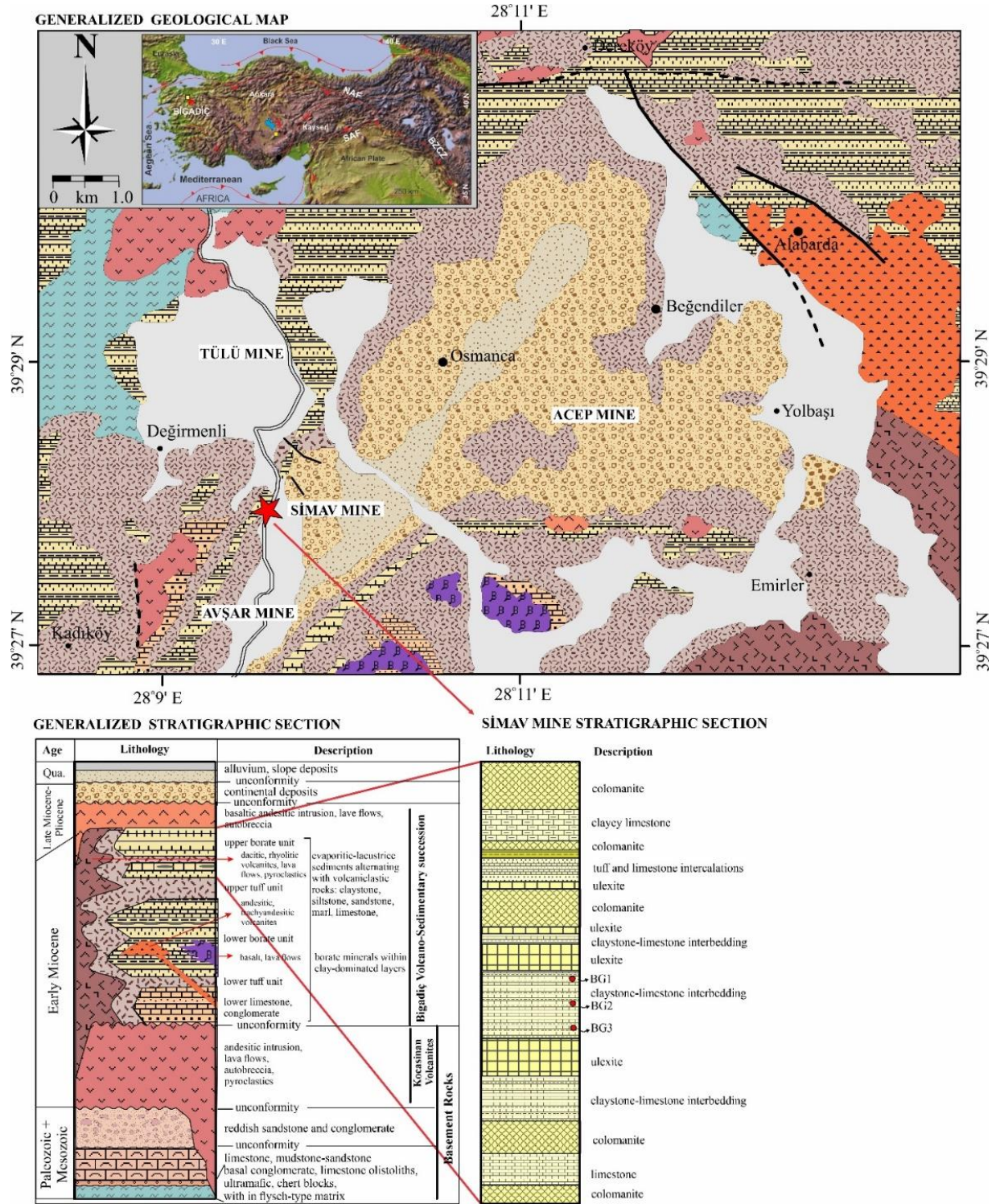
Figure 1. Generalized geological map and stratigraphic section (without scale) of Bigadiç Borate Basin, (the formation colors correspond to the generalized stratigraphic section) (Modified from [30, 41]).

The cation exchange capacities (CEC) of the clays were determined using the methylene blue technique. The technique estimates the quantity of exchangeable cations present in reactive clays. The reaction in this method is the replacement of the methylene blue cations by exchangeable cations of the clay. Clay adsorbs methylene blue in the quantity of exchangeable cations. After saturation, the added methylene blue ions are released into the dispersion. Since the amount of methylene blue added is known, the amount of methylene blue adsorbed by the clay can be calculated and as a result, it can be said that the clay has a cation exchange capacity equal to the amount of charge adsorbed. In the present study, 3.20 g of methylene blue ($C_{16}H_{18}N_3SCl$) was dissolved in 1L of water and thus 0.01 meq load was obtained in 1 cm3 volume [45]. The methylene blue solution was added to 1 g of dry clay in 0.5 ml volumes. After each addition of methylene blue, the clay was mixed and dripped from the dispersion onto the filter paper. The process was continued until the color left by pure methylene blue on the filter paper was formed around the clay dripped onto the filter paper. The cation exchange capacity of the clay was calculated from the amount of methylene blue that was added until the blue ring was formed around the clay.

Field emission scanning electron microscope (FE-SEM) analyses were performed to determine the micromorphological properties of the samples. The micromorphological analysis of clays was carried out using a ZEISS GeminiSEM 500 model scanning electron microscope at Necmettin Erbakan University, Science and Technology Research and Application Centre (BİTAM), Konya, Turkey. The operating conditions of the FE-SEM are 15 kV acceleration voltage, 5-15 mA current and 10-20 s counting time for each element. The iridium coating process was performed using a Leica EM ACE600 model spray coater at 0.06 nm/s at 23 °C, at 0.4 nm. Li and Mg contents of the clays were analyzed by ICP-OS, Perkin Elmer 7000 DV model instrument at Selçuk University, Advanced Technology Research and Application Center (İLTEK), Konya, Turkey.

2.2. The Lithium Extraction Process

To increase their surface area, lithium-containing clay samples (BG1, BG2 and BG3) were ground in a ball mill for 30 min. Three different cation sources with different cation charges were used to perform the cation exchange in the Li extraction process, these are: sodium chloride (NaCl), calcium chloride ($CaCl_2$) and ferric chloride ($FeCl_3$) (Figure 2.). The anion of the cation source was selected from the halide combinations in all experimental groups. These cations were chosen mainly because their ion diameters and enthalpies of hydration (ΔH_{hyd}) were different from each other, and thus ions with different physicochemical properties were aimed to clearly observe the behavior of the ions during the extraction. In this experimental phase partially used the technique applied to cation exchange tested by Sun et al., (2021). In the experimental groups, the mass ratio of the cation source to the clay mineral is 1: 5. Each clay (Cl) sample were mixed with a cation source (CS), then Cl-SC (BG1-NaCl, BG1-CaCl2, BG1-FeCl3, BG2-NaCl, BG2-CaCl2, BG2-FeCl3, BG3-NaCl, BG3-CaCl2, and BG3-FeCl3) experimental groups formed (see Figure 2). It was then powdered in a ball mill for 2 hours to allow the cations to adsorb onto the clay surface and to obtain a homogeneous mixture. Nano-multimix X 50 S, high-energy ball mill with 50 mL chamber at the Biochemistry Laboratory of Selçuk University in Konya/Turkey, was used to grind, mix the samples, and increase their surface area. All processes involving mixing the clay with the cation source were collectively referred to as the " Process-A " (Figure 2).

3 g Cl-SC samples were taken from each group and mixed with 50 ml 1M sulfuric acid (A) (process-A) and Clay-Cation Source-Acid (Cl-CS-A) solution was prepared (Figure 2). This solution was sloshed in an Erlenmeyer flask at 90°C for 24 hours in an ultrasonic bath. After the sloshing procedure, the solutions were percolated with filter paper (pore size 0.45 μm) and each solution was named accordingly as shown in Figure 2. The mixing process of the Cl-CS-A was called the "Process-B". After all of these "Processes-A and B", chemical measurements were performed on the filtrate (Figure 2).
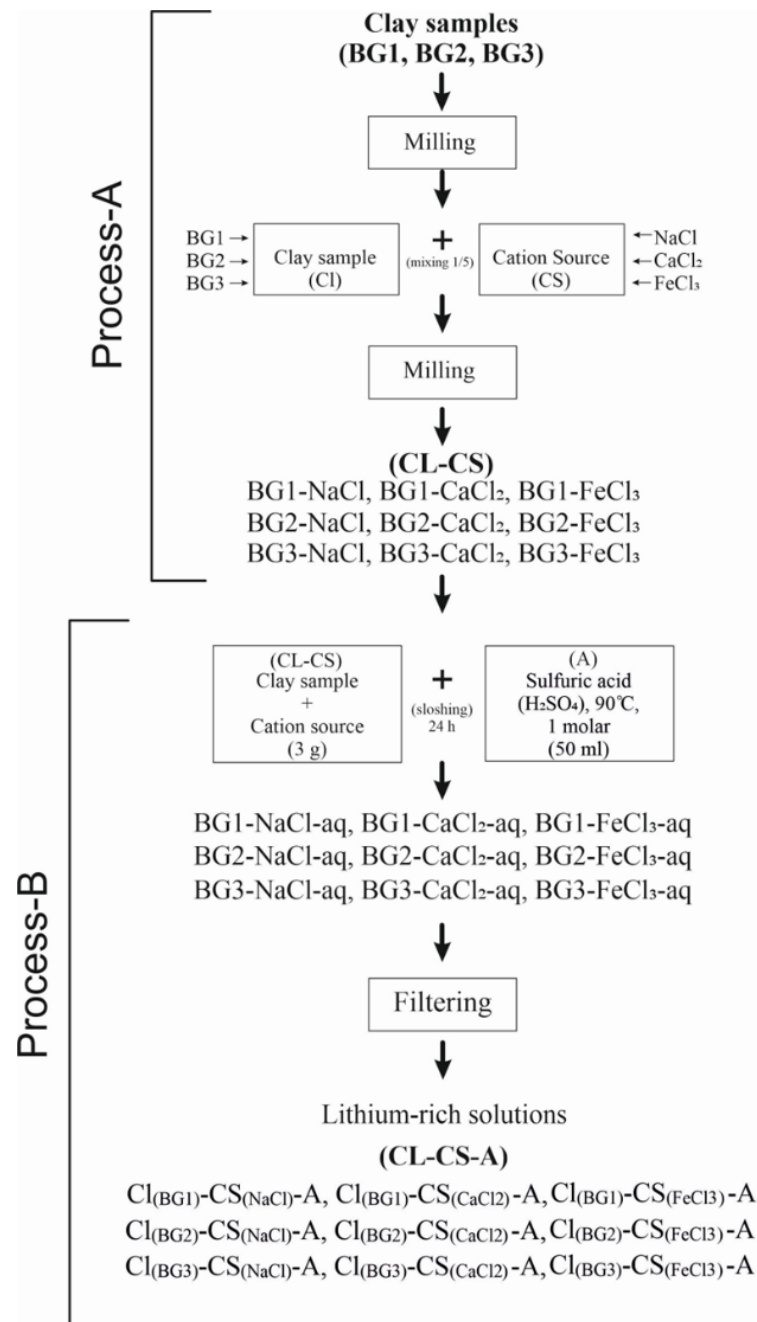
Figure 2. Flowchart outlining the methodology section, including the processes-A and B.

3. RESULTS

The mineralogical characterization of the Li-rich clay samples was carried out XRD analysis and is presented in Figure 3. After the treatment of the ethylene glycol (EG) on the clay sample, it was determined that at the XRD analysis the 001 reflection of the BG1 expanded from 13.01Å to 17.17Å, BG2 from 13.25Å to 17.29Å and the BG3 from 12.04Å to 16.73Å (Figure 3, left). After heating for 30m at 400 and 550 °C, the reflections were observed to have collapsed to about 9.5 to 10 Å. The 060 reflections from the randomly oriented XRD analysis of the samples were detected as 1.539 Å for BG1, 1.530 Å for BG2 and 1.528 Å for BG3 (Figure 3, middle).

The CEC of samples BG1, BG2 and BG3 was determined using the methylene blue cation exchange technique and was found to be 62 mmol/100 g, 54 mmol/100 g and 52 mmol/100 g respectively. In order

to determine the micromorphological structure of smectites, FE-SEM analysis was performed from BG1, BG2 and BG3 samples and wavy subhedral smectite flakes and irregular outlines were observed in each sample (Figure 3, right).

To determine the behavior of Li and Mg during the extraction of Li from the crystal structure of hectorite, the amount of Li and Mg elements was determined by chemical analysis. The Li contents of the raw clay samples (BG1, BG2 and BG3) are 2326.58 ppm, 1446.80 ppm and 1857.27 ppm, respectively. The Mg content is quite high and varies between 15.12%, 15.72% and 13.18% (Table 1).
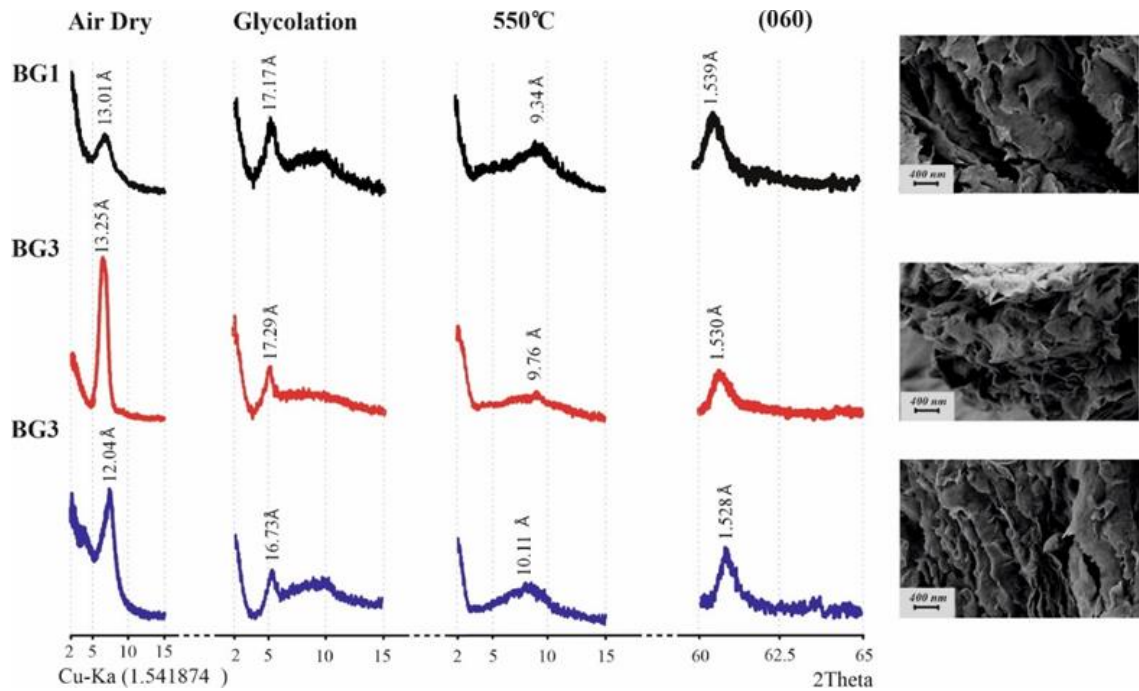
Figure 3. X-ray diffraction (XRD) patterns of clay-sized fractions separated from powdered clay samples at Bigadiç borate deposits Low-angle XRD patterns from 2θ: 2 to 15 ° for air-dried, ethylene-glycolate and thermally heated at 550°C vertically oriented to the c-axis of clay minerals at the left and middle. High angle XRD patterns from 2θ: 60 to 65° including 060 reflections from randomly oriented clay samples at right. FE-SEM images of the samples are shown to the right of the figure.

Table 1. The table displays the Li and Mg levels in the BG1, BG2, and BG3 clays and the clay-cation source-acid (Cl-CS-A) solutions.

	ppm (clay)	ppm (Cl-CS$_{(NaCl)}$-aq)	ppm (Cl-CS$_{(CaCl2)}$-aq)	ppm (Cl-CS$_{(FeCl3)}$-aq)	Recovery %(*)		
	BC1	BC1-NaCl-Aq	BC1-CaCl₂-Aq	BC1-FeCl₃-Aq	NaCl	CaCl	FeCl
Li	2326,5	1821,6	1652	603,3	78,29	71,00	25,93
Mg	151227,9	5443,3	6178,3	4249,1	3,59	4,08	2,80
	BC2	BC2-NaCl-aq	BC2-CaCl2-aq	BC2-FeCl3-aq			
Li	1446,8	843,3	990,5	457,1	58,28	68,46	31,59
Mg	157234,0	4271,5	4229,5	3901	2,71	2,68	2,48
	BC3	BC3-NaCl-aq	BC3-CaCl2-aq	BC3-FeCl3-aq			
Li	1857,2	1216,7	933,1	613,9	65,51	50,24	33,05
Mg	131810	4584,8	5031,63	4500,2	3,47	3,81	3,41

(*) The right three columns illustrate the percentages of Li and Mg elements that transition from the clay to the solution.

3.2 Chemical Composition and Extraction Process of Clays

The extraction of lithium-rich samples BG1, BG2 and BG3 were carried out through two separate steps, Process-A and Process-B (see Section the Lithium Extraction Process), further details of the procedure can

be found in [22]. Li and Mg concentrations were measured in all experimental groups following the processes-A and B. Among Cl-CS$_{(NaCl)}$-A solutions, the highest concentration of Li was obtained from Cl$_{(BG1)}$-CS$_{(NaCl)}$-A solution with 1821.6 ppm (Table 1). The Mg content of these solutions varies between 4271.5 ppm and 5443.3 ppm and increases in direct proportion to the Li content. The magnesium content of these solutions ranges from 4271.5 to 5443.3 ppm (Table 1). In Cl-CS$_{(CaCl2)}$-A solutions, the highest Li concentration was determined as 1652.0 ppm in Cl$_{(BG1)}$-CS$_{(CaCl2)}$-A solution. The Mg content of these solutions increases up to 6178.3 ppm. Li contents of Cl-CS$_{(FeCl3)}$-A solutions are quite low, varying between 457.1 ppm and 613.9 ppm. The Mg content of the same samples is ranging from 3901.0 ppm to 4249.1 ppm (Table 1) (Figure 4). As the Li content increases within the chemical composition of all solutions, so too does the Mg content. The percentage of Li and Mg transferred from clay into solution was calculated from the chemical data (Table 1). For all experimental groups, the percentage of Li transferred from the clay to the solution was quite variable, ranging from 78% (for Cl-CS$_{(NaCl)}$-A solutions) to 25% (for Cl-CS$_{(FeCl3)}$-A solutions) (Table 1) (Figure 4). For Cl-CS$_{(NaCl)}$-A solutions, the highest Li% was found in the Cl$_{(BG1)}$-CS$_{(NaCl)}$-A sample with 78%. Among the Cl-CS$_{(CaCl2)}$-A solutions, the highest Li content was found in the Cl$_{(BG1)}$-CS$_{(CaCl2)}$-A sample with 71%. The amount of Li% that was transferred from the Cl-CS(FeCl3)-A samples to the solution was detected to be quite low and was determined to be between 25% and 33% (Table 1) (Figure 4). For all experimental groups, the Mg% rate transferred from the clay to the solution was quite low and was calculated between 2.48% and 4.08% (Table 1, right). The rate of lithium release from clay into solution is quite high in comparison with magnesium and, proportionally, the amount of Mg increased as the amount of Li increased (Figure 4, left).
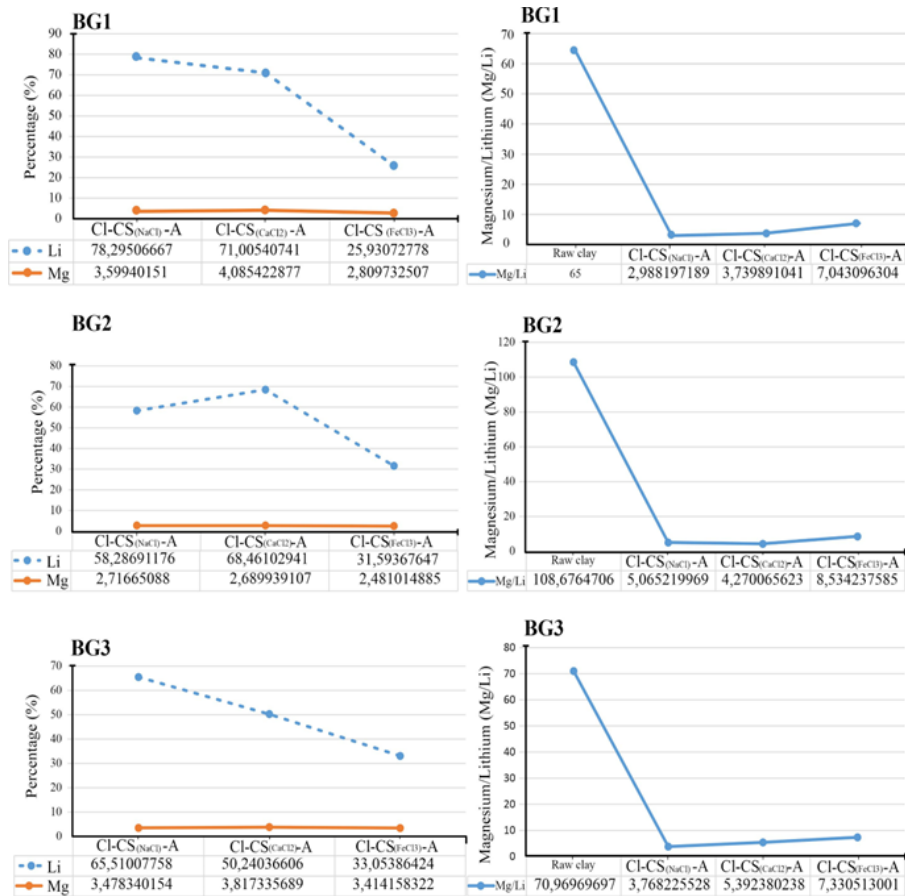
Figure 4. Graphs display the percentages of Li and Mg elements being released from clay minerals into Cl-CS-A solution (Left). Calculation is based on the ratio of Li content in solution to Li content in raw hectorite, and Mg content in solution to Mg content in raw hectorite. The Mg/Li ratios of raw clay and Cl-CS-A solutions (right).

The molar Mg/Li ratios of BG1, BG2 and BG3 clays are 65, 108.6 and 70.9 respectively. After applying the "A + B process", the molar Mg/Li ratio in the solutions decreased to 2.9 - 5.0 for Cl-CS(NaCl)-A solutions, to 3.7 - 5 for Cl-CS(CaCl2)-A solutions and to 7.0 - 8.5 for Cl-CS(FeCl3)-A solutions (Table 2) (Figure 4).The Mg/Li ratios of the clays BG1, BG2, and BG3 were 65, 108.6, and 70.9, respectively. After applying the " process-A + B " with Cl-CS(NaCl)-A, the Mg/Li ratio in the solutions for Cl(BG1)-CS(NaCl)-A, Cl(BG2)-CS(NaCl)-A and Cl(BG3)-CS(NaCl)-A decreased to 2.9, 5.0, and 3.7, respectively (Figure 4, right) (Table 2). The application of the " process-A+B " resulted in Mg/Li ratios ranging from 3.7 to 5.3 for Cl-CS(CaCl2)-A solutions. Molar ratios of Mg/Li were calculated for the solutions Cl(BG1)-CS(FeCl3)-A, Cl(BG2)-CS(FeCl3)-A and Cl(BG3)-CS(FeCl3)-A, resulting in ratios of 7.0, 8.5 and 7.3 (Table 2) (Figure 4).

Table 2. The calculated Mg/Li ratios in BG1, BG2 and BG3 raw hectorite and the Cl-CS-A solutions.

Sample ID	Mg/Li Rations of	Mg/Li Rations of Solutions		
	Raw Clays	(Cl-CS (NaCl)-A)	(Cl-CS(CaCl2)-A)	(Cl-CS(FeCl3)-A)
BG1	65,00	2,98	3,73	7,04
BG2	108,67	5,06	4,27	8,53
BG3	70,96	3,76	5,39	7,33

Table 3. Li and Mg contents of BG1, BG2, and BG3 raw hectorite samples and calculated partition coefficients of Li contents in Cl-CS-A solutions.

	Raw Hectorite			Li partition coeff. ppm/ppm						Correction		
				D_{Li}			$D'_{Li/Mg}$			$logD_{Li}$		
Sample ID	Li (ppm)	Mg (ppm)	Li/(Li+Mg) at./at.	Cl-CS(NaCl)-A	Cl-CS(CaCl2)-A	Cl-CS(FeCl3)-A	Cl-CS(NaCl)-A	Cl-CS(CaCl2)-A	Cl-CS(FeCl3)-A	Cl-CS(NaCl)-A	Cl-CS(CaCl2)-A	Cl-CS(FeCl3)-A
BG1	2326	151227	0.015	1.277	1.408	3.856	0.045	0.057	0.108	9.211	9.114	8.106
BG2	1446	157234	0.009	1.715	1.460	3.165	0.046	0.039	0.078	8.441	8.602	7.828
BG3	1857	131810	0.013	1.526	1.990	3.025	0.053	0.075	0.103	8.808	8.542	8.123

D_{Li} = [Li(clay)]/[Li(aq)], D'_{Li}-Mg = ([Li(clay)]/[Mg(clay)])/([Li(aq)]/[Mg(aq)]), $logD_{Li}$ = -1319/T(K) + 5.5 ([Li(aq)])$^{-0.0806}$

3.3 Calculation of Li partition coefficients in Cl-CS-A solutions

To interpret the data from the processes-A and B intelligibly, this study computes the partition coefficients of Li contents in Cl-CS-A solutions. Partition coefficients values are given in Table 3 and Figure 5, they are displayed either as D_{Li}=[Li(clay)]/[Li(aq)](ppm/ppm) or $D'_{Li/Mg}$ =(Li/Mg)(clay)/(Li/Mg)(aq) (ppm/ppm) [11]. Depending on the cation source, the calculated D_{Li} and $D'_{Li/Mg}$ ratios vary (Figure 5). The ratio of D_{Li} for the Cl-CS(NaCl)-A solutions of all the samples is between 1.27 and 1.71, while for the Cl-CS(CaCl2)-A solutions it is between 1.40 and 1.99. In Cl-CS(FeCl3)-A solutions the DLi ratio increases, varying between 3.02 and 3.85 (Table 3) (Figure 5). For Cl-CS(NaCl)-A solutions the D'Li/Mg ratio is quite low, ranging from 0.04 to 0.05, while for Cl-CS(CaCl2)-A solutions it is slightly increased to 0.04-0.07. The D'Li/Mg ratio increases up to 0.8-1.0 in Cl-CS(FeCl3)-A solutions (Table 3) (Figure 5). A more general expression for the D_{Li} has been established by using the formula $logD_{Li}$. This formula is known as Van't Hoff's law, which is $logD_{Li}$ =

a103/T+b Van't Hoff's law formula and a (slope) and b (intercept) is parameters (see: [11] for details). This formula was utilized in this study to determine the different behavior of different cation sources at constant temperatures. In this formula, the (T) is 90°C and b is $5.5([Li_{(aq)}])^{-0.0806}$, where $[Li_{(aq)}]$ is in mg/L, and also $([Li_{(aq)}])$ reflects the Li value transferred to the solution by extraction. The data of previous study were applied to the equation $logD_{Li}=-1319/T_{(K)}+5.5([Li_{(aq)}])^{-0.0806}$ (see: [11] for details). The calculated $logD_{Li}$ values show an increase as the amount of Li in the solution composition increases. While the calculated value for Cl-CS$_{(NaCl)}$-A and Cl-CS$_{(CaCl2)}$-A solutions are up to 8.4, it is between 7.8 and 8.1 for Cl-CS$_{(FeCl3)}$-A solutions (Table 3) (Figure 5).

a) BG1

	Cl-CS$_{(NaCl)}$-A	Cl-CS$_{(CaCl2)}$-A	Cl-CS$_{(FeCl3)}$-A
-BG1	1,27721968	1,408343444	3,856428591
BG2	1,715651026	1,460685018	3,165190354
-BG3	1,526482699	1,990431357	3,025364879

b) BG2

	Cl-CS$_{(NaCl)}$-A	Cl-CS$_{(CaCl2)}$-A	Cl-CS$_{(FeCl3)}$-A
-BG1	0,045972264	0,057536785	0,108355328
BG2	0,046608249	0,039291538	0,078528844
-BG3	0,053096261	0,075981447	0,103290747

c) BG3

	Cl-CS$_{(NaCl)}$-A	Cl-CS$_{(CaCl2)}$-A	Cl-CS$_{(FeCl3)}$-A
-BG1	9,211948124	9,114191791	8,106345761
BG2	8,441486501	8,602460465	7,828571935
-BG3	8,808240663	8,542732364	8,123777335

Figure 5. Calculated partition coefficients for lithium content in Cl-CS-A solutions. a: D_{Li} exchange against Cl-CS$_{(NaCl)}$-A, Cl-CS$_{(CaCl2)}$-A and Cl-CS$_{(FeCl3)}$-A solutions, b: $D_{Li/Mg}$ exchange against Cl-CS$_{(NaCl)}$-A, Cl-CS$_{(CaCl2)}$-A and Cl-CS$_{(FeCl3)}$-A solutions and c: $logD_{Li}$ exchange against Cl-CS$_{(NaCl)}$-A, Cl-CS$_{(CaCl2)}$-A and Cl-CS(FeCl3)-A solutions.

4. DISCUSSION

4.1 Characterization of Clay Mineral

The widening of 001 reflection to approximately 17 Å with the use of ethylene glycol or glycerol in the identification of smectite group clays is one of the most important identification techniques in X-ray diffraction pattern analysis of crystallographically oriented clay minerals. Smectite group is clearly distinguishable from other non-expandable clays with this method [46-48]. [31] and [49] in their characterization studies of clays from the borate zones of Bigadiç; state that the 060 reflectance is >1.52 Å and the 001 reflectance of smectites after treatment ethylene glycol is 17 Å. In this study, after the treatment of the EG, it was determined that the 001 reflection of samples expanded up to 17.45 Å (Figure 3). 001 reflections collapse to almost 9.5 to 10 Å after heating to 400 and 550 C, EG application and heat treatments indicate that the clays investigated are 2:1 smectite clays with swelling properties (Figure 3). The 2:1 type smectites have various cation substitutions in both tetrahedral and octahedral positions and depending on the properties of these cations, smectites are defined as di- and tri-octahedral [46]. The positioning of Mg and Fe (II) and divalent ions in the octahedral structure results in the formation of trioctahedral smectites, whereas the placement of Al and Fe (III) ions in the octahedral structure results in dioctahedral smectites [50-52]. The 060 reflections of samples BG1, BG2 and BG3 were determined to be >1.528 Å in the detailed XRD diffractogram, indicating that these clays can have trioctahedral structures. Mg, which is one of the substantial components of the trioctahedral smectite is constantly found in the interlayer space beside the octahedral structure [50, 51]. The % MgO content of the Li rich clays representing the Bigadiç region was reported to be 23.33% by [31] and 22.5% by [49]. The MgO content of the samples examined in this investigation falls within the range of around 21.85% - 26.08%. The results suggest that the clays found in the Bigadiç region possess a trioctahedral structure and are compatible with the MgO content (27.5%) of raw hectorite [53, 54]. The smectite in the Bigadiç region must have a trioctahedral structure because trioctahedral smectites tend to contain more Li than dioctahedral smectites [55]. Despite several studies suggesting that hectorite should contain a Li_2O content greater than 1.0%, no minimum limit has been established. Using the term 'hectorite' for clay that has less than 1.0% Li_2O is acceptable [55-57]. Studies involving chemical analysis of smectites in the region have revealed that the Bigadiç clays contain Li_2O within the range of 1462 - 3000 ppm [31, 34, 49]. The Li concentration in samples BG1, BG2 and BG3 have recorded 2326.5 ppm, 1446.8 ppm and 1857.2 ppm, respectively (Table 1). Based on the mineralogical and chemical data presented above, it was determined that samples BG1, BG2, and BG3 are hectorite with a 2:1 trioctahedral structure. The key feature of hectorite is the substitution of Li^+ with some of the coordinated states of Mg^{2+} at the octahedral sheets, leading to layer charge and determining the CEC of clays. The CEC of the hectorite ranges from 50 to 150 mmol/100 g in the pH range of 6 to 13 [10]. CEC of the BG1, BG2 and BG3 clays samples were determined as 62 mmol/100 g, 54 mmol/100 g and 52 mmol/100 g, respectively and these values are in agreement with the CEC values observed in raw hectorite.

4.2 Process of the Lithium Extraction

Lithium extraction study conducted on clays from Bigadiç and other borate deposits in the region evaluated chemical processes including the utilization of sulfuric acid and hydrochloric acid, as well as roasting water leaching methods [34, 35, 58, 59]. In this study, unlike previous research, the clay samples were mixed and ground with a cation source before being mixed with acid. Grinding the clay with the cation source increases the specific surface area of the clay. This significantly enhances the ion exchange potential of the charged clay, facilitating the adsorption of the cation onto the clay surface. The extraction of lithium from clays via the ion exchange method relies on the interplay between appropriate cations and the lithium within clay crystal structures. Several studies have demonstrated that organic cations can be included within the interlayer space of hectorite through an ion exchange reaction, in addition to inorganic ions [14-22]. Hectorite has many active sites used for cation exchange, interlayer-, surface-, edge- and inter-particle sites for the ion-exchange reaction. These active sites of clays can easily interact with other

components and cause different types of reactions to occur, so this can be used to change the structure and functionality of hectorite in particular [9].

In this study, three different inorganic salts containing monovalent (NaCl), divalent ($CaCl_2$) and trivalent ($FeCl_3$) ions were applied to raw hectorite samples (BG1, BG2 and BG3). The reason for choosing these three different cation sources is to determine the change in the amount of lithium passing from the crystal structure of hectorite to the solution according to the type of cation source and to calculate the partition coefficient for more interpretable results. According to the results, comparing the Li contents of the solutions after proceses-A+B, the Li contents of the Cl-CS$_{(NaCl)}$-A and Cl-CS$_{(CaCl2)}$-A solution o are quite high compared to Cl-CS$_{(FeCl3)}$-A (Table 1). Although the ionic radii of the Na^+ and Ca^{2+} (102 and 100 pm, respectively, [60]) were larger than those of the Li^+ (76 pm, [60]), the highest lithium content in the end-solution was measured in the CS$_{(NaCl)}$-A and Cl-CS$_{(CaCl2)}$-A solutions. In general, divalent cations be more tend to preferentially to adsorbed on clay exchange zones than monovalent cations, which explains the displacement of the Li^+ against the Ca^{2+} ion and also Li enrichment in solution [11]. The situation is different for monovalent Na^+, and the dominant process in the displacement between Na^+ and Li^+ during the Cl-CS-A interaction is related to the hydration energy of the ions. The hydration energy (ΔH_{Hyd}), which is also correlated with $Z^{2/r}$ (Z = charge on the cation, r = cationic radius (pm)), indicates how strongly an ion attracts water molecules [61, 62]. The larger the atomic size lesser the hydration energy or the energy decreases [63] because the activity coefficient is affected by the radius of the hydrated ion. The ionic diameter of the Na^+ is larger than the Li^+ but the ΔH_{Hyd} of Li^+ (-520 kJ/mol) is higher than that of the Na^+ (-406 kJ/mol). This becomes effective in the Cl-CS-A solution interaction, the transition of lithium from exchangeable positions in the clay crystal lattice into solution and the preferential displacement of these elements. Although the ion radius of Fe^{3+} (64.5 pm) is close to that of Li^+ (76 pm) or even smaller in diameter, the amount of Li^+ in the Cl-CS$_{(FeCl3)}$-A solutions is quite low (Table 1). The fact that Fe^{+3} has a higher ΔH_{Hyd} potential (-4430 kJ/mol) compared to the ΔH_{Hyd} potential of Li^+ (-520 kJ/mol) caused a lower exchange rate of Li^+ and Fe^{3+} in the solution-clay interaction, because as the water cluster binding studies indicate that the ions with high charge densities bind larger water clusters more strongly than those with lower charge densities [62, 64, 65].

The main problem with Li extraction is the presence of both univalent and divalent cations in the clay surface, as this creates significant differences regarding the nature of the exchanger and the concentration of the solution. Bivalent ions are more strongly bound to clay minerals than univalent ions, but this assumption is not valid for Li+ and Mg^{2+}. The diameter of Li^+ (76 pm) is larger than that of Mg^{2+} (72 pm), but the ΔH_{Hyd} of Mg^{2+} (-1921 kJ/mol) is higher than that of Li^+ (-520 kJ/mol). The high hydration energy means that when Li^+ and Mg^{2+} bound to the clay surface come into contact with the solution, Mg^{2+} preferentially transfers into the solution more, which is one of the main problems in Li extraction. As a result of the experimental studies carried out as part of this study, it was found that the transition of the Mg^{2+} into solution was significantly lower than that of the Li+. The recovery of lithium from the-CS(NaCl)-A solutions ranges from 58 to 78% and that of magnesium from 3.5 to 2.7% and the ranges from 50 to 71% and that of magnesium from 2.68 to 4.08% for Cl-CS($CaCl_2$)-A solutions when the process-A and B is applied to clays (Table 1). These favorable results show that Mg-poor and Li-rich solutions can be obtained with the addition of Na^+ and Ca^{2+} cation sources to the Bigadiç clays. Detailed explanations about this are given below.

In this study, Li^+ in the exchangeable cation position in the interlayer position of the clay and Li+ in the octahedral sheets were intended, and for this purpose, 1 M H_2SO_4 at 90°C was used in the process-B. The main reason for avoiding the heating process is that heating induces the small cations to migrate out of their interlayer space. When this effect is evaluated by considering Li rich clays, heating of the Li rich clay causes Li^+ to migrate from the interlayer space into the vacant octahedral sites or hexagonal holes of the tetrahedral sheets, or both [66]. [67] have detected that from X-ray photoelectron spectroscopy of Li-Montmorillonite heated at 250 and 350 °C, the Li^+ cations migration from interlayer space to hexagonal and octahedral sites with occupancies of 60 and 40% respectively. In addition, the heating process causes reduction in layer charge, this is called the Hofmann-Klemen effect and refers to the reduction of the layer

charge by heating octahedrally charged smectites saturated with small cations (e.g. Li, Mg, Cu) after heat treatment (when heated to 110°C or more) [66, 68-72]. Acid treatment is one of the most applied solvent extraction methods for the recovery of Li from the hectorite because acid treatment chemically leads to controlled, ion-exchange, and partial dissolution of the hectorite structure. Protonated hectorite is produced by the treatment with mild acid [73, 74], but if the acid is strong enough, the proton strongly attacks the oxygen regions connecting the octahedral and tetrahedral sheets at the edge of the surfaces and partially disrupts the hectorite structure. This increases the specific surface area and average pore volume of the acid-activated hectorite [75-77]. Komadel et al. (1996) [76] indicated that the dissolution rate of Li^+ is slightly higher than that of Mg^{2+} at lower acid concentrations and stated that protons preferentially attack Li^+ octahedra. Based on the above explanations, the fact that the transfer of Li^+ from hectorite to the solution is much higher than the transfer of Mg^{2+} can be interpreted in this study in two ways. i) First, lithium is found in higher concentrations than magnesium in the interlayer position of hectorites. It is supported by the results obtained from Cl-CS(CaCl2)-A solutions that lithium is more abundant in the interlayers position of hectorites (The % Mg composition transfer into the solution is much lower than the % Li composition). The application of CaCl2 is a useful methodology for determining interlayer Li^+ quantities or for the separation of lithium from interlayers. [78] and [11] recommended the application of 1 N CaCl2 to eliminate all exchangeable lithium that exists in the interlayer sites of the clays synthesized. ii) Secondly, the Li element located in the octahedral site can show more susceptibility to the acidic process, as mentioned above.

The Mg/Li ratio in the final solution is pivotal in all lithium extraction processes. If the Mg/Li ratio is less than 6, a simple precipitation technique produces a Li-rich precipitate phase and effectively separates Mg from Li. Nonetheless, should the Mg/Li ratio exceed 6, lithium extraction becomes a more arduous [79] and costlier process. Although the Mg/Li ratios of the raw clays (BG1, BG2 and BG3) extracted from the field are higher (>6) the ranges suitable for Li extraction, the Mg/Li ratios of the Cl-CS(NaCl)-A and Cl-CS(CaCl2)-A solutions are lower than six (<6) (Table 2). The Cl-CS(FeCl3)-A solutions have an approximate Mg/Li ratio of 7 to 8. These findings demonstrate that NaCl and CaCl2 can be used as cation sources to attain low Mg/Li ratios (<6) in Bigadiç hetorite. Li-Mg substitution in raw hectorites is constrained to a Li/(Li + Mg) atomic ratio approaching 0.1, according to [80]. [78] found that hectorites with Li concentrations greater than 3600 ppm cannot be obtained experimentally, most likely because it represents the structural limit. At higher content of Li, the structure of the clay becomes unstable and breaks down (when no OH- for F- substitutions occur, [11]. The Li/ (Li + Mg) ratios of BG1, BG2, and BG3 clays are 0.015, 0.009, and 0.013, respectively. These low ratios are linked to the high Mg content present in the clays of the region (Table 3).

DLi partition coefficient calculations were conducted to present the data in a clear and comprehensible way. An apparent decrease in DLi partition coefficient was observed with an increase in Li concentration in the solution, indicating a negative correlation (Table 3) (Figure 5). Such a negative correlation is interpreted as a structural cation substitution occurring during the ion exchange process [11]. As the ratio of Mg/Li in the solution decreased, we observed a decrease in the DLi partition coefficient values. Considering the overall data, an efficiency of 70% or greater from a solution with a Mg/Li ratio below roughly 4 may be achieved by ensuring that the D_{Li} ratio is below about 1.99. For an efficiency of 70%, it is recommended that $D'_{Li/Mg}$ use a partition coefficient value lower than 0.075. All these data was tested with the formula $\log D_{Li} = -1319/ T_{(K)} + 5.5 ([Li_{(aq)}])^{-0.0806}$. The findings indicate a direct correlation between the concentration of lithium in the solution and $\log D_{Li}$. This correlation increases at a constant temperature and in relation to the ionic radii [11]. Additionally, for an Mg/Li ratio lower than approximately 6, the $\log D_{Li}$ value should exceed 8.

5. CONCLUSIONS

The importance of lithium deposits worldwide is increasing as lithium is the main component of lithium-ion batteries used in various fields such as electric vehicles and portable devices. In addition, as the need for clean energy solutions grows, lithium plays an important role in renewable energy storage

systems and in the storage of energy from sources such as solar and wind power. As a result, lithium is gaining strategic importance. From Turkey's point of view, it appears to be an important source of lithium in clay deposits. Turkey can benefit economically from this strategic resource through detailed investigation of lithium-rich clays. This study has achieved very important results in terms of bringing clays into the Turkish economy economically and easily.
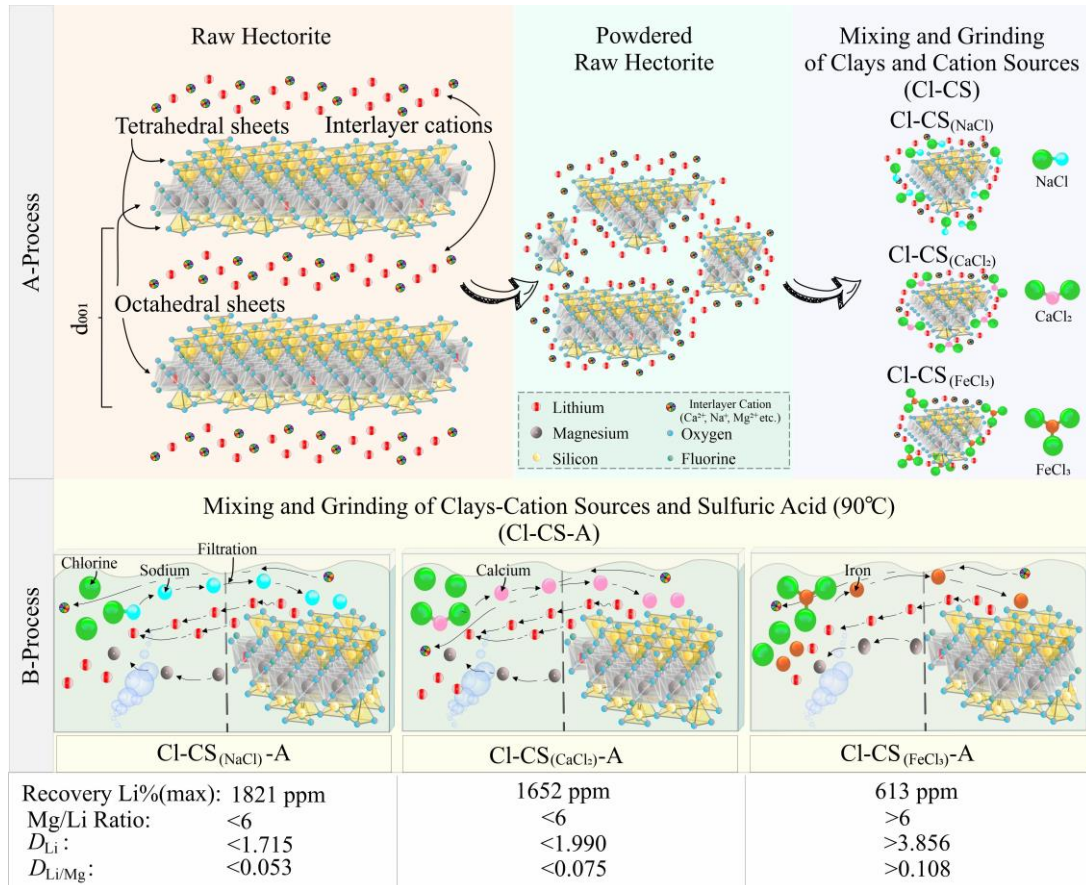
Figure 6. Modal of the lithium extraction process, Process-A(upper): represents powdering raw hectorite, increasing the surface area, grinding and mixing BG1, BG2, BG3 clays with NaCl, CaCl₂, and FeCl₃ cations and absorbing the cations onto the clay surface. Process-B (below): It represents the mixing of sulfuric acid and clays mixed with cations at 90 ºC and the selective displacement and filtration of cations. Numerical proportions were not considered in the model, and it was drawn without a scale, utilizing the Corel Draw software.

Bigadiç borate basins hold a global recognition for their extensive borate deposits which are often interlayered with Li-rich clay occurrences. Owing to the boost in the global Li demand, investigation of unconventional sources such as clay deposits with the help of technological advancements has become an important task. Within this scope, sets of Cl-CS experiments were conducted on borate basin Li-rich clays using cation sources like NaCl, CaCl₂, and FeCl₃. Each set has been treated with of H_2SO_4 at a temperature of 90 ºC and filtered. As a result, a solution rich in lithium have been obtained. The processes-A and B are depicted and modelled in Figure 6 without any scaling.

In the results of this study, in which selective cation exchange was aimed, it was found that the Cl(BG1)-CS(NaCl)-A and Cl(BG1)-CS(CaCl₂)-A solutions of the BG1 sample yielded over 1800 ppm Li with an efficiency exceeding 70%. High concentrations of lithium were also detected in the Cl-CS(NaCl)-A and Cl-CS(CaCl₂)-A solutions obtained from other experiments. The lithium content in solutions of Cl-CS(FeCl₃)-A is relatively low which is associated with the hydration enthalpy of Fe^{3+} (Figure 6). One of the most important findings of these investigations is that the transition of Mg into solution from clays

containing large amounts of Mg (between 13 and 15%) is severely limited. The research demonstrated the impact of ion diameters on the extraction of lithium-rich and magnesium-poor solutions from Li-rich clays, and the correlation between hydration enthalpy and Li extraction.

The Mg/Li ratio, which is the easy and economical recovery limit for Li, is <6. This value was approximately obtained in all the Cl-CS-A solutions obtained in this study. The DLi partition coefficient value was calculated to be less than 2.0 and the $D'_{Li/Mg}$ value to be less than 0.075 in solutions with Mg/Li ratios of less than 6. Together with the calculated $\log D_{Li}$ value, it was found that the Li content is related to the ionic radius at constant temperature. However, cation exchange reactions in natural environments are highly complicated due to the unpredictability of ion concentration in liquid that passes through clay. Consequently, regional studies and information collected in this study will aid in identifying variations in the reactions of local clays, as well as extracting Li from other Li-rich clay formations worldwide and accurate data interpretation.

Declaration of Competing Interest

Acknowledgements

Funding

Data Availability

No data was used for the research described in the article.

REFERENCES

[1]   D. C. Bradley, A. D. McCauley, and L. L. Stillings, "Mineral-deposit model for lithium-cesium-tantalum pegmatites," US Geological Survey, 2328-0328, 2017.

[2]   T. Bibienne, J.-F. Magnan, A. Rupp, and N. Laroche, "From mine to mind and mobiles: Society's increasing dependence on lithium," Elements: An International Magazine of Mineralogy, Geochemistry, and Petrology, vol. 16, no. 4, pp. 265-270, 2020.

[3]   R. J. Bowell, L. Lagos, C. R. de los Hoyos, and J. Declercq, "Classification and characteristics of natural lithium resources," Elements, vol. 16, no. 4, pp. 259-264, 2020.

[4]   D. E. Garrett, Handbook of lithium and natural calcium chloride. Elsevier, 2004.

[5]   L. Wiklander and M. Elgabaly, "Relative uptake of adsorbed monovalent and divalent cations by excised barley roots as influenced by the exchange capacity," Soil Science, vol. 80, no. 2, pp. 91-94, 1955.

[6]   W. Kelley, "Soil properties in relation to exchangeable cations and kinds of exchange material," Soil Science, vol. 98, no. 6, pp. 408-412, 1964.

[7]   N. Kumari and C. Mohan, "Basics of clay minerals and their characteristic properties," Clay Clay Miner, vol. 24, pp. 1-29, 2021.

[8]   L. Delavernhe, M. Pilavtepe, and K. Emmerich, "Cation exchange capacity of natural and synthetic hectorite," Applied Clay Science, vol. 151, pp. 175-180, 2018.

[9]   J. Zhang, C. H. Zhou, S. Petit, and H. Zhang, "Hectorite: Synthesis, modification, assembly and applications," Applied Clay Science, vol. 177, pp. 114-138, 2019.

[10]   N. Hegyesi, R. T. Vad, and B. Pukánszky, "Determination of the specific surface area of layered silicates by methylene blue adsorption: The role of structure, pH and layer charge," Applied Clay Science, vol. 146, pp. 50-55, 2017.

[11]   A. Decarreau, N. Vigier, H. Pálková, S. Petit, P. Vieillard, and C. Fontaine, "Partitioning of lithium between smectite and solution: An experimental approach," Geochimica et Cosmochimica Acta, vol. 85, pp. 314-325, 2012.

[12]   P. Stoffynegli and F. T. Mackenzie, "Mass balance of dissolved lithium in the oceans," Geochimica et Cosmochimica Acta, vol. 48, no. 4, pp. 859-872, 1984.

[13]   A. Hamzaoui, A. M'nif, H. Hammi, and R. Rokbani, "Contribution to the lithium recovery from brine," Desalination, vol. 158, no. 1-3, pp. 221-224, 2003.

[14]   J. Velasco et al., "Foaming behaviour and cellular structure of LDPE/hectorite nanocomposites," Polymer, vol. 48, no. 7, pp. 2098-2108, 2007.

[15]   W. H. Awad et al., "Material properties of nanoclay PVC composites," Polymer, vol. 50, no. 8, pp. 1857-1867, 2009.

[16]   L. Yu and P. Cebe, "Crystal polymorphism in electrospun composite nanofibers of poly (vinylidene fluoride) with nanoclay," Polymer, vol. 50, no. 9, pp. 2133-2141, 2009.

[17]   L. M. Dykes, J. M. Torkelson, W. R. Burghardt, and R. Krishnamoorti, "Shear-induced orientation in polymer/clay dispersions via in situ X-ray scattering," Polymer, vol. 51, no. 21, pp. 4916-4927, 2010.

[18]   A. Walther and A. H. Muller, "Janus particles: synthesis, self-assembly, physical properties, and applications," Chemical reviews, vol. 113, no. 7, pp. 5194-5261, 2013.

[19]   H. Tan et al., "ASA-in-water emulsions stabilized by laponite nanoparticles modified with tetramethylammonium chloride," Chemical Engineering Science, vol. 116, pp. 682-693, 2014.

[20]   M. Stöter et al., "Controlled exfoliation of layered silicate heterostructures into bilayers and their conversion into giant Janus platelets," Angewandte Chemie, vol. 128, no. 26, pp. 7524-7528, 2016.

[21]   M. Daab et al., "Two-step delamination of highly charged, vermiculite-like layered silicates via ordered heterostructures," Langmuir, vol. 33, no. 19, pp. 4816-4822, 2017.

[22]   Z. Sun, H. Chen, T. B. Caldwell, and A. M. Thurston, "Selective extraction of lithium from clay minerals," ed: Google Patents, 2021.

[23]   B. Sawhney, "Sorption and fixation of microquantities of cesium by clay minerals: effect of saturating cations," Soil Science Society of America Journal, vol. 28, no. 2, pp. 183-186, 1964.

[24]   D. Carroll, "Ion exchange in clays and other minerals," Geological Society of America Bulletin, vol. 70, no. 6, pp. 749-779, 1959.

[25]   D. Eberl, "Clay mineral formation and transformation in rocks and soils," Philosophical Transactions of the Royal Society of London. Series A, Mathematical and Physical Sciences, vol. 311, no. 1517, pp. 241-257, 1984.

[26]   B. B. Velde and A. Meunier, The origin of clay minerals in soils and weathered rocks. Springer Science & Business Media, 2008.

[27]   S. C. Aboudi Mana, M. M. Hanafiah, and A. J. K. Chowdhury, "Environmental characteristics of clay and clay-based minerals," GeoloGy, ecoloGy, and landscapes, vol. 1, no. 3, pp. 155-161, 2017.

[28]   F. Anouar, A. Elmchaouri, N. Taoufik, and Y. Rakhila, "Investigation of the ion exchange effect on surface properties and porous structure of clay: Application of ascorbic acid adsorption," Journal of Environmental Chemical Engineering, vol. 7, no. 5, p. 103404, 2019.

[29]   G. Ataman and O. Baysal, "Clay mineralogy of Turkish borate deposits," Chemical Geology, vol. 22, pp. 233-247, 1978.

[30]   C. Helvaci, "Stratigraphy, mineralogy, and genesis of the Bigadiç borate deposits, Western Turkey," Economic Geology, vol. 90, no. 5, pp. 1237-1260, 1995.

[31]   C. Helvaci, H. Mordogan, M. Çolak, and I. Gündogan, "Presence and distribution of lithium in borate deposits and some recent lake waters of west-central Turkey," International Geology Review, vol. 46, no. 2, pp. 177-190, 2004.

[32]   M. m. Çolak, C. Helvaci, and M. Maggetti, "Saponite from the Emet colemanite mines, Kutahya, Turkey," Clays and Clay Minerals, vol. 48, no. 4, pp. 409-423, 2000.

[33]   B. Ertan and Y. Erdoğan, "Emet-Espey bölgesindeki borlu killerde eser element tayini," Journal of Science and Technology of Dumlupınar University, no. 033, pp. 25-32, 2014.

[34]   W.-J. Lee et al., "Lithium extraction from smectitic clay occurring in lithium-bearing boron deposits in Turkey," Journal of the Mineralogical Society of Korea, vol. 29, no. 4, pp. 167-177, 2016.

[35]   A. Obut, İ. Ehsani, Z. Aktosun, A. Yörükoğlu, İ. Girgin, A. Temel and H. Deveci, "Leaching behaviour of lithium from a clay sample of Kırka borate deposit in sulfuric acid solutions," Journal of Boron, vol. 5, no. 4, pp. 170-175, 2020.

[36]   H. Şensöz, Z. E. Sayın, M. Savaş, and Y. Erdoğan, "Emet Bor Üretim Tesisleri Atıklarının Lityum İçeriğinin İncelenmesi," Afyon Kocatepe Üniversitesi Fen Ve Mühendislik Bilimleri Dergisi, vol. 21, no. 6, pp. 1460-1469, 2021.

[37]   H. Mordoğan, M. Akdağ, and C. Helvacı, "Lithium recover from low-grade lithium-bearing clays by H2SO4 and roast-water leach processes," Geosound (Yerbilimleri), vol. 24, pp. 141-150, 1994.

[38]   C. Helvacı and O. Alaca, "Geology and Mineralogy of the Bigadiç Borate Deposıts and Vicinity," Bulletin of the Mineral Research and Exploration, vol. 113, no. 113, pp. 31-63, 1991.

[39]   A. I. Okay, "Was the Late Triassic orogeny in Turkey caused by the collision of an oceanic plateau?," Geological Society, London, Special Publications, vol. 173, no. 1, pp. 25-41, 2000.

[40]   İ. Koçak and Ş. Koç, "Trace element contents of Bigadiç and Kestelek borate deposits," to Boron, p. 232, 2011.

[41]   İ. Koçak and Ş. Koç, "Major and trace element geochemistry of the Bigadiç Borate deposit, Balikesir, Turkiye," Geochemistry International, vol. 50, pp. 926-951, 2012.

[42]   Y. Y. Öztürk, A. Selin, and C. Helvacı, "Bor Minerallerinin Duraylı İzotop Jeokimyası: Bigadiç (Balıkesir) Borat Yatağından Bir Örnek," Yerbilimleri, vol. 35, no. 1, pp. 141-168, 2014.

[43]   Y. Dilek and Ş. Altunkaynak, "Geochemical and temporal evolution of Cenozoic magmatism in western Turkey: mantle response to collision, slab break-off, and lithospheric tearing in an orogenic belt," Geological Society, London, Special Publications, vol. 311, no. 1, pp. 213-233, 2009.

[44]   F. Gulmez, H. U. Ercan, N. Lom, G. Gocmengil, and E. Damci, "The inherited structure of the Gediz Graben (Aegean Extensional Province, Turkey): insights from the deep geothermal wells in the Alasehir sub-basin," International Journal Of Earth Sciences, 2023.

[45]   S. İşçi, "Kil/PVA ve organokil/PVA nanokompozitlerin sentezi ve karakterizasyonu," Fen Bilimleri Enstitüsü, 2007.

[46]   G. Brown, Crystal structures of clay minerals and their X-ray identification. The mineralogical society of Great Britain and Ireland, 1982.

[47]   D. M. Moore and R. C. Reynolds Jr, X-ray Diffraction and the Identification and Analysis of Clay Minerals. Oxford University Press (OUP), 1989.

[48]   S. Yamashita, H. Mukai, N. Tomioka, H. Kagi, and Y. Suzuki, "Iron-rich smectite formation in subseafloor basaltic lava in aged oceanic crust," Scientific Reports, vol. 9, no. 1, p. 11306, 2019.

[49]   S. Kadir, T. Külah, H. Erkoyun, C. Helvacı, M. Eren, and B. Demiral, "Mineralogy, geochemistry, and genesis of lithium-bearing argillaceous sediments associated with the Neogene Bigadiç borate deposits, Balıkesir, western Anatolia, Türkiye," Applied Clay Science, vol. 242, p. 107015, 2023.

[50]   M. D. Foster, "The importance of exchangeable magnesium and cation-exchange capacity in the study of montmorillonitic clays," American Mineralogist: Journal of Earth and Planetary Materials, vol. 36, no. 9-10, pp. 717-730, 1951.

[51]   J. Mering, "Smectites," in Soil Components: Vol. 2: Inorganic Components: Springer, 1975, pp. 97-119.

[52]   S. Petit, A. Decarreau, W. Gates, P. Andrieux, and O. Grauby, "Hydrothermal synthesis of dioctahedral smectites: The Al–Fe3+ chemical series. Part II: Crystal-chemistry," Applied Clay Science, vol. 104, pp. 96-105, 2015.

[53]   Y. Tardy, G. Krempp, and N. Trauth, "Le lithium dans les minéraux argileux des sédiments et des sols," Geochimica et Cosmochimica Acta, vol. 36, no. 4, pp. 397-412, 1972.

[54]   A. Decarreau, "Cristallogènese expérimentale des smectites magnésiennes: Hectorite, stévensite," Bulletin de minéralogie, vol. 103, no. 6, pp. 579-590, 1980.

[55]   H. C. Starkey, The role of clays in fixing lithium (no. 1278). US Government Printing Office, 1982.

[56]   C. S. Ross and S. B. Hendricks, Minerals of the montmorillonite group: Their origin and relation to soils and clays (no. 205). US Government Printing Office, 1945.

[57]   E. F. Brenner-Tourtelot and R. K. Glanzman, "Lithium-bearing rocks of the horse spring formation, Clark County, Nevada," in Lithium Needs and Resources: Elsevier, 1978, pp. 255-262.

[58]   H. J. Koo, B. Y. Lee, H. G. Cho, and S. M. Koh, "Study of Heat and Acid Treatment for Hectorite in Turkey Boron Deposit," Journal of the Mineralogical Society of Korea, vol. 29, no. 3, pp. 103-111, 2016.

[59]   A. Obut, Z. Aktosun, İ. Girgin, H. Deveci, and A. Yörükoğlu, "Characterization and treatment of clayey waste using a sulfuric acid roasting-water leaching process for the extraction of lithium," Physicochemical Problems of Mineral Processing, vol. 58, no. 4, 2022.

[60]   R. D. Shannon, "Revised effective ionic radii and systematic studies of interatomic distances in halides and chalcogenides," Acta crystallographica section A: crystal physics, diffraction, theoretical and general crystallography, vol. 32, no. 5, pp. 751-767, 1976.

[61]   K. Birdi, Handbook of surface and colloid chemistry. CRC press, 2008.

[62]   B. Tansel, "Significance of thermodynamic and physical characteristics on permeation of ions during membrane separation: Hydrated radius, hydration free energy and viscous effects," Separation and purification technology, vol. 86, pp. 119-126, 2012.

[63]   B. J. Teppen and D. M. Miller, "Hydration energy determines isovalent cation exchange selectivity by clay minerals," Soil Science Society of America Journal, vol. 70, no. 1, pp. 31-40, 2006.

[64]   M. W. Washabaugh and K. D. Collins, "The systematic characterization by aqueous column chromatography of solutes which affect protein stability," Journal of Biological Chemistry, vol. 261, no. 27, pp. 12477-12485, 1986.

[65]   J. Havel and E. Högfeldt, "Evaluation of water sorption equilibrium data on Dowex ion exchanger using WSLET-MINUIT program," Scripta Fac. Sci. Nat. Univ. Masaryk. Brun. Chem, vol. 25, pp. 73-84, 1995.

[66]   P. R. Bodart, L. Delmotte, S. Rigolet, J. Brendlé, and R. D. Gougeon, "7Li {19F} TEDOR NMR to observe the lithium migration in heated montmorillonite," Applied Clay Science, vol. 157, pp. 204-211, 2018.

[67]   T. Ebina, T. Iwasaki, And A. Chatterjee, "XPS and DFT study on the migration of lithium in montmorillonite," Clay science, vol. 10, no. 6, pp. 569-581, 1999.

[68]   U. Hofmann and R. Klemen, "Verlust der austauschfähigkeit von lithiumionen an bentonit durch erhitzung," Zeitschrift für anorganische Chemie, vol. 262, no. 1-5, pp. 95-99, 1950.

[69]   R. Greene-Kelly, "A test for montmorillonite," Nature, vol. 170, no. 4339, pp. 1130-1131, 1952.

[70]   R. Tettenhorst, "Cation migration in montmorillonites," American Mineralogist: Journal of Earth and Planetary Materials, vol. 47, no. 5-6, pp. 769-773, 1962.

[71]   P. Komadel, J. Madejová, and J. Bujdák, "Preparation and properties of reduced-charge smectites—a review," Clays and Clay Minerals, vol. 53, pp. 313-334, 2005.

[72]   B. K. G. Theng, Formation and properties of clay-polymer complexes. Elsevier, 2012.

[73]   I. Tkáč, P. Komadel, and D. Müller, "Acid-treated montmorillonites—a study by 29Si and 27Al MAS NMR," Clay Minerals, vol. 29, no. 1, pp. 11-19, 1994.

[74]   C. Breen, J. Madejová, and P. Komadel, "Characterisation of moderately acid-treated, size-fractionated montmorillonites using IR and MAS NMR spectroscopy and thermal analysis," Journal of Materials Chemistry, vol. 5, no. 3, pp. 469-474, 1995.

[75]   B. R. Bickmore, D. Bosbach, M. F. Hochella Jr, L. Charlet, and E. Rufe, "In situ atomic force microscopy study of hectorite and nontronite dissolution: Implications for phyllosilicate edge

surface structures and dissolution mechanisms," American Mineralogist, vol. 86, no. 4, pp. 411-423, 2001.

[76]   P. Komadel, "Acid activated clays: Materials in continuous demand," Applied Clay Science, vol. 131, pp. 84-99, 2016.

[77]   F. Franco, M. Pozo, J. A. Cecilia, M. Benitez-Guerrero, and M. Lorente, "Effectiveness of microwave assisted acid treatment on dioctahedral and trioctahedral smectites. The influence of octahedral composition," Applied Clay Science, vol. 120, pp. 70-80, 2016.

[78]   N. Vigier, A. Decarreau, R. Millot, J. Carignan, S. Petit, and C. France-Lanord, "Quantifying Li isotope fractionation during smectite formation and implications for the Li cycle," Geochimica et Cosmochimica Acta, vol. 72, no. 3, pp. 780-792, 2008.

[79]   Z. Zhao, X. Si, X. Liu, L. He, and X. Liang, "Li extraction from high Mg/Li ratio brine with LiFePO4/FePO$_4$ as electrode materials," Hydrometallurgy, vol. 133, pp. 75-83, 2013.

[80]   G. t. Brown and G. Brindley, "X-ray diffraction procedures for clay mineral identification," 1980.

SITE SUPERVISOR SELECTION WITH ANALYTIC HIERARCHY PROCESS (AHP) AND CASE STUDY

[1] **Oğuzhan BÜLBÜL** [ID], [2,*] **Recep KANIT** [ID]

[1,2] *Gazi University, Graduate School of Natural and Applied Sciences, Technology Faculty, Civil Engineering Department, Ankara, TÜRKİYE*
[1] oguzhanbulbul@yahoo.com, [2] rkanit@gazi.edu.tr

Highlights

- Site supervisor is the most important technical personnel in construction work.

- Selection of the site supervisor is vitally important for construction work.

- This study aims to develop a methodology for site supervisor selection.

- Case study was conducted with 3 companies to comfirm the method developed in study.

*Corresponding Author: Oğuzhan BÜLBÜL, oguzhanbulbul@yahoo.com

SITE SUPERVISOR SELECTION WITH ANALYTIC HIERARCHY PROCESS (AHP) AND CASE STUDY

[1] Oğuzhan BÜLBÜL [iD] , [2, *] Recep KANIT [iD]

[1,2] *Gazi University, Graduate School of Natural and Applied Sciences, Technology Faculty, Civil Engineering Department, Ankara, TÜRKİYE*
[1] oguzhanbulbul@yahoo.com, [2] rkanit@gazi.edu.tr

ABSTRACT: The purpose of this study is to develop a methodology for the selection of site supervisors for construction companies carrying out medium-sized building construction works. For this purpose, 3 construction companies were interviewed and the developed method was used for the site supervisor selection of these companies. In this context, 4 candidates who applied to Company A were given scores by the company official according to the selection criteria used in this study and analyses were made with AHP. Candidate 3 ranked first with a priority value of 26.57%. This result was compared with the results of the simultaneous selection by the company using its own method and it was seen that the company selected the same candidate. Same procedure was used for companies B and C. Three different candidates had applied to each company. According to the results, Candidate 3 was selected by Company B with a priority value of 37.52% and Candidate 1 was selected by Company C with a priority value of 35.87%. It was observed that the selection results of both companies carried out simultaneously with their own methods were the same with the candidates found in the study.

Keywords: AHP, Building Construction Companies, Construction Industry, Field Work, Site Supervisor Selection

1. INTRODUCTION

1.1. Importance of the Subject

The site supervisor is the most important technical personnel in charge of the execution of a construction work. Pursuant to the Regulation on Construction Site Supervisors, the construction site supervisor refers to the technical personnel who manages and implements the construction / demolition works on behalf of the building contractor. The duty of the construction site supervisor regarding the construction work starts from the receipt of the building license and ends with the receipt of the occupancy permit. The site supervisor is responsible for ensuring the construction and work organization necessary for the realization of the construction / demolition work on behalf of the building contractor in accordance with the license and the surveys and projects attached to the license, taking, implementing and enforcing all kinds of measures stipulated by the legislation [1]. According to the 3194 Zoning Law, it is not possible to continue the construction work without a construction site supervisor. Although the responsibility of technical personnel is limited to their own technical field, according to the law, the responsibility of the site supervisor is at the same level with the building contractor. This responsibility includes the construction of the building in accordance with the legislation, technical documents, standards and technical specifications [2].

The selection of the site supervisor, who has such important duties and responsibilities and who is expected to manage resources (time, money, labor, authority, talent, etc.) in the best way, is vitally important for the completion of the construction work as desired. Making this selection with a data-based scientific method will be beneficial for both the contractor company and the person/institution that demands the construction. This study aims to develop such a scientific method.

*Corresponding Author: Oğuzhan BÜLBÜL, oguzhanbulbul@yahoo.com

1.2. Analytic Hierarchy Process (AHP)

It can be difficult to choose between alternatives when there are multiple criteria for decision making. Multi-criteria decision-making (MCDM) methods are analytical methods used in the evaluation of alternatives. There are many types of MCDM methods such as ELECTRE, TOPSIS, PROMETHEE, VIKOR, ANP, AHP and many others [4].

AHP, one of the most popular MCDM methods, was developed by Thomas L. Saaty to find solutions to complex multi-criteria problems [3]. It is based on the principle of determining the relative importance of decision criteria according to each other by subjecting them to pairwise comparisons. For this, the decision maker (expert) opinion is used. The alternatives are prioritized on the basis of the criteria and the selection is made. The most important advantages of AHP among other MCDM methods are its ease of use and the fact that it can be successfully applied in complex decision problems that include subjective judgments as well as objective judgments.

The problem of selecting the best site supervisor involves both quantitative and qualitative criteria. The quantitative criteria (such as having a certificate, experience by years, English level, etc.) can be analyzed numerically while the qualitative criteria (such as self-confidence, general experience, reliability, etc.) should be evaluated personally with expert knowledge of the decision maker. AHP supplies an easily applicable method for both of these two types of criteria. In addition, there is a need to classify and handle many criteria related to different fields, thus the problem can be detailed and decomposed. When evaluated in terms of suitability for the purpose in this study, it was decided that it would be appropriate to use AHP in this study because of the advantages and superiority of it compared with other MCDM methods.

The solution stages of the AHP method consist of 5 steps [5].

Step 1 (Creating the Hierarchical Structure): A top-down structure is created. The objective is written at the top. In the middle are the criteria and sub-criteria, and at the bottom are the alternatives.

Step 2 (Pairwise Comparison Matrices and Determination of Superiorities): After the hierarchical structure is established, the (nxn) pairwise comparison matrix shown in equation (2.1) is created.

$$A = \begin{bmatrix} 1 & a_{21} & a_{31} & \dots & a_{n1} \\ 1/a_{21} & 1 & a_{32} & \dots & a_{n2} \\ 1/a_{31} & 1/a_{32} & 1 & \dots & a_{n3} \\ \vdots & \vdots & \vdots & \ddots & \vdots \\ 1/a_{n1} & 1/a_{n2} & 1/a_{n3} & \dots & 1 \end{bmatrix} \tag{2.1}$$

Each criterion given in equation (2.1) is scored according to their importance. Here, the 9-digit importance scale developed by Saaty should be used to determine the superiority [4].

Step 3 (Determination of the Eigen Vector (Relative Importance Vector)): After the pairwise comparison matrices are created, the eigenvector showing the importance of each value in the matrix relative to the other values is calculated. The eigenvector of the matrix in nx1 dimension is given in equation (2.2).

where i =1,2,3.....,n and j=1,2,3,....n

$$b_{ij} = \frac{a_{ij}}{\sum_{i=1}^{n} a_{ij}}) \text{ and } w_i = \frac{\sum_{j=1}^{n} b_{ij}}{n} \tag{2.2}$$

The column vector W is obtained from the arithmetic mean of the row elements of the matrix formed by the b_{ij} values specified in equation (2.2).

Step 4 (Calculating the Consistency of the Eigenvector): The inconsistency ratio (CR) is calculated for each pairwise comparison matrix. The inconsistency ratio should be below 0.10 [4]. If it is above this value, the scoring should be redone. To calculate the inconsistency ratio, the largest eigenvector of matrix A, i.e. λmax is calculated (equation 2.3).

where i =1,2,3…..,n and j=1,2,3,….n

$D = [aij]_{mxn} \quad x \, [w_i]_{nx1} = [d_i]_{nx1}$

$$\lambda_{max} = \frac{\sum_{i=1}^{n} \frac{d_i}{wi}}{n} \tag{2.3}$$

In order to calculate the inconsistency ratio, the randomness index (RI) value is needed. This value is taken from the random value index table [4].

In accordance with this information, the calculation of the inconsistency ratio CR is given in equation (2.4). In order to obtain a reliable result, the CR inconsistency ratio should not exceed 0.10 [4].

$$CR = \frac{\lambda_{max} - n}{(n-1).RI} \qquad \qquad \textbf{(Hata!}$$

Belgede belirtilen stilde metne rastlanmadı..4)

Step 5: The first four steps for obtaining the priority values are calculated for the entire hierarchical structure. At this stage, the superiority column vectors of mx1 dimension generated by each of the n criteria in the hierarchical structure are combined to form the DW decision matrix of mxn dimension with equation (2.5). The result vector R is obtained by multiplying the matrix with the superiority vector

where i =1,2,3…..,n and j=1,2,3,….n

$DW = [w_i]_{mxn}$ **(Hata!**

Belgede belirtilen stilde metne rastlanmadı..5)
W by equation (2.6) [5].

1.3. Literature Review

There are many studies in the literature on selection with MCDM methods, here especially studies with AHP are focused. In these studies, selection problems have been evaluated in different areas such as recruitment of personnel for workplaces belonging to various sectors, priority/performance evaluation for the purpose of assigning personnel within the organization to a position, selection of the most suitable contractor/bid.

Özyürek et al. [6-8] utilized AHP in their studies on the evaluation of tender bids within the scope of 4734 Public Procurement Law. In this framework, solutions were proposed for the selection of the most suitable bidder by using AHP in the areas of; evaluating quality and bid price together [6], evaluating the quality of bidders [7], evaluating the qualification criteria of bidders in the law [8].

Yılmaz [9] addressed the problem of selecting a research assistant for a private university in Germany by using AHP. It was revealed that if the personnel who is prioritized at result of the study is selected, the research assistant with the most important characteristics of the decision makers will be recruited and the highest efficiency can be achieved.

In the study conducted by Şener [10], the problem of selecting one of the existing personnel as quality control personnel for a new production line to be established in an integrated textile enterprise was solved with AHP. As a result of the study, it was revealed that the classical performance evaluation

applied by the organization is based only on quantitative criteria while ignoring qualitative criteria; however, by taking qualitative criteria into consideration in AHP analysis, the selection results can be based on a more comprehensive study.

In the study conducted by Çoban [11], it was aimed to realize the personnel selection process by applying AHP in the recruitment of engineers for a drip irrigation manufacturing company. As a result of the study; it was concluded that subjective criteria (creative thinking and research skills) had a high impact on the selection and that AHP can be used not only in personnel selection but also in solving all decision problems.

Erdemir et al. [12] conducted a performance evaluation of one hundred personnel working in a municipality by considering public performance requirements. As a result of the findings, it was revealed that the AHP integrated fuzzy TOPSIS model can achieve different and effective results in performance evaluation than the existing evaluation.

Koyuncu et al. [13] aimed to compare the effectiveness of AHP and TOPSIS methods in personnel selection process. In this context, a personnel selection study was conducted in a manufacturing company operating in the automotive sector. Six engineers who started to work in the company within the last year were evaluated with the two methods, and the ranking results obtained were compared with the performance scores of these employees. According to the comparison, it was determined that the method showing the least deviation was AHP.

Turan et al. [14] focused on personnel selection in the health sector and examined the use of AHP in nurse selection for hospitals. As a result of the study, AHP method was applied for the criteria and the importance level of the criteria was quantified.

Vural et al. [15] addressed the personnel selection problem of a medium-sized enterprise located in the Organized Industrial Zone of Kayseri province. Candidates who applied for a job were ranked according to their level of having the specified criteria. The results showed that AHP and VIKOR methods can be used effectively in an integrated manner in personnel selection.

Supçiller et al. [16] used AHP method to find the weights of the criteria in the optimal supplier selection problem for a company, and 7 different MCDM methods together with AHP in the selection of the supplier. As a result of the study, it was observed that AHP gave results compatible with other methods.

Önel [17] studied personnel selection with fuzzy AHP for a concrete plant. With this method, it was revealed that linguistic variables can be processed mathematically and the selection process can be realized.

In the study by Hankılıç [18], a fuzzy AHP decision making model was developed and applied for personnel selection with job/position and organizational requirements criteria. While individuals cannot compare more than seven objects at the same time, it is shown that it is possible to compare the data of a large number of candidates with this method.

In the study conducted by Keser [19] on bank personnel selection, AHP and fuzzy AHP methods were used. The data of the interviews conducted with 250 candidates by the human resources department of a bank were reinterpreted with AHP and fuzzy AHP. It was seen that AHP and fuzzy AHP are very effective methods in deciding which of the alternatives to select from the data sets with high sample size.

In the study by Özbek [20], the personnel selection problem was solved with AHP, one of the MCDM techniques that is frequently used in solving such problems, and the AHP solution algorithm was turned into a web-based application.

In the study conducted by Uğur [21], the selection of a project manager who will take part in the management of a large construction project to be carried out in a foreign country (Russia) was made with MOORA, one of the MCDM methods.

Anbarcı et al. [22] developed a fuzzy logic evaluation model for technical personnel selection, which is usually based on the subjective evaluations of the people responsible for personnel selection in the company. The model was applied to site supervisor selection and the results showed that the proposed

method can be effective and useful for the site supervisor selection problem.

Acer et al. [23] evaluated the field operation personnel selection process in Trabzon Port, one of the most important ports of Türkiye, by using AHP and MOORA methods. With the findings obtained, it was shown that post-application criteria (interview, exam results and references) were the most important factors in the personnel selection process and a prioritized candidate was determined for selection.

Karabayır et al. [24] used multi-criteria decision-making methods for selecting the most convenient supplier for construction companies. Fuzzy AHP was used for the calculation of decision criteria weights, and then Fuzzy TOPSIS was applied for ranking the alternatives. The approach was tested for two construction companies and selection decisions of two different sized companies having the same supplier pool was compared.

In the study by Uluskan et al. [25] suppliers of a public institution operating in the railway industry were evaluated using MCDM methods. The criteria were weighted through AHP, Fuzzy AHP and Level Based Weight Assessment (LBWA) methods, whereas, the alternatives were ranked via Complex Proportional Evaluation (COPRAS) method. The AHP method was utilized due to its effectiveness in criterion weighting and its usability with other methods. As there is a large number of subjective criteria in the study, the uncertainties were decided to be eliminated through FAHP method.

Kantoğlu et al. [26] studied the supplier selection problem in a chocolate production company. Factors such as quality, price, delivery, performance, interaction and a large number of sub-criteria create a complex structure in evaluating supplier selection. In this study, the Fuzzy AHP Method was used to determine the important criteria for supplier selection.

Akkaya [27] analyzed determining the sludge dewatering process in a wastewater treatment plant using the analytical hierarchy process (AHP), as it is necessary to choose low-cost methods that are suitable for the plant and provide high solids content. The criteria were created for the selection of sludge dewatering equipment, these criteria were compared and analyzed in the SuperDecision software and the best sludge dewatering equipment was determined.

Paçacı et al. [28] focused on logistics center selection problem. AHP was used for evaluation of the order of importance of the main and sub-criteria determined for the logistics center location.

In the study conducted by Aykan et al. [29], choosing the right candidate for the position of assistant human resources specialist in a production enterprise operating in the Kayseri Free Zone was studied with the help of AHP and TOPSIS methods. With the help of the results obtained from the AHP method, the TOPSIS method was applied and the most suitable candidate was selected among 8 candidates.

Gümüşhan et al. [30] studied selection of a suitable e-learning system, which is being actively used more and more in normal life starting from the Pandemic period. The criteria for selection were listed using the fuzzy AHP method. The most effective criterion in the study was found to be interaction, which is followed by ease of use, content and reliability criteria.

In the study by Şahintürk et al. [31], appropriate Enterprise Architecture (EA) selection problem was analyzed. EA is a methodology that aims to ensure continuous harmony between the institution's strategy, goals, organizational structure, business processes and information technology infrastructure. In the study, the selection of a EA framework suitable for the business processes of an institution that will start a digital transformation project is explained. AHP and ELECTRE I techniques were used and the TOGAF framework was determined to be the most appropriate one.

Çetin et al. [32] studied company performance with AHP based Balanced Scorecard (BSC) method. AHP was used to determine the weight of performance measurement criteria. The performance of a company operating in the metal plating sector in Izmir was evaluated with BSC. The importance levels of BSC's financial dimension, customer dimension, internal processes dimension and learning and development dimensions in performance evaluation were measured with AHP. The performance evaluation of the company for the determined years was obtained.

Aslan's study [33] was carried out in order to model and evaluate the groundwater potential and quality of Van (Türkiye). In order to evaluate the groundwater potential of Van, remote sensing data

with AHP and Fuzzy AHP methods were used. The evidence obtained by validating the results is consistent with the flow calculation values.

Özen et al. [34] studied supplier selection in automotive sub-industry sector using AHP, fuzzy AHP and fuzzy TOPSIS approaches. In the study, the impact of Covid-19 epidemic on supplier selection in the automotive industry is emphasized. Selection of the most suitable supplier was evaluated among the 4 candidate suppliers with three different expert decision makers. Finally, by conducting sensitivity analysis, suppliers were examined and interpreted under different circumstances.

2. MATERIAL AND METHODS

2.1. Material

The aim of this study is to develop a scientific method that construction companies can use for the selection of personnel to be employed as site supervisors. For this purpose, the study was initiated by researching and obtaining the material that can be used in the analysis.

First of all, the decision criteria that can be used in site supervisor selection were investigated. For this purpose, a literature review on personnel selection and interviews were conducted with the relevant people within the scope of the study. The relevant people whose information and opinions were obtained in the field study were company owners, board members and company managers. In addition to these, missing criteria were produced through research (recruitment advertisements, etc.) and personal experience. The decision criteria obtained were shown on a table and a Personnel Selection Criteria Matrix was created (Table 1).

The criteria were categorized in a logical and consistent manner and a questionnaire was created with 66 sub-criteria under 10 criteria. The purpose of the questionnaire is to determine the importance levels of the criteria and sub-criteria. In order to test the comprehensibility, the questionnaire was sent to a limited number of related people through a Pilot Research Application. As a result of this application, it was realized that the target group of the questionnaire should be more specific. When the questionnaire was first created, it was aimed to be applied to all construction companies. However, it was found that this target caused difficulties in the design of the survey questions (decision criteria).

The construction sector consists of many sub-areas. For example; building construction, soil mechanics applications, steel structures, paved field manufacturing, etc. If the questions are designed to address companies operating in all areas, there is a need to make generalizations, and if the questions are detailed according to different construction areas, the number of questions increases exponentially.

It was evaluated that the survey questions related to a specific construction area, rather than all of these areas, would increase comprehensibility, validity and reliability, and thus the universe for application of the questionnaire was limited. It was decided that applying the questionnaire in the field of "building construction" would provide the opportunity to reach the largest number of participants. Thus, the scope of the study was determined as construction companies operating in the construction sector and carrying out medium-sized building construction works. As a result of the study, it was evaluated that studies addressing different construction areas could be conducted by changing the decision criteria after the method for the selection of the construction site supervisor was established.

Finally, the Site Supervisor Selection Decision Criteria Survey was finalized to consist of 51 sub-criteria under 8 criteria (Table 2). The purpose of the survey is to determine the level of importance of the decision criteria and sub-criteria in the selection of a site supervisor. The survey was prepared in such a way that one of the 5 levels, namely "Very High", "High", "Medium", "Low", "Very Low", could be preferred for the importance levels of the sub-criteria. Participants were not asked to determine the level of importance for the criteria, it was aimed to obtain the importance levels of the criteria from the average of their sub-criteria for internal consistency.

Table 1. Personnel Selection Criteria Matrix (a part of it is shown because it is voluminous)

			Pre-Selection Criteria						Experience		
			Gender	To have done military service	Diploma	Other Legislative Obligations	Experience period (years)	Age	Experience in the Construction Industry	Experience as Site Supervisor	Similar Project Experience
USED IN ACADEMIC STUDIES	1	Personnel Selection with Anp and Dematel - E.Aksakal, ... (Industrial Engineer for an international company)								√√	
	2	Personnel Selection with Fuzzy Ahp - E.Özgörmüş, ... (Supply Planning Engineering for the food industry)								√√	
	3	Site Supervisors Qualifications - L.O.Uğur, ... (leader qualified Site Supervisor)									
	4	(PhD) Fuzzy Logic in Human Resources Selection - B.Doğanalp (Mechanical Maintenance Engineer for a business organization in the manufacturing sector)							√		
	5	Salesperson Candidates with F.Topsis - Z.Başkaya, ... (Salesperson to work in top level store)								√√	
	6	Integrated Fuzzy For Architect - V.Keršulienė, ... (Architect to work as project manager)									
	7	(PhD) F.Topsis F.AHP - B.Öztürk (Salesperson for chain of stores)								√√	
	8	(Master's degree) Nurse Selection with F.Topsis - M.K.Bingöllü (Nurse selection from internal sources)									
	9	Group Decision in Fuzzy Environment with F.Topsis - F.Ecer (Salesperson in national retail stores)								√√	
	10	Topsis for group decision under F.Environment - C.T.Chen *(System Analysis Engineer for software company)*								√√	
FROM CONTRACTORS		BÜLENT SAVAŞ KILINÇ / EYLÜL BİLİŞİM MÜH.İNŞ.TİC.LTD.ŞTİ. (Company owner, Civil Engineer)	√	√						√√	
		MUSTAFA KAYA / YAPTEK İNŞ.TUR.TAAH.TİC.LTD.ŞTİ. (Company partner, Civil Engineer)								√√	
		ALİ ILGAR / A YAPI TAAH.SAN.TİC.LTD.ŞTİ. (Company partner, Civil Engineer)								√√	
		ALAATTİN AKCİN / ÖZ ARGE İNŞAAT SAN.VE TİC.LTD.ŞTİ. (Company owner, Civil Engineer)	√	√					√		√
		Contractor Reported Criteria									
		Self Generated Criteria									
		√ sub-criteria used									
		√√ criteria used									

Table 2. Site Supervisor Selection Decision Criteria Survey

At what level are the following criteria important for the selection of a site supervisor?					
Criteria / Sub Criteria	**Importance for Selection***				
1. EDUCATION / CERTIFICATE	**VH**	**H**	**M**	**L**	**VL**
1.1 Undergraduate Education (candidate's university of graduation)					
1.2 Master's Degree (university candidate graduated/continues)					
1.3 Having "Class A Occupational Safety Specialist Certificate"					
1.4 Having a "First Aid Certificate"					
1.5 Having a "Driver's License"					
1.6 Vocational Trainings Received (certified)					
2. EXPERIENCE	**VH**	**H**	**M**	**L**	**VL**
2.1 Total Experience as a Site Supervisor in All Construction Areas					
2.2 Experience as a Site Supervisor in Building Construction					
2.3 Experience of Managing a Construction Site from Start to Finish					
2.4 Number of Works Completed as Site Supervisor					
2.5 Size of the Work(s) Completed as Site Supervisor (area, cost)					
2.6 Total Number of Years of Employment in the Construction Sector					
2.7 Total Number of Years Worked in the Field of Building Construction					
2.8 Previous Companies and Duration of Employment (stability)					
3. BUSINESS KNOWLEDGE	**VH**	**H**	**M**	**L**	**VL**
3.1 Planning Knowledge (to be able to prepare and follow the work program)					
3.2 Quantity Survey, Progress Payment, Final Account Information					
3.3 Equipment and Technology Knowledge (construction machinery, etc.)					
3.4 Construction Materials Knowledge (concrete, admixtures, paint, etc.)					
3.5 Knowledge of Records to be kept at the construction site					
3.6 Knowledge of Construction Legislation					
3.7 Knowledge of Labor Law (Labor Law and related legislation)					
3.8 Knowledge of Occupational Health and Safety					
3.9 Knowledge of Resource Management (material, labor, money, time, etc.)					
3.10 Knowledge of Cost Management (cost of construction works)					
3.11 Environmental Management Knowledge					
3.12 Knowledge of General Economics and Construction Economics					
3.13 Knowledge of Productivity Management (optimum resources)					
4. COMPUTER KNOWLEDGE	**VH**	**H**	**M**	**L**	**VL**
4.1 Using MS Office Programs					
4.2 Using Autocad Program					
4.3 Using Planning Program (Primavera, MS Project etc.)					
5. FOREIGN LANGUAGE KNOWLEDGE	**VH**	**H**	**M**	**L**	**VL**
5.1 General English Level					
5.2 Vocational English Level (mastery of technical terminology)					
6. CANDIDATE'S DEMANDS	**VH**	**H**	**M**	**L**	**VL**
6.1 Fee Requested by the Candidate					
6.2 Whether the candidate needs accommodation, whether the company should provide it, and if so, the cost to the company					
6.3 Whether the candidate needs a vehicle, whether the company should provide it, and if so, the cost to the company					
7. SKILLS AND PERSONAL CHARACTERISTICS	**VH**	**H**	**M**	**L**	**VL**
7.1 Desire to succeed (enthusiasm for work, ownership of work)					
7.2 Reliability (to be supported by previous workplaces, references, etc.)					
7.3 Self-confidence					
7.4 Activity and Dynamism (practicality, quick thinking and acting)					
7.5 Tidiness and Orderliness					
7.6 Ability to Represent (appearance and speaking style)					
7.7 Coordination Skills (providing information flow up, down and horizontally)					
7.8 Team Management Skills					
7.9 Ability to take initiative when faced with a problem					
7.10 Predisposition to Personal Career Development					
7.11 Whether he/she has harmful/bad habits (gambling, smoking, alcohol)					
8. OTHER	**VH**	**H**	**M**	**L**	**VL**
8.1 References					
8.2 The size of the construction site that the candidate will manage if hired					
8.3 If he/she knows the location of the construction site he/she will manage					
8.4 Whether the construction site is located in the candidate's hometown					
8.5 The status of the candidate's spouse and children (whether the family can come to the location of the construction site, etc.)					
* VH: Very High / H: High / M: Medium / L: Low / VL: Very Low					

2.2. Method

AHP was used for data analysis. For the AHP analysis, data was collected from construction companies by conducting a field study. The data was entered into Super Decisions software and AHP analysis was performed. The flow chart of the processes carried out in accordance with the method from the beginning to the end of the study is given in Figure 1.
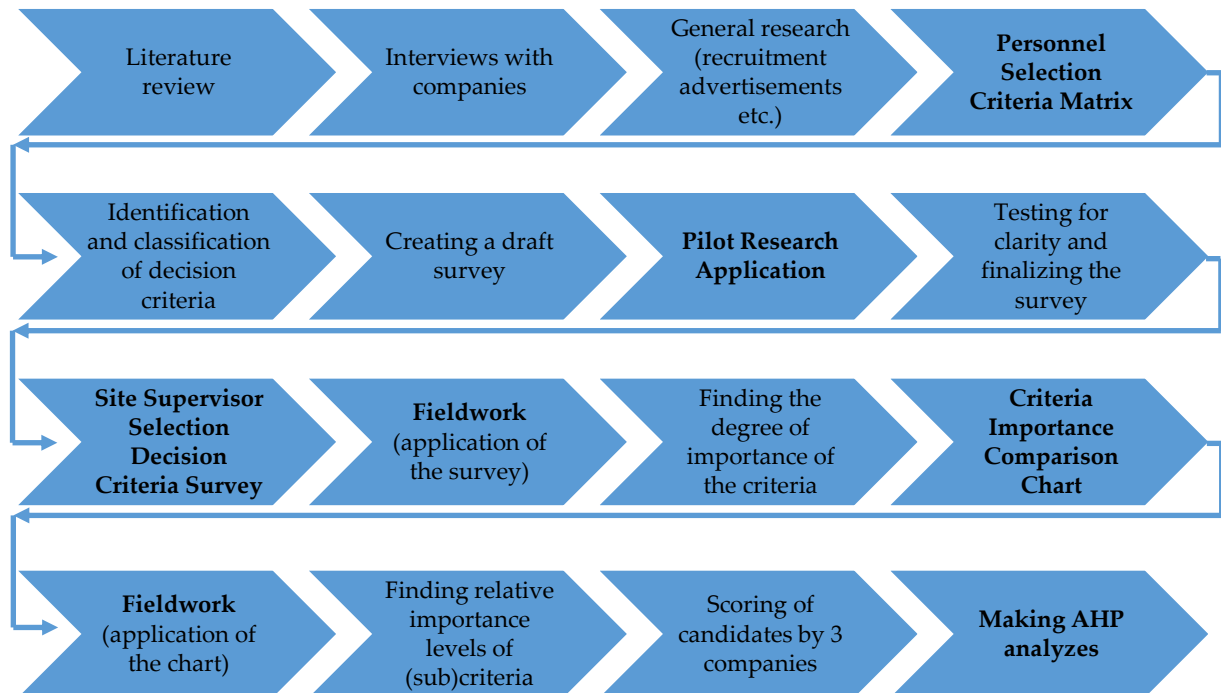
Figure 1. Flow Chart of Processes Conducted in Study (each line is continuation of the previous one)

2.2.1. Fieldwork for AHP

Site Supervisor Selection Decision Criteria Survey was applied to the relevant people and the answers were received. For this purpose, the Ministry of National Defense Construction Real Estate organization, which is responsible for the construction works of the Ministry of National Defense, was worked with. The target group of the survey is the construction companies that carry out medium-sized building construction works participating in the construction tenders of the organization throughout the country. Of these, 48 construction companies were selected to represent the country. The survey was administered through face-to-face interviews where possible, and when this was not possible, it was sent to the companies via the official e-mail address of the organization. As a result, 32 companies were interviewed or returned the questionnaire. Due to the July 15 treacherous coup attempt and Covid-19 pandemic events, this number of interested people could be reached due to the shock, stagnation and contraction in military units and the construction sector. Thus, the importance levels of the sub-criteria were determined. The importance level of each criterion was calculated by taking the average of its sub-criteria (Table 3). In this calculation, it is accepted that the answer "Very High" in the survey is 5 points and the answer "Very Low" is 1 point. These numbers were used in the next stage to find the relative importance levels of the criteria in comparison with each other.

In order to determine the comparative (relative) importance levels of the sub-criteria with each other, the "Decision Criteria Importance Comparison Chart" was created. A score of 1 indicates that the

importance levels of the sub-criteria are equal, and a score between 2 and 9 indicates the level of importance compared to the other sub-criteria (2 being the lowest and 9 being the highest relative importance level). To obtain expert opinion for the chart, face-to-face interviews were conducted with the company managers/board members of 3 construction companies. The scores of the experts were averaged to obtain the comparative (relative) importance levels of the sub-criteria (Table 4).

Table 3. Importance Levels of Decision Criteria (Scores Calculated Using Sub-Criteria)

Decision Criteria	Average Score
1. EDUCATION / CERTIFICATE	3,89
2. EXPERIENCE	4,46
3. BUSINESS KNOWLEDGE	4,13
4. COMPUTER KNOWLEDGE	4,55
5. FOREIGN LANGUAGE KNOWLEDGE	3,00
6. CANDIDATE'S DEMANDS	3,00
7. SKILLS AND PERSONAL CHARACTERISTICS	4,12
8. OTHER	3,40

Table 4. Comparative (Relative) Importance Levels of The Sub-Criteria (a part of it is shown)

1. EDUCATION / CERTIFICATE	9	8	7	6	5	4	3	2	1	2	3	4	5	6	7	8	9	
1.1 Undergraduate Education (candidate's university of graduation)								X										1.2
1.1												X						1.3
1.1			X															1.4
1.1														X				1.5
1.1											X							1.6
1.2 Master's Degree (university candidate graduated/continues)												X						1.3
1.2										X								1.4
1.2																	X	1.5
1.2										X								1.6
1.3 Having "Class A Occupational Safety Specialist Certificate"		X																1.4
1.3																	X	1.5
1.3								X										1.6
1.4 Having a "First Aid Certificate"																	X	1.5
1.4													X					1.6
1.5 Having a "Driver's License"				X														1.6

In order to obtain the comparative (relative) importance levels of the criteria, the importance level scores given in Table 3 were used. These were mathematically compared with each other to obtain the comparative (relative) importance levels of the criteria according to the comparison chart (Table 5).

Three construction companies were contacted, and the developed method was used for the selection of site supervisors for these companies. These selection results were then compared with the results of the simultaneous selection process conducted by the companies using their own methods. Candidates who wanted to work as a construction site supervisor applied to companies A, B and C. The candidates who applied to the companies are different people. After pre-selecting the applicants, the companies assigned scores to the best remaining candidates (alternatives) to apply this method.

The method developed in this study was applied in the selection of the best 4 candidates among the

candidates (alternatives) who applied to Company A for the position of construction site supervisor. The candidates were given scores by the company official according to the sub-criteria (Appendix A). This method was applied in the selection of the best 3 candidates among the candidates (from the alternatives) who applied for the position of construction site supervisor in Company B. The scores given to the candidates by the company official are given in Appendix B. Similarly, the scores given by the company official to the top 3 candidates who applied for the position of construction site supervisor at Company C are shown in Appendix C. The data obtained from the field studies and the scores given to the candidates were used in the AHP analyses. The voluminous score tables are given in appendices for the sake of orderliness of main text.

Table 5. Comparative (Relative) Importance Levels of Decision Criteria

	9	8	7	6	5	4	3	2	1	2	3	4	5	6	7	8	9	
1. EDUCATION / CERTIFICATE										X								2.
1									X									3.
1										X								4.
1							X											5.
1							X											6.
1									X									7.
1								X										8.
2. EXPERIENCE								X										3.
2									X									4.
2						X												5.
2						X												6.
2							X											7.
2								X										8.
3. BUSINESS KNOWLEDGE										X								4.
3							X											5.
3							X											6.
3									X									7.
3							X											8.
4. COMPUTER KNOWLEDGE						X												5.
4						X												6.
4							X											7.
4						X												8.
5. FOREIGN LANGUAGE KNOW.									X									6.
5											X							7.
5										X								8.
6. CANDIDATE'S DEMANDS											X							7.
6										X								8.
7. SKILLS AND PERSONAL CH.								X										8. OTHER

2.2.2. AHP Analyses

Super Decisions software was used for AHP analyses. In the software, firstly the decision problem was defined and the objective was determined as "Best site supervisor selection". The decision criteria and sub-criteria created to realize the objective were entered into the software. The criteria are linked to the objective and each sub-criteria is linked to its own criterion. Three different hierarchical structures were created for three different companies (companies A, B, C). The hierarchical structure for Company A is given in Figure 2.

First, the comparison results of the decision criteria shown in Table 5 were entered into the software (Table 6). The comparison matrix of the criteria is given in Table 7 and the priority values according to the comparison results are given in Table 8. Accordingly, 'K2 Experience' and 'K4 Computer Knowledge' criteria were determined as the most prioritized criteria with 22.34%. Table 8 shows that the inconsistency rate is 0.00893. The fact that this ratio is less than 0.10 indicates that the relevant data are consistent [4].

For the comparison of the importance levels of sub-criteria, the expert opinion results presented in Table 4 were entered into the software. Here, as an example, the comparison results of the sub-criteria of the "K1 Education / Certificate" criterion are shown as entered the software (Table 9). The comparison matrix of the same sub-criteria is given in Table 10 and the priority values according to the comparison results are given in Table 11. Accordingly, among the sub-criteria of criterion K1, sub-criterion 'K1.5 Having a "Driver's License"' is the most prioritized sub-criterion with 52.34% priority value. The

inconsistency rate is 0.09848.
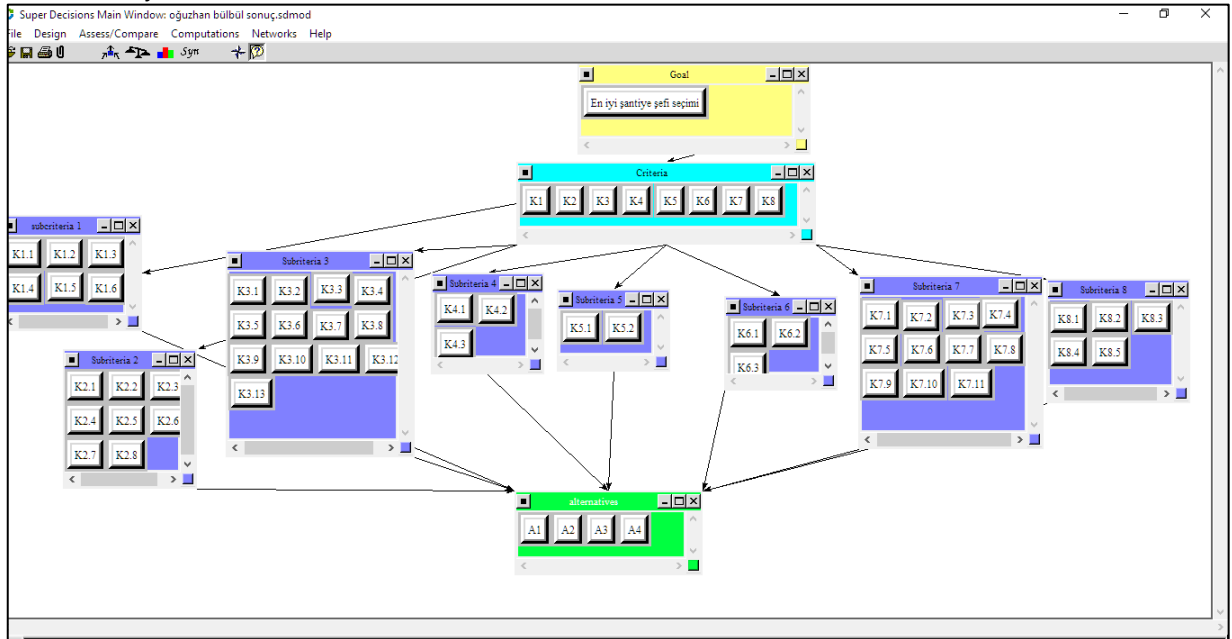
Figure 2. Hierarchical Structure for Company A

Table 6. Entering the comparison results of the criteria into the software (a part of it is shown)

Table 7. Comparison matrix of criteria (a part of it is shown)

Graphical Verbal **Matrix** Questionnaire Direct

Comparisons wrt " Best site supervisor selection in "Criteria" cluster
K2 is 2 times more important than K1

Inconsistency	K2 ~	K3 ~	K4 ~	K5 ~	K6 ~	K7 ~	K8 ~
K1 ~	↑ 2	← 1	↑ 2	← 3	← 3	← 1	← 2
K2 ~		← 2	← 1	← 4	← 4	← 2	← 3
K3 ~			↑ 2	← 3	← 3	← 1	← 3
K4 ~				← 4	← 4	← 2	← 3
K5 ~					← 1	↑ 3.0000	↑ 2
K6 ~						↑ 3.0000	↑ 2

Table 8. Priority values of the criteria according to the comparison results

Inconsistency: 0.00893

K1		0.12737
K2		0.22339
K3		0.13616
K4		0.22339
K5		0.04559
K6		0.04559
K7		0.12737
K8		0.07112

Table 9. Entering comparison results of K1 criterion's sub-criteria into the software (a part of it is shown)

Graphical Verbal Matrix **Questionnaire** Direct

Comparisons wrt "K1" node in "subcriteria 1" cluster
K1.1 is equally to moderately more important than K1.2

		>=9.5	9	8	7	6	5	4	3	2	1	2	3	4	5	6	7	8	9	>=9.5	No comp.	
1.	K1.1	>=9.5	9	8	7	6	5	4	3	**2**		2	3	4	5	6	7	8	9	>=9.5	No comp.	K1.2
2.	K1.1	>=9.5	9	8	7	6	5	4	3	2		**2**	3	4	5	6	7	8	9	>=9.5	No comp.	K1.3
3.	K1.1	>=9.5	9	8	**7**	6	5	4	3	2		2	3	4	5	6	7	8	9	>=9.5	No comp.	K1.4
4.	K1.1	>=9.5	9	8	7	6	5	4	3	2		2	3	4	5	**6**	7	8	9	>=9.5	No comp.	K1.5
5.	K1.1	>=9.5	9	8	7	6	5	4	3	2		**2**	3	4	5	6	7	8	9	>=9.5	No comp.	K1.6
6.	K1.2	>=9.5	9	8	7	6	5	4	3	2		2	3	**4**	5	6	7	8	9	>=9.5	No comp.	K1.3
7.	K1.2	>=9.5	9	8	7	6	5	4	3	2		**2**	3	4	5	6	7	8	9	>=9.5	No comp.	K1.4
8.	K1.2	>=9.5	9	8	7	6	5	4	3	2		2	3	4	5	6	7	8	**9**	>=9.5	No comp.	K1.5
9.	K1.2	>=9.5	9	8	7	6	5	4	3	2		**2**	3	4	5	6	7	8	9	>=9.5	No comp.	K1.6
10.	K1.3	>=9.5	9	**8**	7	6	5	4	3	2		2	3	4	5	6	7	8	9	>=9.5	No comp.	K1.4
11.	K1.3	>=9.5	9	8	7	6	5	4	3	2		2	3	4	5	**6**	7	8	9	>=9.5	No comp.	K1.5
12.	K1.3	>=9.5	9	8	7	6	5	4	3	**2**		2	3	4	5	6	7	8	9	>=9.5	No comp.	K1.6

Table 10. Comparison matrix of K1 criterion's sub-criteria

Graphical	Verbal	Matrix	Questionnaire	Direct						
Comparisons wrt "K1" node in "subcriteria 1" cluster										
K1.1 is 2 times more important than K1.2										
Inconsistency	K1.2 ~		K1.3 ~		K1.4 ~		K1.5 ~		K1.6 ~	
K1.1 ~	← 2		↑ 2		← 7		↑ 5.9999		↑ 2	
K1.2 ~			↑ 4		↑ 2		↑ 9.0000		↑ 2	
K1.3 ~					← 8		↑ 5.9999		← 2	
K1.4 ~							↑ 8		↑ 5	
K1.5 ~									← 5	

Table 11. Priority values of the K1 criterion's sub-criteria according to the comparison results

Inconsistency: 0.09848	
K1.1	0.10281
K1.2	0.04125
K1.3	0.17671
K1.4	0.03712
K1.5	0.52338
K1.6	0.11874

Likewise, the comparison results of the sub-criteria of K2, K3, K4, K5, K6, K7 and K8 criteria within their groups were entered into the software and comparison matrices and priority values were obtained. In all cases, the inconsistency rate is below 0.10. Up to this point, hierarchical structures are common to the three companies A, B and C. From this point on, the structures change as candidates are entered into the software as data.

For Company A, hierarchical structure given in Figure 2 is used. The 4 candidates (alternatives A1, A2, A3, A4) who applied to Company A were compared according to each sub-criteria, based on their scores given in Appendix A. For example, comparison of alternatives according to the 'K1.1 Undergraduate Education (candidate's university of graduation)' sub-criterion is in Table 12. The comparison matrix of this process is given in Table 13, and the priority values are given in Table 14. According to the K1.1 sub-criterion, Candidate 3 is the highest priority candidate with 51.58% priority value. The inconsistency rate is 0.00772.

Table 12. Comparison of Company A's candidates according to the K1.1 sub-criterion

Graphical	Verbal	Matrix	Questionnaire	Direct
Comparisons wrt "K1.1" node in "alternatives" cluster				
A1 is equally to moderately more important than A2				

1. A1	>=9.5	9	8	7	6	5	4	3	2	1	2	3	4	5	6	7	8	9	>=9.5	No comp.	A2
2. A1	>=9.5	9	8	7	6	5	4	3	2	1	2	3	4	5	6	7	8	9	>=9.5	No comp.	A3
3. A1	>=9.5	9	8	7	6	5	4	3	2	1	2	3	4	5	6	7	8	9	>=9.5	No comp.	A4
4. A2	>=9.5	9	8	7	6	5	4	3	2	1	2	3	4	5	6	7	8	9	>=9.5	No comp.	A3
5. A2	>=9.5	9	8	7	6	5	4	3	2	1	2	3	4	5	6	7	8	9	>=9.5	No comp.	A4
6. A3	>=9.5	9	8	7	6	5	4	3	2	1	2	3	4	5	6	7	8	9	>=9.5	No comp.	A4

Table 13. Comparison matrix of Company A's candidates according to the K1.1 sub-criterion

Graphical	Verbal	Matrix	Questionnaire	Direct

Comparisons wrt "K1.1" node in "alternatives" cluster
A1 is 2 times more important than A2

Inconsistency	A2 ~	A3 ~	A4 ~
A1 ~	← 2	↑ 3.0000	← 1
A2 ~		↑ 4	↑ 2
A3 ~			← 3

Table 14. Priority values of Company A's candidates according to the K1.1 sub-criterion

Inconsistency: 0.00772

A1	0.18941
A2	0.10539
A3	0.51579
A4	0.18941

Candidates of Company A were compared with each other according to each of the 51 sub-criteria. As explained above, each comparison was entered into Super Decisions software and comparison matrices and priority values were obtained. Other results are not shown here to save space. The inconsistency rate is less than 0.10 in all comparisons.

Finally, an Unweighted Super Matrix of 64x64 size was created by combining all the data (objective, criteria, sub-criteria, candidates) of Company A and normalized to obtain the Weighted Super Matrix (Table 15). The Limit Matrix, which reveals the priorities of the objective, criteria, sub-criteria and alternatives, is in Table 16. The selection results of Company A obtained as a result of these procedures are presented in the "3. Results and Discussion" section.

Table 15. Weighted Super Matrix of Company A (a part of it is shown)

Super Decisions Main Window: oğuzhan bülbül sonuç.sdmod: Weighted Su... — □ ×

Cluster Node Labels		Goal: Best site supervisor selection	subcriteria 1						Subriteria 2
			K1.1	K1.2	K1.3	K1.4	K1.5	K1.6	K2.1
alternatives	A1	0.000000	0.189406	0.510316	0.087847	0.290339	0.315789	0.225719	0.469434
	A2	0.000000	0.105394	0.086097	0.055322	0.496616	0.315789	0.123501	0.078875
	A3	0.000000	0.515793	0.325741	0.713340	0.127957	0.315789	0.516638	0.137110
	A4	0.000000	0.189407	0.077846	0.143491	0.085089	0.052632	0.134142	0.314582
Criteria	K1	0.127369	0.000000	0.000000	0.000000	0.000000	0.000000	0.000000	0.000000
	K2	0.223394	0.000000	0.000000	0.000000	0.000000	0.000000	0.000000	0.000000
	K3	0.136163	0.000000	0.000000	0.000000	0.000000	0.000000	0.000000	0.000000
	K4	0.223394	0.000000	0.000000	0.000000	0.000000	0.000000	0.000000	0.000000

Done

Table 16. Limit Matrix of Company A (a part of it is shown)

Cluster Node Labels		Criteria							
		K1	K2	K3	K4	K5	K6	K7	K8
alternatives	A1	0.129452	0.131938	0.106073	0.149494	0.078960	0.150363	0.150396	0.097583
	A2	0.111269	0.089047	0.120766	0.070995	0.208396	0.161996	0.116059	0.162956
	A3	0.211944	0.142702	0.128351	0.126043	0.125222	0.089152	0.096018	0.089346
	A4	0.047336	0.136313	0.144811	0.153468	0.087422	0.098489	0.137527	0.150115
Criteria	K1	0.000000	0.000000	0.000000	0.000000	0.000000	0.000000	0.000000	0.000000
	K2	0.000000	0.000000	0.000000	0.000000	0.000000	0.000000	0.000000	0.000000
	K3	0.000000	0.000000	0.000000	0.000000	0.000000	0.000000	0.000000	0.000000
	K4	0.000000	0.000000	0.000000	0.000000	0.000000	0.000000	0.000000	0.000000

Similar to Company A, the candidates of Companies B and C were also compared according to 51 sub-criteria. The comparison of the 3 candidates who applied to company B was made according to the sub-criteria based on the scores given in Appendix B. For example, the comparison data for the sub-criterion 'K1.1 Undergraduate Education (candidate's university of graduation)' is given in Table 17. The comparison matrix of this process is given in Table 18 and the priority values are given in Table 19. According to sub-criterion K1.1, Candidate 2 and Candidate 3 have equal priority with 42.86%. The inconsistency rate is 0.00000.

Based on the scores given in Appendix C, 3 candidates who applied to Company C were compared according to the sub-criteria. For example, the comparison data according to the sub-criterion 'K1.1 Undergraduate Education (candidate's university of graduation)' is in Table 20. The comparison matrix of this process is given in Table 21 and the priority values are given in Table 22. According to sub-criterion K1.1, Candidate 3 is the most prioritized candidate with 64.42%. The inconsistency rate is 0.05156.

Other results for companies B and C are not shown here to save space. The inconsistency rate is less than 0.10 in all comparisons. The selection results of companies B and C are presented in the "3. Results and Discussion" section.

Table 17. Comparison of Company B's candidates according to the K1.1 sub-criterion

Graphical | Verbal | Matrix | Questionnaire | Direct

Comparisons wrt "K1.1" node in "alternatives" cluster
A2 is moderately more important than A1

1. A1	>=9.5	9	8	7	6	5	4	3	2	1	2	3	4	5	6	7	8	9	>=9.5	No comp.	A2
2. A1	>=9.5	9	8	7	6	5	4	3	2	1	2	3	4	5	6	7	8	9	>=9.5	No comp.	A3
3. A2	>=9.5	9	8	7	6	5	4	3	2	1	2	3	4	5	6	7	8	9	>=9.5	No comp.	A3

Table 18. Comparison matrix of Company B's candidates according to the K1.1 sub-criterion

Table 19. Priority values of Company B's candidates according to the K1.1 sub-criterion

Table 20. Comparison of Company C's candidates according to the K1.1 sub-criterion

Table 21. Comparison matrix of Company C's candidates according to the K1.1 sub-criterion

Table 22. Priority values of Company C's candidates according to the K1.1 sub-criterion

3. RESULTS AND DISCUSSION

The outcome, which is the objective of this study, is the final priority values of the candidates (alternatives). The candidate with the highest priority value will be preferred.

This result for Company A is given in Table 23. Accordingly, the priority values (from highest to

lowest) are 26.57% for Candidate 3, 26.07% for Candidate 1, 25.43% for Candidate 4 and 21.93% for Candidate 2. According to these results, Candidate 3 ranked first with a priority value of 26.57% and was selected as the site supervisor.

An important detail is that the priority values of Candidate 3 and Candidate 1 are very close to each other. There is only a 0.5% difference between them. There is a difference of 1.14% between Candidate 3 and Candidate 4 and a difference of 4.64% between Candidate 3 and Candidate 2. These results show that with the method developed in this study, it is possible to make a choice even between alternatives with very close selection values. With this method, it is possible to scientifically determine the priorities that may not be realized in subjective choices and to select the best site supervisor.

Table 23. Final Priority Values for Company A's Candidates

Name	Graphic	Ideals	Normals	Raw
A1		0.981088	0.260707	0.086902
A2		0.825102	0.219257	0.073085
A3		1.000000	0.265733	0.088578
A4		0.956991	0.254304	0.084768

The total priority values for Company B's candidates are given in Table 24. Accordingly, the priority values (from highest to lowest) are 37.52% for Candidate 3, 33.61% for Candidate 1 and 28.87% for Candidate 2. According to these results, Candidate 3 ranks first with a priority value of 37.52% and is selected as the site supervisor.

Table 24. Final Priority Values for Company B's Candidates

Name	Graphic	Ideals	Normals	Raw
A1		0.895894	0.336107	0.112036
A2		0.769606	0.288728	0.096243
A3		1.000000	0.375164	0.125055

The total priority values for Company C's candidates are given in Table 25. Accordingly, the priority values (from highest to lowest) are 35.87% for Candidate 1, 35.17% for Candidate 3 and 28.95% for Candidate 2. According to these results, Candidate 1 ranks first with a priority value of 35.87% and is selected as the site supervisor.

Similar to Company A, the priority values of the top two candidates of Company C are very close to each other. There is only a 0.70% difference between Candidate 1 and Candidate 3. It is seen that the selection method developed in the study allows the selection between candidates with very close priority values in the three-candidate selection.

Table 25. Final Priority Values for Company C's Candidates

Name	Graphic	Ideals	Normals	Raw
A1		1.000000	0.358738	0.119579
A2		0.807126	0.289547	0.096516
A3		0.980422	0.351715	0.117238

An important part of the study is that the construction companies, with which this study was carried out, conducted the selection of the construction site supervisor with their own selection methods simultaneously with the study and the results of this study were compared with the results of the

companies' own selection. Firms A, B and C conducted the selection process with their own methods simultaneously. It was seen that the candidates selected by the companies with their own methods were the same as the candidates selected as a result of the AHP analysis applied according to the method developed in this study (Table 26).

Table 26. The Candidates Selected with AHP Analyses Applied According to the Methodology Developed in this Study and the Candidates Selected by the Companies' Own Methods

Companies	Candidates and Priority Values	Candidates Selected with AHP Analyses	Candidates Selected by the Companies' Own Methods
A	Aday 3 (%26,57) Aday 1 (%26,07) Aday 4 (%25,43) Aday 2 (%21,93)	A3	A3
B	Aday 3 (%37,52) Aday 1 (%33,61) Aday 2 (%28,87)	A3	A3
C	Aday 1 (%35,87) Aday 3 (%35,17) Aday 2 (%28,95)	A1	A1

In the literature review of personnel selection studies conducted with AHP, it has been revealed that AHP generally gives successful results for priority assessment.

Yılmaz [9] used AHP in the selection of research assistants for a university. Şener [10] studied a quality control personnel selection problem in a textile company. Çoban [11] utilized AHP for the selection of engineers for a drip irrigation manufacturing company. Erdemir et al. [12] used AHP integrated fuzzy TOPSIS model to identify and prioritize criteria for the personnel working in a public institution (municipality) and evaluated their performance. Koyuncu et al. [13] compared the effectiveness of AHP and TOPSIS methods in personnel selection in a manufacturing company operating in the automotive sector. Turan et al. [14] examined the use of AHP in nurse selection for hospitals. Vural et al. [15] examined the integrated use of AHP and VIKOR methods in the personnel selection problem of a medium-sized enterprise located in Kayseri Organized Industrial Zone. Önel [17] studied personnel selection with fuzzy AHP for a concrete factory. In the study by Hankılıç [18], a fuzzy AHP decision making model for personnel selection was developed and applied. AHP and fuzzy AHP methods were used in the study conducted by Keser [19] on bank personnel selection. In the study by Özbek [20], AHP solution algorithm for personnel selection problem was turned into a web-based application. In the study conducted by Uğur [21], the selection of the project manager for a construction project was made with MOORA, one of the MCDM methods. Anbarcı et al. [22] developed a fuzzy logic evaluation model for site supervisor selection. Acer et al. [23] studied the selection of field operation personnel for a port by using AHP and MOORA, two MCDM methods. Karabayır et al. [24] used Fuzzy AHP and Fuzzy TOPSIS for selecting the most convenient supplier for construction companies. Uluskan et al. [25] studied supplier selection of a public institution operating in the railway industry with the help of fuzzy AHP. Kantoğlu et al. [26] studied the supplier selection problem in a chocolate production company with fuzzy AHP. Akkaya [27] analyzed determining the sludge dewatering process in a wastewater treatment plant using SuperDecision software for AHP analyzes. Paçacı et al. [28] focused on logistics centers selection problem using AHP. Aykan et al. [29] studied selection of assistant human resources specialist in a production enterprise with the help of AHP and TOPSIS methods. Gümüşhan et al. [30] studied selection of a suitable e-learning system using the fuzzy AHP method. Çetin et al. [32]

studied company performance with AHP based Balanced Scorecard (BSC) method. Özen et al. [34] studied supplier selection in automotive sub-industry sector using AHP, fuzzy AHP and fuzzy TOPSIS approaches, emphasizing the impact of Covid-19 epidemic.

Many types of selection and priority determination problems were studied using AHP method. In these studies, AHP was used both alone to analyze the problem as well as an accompanying method besides other MCDM methods successfully. To be easily combined with other methods is another powerful property of AHP.

In this study, the problem of site supervisor selection with AHP for construction companies is analyzed. As a result, findings confirming the results of similar studies on selection problems were obtained.

4. CONCLUSIONS

Site supervisor selection problem was studied and the criteria for selection were analyzed using AHP method. The priorities for both criteria and site supervisor candidates were evaluated successfully with the help of Super Decisions software. The candidates with highest priorities were determined for three companies. It was observed that the selection results of all three companies with their own methods coincided with the results of the method developed in this study and the success of the method was 100% according to the available data.

Even if a different candidate had been selected by the companies with their own methods among the candidates with very close values, it would not have reduced the value of this study, but it was considered that the study was confirmed by seeing that the same alternatives were selected.

This study has been conducted to benefit the selection of site supervisors for contractor construction companies carrying out medium-sized building construction works. Similar studies can be developed for companies operating in different fields in the construction industry by using criteria specific to the relevant field.

Declaration of Ethical Standards

Authors declare that all ethical guidelines including authorship, citation, data reporting, and publishing original research are followed.

Credit Authorship Contribution Statement

O.Bülbül and R.Kanıt both contributed to all stages of study and composing the article. Besides, O.Bülbül performed writing of article while R.Kanıt performed editing and supervision.

Declaration of Competing Interest

Authors declare that there is no competing interest that influence this study.

Funding / Acknowledgements

The authors received no financial support for the research.

Data Availability

The data related to this study is available from O.Bülbül upon reasonable request.

REFERENCES

[1]   *Regulation on Construction Site Supervisors.*

[2]   *3194 Zoning Law*, article 28.

[3]   T.L. Saaty, *The Analytic Hierarchy Process,* Mcgraw-Hill, New York, 1980.

[4]   B. F. Yıldırım, E. Önder, "Analitik Hiyerarşi Süreci" in *Çok Kriterli Karar Verme Yöntemleri,* Dora Yayıncılık, 1st Edition, 2014, pp.21-74.

[5]   Y.Sarar, *Multi-Criteria Selection Of Carrier Systems For Aluminum Curtain Walls (MSc Thesis).* Düzce University, Graduate School of Natural and Applied Sciences, Department of Civil Engineering, 2018.

[6]   İ.Özyürek, M.Erdal, "Solution Proposals based on Fuzzy AHP-TOPSIS Hybrid Model to the Problems in Public Works Procurement in Turkey" *Turkish Journal of Civil Engineering,* vol. 34, no. 1, pp.153-165, 2023.

[7]   İ.Özyürek, M.Erdal, "Crisp and fuzzy appraisal of tenderer's qualifications in public works procurement in Turkey" *Journal of Public Procurement,* vol. 23, no. 1, pp.78-99, 2023.

[8]   İ.Özyürek, M.Erdal, "Assessment of qualification criteria described in public procurement law code 4734 in construction works by Analytic Hierarchy Process (AHP)" *Gazi University Journal of Science,* vol. 31, no. 2, pp.437-454, 2018.

[9]   N.T.Yılmaz, *Personel Seçim Problemine Analitik Hiyerarşi Yöntemi ile Bir Yaklaşım (MSc Thesis).* Marmara Üniversitesi Sosyal Bilimler Enstitüsü Ekonometri Anabilim Dalı, 2009.

[10]   T.Şener, *Analytic Hierarchy Process in Personnel Selection Problem: A Sample Application for the Textile Sector (PhD Thesis).* Selçuk Üniversitesi Sosyal Bilimler Enstitüsü İşletme Anabilim Dalı, 2011.

[11]   M.Çoban, *Using Analytic Hierarchy Process In Personnel Selection And A Research On Manufacturing Industry (MSc Thesis).* Balıkesir Üniversitesi Sosyal Bilimler Enstitüsü İşletme Anabilim Dalı, 2012.

[12]   N.Erdemir, F.Öztürk, G.K.Kaya, "Integrated decision support model for performance evaluation of public staff: using AHP and fuzzy TOPSIS" *Journal of the Faculty of Engineering and Architecture of Gazi University,* no. 37:4, pp.1809-1821, 2022.

[13]   O.Koyuncu, M.Özcan, "Comparison of AHP and TOPSIS Methods in Personnel Selection Process: An Empirical Study in Automative Industry" *Hacettepe Üniversitesi İktisadi ve İdari Bilimler Fakültesi Dergisi,* vol. 32, no. 2, pp.195-218, 2014.

[14]   H.Turan, G.Turan, "Implementing analytical hierarchy proses in the nurse selection" *Sağlık Akademisyenleri Dergisi,* vol. 3, no. 1, pp.26-30, 2016.

[15]   D.Vural, E.Köse, B.Bayam, "Personnel Selection by AHP and VIKOR Methods" *Yalova Üniversitesi Sosyal Bilimler Dergisi,* vol. 10, no. 21, pp.70-89, 2020.

[16]   A.A.Supçiller, K.Deligöz, "Compromise Solution of Supplier Selection Problem By Multi-Criteria Decision Making Methods" *International Journal of Economic and Administrative Studies,* (18. EYİ Özel Sayısı), pp.355-368, 2018.

[17]   C.B.Önel, *Personel Selection with Fuzzy Analytical Hierarchy Process and Application (MSc Thesis).* Çukurova Üniversitesi Fen Bilimleri Enstitüsü Endüstri Mühendisliği Anabilim Dalı, 2014.

[18]   H.Kankılıç, *Development Of A Fuzzy Decision Making Model For Personnel Selection (MSc Thesis).* Gaziantep University Graduate School of Natural & Applied Sciences Industrial Engineering, 2005.

[19]   İ.Keser, *A Case Study on a Precise Staff Selection Using Fuzzy Multi-Criteria Decision-Making Methodology on a Bank Application (MSc Thesis).* Maltepe Üniversitesi Lisansüstü Eğitim Enstitüsü Endüstri Mühendisliği Anabilim Dalı, 2022.

[20]   D.Özbek, *The Effective Personnel Selection via Multi-Criteria Decision Making Method Analytic Hierarchy Process (AHP): A Web Based Application (MSc Thesis).* Dokuz Eylül Üniversitesi Sosyal Bilimler Enstitüsü Yönetim Bilişim Sistemleri Anabilim Dalı, 2018.

[21]   L.O.Uğur, "Construction Project Maneger Selection With the MOORA Optimisation Method: A Multi-Objective Optimization Application" *Journal of Polytechnic,* no. 20 (3), pp.717-723, 2017.

[22]   M.Anbarcı, B.Öz, "A Fuzzy Logic Evaluation Model To Select A Site Chief For Construction

Projects" *Marmara Fen Bilimleri Dergisi,* no. 4: pp.104-113, 2015.

[23] A.Acer, H.İnci, "The Evaluation of Personnel Selection Process with AHP Based MOORA Method: An Application on Selection of Port Field Operations Staff" *OPUS– -International Journal of Society Researches*, vol. 16 (Special Issue), pp.3689-3713, 2020.

[24] A.N.Karabayır, A.R.Botsalı, "Supplier Selection Among Different Scale Construction Companies Using Fuzzy AHP And Fuzzy TOPSIS", *El-Cezerî Journal of Science and Engineering*, Vol: 9, No: 1, 35-48, 2022

[25] M.Uluskan, D.Topuz, C.Çimen, "Supplier Evaluation Through AHP, FUZZY AHP, LBWA and COPRAS Methods: An Application In The Railway Industry" *ESOGÜ Müh Mim Fak Derg.*, 30(3), 412-430, 2022

[26] B.Kantoğlu, Ş.Gökçe, "Supplier Selection With Fuzzy AHP Method In Chocolate Industry" *Düzce Üniversitesi Bilim ve Teknoloji Dergisi*, 11, 1666-1685, 2023

[27] G.K.Akkaya, "Decision making in Sewage sludge dewatering equipment selection: AHP approach" *International Journal of Environmental Trends (IJENT)*, 6 (1), 21-30, 2022

[28] B.Paçacı, S.Erol, M.K.Çubuk, "AHP Application for Logistics Center Location Selection According to Criteria" *Bitlis Eren University Journal Of Science*, 11 (4), 943-952, 2022

[29] E.Aykan, O.Çataltepe, "Selection Of Human Resources Assistant Expert with AHP and TOPSIS" *Süleyman Demirel University Journal of Human Resources Management*, Volume: 1, No: 1, 41-51, 2022

[30] Y.S.Gümüşhan, F.S.Çakır, "Ranking the Criteria Effective in the Selection of E-Learning System by Fuzzy AHP (F-AHP) Method" *Journal of Theoretical Educational Science*, 16(4), 749-768, 2023

[31] L.Şahintürk, N.Fığlalı, Z.Aladağ, B.Denizhan, "Enterprise Architecture Framework Selection with AHP and ELECTRE I Methods" *International Journal of Management Information Systems and Computer Science*, 8(1), 15-40, 2024

[32] N.Çetin, D.T.Coşansu, "Company Performance Evaluation With AHP Based BSC Method" *Manisa Celal Bayar University Journal of Social Sciences*, 21 (1), 261-278, 2023

[33] V.Aslan, "Determination of Van Basin Groundwater Potential by GIS Based, AHP and Fuzzy-AHP Methods" *Journal of Agricultural Sciences*, 30 (1), 47-60, 2024

[34] M.Özen, O.Borat, "AHP, FUZZY AHP and FUZZY TOPSIS Approach In Supplier Selection In Automotive Sub-Industry Sector" *İstanbul Ticaret Üniversitesi Fen Bilimleri Dergisi*, 19 (38), 152-171, 2020

APPENDICES

Appendix A. Scores of Site Supervisor Candidates of Company A

Criteria / Sub Criteria	Scores of Candidates			
1. EDUCATION / CERTIFICATE	**A1**	**A2**	**A3**	**A4**
1.1 Undergraduate Education (candidate's university of graduation)	8	7	10	8
1.2 Master's Degree (university candidate graduated/continues)	10	2	9	2
1.3 Having "Class A Occupational Safety Specialist Certificate"	3	2	10	4
1.4 Having a "First Aid Certificate"	8	10	5	3
1.5 Having a "Driver's License"	10	10	10	4
1.6 Vocational Trainings Received (certified)	8	7	10	7
2. EXPERIENCE	**A1**	**A2**	**A3**	**A4**
2.1 Total Experience as a Site Supervisor in All Construction Areas	10	4	6	8
2.2 Experience as a Site Supervisor in Building Construction	10	4	8	6
2.3 Experience of Managing a Construction Site from Start to Finish	6	8	10	4
2.4 Number of Works Completed as Site Supervisor	6	8	10	4
2.5 Size of the Work(s) Completed as Site Supervisor (area, cost)	6	7	8	10
2.6 Total Number of Years of Employment in the Construction Sector	10	4	6	8
2.7 Total Number of Years Worked in the Field of Building Construction	10	4	8	6
2.8 Previous Companies and Duration of Employment (stability)	4	6	4	10
3. BUSINESS KNOWLEDGE	**A1**	**A2**	**A3**	**A4**
3.1 Planning Knowledge (to be able to prepare and follow the work program)	4	8	10	3
3.2 Quantity Survey, Progress Payment, Final Account Information	8	5	7	10
3.3 Equipment and Technology Knowledge (construction machinery, etc.)	8	6	7	8
3.4 Construction Materials Knowledge (concrete, admixtures, paint, etc.)	7	8	6	9
3.5 Knowledge of Records to be kept at the construction site	6	8	10	7
3.6 Knowledge of Construction Legislation	10	8	6	9
3.7 Knowledge of Labor Law (Labor Law and related legislation)	9	8	10	7
3.8 Knowledge of Occupational Health and Safety	8	9	7	7
3.9 Knowledge of Resource Management (material, labor, money, time, etc.)	8	7	9	10
3.10 Knowledge of Cost Management (cost of construction works)	8	9	9	8
3.11 Environmental Management Knowledge	10	8	9	7
3.12 Knowledge of General Economics and Construction Economics	8	8	9	10
3.13 Knowledge of Productivity Management (optimum resources)	8	9	8	7
4. COMPUTER KNOWLEDGE	**A1**	**A2**	**A3**	**A4**
4.1 Using MS Office Programs	7	8	10	10
4.2 Using Autocad Program	10	8	10	9
4.3 Using Planning Program (Primavera, MS Project etc.)	10	9	8	10
5. FOREIGN LANGUAGE KNOWLEDGE	**A1**	**A2**	**A3**	**A4**
5.1 General English Level	9	6	7	8
5.2 Vocational English Level (mastery of technical terminology)	5	10	8	7
6. CANDIDATE'S DEMANDS	**A1**	**A2**	**A3**	**A4**
6.1 Fee Requested by the Candidate	10	8	9	10
6.2 Whether the candidate needs accommodation, whether the company should provide it, and if so, the cost to the company	4	5	3	2
6.3 Whether the candidate needs a vehicle, whether the company should provide it, and if so, the cost to the company	8	7	6	10
7. SKILLS AND PERSONAL CHARACTERISTICS	**A1**	**A2**	**A3**	**A4**
7.1 Desire to succeed (enthusiasm for work, ownership of work)	6	8	10	8
7.2 Reliability (to be supported by previous workplaces, references, etc.)	10	7	8	10
7.3 Self-confidence	10	9	10	8
7.4 Activity and Dynamism (practicality, quick thinking and acting)	9	10	7	6
7.5 Tidiness and Orderliness	6	7	9	8
7.6 Ability to Represent (appearance and speaking style)	10	8	9	7
7.7 Coordination Skills (providing information flow up, down and horizontally)	10	9	8	9
7.8 Team Management Skills	10	8	9	10
7.9 Ability to take initiative when faced with a problem	10	8	7	9
7.10 Predisposition to Personal Career Development	6	9	8	7
7.11 Whether he/she has harmful/bad habits (gambling, smoking, alcohol)	6	10	7	8
8. OTHER	**A1**	**A2**	**A3**	**A4**
8.1 References	10	9	8	10
8.2 The size of the construction site that the candidate will manage if hired	8	9	9	10
8.3 If he/she knows the location of the construction site he/she will manage	5	9	6	4
8.4 Whether the construction site is located in the candidate's hometown	6	7	9	8
8.5 The status of the candidate's spouse and children (whether the family can come to the location of the construction site, etc.)	7	6	5	10

Appendix B. Scores of Site Supervisor Candidates of Company B

Criteria / Sub Criteria	Scores of Candidates		
	A1	A2	A3
1. EDUCATION / CERTIFICATE	**A1**	**A2**	**A3**
1.1 Undergraduate Education (candidate's university of graduation)	6	8	8
1.2 Master's Degree (university candidate graduated/continues)	9	5	3
1.3 Having "Class A Occupational Safety Specialist Certificate"	2	10	2
1.4 Having a "First Aid Certificate"	10	2	2
1.5 Having a "Driver's License"	9	6	10
1.6 Vocational Trainings Received (certified)	3	6	2
2. EXPERIENCE	**A1**	**A2**	**A3**
2.1 Total Experience as a Site Supervisor in All Construction Areas	5	9	9
2.2 Experience as a Site Supervisor in Building Construction	6	7	8
2.3 Experience of Managing a Construction Site from Start to Finish	7	9	10
2.4 Number of Works Completed as Site Supervisor	6	8	9
2.5 Size of the Work(s) Completed as Site Supervisor (area, cost)	10	6	9
2.6 Total Number of Years of Employment in the Construction Sector	5	10	10
2.7 Total Number of Years Worked in the Field of Building Construction	7	8	8
2.8 Previous Companies and Duration of Employment (stability)	10	5	7
3. BUSINESS KNOWLEDGE	**A1**	**A2**	**A3**
3.1 Planning Knowledge (to be able to prepare and follow the work program)	8	10	10
3.2 Quantity Survey, Progress Payment, Final Account Information	7	9	8
3.3 Equipment and Technology Knowledge (construction machinery, etc.)	10	6	8
3.4 Construction Materials Knowledge (concrete, admixtures, paint, etc.)	6	9	10
3.5 Knowledge of Records to be kept at the construction site	8	10	9
3.6 Knowledge of Construction Legislation	7	10	8
3.7 Knowledge of Labor Law (Labor Law and related legislation)	5	7	7
3.8 Knowledge of Occupational Health and Safety	4	10	3
3.9 Knowledge of Resource Management (material, labor, money, time, etc.)	8	7	8
3.10 Knowledge of Cost Management (cost of construction works)	6	8	6
3.11 Environmental Management Knowledge	6	3	4
3.12 Knowledge of General Economics and Construction Economics	7	8	6
3.13 Knowledge of Productivity Management (optimum resources)	9	6	8
4. COMPUTER KNOWLEDGE	**A1**	**A2**	**A3**
4.1 Using MS Office Programs	10	8	5
4.2 Using Autocad Program	8	4	9
4.3 Using Planning Program (Primavera, MS Project etc.)	5	8	5
5. FOREIGN LANGUAGE KNOWLEDGE	**A1**	**A2**	**A3**
5.1 General English Level	9	5	10
5.2 Vocational English Level (mastery of technical terminology)	8	2	6
6. CANDIDATE'S DEMANDS	**A1**	**A2**	**A3**
6.1 Fee Requested by the Candidate	10	8	6
6.2 Whether the candidate needs accommodation, whether the company should provide it, and if so, the cost to the company	8	5	4
6.3 Whether the candidate needs a vehicle, whether the company should provide it, and if so, the cost to the company	3	10	6
7. SKILLS AND PERSONAL CHARACTERISTICS	**A1**	**A2**	**A3**
7.1 Desire to succeed (enthusiasm for work, ownership of work)	9	7	8
7.2 Reliability (to be supported by previous workplaces, references, etc.)	8	9	6
7.3 Self-confidence	10	7	7
7.4 Activity and Dynamism (practicality, quick thinking and acting)	9	7	8
7.5 Tidiness and Orderliness	6	5	9
7.6 Ability to Represent (appearance and speaking style)	7	5	9
7.7 Coordination Skills (providing information flow up, down and horizontally)	8	9	6
7.8 Team Management Skills	7	8	10
7.9 Ability to take initiative when faced with a problem	9	7	9
7.10 Predisposition to Personal Career Development	7	6	3
7.11 Whether he/she has harmful/bad habits (gambling, smoking, alcohol)	4	9	7
8. OTHER	**A1**	**A2**	**A3**
8.1 References	6	8	10
8.2 The size of the construction site that the candidate will manage if hired	10	6	9
8.3 If he/she knows the location of the construction site he/she will manage	5	10	3
8.4 Whether the construction site is located in the candidate's hometown	4	10	2
8.5 The status of the candidate's spouse and children (whether the family can come to the location of the construction site, etc.)	8	7	3

Appendix C. Scores of Site Supervisor Candidates of Company C

Criteria / Sub Criteria	Scores of Candidates		
	A1	A2	A3
1. EDUCATION / CERTIFICATE	**A1**	**A2**	**A3**
1.1 Undergraduate Education (candidate's university of graduation)	8	5	10
1.2 Master's Degree (university candidate graduated/continues)	10	2	2
1.3 Having "Class A Occupational Safety Specialist Certificate"	2	10	10
1.4 Having a "First Aid Certificate"	2	10	2
1.5 Having a "Driver's License"	10	8	5
1.6 Vocational Trainings Received (certified)	3	5	9
2. EXPERIENCE	**A1**	**A2**	**A3**
2.1 Total Experience as a Site Supervisor in All Construction Areas	8	7	5
2.2 Experience as a Site Supervisor in Building Construction	6	5	4
2.3 Experience of Managing a Construction Site from Start to Finish	8	7	5
2.4 Number of Works Completed as Site Supervisor	5	4	3
2.5 Size of the Work(s) Completed as Site Supervisor (area, cost)	7	10	9
2.6 Total Number of Years of Employment in the Construction Sector	8	7	5
2.7 Total Number of Years Worked in the Field of Building Construction	6	5	4
2.8 Previous Companies and Duration of Employment (stability)	5	9	10
3. BUSINESS KNOWLEDGE	**A1**	**A2**	**A3**
3.1 Planning Knowledge (to be able to prepare and follow the work program)	10	8	9
3.2 Quantity Survey, Progress Payment, Final Account Information	8	9	6
3.3 Equipment and Technology Knowledge (construction machinery, etc.)	6	9	5
3.4 Construction Materials Knowledge (concrete, admixtures, paint, etc.)	6	9	4
3.5 Knowledge of Records to be kept at the construction site	8	6	9
3.6 Knowledge of Construction Legislation	7	5	6
3.7 Knowledge of Labor Law (Labor Law and related legislation)	6	5	6
3.8 Knowledge of Occupational Health and Safety	4	8	10
3.9 Knowledge of Resource Management (material, labor, money, time, etc.)	7	8	9
3.10 Knowledge of Cost Management (cost of construction works)	5	8	9
3.11 Environmental Management Knowledge	3	2	5
3.12 Knowledge of General Economics and Construction Economics	5	7	7
3.13 Knowledge of Productivity Management (optimum resources)	7	6	8
4. COMPUTER KNOWLEDGE	**A1**	**A2**	**A3**
4.1 Using MS Office Programs	10	7	9
4.2 Using Autocad Program	8	6	9
4.3 Using Planning Program (Primavera, MS Project etc.)	10	3	5
5. FOREIGN LANGUAGE KNOWLEDGE	**A1**	**A2**	**A3**
5.1 General English Level	8	5	10
5.2 Vocational English Level (mastery of technical terminology)	6	2	5
6. CANDIDATE'S DEMANDS	**A1**	**A2**	**A3**
6.1 Fee Requested by the Candidate	6	10	8
6.2 Whether the candidate needs accommodation, whether the company should provide it, and if so, the cost to the company	6	7	9
6.3 Whether the candidate needs a vehicle, whether the company should provide it, and if so, the cost to the company	5	6	9
7. SKILLS AND PERSONAL CHARACTERISTICS	**A1**	**A2**	**A3**
7.1 Desire to succeed (enthusiasm for work, ownership of work)	7	8	9
7.2 Reliability (to be supported by previous workplaces, references, etc.)	9	6	7
7.3 Self-confidence	7	8	6
7.4 Activity and Dynamism (practicality, quick thinking and acting)	7	8	9
7.5 Tidiness and Orderliness	10	6	7
7.6 Ability to Represent (appearance and speaking style)	9	5	7
7.7 Coordination Skills (providing information flow up, down and horizontally)	5	9	8
7.8 Team Management Skills	8	10	7
7.9 Ability to take initiative when faced with a problem	7	8	6
7.10 Predisposition to Personal Career Development	8	4	10
7.11 Whether he/she has harmful/bad habits (gambling, smoking, alcohol)	5	9	7
8. OTHER	**A1**	**A2**	**A3**
8.1 References	8	9	6
8.2 The size of the construction site that the candidate will manage if hired	7	10	9
8.3 If he/she knows the location of the construction site he/she will manage	8	5	9
8.4 Whether the construction site is located in the candidate's hometown	5	2	9
8.5 The status of the candidate's spouse and children (whether the family can come to the location of the construction site, etc.)	6	9	5